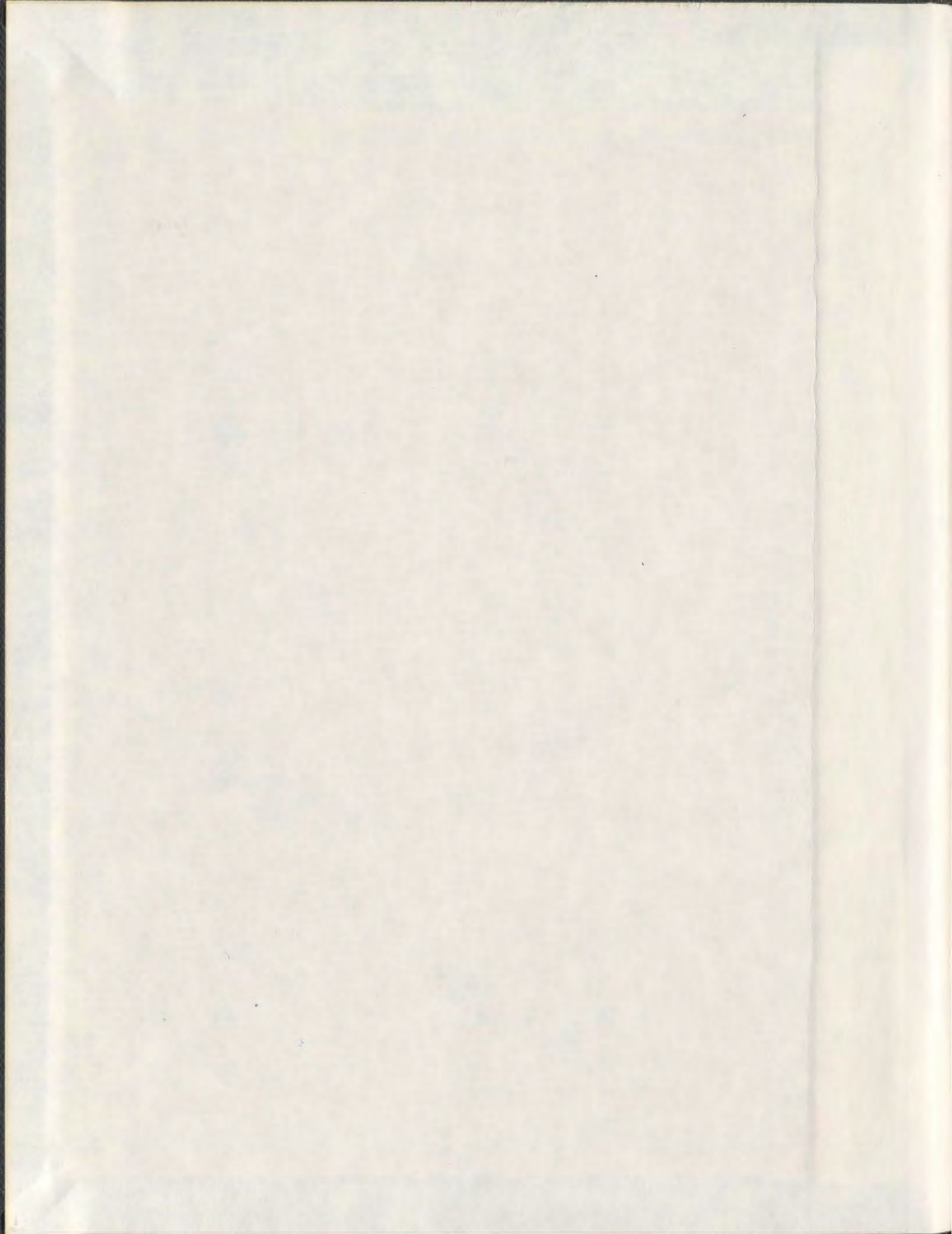


ANALYSIS OF SCALE EFFECT IN COMPRESSIVE ICE
FAILURE AND IMPLICATIONS FOR DESIGN

ROCKY SCOTT TAYLOR



001311



Analysis of Scale Effect in Compressive Ice Failure and Implications for Design

by

©Rocky Scott Taylor, B.Eng., M.Eng., P.Eng.

A thesis submitted to the School of Graduate Studies
in partial fulfillment of the requirements for the
degree of Doctor of Philosophy

Faculty of Engineering and Applied Science
Memorial University of Newfoundland

March 2010

St. John's Newfoundland and Labrador Canada

Abstract

The main focus of the study was the analysis of scale effect in local ice pressure resulting from probabilistic (spalling) fracture and the relationship between local and global loads due to the averaging of pressures across the width of a structure.

A review of fundamental theory, relevant ice mechanics and a critical analysis of data and theory related to the scale dependent pressure behavior of ice were completed. To study high pressure zones (*hpzs*), data from small-scale indentation tests carried out at the NRC-IOT were analyzed, including small-scale ice block and ice sheet tests. Finite element analysis was used to model a sample ice block indentation event using a damaging, viscoelastic material model and element removal techniques (for spalling).

Medium scale tactile sensor data from the Japan Ocean Industries Association (JOIA) program were analyzed to study details of *hpz* behavior. The averaging of non-simultaneous *hpz* loads during an ice-structure interaction was examined using local panel pressure data. Probabilistic averaging methodology for extrapolating full-scale pressures from local panel pressures was studied and an improved correlation model was formulated. Panel correlations for high speed events were observed to be lower than panel correlations for low speed events. Global pressure estimates based on probabilistic averaging were found to give substantially lower average errors in estimation of load compared with methods based on linear extrapolation (no averaging). Panel correlations were analyzed for Molikpaq and compared with JOIA results. From this analysis, it was shown that averaging does result in decreasing pressure for increasing structure width.

The relationship between local pressure and ice thickness for a panel of unit width was studied in detail using full-scale data from the STRICE, Molikpaq, Cook Inlet and Japan Ocean Industries Association (JOIA) data sets. A distinct trend of decreasing pressure with increasing ice thickness was observed. The pressure-thickness behavior was found to be well modeled by the power law relationships $P_{avg} = 0.278h^{-0.408}$ MPa and $P_{std} = 0.172h^{-0.273}$ MPa for the mean and standard deviation of pressure, respectively.

To study theoretical aspects of spalling fracture and the pressure-thickness scale effect, probabilistic failure models have been developed. A probabilistic model based on Weibull theory (tensile stresses only) was first developed. Estimates of failure pressure obtained with this model were orders of magnitude higher than the pressures observed from benchmark data due to the assumption of only tensile failure. A probabilistic fracture mechanics (PFM) model including both tensile and compressive (shear) cracks was developed. Criteria for unstable fracture in tensile and compressive (shear) zones were given. From these results a clear theoretical scale effect in peak (spalling) pressure was observed. This scale effect followed the relationship $P_{p,th} = 0.15h^{-0.50}$ MPa which agreed well with the benchmark data.

The PFM model was applied to study the effect of ice edge shape (taper angle) and hpz eccentricity. Results indicated that specimens with flat edges spall at lower pressures while those with more tapered edges spall less readily. The mean peak (failure) pressure was also observed to decrease with increased eccentricity. It was concluded that hpz s centered about the middle of the ice thickness are the zones most likely to create the peak pressures that are of interest in design.

Promising results were obtained using the PFM model, which provides strong support for continued research in the development and application of probabilistic fracture mechanics to the study of scale effects in compressive ice failure and to guide the development of methods for the estimation of design ice pressures.

Acknowledgements

I would like to first thank Dr. Ian Jordaan for his continued support and guidance. His creativity, passion and tremendous work ethic have made this program of study a very invigorating and enjoyable experience. His expert advice in the areas of ice mechanics, applied probability and engineering judgment are gratefully acknowledged. His patient and persistent feedback has been invaluable in helping me complete my program. Thank you for challenging, inspiring and supporting me.

Sincere gratitude to Dr. Ahmed Derradji-Aouat for his ongoing support. His assistance in arranging for use of the NRC-IOT testing facilities is much appreciated. Thank you to Dr. Brian Veitch for his continued support and for helping me successfully progress from my undergraduate studies through to the present.

I would like to express my gratitude to Dr. Charles Randell and to C-CORE for granting me educational leave to pursue this work, and for providing me with practical and financial support over the past several years. Sincere thanks to my colleagues, Mr. Freeman Ralph, Mr. Jonathan Bruce, Ms. Jennifer Wells, Dr. Chuanke Li, Mr. John Barrett, Mr. Aiman Al-Showaiter and Mr. Richard Harvey. Thank-you to Dr. Mark Fuglem for his technical insights and practical advice.

Sincere appreciation is extended to Dr. Robert Frederking for the stimulating discussions. I would also like to thank Dr. Katna Munaswamy for his insights on fracture mechanics. Use of the facilities at the National Research Council of Canada - Institute for Ocean Technology are gratefully acknowledged, along with technical support provided by

Mr. Austin Bugden. To Mrs. Moya Crocker I would like to extend my sincere gratitude for all the help and support she has given over the years.

Financial support from the School of Graduate Studies at Memorial, NSERC, The Link Foundation, C-CORE, The National Research Council of Canada, Engineers Canada - Manulife Financial, The George Weston Foundation, The Society of Naval Architects and Marine Engineers Arctic Section and The Department of Education, Government of Newfoundland and Labrador are gratefully acknowledged.

A special thank-you to my parents, Lloyd and Kay Taylor, for their unwavering support throughout my life. The love of learning that you instilled in me during my childhood years will serve as the cornerstone of any success that I may have in life.

Finally, I would like to thank my beautiful wife Skye, and our dear children Alexander and Anna for their boundless love, support and encouragement. Without your support this would not have been possible.

Contents

Chapter 1: Introduction.....	1
1.1 General Overview	1
1.2 Designing Structures for Ice Environments	2
1.3 Ice Mechanics	4
1.3.1 Compressive Ice Failure Processes.....	4
1.3.2 Pressure-Area Scale Effect	5
1.4 Estimation of Local and Global Loads	7
1.4.1 Definition of Local and Global Areas.....	8
1.4.2 Ice Load Estimation Methods	9
1.5 Scope of Thesis.....	10
Chapter 2: Fundamental Theory.....	13
2.1 Scope.....	13
2.2 Viscoelasticity Theory	13
2.2.1 Linear Theory.....	13
2.2.2 The Broad-Spectrum Approach	15
2.2.3 Nonlinear Viscoelasticity Theory	16
2.2.4 Modified Superposition Principle.....	18
2.3 Damage Mechanics.....	19
2.3.1 The Area-Based Approach to Damage	20
2.3.2 The Crack Density Approach to Damage	21
2.3.3 The Stress-History Approach to Damage	24
2.4 Fracture Mechanics.....	25
2.4.1 Linear Elastic Fracture Mechanics.....	25

2.4.2	J-Integral Theory for Elastic and Plastic Cases	29
2.4.3	J-Integral Theory for Nonlinear Viscoelastic Case.....	30
2.5	Statistical Approach to Fracture.....	36
2.5.1	Weakest-Link Theory	37
2.5.2	Complex Stress States and Reduced Volume Formulation	39
Chapter 3: Review of Ice Mechanics		41
3.1	Scope.....	41
3.2	Ice Properties and Behavior	41
3.2.1	Overview.....	41
3.2.2	Viscoelasticity and Creep Behavior of Ice.....	42
3.2.3	Elastic Ice Response for Fast Loading Rates.....	47
3.3	Microstructural Damage in Ice	48
3.3.1	Damage Processes at Slow Loading Rates	48
3.3.2	Damage Processes at High Loading Rates.....	51
3.3.3	High Pressure Zones and Damage Failure.....	56
3.3.4	Application of Damage Mechanics to Ice.....	60
3.4	Fracture Behavior of Ice	63
3.4.1	Crack Nucleation	64
3.4.2	Modes of Ice Fracture	69
3.4.3	Spalling Fracture.....	71
3.4.4	Theoretical Fracture Models Relevant to Spalling	74
Chapter 4: Critical Analysis of Scale Effects.....		92
4.1	Scope.....	92
4.2	Classical Materials.....	92
4.3	General Observations on Ice Behavior	97
4.4	Probabilistic Averaging and Scale Effect	103
4.4.1	Non-simultaneous Failure.....	103
4.4.2	Probabilistic Averaging	106
4.5	Scale Effects Resulting from Mechanics	109

4.5.1	Fracture Mechanics Models.....	110
4.5.2	Weibull Statistical Strength Models	117
4.5.3	Probabilistic Fracture Mechanics Models.....	123
4.6	High Pressure Zone Behavior at Different Scales	126
Chapter 5: High Pressure Zone Behavior and Averaging		128
5.1	Scope.....	128
5.2	Overview.....	129
5.3	Small-scale Ice Indentation Experiments.....	129
5.3.1	Analysis of Sample Indentation Event.....	130
5.4	Preliminary Ice Sheet Indentation Tests	139
5.4.1	Test Set-up	140
5.4.2	Sample Test Results and Discussion.....	141
5.5	Medium Scale Field Indentation Test (JOIA).....	144
5.5.1	JOIA Program Background.....	145
5.6	High Pressure Zone Behavior	148
5.6.1	Analysis of JOIA Tactile Sensor Data	149
5.6.2	Failure Modes and Consequences.....	150
5.7	Multiple High Pressure Zones and Averaging.....	159
5.7.1	Analysis of JOIA Local Pressure Data	159
5.7.2	Preparation of Data	160
5.7.3	Statistical Characteristics of Data	166
5.7.4	Probabilistic Averaging: Autoregressive Approach	174
5.7.5	Local Panel Correlation Analysis	175
5.7.6	Correlation Modeling (Standard Approach).....	181
5.7.7	Global Pressure Estimates (Standard Approach).....	186
5.7.8	Correlation Modeling (Composite Approach).....	194
5.7.9	Global Pressure Estimates (Composite Approach).....	197
5.7.10	Comparison of Global Pressure Estimation Approaches.....	200
5.8	Full-scale Data Analysis	201
5.8.1	Global Load Estimation Using Molikpaq Data	201

5.8.2	Discussion of Scale Issues: JOIA vs. Molikpaq Scale.....	202
5.8.3	Molikpaq Correlation Analysis (Standard).....	206
5.8.4	Molikpaq Correlation Analysis (Composite).....	208
5.8.5	Correlation Scaling: Preliminary Investigation	209
5.8.6	Discussion of Results.....	212
5.9	Summary and Conclusions	214
Chapter 6: Pressure-Thickness Scaling From Data		219
6.1	Scope.....	219
6.2	Overview.....	220
6.3	Scale Effect for Remote Ice Edges	220
6.4	Pressure-Thickness Effect in STRICE Data	222
6.5	Thickness Effects in Full-scale Pressure Data	225
6.5.1	Detailed Analysis and Filters for Molikpaq Data	226
6.5.2	Filters for STRICE Data	234
6.5.3	Filters for JOIA Data	235
6.5.4	Filters for Cook Inlet Data	235
6.5.5	Thickness Scaling Analysis Results.....	236
6.5.6	Discussion.....	255
6.6	Summary and Conclusions	258
Chapter 7: Theoretical Analysis of Pressure-Thickness Scaling.....		260
7.1	Scope.....	260
7.2	Introduction.....	261
7.2.1	Overview of the Ice Failure Process	261
7.2.2	Analysis of Tactile Sensor Data for Sample Event.....	262
7.2.3	Problem Definition for Analysis of Ice Edge Spalling	264
7.3	Elastic Stress Field Analysis.....	267
7.3.1	Background	268
7.3.2	Finite Element Implementation.....	270
7.4	Weibull Failure Model.....	273

7.4.1	Overview of Weibull Model	273
7.4.2	Implementation of Weibull Model (Tension Only)	274
7.5	Probabilistic Fracture Mechanics Model	275
7.5.1	Overview of Model	276
7.5.2	Crack Model I: Tensile Crack (No Confinement)	282
7.5.3	Crack Model II: Shear Crack (Subject to Confinement)	290
7.6	Investigation of Scaling Behavior using PFM Model.....	298
7.6.1	Thickness Scaling for Flat Ice Edge ($\omega = 0^\circ$)	299
7.6.2	Effect of Ice Edge Shape.....	305
7.6.3	Effect of Proximity to the Edge	308
7.7	Discussion and Conclusions	312
Chapter 8: Conclusions.....		316
8.1	Summary and Conclusions	316
8.1.1	Critical Analysis of Scale Effects	316
8.1.2	Analysis of High Pressure Zones.....	317
8.1.3	Study of Probabilistic Averaging Effects	318
8.1.4	Analysis of Thickness Scaling in Full-scale Data.....	319
8.1.5	Theoretical Modeling of Spalling Fracture and Scale Effects	320
8.2	Recommendation for Future Work	323
Bibliography.....		326
Appendix A: Related Mechanics.....		349
A.1	Derivation of Wing Crack Stress Intensity Factor	349
A.2	Radial and Circumferential Cracking	360
A.3	Dimensional Analysis	365
Appendix B: JOIA Data Information		368
B.1	Global Load Data.....	368
B.2	Event Definition Sensitivity.....	370
B.3	Sample Spectral Analysis	373

B.4	Stationarity	374
Appendix C: Data Analysis Details		378
C.1	Molikpaq Events	378
C.2	Explanation of Event Trimming Process	379
C.3	Residuals of Pressure Data for Analysis Case 10	381
Appendix D: Distribution Fitting		382
D.1	Sample Probability Plot	382

List of Figures

Figure 1.1: Relevant ice mechanics topics and their relationship to ice load estimation. . .	3
Figure 1.2: Schematic representation of the link between load cycling and layer dynamics (Jordaan et al., 2008).....	5
Figure 1.3: (a) Statistical flaw distribution in large and small samples; (b) Weibull fit of compressive ice failure data (after Jordaan and Pond, 2001).	6
Figure 1.4: Comparison of variation in local pressure measurements and in global pressures estimated using the probabilistic averaging approach (Li, 2007).	7
Figure 1.5: Illustration of (a) global interaction area and (b) local design area.....	8
Figure 2.1: Schematics of: (a) a Kelvin unit; (b) a Maxwell unit.....	14
Figure 2.2: Modes of fracture: (a) tensile mode; (b) in-plane shear; (c) anti-plane shear. (after Sih and Liebowitz, 1968).	25
Figure 2.3: Schematic of a crack in an infinite plate (Broek, 1986).....	27
Figure 2.4: Illustration of J-Integral around the crack tip (Li, 2007).....	29
Figure 2.5: Illustration of Schapery's crack tip idealization (from Xiao, 1997).....	30
Figure 2.6: Non-linear elastic stress-strain curve, showing strain energy W and complementary strain energy W^c (from Xiao, 1997).	33
Figure 2.7: (a) Time dependent crack growth during instability for different values of k ; (b) change of complementary strain energy with increasing damage; event E represents a large fracture event, such as a spall, resulting in a large jump in W^c (Jordaan and Xiao, 1992).	36
Figure 2.8: Specimen in tension; failure results in total loss of strength.....	38

Figure 3.1: Typical constant strain rate creep curves for ice (Nadreau and Michel, 1984).	42
Figure 3.2: Typical creep curves for ice under constant stress (Nadreau and Michel, 1984).	43
Figure 3.3: Burgers model consisting of a Maxwell unit and Kelvin Unit in Series.....	44
Figure 3.4: Schematic representation of: (a) creep zone during very slow loading; (b) dislocation glide (and climb) in grain (after Sanderson, 1988).....	49
Figure 3.5: Schematic representation of: (a) creep and damaged zone at slow speeds; (b) slow (0.03 cm/s) test results from Hobson's Choice Ice Island experiments (Frederking et al., 1990).	50
Figure 3.6: Ductile failure observed for slow test ($v = 0.03$ cm/s) during Rae Point experiments with 1 m^2 spherical indenter (Masterson et al., 1999).....	51
Figure 3.7: (a) schematic of brittle failure at higher loading rates; (b) brittle failure observed for fast test ($v = 1.0$ cm/s) during Rae Point experiments with 1 m^2 spherical indenter (Masterson et al., 1999).	52
Figure 3.8: Plot of pressure melting data for ice (after Nordell, 1990).	55
Figure 3.9: Wide interaction area, showing possible internal spall. (Jordaan, 2001).	57
Figure 3.10: Photographic example of dynamic loading events observed during crushing events at three scales. (a) small-scale laboratory tests (Wells et al, 2009); (b) Extrusion of crushed ice during a medium-scale test at Hobson's Choice (Jordaan, 2001) (c) Mound of crushed ice that developed during the April 12, 1986 event at the Molikpaq.	58
Figure 3.11: Sections taken from the central region of ice-indentation zone for: (a) Hobson's Choice medium-scale indentation tests (Jordaan, 2001); (b) laboratory scale indentation test (Barrette et al., 2002).....	59
Figure 3.12: Crack formation due to grain boundary sliding for (a) triple point junction of three grains; (b) 'wing' cracks between two grain boundaries (Jordaan and McKenna, 1988).	66
Figure 3.13: Illustrations of fracture modes: (a) radial cracking; (b) circumferential cracking; (c) spalling (modified after Sanderson, 1988).	69
Figure 3.14: Deformation mode map as function of indentation rate and aspect ratio (Sanderson, 1988 based on Timco, 1986).....	70
Figure 3.15: Schematic of flaw types considered in tank tests (modified from Timco, 1987).	71

Figure 3.16: Arrays of high pressure zones for various geometries (Jordaan et al., 2008).	72
Figure 3.17: Idealization of spalling near a single high pressure zone: (a) 2D flat edge; (b) 2D wedge-shaped edge; (c) 3D flat edge; (d) 3D wedge-shaped edge.....	73
Figure 3.18: Model of compressive indentation proposed by Kendall (1978).	74
Figure 3.19: Kendall's theory applied to in-plane ice spalling (after Wierzbiki, 1985)...	75
Figure 3.20: Kendall's model for off-center cracks in compression (from Kendall, 1978).	76
Figure 3.21: Struts with no constraints at free ends (from Zou et al., 1996).	77
Figure 3.22: Comparison of the models of: (a) Kendall (1978); (b) DeFranco and Dempsey (1990).	77
Figure 3.23: Results of strain energy release rate analysis (from Zou et al., 1996).	79
Figure 3.24: (a) Non-centrally located crack; (b) plot of G vs. $1/D$ (from Zou et al., 1996).	79
Figure 3.25: (a) Model of spalling due to edge loads (Thouless et al., 1987); (b) generalized beam model developed by Suo (1990).	80
Figure 3.26: Crack propagation angle as a function of K_I/K_{II} (Palaniswamy and Knauss, 1974).	83
Figure 3.27: (a) Crack locations used in analysis; (b) G vs. a/D for three selected locations (from Zou et al., 1996).	84
Figure 3.28: Schematics of (a) wing crack coordinates, stresses and angles (Ashby and Hallam, 1986); (b) crack dimensions for idealized wing crack geometry.	86
Figure 4.1: Scale effect for classical and fracturing materials.....	93
Figure 4.2: Schematic of two self-similar deformable bodies for: (a) Case 1 (unscaled geometry); (b) Case 2 (geometry scaled by constant factor λ)	93
Figure 4.3: Rigid cylinder indenting elastic half-space.	95
Figure 4.4: Illustrations of: (a) the Maxwell model; (b) creep response; (c) relaxation response.....	96
Figure 4.5: Schematics of (a) ice-structure interaction; (b) associated global and local areas.	98

Figure 4.6: Measured ice failure pressure versus contact area for a wide range of interaction and loading situations for various ice types, temperatures and strain rates (from Blanchet, 1990. After Sanderson, 1988).....	99
Figure 4.7: Plot of α_L vs. area for ship-ice interaction data (Taylor et al., 2009).	102
Figure 4.8: Non-simultaneous failure illustrated by tests on brittle wax (Ashby et al., 1986).	104
Figure 4.9: Idealized model of non-simultaneous failure (Ashby et al., 1986).	104
Figure 4.10: Relationship between critical-stress intensity factor K_{Ic} and \dot{K}_I for pure ice with average grain size of 5 to 10 mm, tested at -20°C (Urabe and Yoshitake, 1981)...	112
Figure 4.11: Critical stress as a function of crack size for self-similar geometry for two constant values of K_{Ic} , as well as a for scale dependent fracture toughness.	113
Figure 4.12: Fracture process zone at sharp crack tip for: (a) brittle material; (b) ductile material; (c) quasi-brittle material; (Bazant and Planas, 1998).	114
Figure 4.13: Fractal geometry models of: (a) Bhat (1990); (b) Palmer and Sanderson (1991).	116
Figure 4.14: Illustration of Weibull scaling applied to both mean pressure and extreme pressures.....	120
Figure 4.15: Scale effect for: (a) flexural failure data; (b) compressive failure data. References for the sources of data may be found in Jordaan and Pond (2001).	122
Figure 5.1: LVDT and MTS load cell data for event I07_V5P0_C_062 showing time traces of: (a) nominal indentation area; (b) total force on the indenter; (c) mean nominal stress on indenter; modified from Wells et al. (2009).	131
Figure 5.2: Pictures from event I07_V5P0_C_062 showing: (a) indentation zone immediately after testing; (b) pressure distribution given by tactile sensor for last frame before end of test; (c) overlay of <i>hpz</i> outline from tactile sensor, showing general agreement between locations of <i>hpz</i> 'core' area and darker colored recrystallized zone (photos modified from Wells et al., 2009).	132
Figure 5.3: Inverted color images of thin-sections from I07_V5P0_C_062 shown under (a) polarized lighting; (b) side-lighting; (c) combined polarized and side-lighting conditions; (d) inset showing plane of thin-section (modified from Wells et al., 2009).	133
Figure 5.4: Spalling event during test I07_V10P0_C_041: (a) pressure distribution before spalling; (b) pressure distribution after spalling; (c) load drop due to spalling.	134

Figure 5.5: Finite element model of ice block and indenter used in indentation analysis.	135
Figure 5.6: Schematic of idealized spall geometry used for finite element analysis.....	137
Figure 5.7: Plot of experimental and simulated pressure data from finite element model.	138
Figure 5.8: (a) Set-up for ice sheet tests; (b) Tekscan USB handle and sensor array.....	140
Figure 5.9: Results for indentation test A03, showing: (a) time trace of force on the tactile sensor; (b) 2D contour plot of pressure at $t = t_1$; (c) 3D contour plot of pressure at $t = t_1$	141
Figure 5.10: Photographs of specimen A03 after testing showing: (a) front view and, (b) isometric view of indentation zone showing sintered layer of extruded ice.	142
Figure 5.11: (a) Microtome used for thin-sectioning of ice; (b) light table used for lighting thin-sections (photos courtesy of Jennifer Wells).	143
Figure 5.12: Thin-sections of specimen A03 showing: (a) extensive microcracking viewed using side-lighting; (b) microstructure of the ice specimen.	144
Figure 5.13: Plan view of the test site (Sodhi et al., 1998).....	145
Figure 5.14: Indentation instrumentation and structure: (a) elevation view; (b) plan view (Sodhi et al., 1998).....	146
Figure 5.15: Indenter used in MSFIT program; dimensions in mm (after Sodhi et al., 1998).....	146
Figure 5.16: Schematic of tactile sensor configurations used in: (a) 1998, 1999; (b) 2000. (after Sodhi et al. (2001)).....	147
Figure 5.17: Tactile sensor data showing: (a) 3D contour plot; (b) 2D contour map.....	148
Figure 5.18: Total tactile sensor force vs. time.....	151
Figure 5.19: Tactile sensor data for (a) peak of 'break-out' load; (b) onset of crushing.	152
Figure 5.20: Simplified schematic of hpz pressure distribution before ($t = t_0$) and after ($t = t_1$) failure for (a) crushing; (b) spalling.	153
Figure 5.21: Tactile sensor data regions used in the identification of dominant failure events.	154
Figure 5.22: Tactile sensor data for interval from 55 to 65 seconds; data correspond to total sensor load, as well as loads for the four regions identified in Figure 5.21.	154

Figure 5.23: Pressure distributions from selected regions for Failure Event 1 (local spalling): (a) 2-D plan view before failure; (b) 3-D view before failure; (c) 2-D plan view after failure; (d) 3-D view after failure.	156
Figure 5.24: Pressure distributions from selected regions for Failure Event 2 (local crushing): (a) 2-D plan view before failure; (b) 3-D view before failure; (c) 2-D plan view after failure; (d) 3-D view after failure.	156
Figure 5.25: Pressure distributions from all regions for Failure Event 3 (simultaneous crushing): (a) 2-D plan view before failure; (b) 2-D plan view after failure; (c) 3-D view before failure; (d) 3-D view after failure.	157
Figure 5.26: Sample event time traces showing: (a) global pressure; (b) local pressures.	162
Figure 5.27: Observed edge effects in normalized pressures for event 2-1.....	164
Figure 5.28: Timoshenko elastic solution compared with average normalized JOIA results for three speed ranges considered.....	164
Figure 5.29: Maximum, mean and standard deviation of pressures for sample fast result.	167
Figure 5.30: Local pressure plots (P1-P9) for sample fast event.....	168
Figure 5.31: Local pressure (P10-P15) and global pressure plots for sample fast event.....	168
Figure 5.32: Maximum, mean and standard deviation of pressures for sample medium speed event.....	169
Figure 5.33: Local pressure plots (P1-P9) for sample medium speed event.	170
Figure 5.34: Local pressure (P10-P15) and global pressure for medium speed event. ..	170
Figure 5.35: Maximum, mean and standard deviation of pressures for sample slow event.	171
Figure 5.36: Local pressure plots (P1-P9) for sample slow speed event.	172
Figure 5.37: Local pressure (P10-P15) and global pressure for sample slow speed event.	172
Figure 5.38: (a) Individual panel correlations for sample panel (P7); (b) correlation coefficient matrix 3-D bar chart for sample fast result.	176
Figure 5.39: Correlation coefficient matrix contour plot; sample fast result (event 2-1)	177
Figure 5.40: (a) Individual panel correlations for sample panel (P7); (b) correlation coefficient matrix 3-D bar chart for sample medium speed event.....	178

Figure 5.41: Correlation coefficient contour plot; sample medium speed event.	178
Figure 5.42: (a) Individual panel correlations for sample panel (P7); (b) correlation coefficient matrix 3-D bar chart for sample slow event.	179
Figure 5.43: Correlation coefficient matrix contour plot; sample slow event.	180
Figure 5.44: Event averaged individual panel correlations for single sample panel (P7) for: (a) all fast events; (b) all medium speed events; (c) all slow events.	181
Figure 5.45: Plot of ρ vs. distance; autoregressive fit; fast event data (P1-P15).	182
Figure 5.46: Plot of ρ vs. distance; autoregressive fit; medium event data (P1-P15)...	183
Figure 5.47: Plot of ρ vs. distance; autoregressive fit; slow event data (P1-P15).	183
Figure 5.48: Plot of ρ vs. distance; autoregressive fit; fast event data (P2-P14).	185
Figure 5.49: Plot of ρ vs. distance; autoregressive fit; medium event data (P2-P14)...	185
Figure 5.50: Plot of ρ vs. distance; autoregressive fit; slow event data (P2-P14).	186
Figure 5.51: Global pressure estimates for event 2-1; $v = 3.0$ cm/s.	188
Figure 5.52: Global pressure estimates for event 1-1; $v = 0.30$ cm/s.	190
Figure 5.53: Global pressure estimates for event 3-1; $v = 0.03$ cm/s.	192
Figure 5.54: Plot of ρ vs. distance; composite fit; fast event data (P2-P14).	195
Figure 5.55: Plot of ρ vs. distance; composite fit; medium event data (P2-P14).	196
Figure 5.56: Plot of ρ vs. distance; composite fit; slow event data (P2-P14).	196
Figure 5.57: Global pressure estimates for event 2-1 (composite approach).	198
Figure 5.58: Global pressure estimates for event 10-1 (composite approach).	199
Figure 5.59: Global pressure estimates for event 3-1 (composite approach).	199
Figure 5.60: Molikpaq Medof panel configurations.	203
Figure 5.61: Molikpaq sample event: (a) global and local load traces; (b) comparative plot of column data illustrating apparent correlation.	204
Figure 5.62: Molikpaq local subevent: (a) global and local load traces; (b) comparative plot of column data illustrating local correlation.	205

Figure 5.63: Comparison of JOIA and Molikpaq correlations: fast events (autoregressive).....	207
Figure 5.64: Comparison of JOIA and Molikpaq correlations: slow events (autoregressive).....	207
Figure 5.65: Comparison of JOIA and Molikpaq correlations: fast events (composite).	208
Figure 5.66: Comparison of JOIA and Molikpaq correlations: slow events (composite).	209
Figure 5.67: Comparison of JOIA and Molikpaq correlations: fast events (non-dimensionalized by thickness).	210
Figure 5.68: Comparison of JOIA and Molikpaq correlations: slow events (non-dimensionalized by thickness).	211
Figure 6.1: Illustration of (a) pressure-area effect; (b) increasing area for constant width panel with increasing thickness.	220
Figure 6.2: Indentation test scale effects for different speeds (after Li et al., 2004)	221
Figure 6.3: (a) Norstromsgrund lighthouse; (b) lighthouse location (Kärnä and Yan, 2006).	223
Figure 6.4: STRICE measurement panels: (a) schematic of panel numbering and orientation; (b) mounting configuration (Kärnä and Yan, 2006).....	224
Figure 6.5: Mean local pressure versus ice thickness for STRICE event data.	224
Figure 6.6: Illustration of pressure-thickness effect based on pressure data for individual events for JOIA, STRICE and Molikpaq data.	226
Figure 6.7: Medof panel array numbering (letters represent columns).	227
Figure 6.8: Illustration of selected columns of Medof panel data (dark panels represent broken panels) used for: (a) thin ice events; (b) thick ice events; (c) ridge/rubble events.	228
Figure 6.9: Plots showing a sample Molikpaq event with: (a) linked untrimmed data, and (b) linked trimmed data.....	230
Figure 6.10: Data for a sample STRICE event: (a) untrimmed data and (b) a trimmed event (after Kärnä and Yan, 2006).....	231
Figure 6.11: Initial comparison of STRICE and Molikpaq results corresponding to similar ice conditions, showing the discrepancy between values measured on each structure. .	233

Figure 6.12: Case 1 (Molikpaq recalibration correction off; STRICE level ice filter on, duration filter off; JOIA unfiltered; Cook Inlet level ice filter on; unweighted mean) data and curve fits for: (a) mean pressure results; (b) standard deviation of pressure results.243

Figure 6.13: Case 2 (Molikpaq recalibration correction on; STRICE level ice filter on, duration filter off; JOIA unfiltered; Cook Inlet level ice filter on; unweighted mean) data and curve fits for: (a) mean pressure results; (b) standard deviation of pressure results.244

Figure 6.14: Case 3 (Molikpaq recalibration correction off; STRICE level ice filter on, duration filter off; JOIA unfiltered; Cook Inlet data excluded; weighted mean) data and curve fits for: (a) mean pressure results; (b) standard deviation of pressure results..... 245

Figure 6.15: Case 4 (Molikpaq recalibration correction on; STRICE level ice filter on, duration filter off; JOIA unfiltered; Cook Inlet excluded; weighted mean) data and curve fits for: (a) mean pressure results; (b) standard deviation of pressure results. 246

Figure 6.16: Case 5 (Molikpaq recalibration correction on; STRICE level ice filter on, duration filter on; JOIA unfiltered; Cook Inlet level ice filter on; unweighted mean) data and curve fits for: (a) mean pressure results; (b) standard deviation of pressure results.247

Figure 6.17: Case 6 (Molikpaq recalibration correction on; STRICE level ice filter on, duration filter on; JOIA unfiltered; Cook Inlet data excluded; weighted mean) data and curve fits for: (a) mean pressure results; (b) standard deviation of pressure results..... 248

Figure 6.18: Case 7 (Molikpaq recalibration correction on; STRICE level ice filter off, duration filter off; JOIA unfiltered; Cook Inlet data level ice filter off; unweighted mean) data and curve fits for: (a) mean pressure results; (b) standard deviation of pressure results 249

Figure 6.19: Case 8 (Molikpaq recalibration correction on; STRICE level ice filter on, duration filter on; JOIA unfiltered; Cook Inlet data excluded; unweighted mean) data and curve fits for: (a) mean pressure results; (b) standard deviation of pressure results..... 250

Figure 6.20: Case 9 (Molikpaq recalibration correction off; STRICE level ice filter on, duration filter on; JOIA excluded; Cook Inlet data excluded; unweighted mean) data and curve fits for: (a) mean pressure results; (b) standard deviation of pressure results..... 251

Figure 6.21: Case 10 (Molikpaq recalibration correction on; STRICE level ice filter on, duration filter on; JOIA excluded; Cook Inlet data excluded; unweighted mean) data and curve fits for: (a) mean pressure results; (b) standard deviation of pressure results..... 252

Figure 6.22: Case 11 (Molikpaq recalibration correction off; STRICE level ice filter on, duration filter on; JOIA excluded; Cook Inlet data excluded; weighted mean) data and curve fits for: (a) mean pressure results; (b) standard deviation of pressure results..... 253

Figure 6.23: Case 12 (Molikpaq recalibration correction on; STRICE level ice filter on, duration filter on; JOIA excluded; Cook Inlet data excluded; weighted mean) data and curve fits for: (a) mean pressure results; (b) standard deviation of pressure results..... 254

Figure 7.1: Illustrations of: (a) an idealized pressure time trace showing peak pressures, crushing behavior and overall event mean pressure; (b) idealization of a fracture event comprised of a loading phase (AB), a fracture event (B) and a consequence phase (BC).	261
Figure 7.2: Results from analysis of tactile data for sample JOIA event, showing: (a) pressure distribution at $t \approx 6$ sec; (b) time series plot of contact area; (c) time series plot of total forces; (d) time series plot of contact pressure; (e) cross-section of pressure through an <i>hpz</i>	263
Figure 7.3: Three dimensional idealization of semi-infinite ice sheet.	265
Figure 7.4: Two dimensional idealization of ice edge on interaction face, showing (a) edge geometry; (b) assumed pressure distribution.	265
Figure 7.5: Illustration of zones for potential shear and tensile cracking.	267
Figure 7.6: Illustration of element stress components for a two-dimensional general state of stress (left) and stress components after transformation to the principal plane (right).	269
Figure 7.7: Mohr's circle for a two-dimensional element subject to: loading case 1 (left); loading case 2 (centre); loading case 3 (right).	270
Figure 7.8: Meshed geometry for sample analysis case.	271
Figure 7.9: Stress contour plots for sample event showing: (a) σ_{xx} ; (b) σ_{yy}	272
Figure 7.10: Results of Weibull analysis corresponding to three sets of model parameters.	275
Figure 7.11: Spalling fracture idealization, showing: (a) shear crack spalling mechanism; (b) wing crack growth model used to estimate probability of spalling.	278
Figure 7.12: Illustration of combined elemental stress and idealized wing crack analysis	279
Figure 7.13: Structure of probabilistic fracture mechanics analysis main routine	280
Figure 7.14: Cross-section of an idealized crack (Schapery, 1975)	282
Figure 7.15: Through crack in an infinite plate for general case where the principal stress is not perpendicular to the crack plane in terms of: (a) general state of stress; (b) maximum principal stress (modified from Anderson, 2005).	283
Figure 7.16: Illustrations showing (a) fracture path deviating from the original crack plane for uniaxial loading; (b) infinitesimal kink at the tip of a macroscopic crack (modified from Anderson, 2005).	284

Figure 7.17: Optimum propagation angle for crack oriented at angle β relative to normal stress as a function of biaxiality (Anderson, 2005).....	286
Figure 7.18: Structure of failure probability routine for unconfined tensile element.	287
Figure 7.19: Discretization of flaw orientation distribution <i>cdf</i> into <i>b</i> intervals of width $\Delta\beta_j$	288
Figure 7.20: Through crack in an infinite plate for general case where the principal stress is not perpendicular to the crack plane in terms of: (a) general state of stress; (b) maximum principle stress.	290
Figure 7.21: Idealized wing crack geometry.....	291
Figure 7.22: Illustration of: (a) orientation of the principal stress, and precursor flaw relative to the horizontal plane; (b) projected intersection of a wing crack with the free surface.	293
Figure 7.23: Discretization of flaw size distribution <i>cdf</i> into <i>k</i> intervals of width Δa_k .	294
Figure 7.24: Structure of confined crack element failure probability routine	296
Figure 7.25: Probability of spalling as a function of stress for Case 3 ($h = 0.2\text{m}$).	300
Figure 7.26: Probability of spalling as a function of stress for Case 6 ($h = 0.5\text{m}$).	301
Figure 7.27: Probability of spalling as a function of stress for Case 9 ($h = 1.0\text{m}$).	302
Figure 7.28: Probability of spalling as a function of stress for Case 12 ($h = 2.0\text{m}$).	303
Figure 7.29: Pressure-thickness plot for $\bar{P}_{h,50}$ data from Table 6.4.	304
Figure 7.30: Geometric configurations considered: (a) $\omega = 45^\circ$; (b) $\omega = 20^\circ$; (c) $\omega = 0^\circ$	305
Figure 7.31: Plot of pressure coefficient <i>C</i> as a function of flaw density ρ_c for three different effective taper angles.....	307
Figure 7.32: Plot of pressure exponent <i>D</i> as a function of flaw density ρ_c for three different effective taper angles.....	307
Figure 7.33: Four eccentricity cases: (a) $e_1 = 0q$; (b) $e_2 = 3q$; (a) $e_3 = 6q$; (a) $e_1 = 9q$	309
Figure 7.34: Model geometry used for study of eccentricity effects.	310

Figure 7.35: Plot of pressure coefficient C for each of the eccentricity cases. 311

Figure 7.36: Plot of pressure exponent D for each of the eccentricity cases..... 311

List of Tables

Table 5.1: Calibrated model parameters used for the UMAT routine (from Li, 2007)..	136
Table 5.2: Characteristics of selected event.....	150
Table 5.3: Classification of the degree of influence of each region on total load drop during identified failure events and assessment of domination failure type using qualitative approach.	155
Table 5.4: Percent drop in force, area and pressure during failure events for each region	158
Table 5.5: Selected JOIA Datasets used in probabilistic averaging analysis	161
Table 5.6: Values of local and global event pressures: (a) means; (b) standard deviations.	173
Table 5.7: Percent error in global pressure estimates (autoregressive) compared with measured global pressure.....	193
Table 5.8: Percent error in global pressure estimates (composite) compared with measured global pressure (based on P2-P14)	200
Table 5.9: Percent error for different global pressure estimation approaches	201
Table 5.10: Event averaged mean estimation error for various estimation approaches .	214
Table 6.1: Displacement rates for the three test series (a, b and c) each with five indenter sizes; details of test results are provided in Li et al. (2004).....	221
Table 6.2: Description of cases considered in analysis.....	237
Table 6.3: Power law parameters fit to mean and standard deviation data for analysis cases	255
Table 7.1: Weibull parameter values for freshwater ice (after Parsons et al., 1992).....	274

Table 7.2: Summary of baseline parameters used in PFM model	298
Table 7.3: Matrix of analysis cases used to study thickness effect for flat ice edge.	299
Table 7.4: Values of $\bar{P}_{h,50}$ for Case 3, Case 6, Case 9, and Case 12.....	303
Table 7.5: Matrix of model geometry for analysis of effects of ice edge shape.....	305
Table 7.6: Matrix of model geometry for analysis cases used to study eccentricity effects.	310

Table of Symbols

E	Elastic modulus.
ν	Poisson's ratio.
K_{Ic}	Mode I fracture toughness.
σ_{ij}	Stress tensor.
ϵ_{kl}	Strain tensor.
C_{ijkl}	Stiffness matrix.
$X(t)$	Autoregressive random series.
$U(t)$	Background random noise.
$B_x(\tau)$	Covariance function.
σ_p^2	Variance.
τ	Lag distance.
$\rho(t)$	Correlation coefficient.
c	Characteristic correlation length.

σ_G^2	Variance of global pressure.
σ_L^2	Variance of local pressure.
T	Averaging distance.
$\gamma(T)$	Variance reduction function.
c_1, c_2	Characteristic correlation lengths (composite correlation method).
q_1, q_2	Weighting factors (composite correlation method).
γ_1, γ_2	Variance reduction factors (composite correlation method).
$\mu_{L,i}$	Mean local panel pressure for the i^{th} panel.
$\sigma_{L,i}$	Standard deviation of the local pressure for the i^{th} panel.
$\mu_{L,avgP1-P15}$	Average value of mean local pressure over panels P1-P15.
$\sigma_{L,avgP1-P15}$	Average standard deviation of the local pressure over panels P1-P15.
$\mu_{L,avgP2-P14}$	Average value of mean local pressure over panels P2-P14.
$\sigma_{L,avgP2-P14}$	Average standard deviation of the local pressure over panels P2-P14.
α_L	Pressure coefficient for the event maximum method.
C	Coefficient of power law for mean pressure.
D	Exponent of power law for mean pressure.
E	Coefficient of power law for standard deviation of pressure.
F	Exponent of power law for standard deviation of pressure.

T_i	Random strength of the i^{th} element.
$F_T(t)$	Strength distribution function.
W	Event that the weakest link fails.
$F_W(\sigma)$	Failure probability of the system.
v_0	Reference volume (for Weibull function).
$m(\sigma)$	Material function (for Weibull function).
α_W	Weibull shape parameter.
σ_W	Weibull scale parameter.
σ_0	Weibull constant (here lower limit on strength).
$\langle R \rangle$	Expected specimen strength.
σ_R	Standard deviation of strength.
s_i	Constant corresponding to probability of exceedence.
E_i	Extreme pressure.
a_s	Spall depth based on idealized geometry.
b_s	Spall distance from center of indentation.
$2q$	Width of contact zone.
ω	Effective taper angle of ice edge (in degrees).
P_0	Reference state (maximum peak pressure).

\bar{P}_c	Mean contact pressure (over contact area).
\bar{P}_h	Overall mean pressure (over nominal area).
F_{TOT}	Total force on specimen.
$\bar{P}_{h,50}$	Mean overall pressure corresponding to 50% probability of spalling.
σ_x	Stress component in x-direction.
σ_y	Stress component in y-direction.
τ_{xy}	Shear stress component.
σ_1	Maximum principal stress.
σ_2	Minimum principal stress.
θ_p	Principal angle.
$\sigma'(x_i)$	Normalized stresses at i^{th} element.
$\sigma(x_i)$	Stresses at i^{th} element.
r	Reference stress value (scalar).
σ'_{ij}	Normalized stress tensor.
d_g	Mean grain size.
A_G	Weibull scale parameter for grain size distribution.
B_G	Weibull shape parameter for flaw size distribution.
a	Crack half-length.

a_{crit}	Critical crack half-length.
n	Number of elements.
ΔV_i	Volume of the i^{th} element.
x_i	Center coordinates of the i^{th} element.
F	Specimen failure event (occurrence of a spall).
E_i	Event that the i^{th} element fails (triggers unstable fracture).
C_i	Event that the i^{th} element contains a crack.
U_i	Event that unstable crack propagation occurs.
ρ_c	Flaw density per unit volume.
β	Orientation angle of precursor flaw.
B	Biaxiality ratio.
k_I	Local mode I stress intensity factor at kinked crack tip.
k_{II}	Local mode II stress intensity factor at kinked crack tip.
C_{11}, C_{12}	Geometric functions of crack kink angle.
G	Strain energy release rate.
G_c	Critical strain energy release rate.
α_c	Crack kink angle at which G is maximum.
$\bar{\beta}_j$	Mean values of the $\Delta\beta_j$ interval.

ψ	Direction of principal compression.
ℓ_k	Critical wing crack length corresponding to k^{th} interval of precursor crack.
T_f	Temperature (in degrees C).
μ_f	Internal coefficient of friction.
x_C	x-coordinate of precursor crack centroid.
y_C	y-coordinate of precursor crack centroid.
x_B	x-coordinate of intersection point of crack with free surface.
y_B	y-coordinate of intersection point of crack with free surface.
$F_A(a)$	Cumulative distribution function (<i>cdf</i>) of precursor crack half-length.
Δa_k	Interval of flaw length distribution discretized into k intervals.
\bar{a}_k	Mean precursor crack half-length corresponding to the k^{th} interval.
Λ	Ratio of wing crack length to precursor crack half-length.
ℓ	Length of a single wing crack.
Γ	Constant with a value of approximately 0.4.
λ	Ratio of stresses for compressive (shear) crack model.
μ	Coefficient of friction across the crack.
Λ_k	Critical crack length ratio for the k^{th} interval.
e_i	High pressure zone eccentricity value.

μ_e Event mean for benchmark data.

σ_e Event standard deviation for benchmark data.

Chapter 1: Introduction

1.1 General Overview

Increased global demand for energy has stimulated interest in the development of arctic and sub-arctic oil and gas resources. Design of offshore structures for these regions requires consideration of compressive failure of ice, particularly for structures with vertical faces. Engineers require estimates of local and global forces for design. These are based on estimates of pressures acting over an appropriate area. The designer is tasked with balancing safety, environmental protection and economic aspects of the structural design. Some conservatism is included to account for uncertainty in ice load estimation. The reduction of pressures with increasing area constitutes an important consideration in the design process; yet uncertainty associated with the relationship should also be modeled.

The objective of this research is to evaluate the present understanding of ice failure processes and investigate links between various aspects of these processes, with the goal of improving ice load modeling. Areas to be considered include: crushing, high pressure zone characteristics, fracture, non-simultaneity, probabilistic averaging, the scale-effect, and local and global pressure models. While considerable research has been carried out for many facets of the compressive failure process, opportunities exist to enhance the understanding of the interplay between these different aspects of failure. This will aid in the development of more complete ice failure models and provide insight into the interpretation of full-scale local pressure data. The aim of this chapter is to identify the relationship between the proposed research and engineering practice, and provide an introduction to ice mechanics topics that are examined in this research program.

1.2 Designing Structures for Ice Environments

The design of structures for ice environments is a complex subject and requires integrated examination of three key subject areas: ice conditions, ice mechanics and risk analysis. The Canadian Standards Association Standard S471-04 (CSA, 2004) and ISO/DIS 19906 (2010) suggests that information on ice conditions required for design depends on geographical location, season, ice feature type, interaction scenario and structural configuration to be considered. For sea ice, statistics regarding ice type and morphology, floe sizes, ice thickness, total and partial ice concentration, and seasonal and annual variations may be of interest. Information regarding the occurrence of specific features such as icebergs, rubble fields, ridges and ice islands must also be considered. For these discrete features, statistics regarding arrival rate, mass distributions, shape and possible eccentricity of impact are needed. Probability distributions of velocity must also be determined based on field data and analysis of interactions between ocean currents, wind, waves and ice. Mechanical and physical properties based on the site location and season are also required. Data on ice conditions are available from sources such as the Canadian Ice Service (CIS) and the National Ice Center (NIC) in the United States. For some regions additional information may be available from industry studies, field program databases, data from open literature or other government agencies. While gaps in the data remain, renewed interest in Northern resources has stimulated further research, which combined with technological advances, is helping to fill these gaps.

Risk analysis is generally well developed and has been applied in many industries. Monte Carlo simulations are relatively straightforward to implement using modern software packages such as Matlab. Probabilistic ice load models, such as those developed by Jordaan et al. (1993) for local pressure estimation and Jordaan et al. (1996) for global load estimation, may be readily integrated into risk-based designs. This approach provides estimates of design load as a function of annual probability of exceedence, offering the designer an awareness of the relationship between design load and estimated levels of safety. The above-mentioned models will be discussed in further detail later in the chapter.

The areas of ice mechanics of interest in the proposed research program are summarized in Figure 1.1. From a high level, the two most important questions of ice mechanics are: (1) how does ice behave? (2) how do we model the way ice behaves? To reflect these questions, the diagram below shows ice mechanics as being divided into two categories: fundamental research and engineering research.

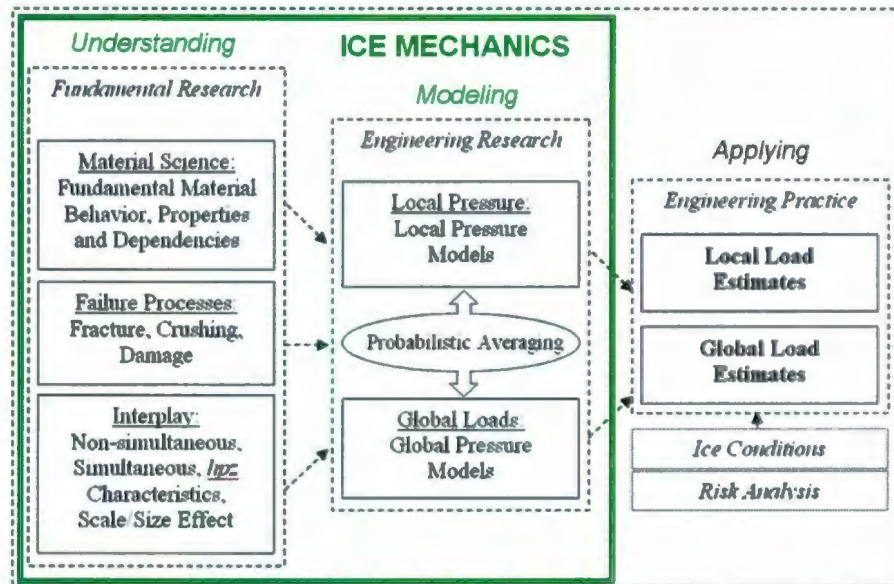


Figure 1.1: Relevant ice mechanics topics and their relationship to ice load estimation.

Fundamental research is focused on enhancing our understanding of ice material behavior, failure mechanisms and the interplay between these processes. This aspect of research aims to improve understanding of how ice behaves under a variety of conditions at different geometric scales. Engineering research is focused on incorporating knowledge of fundamental behavior into mathematical models that can be used in the estimation of ice loads on structures. Many questions remain to be answered in these areas. The goal of the present research is to identify and exploit opportunities to contribute to both fundamental and engineering aspects of ice mechanics research.

1.3 Ice Mechanics

From an engineering perspective, one of the most significant challenges when designing offshore structures for ice environments is the determination of ice load criteria. Compressive ice failure is often an important design condition, particularly for vertical-walled structures. This section explores various aspects of ice mechanics related to compressive failure of ice.

1.3.1 Compressive Ice Failure Processes

Ice failure processes serve as one of the mechanisms limiting load build-up on structures in ice. Croasdale et al. (1984) described other possible mechanisms such as limiting kinetic energy and limiting force which may also limit load build-up, but the present work focuses on ice strength. Understanding and modeling the causes and consequences of failure is an important aspect of ice load modeling. The compressive failure process is complex and as a result of its often cyclic nature, may cause ice induced vibrations in the structure; Jordaan et al. (2008). During compressive failure, spalls and splits lead to the formation of small zones of high pressure through which the majority of ice loads are transmitted. For ice sheets it has been observed that these high pressure zones (*hpzs*) may cover only 10% of the global interaction area (Taylor et al., 2008). As illustrated in Figure 1.2, at the onset of the interaction, microcracking accompanied by recrystallization begins to occur near the outside of the *hpz* (A). This results in the formation of a ‘white zone’ containing small air pockets and cracks near the edge of the zone, which eventually fragments into small particles of ice. Due to high confinement and pressure in the center of the *hpz* a zone of fine-grained, recrystallized ice is formed (B). Crushed and pressure-softened ice are extruded, resulting in a decrease in *hpz* pressure (C). As a result of the release of pressure, the layer hardens again (D). It is this cycle of pressure-softening and hardening that produces the load cycling behavior that is associated with the crushing process.

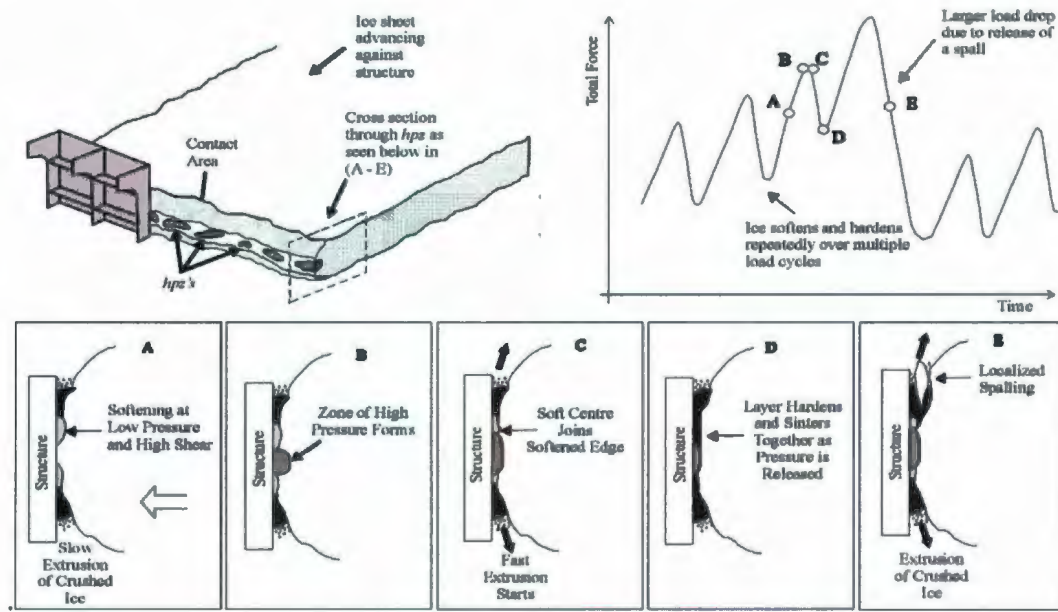


Figure 1.2: Schematic representation of the link between load cycling and layer dynamics (Jordaan et al., 2008).

Localized spalling fractures reduce the contact area, resulting in a redistribution of pressure and a drop in force (E). In small or medium scale tests, spalling may disrupt the load cycling until sufficient pressure builds to resume the cycle of pressure softening and hardening. Full-scale interactions involve many *hpzs*, reducing the influence of individual spalls in the overall crushing process. Detailed descriptions of the mechanisms of high pressure zone formation and evolution are provided in Jordaan et al. (2008).

1.3.2 Pressure-Area Scale Effect

The estimation of ice loads is further complicated by the presence of a scale effect, whereby average pressure on the structure decreases with increasing contact area (Sanderson, 1988). The scale effect in ice-structure interaction has been attributed to two main causes: (1) fracture of ice, and (2) probabilistic averaging.

The importance of fracture in ice failure was introduced by Gold (1972) and subsequently Palmer et al. (1983). Ice is a geophysical material and contains many natural flaws. The statistical distribution of flaws in ice is believed to play a significant role in the fracture

behavior of ice. As illustrated in Figure 1.3 (a), larger samples of ice have a higher probability of containing critical flaws and therefore it is more likely that larger specimens would fracture at lower stress levels. The relationships between statistical aspects of fracture and the scale effect has been discussed by Sanderson (1988), Jordaan and Pond (2001), and others.

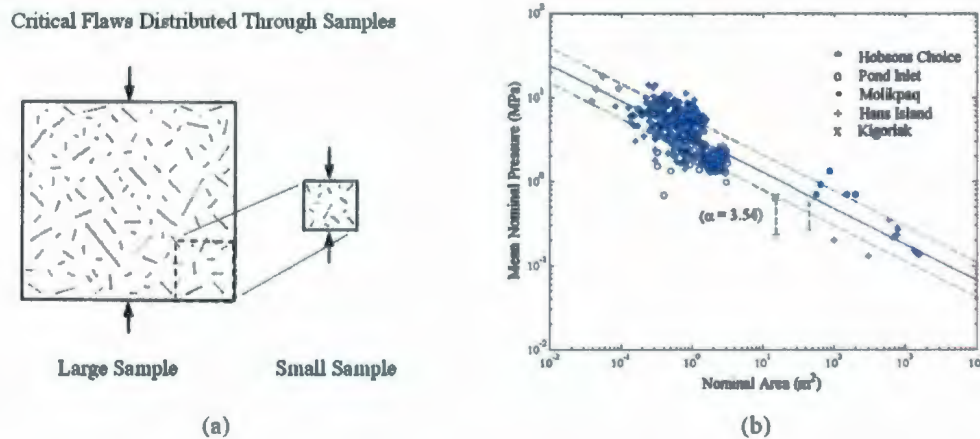


Figure 1.3: (a) Statistical flaw distribution in large and small samples; (b) Weibull fit of compressive ice failure data (after Jordaan and Pond, 2001).

In applying Weibull-type models to the case of compressive failure, the weakest-link assumptions must be re-evaluated since they were originally developed for tensile failure. Probabilistic failure theories offer an excellent direction for dealing with the decrease of global average pressure with area. In understanding and estimating local and global pressures, it is important to understand the effects of splits and fractures in the ice on the position and density of *hpzs*. Research is needed to help understand the causes and consequences of fracture, the role it plays in the compressive ice failure process and how to incorporate this knowledge into ice-load models.

As discussed in Taylor et al. (2008), pressures over small areas show large systematic and random fluctuations as a result of the formation of high-pressure zones in areas of compressive failure. Averaging across the width of a structure results from the fact that ice pressures over increasing areas are the sum of the forces in the high-pressure zones averaged over the area of interest. Non-simultaneous failure of ice across a wide structure results in a

statistical averaging of pressures from *hpzs*. This averaging effect results in a global pressure that has the same mean as local pressure measurements, but with a considerably smaller global pressure standard deviation.

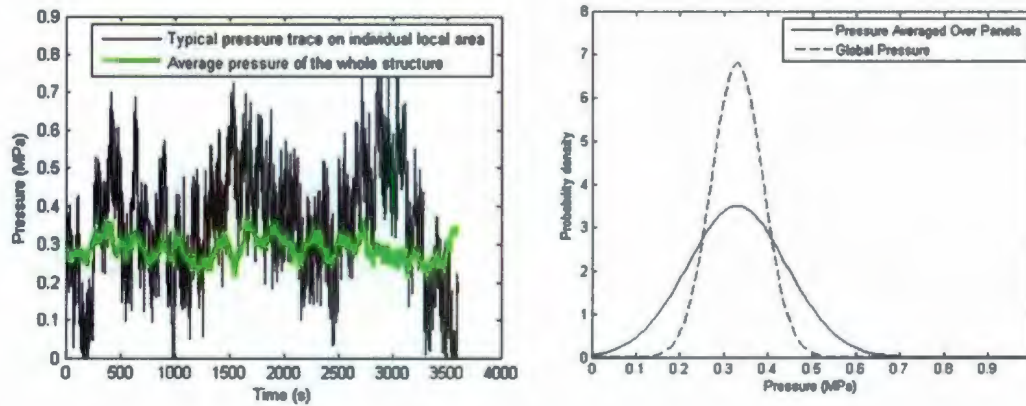


Figure 1.4: Comparison of variation in local pressure measurements and in global pressures estimated using the probabilistic averaging approach (Li, 2007).

Probabilistic averaging has been found to reduce the variation of global pressure significantly, indicating that using local information only to estimate the global pressure is very conservative. The effects of probabilistic averaging are illustrated in Figure 1.4. Further efforts to evaluate and expand on the probabilistic averaging method are recommended to enhance understanding of links between local and global pressure behavior. Through better understanding of statistical fracture and probabilistic averaging aspects of ice failure this research aims to improve the understanding of the observed pressure-area scale effect.

1.4 Estimation of Local and Global Loads

Methodologies used for ice load estimation link our fundamental understanding of ice behavior with engineering practice. To have practical application, the methodology should offer the engineer with a workable method that can readily integrate with available input information and extremal analysis techniques to produce a probability distribution of ice loadings on the structure. Complex parametric models for which the typical designer would have no basis to either understand or estimate parameter values (for instance local grain size

distributions) are of limited utility to the practicing engineer. The challenge then for the research engineer is to develop methodology which safely and effectively captures the essence of actual ice failure processes, without using excessively complex models. Definitions of local and global areas, as well as a discussion of some ice load estimation methods commonly used in practice are given below.

1.4.1 Definition of Local and Global Areas

The global area (also referred to as ‘global interaction area’ or the ‘nominal interaction area’) is the area determined by projecting the structure onto the original shape of the ice feature. As indicated in Figure 1.5 (a), during an interaction large areas may spall from the ice feature. While this will likely affect the actual contact area, the global area definition does not account for any loss of contact area due to fractures or spalls. The global area also contains regions carrying little or no pressure, as well as *hpzs*. The global area is simply based on the shape of the structure and the shape of the ice feature. Local design area is the area used in the design of shell or stiffening elements of a structure considered in design. Figure 1.5 (b) illustrates the concept of the local design area.

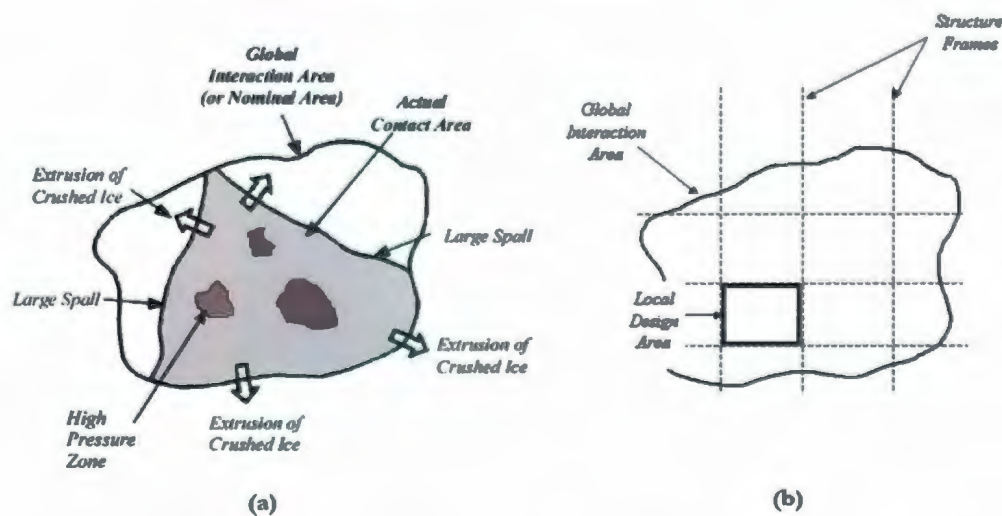


Figure 1.5: Illustration of (a) global interaction area and (b) local design area.

1.4.2 Ice Load Estimation Methods

In the estimation of ice loads on structures, probabilistic methods are often used since they allow the designer to estimate loads and model uncertainty associated with the estimates. The modeling of uncertainty and evaluation of design load sensitivity to input selection represents an important aspect of ice load estimation. The Canadian Standards Association S471-04 guideline recommends different strategies for environmental loading scenarios depending on whether the scenario is categorized as frequent or rare. Frequent environmental processes such as wind, waves, currents, and sea ice may encounter several extreme events each year. By comparison, rare environmental events such as iceberg impacts, seismic events or tsunamis may have a return period of tens of years or longer. Furthermore, the prescribed level of safety depends on the Safety Class assigned to the structure or its structural elements. Safety Class 1 corresponds to a scenario where failure of the structure or structural element would result in a great risk to life or a high potential for environmental damage. Safety Class 2 refers to scenarios where failure would result in small risk to life and a low potential for environmental damage. According to CSA S471-04, for frequent events the annual probability of exceedence shall not be greater than 10^{-2} for Safety Classes 1 and 2. For rare events, the annual probability of exceedence is to be not greater than 10^{-2} for Safety Class 2 and typically not greater than 10^{-4} for Safety Class 1.

For the estimation of local ice pressures, the CSA recommends a probabilistic approach based on extremal analysis developed by Jordaan et al. (1993). The expression for local pressure given is

$$F_x(x) = 1 - \exp(-(x - x_0) / \alpha) \quad (1.1)$$

where x is the local ice pressure and α and x_0 are constants for a given area. Data corresponding to maximum pressures during ice ramming events recorded on the Kigoriak during its 1981 Arctic voyage have been used in the design of structures for offshore Eastern Canada. Using these data, the parameter α has been modeled as a function of area according to the expression $\alpha = 1.25A_1^{-0.7}$. Taylor et al. (2009) and Li (2007) have examined other

expressions for α and x_0 parameters based on ship ram data from other ice breakers, such as the Polar Sea.

In modeling global pressure behavior, a number of different approaches have been employed. The power-law relationship developed by Jordaan et al. (1996) for structures on the Grand Banks of Newfoundland was developed for loads governed by limiting kinetic energy using ship ram data. This relationship is expressed as

$$P = CA^p, \quad (1.2)$$

where A is the global area, C is a lognormally distributed model parameter and D is a normally distributed model parameter. As discussed by Jordaan et al. (2005), field data indicates that global ice loads may be less than previously estimated. This prompted further research to investigate various aspects of failure processes during global loading.

Work by Li (2007) has examined probabilistic averaging methodology for wide structures where loading is governed by limiting stress cases. A key contribution of this work is in linking the reduction of global pressure variance to the statistical averaging of local failure processes that occur across the width of the structure. This approach is well suited to the estimation of global loads based on local measurements. The variance of global pressure, σ_g^2 has been linked to variance of the local pressure, σ_L^2 by the expression

$$\sigma_g^2 = \gamma(w)\sigma_L^2, \quad (1.3)$$

where $\gamma(w)$ is the variance reduction factor as a function of width derived by Vanmarcke, (1983). This approach has been explored to explain discrepancies between pressure-area and pressure-aspect ratio curves used in the estimation of global loads. Aspects of probabilistic averaging are discussed in further detail in Chapter 4.

1.5 Scope of Thesis

The research presented in this thesis focuses on limiting stress for ice sheets interacting with rigid vertical structures. Emphasis has been placed on enhancing the understanding and

modeling of aspects of the compressive ice failure process, and linking this behavior with the observed scale-dependent pressure behavior. Factors such as salinity and porosity have not been explicitly considered in the present research. Focus has been placed on statistical aspects of fracture behavior, and the role of flaws in the scale effect. The scope of this work may be categorized as follows:

- Review of fundamental theory relating to viscoelasticity, damage mechanics, fracture mechanics and the statistical treatment of fracture.
- Review of ice properties and behavior, relevant ice mechanics literature, as well as various theoretical models of ice fracture.
- Examine potential contributing factors to the scale dependent pressure behavior of ice including the role of material behavior, material properties, fracture behavior and statistical aspects of fracture.
- Study high pressure zone behavior and probabilistic averaging effects. Study damage layer and spalling fracture in small-scale experiments. Examine the interplay between crushing, and spalling fracture. Use damage mechanics material model and simulate a fracture event from a sample indentation test. Analyze medium-scale field data from Japan Ocean Industries Association (JOIA) to investigate crushing, spalling fracture, non-simultaneity, *hpz* behavior, spatial correlations, and probabilistic averaging effects. Examine JOIA and Molikpaq panel data to compare correlation behavior associated with ice sheets of different thickness.
- Study pressure-thickness effects at full-scale. Analyze experimental data to study scale effects for remote ice edges. Analyze local panel data from JOIA, STRICE, Cook Inlet and Molikpaq datasets to study thickness scaling. Examine influence of recalibration of Molikpaq panel data on pressure thickness data. Obtain a representative expression for the observed pressure-thickness behavior.
- Study theoretical aspects of thickness scaling using a probabilistic approach. Develop numerical tools for modeling ice failure to enhance understanding of the failure processes in ice. Model near field elastic stresses in an edge-loaded ice sheet using finite element analysis. Study failure probability of ice sheets using a Weibull model (tensile zones only). Develop probabilistic fracture mechanics model to include

effects of both tensile fracture and shear cracking (associated with grain boundary sliding). Simulate statistical aspects of brittle fracture in an elastic medium containing distributed flaws. Examine effects of ice edge geometry and proximity of *hpz* to ice edge on spalling failure probability.

- Summarize conclusions and recommendations for future research.

Chapter 2: Fundamental Theory

2.1 Scope

In this chapter, a review of fundamental theory pertinent to the research carried out in this study has been summarized. Linear viscoelasticity, broad-spectrum, non-linear viscoelasticity and modified superposition theories have been reviewed as background to the numerical routines implemented in this work. Fundamental aspects of fracture mechanics theory are also presented, including linear elastic fracture mechanics and a discussion of relevant aspects of J-Integral theory. Weibull weakest-link theory is discussed in the context of statistical fracture modeling for both homogeneous and inhomogeneous stress states. A review of relevant damage mechanics theories is given.

2.2 Viscoelasticity Theory

2.2.1 Linear Theory

Given the viscoelastic nature of ice, a review of some basic viscoelastic theories is provided. For ice the creep strain may be expressed as a function of stress σ , temperature T and time t as: $\varepsilon = F(\sigma, T, t)$. For the uniaxial case the integral forms of linear viscoelastic stress and strain, as first suggested by Volterra (1909), are

$$\sigma(t) = \int_0^t E(t-\tau) \frac{d\varepsilon(\tau)}{d\tau} d\tau, \quad (2.1)$$

$$\varepsilon(t) = \int_0^t D(t-\tau) \frac{d\sigma(\tau)}{d\tau} d\tau, \quad (2.2)$$

where τ is a point of interest on the interval $[0, t]$ and the stress σ and strain ε are assumed to be zero for $t < 0$; $E(t)$ is the relaxation function (or relaxation modulus), which is a memory function that describes the history dependence of the stress; $D(t)$ is the creep function (also called the creep compliance) which describes the strain per unit stress in time.

Biot (1954) developed expressions for relaxation and creep functions in terms of material constants E_i, μ_i, E'_i, μ'_i and are given as:

$$E(t) = E_1 + \sum_{i=2}^N E'_i \exp\left(-\frac{E'_i}{\mu_i} t\right), \quad (2.3)$$

$$D(t) = \frac{1}{E_1} + \frac{t}{\mu_1} + \sum_{i=2}^N \frac{1}{E_i} \left\{ 1 - \exp\left(-\frac{E_i}{\mu_i} t\right) \right\}. \quad (2.4)$$

These expressions represent the classical formulation of viscoelasticity theory and are based on the thermodynamics of irreversible processes.

The above equations represent a series of spring and viscous dashpot elements. The two most commonly used combinations of these elements are the Kelvin unit and the Maxwell unit; see Figures 2.1 (a) and 2.1 (b), respectively.



Figure 2.1: Schematics of: (a) a Kelvin unit; (b) a Maxwell unit.

The material constants E_i , μ_i , E_i' , and μ_i' in Eq. 2.3 and Eq. 2.4 may be interpreted as the stiffnesses and viscosities of the spring and dashpot elements, respectively. The creep compliance defined by Eq. 2.4 represents a Kelvin chain in series with a Maxwell chain having elements E_1 and μ_1 . For many materials the summation term in Eq. 2.4 may be approximated by a power-law term t^b to give a simplified expression:

$$D(t) = D_0 + D_1 t + D_2 t^b, \quad (2.5)$$

where D_0 , D_1 , D_2 and b are material constants; the term $D_2 t^b$ represents a simplified approximation of the broad spectrum approach. For appropriate applications, Equation 2.5 is a useful alternative to the full expression given in Eq. 2.4.

For materials with more complex behavior, proper representation of the material creep behavior may be better accomplished using chains of Kelvin or Maxwell units with a spectrum of values for the spring and dashpot elements.

2.2.2 The Broad-Spectrum Approach

The behavior of a viscoelastic material (especially when nonlinearity is involved) may be better modeled using chains of Kelvin and Maxwell units with a spectrum of values for the spring and dashpot elements. While improved modeling capabilities may be afforded by employing this approach compared with using a single unit, additional difficulties are encountered in modeling and fitting the experimental data. Application of the broad-spectrum collocation method for fitting experimental data developed by Schapery (1962) was explored in the context of modeling ice behavior by Xiao (1997). For this approach, the relaxation modulus is defined as:

$$E(t) = E_1 + \sum_{i=2}^N E_i \exp\left(-\frac{E_i}{\mu_i} t\right). \quad (2.6)$$

Letting $\tau_i = \mu_i/E_i$, we can rewrite Eq. 2.6 as:

$$E(t) - E_1 = \sum_{i=2}^N E_i \exp\left(-\frac{t}{\tau_i}\right) \quad (2.7)$$

where $E_1 = E(\infty)$. To fit Eq. 2.7 to a set of experimental data, a set of collocation points for t are chosen, for instance $t_1 = 0$ and $t_j = 10^{(j-3)}$, ($j = 2, 3, \dots, n$). Xiao (1997) suggested using the somewhat arbitrary values of $\tau_i = 2t_i = 2 \times 10^{(i-3)}$, ($i = 1, 2, 3, \dots, n$). Equating $E(t_j)$ to the values of experimental data at time t_j produces a set of n linear algebraic equations for the unknown values of E_j , ($j = 1, 2, 3, \dots, n$). In matrix notation this may be written as:

$$\{E(t_j) - E_1\} = \{a_{ij}\} \{E_j\}, \quad (2.8)$$

where $a_{ij} = \exp(-t_j/\tau_i)$, ($i, j = 1, 2, 3, \dots, n$). Solving 2.8 gives values of E_j , which can be substituted into Eq. 2.6 to give a model response which may be compared with the experimental data. Refinement of the model may be accomplished by adjusting t_j and τ_i . Solutions with very small E_j values for some units may be simplified since these units contribute little to the model response. To simplify the model, save computation time and data storage, units having small E_j values can be eliminated.

2.2.3 Nonlinear Viscoelasticity Theory

Schapery (1969) generalized the equations developed by Biot (1954) to account for nonlinearities in time-dependent material behavior, to give the expressions

$$\sigma(t) = \int_0^t E(\psi(t) - \psi(\tau)) \frac{d\varepsilon(\tau)}{d\tau} d\tau, \quad (2.9)$$

$$\varepsilon(t) = \int_0^t D(\psi(t) - \psi(\tau)) \frac{d\sigma(\tau)}{d\tau} d\tau. \quad (2.10)$$

The primary difference between the above expressions and the linear forms given in Equations 2.1 and 2.2 is the replacement of time t with the term, $\psi(t)$ which is called the reduced time. The reduced time is defined as

$$\psi(t) = \int_0^t \frac{d\tau}{a_d}, \quad (2.11)$$

where a_d is an entropy production coefficient. Nonlinearities in response due to the effects of temperature, stress, strain or other such factors can be included through this coefficient.

Jordaan and McKenna (1988) applied non-linear theory to model ice behavior using a Burgers unit, which consists of a Maxwell unit and a Kelvin unit in series. In this model the authors used linear springs and nonlinear dashpots having stress dependent viscosity, i.e. $\mu = \mu(\sigma')$, where σ' is the stress in the dashpot. When subjected to a constant overall stress σ applied at $t = 0$, the equilibrium stress for the Kelvin unit may be expressed as a function of the elastic modulus of the spring, E_k and the viscosity of the dashpot μ_k of the Kelvin unit to give:

$$\sigma = E_k \varepsilon^d + \mu_k \dot{\varepsilon}^d. \quad (2.12)$$

This expression can be solved to give the deformation of the Kelvin unit $\varepsilon^d(t)$,

$$\varepsilon^d(t) = \frac{\sigma}{E_k} \left[1 - \exp \left\{ - \int_0^t \frac{E_k}{\mu_k(\sigma_d)} dt \right\} \right], \quad (2.13)$$

where the term σ_d is the stress in the dashpot of the Kelvin unit.

For the case where the Kelvin unit dashpot is modeled as having a viscosity μ_k that exhibits a power-law dependence on stress, the viscosity may be expressed as

$$\mu_k(\sigma_d) = \frac{1}{A_k \sigma_d^{n-1}}, \quad (2.14)$$

where the term n is a constant; A_k is the viscosity parameter. As explained in Xiao (1997), considering the equilibrium equation for the Kelvin unit, $(\dot{\sigma} - \dot{\sigma}_d)/E_k = \sigma_d/\mu_k(\sigma_d)$, it may be shown that the viscosity is a linear function of time, as given by

$$\mu_k = (n-1)E_k t + \mu_{k0}, \quad (2.15)$$

where the term μ_{k0} is the viscosity at $t = 0$. Substituting this equation into Eq. 2.13 and solving for the Kelvin unit deformation gives

$$\varepsilon^d(t) = \frac{\sigma}{E_k} \left\{ 1 - [(n-1)\omega t + 1]^{1/(1-n)} \right\}, \quad (2.16)$$

where the term $\omega = E_k/\mu_{k0}$.

2.2.4 Modified Superposition Principle

Another approach, known as the modified superposition principle (Findley et al., 1976), was developed using generalized linear viscoelasticity theory. Schapery (1981) applied the modified superposition principle to the case of a uniaxial state of stress to give an expression

$$\varepsilon(t) = E_R \int_0^t D(t-\tau) \frac{\partial \varepsilon^0(\sigma, \tau)}{\partial \tau} d\tau, \quad (2.17)$$

where $D(t)$ is a linear compliance, E_R is a reference elastic modulus. The term ε^0 is known as pseudostrain, which includes the applied stress σ and has units of strain. For the special case where the compliance is given as $D(t-\tau) = 1/E_R$, the pseudostrain is equal to the total strain i.e. $\varepsilon(t) = \varepsilon^0$, which corresponds to the elastic case. If instead the pseudostrain is given as $\varepsilon^0 = \sigma/E_R$, then Eq. 2.17 simplifies to the case of uniaxial linear viscoelasticity.

For the case where the stress-strain behavior is assumed to be nonlinear and which can be represented by a power-law relationship (i.e. $\dot{\varepsilon} = A\sigma^n$, where σ is a constant for $t \geq 0$), the nonlinearity may be reflected in the pseudostrain term. This is accomplished by letting $\varepsilon^0 = \sigma^n$ and $D(t-\tau) = A(t-\tau)/E_R$ in Eq. 2.17, to give

$$\varepsilon(t) = E_r \int_0^t \frac{A(t-\tau)}{E_r} \frac{d(\sigma^n)}{d\tau} d\tau . \quad (2.18)$$

For the case where $\tau = 0$ and σ is constant (for $t \geq 0$), Eq. 2.33 simplifies to $\varepsilon(t) = At\sigma^n$, from which the power-law relationship may be derived

$$\dot{\varepsilon}(t) = A\sigma^n . \quad (2.19)$$

In terms of the complementary strain energy W^c the pseudostrain ε^0 can be written as

$$\varepsilon^0 = \frac{\partial W^c}{\partial \sigma} = \frac{1}{E_r} \int_0^t E(t-\tau) \frac{\partial \varepsilon(t)}{\partial \tau} d\tau , \quad (2.20)$$

where $E(t)$ is the relaxation function (see Eq. 2.3). Recall that the creep compliance $D(t)$ and the relaxation modulus $E(t)$ are inversely related according to $s^2 \overline{D}(s) \overline{E}(s) = 1$, where the overbar denotes the Laplace transform and s is the transform parameter. From Eq. 2.20 the strain equation for nonlinear behavior may be determined to be

$$\varepsilon(t) = E_r \int_0^t D(t-\tau) \frac{\partial}{\partial \tau} \left(\frac{\partial W^c}{\partial \sigma} \right) d\tau . \quad (2.21)$$

Using the above expressions, nonlinear viscoelastic behavior may be modeled based on the modified superposition principle. Schapery (1981) used this result as input into his J-Integral analysis and in the application of correspondence principles for viscoelastic materials. Extension of this approach to include the effects of damage will be discussed later in the chapter.

2.3 Damage Mechanics

The concept of damage was introduced to account for the presence of microcracks and voids which permanently affect the material behavior through modification of properties, such as the elastic moduli. Kachanov (1958) first introduced the concept of a scalar damage factor equal to the ratio of the area of voids to the area of the whole cross-section. Much of the early

work in damage mechanics, including its application to ice, was based on this concept. This approach was effective in developing a rational framework for relating current material properties to the accumulation of damage. The area-based approach along with subsequent crack density and stress-history approaches are reviewed below.

2.3.1 The Area-Based Approach to Damage

Kachanov (1958) introduced an area-based definition of damage for the case of uniaxial loading by first considering the nominal stress in an undamaged body σ as

$$\sigma = \frac{P}{A_0}, \quad (2.22)$$

where P is the uniaxial force and A_0 is the overall cross-sectional area. A scalar measure of isotropic damage D was introduced as the ratio of the overall area A_0 to the area of the void spaces and microcracks (i.e. damaged area) A , as given by

$$D = \frac{A}{A_0}; \quad (0 \leq D \leq 1). \quad (2.23)$$

In this model, as damage increases the load is carried over a progressively smaller intact area. To include these effects, the 'effective stress' σ_a was expressed as

$$\sigma_a = \frac{P}{A_0 - A} = \frac{P}{A_0(1 - D)} = \frac{\sigma}{1 - D}. \quad (2.24)$$

It was then assumed that the effects of damage on the strain can be completely defined by the stress-strain relationship

$$\varepsilon = \frac{\sigma_a}{E_0} = \frac{\sigma}{E_0(1 - D)} = \frac{\sigma}{E}. \quad (2.25)$$

In the above expression, E_0 is the Young's modulus of the virgin material. The parameter E is the 'effective' modulus, which accounts for the reduction of the modulus as a result of the effects of damage and is defined by

$$E = E_0(1 - D). \quad (2.26)$$

The above concept of damage establishes a rational way to relate the accumulation of damage to the internal and state variables of the material, but does not directly relate the damage to cracks and other flaws in the specimen.

2.3.2 The Crack Density Approach to Damage

Microcracks and other defects play an important role in the accumulation of damage in a material. Much research into the relationship between the behavior of materials and these damage processes has been carried out; see for instance Schapery (1981, 1984, 1988); Krajcinovic (1983, 1989). An important advancement in modeling the effects of damage resulted from the development of approaches which relate damage evolution to crack density. Such models rely on 'crack smearing' techniques which average out the effects of individual cracks and rather describe the continuum behavior as a function of a crack-density dependent damage law. Continuum damage models are well suited for use with numerical analysis tools, such finite element analysis. Advances in numerical modeling methods and computing technology, along with advances in fracture mechanics, have helped broaden the use of damage mechanics in engineering applications.

One of the earliest models relating the 'effective' elastic moduli to the crack density was given by Budiansky and O'Connell (1976). In their model of a damaging elastic body, the authors assumed the material contained an isotropic array of flat circular cracks. This model related the decrease in strain energy associated with the nucleation of cracks to the elastic moduli of the material. The damage measure defined in this model was related to the crack density according to

$$D = a^3 N, \quad (2.27)$$

where a is the crack radius, and N is the crack density. In this model, all cracks were assumed to remain open and while the effects of interaction between cracks were included the analysis did not include tractions acting on the crack surfaces. Based on their analysis, the authors developed expressions relating the elastic properties of the damaged material (denoted by the prime) to the virgin properties of the material, as given by

$$E'/E = 1 - [16(1 - \nu'^2)(10 - 3\nu')]/[45(2 - \nu')]D, \quad (2.28)$$

$$K'/K = 1 - [16(1 - \nu'^2)]/[9(1 - 2\nu')]D, \quad (2.29)$$

where E is the Young's modulus, K is the bulk modulus, and ν is Poisson's ratio. The damage measure was solved in terms of ν and ν' to give

$$D = [45(\nu - \nu')(2 - \nu')]/[16(1 - \nu'^2)(10\nu - \nu'(1 + 3\nu))]. \quad (2.30)$$

While the above model is appropriate for tensile loading, under compression some of the microcracks will close. Correspondingly, the effects of cracks on the elastic properties of materials subject to compressive loading will be less than for the tensile case. Under these conditions, the closed cracks will still be able to transmit tractions and shear stresses across the crack surfaces.

To account for this, Horii and Nemat-Nasser (1983) developed solutions for the general case of a two-dimensional body containing an array of plane strain cracks subjected to compressive stresses, including the effects of friction on the crack surfaces. Using numerical analysis, the authors studied the relationship between the elastic properties and the applied normal stress σ_p , the applied shear stress s , and the friction coefficient η . Based on their results, the authors developed the functional relationships

$$(1 - K'/K)^2 = [1.8aD(\sigma_p/s + 1)], \quad (2.31)$$

$$(1 - G'/G) = 0.9D\{\sigma_p/s + 1 + \exp[\eta(\sigma_p/s - 1)]\}, \quad (2.32)$$

The above model is applicable only for cases of proportional loading where the ratio of normal stresses and shear stresses (i.e. σ_p / s) remains constant. For the case where $\sigma_p / s \geq 1$, all cracks are open; all cracks are closed for $\sigma_p / s \leq -1$.

Kachanov (1993) studied a variety of problems involving solids containing different configurations of crack arrays, with emphasis on examining the effects of crack interactions, including their effects on crack tip stress intensity factors. The author also studied the interaction between microcrack arrays and a macrocrack, as well as the influence of cracks on the elastic moduli of the material. Of most relevance to modeling damage in ice is Kachanov's three dimensional solution for the case of non-interacting cracks with isotropic random distribution. The solution he developed for this scenario assumed an applied stress σ^0 at the remote boundary of an elastic solid having N cracks per unit volume, with each crack having a normal n^i and a surface traction of $f^o = n^i \sigma^o$. The resulting solutions relating virgin material characteristics (denoted with the naught subscript) to the damaged properties were given for the Young's modulus E , shear modulus G and Poisson's ratio ν as

$$\frac{E}{E_0} = (1 + C_1 N)^{-1}, \quad (2.33)$$

$$\frac{G}{G_0} = (1 + C_2 N)^{-1}, \quad (2.34)$$

$$\frac{\nu}{\nu_0} = \frac{E}{E_0} (1 + C_3 N), \quad (2.35)$$

where

$$C_1 = \frac{16(1-\nu_0^2)(1-3\nu_0/10)}{9(1-\nu_0/2)}, \quad (2.36)$$

$$C_2 = \frac{16(1-\nu_0)(1-\nu_0/5)}{9(1-\nu_0/2)}, \quad (2.37)$$

$$C_3 = \frac{8(1-\nu_0^2)}{45(1-\nu_0/2)}. \quad (2.38)$$

As discussed by Xiao (1997) the above solutions provide accurate results for both low and high crack densities, though some simplifications may be possible for low crack densities.

2.3.3 The Stress-History Approach to Damage

Schapery (1981, 1984, 1988, 1989) developed a continuum model for nonlinear viscoelastic materials based on generalized J-Integral theory. Schapery's idealization included modeling of the damaged material near the crack tip and correctly modeled the effects of energy flux into the highly stressed zone at the crack-tip. Schapery (1981) used the modified superposition principle to model nonlinear viscoelastic material behavior, which was also extended to include the effects of microstructural damage processes. The effects of damage were included through a definition of the pseudostrain ε^0 as a function of both the stress σ and a damage measure S , according to

$$\varepsilon^0 = g(S)(\sigma)^r, \quad (2.39)$$

where r is a positive constant. The term $g(S)$ is a damage enhancement factor given by Schapery (1981) as

$$g(S) = \exp(\lambda S), \quad (2.40)$$

where λ is a positive constant. Schapery's damage measure S is based on the integral of the stress-history of the specimen and is given by

$$S = \int_0^t f_1(\sigma)^q d\tau, \quad (2.41)$$

where f_1 is a function representing the material behavior in the crack tip region; q is a positive constant. For the above expression changing f_1 or q results in a different definition of S . For many conditions, the effects of damage may be captured by a single parameter definition. For some materials, such as ice, more than one definition of S may be needed to

capture the effects of different damage processes. A review of the application of damage mechanics to ice is given below.

2.4 Fracture Mechanics

In engineering literature, fracture is generally categorized into the three modes of fracture shown in Figure 2.2 below. These modes correspond to the relative movement of the upper and lower crack surfaces relative to each other (Sih and Liebowitz, 1968).

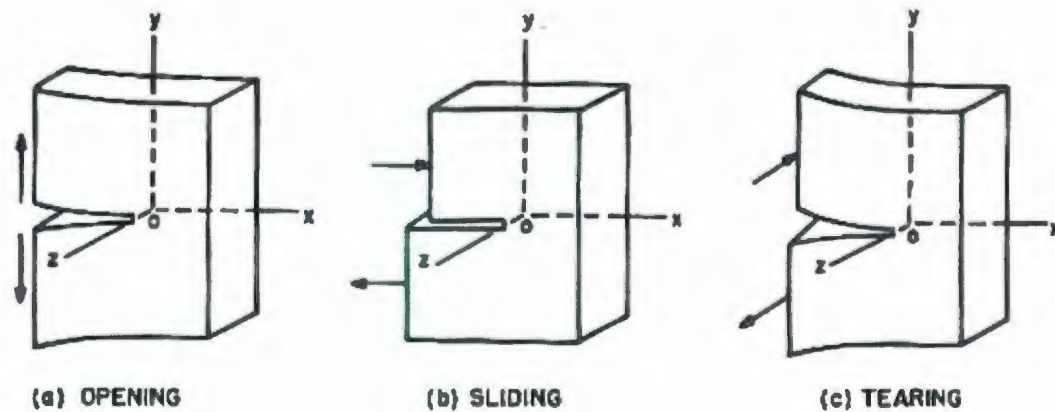


Figure 2.2: Modes of fracture: (a) tensile mode; (b) in-plane shear; (c) anti-plane shear. (after Sih and Liebowitz, 1968).

Depending on the material characteristics, different approaches to modeling fracture may be employed. These different approaches are reviewed below.

2.4.1 Linear Elastic Fracture Mechanics

Pioneering work by Griffith (1920) led to the development of an energy criterion for fracture based on an energy balance approach. His analysis was based on an elliptical crack in an ideally elastic medium. He stated that the reduction in strain energy resulting from crack growth must be greater than or equal to the increase in surface energy required to form the new crack surfaces (Hayes, 1975). This may be expressed as:

$$\frac{dU}{da} \geq \frac{dW}{da}, \quad (2.42)$$

where U is the elastic strain energy, W is the surface energy and da is the crack length increment. The left side of the above equation represents the strain energy release rate for a linear elastic solid, G . This is described in many fracture mechanics texts (see for instance Broek, 1986) for narrow elliptical cracks according to the expressions:

$$G = \frac{\pi\sigma^2 a}{E(1-\nu)}, \quad \text{for plane strain,} \quad (2.43)$$

$$G = \frac{\pi\sigma^2 a}{E}. \quad \text{for plane stress.} \quad (2.44)$$

The right side of Eq. (2.42) represents the rate of increase in surface energy per unit crack growth. For many engineering materials, this is a constant. On this basis, we can define a critical value of energy release rate for a given material, G_c above which failure occurs. This can be expressed as

$$G = G_c, \quad \text{for stable crack growth,} \quad (2.45)$$

$$G > G_c, \quad \text{for unstable crack growth.} \quad (2.46)$$

Irwin (1957) expanded on the original stress analysis work Inglis (1913), which focused on characterizing fracture in terms of the stress in the crack tip region. This approach led to the development of the stress intensity factor as a fracture criterion. Irwin introduced the idea of a flat, inline crack and studied the elastic stress field in the vicinity of the crack tip. For a homogenous, isotropic elastic solid with a sharp crack in plane stress or plane strain, such as the one shown in Figure 2.3, this analysis led to the following stress field expressions:

$$\sigma_x = \sigma_y = \frac{K}{\sqrt{2\pi r}} \cos \frac{\theta}{2} \left(1 - \sin \frac{\theta}{2} \sin \frac{3\theta}{2} \right), \quad (2.47)$$

$$\tau_{xy} = \frac{K}{\sqrt{2\pi r}} \cos \frac{\theta}{2} \sin \frac{\theta}{2} \sin \frac{3\theta}{2}, \quad (2.48)$$

where r is the radial distance from the crack tip, θ is the angle relative to the crack axis, and K is the stress intensity factor.

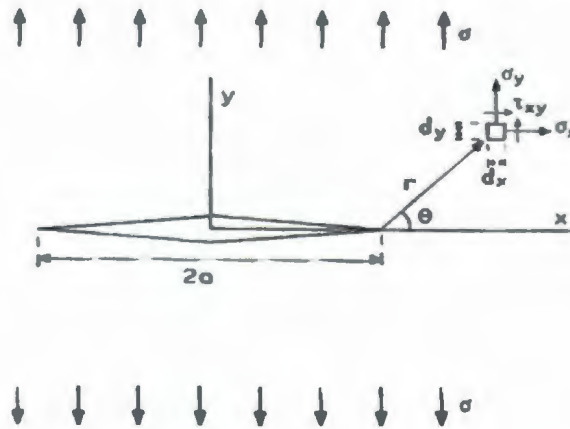


Figure 2.3: Schematic of a crack in an infinite plate (Broek, 1986).

For pure tensile fracture (Mode I), the stress intensity factor K_I may be expressed as

$$K_I = \sigma_a Y \sqrt{\pi a}, \quad (2.49)$$

where σ_a is the applied external stress, Y is a constant based on geometry and a is the crack half-length. Expressions for Y have been derived for a wide number of geometric configurations and may be found in many engineering handbooks or fracture mechanics texts. Considering Equations 2.47-2.48, it may be seen that for a cracked specimen with known geometry, determination of the stress of any point (r, θ) only requires knowledge of the applied external stress σ_a . Failure occurs when the local stress exceeds the material strength. Since the local stress intensity depends on the combination of applied stress and crack size, a failure criterion for brittle materials was developed by Irwin on the basis of a critical stress intensity required to cause unstable crack propagation. On this basis, the criterion for Mode I fracture may be expressed as

$$K_I \geq K_{IC}, \quad (2.50)$$

where K_{IC} is the critical stress intensity factor for Mode I fracture (plane strain). A shortcoming of fracture theories based on elasticity theory is that they predict infinite stresses

at the crack tip, even for low nominal stress. In reality, this is not physically possible and energy near the crack tip is dissipated through some local dissipation mechanism (for instance, creep and damage in ice at low strain rates). For metals, which generally have well defined yield strength, Irwin developed a plastic tip correction model. This model uses the material yield strength as an upper physical limit on local stress and estimates the size of the plastic zone that would be required to dissipate the elastic energy in the crack tip region (Broek, 1986). This work initiated a large body of research into the study of crack-tip plasticity and modeling, including the important strip yield model of Dugdale and work on crack tip cohesion by Barenblatt (Kanninen and Popelar, 1985). The work of Rice (1968) introduced the J-Integral approach, which continues to see broad application in modeling a wide range of fracture problems.

As fracture mechanics expanded to include other material types, the crack tip region became known more generally as the fracture process zone. The fracture process zone is present in all materials, but its characteristics determine which subset of fracture mechanics is appropriate. Bazant and Planas (1998) define the fracture process zone as a nonlinear zone characterized by a region of progressive softening directly adjacent to the crack tip, surrounded by a non-softening, nonlinear zone characterized by either perfect yielding or plastic hardening (in ice this would also include viscoelastic behavior). As deformation increases, the stress in the softening region decreases, while stress in the surrounding region either hardens or remains constant.

For the case where the entire fracture process zone is small relative to the structure size, fracture essentially takes place at a single point. Such materials exhibit classical brittle behavior. The crack tip and entire body are treated as elastic, and the use of linear elastic fracture mechanics (LEFM) is appropriate. In LEFM, the assumption of small-scale yielding (SSY) is an underpinning requirement of the method. A number of authors have examined the validity of applying LEFM to ice. Based on the work presented by Dempsey (1996), Abdel-Tawab and Rodin (1995) and others, it may be concluded that LEFM may be applied to ice for loading rates that are high enough for brittle behavior to dominate and for samples of sufficient size to 'smear' the effects of heterogeneities. For small specimen sizes, Dempsey (1991) suggests micromechanical modeling may be appropriate. At lower strain

rates, where creep and damage processes have sufficient time to activate, more involved methods, such as those developed by Schapery (1981) are required. Given that Schapery's approach builds on the J-Integral method of Rice (1968), a review of J-Integral theory is appropriate here.

2.4.2 J-Integral Theory for Elastic and Plastic Cases

To overcome some of the complexities posed by plasticity theory, Rice (1968) developed the J-Integral method based on the assumption that for non-decreasing stresses, nonlinear elasticity theory can be used to effectively model plastic behavior. The J-Integral expression is a path-independent integral taken around the curve Γ (see Figure 2.4) is given as

$$J = \int_{\Gamma} (W dy - T_s \frac{\delta u}{\delta x} ds), \quad (2.51)$$

where J is the energy release rate, W is the strain energy density (given by

$W(x, y) = W(\epsilon) = \int_0^{\epsilon} \sigma_{ij} d\epsilon_{ij}$), T_s is the traction vector normal to ds , u is the displacement

vector, and ds is a small increment along the path Γ . As with other criteria, stable crack growth occurs for $J = J_c$ and unstable failure occurs when J exceeds the critical value J_c .

For linear elastic materials, Rice (1968) showed that the J-Integral is equal to the energy release rate per unit crack extension, i.e. $J = G = (K^2 / E)(1 - \nu^2)$.

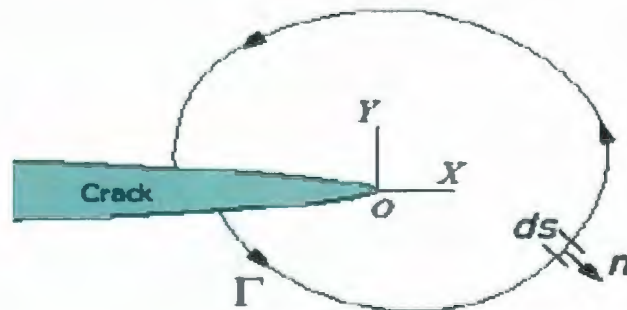


Figure 2.4: Illustration of J-Integral around the crack tip (Li, 2007).

Materials for which the fracture process zone is dominated by plasticity behavior require treatment by elasto-plastic fracture mechanics, such as the J-integral approach outlined

above. Materials in this category follow classical ductile behavior. Treatment of such materials is not given attention here, since ice is viscoelastic material. As discussed previously, for high strain rates the fracture behavior may be treated using LEFM. At lower strain rates, where creep and damage processes have sufficient time to activate, more involved methods, such as those developed by Schapery (1981) for damaging viscoelastic media, are required

2.4.3 J-Integral Theory for Nonlinear Viscoelastic Case

Schapery (1981, 1984) developed a constitutive model of nonlinear viscoelastic material behavior, which included the effects of distributed damage. This led to the development of a generalized J -Integral theory for analyzing fracture in damaging nonlinear viscoelastic materials. Note that this approach provides an exact solution and overcomes some of the limitations of the theory developed by Rice (1968), which approximated plasticity using nonlinear elasticity theory. Schapery's crack tip idealization is shown in Figure 2.5 below. As shown, in this model the crack tip is assumed to be straight with planar surfaces near the tip.

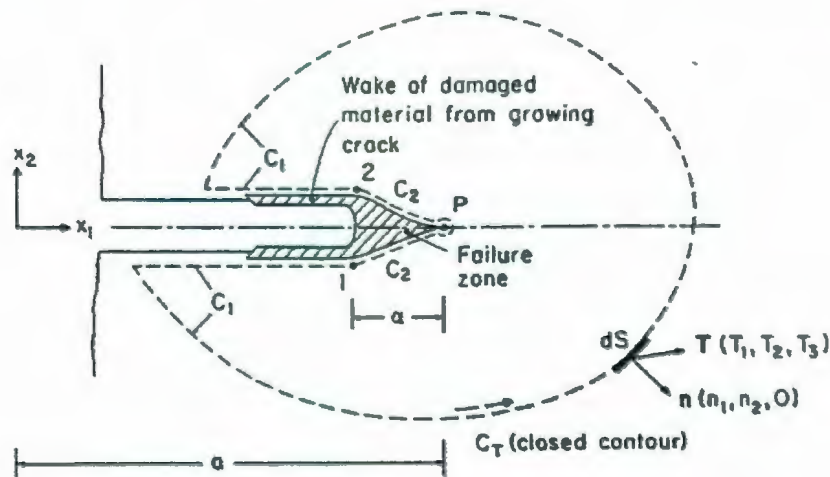


Figure 2.5: Illustration of Schapery's crack tip idealization (from Xiao, 1997).

The failure zone consists of a region of damaged material, which is thin relative to the crack length; as the crack grows a thin wake of damaged material remains along the crack surface.

As with the standard J-Integral approach, an arbitrary closed curve C_T encompasses the crack tip zone. The region inside C_T contains no cracks. As seen in Figure 2.5, for this model the curve is divided into two sections, C_1 and C_2 . The equilibrium equations for any arbitrary point inside the curve C_T is given by:

$$\frac{\partial \sigma_{ij}}{\partial x_j} + T_i = 0, \quad (2.52)$$

where the surface tractions T_i are given by:

$$T_i = \sigma_{ij} n_j, \quad (2.53)$$

The term n_j is the normal to the surface C_T . The stresses σ_{ij} may be expressed in terms of the displacements $u_{i,j}$ and a potential function W according to:

$$\sigma_{ij} = \frac{\partial W}{\partial u_{i,j}}. \quad (2.54)$$

Assuming body forces F_i act on the specimen, these may be expressed as a function of the body force potential W_F as:

$$F_i = -\frac{\partial W_F}{\partial u_i}. \quad (2.55)$$

Multiplying Eq. 2.52 by $-\partial u_i / \partial x_i$ and integrating the equation over the volume V enclosed by the surface C_T gives:

$$J \equiv \int_V \left[\frac{\partial}{\partial x_i} (W + W_F) - \frac{\partial}{\partial x_i} \left(\sigma_{ij} \frac{\partial u_i}{\partial x_j} \right) \right] dV. \quad (2.56)$$

Converting the volume integral in Eq. 2.56 to a surface integral gives:

$$J \equiv \int_{C_2} \left[(W + W_F) n_1 - T_i \frac{\partial u_i}{\partial x_1} \right] dS . \quad (2.57)$$

Relative to the crack length, if it is assumed that the failure zone is very thin in the x_2 direction, for the surface C_2 it may be assumed that $n_1 = 0$ and therefore $J \equiv J_v - J_f = 0$, and thus

$$J_v = J_f , \quad (2.58)$$

where

$$J_v = \int_{C_1} \left[(W + W_F) n_1 - T_i \frac{\partial u_i}{\partial x_1} \right] dS , \quad (2.59)$$

$$J_f = \int_{C_2} \left[T_i \frac{\partial u_i}{\partial x_1} \right] dS . \quad (2.60)$$

Equation 2.58 provides a basic relationship between the material outside the failure zone and failure material at the crack tip. As long as the curve C_1 contains no cracks, the integral J_v is independent of C_1 .

In modeling fracture in a nonlinear viscoelastic material, it is also important to analyze the speed and stability of crack growth. Starting with the case of proportional stressing, the stress σ_{ij} is assumed to be the product of a scalar proportionality σ and a constant tensor σ'_{ij} , given by

$$\sigma_{ij} = \sigma \sigma'_{ij} \quad (2.61)$$

From Figure 2.6 it is seen that the complementary strain energy W^c may be defined as

$$W^c = \int \epsilon d\sigma = \sigma \epsilon - W \quad (2.62)$$

where $W = \int \sigma d\epsilon$ is the strain energy.

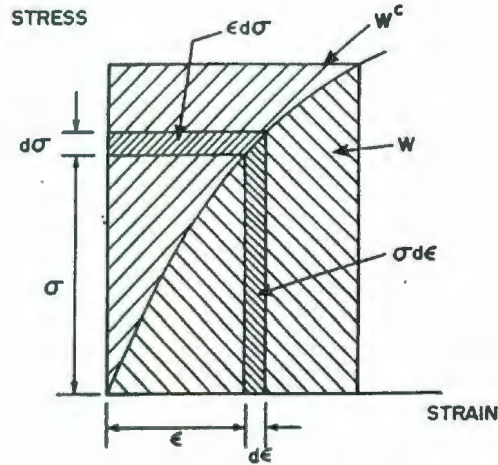


Figure 2.6: Non-linear elastic stress-strain curve, showing strain energy W and complementary strain energy W^c (from Xiao, 1997).

Assuming the strain is power-law nonlinear with stress (i.e. $\varepsilon = A\sigma^r$; r is a constant), W^c may be expressed as:

$$W^c = \int \varepsilon_{ij} d\sigma_{ij} = \int A\sigma_{ij}^r d\sigma_{ij} = A\sigma_{ij}^{r+1}/(r+1). \quad (2.63)$$

For proportional stressing, substitution of Eq. (2.61) into the above expression yields

$$W^c = |\sigma|^{r+1} A\sigma_{ij}'^{r+1}/(r+1) = |\sigma|^{r+1} \int \varepsilon_{ij} d\sigma_{ij}'. \quad (2.64)$$

Comparison of Eq. (2.64) and Eq. (2.63) reveals

$$W^c(\sigma\sigma_{ij}') = |\sigma|^{r+1} W^c(\sigma_{ij}'). \quad (2.65)$$

From Schapery (1981) we find that the J-Integral may be expressed as a function of the complementary strain energy, as given by

$$J = \frac{\partial W^c}{\partial a}, \quad (2.66)$$

since $J = -\partial W/\partial A$ (for a unit thickness, $\partial A = \partial a$) and $W^c = \sigma\varepsilon - W$. For a viscoelastic medium, inclusion of time dependence is required in the analysis. Schapery (1981, 1984) also showed that for nonlinear viscoelastic materials with power-law stress-strain behavior, a power-law relationship exists between the J-Integral J , and the crack growth speed \dot{a} . Here time is introduced through the crack growth speed \dot{a} (as opposed to the crack half length a typically used in elasticity). Similar power-law relationships were observed in experimental results (see for instance Atkin and Mai, 1985), which may be expressed in the form

$$\dot{a} = c_1 J^k, \quad (2.67)$$

where c_1 and k are constants. Substituting of Eq. (2.66) and subsequently Eq. (2.65) into Eq. (2.67) yields

$$\dot{a} = c_1 |\sigma|^{k(r+1)} \left(\frac{\partial W^c}{\partial a} \right)^k. \quad (2.68)$$

Schapery found that for penny-shaped cracks of radius a , it can be shown that $\partial W^c/\partial a \propto a$. On this basis Eq. (2.68) can be rewritten as

$$\dot{a} = c_1 (c_2 a)^k \sigma^q, \quad (2.69)$$

where c_2 is a constant and $q = k(r+1)$. Integration of Eq. (2.69) gives

$$\frac{a}{a_0} = \frac{1}{[1 - (k-1)(c_2 a)^{k-1} S]^{1/(k-1)}}, \quad (2.70)$$

where a_0 is the initial crack length and S (known as the Schapery damage measure) is the integral of stress history given by

$$S = \int_0^t c_1 \sigma^q d\tau. \quad (2.71)$$

Examination of Eq. (2.70) shows that the crack growth becomes unstable if the denominator tends to zero. This condition will occur when the term $(k-1)(c_2 a)^{k-1} S = 1$, which corresponds to

$$S = \int_0^{t'} c_1 \sigma^k d\tau = \frac{1}{(k-1)(c_2 a)^{k-1}}. \quad (2.72)$$

Thus unstable crack growth in a viscoelastic medium requires that time reaches a critical value (i.e. as t approaches a critical failure time t_f) or if the crack length is sufficiently large to cause the value of J to approach a critical value J_c . The effect of k on crack growth was explored by Jordaan and Xiao (1992); see Figure 2.7 (a).

For polycrystalline ice, Xiao (1997) suggests that microcracks grow incrementally (they are often arrested at grain boundaries) and the propagation time is small relative to the failure time t_f . Since variation occurs from crack to crack, the failure time t_i for the i^{th} crack is given as:

$$S_i = \int_0^{t_i} c_1 \sigma^k d\tau. \quad (2.73)$$

As the crack grows, the energy released (i.e. a decrease of strain energy) will result in an increase in the complementary strain energy W^c . Correspondingly, each microcrack results in a small jump in the complementary strain energy, as is illustrated in Figure 2.7 (b). For small microcracks damage mechanics assumes that the effects of individual cracks are sufficiently small that they may be 'smeared out'. Consequently, in the macro-scale the damage process may be modeled as a smooth function. The summation of S_i associated with each microcrack yields the total damage S , as given by Eq. (2.73). On the basis of the above analysis Schapery (1981, 1984) developed a measure of damage S that links damage theory with fracture mechanics for viscoelastic materials. As shown in Figure 2.7 (b), for larger fractures (i.e. a spall), a large jump in W^c occurs. Since such a large jump violates the assumption of a smooth function, the effects of macroscale fracture must be treated using a different approach than damage mechanics.

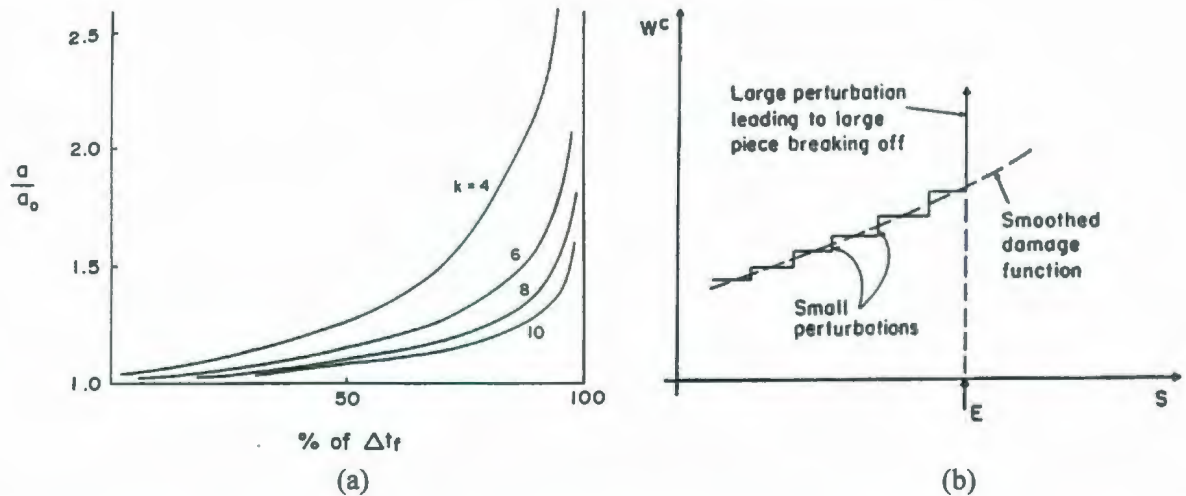


Figure 2.7: (a) Time dependent crack growth during instability for different values of k ; (b) change of complementary strain energy with increasing damage; event E represents a large fracture event, such as a spall, resulting in a large jump in W^c (Jordaan and Xiao, 1992).

2.5 Statistical Approach to Fracture

The statistical treatment of fracture (see for instance, Bolotin, 1969; Freudenthal, 1968) has been applied to a variety of materials, such as ceramics (Batdorf and Heinisch, 1978; Evans, 1979), glass (Reid, 1991), concrete (van Mier, 1997; Bazant and Planas, 1998), and ice (Maes, 1986, 1992). Statistical treatment of fracture is of particular interest in terms of the scale effect, since the probability of encountering larger flaws in the more highly stressed regions increases with specimen size.

Jayatilaka and co-workers have studied various aspects of statistical fracture in brittle media and examined the applicability of Weibull analysis for a specimen containing a single crack subject to uniform tensile stress (see for instance Jayatilaka and Trustrum, 1977). In this work, the stress required to propagate an inclined crack is determined using a strain energy density criterion. To explore the relationship between the flaw size distribution and Weibull modulus, a uniform distribution of crack angle was used, and several assumed distributions of flaw sizes were considered. A main conclusion of this work is that the failure stress distribution is sensitive to flaw size, but insensitive to the particular type of distribution and Weibull analysis is appropriate for all types of flaw size distributions considered (power law,

gamma, lognormal and normal). The relationship between the Weibull modulus and the flaw size distribution was observed to change for different distributions. For power law distributions, it was concluded that the Weibull modulus is directly related to the flaw size distribution. For lognormal distributions, the Weibull modulus was found to depend on the number of cracks (e.g. volume) and a parameter of the flaw size distribution. For exponential, gamma or normal distributions, the Weibull modulus was found to depend only on the logarithm of the number of cracks. Since the number of cracks is proportional to the volume, this implies that for these distributions the probability of failure is proportional to the volume. This work, in combination with the above cited articles, provides a good starting point for the development of a probabilistic fracture model. A more detailed review of weakest-link theory is provided below.

2.5.1 Weakest-Link Theory

Probabilistic failure theories are considered the most appropriate umbrella under which to develop models. Since fractures play a strong role in compressive failure, we consider briefly tensile failure (Figure 2.8). We may consider failure of a brittle solid to result from the propagation of a crack from the most dominant flaw. The 'weakest-link' model (Weibull, 1951) is essentially a chain. If T_i is the (random) strength of the i^{th} element or link, the strengths of the elements are considered to be independent and identically distributed (*iid*) with distribution function $F_r(t)$, for each of the $i = 1, \dots, n$ links of the chain. Failure of the chain occurs when the weakest link fails. We denote this value as W . Thus

$W = \min(T_1, T_2, T_3, \dots, T_n)$, and for *iid* random quantities,

$$F_w(w) = 1 - [1 - F_r(w)]^n = 1 - \exp\left\{-\frac{v}{v_0} \ln[1 - F_r(w)]\right\}. \quad (2.74)$$

For large n , this tends to the following asymptotic distribution:

$$F_w(w) = 1 - \exp\left\{-\frac{v}{v_0} \left(\frac{w - w_0}{w_1}\right)^a\right\}, \quad w \geq w_0. \quad (2.75)$$

Weibull arrived at this equation by suggesting the use of a material function

$m(w) = [(w - w_0)/w_1]^\alpha$ to represent the expression $\{-\ln[1 - F_T(w)]\}$ within Equation

2.74. In this expression, w_1 and α are constants representing the scale and shape parameters respectively; v_0 is a reference volume (i.e. the volume of a standard test specimen subjected to homogeneous stress state). Because of the asymptotic result, there is considerable basis for Weibull's theory: we can interpret it as the asymptotic distribution of the minimum of a set of random strengths with a lower minimum value w_0 .

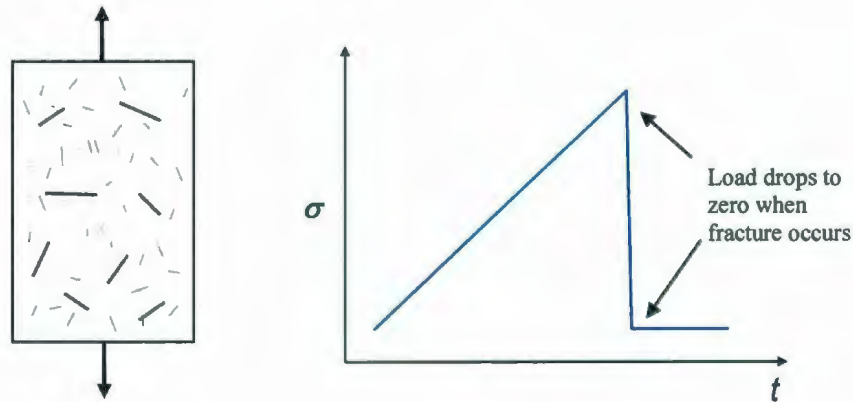


Figure 2.8: Specimen in tension; failure results in total loss of strength.

For compressive failure, the occurrence of a fracture event will lead to a drop in load, but not necessarily to zero. This fundamental difference between compressive and tensile failure necessitates re-examination of the underlying assumptions of the 'weakest link' model.

Scale effects are associated with this theory. From the mean value of W with $w_0 = 0$, we may compare the expected strength $\langle R \rangle$ of two volumes v_1 and v_2 :

$$\frac{\langle R \rangle_1}{\langle R \rangle_2} = \left(\frac{v_2}{v_1} \right)^{\frac{1}{\alpha}}. \quad (2.76)$$

Investigation of the scale effect associated with weakest-link theory and that observed for ice represents an important aspect of proposed modeling efforts.

2.5.2 Complex Stress States and Reduced Volume Formulation

As a starting point we consider the heuristic material function suggested by Weibull (1951), which is based on a power-law equation

$$m(\sigma) = \left(\frac{\sigma - \sigma_0}{\sigma_1} \right)^\alpha, \quad (2.77)$$

where α , σ_0 , and σ_1 are constants. The term σ_0 represents a lower limit on strength, which is often taken as zero, giving the simplified function

$$F_w(\sigma) = 1 - \exp \left[-\frac{1}{v_0} \sum_{i=1}^n \left(\Delta v_i \left(\frac{\sigma(x_i)}{\sigma_0} \right)^\alpha \right) \right], \quad (2.78)$$

where the proportional stressing is assumed (i.e. $\sigma = r \cdot \phi(x_i)$),

$$m(\sigma) = \left(\frac{r \cdot \phi(x_i)}{\sigma_1} \right)^\alpha. \quad (2.79)$$

Substituting this material function into Eq. 2.78 and simplifying gives:

$$F_w(\sigma) = 1 - \exp \left[-\frac{1}{v_0} \left(\frac{r}{\sigma_1} \right)^\alpha \int_V \phi^\alpha(x_i) dv \right]. \quad (2.80)$$

To account for the effects of an inhomogeneous stress state, the concept of ‘reduced volume’ v_r may be used (see for instance, Jordaan, 2005). From the above expression it may be seen that $F_w(w)$ represents the probability of that the material fails at the given level of stress. In other words, it is the probability that all elements in the stressed volume survive at the current stress level. For stress distributions with analytical solutions, the integral form of the reduced volume expression may be solved to give a direct solution. For more complex stress fields, the approach of Hunt and McCartney (1979) may be used in combination with finite element analysis to estimate failure probabilities. The ‘reduced volume’ is defined as

$$v_* = \int_V \phi^\alpha(x) dv. \quad (2.81)$$

Using this definition, Eq. 2.80 may be simplified to give

$$F_w(w) = 1 - \exp\left\{-\frac{v_*}{v_0} \left(\frac{r}{\sigma_1}\right)^\alpha\right\}. \quad (2.82)$$

The terms α and σ_1 are known as the scale and shape parameters, respectively. The scale effects associated with this formulation are the same as that given by Eq. 2.76, except reduced volumes are used.

Chapter 3: Review of Ice Mechanics

3.1 Scope

This chapter is focused on a review of relevant ice mechanics literature. Ice properties and behavior have been summarized, including a discussion of viscoelasticity and creep behavior. A review of damage processes observed at different loading rates has been given, along with a discussion of the role of damage in *hpz* behavior. Approaches to modeling damage in ice have been reviewed and a discussion of crack nucleation and modes of fracture has been given. Since global fracture (radial and circumferential cracking) cannot be relied upon to always occur or to reduce loads if they do occur, spalling fracture plays a crucial in limiting the extreme loads of interest in design. Spalling fracture and relevant theoretical models have been reviewed in detail. Recommendations were made regarding the approach identified as being most appropriate for modeling probabilistic aspects of spalling behavior.

3.2 Ice Properties and Behavior

3.2.1 Overview

Ice is an intriguing and complex material. Understanding fundamental material behavior, as well as the associated mechanics during ice-structure interaction is requisite in the development of ice load models. As discussed briefly in Chapter 1, site- and season-specific information about physical and mechanical properties are required for the design of structures for ice conditions. In typical offshore engineering applications, two different types

of ice exist: glacial ice and sea ice. Glacial ice found in the marine environment calves from freshwater, land-based glaciers where it has formed from perennial snow accumulation. The most commonly observed forms of glacial ice are icebergs or ice islands. Sea ice forms as a result of the seasonal cooling and freezing of sea water. Information about ice microstructure, formation processes, morphologies, physical and mechanical properties are readily available in the open literature and will not be discussed in this review; the reader is referred to Pounder (1965), Hobbs (1974), Michel (1978), Sanderson (1988), and Cammaert and Muggeridge (1988). The work discussed here is focused on the failure of ice sheets (freshwater, first-year sea ice and multi-year sea ice); other morphologies will not be considered.

3.2.2 Viscoelasticity and Creep Behavior of Ice

Ice is a viscoelastic material. For any level of stress, ice will exhibit time-dependent strain. Similarly, when subjected to a fixed strain, ice will exhibit a time-dependent stress relaxation. The time dependence of the stress and strain behavior of ice is reflected in Figure 3.1 and Figure 3.2 respectively. From Figure 3.1 it may be seen that for ice deformed under constant strain rate, increasing the strain rate increases the peak stress.

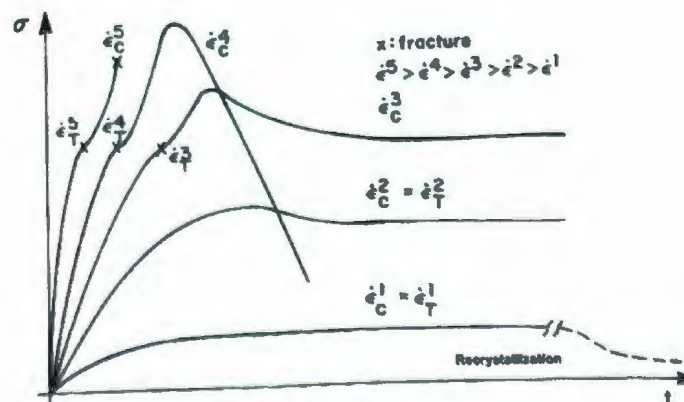


Figure 3.1: Typical constant strain rate creep curves for ice (Nadreau and Michel, 1984).

For low strain rates, the behavior is pure creep and ice behaves similarly under tensile and compressive loading. For intermediate strain rates, pressure softening resulting from the activation of microstructural ‘damage’ processes (microcracking, recrystallization) in the

post-peak region. In this range of strain rates the compressive failure behavior begins to deviate from that of the tensile case. As strain rate is increased further the failure mode changes to brittle fracture behavior. Fracture failure is governed by the nucleation and propagation of cracks in the specimen. As discussed in later sections, the primary mechanisms of compressive crack growth depend on induced shear and tensile stresses, necessitating a higher overall compressive load to activate these mechanisms. As a result, higher failure strength is generally observed for compression than tension (Sanderson, 1988).

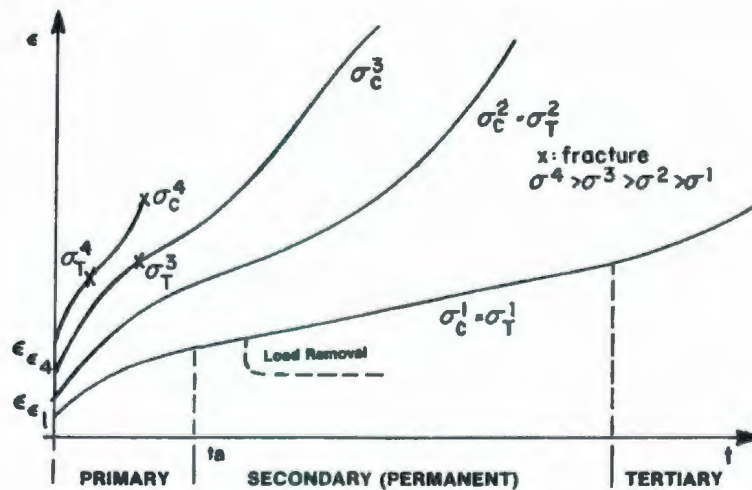


Figure 3.2: Typical creep curves for ice under constant stress (Nadreau and Michel, 1984).

Ice subjected to constant stress deforms instantly as a result of instantaneous elastic strain (shown as a jump on the strain axis at time equal to zero), which is followed by time-dependent creep behavior; see Figure 3.2. This creep behavior is typically divided into three components: primary creep, secondary creep and tertiary creep.

Primary creep is associated with time-dependent delayed elastic strain resulting from reversible grain boundary sliding due to shear stresses at grain boundaries. This creep component occurs in conjunction with elastic deformation of the grain; if compressive stresses are removed the grain tries to recover its undeformed shape (Sanderson, 1988). Secondary creep is the irrecoverable (flow) component of creep behavior and is highly non-linear and time-dependent, since ice creeps at all stresses and shows no yield point. Secondary or steady-state creep results in permanent deformation processes within the ice leading to irreversible rearrangement of the material. The primary mechanism associated

with secondary creep is dislocation glide and climb. Tertiary creep results from damage processes, which soften the ice and accelerate strain-rates. The mechanisms typically associated with this behavior are microcracking and dynamic recrystallization.

Jordaan and McKenna (1988) used a Burgers model to represent the viscoelastic behavior of ice. As shown in Figure 3.3, a Burgers model consists of a Maxwell unit and a Kelvin unit in series.

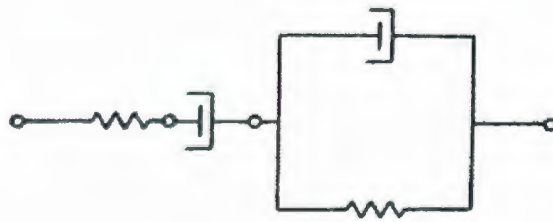


Figure 3.3: Burgers model consisting of a Maxwell unit and Kelvin Unit in Series

In this model, the instantaneous elastic strain is represented by the spring of the Maxwell unit, while the Kelvin unit represents the delayed elastic strain component. The viscous strain is modeled by the dashpot of the Maxwell unit. In this model, the total strain ε is the sum of the instantaneous elastic strain ε^e , the delayed elastic strain ε^d , and the viscous strain ε^v , as given by

$$\varepsilon = \varepsilon^e + \varepsilon^d + \varepsilon^v. \quad (3.1)$$

This model has been used successfully to model ice behavior by Jordaan and Xiao (1992), Xiao (1997), Li (2007) and others. Xiao (1997) examined the use of multiple additional Maxwell units in series to provide a more accurate model, but encountered difficulties in calibrating the parameters for this more complex model. Each of these components is discussed below.

For an isotropic medium, elastic behavior may be expressed in terms of two constants: Young's modulus E and Poisson's ratio ν . The instantaneous elastic strain ε^e may be defined according to Hooke's law and as expressed as

$$\varepsilon^e = \frac{\sigma}{E}. \quad (3.2)$$

The delayed elastic strain term ε^d represents a completely recoverable portion of the strain. Once the specimen is unloaded, this component of strain will recover after sufficient time. This strain component is associated with grain boundary distortion and basal plane sliding as a result of shear stresses between grain boundaries. The model developed by Sinha (1979, 1982) is based on viscoelastic theory for constant, monotonic uniaxial loading and is dependent on grain size and temperature. Sinha's equation for delayed elastic strain is

$$\varepsilon^d = \frac{cd_1}{d} \left(\frac{\sigma}{E} \right)^s [1 - \exp(-(\alpha_T t)^b)], \quad (3.3)$$

where d_1 is a unit grain size, and c, s, α_T and b are constants (α_T is dependent on temperature T). Jordaan and McKenna (1988) proposed a phenomenological model for delayed elastic strain. Their model is based on the assumption that the viscous coefficient of the dashpot of the Kelvin unit could be modeled as having a power-law dependency on stress. They modeled the delayed elastic strain using the expression

$$\varepsilon^d = \frac{\sigma}{E_K} [1 - \exp\{-\int_0^t \frac{1}{\mu_K \sigma_d} d\tau\}], \quad (3.4)$$

where $\int_0^t \frac{1}{\mu_K \sigma_d} d\tau$ is called the reduced time or pseudo time.

The viscous component of strain is the permanent component of the total strain. This mechanism is associated with the movement of dislocation within ice grains. This component of creep behavior is modeled using the widely accepted power-law creep equation known as Glen's law, based on the work of Glen (1955) and expressed as

$$\dot{\varepsilon}^v = A\sigma^n. \quad (3.5)$$

In this expression, n is a material constant and A is a shift factor of temperature given by

$$A = B \exp(-Q/RT), \quad (3.6)$$

where B is a material constant, Q is the activation energy, R is Boltzman's constant ($R=8.314 \text{ J mol}^{-1}\text{K}^{-1}$) and T is the absolute temperature. Later work by Barnes et al. (1971) suggests that Glen's law is appropriate only for low stresses. Laboratory experiments by Sinha (1978) confirmed that for small strain levels ice follows the thermorheologically simple principle and that Glen's law is appropriate for these conditions. This principle refers to behavior of materials for which known behavior at a given temperature can be used to determine material behavior at other temperatures using a shift factor expression, such as the one given in Equation 3.6. To reflect this principle, Sinha related the viscous strain and stress at a given temperature to a reference strain $\dot{\epsilon}_0^v$ and reference stress σ_0 using the following expression

$$\dot{\epsilon}^v = \dot{\epsilon}_0^v (\sigma / \sigma_0)^n. \quad (3.7)$$

Results presented by Meglis et al. (1999) indicate that under higher confining pressures, dynamic recrystallization is an important factor resulting in the enhancement of creep rate. These findings support earlier work by Jonas and Muller (1969), who modeled the effects of dynamic recrystallization on strain rate of ice under high stresses using the expression

$$\dot{\epsilon} = \phi_f \exp\left(-\frac{\Delta H}{KT}\right) \exp\left(\frac{v[\tau - \tau_B]}{KT}\right). \quad (3.8)$$

In this expression ϕ_f is a structure factor, ΔH is the activation enthalpy in the presence of hydrostatic pressure, v is the activation volume, τ is the shear stress and τ_B is the internally generated back stress. Findley et al. (1976) and Schapery (1997) also prepared similar viscoelastic models.

For higher loading rates, delayed elastic and viscous strain components become less dominant, particularly in the far field, since there is insufficient time for the mechanisms associated with these behaviors to activate. Under such conditions, the elastic component of ice behavior tends to dominate, with failure generally resulting from brittle fracture, rather

than the creep mechanisms associated with lower loading rates. Under such conditions, it is reasonable to treat ice in the far field region as a brittle elastic medium. Unlike the far field zone, the damage layer at the interaction interface which forms during crushing exhibits localized pressure softening behavior. To capture this localized behavior in the *hpzs*, ice has been modeled using a damaging nonlinear viscoelastic model (see for instance Xiao, 1997). The effects of this damage layer are an important aspect of crushing failure at high strain rates; the effects of localized damage will be explored later.

3.2.3 Elastic Ice Response for Fast Loading Rates

For the purpose of the present research, initial models will be developed based on freshwater granular ice, and thus isotropic behavior will be assumed. This is seen as a reasonable starting point since the properties of freshwater ice are better known, and results can be more easily validated (Timco, 1987). This has the added advantage of simplifying model development. For full-scale ice sheets, Sanderson (1988) suggested that multiyear ice may be modeled as statistically isotropic as a result of its random microstructure and very low bulk salinity. This is also valid for iceberg (glacial) ice, since it has granular microstructure and is formed from fresh water. For the ductile behavior of sea ice, Sanderson (1988) used temperature and brine volume corrections to relate the bulk properties of sea ice to that of pure ice. For behavior in the brittle range, the effect of brine pockets, microstructure or other such defects may be treated as a statistical distribution of flaws. For columnar ice the grain boundaries may be preferentially oriented, which may be modeled using appropriate modifications to the flaw distribution model. In the present work, flaw orientation is modeled as being random, due to randomness of grain boundary orientations for granular ice.

Of relevance to grain-scale modeling is the work of Schapery (1997), as he showed that the elastic behavior of an individual ice crystal is approximately isotropic. On this basis, ice will initially be modeled as an isotropic elastic material. For isotropic behavior the elasticity of ice can be characterized by two parameters: Young's modulus E and Poisson's ratio ν . The elastic strain is defined according to Hooke's law, as expressed in Equation 3.2.

The classical approach for determining Young's modulus is based on determining the slope of the initial tangent of the stress-strain curve for a very rapid test. Since ice tends to creep for any level of stress, this is not an accurate approach for quantifying the Young's modulus of ice. High frequency measurement systems (see for instance Mellor, 1983) have been used to provide better estimates of these parameters. Glen (1975) developed temperature dependent equations for E and ν based on his study of the effects of temperature on the behavior of ice. Subsequent work by Sinha (1978) determined that temperature effects were not significant and thus could be neglected. Mellor (1983) reported E values in the range of 9 GPa to 9.5 GPa and ν in the range of 0.3 to 0.33 for polycrystalline ice in the temperature range $-10\text{ }^{\circ}\text{C}$ to $-5\text{ }^{\circ}\text{C}$. Sinha (1989) studied the properties of ice over a temperature range of $0\text{ }^{\circ}\text{C}$ to $-50\text{ }^{\circ}\text{C}$ and reported values of Young's modulus varied from 9 GPa to 10.16 GPa and Poisson's ratios varied from 0.308 to 0.365.

3.3 Microstructural Damage in Ice

During the deformation process, ice may undergo microstructural modification, which can result in changes to the constitutive behavior of the material. The term 'damage' is used since these microstructural modifications represent changes to the material which impair its mechanical properties. These processes are generally irreversible, since entropy tends to increase during the damage process. The processes associated with microstructural damage include microcracking, dynamic recrystallization and pressure melting.

3.3.1 Damage Processes at Slow Loading Rates

As illustrated in Figure 3.4 (a), the creep affected zone corresponds to the stressed volume of material near the interaction area. The principal mechanism responsible for steady-state creep behavior is dislocation glide and where necessary for compatibility, dislocation climb; see Figure 3.4 (b). During ductile failure, pressure across the face of the indenter tends to be more uniformly distributed (i.e. non-simultaneous aspects are less dominant) compared with brittle failure.

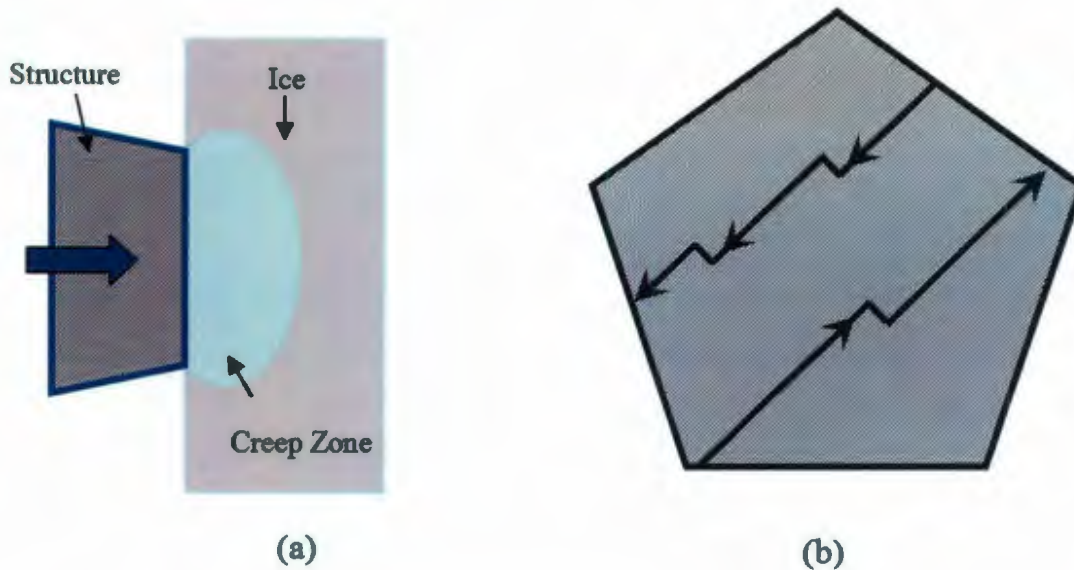


Figure 3.4: Schematic representation of: (a) creep zone during very slow loading;
 (b) dislocation glide (and climb) in grain (after Sanderson, 1988)

As the rate of loading increases, dislocation mechanisms can no longer completely dissipate all of the input strain energy. Dislocations begin to pile up at grain boundaries, particularly in zones where three grains intersect. This dislocation pile-up may contribute to the formation of microcracks or other microstructural modification. In zones of high dislocation density at high temperatures, dynamic recrystallization may result in extensive local rearrangement and disappearance of dislocations resulting in the formation of new, undeformed grains (Sanderson, 1988). During triaxial testing of ice, Meglis et al. (1999) observed similar dynamic recrystallization behavior for ice under high confining pressures. As loading rate increases, fracture and the effects of microstructural change become more dominant. The irrecoverable component of creep becomes particularly enhanced. Damage processes result in the formation of a damage enhanced creep (tertiary creep) zone in the contact region near the indenter; see Figure 3.5.

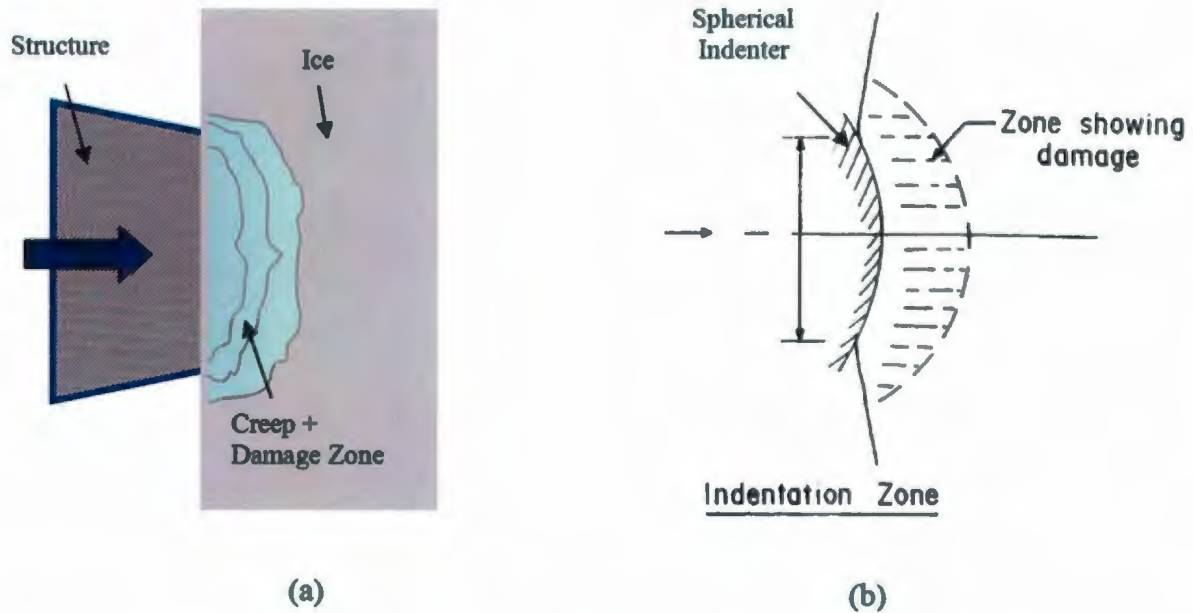


Figure 3.5: Schematic representation of: (a) creep and damaged zone at slow speeds; (b) slow (0.03 cm/s) test results from Hobson's Choice Ice Island experiments (Frederking et al., 1990).

From Hobson's Choice medium-scale experiments, Frederking et al., (1990) reported that during a test with an indentation rate of 0.03 cm/s, a permanent depression with evidence of substantial damage in the vicinity of the indenter was observed. This is illustrated in Figure 3.5 (b). Neither ejection of ice nor localized spalling was observed under these conditions, though a large spall crack did occur. Thin sections of the indentation region revealed significant recrystallization, indicating the presence of a damage zone, but no distinct layer was formed. Similar ductile failures were observed for slow speed tests during Rae Point experiments (Masterson et al., 1999). Results shown in Figure 3.6 for an indentation speed of 0.03 cm/s depict the formation of a permanent depression, with some localized radial cracking near the indentation zone. There are no signs of crushing and ejection or localized spalling of material at this speed, though a damaged region is observed behind the indentation zone.



Figure 3.6: Ductile failure observed for slow test ($v = 0.03$ cm/s) during Rae Point experiments with 1 m^2 spherical indenter (Masterson et al., 1999).

3.3.2 Damage Processes at High Loading Rates

As the rate of loading is further increased, the failure mode changes from ductile to brittle behavior. Damage zones develop into highly damaged layers, and failure results from the crushing and extrusion of pulverized ice. Localized spalling and damage processes lead to the formation of *hpzs* through which most of the force is transmitted. The observation of the damage layer was first reported by Kheisin and Cherepanov (1976) for drop tests conducted using a 300 kg steel ball to impact the surface of an ice sheet. In these tests, microcracking along the basal plane was observed to be an important mechanism.

During medium scale indentation tests at Hobson's Choice Ice Island (Frederking et al., 1990), an extensive white layer of crushed material with occasional 'blue' recrystallized zones was observed (Jordaan, 2001). In these tests, a distinct boundary between the damaged ice and parent ice was visible at some depth from the contact interface, with evidence of

lateral grain motion along the boundary. Muggeridge and Jordaan (1999) also reported observations of a layer of fine-grained and microcracked ice in thin sections of ice samples collected from full-scale iceberg impact tests conducted on Grappling Island, Labrador (Crocker et al., 1997). Muggeridge and Jordaan (1999) describe the “crack-like” layer boundary as being similar to an extrusion plane, where grains within the zone are forced toward the free surface. Similar results for brittle tests during the Rae Point experiments were reported (Masterson et al., 1999).

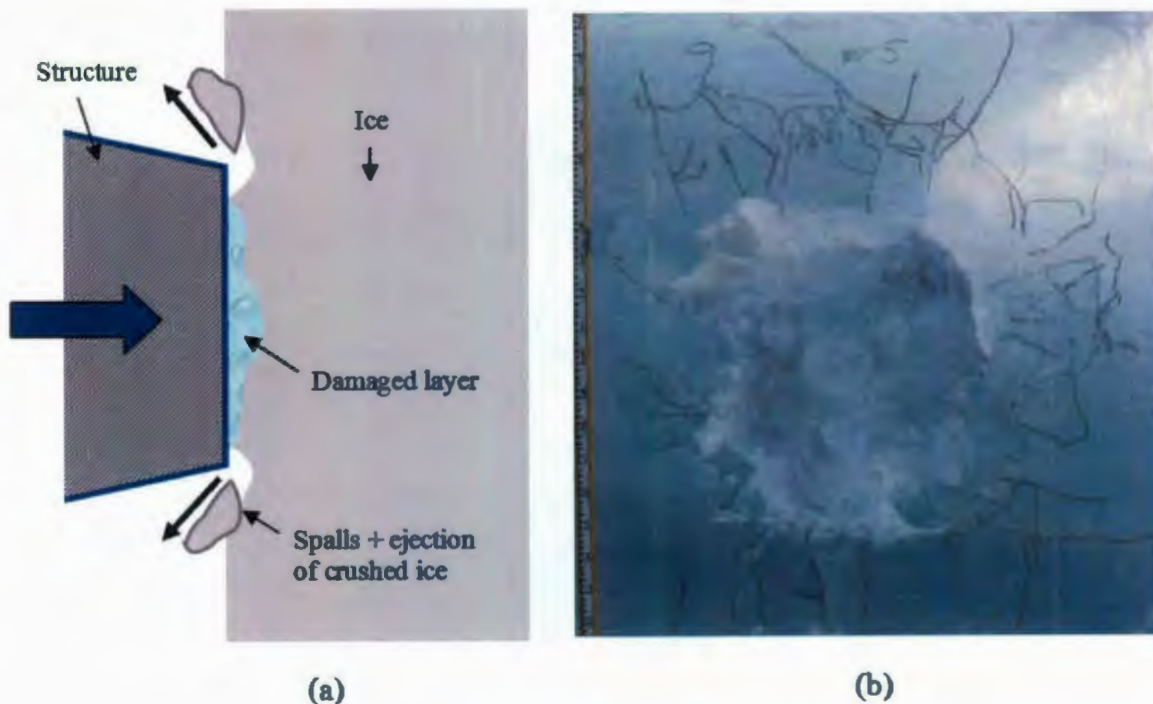


Figure 3.7: (a) schematic of brittle failure at higher loading rates; (b) brittle failure observed for fast test ($v = 1.0 \text{ cm/s}$) during Rae Point experiments with 1 m^2 spherical indenter (Masterson et al., 1999).

As shown in Figure 3.7, spalling and extensive microcracking are prevalent in outer areas of the indentation zone where the ice is subject to high shear and low confining pressures. In the interior regions, which are more highly confined, microcracking and recrystallization accompanied by pressure softening is in evidence. Results of triaxial experiments reported by Meglis et al. (1999) suggest that localized pressure melting may also be a contributing factor in regions of high confinement. Brittle failure is inherently more random, due to the complex

relationship between flaws, fracture and damage processes. As a result, non-simultaneous aspects of the pressure distribution are more dominant for brittle-type failure than for ductile mode. The interplay between damage and fracture has been explored by Jordaan and Xiao (1992), Xiao (1997) and Li (2007) and remains an important area of ice research. The mechanisms associated with damage (microcracking, dynamic recrystallization and pressure melting) are explored further in the sections below. A review of relevant aspects of damage mechanics and their application to ice is presented later in the chapter.

Dynamic Recrystallization

Passchier and Trouw (2005) suggested that grain boundary mobility can serve as a mechanism to lower free energy through the reduction of dislocation densities in deformed polycrystalline materials. The reorganization of material into different grain shapes, orientations, and sizes is known as recrystallization (Vernon, 1981). The term dynamic recrystallization refers to the process of recrystallization which is associated with the progress of deformation; otherwise it is referred to as static recrystallization (Xiao, 1997). Urai et al. (1986) described several ways which dynamic recrystallization affects the mechanical properties of a material. Of most relevance to ice are: (1) changes (increases or decreases depending on stress level) in grain size; (2) changes of grain boundary structure; (3) changes in dislocation density and sub-structure. These effects will result in enhanced ductility and softening (compliance) in the material, resulting in the development of shear zones and strain localization. Material softening effects, in terms of the creep compliance, are more substantial when grain size is reduced, which is governed largely by the flow stress (Xiao, 1997).

Dynamic recrystallization processes resulting from grain boundary formation or migration may result in either a decrease or an increase in grain size. Poirier (1985) modeled the grain size of new grains generated as a result of recrystallization using the expression

$$\frac{D}{b} = K \left(\frac{\sigma}{\mu} \right)^{-r} \quad (3.9)$$

where b, K, μ , and r are constants. For creep loading, the dynamic recrystallization process is a discontinuous one. Duval et al. (1983) discuss the possible role of dynamic recrystallization in creep enhancement observed in ice. During creep loading, a wave of accelerated creep will result from a discontinuous wave or burst of recrystallization. As the strain rate increases, discontinuities disappear leading to a more continuous dynamic recrystallization process, resulting in more pronounced softening effect.

Urai et al. (1986) discussed the driving forces behind dynamic recrystallization and identified four key contributors. These include internal energy sources such as chemical free energy, surface energy of grain boundaries, and intragranular lattice defect energy, as well as elastic energy due to external loading. When waves of recrystallization sweep through old grains, the new grains often have fewer dislocations and straighter grain boundaries resulting in lower free energy (Passchier and Trouw, 2005). Jonas and Muller (1969) studied the deformation of monocrystalline and polycrystalline ice sampled subjected to high internal shear stresses. In their analysis, the authors modeled the influence of dynamic recrystallization on strain rate according to Equation 3.8. The authors conclude that during the deformation of ice, dynamic recrystallization can be initiated once a temperature and applied stress dependent critical strain has been exceeded. For conditions of very low shear stresses, dynamic recrystallization may be avoided.

For intermediate stress states, dynamic recrystallization occurs periodically, resulting in intermittent increases in strain rate. For higher states of stress, a single increase in strain rate is expected as a result of continuous recrystallization, which follows after a period of conventional creep flow. This accumulation of grain dislocations may result from the formation of kink bands in ice grains as a result of different stress states within a crystal. Results presented by Meglis et al. (1999) show that dynamic recrystallization, along with pressure melting, play an important role in the enhancement of creep in ice under higher confining pressures.

Wei and Dempsey (1991) also observed new grain boundaries formed on the fracture surfaces of ice specimens. The growth of these new boundaries was attributed to a 'kinking'

mechanism, and highlights that new grains can form even during very fast processes like brittle crack propagation.

Pressure Melting

For ice subject to high confining pressures, pressure melting and dynamic recrystallization are dominant mechanisms associated with deformation processes. The pressure melting behavior of ice has been studied by a number of authors; see Nordell (1990) for data references. Experimental data for the relationship between melting pressure and temperature is given in Figure 3.8.

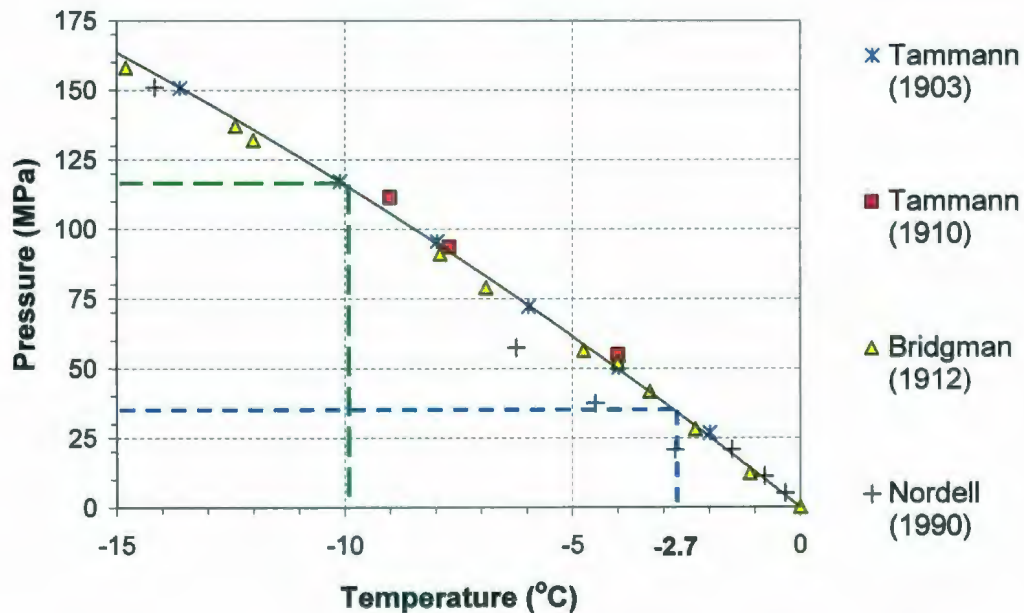


Figure 3.8: Plot of pressure melting data for ice (after Nordell, 1990).

From the above plot it may be seen that pressure melting corresponds to approximately 120 MPa at -10 °C and at approximately 35 MPa at -2.7 °C. Hobbs (1974) suggested that the pressure melting behavior may be modeled on a thermodynamic basis according to the expression

$$\frac{dT_m}{dp} = \frac{(v_w - v_i)}{(s_w - s_i)}, \quad (3.10)$$

where T_m is the melting temperature, p is the melting pressure, v_w is the specific volume of water, v_i is the specific volume of ice, s_w is the entropy of water and s_i is the entropy of ice. From the second law of thermodynamics we see that the denominator of the right-hand term of Equation 3.10 must be positive, while the numerator is negative, since the density of ice is less than the density of water. This suggests that the melting temperature of ice is inversely proportional to pressure, which is in agreement with Figure 3.8. This may also be modeled using the Clausius-Clapeyron equation

$$dT_m = -A dp, \quad (3.11)$$

where A is a temperature dependent constant. For ice at -10°C , $A = 0.0833^\circ\text{C/MPa}$ and at 0°C , $A = 0.0743^\circ\text{C/MPa}$. Results presented by Meglis et al. (1999) and Muggeridge and Jordaan (1999) suggest that pressure melting is in evidence for ice tested under triaxial conditions and also in the damage layer during full-scale indentation tests, respectively.

3.3.3 High Pressure Zones and Damage Failure

During higher speed ice-structure interactions the majority of the force will be transferred to the structure through a series of relatively small zones of high pressure. In their analysis of tactile sensor data from the JOIA MS-FIT program, Taylor et al. (2008) reported that contact only occurred over a region of the order of about 10% of the global interaction area, with no load acting over the remaining area.

The peaks of these *hpzs* vary in both time and location throughout the interaction and are influential in the evolution of the interaction since their presence is linked with localized spalling, damage and softening processes. When *hpzs* occur near the edge of an ice-sheet large-scale spalling fractures can be precipitated. These fracture events significantly reduce the load that is felt by the structure (Jordaan, 2001).

Under compression, high-pressure zones form at all but the slowest interaction speeds. As illustrated Figure 3.9, spalls play an important role in the compressive failure process. A consequence of spalling fracture is to limit load build-up during interaction; this is of

particular importance for ice load modeling. Croasdale (1975) and Croasdale et al. (1977) were first to introduce his line of thinking.

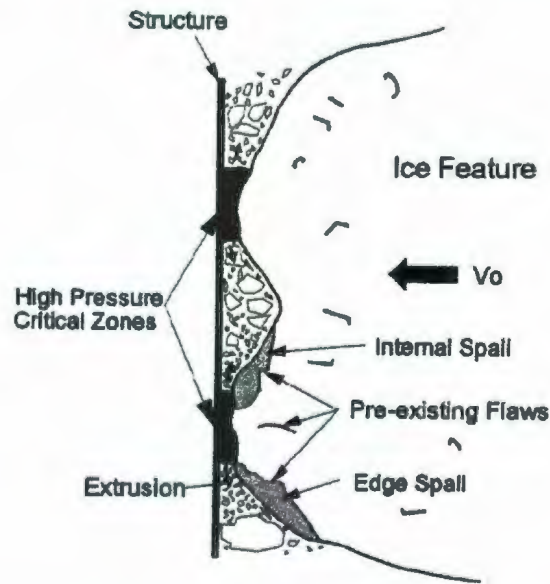


Figure 3.9: Wide interaction area, showing possible internal spall. (Jordaan, 2001).

In the vicinity of the *hpz*, damaged ice forms in a layer. In the center of the *hpz*, where confining pressures are highest, the damaged layer likely consists of a region of recrystallized and pressure-melted ice. Towards the edges of the *hpz* the confining pressures are lower and highly micro-cracked and crushed ice is present. This crushed ice is often extruded away from the interaction area leading to dynamic loading.

Crushing behavior has been studied at both the small and medium scales (for example Barrette et al., 2002; Frederking et al., 1990). Crushing activity observed at these reduced scales agrees well with behavior found during full-scales ice-structure interactions, such as during the deployment of the Molikpaq. Figure 3.10 shows examples of characteristic spalling, pulverization and extrusion behavior observed during small, medium and full-scale interactions.

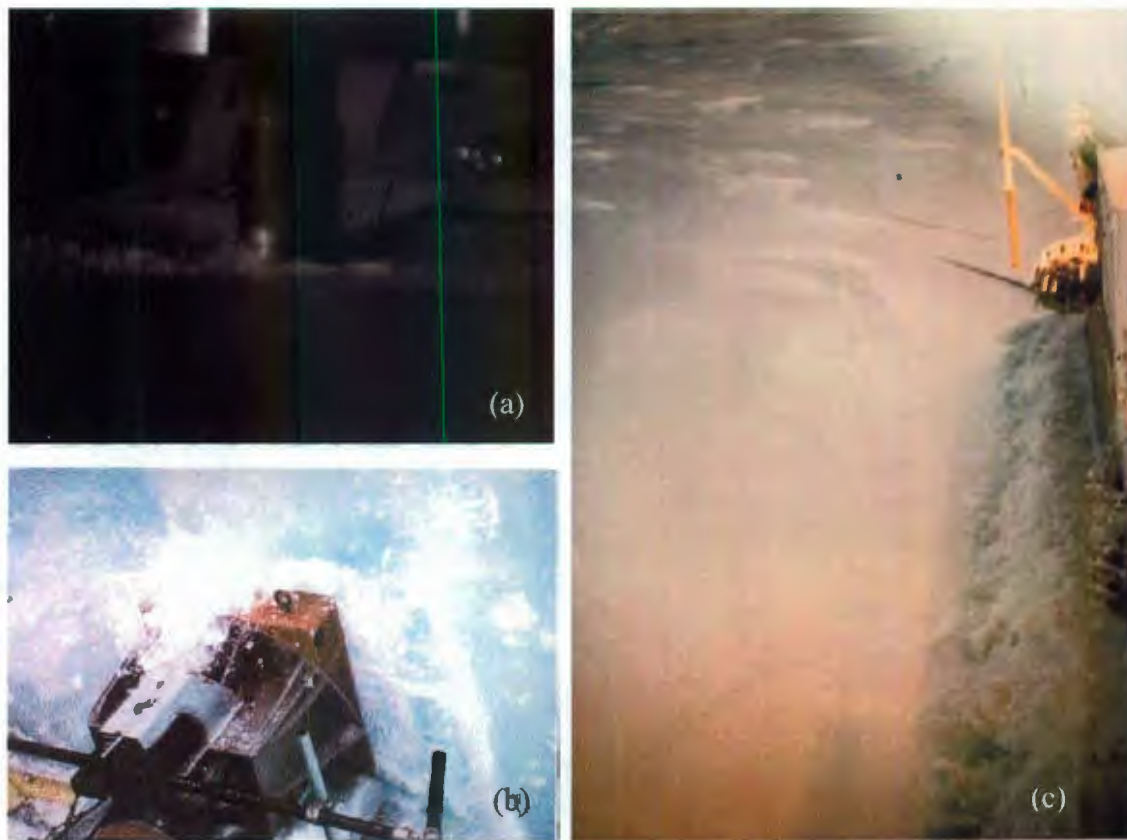


Figure 3.10: Photographic example of dynamic loading events observed during crushing events at three scales. (a) small-scale laboratory tests (Wells et al, 2009); (b) Extrusion of crushed ice during a medium-scale test at Hobson's Choice (Jordaan, 2001) (c) Mound of crushed ice that developed during the April 12, 1986 event at the Molikpaq.

As depicted in Figure 3.11, the composition of the damaged layers in general is found to be similar both at the medium and small scale. Figure 3.11 (a) shows a thick section taken from a medium scale indenter test at Hobson's Choice, while Figure 3.11 (b) is a thin section taken from a small scale laboratory indentation test. Comparison of the two shows remarkable similarity. This strongly suggests that the same mechanical phenomena are at work within the damage zone at both scales. Understanding how *hpzs* scale is important in modeling correlation of pressures for different size structures. That *hpzs* exhibit similar characteristics over all scales of interest to the present work suggests that the relationship between competing damage and fracture processes (i.e. the extent of interplay) remains relative constant over this size range.

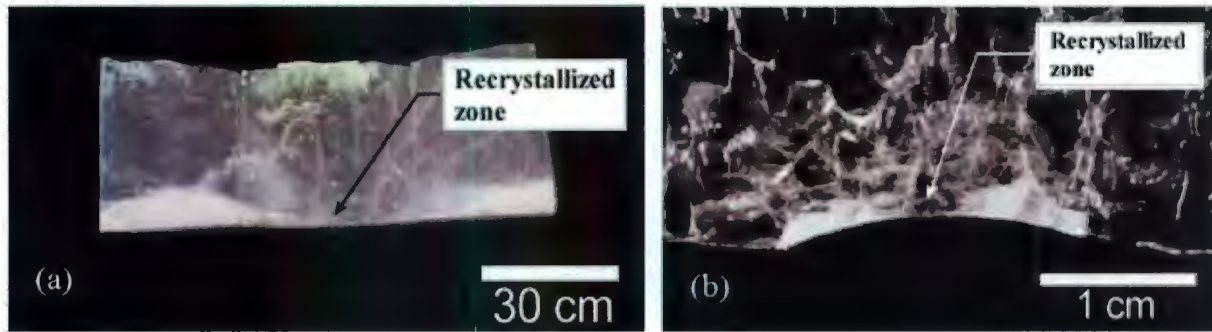


Figure 3.11: Sections taken from the central region of ice-indentation zone for: (a) Hobson's Choice medium-scale indentation tests (Jordaan, 2001); (b) laboratory scale indentation test (Barrette et al., 2002)

A purely damage-based crushing model would give loads that far exceed those measured, thus highlighting the important role of spalls in failure modeling (Jordaan and Xiao, 1992). The result of spalls is to cause localization of damage into zones of high stress concentrations. During an ice-structure interaction, the initial spalls are related to the contact geometry and high stresses associated with the initial rapid rise in stress. Jordaan and Xiao (1992) simulated a spalling event using finite element analysis to model a beam made of a damaging, non-linear viscoelastic material. From this analysis they observed that even if a spall did not cause a large instantaneous drop in the total load, it may still significantly affect the subsequent variation of load with time, as a result of the redistribution and concentration of local pressure.

Matskevitch and Jordaan (1996) considered high pressure zones and accompanying spalls using data from medium-scale field indentation tests at Hobson's Choice Ice Island. An important conclusion of this work is that in the vicinity of contact, ice can experience high confining pressures and thus the existence of high pressure zones does not contradict the traditional knowledge of ice strength. They presented two analytical models for an elastic wedge subjected to uniform edge pressure. Their analysis showed that for a line taken normal to the interaction surface and dropped below the center of an *hpz*, confining pressures were higher for flat specimens than for specimens with highly taper edges. An important implication of this finding is that higher confining pressures in the zone below the contact

correspond to large angles (i.e. a square edge) compared with highly tapered edges (i.e. after spall occurs). In terms of potential for radial cracking, this result suggests that a radial fracture would be more likely to occur for an ice sheet with a spalled edge than for an undamaged ice edge, since spalling reduces some of the confinement associated with the zone of lateral tension. A more detailed examination of stress in the ice surrounding a high pressure zone is considered in Chapter 5.

Zou et al. (1996) studied spalling fracture in a beam-like structure and considered the likely position of critical flaws and identified likely candidates were grain boundaries under shear near the edges of high pressure zones. Similar studies have been carried out by Xiao (1997) and Dempsey (1999). Much of this work was aimed at exploring deterministic aspects of the most likely conditions to be encountered during failure. This has provided valuable insight into the mechanics associated with *hpzs* and spalling fractures. Modeling these processes in a manner that allows for the treatment of observed randomness of spalling and fracture with probabilistic methods is considered in the present work.

3.3.4 Application of Damage Mechanics to Ice

The finite element (FE) method is perhaps the most broadly used and accepted computational analysis technique. In conventional continuum formulations, the material structure and flaw effects are not included directly, but rather the effects are modeled in the constitutive law. The capabilities of such models are a direct function of the constitutive relationships used. FE has been used extensively to model ice in the past (see for instance, Derradji-Aouat et al., 1990; Xiao, 1997; Kim and Shyam Sunder, 1997; Derradji-Aouat and Evgin, 2001; Derradji-Aouat, 2004). Other methods, such as boundary element method (Veitch and Tuhkuri, 1997) have also been used to model different aspects of ice behavior.

Early work by Karr (1985), Cormeau et al. (1986) and others pioneered the application of damage mechanics in modeling ice behavior. A thermodynamic model of damage growth rate defined in terms of dissipation potentials was employed by Sjolind (1987) to model the effects of damage on the elastic modulus. Jordaan and McKenna (1988), McKenna et al. (1989), and Jordaan et al. (1990) developed an isotropic damage model based on a single

damage parameter D . The authors used the damage definition given by Budiansky and O'Connell (1976). Recall that $D = a^3 N$, where a is the crack radius and N is the crack density. This model focused on the effects of damage resulting from microcracking for primarily moderate stress conditions. Microcrack networks were assumed to be randomly oriented, uniformly distributed and their density was linked to the rate of crack formation, which was modeled using rate theory as

$$\dot{N} = \dot{N}_0 \left(\frac{\sigma - \sigma_c}{\sigma_0} \right)^r \quad (3.12)$$

where \dot{N}_0 is a reference rate ($\dot{N}_0 = 0$, if $\sigma \leq \sigma_c$); σ_c is a threshold stress; σ_0 is a constant with units of stress; r is a positive constant. The influence of damage on the elastic moduli was modeled using the expressions developed by Horii and Nemat-Nasser (1983).

To account for the effects of damage enhancement of the creep behavior, Jordaan and McKenna (1989) developed a three dimensional model of exponential form. This model was subsequently redefined by McKenna et al. (1990) to the form $\exp(\beta D)$, where β is a positive constant and D is the damage measure ($D = a^3 N$) as described above. As discussed by Xiao (1997), the $\exp(\beta D)$ term is a more general form of the creep enhancement factor and is equal to the series $\sum_{k=0}^{\infty} b_k D^k$, where b_k are constants.

Karr and Choi (1989) developed a second order tensor model which included two damage parameters. One parameter was defined to account for intergranular cracking, while the second accounted for the effects of intragranular cracking. Based on strain rate, stress level and prior damage levels, the authors defined a law of damage evolution for ice.

Jordaan and Xiao (1992) suggested that the complex nature of compressive ice failure may necessitate two or more damage measures to accurately reflect the behavior of damaged ice. Singh (1993) studied the effects of hydrostatic pressure during a series of triaxial tests and modeled damage processes in ice using the continuum damage theory of Schapery (1989). Schapery's damage measure S was developed using generalized J-integral theory and is expressed as

$$S = \int_0^t f_1(p) \left(\frac{\sigma}{\sigma_0} \right)^q d\tau \quad (3.13)$$

where $f_1(p) = f_1/p$ (based on Singh, 1993); f_1 is a function representing the properties of the crack-tip material; p is the hydrostatic pressure; σ is the overall stress; σ_0 is a unit stress; q is a constant. Xiao and Jordaan (1996) expanded on this model and found that it gave good agreement with experimental results for moderate stress conditions (for applied stress < 10 MPa; confining pressures < 20 MPa).

Subsequent work by Melanson et al. (1998), Xiao (1997), Jordaan et al. (1999), and Meglis et al. (1997) studied damage processes in ice under conditions of higher confinement (up to 60 MPa) and high shear (up to 15 MPa). From this work it became evident that the damage behavior of ice is dependent on two key damage processes: (1) the effects of microcracking and related processes at low confining pressures; (2) the effects of pressure-softening processes (recrystallization and localized pressure melting) at higher confining pressures.

Microcracking has been observed to dominate for low confinement, and tends to be suppressed as hydrostatic pressure increases. For higher confinement, the dominant mechanism shifts to the recrystallization and localized pressure melting processes. To account for these two distinct processes, a damage model was developed based on two damage variables, S_1 and S_2 (see for instance, Jordaan et al., 1999). In this model, the state variable S_1 accounts for the dominant damage processes at low confinement, which is primarily microcracking. The state variable S_2 corresponds to the pressure-softening processes which dominate under higher confinement conditions. These state variables were defined using a damage measure formulation similar to that given in Eq. 3.13, given as

$$S_i = \int_0^t f_i(p) \left(\frac{\sigma}{\sigma_0} \right)^{q_i} d\tau \quad (i = 1, 2) \quad (3.14)$$

where q_i is a constant corresponding to the i^{th} state variable. For S_1 , the $f_1(p)$ function was given as

$$f_1(p) = \begin{cases} 0.712(1 - \frac{p}{37})^2 & \text{if } p < 37 \text{ MPa} \\ 0 & \text{if } p \geq 37 \text{ MPa} \end{cases} \quad (3.15)$$

Similarly, for the state variable S_2 the $f_2(p)$ function was defined as

$$f_2(p) = 0.1 \left(\frac{p}{42.8} \right)^r \quad (3.16)$$

where r is a constant. The total damage evolution law is then taken as the sum of both state variables:

$$S = S_1 + S_2 \quad (3.17)$$

The total damage was related to the creep strain through use of a creep enhancement factor of exponential form, $\exp(\beta S)$ (Xiao and Jordaan, 1996). This work is important in modeling the crushing failure process (which is distinctly different from the spalling failure process) and is associated with damage processes and the softening of the central region of an *hpz* (Jordaan et al., 1999). Further details of the application of this model may be found in Xiao (1997); Melanson (1998); Jordaan (2001); Li (2003); Li (2007).

3.4 Fracture Behavior of Ice

In nature the formation of ice is a geophysical process resulting in many inherent defects, flaws and irregularities. At higher loading rates, ice is extremely brittle and is prone to spalling and other fracture processes. The importance of this brittle behavior in the failure of ice was first recognized by Gold (1973). Crack nucleation and growth, and different modes of ice fracture are discussed below. A detailed review of spalling fracture is presented, with particular emphasis on relevant physics-based models including edge crack, internal flaw and wing crack models.

3.4.1 Crack Nucleation

In the absence of pre-existing flaws in ice, crack nucleation is the first step in mechanical failure (Frost, 1995). True crack nucleation requires the local concentration of stress to levels matching the cohesive or theoretical cleavage strength of the material. The term 'crack nucleation' refers to the point at which cracks appear where none were present before. The nucleation of a crack is sometimes referred to as a crack 'popping-in'. Similarly, the length of the crack at nucleation is sometimes referred to as the 'pop-in' length (Elvin and Shyam Sunder, 1996). The nucleation of cracks in ice also associated with the transition of ice behavior from ductile to brittle. This transition is a result of complex processes involving factors such as strain rate, temperature and load level (Sanderson, 1988). As noted by Schulson et al. (1984), crack nucleation is a physical process which occurs as a means to relieve stress concentrated at grain boundaries.

Frost (2001) provides a thorough discussion of mechanisms of crack nucleation in freshwater ice. The author explores a variety of mechanisms responsible for the local stress concentrations including:

- Elastic stress concentrations due to elastic anisotropy and thermal effects
- Dislocation pile-ups
- Grain-boundary sliding
- Elastic stress concentrations at interior flaws

These mechanisms are discussed below.

Elastic Anisotropy and Thermal Effects

Cole (1988) and Shyam Sunder and Wu (1990) investigated the effects of elastic anisotropy and identified this as a potential source of stress concentration. Later work by Elvin and Shyam Sunder (1996) concluded that the effects of elastic mismatch were not strong and in the absence of grain boundary sliding, required unrealistically high stresses to nucleate cracks. This is in agreement with Frost (2001), who concluded that under no conditions is elastic anisotropy expected to be sufficient to cause crack nucleation without the contribution of other mechanisms and is unlikely to have any major impact on the process. Similarly,

elastic stress concentrations resulting from thermal effects were not identified as a major contributing factor in the nucleation of cracks, though creep anisotropy along the basal plane may potentially result in stress concentrations.

Grain Boundary Sliding

For tensile conditions, Sinha (1984) proposed that when strain associated with grain boundary sliding, reaches some critical value, sufficient stress accumulates at the end of a sliding interface to cause nucleation of a crack. This strain due to grain boundary sliding was identified as the mechanism responsible for the delayed elastic strain in ice ϵ^d . On this basis, Sinha (1984) proposed that the nucleation of cracks depends on exceedence of a critical delayed elastic strain. One issue with this approach is that delayed elastic strain always takes a finite time to develop, suggesting that fractures cannot form immediately, regardless of how high the applied stress is.

For high strain rates Seng-Kiong and Sunder (1985) suggested that total tensile strain is a more appropriate criterion for crack nucleation, since the delayed elastic strain criterion is not valid for these conditions. Sanderson (1988) reported that the critical stress for tensile crack nucleation decreases for increasing grain size and may be expressed as

$$\sigma_N = \sigma_0 + k_1 / \sqrt{d}, \quad (3.18)$$

where σ_0 is 0.6 MPa, k_1 is 0.02 MPa m^{1/2} and d is the grain size. For a specimen under tensile loading, failure occurs once the applied load reaches sufficient level to cause a nucleated crack to propagate unstably.

Failure under compressive loading conditions is a more complex situation and is highly dependent on the loading rate. For compressive loading, as many as 50% of nucleated cracks are transgranular, though this depends on the stress and loading rate (Hallam et al., 1986). Wei and Dempsey (1991) observed that the dominant cleavage planes for transgranular cracking were observed to be the basal {0001} and pyramidal {10 $\bar{1}$ 1} planes. For uniaxial conditions, Seng-Kiong and Sunder (1985) and Hallam (1986) suggest that a tensile strain criterion is appropriate for ice under compression. The authors suggest that for the

compressive case, crack nucleation may be associated with exceedence of critical lateral tensile strain due to Poisson expansion. Given a typical Poisson ratio of 0.33 for ice, one would expect that the nucleation of cracks would require compressive stresses approximately three times higher than for tensile loading. Sanderson (1988) indicates that this agrees well with small-scale data for fine-grained polycrystalline ice, which has brittle tensile fracture strength in the range 1-2 MPa, and brittle compressive fracture strength in the range of 4-6 MPa.

For low confining pressures, failure was observed to occur by axial splitting, as is typical for uniaxial compression tests, while shear fracture was observed to occur for increased confinement (Rist et al., 1988; Weiss and Schulson, 1995). These authors propose that boundary conditions have a significant effect on the observed mode of fracture. Failure of cylindrical specimens under confinement was observed to result from the linkage of microcracks along the direction of maximum shear stress. During grain boundary sliding, shear tractions along these boundaries generate local tensile and compressive stresses. These effects were first modeled by Raj and Ashby (1971). Two possible mechanisms of shear cracks formation due to grain boundary sliding in ice subject to compressive loading are depicted in Figure 3.12 (Jordaan and McKenna, 1988). Schulson (2001) developed a comb crack model based on combined contribution of both wing cracks and secondary cracks to shear fracture.

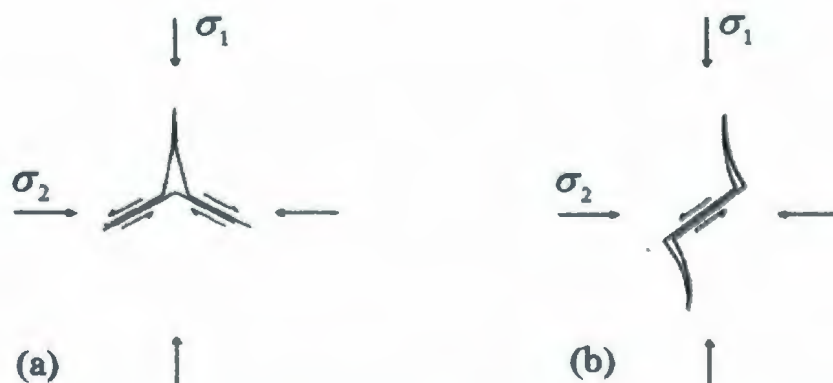


Figure 3.12: Crack formation due to grain boundary sliding for (a) triple point junction of three grains; (b) 'wing' cracks between two grain boundaries (Jordaan and McKenna, 1988).

While the tests discussed above (Kalifa et al., 1989; Schulson et al., 1993; Rist et al., 1988; Weiss and Schulson, 1995; Schulson, 2001) correspond to confining pressures of less than 20 MPa, other workers have examined the effects of confinement for a higher range of pressures. Murrell et al. (1991) showed that for higher confinement, shear fracture is inhibited and the failure becomes dominated by viscoelastic flow. For confinement pressures between 30 MPa and 50 MPa, Melanson (1998) and Li et al. (2005) report that little evidence of microfracture was observed for this range. These studies suggest that for higher confining pressures, dynamic recrystallization and pressure melting become dominant mechanisms in compressive failure.

Dislocation Pile-up

The movement of dislocations through individual ice crystals creates defects in the crystal structure of ice grains. The pile-up of dislocations at grain boundaries can lead to stress concentrations. Experimental results from Gold (1972) suggest that cracks due to dislocation pile-up tend to be parallel to the maximum (tensile) principal stress axis. Such dislocation pile-ups have been observed by Sinha (1978) using surface etching techniques. The work of Schulson et al. (1984), Cole (1986), and Kalifa et al. (1989) supported the role of dislocation pile-up as a source of stress concentration. Kalifa et al. (1989) conducted a series of triaxial experiments to study the effects of confining pressure on ice for confinement up to 10 MPa at a temperature of -10 °C. Results of these tests indicated that crack nucleation requires higher levels of stress and strain for increasing confining pressure, which they modeled using the expression

$$\sigma_1 - \sigma_3 = -2.47 + 0.4\sigma_3, \quad (3.19)$$

where σ_1 and σ_3 are the maximum and minimum principal stresses respectively. From the above expression it may be observed that the crack nucleation is governed by the von Mises stress for a given state of confinement; increasing confining pressure can inhibit the nucleation of cracks. Schulson et al. (1993) performed a similar study under proportional triaxial stress conditions. Compressive conditions were observed to inhibit the propagation of individual cracks resulting in a strong relationship between the failure mode and confining

pressure. Frost (2001) also provides a review of the dislocation pile-up mechanism and summarizes the approaches of Stroh (1957) and Smith and Barnby (1967), which were developed for estimating stress conditions near the tip of dislocation pile-ups in metals. Frost suggests that this mechanism is likely to be of most importance for either single ice crystals or grain geometries that do not permit activation of grain boundary sliding.

Internal Flaws

An insightful assessment of the relative importance of individual nucleation mechanisms was provided by Frost (2001). He concluded that for moderate and higher strain rates, in the absence of inclusions and pre-existing flaws, grain boundary sliding is likely to be an important component of crack nucleation. If grain geometry does not permit grain boundary sliding, nucleation of cracks from the tips of dislocation pile-ups may be expected. At low temperatures or high strain rates, Frost (2001) suggests that nucleation from pre-existing flaws and inclusions are inevitable, given the large numbers of flaws occurring in natural ice. This final conclusion, which highlights the importance of pre-existing flaws in brittle failure at high strain rates, is of particular significance to this research proposal.

Summarizing Discussion

In light of the above review, it may be concluded that a number of different nucleation mechanisms may be observed in laboratory-grown ice under controlled conditions. Sanderson (1988) highlights that natural ice, which contains many inherent defects and flaws (including large favorably oriented grain boundaries), will likely experience fracture due to the propagation of existing flaws prior to the nucleation of new cracks. Here it is assumed that the most likely sites of the crack growth responsible for spalling fracture are grain-scale flaws, especially grain boundaries, which are inherent to the ice. Cole (1986) suggests that observed cracks of length $2a$ were related to grain size d_G , as given by the approximate relationship $2a = 0.65d_G$. In the present work, this expression has been used in to relate the size distribution of flaw to the size distribution of grains in the ice.

3.4.2 Modes of Ice Fracture

During an interaction between an ice sheet with a vertical-walled structure, a number of types of fracture are commonly observed. In his discussion of ice failure modes on vertical structures, Sanderson (1988) identified two types of 'global' fractures (radial cracking and circumferential cracking) and one type of 'local' fracture (spalling). These fracture modes are illustrated in Figure 3.13 below. Attention is not given to other failure modes such as creep, buckling and crushing in this section.

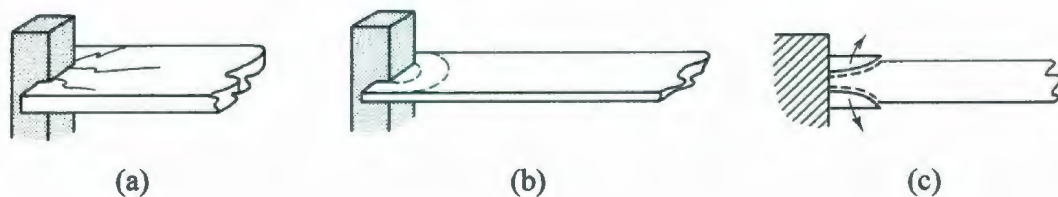


Figure 3.13: Illustrations of fracture modes: (a) radial cracking; (b) circumferential cracking; (c) spalling (modified after Sanderson, 1988).

Palmer et al. (1983) described radial cracking as fracture involving the growth of vertical cracks directed radially from the contact region and running through the whole thickness. Circumferential cracks result from an out-of-plane bending moment due to eccentric loading or as a result of elastic buckling (Sanderson, 1988). In large ice sheets, combined radial and circumferential cracking can cause the sheet to break into triangular and trapezoidal fragments. While load reductions may result for some global fracture events, these mechanisms cannot be relied upon to always occur, and design conditions are often assumed to the case where global fracture does not occur.

Local spalling or flaking, is characterized by the formation of relatively large fragments of ice which occur near high pressure zones and run to a free surface. At full-scale failure is often mixed modal and local crushing may be accompanied by spalling, as well as radial and circumferential cracking. To provide some guidance as to what failure modes to expect for different conditions, Palmer et al. (1983) proposed a deformation mode map based on observed failure modes for different strain rates and aspect ratios.

For small-scale ice indentation tests, Timco (1986) also studied different failure modes as a function of indentation rate and aspect ratio, which were reported using a similar failure map; see Figure 3.14. From this work, radial cracks were observed to occur most commonly for high aspect ratios and typically radiated from the corners of the indenter. Radial cracks also tended to be initially stable and of limited length. At low indentation rates and high aspect ratios, Timco (1986) reported that radial and circumferential cracking occurred without any crushing. As indentation rate is increased, particularly for thick ice, failure tends to change to spalling and crushing behavior.

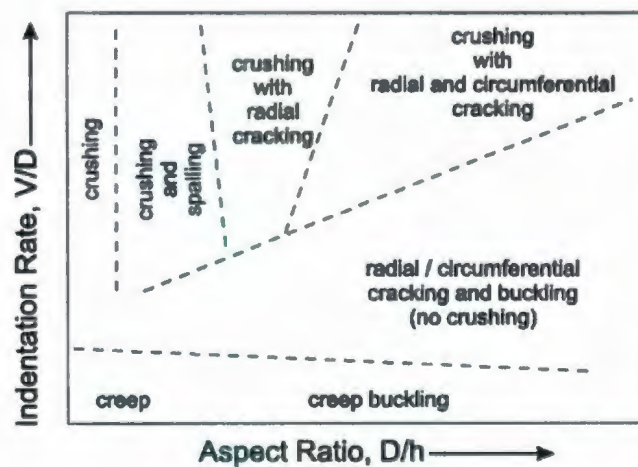


Figure 3.14: Deformation mode map as function of indentation rate and aspect ratio (Sanderson, 1988 based on Timco, 1986).

While a deformation mode map may help illustrate the relationship between different mechanisms for laboratory-scales, as discussed by Sanderson (1988) it is unwise to make quantitative generalizations about failure modes, since such figures are certainly not universal. Other factors (for instance absolute thickness) can affect failure modes and are not reflected in deformation mode maps.

Later work by Timco (1987) reported results of a series of indentation experiments on a 6 cm diameter piled towed through freshwater ice containing flaws. The effects of several types of macro scale flaws were explored, such as short flaws, long flaws and round flaws, as shown in Figure 3.15.

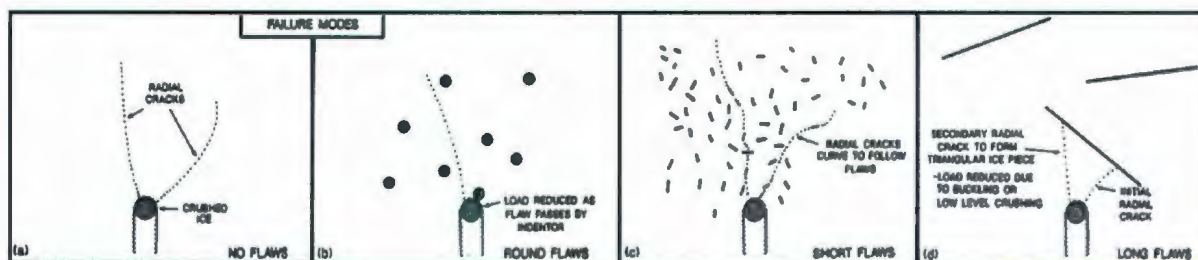


Figure 3.15: Schematic of flaw types considered in tank tests (modified from Timco, 1987).

Based on these tests Timco concluded that load reduction was often observed when radial cracks emanating from the structure extended and interacted with the large pre-existing flaws (several times the structure width).

For design, load reductions associated with global fracture events and large crack interactions cannot be relied upon to always occur. The design case then corresponds to the event where global fractures do not occur, and loads are limited by spalling and crushing failure. Details of spalling fracture are explored below.

3.4.3 Spalling Fracture

This type of fracture is one of the mechanisms governing local ice pressure behavior. A direct consequence of this type of failure is a reduction of contact area through the removal of ice at the interaction interface, along with an associated load drop. This type of fracture plays an important role in the localization of loads into high pressure zones and scale effects in ice pressure behavior (Jordaan, 2001). This mode of failure has been referred to in the literature using a variety of descriptions, such as (edge/in-plane/indentation) spalling, flaking, chipping or splitting. In-plane splitting should not be confused with floe splitting (radial cracking), which is a global failure mechanism. Here this failure mode is termed 'spalling fracture', or simply 'spalling'. A review of theoretical fracture models of relevance to this failure mode are discussed below.

Overview of Spalling

Croasdale (1975) and Croasdale et al. (1977) were first to highlight the tendency of fractures to run to free edges during spalling failure. In this early work, an initial ice load model was

developed using plasticity theory to provide an upper-bound estimate of ice loads. Croasdale et al. (1977) used a Tresca yield criterion and assumed failure occurred on slip planes as a result of plastic yielding. This model was applied to a series of failures along parallel shear planes and was developed to provide an estimate of maximum quasi-static load during an interaction. As illustrated in Figure 3.16, the tendency of fractures to run to free edges during spalling has important implications in the formation of high pressure zones (Jordaan, 2001). This results in a tendency for less *hpzs* to form near the edge of an ice feature.

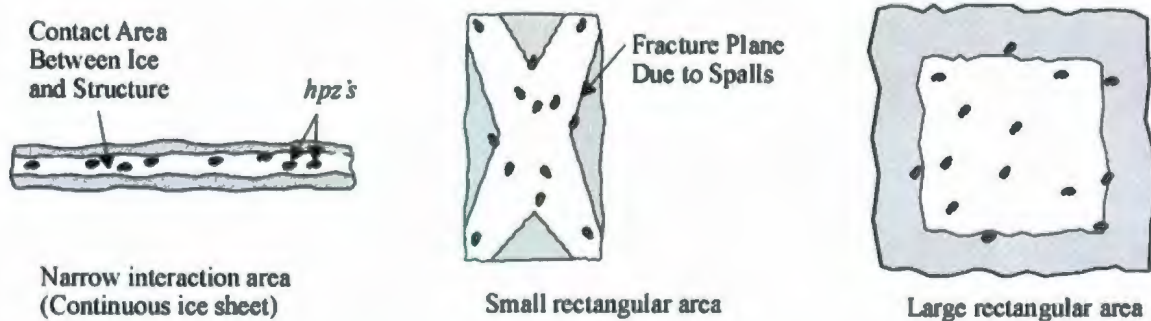


Figure 3.16: Arrays of high pressure zones for various geometries (Jordaan et al., 2008).

For interactions involving sheet ice this tendency is particularly evident, as *hpzs* tend to be concentrated near the center of the ice sheet. This concept of 'line-load' contact geometry was first introduced by Joensuu and Riska (1989) and explored further by Fransson et al. (1991) and Tuhkuri (1993). Daley (1991) developed a process model for ice sheet failure based on the assumption that brittle failure results from a sequence of through-body shear cracks which are triggered once the stress on a failure plane reaches a critical limit. In this model it was assumed that all drops in force result from sudden flaking events due to shear fracture. In this model, a simple Coulomb failure criterion was used to check if a flake formed. Daley et al. (1998) provided a review of discrete failure events in ice and described ice failure as a nested hierarchy of discrete failure events. An event tree for local failure was presented based on the assumed failure models. In this approach, probabilistic methods and links to fracture mechanics (including the effects of confining pressure) were not explored, but rather the model attributed the randomness of ice loads to chaotic behavior associated with the hierarchical nature of the assumed model.

For large multi-year floes or other massive ice features, internal spalls may form near the edges of *hpzs* where the fractures propagate to a free surface within the interaction area. This is a highly random process and internal flaws play an important role in this process (Jordaan, 2001). Internal spalls, are in evidence in medium-scale test results (Masterson et al., 1992; Masterson et al., 1993; Masterson et al., 1999). This has important implications for the estimation of loads from thick ice sheets, since this suggests that *hpzs* do not form in ‘line-load’ configurations as for thinner ice sheets. This highlights the need to consider the effect of increasing thickness on *hpz* distribution, which is in turn a likely factor affecting the observed scale effect in ice.

Several idealizations of spalling failure are illustrated in Figure 3.17. During the initial stages of an ice-structure interaction, the edge of the ice sheet may be idealized as having a flat edge (Figure 3.17(a) and 3.17(c)). Towards the midplane of the ice sheet, triaxial constraint tends to suppress fracture, while lower confinement near the edges promote it. As the interaction progresses, spalls form and produce an edge that is more wedge-shaped in profile (Figure 3.17 (b) and Figure 3.17 (d)).

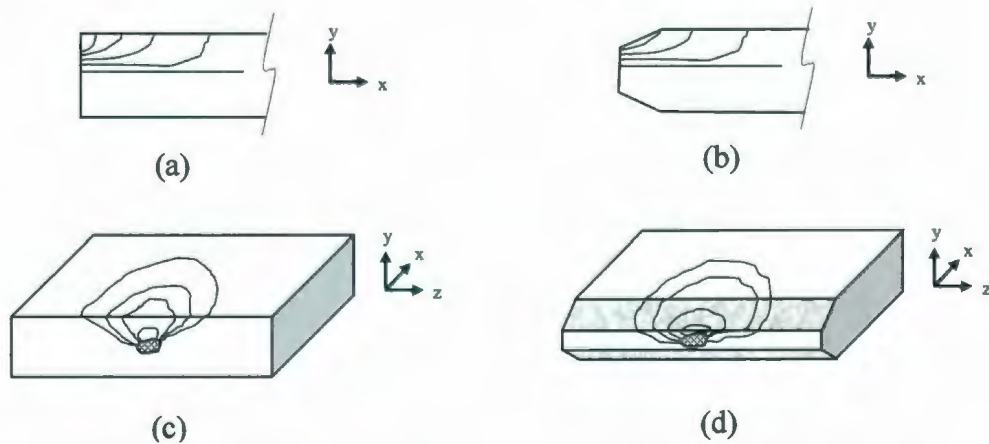


Figure 3.17: Idealization of spalling near a single high pressure zone: (a) 2D flat edge; (b) 2D wedge-shaped edge; (c) 3D flat edge; (d) 3D wedge-shaped edge.

Crushing processes result in the pulverization and removal of material from the contact zone producing a flatter ice edge, which results in a redistribution of stress. Subsequent spalling leads to the reoccurrence of wedge-shaped edges, resulting in a continual evolution of the ice

edge geometry. The role of evolving ice edge geometry in the interplay between crushing and spalling failure is discussed in Chapter 7.

3.4.4 Theoretical Fracture Models Relevant to Spalling

A review of theoretical fracture models of relevance to this failure mode are discussed below.

Edge Crack Models

Kendall (1978) provided an analysis of compressive splitting failure based on simple beam theory using the double cantilever beam approach. In this model the total compressive force F was decomposed into two eccentric components $F/2$. This approach assumed that the crack effectively divides the specimen into two beams that can bend and shear outwards under compression, resulting in the opening of a central gap.

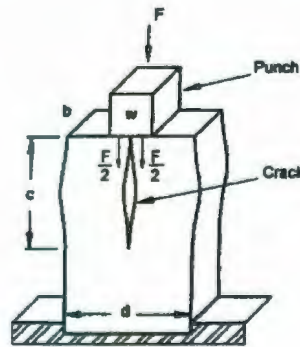


Figure 3.18: Model of compressive indentation proposed by Kendall (1978).

Using elastic beam theory and an energy-based approach, Kendall developed an equation for splitting force as a function of geometry, elastic modulus E and fracture energy R , but which is also independent of crack length. His analysis gave the splitting force F_s as

$$F_s = \frac{b}{1-w/d} \left(\frac{2}{3} ERd \right)^{1/2} \quad (3.20)$$

where b is the specimen thickness, w is the indenter width and d is the specimen width. In this model, the strain energy due to the applied load has two major components: direct

compression and a bending moment due to the eccentricity of the load. It is noted that Eq. 3.20 is independent of crack length.

Kendall's analysis was used in the context of ice spalling by Wierzbiki (1985). He adapted the analysis to represent an ice sheet by assuming plane strain conditions (see Figure 3.19).

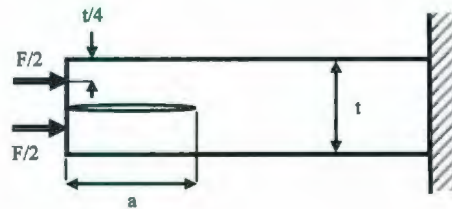


Figure 3.19: Kendall's theory applied to in-plane ice spalling (after Wierzbiki, 1985).

Treating ice as an elastic brittle material, where $K_{Ic} = \sqrt{2ER}$, Wierzbiki gave an equation for the critical force per unit width F_s for in-plane spalling as

$$F_s = \left(\frac{K_{Ic} t^{1/2}}{(3(1 - \nu^2))^{1/2}} \right) \quad (3.21)$$

where K_{Ic} is the fracture toughness, t is the thickness of the ice sheet, and ν is the Poisson ratio of ice. Based on this equation, Tomin et al. (1986) gave the normalized spalling stress per unit width σ_s as

$$\sigma_s = \frac{F_s}{t} \quad (3.22)$$

For freshwater ice, Sanderson (1988) suggested values of $K_{Ic} = 0.1 \text{ MPa m}^{1/2}$, and $\nu = 0.3$. Substituting these values into Eq. 3.21 and Eq. 3.22 yields an expression (based on the double cantilever model) for spalling stress per unit width as a function of thickness

$$\sigma_s = 0.06t^{-1/2} \quad (3.23)$$

As discussed by Tomin et al. (1986) for an ice thickness of 0.025 m, Eq. 3.23 yields a spalling fracture stress of $\sigma_s = 0.38$ MPa. This value is considerably smaller than the standard range of compressive (crushing) stress of ice, which is typically in the range of 4 to 8 MPa (Sanderson, 1988). From Eq. 3.23, it is observed that dependence on the $t^{-1/2}$ term suggests that larger ice features would see a smaller average stress. This observation supports the presence of a thickness scale effect.

Kendall (1978) also used similar principles to derive an expression for splitting force for the case of off-center cracks; see Figure 3.20 (a). As illustrated in Figure 3.20 (b) this model predicted that the force to propagate a crack would be minimum when the crack is located on the center line. On this basis Kendall concluded that “there will be a preference for cracks to travel on the center plane.”

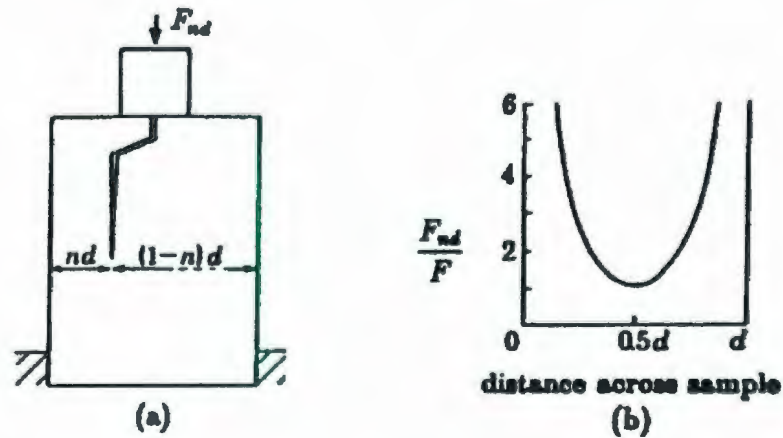


Figure 3.20: Kendall's model for off-center cracks in compression (from Kendall, 1978).

Kendall's model assumed there were no lateral restraints on the free ends of the struts. As discussed by Zou et al. (1996), when no lateral restraint is included in the model, the free ends of the struts are free to run into each other; see Figure 3.21. In reality, reaction forces would be present on the inside faces of the struts, causing additional bending in the struts.

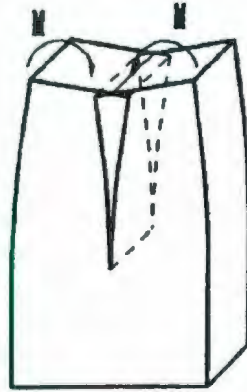


Figure 3.21: Struts with no constraints at free ends (from Zou et al., 1996).

To address this issue, DeFranco and Dempsey (1990) developed a model based on the assumption that the free ends are completely restrained (the boundary conditions of the two models are illustrated in Figure 3.22). This work builds on an earlier augmented double cantilever beam model developed by Kanninen (1973).

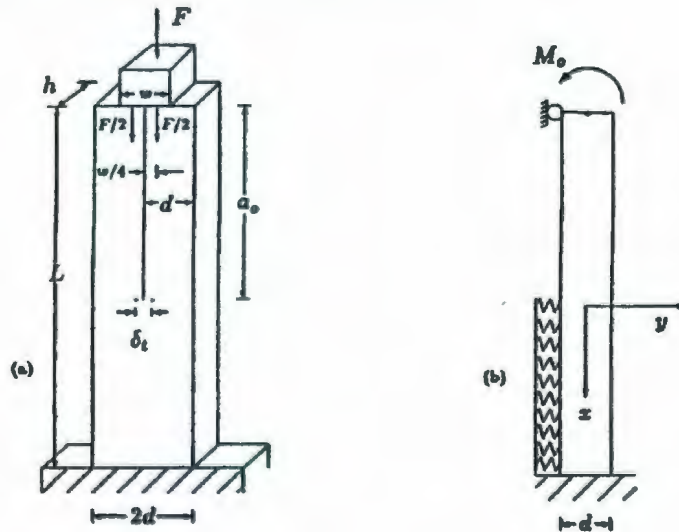


Figure 3.22: Comparison of the models of: (a) Kendall (1978); (b) DeFranco and Dempsey (1990).

For the double cantilever beam model shown in Figure 3.22 (b), DeFranco and Dempsey (1990) derived an expression for fracture driving force using energy balance criteria to give:

$$F_s = \frac{b}{1-w/d} \left(\frac{16}{3} ERd \right)^{1/2} \quad (3.24)$$

Comparison of Eq. 3.24 with Eq. 3.20 shows that the DeFranco and Dempsey (1990) model suggests a fracture driving force that is nearly three times larger. In reality, the strut end condition may be between free and completely restrained and may involve friction, pressure melting and sintering processes (Zou et al., 1996).

For small crack lengths, simplifying the strut deflection as pure bending may not be appropriate. Compressive stresses dominate in the zone near the indentation interface and tend to stabilize or close cracks. On this basis Wierzbicki (1985), concluded that the double cantilever beam models were invalid until the initial cracks grow to such an extent that simple beam theory can be used.

To examine the effects of these assumptions, Zou et al. (1996) numerically investigated the strain energy release rate G at crack tips of flaws of various lengths at different locations. The values of G at crack tips were evaluated for different crack lengths using finite element analysis and compared with values obtained from the models of Kendall (1978) and DeFranco and Dempsey (1990).

For ice the value of G ranges between 1-2 J/m²; Zou et al. (1996) used a value of 1 J/m² for their analysis. The G values found using each model were plotted as a function of the ratio of crack length a to ice thickness D ; see Figure 3.20. Recalling that $G = K_{ic}^2/E$, we see that the strain energy release rate of DeFranco and Dempsey is one eighth the value predicted by Kendall's theory. As shown in Figure 3.22 (b), for a/D less than 0.22 no crack growth is expected since the value of G is less than the critical value. As a/D increases, the numerical results approach a constant close to the value predicted by DeFranco and Dempsey (1990).

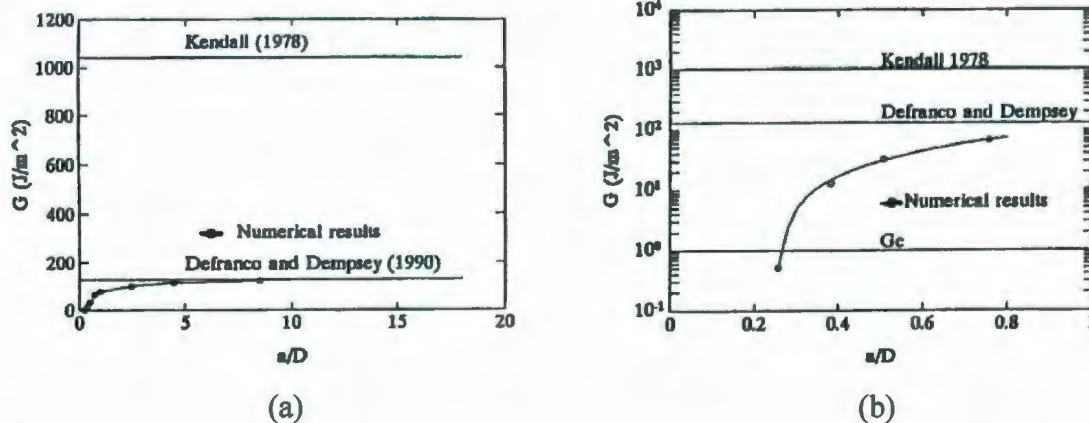


Figure 3.23: Results of strain energy release rate analysis (from Zou et al., 1996).

Kendall's model was originally developed for a central crack and omitted the effects of shear strain energy. Extending this model to non-centrally located cracks, as shown in Figure 3.24, where shear may dominate, presents difficulties. To investigate this further, Zou and his coworkers conducted a numerical analysis of G as a function of distance from the central plane l for a crack of fixed length (0.5 m); see Figure 3.24 (a). These results, shown in Figure 3.24(b), were compared with predictions made using Kendall's model. From this figure it is observed that Kendall's model suggests G will be maximum for a central crack, in contrast with the results of Zou et al., 1996 which suggest that G increases when the crack is off the central plane.

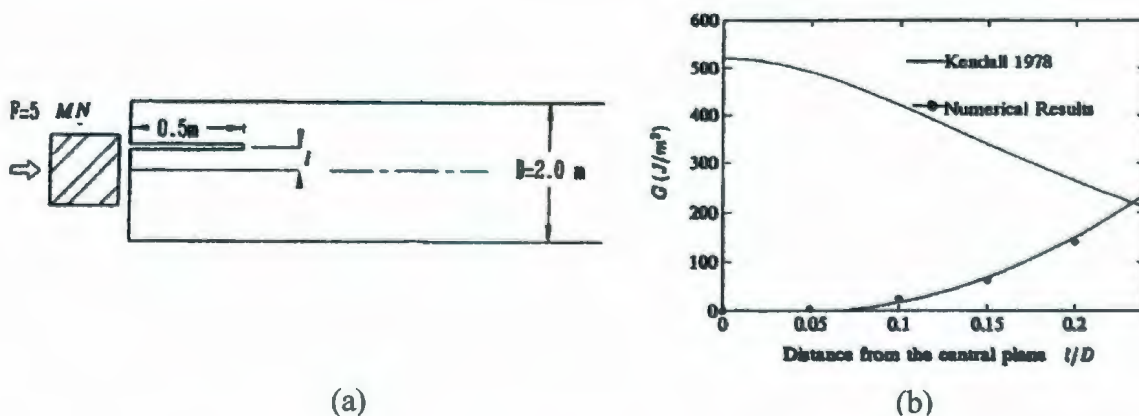


Figure 3.24: (a) Non-centrally located crack; (b) plot of G vs. l/D (from Zou et al., 1996).

Thouless et al. (1987) developed a model similar to Kendall's for an edge crack in a brittle plate; Figure 3.25 (a). Complete solutions for stress intensity factors corresponding to this model were given by Hutchinson and Suo (1992) as:

$$K_I = \frac{1}{\sqrt{2}} [Ph^{-1/2} \cos \omega + 2\sqrt{3}Mh^{-3/2} \sin \omega] \quad (3.25)$$

$$K_{II} = \frac{1}{\sqrt{2}} [Ph^{-1/2} \sin \omega + 2\sqrt{3}Mh^{-3/2} \cos \omega] \quad (3.26)$$

where P is the compressive force, M is the bending moment, h is the distance from the free surface and $\omega = 52.7^\circ$. A more generalized beam model of spalling was developed by Suo (1990). This model is detailed by Hutchinson and Suo (1992), who give the strain energy release rate at the crack tip as

$$G = \frac{1}{2\bar{E}} \left[\frac{P_1^2}{h} + 12 \frac{M_1^2}{h^3} + \frac{P_2^2}{H} + 12 \frac{M_2^2}{H^3} - \frac{P_3^2}{h+H} + 12 \frac{M_3^2}{(h+H)^3} \right] \quad (3.27)$$

where \bar{E} is the effective Young's modulus, $P_1, P_2, P_3, M_1, M_2, M_3, h$ and H are defined in Figure 3.25 (b). The approach of Thouless et al. (1987) may be treated as a special case of the Hutchinson and Suo (1992) model.

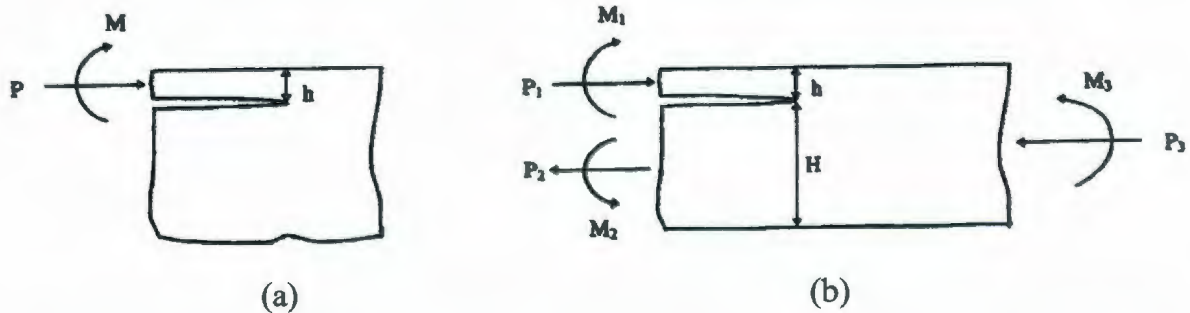


Figure 3.25: (a) Model of spalling due to edge loads (Thouless et al., 1987); (b) generalized beam model developed by Suo (1990).

Hutchinson and Suo (1992) also provided a criterion for mixed-mode fracture based on a ratio of K_I to K_{II} , the direction of crack propagation, a crack tip traction parameter and the

mode I strain energy release rate. Their model suggests that a mixed mode crack will propagate at an 'apparent strain energy release rate' that is less than the G value based on K_{Ic} .

In their discussion of different modeling approaches, Zou et al. (1996) suggest that the approach of Hutchinson and Suo (1992) may be the most appropriate double cantilever beam approach. The model of Kendall (1978) was identified as being suitable only for large cracks, though extending it for non-central cracks presented difficulties. For large crack lengths, the model of DeFranco and Dempsey (1990) was found to provide a good prediction of G when compared with numerical analysis results. In reality, when cracks become long it is likely that subdivided layers will spall off or fail due to flexural cracking. Wierzbiki (1985) suggested that cleavage of the ice sheet into thinner layers and the subsequent spalling of the outer layers, promotes a progressive type of failure where there is always a local failure mechanism which produces eccentricity, and thus leads to flexural cracking. In cases where the crushed ice and rubble accumulate around the structure, the additional weight of broken ice on top of the sheet (or buoyancy if submerged below) may contribute to bending loads, and promote flexural failure modes.

Zou and his co-workers concluded that double cantilever beam theory may be appropriate for large splitting type fractures, but in general is not suitable for the analysis of ice spalling. This type of model implies that the proximity of the crack to the edge affects the degree to which bending stresses affect the crack trajectory. Li (2007) investigated this numerically and experimentally and concluded that cracks located nearer to the edge of a specimen tend to propagate at lower stress levels, and deviate towards the free surface more readily. In reality, spalls may result from the propagation of cracks of various locations, not simply large edge cracks as suggested in the above models. The large, open cracks implied by the double cantilever beam theory are rarely found in nature, and are not representative of the spalling process in local ice failure. On this basis, Zou et al. (1996) extended their analysis to include a numerical investigation of the behavior of small internal cracks at different locations in the ice sheet. A discussion of internal flaw models is provided below.

Internal Flaw Models

It is highly probable that small internal flaws, such as weak grain boundaries, exist in natural ice, which may serve as precursor cracks that lead to the formation of spalls. These cracks may propagate in a tensile mode, a shear mode or a mixed mode. Mixed mode fracture has been studied extensively in the past (see for instance, Sih (1973); Palaniswamy and Knauss (1974); Conrad (1976); Cotterell and Rice (1980); Sih and Tzou (1983); Hutchinson and Suo (1992)). In assessing the consequences of fracture, it is also important to estimate the size and shape of the failed zone, and the shape of the remaining specimen. In addition to modeling the conditions under which cracks will propagate, this also requires prediction of the trajectory of propagating cracks. Crack trajectory has been studied extensively by a number of authors (see for instance Sih (1973); Palaniswamy and Knauss (1974); Conrad (1976); Sih and Tzou (1983); Zou (1996)).

There are three principal theories commonly used in the assessment of crack propagation trajectory for mixed mode fracture. These include: (1) the direction of maximum strain energy release rate (SERR); (2) the direction at right angles to the maximum tensile stress ($K_{II} = 0$) approach; (3) the direction of minimum strain energy density. In their evaluation of these theories, Zou et al. (1996) concluded that the SERR approach is the most fundamental since cracks would naturally be expected to propagate in this direction, as this is actually the same criterion for propagation itself – the crack having the maximum SERR will be the first to propagate. The second approach, which suggests that cracks follow a direction perpendicular to the maximum tensile stress, has been shown to be essentially equivalent to the first approach (Xiao, 1997).

In general, all three modes of fracture (I, II and III) are of interest in modeling crack trajectory. For many cases of interest in ice mechanics the assumption of plane strain conditions at the crack tip is appropriate. For these conditions, only tensile (mode I) and shearing (mode II) crack propagation need be considered; this type of analysis is also well suited to use of the J -Integral approach. The relationship between the angle of crack propagation θ and the ratio of K_I/K_{II} was explored by Palaniswamy and Knauss (1974); see Figure 3.26.

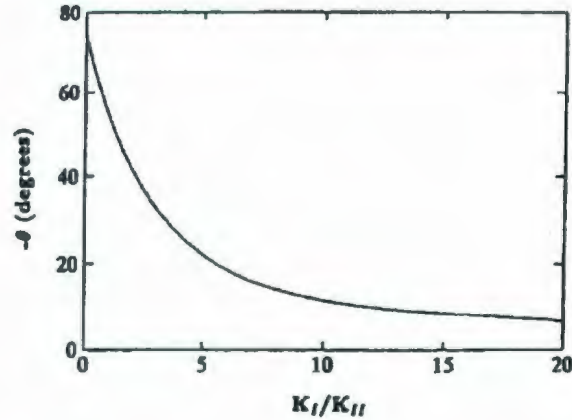


Figure 3.26: Crack propagation angle as a function of K_I/K_{II} (Palaniswamy and Knauss, 1974).

A finite element analysis of mixed-mode fracture by Conrad (1976) yielded similar results to those of Palaniswamy and Knauss except for low K_I/K_{II} where shear stress dominates. The work of Shen and Lin (1986) on mixed-mode fracture in ice showed good agreement between experimental results and the result of SERR analysis based on Palaniswamy and Knauss (1974). For ice, Smith and Schulson (1993) also suggest that cracks may propagate if the crack tip is under confining pressure and shear stresses. In reality, propagation under these conditions would be less likely than for crack tips subjected to mixed mode shear and tensile loading.

The analysis of Zou and coworkers considered a horizontal crack of length a at three different locations for an ice sheet of thickness D subject to indentation loading. Crack locations, along with trajectories based on Conrad (1976) are shown in Figure 3.27 (a). A parabolic loading function was assumed based on prior damage analysis applied to indentation by Xiao and Jordaan (1991). The crack at location one was subject to primarily shear mode cracking, location two was mixed-mode and location three was primarily tensile mode. Results are shown in Figure 3.27 (b). As may be observed, G increases with crack length and the most likely regions from which fractures will initiate were identified as shear zones with low confining pressure and tensile zones. For all locations, the crack size associated with exceedence of the critical strain energy release rates are small compared with critical crack lengths for Kendall-type analysis. The mode II critical strain energy release rate

was taken as $G_{IIc} \approx 0.6G_{Ic}$ and mixed-mode cracks will propagate for a G value between G_{Ic} and G_{IIc} . Cracks in locations one and two may result in spalling and the removal of discrete ice pieces. Cracks in location three may result in tensile splits in the ice sheet, such as those discussed by Kärnä and Muhonen (1990). Wierzbiki (1985) presented observations of similar cleavage cracks to Kry et al. (1978).

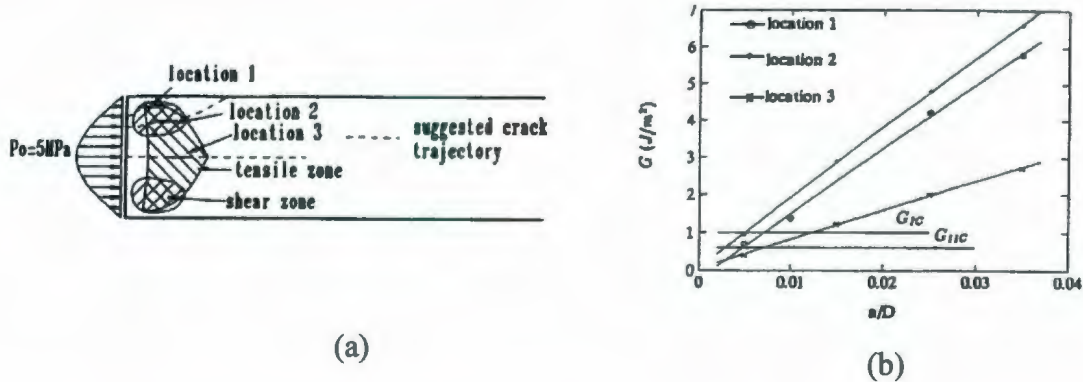


Figure 3.27: (a) Crack locations used in analysis; (b) G vs. a/D for three selected locations (from Zou et al., 1996).

Kendall-type flaws have been identified as being less likely to propagate than small internal cracks; Kendall-type flaws would also have to be located in specific planes (Zou et al., 1996). Given that flaws in ice are random in nature, a probabilistic model of fracture is recommended. Early efforts in the modeling of spalling fracture from small internal cracks were described by Xiao and Jordaan (1991), who analyzed the occurrence of spalls in terms of the propagation of a flaw located near the ice-structure interface using finite element analysis.

Xiao and Jordaan (1991) found that the propagation of such flaws led to the formation of spalls and an associated load drop. They found that during indentation the pressure distribution is an inverse parabola in shape when the contact is initially elastic. As the ice near the interface becomes damaged, the distribution becomes uniform and then parabolic in shape. Loads required for crack propagation were found to be about one tenth of those found using damage analysis only, highlighting the importance of spalls in the formation of *hpzs*. Flaws were found to propagate in tensile, shear or mixed-modes and to propagate more

readily in zones located near the free surface, which tend to have lower confining pressure. For edge-indentation of an ice sheet, a large zone of compression develops behind the *hpz*; fracture is unlikely in the highly confined regions. The authors found tensile zones near the free surface of the ice often were small; zones of high shear stress tend to be larger and to have a higher probability of containing a flaw.

Earlier work by Evans et al. (1984) put forward a semi-quantitative model of spalling based on an idealization of an edge-loaded ice sheet as an elastic-perfectly plastic material. This model was based on elastic plate bending theory and plane-strain cavity expansion theory (Hill, 1950). While this model was used to show that the forces require to propagate spalling cracks are relatively small, the model parameters proved to be difficult to calibrate with experiments.

Wing-crack Models

Zou et al. (1996) reported that the most likely regions from which fractures will emanate are shear zones with low confining pressures, as well as zones of tension. While linear elastic fracture mechanics theory for tensile cracks is well developed, the application of fracture mechanics to zones of compressive loading is more complex. One of the main differences between cracks subjected to compression and those subjected to tension, is crack face contact. Tensile stresses cause crack faces to separate (i.e. there is no contact), while compressive loading often results in contact between opposing crack surfaces. This contact introduces a frictional force component along the crack interface, which affects the details of the crack mechanics.

As compression increases, shear stresses acting along the faces of the crack create tensile zones at the crack tips. Once the local stress level exceeds some critical value 'wing cracks' begin to form and propagate from these tensile zones (Kachanov, 1982).

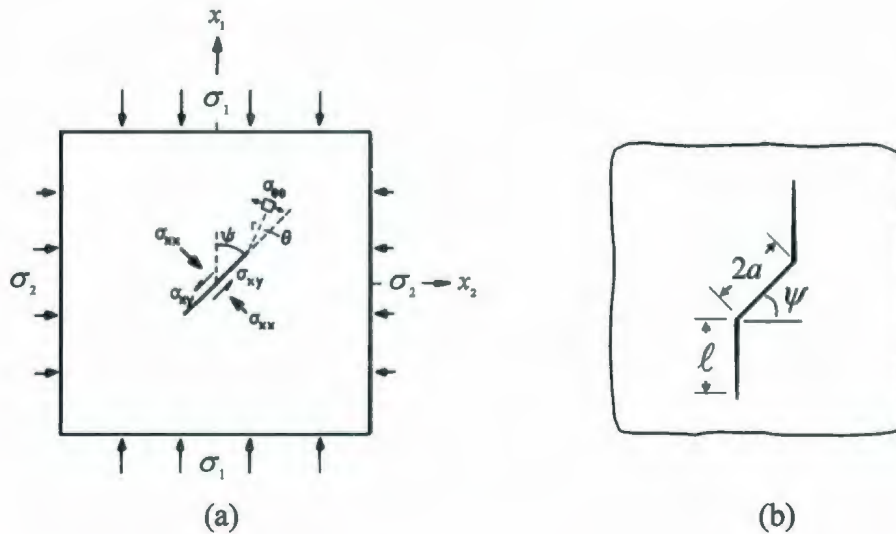


Figure 3.28: Schematics of (a) wing crack coordinates, stresses and angles (Ashby and Hallam, 1986); (b) crack dimensions for idealized wing crack geometry.

As the ‘wing cracks’ grow, they begin to align themselves with the direction of principal compressive stress, as shown for the idealized geometry given in Figure 3.28. While a specimen may contain many precursor flaws, only those favorably oriented to the local stress field will become ‘active’. Ashby and Hallam (1986) suggest that cracks in the approximate range of orientations between 30° and 60° relative to the principal compression will nucleate since these angles are most favorable for sliding. Flaws oriented at angles outside this range require significantly higher stresses to form cracks.

Hoek and Bieniawski (1965) studied the extension of elliptical ‘Griffith’ cracks (no crack face contact) in glass as a function of uniaxial compressive load. The authors observed a linear relationship between compressive load and crack growth, and found that wing cracks grow stably under compression. Kobayashi (1971) extended this work to include ‘closed’ cracks (having crack face contact). He found that ‘closed’ cracks exhibit a non-linear relationship, with crack growth accelerating for increasing compression. His work also included a study of stable crack length as a function of the biaxiality ratio for both open and closed cracks, and examined crack interactions for different crack arrays.

Kachanov (1982) developed an analytical expression of wing crack growth by assuming that the Mode I stress intensity factor at the tip of a wing crack is given as the sum of two contributions, given by:

$$K_I = 1.15 \tau_{xy} \sqrt{\pi a} + \sigma_n \sqrt{\pi \ell / 2}. \quad (3.28)$$

The first term is the opening contribution due to shear τ_{xy} along the face of the precursor crack. The second term is the contribution due to the normal (confining) stresses acting on the wing crack; σ_n is negative and is associated with the surrounding compressive field, which tends to close the crack. The parameter a is the crack half-length and ℓ is the wing crack length. For given stress conditions, the equilibrium wing crack length ℓ is the value which gives $K_I = K_{Ic}$. In his analysis Kachanov assumes that the cracks grow in the direction of initiation, which makes it best suited for short crack lengths ($\ell < a/4$). As discussed above, when the wing cracks extend they align with the principal compressive stress and other analysis approaches are required.

For longer cracks the driving force for crack extension changes from the field surrounding the precursor crack to the wedging action due to sliding along the precursor crack. Nemat-Nasser and Horii (1982) produced a classic paper on compressive crack growth in brittle media, which has served as a benchmark for much work done since. Nemat-Nasser and Horii modeled fracture using a closed crack with friction acting between the surfaces. They replaced the wing crack by a continuous distribution of dislocations, and numerically solved for the stress intensity factors at the wing crack tip. This approach was used to analyze crack initiation and growth and to estimate the stable wing crack length ℓ for given stress conditions. This work was used by Ashby and Hallam (1986) to justify simplifications made to their analytical crack models, which serve as an important part of the present modeling efforts.

Ashby and Hallam (1986) described an analytical model for the stress intensity factor of a two dimensional wing crack subject to multiaxial loading. Given its importance to the present work, the full derivation of the stress intensity factor expression of Ashby and Hallam (1986)

has been detailed in Appendix A.1. In modeling fracture behavior, the primary expression of interest is that of the wing-tip stress intensity factor, given as:

$$K_{Ic} = \frac{\sigma_1 \sqrt{\pi a}}{(1 + \Lambda)^{3/2}} \left[1 - \lambda - \mu(1 + \lambda) - \frac{\sqrt{3} \lambda \Lambda}{\Gamma} \left[\frac{\Gamma \Lambda}{\sqrt{3}} + \frac{1}{\sqrt{3}(1 + \Lambda)^{1/2}} \right] \right], \quad (3.29)$$

where K_{Ic} is the fracture toughness, a is the half-length of the original crack, ℓ is the length of a single wing crack and $\Lambda = \ell / a$. The parameter Γ is a constant with a value of approximately 0.4, $\lambda = \sigma_2 / \sigma_1$ (ratio of confinement to compression) and μ is the coefficient of friction across the crack.

Schulson (1987, 1990) developed a model for failure stress σ_f based on the Ashby and Hallam model for the propagation of wing cracks, which he gave as:

$$\sigma_f = \frac{Z K_{Ic} d^{-1/2}}{(1 - \mu)}, \quad (3.30)$$

where Z is a constant, K_{Ic} is the plane strain fracture toughness of ice, d is the grain size of the ice and μ is the coefficient of friction for ice-on-ice sliding contact at the temperature and rate of interest. In Schulson's model, it was assumed that the wing cracks would grow until they reached a certain length after which instability occurred, resulting in unstable fracture. Schulson (1990) gave values of $Z = 1.8 \pm 0.2$ for axial splitting, and $Z = 2.5 \pm 0.3$ for shear faulting. Schulson et al., (1991) suggest that grain boundaries may be sites for the inclined parent crack nucleation and transgranular wing cracks then form at the tips of these cracks and run parallel to the compressive stresses.

Comparing the model of Schulson with that of Ashby and Hallam, Nixon (1996) developed a propagation criterion for Eq. 3.30 as corresponding to a Z value given by the expression:

$$Z = 3.5 \Lambda_c^{1/2}, \quad (3.31)$$

where $\Lambda_c = \ell_c / a$, with ℓ_c being the critical wing crack length, and a is the precursor crack half-length. Based on the Z values given by Schulson, the critical normalized crack lengths

would be $\Lambda_c = 0.51$ for shear faulting, and $\Lambda_c = 0.26$ for axial splitting. These critical lengths are significantly smaller than wing-cracks observed during testing. Nixon (1996) suggested that the values of Z given by Schulson were empirically developed, and are dependent upon the assumed values of μ and K_{Ic} , and may not be representative.

Sanderson (1988) applied the analytical model of Ashby and Hallam (1986) to provide estimates of the compressive strength of ice. For the uniaxial case, Sanderson first simplified Eq. 3.29 by assuming zero confinement for uniaxial conditions (i.e. stress ratio, $\lambda = 0$), which gives:

$$K_{Ic} = \frac{\sigma_1 \sqrt{\pi a} (1 - \mu)}{(1 + \Lambda)^{3/2}} \left[\frac{\Gamma \Lambda}{\sqrt{3}} + \frac{1}{\sqrt{3}(1 + \Lambda)^{1/2}} \right]. \quad (3.32)$$

To further simplify this expression, he assumed values of $\mu = 0.3$, $\Gamma = 0.4$ and that the wing cracks were much longer than the precursor cracks, giving $\Lambda \gg 1$, which simplifies Eq. 3.32 to give:

$$\sigma_f \approx 3.5 K_{Ic} \sqrt{\ell / a^2}. \quad (3.33)$$

Using this expression, Sanderson estimated that a stress of approximately 14 MPa was required to propagate a wing crack of length 10mm from an initial crack of length 5mm.

Sanderson (1988) also developed a crack linkage model based on Eq. 3.33, which assumed that failure occurs by the coalescence of cracks. For an average crack separation distance of Δ_f between adjacent cracks, Sanderson assumed that failure would occur soon after the wing cracks grew to a length of $\ell \approx \Delta_f / 2$. Based on this assumption, he gave the general equation for the failure stress due to crack linkage:

$$\sigma_f \approx 3.5 \frac{K_{Ic}}{a} \sqrt{\frac{\Delta_f}{2}}. \quad (3.34)$$

Using the work of Cole (1986) as a guide, Sanderson assumed that the average crack length is $2a = 0.65d$ and the initial crack density is on the order of one per grain (i.e. $\Delta_f \approx d$). This yielded an expression for the failure stress of ice as a function of grain diameter d , given by:

$$\sigma_f \approx 7.6 K_{Ic} / \sqrt{d}. \quad (3.35)$$

This expression was shown to give a reasonable (albeit higher) result compared with peak uniaxial compressive stresses measured during lab tests. Sanderson suggests that Eq. 3.35 embodies a number of simplifying approximations which may be modeled more completely by: (1) adjusting the model to include only active cracks (i.e. with favorable orientation); (2) accounting for temperature effects in the internal friction model.

The damage model of Ashby and Sammis (1990) based on wing crack propagation was applied by Nixon (1996) to model failure resulting from progressive damage weakening of the material. Given the focus of the present work on spalling fracture, further consideration of the Ashby and Sammis model is not considered.

Nixon (1996) also developed two new models for the failure stress of ice based on wing crack formation and propagation. His first model was similar to those reviewed above in that crack growth is assumed to be stable until a critical length is reached, after which instability occurs. This model is not materially different from that of Schulson. Nixon's second model considered the possibility that the formation of a wing crack will immediately lead to instability. These models are not considered further in the present work and the reader is referred to Nixon (1996) for additional detail.

Summary of Spall Modeling

In light of the edge crack, internal flaw and wing crack models reviewed above, it is concluded that tensile and shear (wing) crack models are most fundamental in modeling the fracture processes associated with spalling failure. The possibility of an ice sheet containing a large, pre-existing crack that is located at the center of the ice sheet (i.e. the conditions required for edge crack models) is quite remote. Internal flaw and wing crack models are seen as most fundamental compressive ice failure. Flaws, grain boundaries and inclusions in

ice are random in nature, resulting in the need for probabilistic treatment of fracture. Scale effects arise from the probabilistic nature of random spalling fracture, as well as from statistical averaging of non-simultaneous loading across the structure. The extreme local pressures of interest in design are assumed to occur when global fractures (radial and circumferential cracking) do not; these modes are discussed further in Appendix A.2. Scale effects associated with ice failure processes are discussed in Chapter 4.

Chapter 4: Critical Analysis of Scale Effects

4.1 Scope

In this chapter focus is placed on critically analyzing potential causes of the scale dependence observed in measured ice pressures. A variety of theories have been put forward in the literature as possible explanations for the scale effect in ice. The two main contributing factors to the scale dependence of pressure behavior are: (i) scale effects due to statistical aspects of failure (averaging), and (ii) scale effects that arise from mechanics. Scale effects associated with local pressure behavior (for instance on a structural panel of a ship or offshore structure) are associated with spalling fracture. The non-simultaneous nature of local pressure results in statistical averaging of pressures over larger areas. A critical analysis of the potential causes of this behavior is provided.

4.2 Classical Materials

For classical material models (elastic, viscoelastic, plastic, for example), a change of scale does not affect the failure pressure. Such behavior is depicted by the horizontal line in Figure 4.1. This is a consequence of the fact that the stress-strain relationships do not contain a parameter related to length and is based on the supposition that fractures do not occur. Since fracturing materials are inherently scale dependent (larger flaws fail at lower stresses), ice is expected to exhibit a scale effect for conditions which trigger fracture. Since ice is

viscoelastic, the correct normalization of speed was required to ensure appropriate scaling of strain rates for different sizes of indenters. The intrinsic (i.e. scale independent) strength σ_i of ice will be rate- and geometry-dependent.

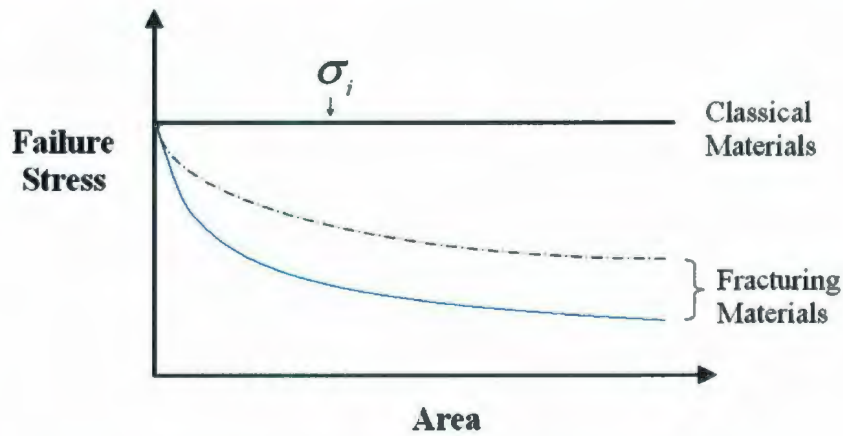


Figure 4.1: Scale effect for classical and fracturing materials

Classical continuum models are scale independent. Consider two self-similar deformable bodies, where the second case (Figure 4.2 (b)) corresponds to the first case (Figure 4.2 (a)) with all linear dimensions scaled by a constant factor λ .

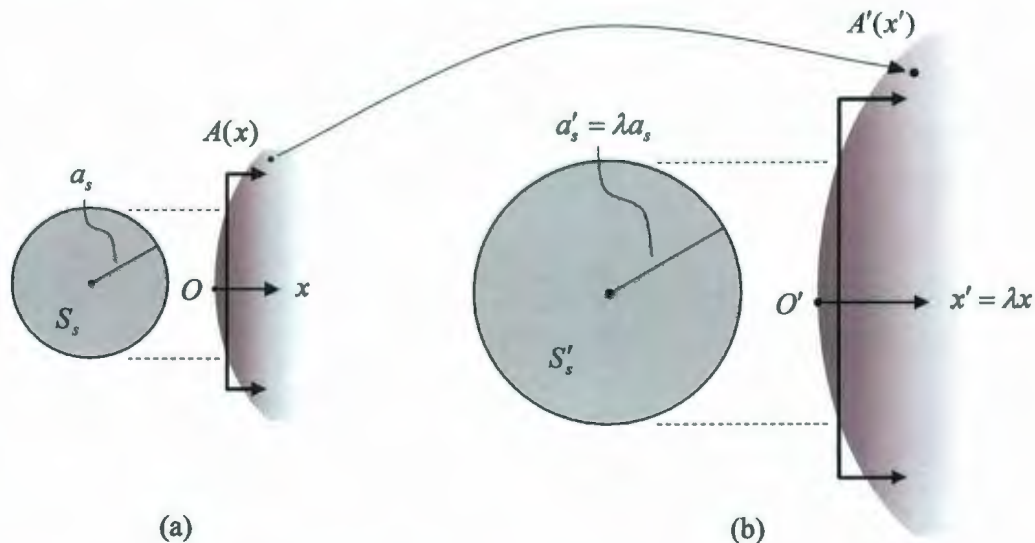


Figure 4.2: Schematic of two self-similar deformable bodies for: (a) Case 1 (unscaled geometry); (b) Case 2 (geometry scaled by constant factor λ)

Each point $A(x)$ at some location x in the first body then maps to a corresponding point in the scaled geometry $A'(x')$ at a scaled location $x' = \lambda x$. Here x stands for generalized location (e.g. x_1, x_2, x_3). Consider for Case 1 a region with projected area S_s (for example this could be the loaded area). For Case 2 a corresponding region with projected area S'_s scales according to $S'_s = \lambda^2 S_s$ since the radii are related as $a'_s = \lambda a$. Assuming both bodies are at rest and neglecting body forces, then the stress equilibrium equations are the same, and may be written as:

$$\frac{\partial \sigma_{ij}(x)}{\partial x_j} = 0, \quad (4.1)$$

with x' replacing x for Case 2.

For Case 1 (unscaled geometry), the strain-displacement equation at x may be written

$$\varepsilon_{kl}(x) = \frac{1}{2} \left\{ \frac{\partial u_k(x)}{\partial x_l} + \frac{\partial u_l(x)}{\partial x_k} \right\} \quad (4.2)$$

Since all linear dimensions are scaled by a factor λ , deformations scale as $u'_k = \lambda u_k$ and $u'_l = \lambda u_l$. Equation 4.2 may be written for Case 2 as:

$$\varepsilon'_{kl}(x') = \frac{1}{2} \left\{ \frac{\partial u'_k(x')}{\partial x'_l} + \frac{\partial u'_l(x')}{\partial x'_k} \right\} \quad (4.3)$$

Taking partial derivatives of the deformation terms for Case 2 gives:

$$\frac{\partial u'_k}{\partial x'_l} = \frac{\partial(\lambda u_k)}{\partial(\lambda x_l)} = \frac{\partial u_k}{\partial x_l}, \text{ and} \quad (4.4)$$

$$\frac{\partial u'_l}{\partial x'_k} = \frac{\partial(\lambda u_l)}{\partial(\lambda x_k)} = \frac{\partial u_l}{\partial x_k}. \quad (4.5)$$

Substituting Eq. 4.4 and 4.5 into Eq. 4.3 and comparing with Eq. 4.2, we see that:

$$\varepsilon'_{kl} = \varepsilon_{kl} \quad (4.6)$$

The solutions for stress and strain are then identical for each case since

$$\sigma_{ij} = C_{ijkl} \varepsilon_{kl} \quad (4.7)$$

where the constitutive relation of the material is embodied in C_{ijkl} , and is constant for both specimens. The above applies for elasticity, viscoelasticity, and plasticity, but breaks down if the constitutive relation contains a length scale (fracture).

Examples

Consider the indentation problem from Timoshenko and Goodier (1967) for a rigid cylinder indenting an elastic half-space shown in Figure 4.3.

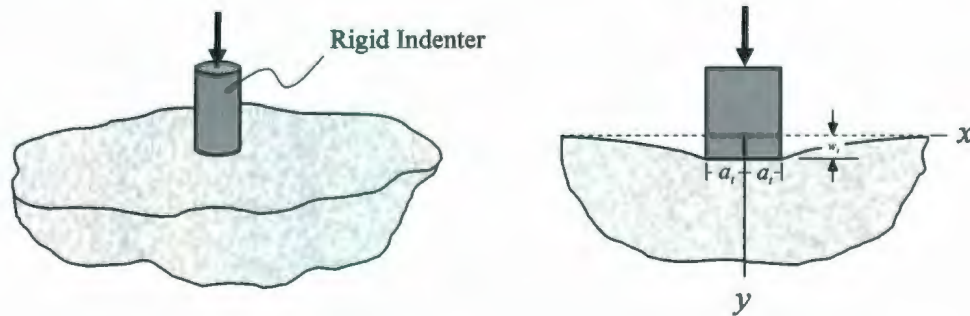


Figure 4.3: Rigid cylinder indenting elastic half-space.

Here the mean pressure \bar{P} over the contact face may be written as:

$$\bar{P} = \frac{2a_i w_i E}{(1-\nu^2)\pi a_i^2}, \quad (4.8)$$

where a_i is the radius of the indenter, w_i is the indentation depth, E is the elastic modulus, and ν is Poisson's ratio. To illustrate the scale independence, we assume two self-similar specimens where linear dimensions of the second specimen correspond to those of the first (a_i and w_i) scaled by a constant λ . Assuming the mean pressure for the first specimen is

given by Eq. 4.8, we may show that the mean pressure for the second (scaled) specimen is given by an expression identical to Eq. 4.8:

$$\bar{P} = \frac{2(\lambda a_i)(\lambda w_i)E}{(1-\nu^2)\pi(\lambda a_i)^2} = \frac{\lambda^2 2a_i w_i E}{\lambda^2 (1-\nu^2)\pi a_i^2} = \frac{2a_i w_i E}{(1-\nu^2)\pi a_i^2}.$$

For slow loading rates ice exhibits viscoelastic material behavior. A simple viscoelastic model is the Maxwell model, as depicted in Figure 4.4, which consists of an elastic spring, with elastic modulus E , in series with a dashpot having a viscosity modulus η .

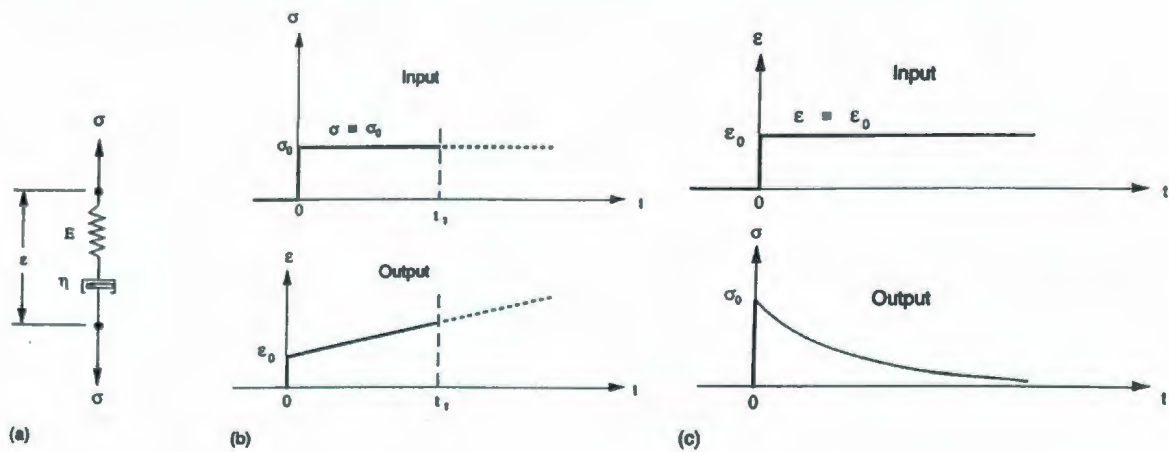


Figure 4.4: Illustrations of: (a) the Maxwell model; (b) creep response; (c) relaxation response.

The same scaling applies to linear viscoelastic materials as discussed above for the elastic case, provided that specimens are geometrically self-similar and strain rate similitude is maintained. When comparing results for specimens of a viscoelastic material at different geometric scales, speed must also be scaled by λ to avoid strain rate effects.

For nonlinear viscoelastic and plastic materials, scale independence also applies. Consider for example, the Prandtl solution for plane-strain compression, and that for axisymmetric indentation, where average pressures at failure are given by

$$\bar{P} = k\sigma_y, \quad (4.9)$$

where σ_y is the yield stress and $k = 2.57$ and 3.0 for plane-strain compression and axisymmetric indentation, respectively. Since σ_y is a constant material property and k is a constant, the ratio of average pressures for two self-similar specimens of different sizes equals unity (assuming both are subject to the same loading conditions).

Damage theories applied to ice (see Section 3.3.4.) are also scale independent, since they are based on stress history outputs from a nonlinear viscoelastic material model. For two geometrically self-similar specimens loaded such that strain rate similitude is maintained, the corresponding values of the damage parameters and stresses would be identical.

Summarizing Discussion

From the above examples and discussion, it is evident that there are no scale effects for continuum constitutive models that do not contain length scales. This is consistent with observations from ice indentation tests carried out at slow loading rates, where ice exhibits scale-independent continuum behavior (Li et al., 2004).

4.3 General Observations on Ice Behavior

The pressure-area scale effect, whereby pressure is observed to decrease for increasing area is generally well-accepted amongst the ice engineering community. In the literature some authors have attempted to distinguish between a scale effect and a size effect. For instance, Iyer (1983) defines a scale effect as a decrease in pressure due to changes in failure mechanisms with increasing interaction width; a size effect is defined as being associated with a decrease in strength due to larger critical flaws in larger material samples (assumed inherent to the material). Here the term scale effect and size effect are considered interchangeable and refer to the decrease in pressure with increasing size. Decreasing ice pressure has also been observed for increasing volume, ice thickness and interaction width. For cases where the scale dependent behavior of pressure with some geometric parameter is under consideration (i.e. pressure-area or pressure-thickness), the specific geometric dimensions of interest are identified.

The pressure-area scale effect has important implications for design. The selection of strengthening for full-scale structures based on laboratory-scale ice pressure data would result in highly conservative (and more expensive) designs. Another consequence of the scale effect is that local design areas (order of 1 m^2) must be designed to withstand significantly higher pressures than are required for global design (areas order of 100 m^2).

Figure 4.5 shows the two key areas of interest, the global interaction area and the local design area. The global interaction area (which has also been termed the nominal interaction area) is the area determined by the projection of the structure onto the original shape of the ice feature at a particular point of time in the interaction, without any reduction of the area for spalls and fractures that take place during the interaction.

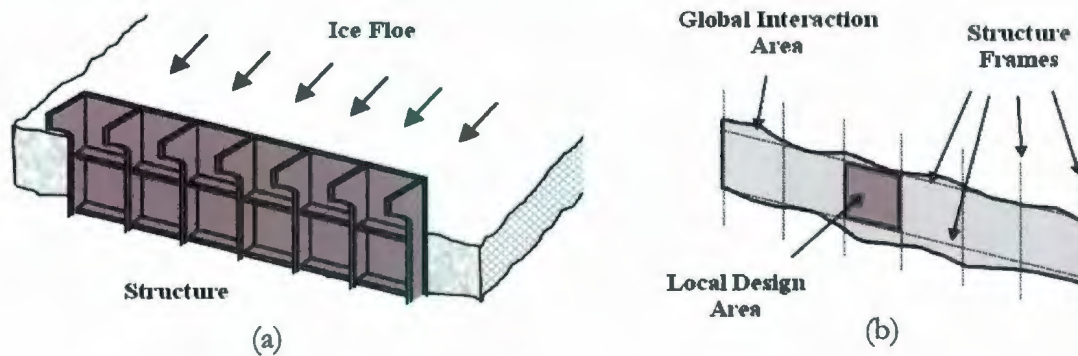


Figure 4.5: Schematics of (a) ice-structure interaction; (b) associated global and local areas.

The global interaction area can be determined from the shape of the ice feature and the shape of the structure. Within this area, there will be areas that carry little or no pressure, as well as zones of high-pressure. Large fracture events, such as floe splitting or flexural failures may result in regions of little or no loads on the structure. For design, a conservative assumption of full contact across the structure width is often used, since global fracture events cannot be relied upon to always occur or to result in load drops when they do happen. The extreme pressures of interest in design will result when global fractures do not. For these conditions, loads will be limited by crushing and spalling failure. Here it is assumed that global contact occurs across the full structure width.

Global Pressure Behavior and Scale-effect

Ice does not have a simple 'failure pressure' or compressive strength value which can be used in the design of structures for ice environments. Pressure is observed to decrease with increasing area for a broad range of scales of interest in engineering design. This pressure-area relationship is governed by the mechanics of ice failure, not by those of the structure the ice is interacting with. For compliant structures it has been observed structural dynamics can contribute to and modify the ice failure behavior. For the present work the structure is treated as essentially rigid.

Global pressures for full-scale structures are generally associated with areas ranging from about ten square meters to hundreds of square meters, as shown in Figure 4.6. Global design issues may include structural stability (foundation sliding and overturning resistance, station-keeping ability), integrity (ultimate load capacity, fatigue), and operability (severity of vibrations, pitching/rolling motions). In the context of the present work, only quasi-static loading due to ice failing on a rigid structure is considered.

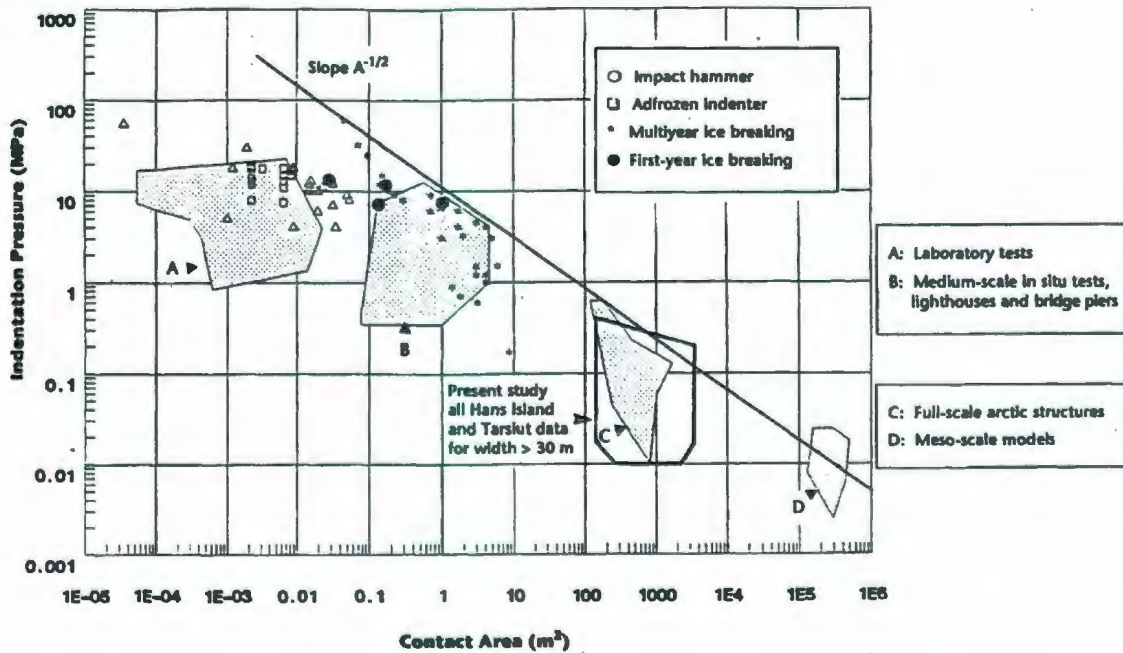


Figure 4.6: Measured ice failure pressure versus contact area for a wide range of interaction and loading situations for various ice types, temperatures and strain rates (from Blanchet, 1990. After Sanderson, 1988).

Since fracture plays an important role in ice failure behavior, it follows from mechanics that the flaws inherent to ice are also important. Sanderson (1988) considered three possible assumptions about the size of flaws in ice: (i) flaw size is constant over all scales; (ii) flaw size scales geometrically; (iii) larger size specimens represent larger samples from the parent flaw distribution.

The first assumption would yield no scale effect, since from fracture mechanics we see that the same stress would be required to fail the same size flaw. The second assumption gives a scale effect due to fracture mechanics, since increasing the length of the sample and its associated flaws by a factor λ results in a decrease in fracture strength by a factor $\lambda^{-1/2}$ (see Section 4.5.1 for further detail). Since area A is proportional to a linear dimension squared, this suggests a scale effect of $\sigma \propto A^{-1/4}$. While this is an interesting result, there is no physical reason why doubling the sample size exactly doubles the flaw length, since this implies that somehow the material changes with scale (Sanderson, 1988). There is no physical basis for this assumption and it is unlikely that this is a primary cause of scale the effect.

The assumption of statistical (fracture) effects starts with the premise that the material contains a statistical population of flaws of different sizes. Larger specimens will likely contain larger flaws, which in turn will trigger fracture at lower stress levels. Weibull's failure theory (see Section 4.5.2 for details) assumes that the 'weakest-link' (i.e. most critical flaw) controls tensile strength; this is not necessarily true for compression. Sanderson (1988) suggests that if compressive failure were to behave the same way, then strength σ should be a function of volume V of the form $\sigma \propto V^{-1/\alpha}$, where α_w is the shape parameter of the Weibull function (here assumed to characterize flaw distribution). For a specimen where linear dimensions are scaled by a factor λ , the volume scales by λ^3 and the stress should scale $\sigma \propto \lambda^{-3/\alpha}$. Since area $A \propto \lambda^2$, stress can be expressed as $\sigma \propto A^{-3/2\alpha}$. This result agrees with the observed relation from Figure 4.6 for the case where $\alpha_w \approx 3$. As discussed in Section 4.5.2, results from data are promising, and support the assumption that statistical aspects of fracture are a main contributor to the scale effect in ice pressure. Scale effects arising from mechanics are discussed in greater detail later in the chapter.

Local Pressure Behavior and Scale-effect

For full-scale structures, local areas of interest for design typically range between 0.6 m² and 10 m². Over this range, the primary modes of interest for design loads are crushing, with spalling fracture (see Chapter 3 for a review of theoretical ice fracture models).

A detailed discussion of local ice pressure estimation using the ‘event-maximum’ method developed by Jordaan et al. (1993), has been provided in Taylor et al. (2009). In this paper the authors present results for ship-ram data analyzed using the event-maximum method, along with a discussion of how to apply the method in practice. These results are compared with the design curve developed by Jordaan and his co-workers to model the α_L -area relationship as

$$\alpha_L = 1.25A^{-0.7} \quad (4.10)$$

where α_L is a pressure coefficient, and A is the local area of interest (see Jordaan et al., 1993 for details of the method and how to calculate α_L). From Figure 4.7 it is evident that a clear trend of decreasing pressure coefficient exists for increasing area, with the expression $\alpha_L = 1.25A^{-0.7}$ representing an upper bound to the available data.

Fitting curves of the form $\alpha_L = CA^D$ to all datasets considered, the exponent of the area term D was found to be well represented by a constant value of approximately -0.7 for all sets. The value of the C coefficient was found to vary from dataset to dataset, and is believed to be linked to the characteristics of the ice. For thinner ice sheets, flexural failure of the ice may also play a role in the observed lower pressures. Given the striking similarity of the trends observed for all datasets, these results suggest that there is a systematic cause of the scale effect.

The localization of loads into *hpzs* results in significant spatial and temporal variation in pressure across the width of the structure. Spalling fractures (on the scale of a single *hpz*)

contribute to the non-simultaneity of local failures and play an important part in the random averaging of loads.

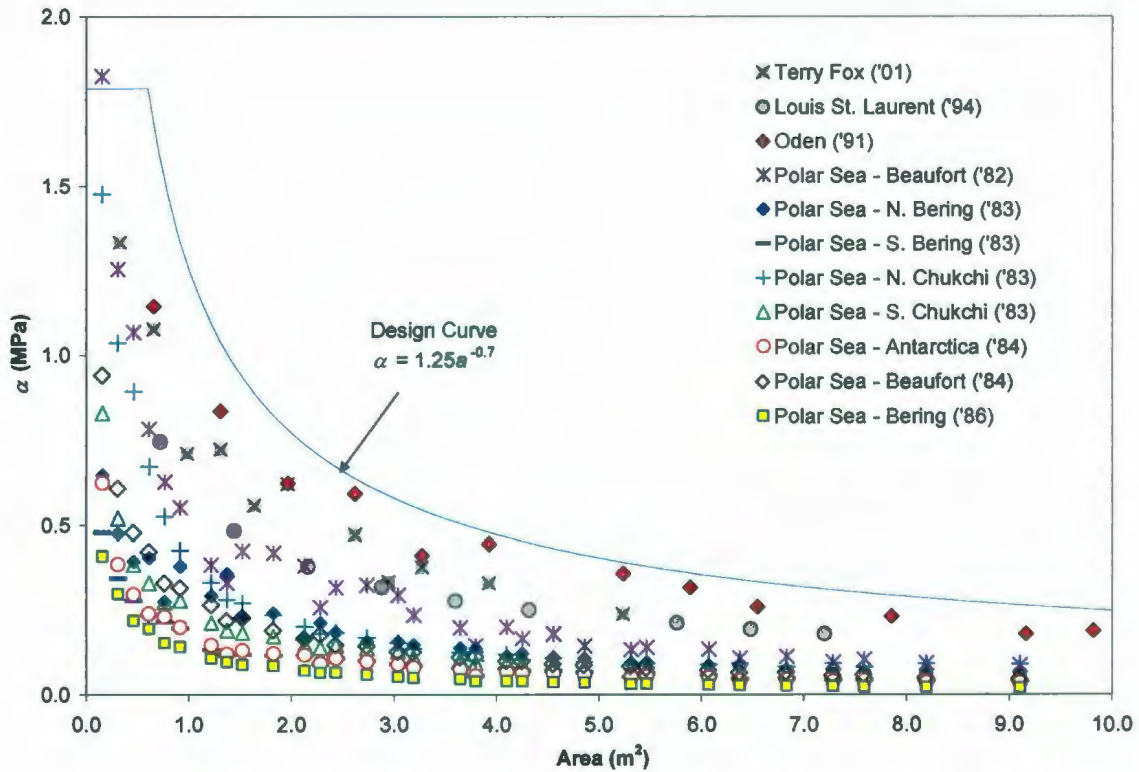


Figure 4.7: Plot of α_L vs. area for ship-ice interaction data (Taylor et al., 2009).

Since global loads result from the sum of local loads, understanding *hpzs* and local pressure behavior is seen as being fundamental to the modeling of scale effect over all scales of interest for design. Issues of particular relevance to modeling global loads, such as probabilistic averaging and correlation between adjacent panel pressures, are discussed later in the chapter.

Summarizing Discussion

In light of the above discussion, focus has been placed on exploring local pressure scale effects due to mechanics (particularly probabilistic aspects of spalling fracture) and studying

links between local pressures and global loads by accounting for statistical averaging across the width of a structure.

4.4 Probabilistic Averaging and Scale Effect

An important contributing factor to the scale-effect is associated with the statistical averaging of local loads across the width of the structure as a result of non-simultaneous failure. This section is focused on scale effects arising from statistical averaging. Scale effects associated with probabilistic aspects of individual fracture events are treated in Section 4.5.3.

4.4.1 Non-simultaneous Failure

Non-simultaneous failure arises as a result of random failures in and around *hpzs* across the interaction region. The birth, evolution and death of individual *hpzs*, which is responsible for this type of failure, are associated primarily with crushing and spalling fracture processes. For conditions which do not favor non-simultaneous failure, such as slower (creep) loading rates, the effects of probabilistic averaging are less significant.

The earliest contact pressure model for vertical structures in level ice was developed by Korzhavin (1971). This model assumed that the pressure on a structure is related to the uniaxial compressive strength, structure shape, contact length and number of contact points, which were accounted for using empirical coefficients. In this model, statistical aspects of non-simultaneous failure are buried in the empirical parameters. Later work by Varsta (1983) and Riska and Frederking (1987) extended this formulation to include multiaxial states of stress.

In modeling stochastic aspects of loads during an ice structure interaction, several process models have been developed based on the idealization of ice failure as a series of discrete failure events. Kry (1978) presented the first statistical treatment of non-simultaneous ice failure and introduced the concept of statistically independent failure zones. He suggested that the indenter used to capture failure zone statistics be at least as wide as the largest pieces observed to fail independently. As a practical lower limit on indenter width, Kry

recommended a width of four or five times the ice thickness; this recommendation was based on the reduction of indenter end effects as suggested by Neill (1975).

The work of Ashby et al. (1986) built on this concept and they used the failure of a brittle wax sheet indented by a cylindrical structure to illustrate the concept of non-simultaneous failure. As shown in the Figure 4.8, at any given time the load is transmitted through several distinct points, the position of which change in time as a result of fractures and spalls. As suggested by the above authors, such loading requires a probabilistic approach.

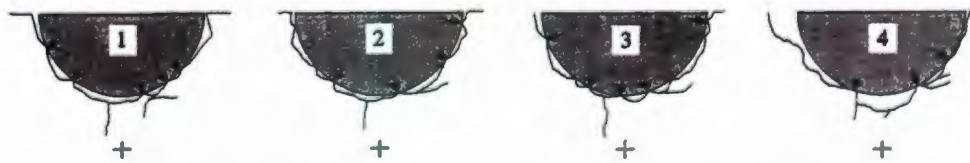


Figure 4.8: Non-simultaneous failure illustrated by tests on brittle wax (Ashby et al., 1986).

Ashby et al. (1986) introduced a theoretical model of non-simultaneous failure based on contact occurring through statistically independent failure zones. They assumed that during an interaction between an ice feature and a structure of width D_A contact would occur through independent contact zones of width L_i ; see Figure 4.9 (a).

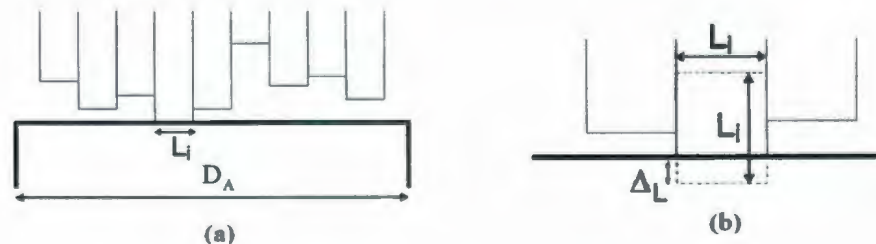


Figure 4.9: Idealized model of non-simultaneous failure (Ashby et al., 1986).

During an interaction, load was assumed to build up proportionally to the displacement of the independent contact zones. Fracture was assumed to occur at some limiting value of displacement Δ_L and result in the removal of a piece of ice with an area of L_i^2 , as shown in Figure 4.9 (b). In this model, the concept of independent failure zones was directly linked to a finite failure depth and did not account for the mechanics of ice failure.

As discussed by Palmer et al. (1983), Timco (1986) and others, different failure modes are associated with ice failure processes. From the laboratory-scale ice indentation tests in freshwater ice conducted by Timco (1986) it was suggested that the aspect ratio of the contact zone, as well as the indentation rate, had a significant impact on the observed ice failure mode.

A probabilistic model based on an idealization of *hpzs* as randomly sized point loads that are randomly distributed over a design area according to a spatial Poisson process has been developed by Jordaan, Xiao and Zou (1993). Comparison of this model with local pressures measured from full-scale ship ram data has indicated good agreement (in a statistical sense); see Johnston et al., 1998; Zou, 1996.

Dunwoody (1991) developed a model of non-simultaneous failure linking global loads to loads on a local panel. A spatial distribution model of local loads on an offshore structure was developed based on data from the Molikpaq. The logarithms of the local loads were modeled as a spatially-stationary Gaussian random process with a slowly varying mean and a negative exponential spatial correlation function given as $0.7 \exp(-|x|/30)$, where x is the separation distance in meters. Based on this spatial distribution model, the mean and standard deviation of the global force was modeled solely as a function of the mean and spatial correlation of the local force. End effects near the edges of the structure were ignored, since insufficient data were available to calibrate such a model, and the data that were available did not support significant end effect.

Takeuchi and Saeki (1994) used a shot-noise model to simulate time series of local ice pressures and study the effects of non-simultaneity. Kujala (1996) developed a model of ice crushing as a Poisson random process using statistical parameters based on full-scale PVDF measurements from the IB Sampo operating in the northern Baltic Sea.

Kamesaki et al. (1997) studied non-simultaneous failure characteristics of local segmented panel loads and global loads from laboratory indentation tests for rectangular and cylindrical model structures tested in urea ice. The authors examined the applicability of Korzhavin's

equation in extrapolating results and conclude that another approach would be required for the extrapolation of small-scale data to full-scale. In this study, the assumptions of Kry (1978) were also examined. Over the range of structure widths considered (100 mm to 1500 mm) the mean remained approximately constant, while variance decreased slightly for increasing width. The authors also indicate that the failure zones were approximately on the order of the ice thickness, thus supporting Kry's assumptions. Shi et al. (2002) reported results of a model test study of non-simultaneous failure for model multi-leg and conical structures using urea ice. It is noteworthy that the compressive failure mechanisms of model ice, such as urea or EGADS ice, may not exhibit the same characteristics as freshwater ice. Caution must be exercised in the use of model ice data, since the underlying physics may be different.

Sodhi (1998) presented results of experiments studying non-simultaneous failure, which were performed using a segmented indenter to indent freshwater ice at various speeds. He reported that simultaneous loading was observed on all segments at low velocities, while non-simultaneous failure due to brittle flaking was observed for high velocities. Sodhi applied a model based on the work of Dunwoody (1991) to the laboratory data to give an estimate of the correlation length as a function of ice thickness and indentation velocity.

Fractal concepts have also been explored as an approach to model the statistical nature of ice contact (see for instance Bhat, 1990; Palmer and Sanderson, 1991). Others, such as Blanchet and DeFranco (1996) have provided additional insight into the role of non-simultaneous failures in the scale effect and estimation of global loads.

4.4.2 Probabilistic Averaging

Probabilistic averaging essentially results in a "smoothing out" of peak stresses over the structure width, resulting in a lower overall global pressure on the structure. Statistically, this results in a global pressure having a same mean as the local panel pressures, but with a reduced global standard deviation.

Jordaan et al. (2006) used a probabilistic approach to analyze Molikpaq Medof panel data. The approach used takes into account the fact that only a portion of the structure was

instrumented, leading to estimates of global standard deviation appropriate for extrapolation to determine face loads. An ice-structure interaction event was idealized as a random averaging process, and the assumption was been made that the process is stationary in order to characterize the process. The authors observed that the data has many fluctuations due to fractures, splits, variations in ice thickness and other dimensions. If all of these aspects were known, for instance if local variations in ice thickness were measured, one could develop a model to account for them. To attempt to model a process as being non-stationary is difficult, since there is no basis to develop physical reasoning to explain the non-stationarity. Rather the causes of the load fluctuations are considered as background random events within a stationary process, contributing to the variance. The process is therefore treated as stationary for a given time interval, and modeled as a Markov (autoregressive) process in time.

An autoregressive process refers to a stochastic process that may be described in terms of a weighted sum of previous values plus an uncorrelated random series (white noise). A Markov process in time is a first-order autoregressive process; events depend on only one previous step but not those further in the past. In other words, "knowledge of the present makes the future independent of the past."

For temporal processes correlation is directional since time moves forward only. As discussed by Vanmarcke (1983), the directionality of temporal processes is reflected in the first-order difference equation for an autoregressive random series $X(t)$ according to

$$X(t + 1) = aX(t) + U(t), \quad (4.11)$$

where the following event in the series, $X(t+1)$, is dependent only upon the constant a , the present event $X(t)$ plus the contribution of the background random noise, $U(t)$. For a Markov process in space, no such directionality exists. The present event correlates to both the preceding one and the following one. This can be expressed by the second-order difference equation:

$$X(t) = k[X(t-1) + X(t+1)] + U(t), \quad (4.12)$$

where $X(t)$ is the random series, k is a constant and $U(t)$ is an uncorrelated random series. The associated covariance function is:

$$B_x(\tau) = \sigma_p^2 (|\tau|/c + 1) e^{-|\tau|/c}, \quad (4.13)$$

where σ_p^2 is the variance and τ is the lag distance (noting that space rather than time is the key variable). The lag distance τ is the distance between two points, for instance adjacent panels. The correlation function for the second-order autoregressive model has exponential form

$$\rho(\tau) = \left[1 + \frac{|\tau|}{c} \right] e^{-|\tau|/c}, \quad (4.14)$$

where $\rho(t)$ is the correlation coefficient, τ is the distance between adjacent panels and c is a constant (characteristic correlation length) which can be calculated based on the correlation coefficient and the distance between adjacent panels.

Ice pressure generally follows a non-Gaussian distribution for local areas. For large areas, a Gaussian distribution follows as a result of the central limit theorem. Using this assessment, ice pressure may be modeled as a random averaging process with a Gaussian distribution defined by a mean, standard deviation and a second-order autoregressive correlation function in space.

Using the above model, global ice pressure on a large contact area can be probabilistically defined. The mean global ice pressure is equal to the mean local ice pressure. The standard deviation of global pressure reduces depending on size of the loaded area due to averaging across the width of the structure. The variance of the global pressure σ_G^2 after averaging of a one-dimensional random process with local pressure variance σ_L^2 is

$$\sigma_G^2 = \gamma(T) \sigma_L^2, \quad (4.15)$$

where T is the averaging distance, which is taken as the whole structure width in this case. The variance function $\gamma(T)$ is defined (Vanmarcke, 1983) as

$$\gamma(T) = \frac{2}{T} \int_0^T \left(1 - \frac{\tau}{T}\right) \rho(\tau) d\tau. \quad (4.16)$$

For a second-order autoregressive model, the variance function for one-dimensional space is

$$\gamma(T) = 2 \frac{c}{T} \left(2 + e^{-T/c} - 3 \frac{c}{T} \left(1 - e^{-\frac{T}{c}}\right) \right). \quad (4.17)$$

The square root of the variance function $\sqrt{\gamma(T)}$ is a “reduction factor” to be applied to the local standard deviation σ_L according to the relation

$$\sigma_G = \sqrt{\gamma(T)} \sigma_L. \quad (4.18)$$

The above method requires knowledge of the correlation coefficient $\rho(t)$ as a function of distance, which may be obtained from the analysis of correlation between pressure measurements from pairs of local panels. Using the above approach, estimates of global pressure may be extrapolated from local panel pressure measurements.

4.5 Scale Effects Resulting from Mechanics

The results of dimensional analysis suggest that the property governing scale effects in ice is the fracture toughness, though little insight into the physics of failure is gained from this approach. Flaw length and other details of the physical process are quite important, yet are not accounted for in dimensional analysis; see Appendix A.3 for further detail. As loading rates are increased, fracture takes on a more dominant role in the failure behavior of ice. Relevant aspects of linear elastic fracture mechanics, fracture toughness models, fracture process zones and crack tip mechanics, as well as fractal theories are discussed in the context of scale effects.

Fracture is affected by many factors such as spatial and temporal variations in contact geometry, stress distribution and fields of naturally occurring flaws, such as favorably oriented crack-like grain boundaries. Given the random nature of these factors, a probabilistic

approach to modeling failure is seen as most appropriate. Weibull failure models and probabilistic fracture models are discussed.

4.5.1 Fracture Mechanics Models

Brittle fracture is an important process in the compressive failure of ice; scale effects associated with fracture are discussed below.

Linear Elastic Fracture Mechanics

From fracture mechanics theory, a scale effect is expected. To illustrate this point, we first consider a specimen containing a crack with dimension a . From linear elastic fracture mechanics (see for instance Anderson, 2005) we may write the failure stress as:

$$\sigma = K_{Ic} / \sqrt{2\pi a} \quad (4.19)$$

where K_{Ic} is the Mode I fracture toughness and $2a$ is the crack length. For two geometrically similar specimens with all dimensions scaled with the size of the body, the ratio of stresses may be given as:

$$\frac{\sigma_1}{\sigma_2} = \frac{K_{Ic,1} / \sqrt{2\pi a_1}}{K_{Ic,2} / \sqrt{2\pi a_2}} = \frac{K_{Ic,1} \sqrt{a_2}}{K_{Ic,2} \sqrt{a_1}} \quad (4.20)$$

From the above expression, two possible contributors to the scale effect emerge: (1) scale-dependence due to geometric scaling, and (2) the possibility of scale dependent fracture toughness. Based on this expression, the only way fracturing materials could exhibit scale independent behavior is if the fracture toughness scaled in a manner that was inversely proportional to the length scaling. For the present, it is assumed that fracture toughness is a scale-independent material property; the possible scale dependence of the fracture toughness is explored later. For the geometric scaling factor, $\lambda = a_2 / a_1$, Eq. 4.20 can be simplified to give:

$$\frac{\sigma_1}{\sigma_2} = \frac{K_{Ic}}{K_{Ic}} \sqrt{\frac{a_2}{a_1}} = \sqrt{\lambda} \quad (4.21)$$

From the above it is evident that fracturing materials exhibit scale dependent failure strength. Since area is proportional to a linear dimension squared, we may write:

$$\lambda \propto \sqrt{\frac{A_2}{A_1}}. \quad (4.22)$$

Substituting this result into Eq. 4.22 gives:

$$\frac{\sigma_1}{\sigma_2} \propto \left(\frac{A_1}{A_2}\right)^{-1/4}. \quad (4.23)$$

The above expression highlights that fracture behavior, unlike continuum models, predicts that failure stress for a specimen (and thus the peak contact pressure associated with a failure event) will decrease for increasing specimen size.

Fracture Toughness and Scale Dependence

Another potential cause of the scale effect in ice has been identified as a scale-dependent fracture toughness; see for instance Dempsey et al. (2001). Mulmule and Dempsey (1996) explored experimentally the relationship between fracture toughness and crack length for a wide range of crack lengths. Later work by Dempsey et al. (1999) and Dempsey (1999) reported the results of two major sets of field experiments and provided further insight into fracture processes in both freshwater and first year sea ice.

One series of experiments was conducted on warm freshwater ice covering a size range of 1:81, while the second series was conducted on first year sea ice over scales ranging from 0.5 to 80 m. For both programs the test geometries were self-similar. For the warm freshwater ice tests, fracture energies on the order of 20 Jm^{-2} were calculated; these high values were attributed to the effects of energy absorbing mechanisms such as grain boundary sliding. For sea ice, the size-independent fracture toughness was reported to be on the order of 0.15 to 0.25 MPa m^{1/2}; for a Young's modulus of 10 GPa, this suggests an energy release rate in the range of 2.25-6.25 Jm⁻². The authors attribute this higher fracture energy to creep microcracking in the fracture process zone. Dempsey and his co-workers suggest that the measured values of 'apparent fracture toughness' exhibit scale dependent behavior.

Schulson and Duval (2009) highlight that the key word here is ‘apparent’. A likely cause of the variation with size is the loading rate (i.e. strain rate similitude was not maintained). As highlighted by the work of Urabe and Yoshitake (1981) shown in Figure 4.9, lower fracture toughness values are obtained when faster loading rates are used during testing. This is likely a result of more extensive creep at the crack tip for slower loading rates compared with fast loading rates. The dissipation of additional energy necessitates higher total forces to propagate a fracture when loading rate is slower, resulting in higher apparent fracture toughness values for large specimens (which have lower effective strain rates). It is interesting to note the range of values obtained by Urabe and Yoshitake (1981) well match the range of values reported by Dempsey et al (1999).

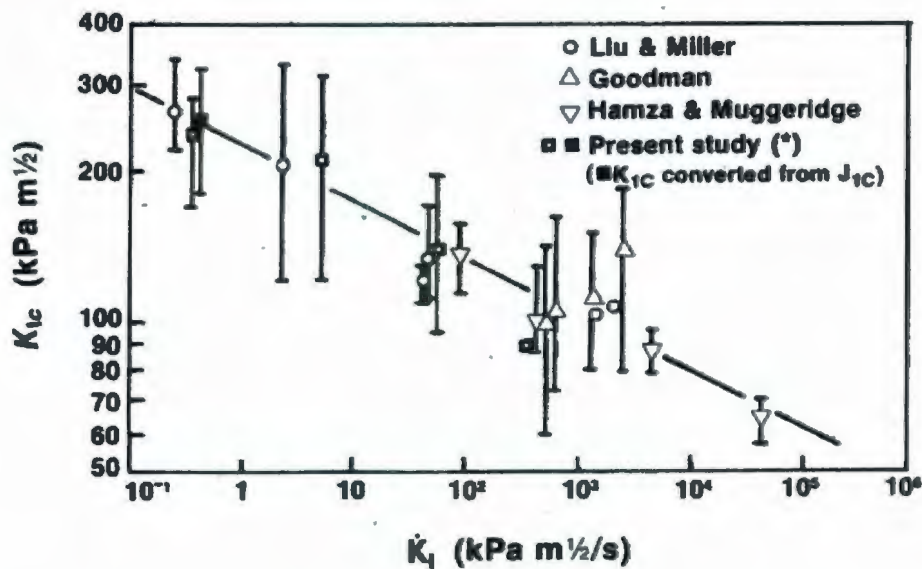


Figure 4.10: Relationship between critical-stress intensity factor K_{Ic} and \dot{K}_I for pure ice with average grain size of 5 to 10 mm, tested at -20°C (Urabe and Yoshitake, 1981).

As a point of practical interest, we consider the relative effect of the variation of apparent fracture toughness over the range of values given in Figure 4.10. We start by assuming the critical stress may be modeled as $\sigma_c = K_{Ic} / \sqrt{2\pi a}$, where K_{Ic} is fracture toughness and a is the crack length. Three cases are considered below: (1) fracture toughness is constant with value of $K_{Ic} = 0.125 \text{ MPa}\cdot\text{m}^{1/2}$; (2) fracture toughness is constant with value of $K_{Ic} = 0.25 \text{ MPa}\cdot\text{m}^{1/2}$; (3) fracture toughness as a function of size as reported by Dempsey. Calculated

values of critical stress corresponding to different crack length ranging from less than 1 m to approximately 100 meters are presented in Figure 4.11 for each of the cases.

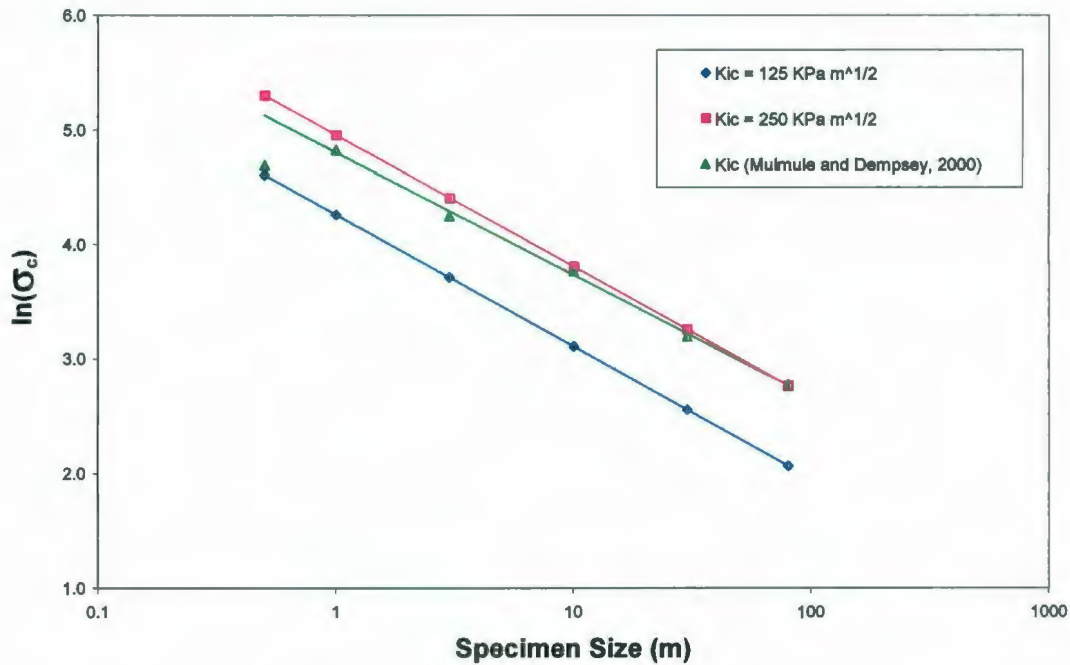


Figure 4.11: Critical stress as a function of crack size for self-similar geometry for two constant values of K_{Ic} , as well as a for scale dependent fracture toughness.

As may be observed from the above figure, the length of the crack will have a much more significant effect on the observed scale effect than will the value of the fracture toughness. Furthermore, a scale dependent 'apparent toughness' would result in a toughening with increasing size, not the softening behavior observed. Based on this observation, it is evident that the ice pressure scale effect cannot be attributed to scale dependent fracture toughness.

While some variation in fracture toughness may be associated with grain size, microstructure, temperature and salinity (see for instance Dempsey, 1996), it is natural to make the assumption that the fracture toughness is approximately constant over certain reasonable ranges of flaw size. On this basis it is concluded that fracture toughness is not a significant contributor to the ice pressure scale effect. Fracture toughness is treated as a constant material property in the present work.

Fracture Process Zones and Crack-tip Mechanics

Flaws and cracks in a material serve as stress concentrators. Stresses are particularly high in the region directly surrounding the tip of a crack, which can locally affect the material behavior. The region surrounding the crack tip for which the material behavior differs from the surrounding continuum is often termed the 'fracture process zone'. Perfectly elastic materials do not exhibit nonlinear behavior near the crack tip. Elasticity theory shows that for such materials, crack tip stresses tend to infinity as the distance from the crack tip tends to zero. In reality no material is perfectly elastic, since some dissipation process is required in the region directly adjacent to the crack tip to avoid the development of infinite stresses. Linear elastic fracture mechanics requires that the fracture process zone is small relative to the crack size, as shown in Figure 4.12 (a).

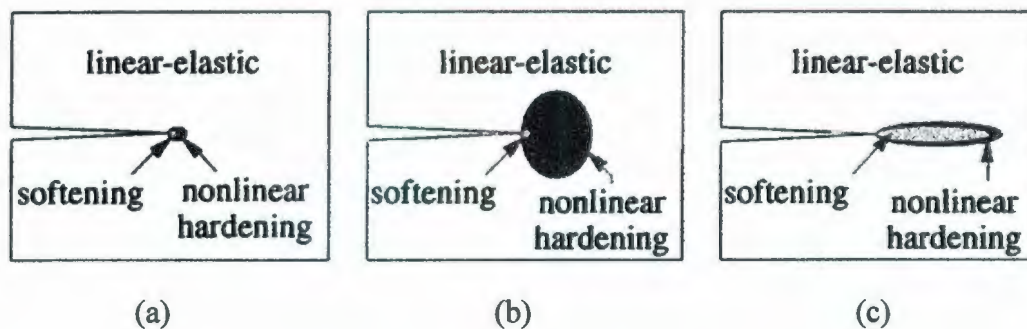


Figure 4.12: Fracture process zone at sharp crack tip for: (a) brittle material; (b) ductile material; (c) quasi-brittle material; (Bazant and Planas, 1998).

For plastic materials, if local stresses exceed the yield strength, the material surrounding the crack tip will yield; see Figure 4.12 (b). For other materials such as concrete, high local crack tip stresses result in microcracks surrounding the crack tip, leading to non-linear softening behavior in this zone; Figure 4.12 (c). Materials such as concrete, which are nominally brittle, but which exhibit local material softening due to damage processes are referred to as 'quasibrittle'.

For practical purposes, it is often assumed that the size of this process zone is negligible relative to the size of the specimen, and as a result non-linearity at the crack-tip does not significantly affect the failure behavior. This assumption, often called the small scale

yielding (SSY) assumption, simplifies the analysis of crack tip stresses and allows for the implementation of linear elastic fracture mechanics (LEFM). For materials for which the process zone size is large relative to the specimen size, linear elastic fracture mechanics cannot be employed.

For concrete and other quasi-brittle materials, size effects are associated with scale dependence of the fracture process zone relative to the specimen size. On this basis size-effect laws have been developed to account for such effects (see for instance, Bazant and Planas, 1998). The authors suggest that quasibrittle materials, particularly concrete, contain many microcracks and failure does not occur as soon as one of these microcracks starts to grow. Failure only occurs once a macroscopic fracture process zone forms as a result of the growth and coalescence of many microcracks. The authors propose that a fracture mechanics size effect occurs due to the release of stored energy of the structure into the fracture front. Unlike ice, concrete structures only fail after a large stable growth of cracking fronts and fractures. The stable crack growth of large fractures in concrete causes large stress redistributions and a release of stored energy, which, according to Bazant and Planas (1998), dominates over any statistical size effects. Bazant and Planas (1998) have explored size effects associated with such failure mechanisms in concrete based largely of crack band theory (for example, Bazant and Kim, 1986).

The extent to which crack-band theory applies to ice fracture is not clear. During small and medium scale interactions of interest to *hpz* mechanics, spalls frequently result from rapid, unstable crack propagation, not the growth of large stable cracks due to microcrack coalescence. Based on this observation, it is concluded that investigations of spalling and ice fracture are more appropriately treated using probabilistic fracture mechanics rather than crack band theory and its associated size effect laws.

Recall that the fracture toughness of ice has been measured over a large range of scales, and shown to be relatively invariant with specimen size once strain rate is accounted for. This suggests that explanations of size effect based on fracture process zones and quasibrittle behavior are an unlikely source of the scale effect in ice. No further consideration of quasibrittle size effect laws is given.

Fractal Theories

Some workers have used fractals and self-similarity as a possible approach to use in explaining scale effect (Bhat, 1990; Parsons, 1991; Palmer and Sanderson, 1991). According to proponents of fractal theories, the pressure-area effect is a natural outcome of the fractal geometry. Bhat (1990) proposed the concept of fractal edge geometry for an ice edge resulting from a series of discrete failure events during an interaction; see Figure 4.13 (a). According to this model, a zone of width w has order $r + 1$, and a zone of order r has a width of $\lambda w / 2$, where λ is a 'fractal contact factor'. Palmer and Sanderson (1991) expanded the concept of fractals to three-dimensions (Figure 4.13 (b)) and discussed this approach in the context of brittle ice crushing. In this model, a cube is divided into a hierarchy of cubic elements. Each fragment of order r has a probability of $p = 0.75$ of being crushed into $n = 8$ fragments of order $r - 1$. The premise of this model is based on the work of Sammis et al. (1987), which suggests that the probability of failure of a fragment largely depends on the relative size of the neighboring fragments. This comminution mechanism was believed to result in a fractal fragment size distribution. The total force acting on a plane of the fragmenting solid F_r is carried by a fractal hierarchy of elements of dimension less than or equal to d_r , where d_r is the diameter of a fragment of order r .

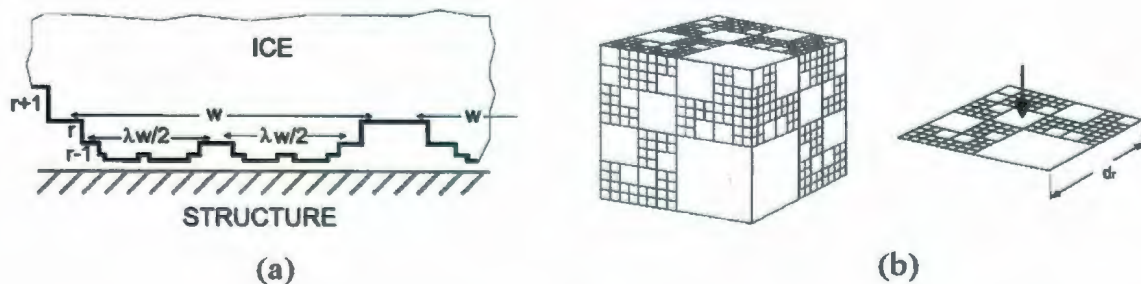


Figure 4.13: Fractal geometry models of: (a) Bhat (1990); (b) Palmer and Sanderson (1991).

Considering the microstructure of ice, one may conclude there is insufficient physical basis to justify the assumption of self-similarity. Microstructure and flaws are known to play an important role in fracture behavior of ice, and as discussed by Sanderson (1988), there is no physical justification for why doubling a sample size should automatically and precisely double the flaw size. This would be unexpected, since it actually implies that the material has

changed. Later work by Tuhkuri (1994), which examined the particle size distributions of crushed ice, did not support the assumption of fractal size distribution. On this basis, fractals are not considered further in this study of scale effect.

4.5.2 Weibull Statistical Strength Models

There is considerable basis for Weibull's approach as a result of its asymptotic tendency. Scale effects are associated with this theory. For engineering design, it is the extreme pressures that are of concern. This necessitates consideration of both mean and standard deviations of pressure.

Overview of Weibull Model

In its most general form, the weakest-link approach models the failure of a system of components as being governed by its weakest component. In other words, the maximum capacity of the system is governed by the minimum of the component capacities. For increasing demand, system failure will not occur until the capacity of the limiting element is exceeded.

When the edge of an ice sheet is subjected to a pressure, a stress distribution occurs in the ice sheet. Spalling fracture will not occur unless at some location the internal stress (demand) exceeds the capacity of the ice. If no failure occurs for the given pressure level, the pressure can continue to increase until the capacity is exceeded at some location and a spall occurs. For local fracture, the maximum capacity of the ice is governed by the minimum capacity of some portion of the ice specimen. We can interpret this as the asymptotic distribution of the minimum of a set of random strengths. On this basis, it may be concluded that a weakest-link type model is appropriate for spalling fracture in ice.

For homogenous stress, if T_i is the (random) strength of the i^{th} element in a weakest-link model with distribution function $F_r(t)$, for each of the $i = 1, \dots, n$ elements, the system fails when the weakest element fails. We denote this value as W . Thus

$W = \min(T_1, T_2, T_3, \dots, T_i, \dots, T_n)$ and for independent and identically distributed (*iid*) random

quantities, the failure probability of the system $F_W(\sigma)$ is the probability that all elements survive at a given stress. This may be expressed as

$$F_W(\sigma) = 1 - [1 - F_T(\sigma)]^n. \quad (4.24)$$

For a structure composed of $n = v/v_0$ elements, this may be written as:

$$F_W(\sigma) = 1 - \exp\left\{\frac{v}{v_0} \ln[1 - F_T(\sigma)]\right\}. \quad (4.25)$$

The value v_0 should be interpreted as a reference volume, such as that of a standard test specimen (see for instance, Bolotin, 1969).

For the conditions of interest to this research, the stress field will be inhomogeneous. A specimen of volume V having an inhomogeneous state of stress may be approximated as an assemblage of n homogeneously stressed elemental volumes ΔV_i , where $i = 1 \dots n$ (Jordaan, 2005). For each ΔV_i , the center coordinates of the element are given by x_i . Since the elemental stresses $\sigma(x_i)$ at positions x_i may be expressed as a function of the maximum stress σ , the failure probability of the specimen is:

$$F_W(\sigma) = 1 - \exp\left[\frac{1}{v_0} \sum_{i=1}^n (\Delta V_i \ln\{1 - F_T(\sigma(x_i))\})\right] \quad (4.26)$$

In this expression, the sum may be replaced with an integral to give

$$F_W(\sigma) = 1 - \exp\left\{\frac{1}{v_0} \int_V \ln\{1 - F_T(\sigma(x_i))\} dv\right\} \quad (4.27)$$

Weibull suggested the use of a power-law material function $m(\sigma)$ to represent the term $\{-\ln[1 - F_T(\sigma(x_i))]\}$ as given by:

$$m(\sigma) = \left(\frac{\sigma - \sigma_0}{\sigma_w}\right)^\alpha, \quad (4.28)$$

where α , σ_0 and σ_w are constants with σ_0 representing a lower limit on strength (often assumed to be zero to simplify the analysis).

Scaling Relationships from Weibull Theory

From the mean value of strength, with a lower minimum value σ_0 of zero, we may compare the expected strength $\langle R \rangle$ of two volumes v_1 and v_2 :

$$\frac{\langle R \rangle_1}{\langle R \rangle_2} = \frac{\left(\sigma_0 + \sigma_w \left(\frac{v_1}{v_0} \right)^{-\frac{1}{\alpha_w}} \Gamma \left(1 + \frac{1}{\alpha_w} \right) \right)}{\left(\sigma_0 + \sigma_w \left(\frac{v_2}{v_0} \right)^{-\frac{1}{\alpha_w}} \Gamma \left(1 + \frac{1}{\alpha_w} \right) \right)} = \left(\frac{v_2}{v_1} \right)^{\frac{1}{\alpha_w}} \quad (4.29)$$

Similarly we may compare the standard deviation of the strength distribution for two volumes v_1 and v_2 :

$$\frac{\sigma_{R,1}}{\sigma_{R,2}} = \frac{\left(\sigma_w \left(\frac{v_1}{v_0} \right)^{-\frac{1}{\alpha_w}} \left[\Gamma \left(1 + \frac{2}{\alpha_w} \right) - \Gamma^2 \left(1 + \frac{1}{\alpha_w} \right) \right]^{\frac{1}{2}} \right)}{\left(\sigma_w \left(\frac{v_2}{v_0} \right)^{-\frac{1}{\alpha_w}} \left[\Gamma \left(1 + \frac{2}{\alpha_w} \right) - \Gamma^2 \left(1 + \frac{1}{\alpha_w} \right) \right]^{\frac{1}{2}} \right)} = \left(\frac{v_2}{v_1} \right)^{\frac{1}{\alpha_w}} \quad (4.30)$$

For design, extreme pressures corresponding to a specified probability of exceedence are of interest. There are important differences between modeling means and standard deviations, and using these to estimate extreme pressures, compared with basing an analysis on maxima. The use of maximum pressures is to be avoided. These values can be significantly affected by factors such as event duration, the number of repetitions during testing, interaction events during a season, or how the data were processed (i.e. recorded only the peak values over a five minute interval). This may be illustrated by considering the extreme pressure E_1 corresponding to a specified probability of exceedence:

$$E_1 = \langle R \rangle_1 + s_1(\sigma_{R,1}) \quad (4.31)$$

where the term s_1 is a constant corresponding to a specified probability of exceedence. In the case of a normal distribution, a value of $s_1 = 3$ corresponds to the case where approximately 99.7% of observations are within 3 standard deviations of the mean. The implications of scaling on both mean and standard deviation are illustrated in Figure 4.14.

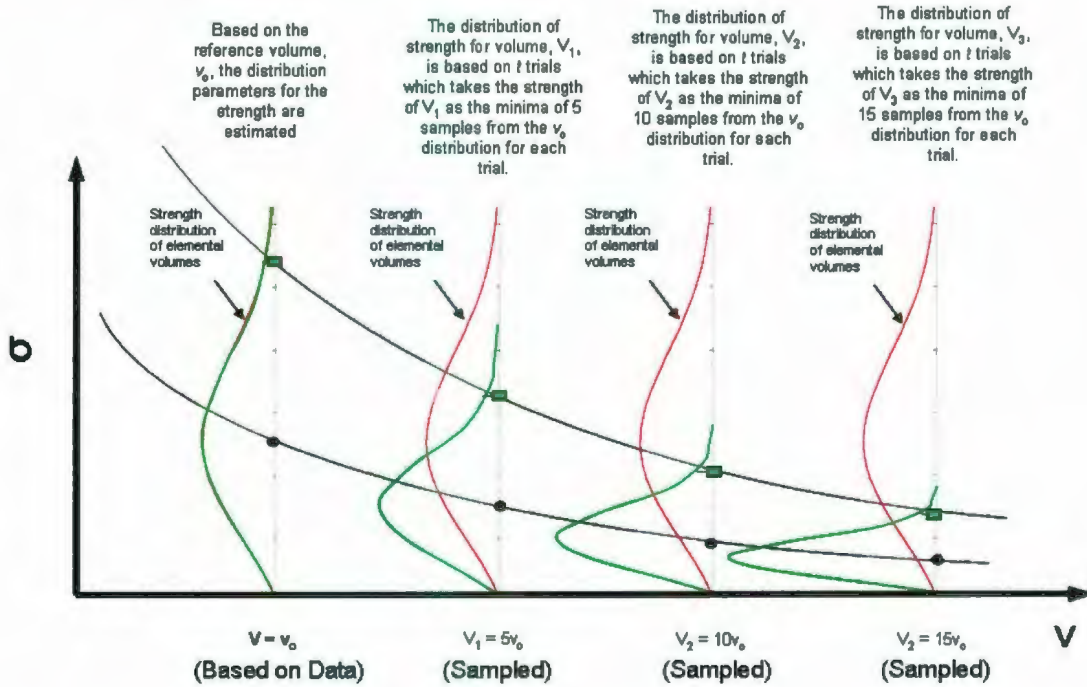


Figure 4.14: Illustration of Weibull scaling applied to both mean pressure and extreme pressures.

When peak pressures are identified from different dataset, they may correspond to different exceedence probabilities. Comparing the maximum strengths from two sets of test results with two different volumes v_1 and v_2 we get:

$$\frac{E_1}{E_2} = \frac{\langle R \rangle_1 + s_1(\sigma_{R,1})}{\langle R \rangle_2 + s_2(\sigma_{R,2})} \quad (4.32)$$

$$\frac{E_1}{E_2} = \frac{\left(\left(\sigma_0 + \sigma_w \left(\frac{v_1}{v_0} \right)^{-\frac{1}{\alpha_w}} \Gamma \left(1 + \frac{1}{\alpha_w} \right) \right) + s_1 \left(\sigma_w \left(\frac{v_1}{v_0} \right)^{-\frac{1}{\alpha_w}} \left[\Gamma \left(1 + \frac{2}{\alpha_w} \right) - \Gamma^2 \left(1 + \frac{1}{\alpha_w} \right) \right]^{\frac{1}{2}} \right) \right)}{\left(\left(\sigma_0 + \sigma_w \left(\frac{v_2}{v_0} \right)^{-\frac{1}{\alpha_w}} \Gamma \left(1 + \frac{1}{\alpha_w} \right) \right) + s_2 \left(\sigma_w \left(\frac{v_2}{v_0} \right)^{-\frac{1}{\alpha_w}} \left[\Gamma \left(1 + \frac{2}{\alpha_w} \right) - \Gamma^2 \left(1 + \frac{1}{\alpha_w} \right) \right]^{\frac{1}{2}} \right) \right)} \quad (4.33)$$

For the case where $\sigma_0 = 0$, the relationship between the maximum strengths may be written as:

$$\frac{E_1}{E_2} = \frac{\left(\sigma_w \left(\frac{v_1}{v_0} \right)^{-\frac{1}{\alpha_w}} \left(\Gamma \left(1 + \frac{1}{\alpha_w} \right) \right) + s_1 \left(\left[\Gamma \left(1 + \frac{2}{\alpha_w} \right) - \Gamma^2 \left(1 + \frac{1}{\alpha_w} \right) \right]^{\frac{1}{2}} \right) \right)}{\left(\sigma_w \left(\frac{v_2}{v_0} \right)^{-\frac{1}{\alpha_w}} \left(\Gamma \left(1 + \frac{1}{\alpha_w} \right) \right) + s_2 \left(\left[\Gamma \left(1 + \frac{2}{\alpha_w} \right) - \Gamma^2 \left(1 + \frac{1}{\alpha_w} \right) \right]^{\frac{1}{2}} \right) \right)} \quad (4.34)$$

Assuming the same reference volume is used for both scales, and the peak values correspond to the same exceedence level (i.e. $s_1 = s_2$), then the relationship $\frac{\langle R \rangle_1}{\langle R \rangle_2} = \left(\frac{v_2}{v_1} \right)^{\frac{1}{\alpha}}$ holds.

Weibull theory is relevant to the local pressure scale effect where extreme forces are governed primarily by spalling, though shear cracks emanating from compressive zones are an important contributor to spalling. Classical Weibull theory is limited to the case of tensile fracture. Global pressures involve other factors, such as probabilistic averaging and global fracture mechanism, which would need to be incorporated into the model.

Weibull Scaling Applied to Ice

The asymptotic tendency of Weibull's approach makes it an attractive starting point for a probabilistic treatment of ice failure. Recall from the preceding section that the ratio of mean strengths of two volumes v_1 and v_2 is $\langle R \rangle_1 / \langle R \rangle_2 = (v_2 / v_1)^{1/\alpha}$. The stressed volume is proportional to a linear dimension ℓ cubed, with contact area a proportional to ℓ^2 . Then

stress is proportional to $A^{-3/2\alpha}$ or $\ell^{-3/\alpha}$. On this basis, a value of $\alpha_w \approx 3$ would be required to give stress proportional to $A^{-1/2}$ (i.e. to give agreement with the pressure-area exponent of approximately -0.5 given by Sanderson, 1988).

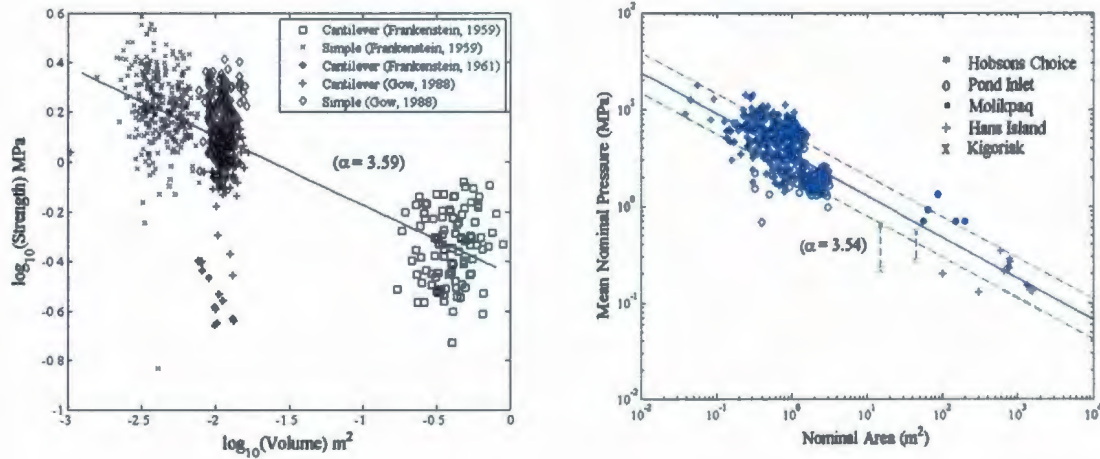


Figure 4.15: Scale effect for: (a) flexural failure data; (b) compressive failure data.

References for the sources of data may be found in Jordaan and Pond (2001).

Consideration of available flexural and compressive failure data (Figure 4.15) highlights the potential of this approach in modeling scale-effect. Figure 4.15 (a) shows the variation of flexural strength with volume for freshwater cantilever and 3-point bending experiments. Analysis of this data gives $\alpha_w = 3.59$, corresponding to a pressure-area exponent of approximately -0.4 . Analysis of the compressive data plotted in Figure 4.15 (b) result in a value of $\alpha_w = 3.54$, leading to an exponent of approximately -0.4 . These data correspond to a variety of situations and the analysis is consequently approximate. Further investigation is required to investigate the suitability of Weibull theory in modeling details of the scale effect.

Limitations of Weibull Theory

Weibull statistical theory has some limitation in modeling statistical aspects of fracture. Bazant and Planas (1998) discussed the limited ability of Weibull theory in dealing with fracture of a specimen containing large macrocracks due to the presence of stress singularities at crack tips. The authors suggest that such singularities will lead to exceedence

of material strength for vanishingly small stress. Such limitations may be readily overcome by restricting the application of the model to its intended range of applicability.

Bazant and Planas (1998) also suggest that for classical Weibull theory every structure is mathematically equivalent to a uniaxially stressed bar, which means that no information on the failure mechanism is taken into account. This issue stems from the assumption that the specimen strength is governed by the material tensile strength. Exceedence of this tensile strength results in failure of the specimen. For an ice specimen subjected to compressive loading, the stable growth of (shear) cracks from compressive zones is an important consideration. Further, the occurrence of a fracture event results in a load drop, but not to zero. The treatment of such failure mechanisms is beyond the scope of Weibull theory, and requires the development of a probabilistic fracture mechanics model.

4.5.3 Probabilistic Fracture Mechanics Models

It is central to the notion of scale effects that failure is initiated at defects and flaws in the material. In the compressive ice failure process, spalls and splits form in unconfined regions near the edges of the ice-structure interface. Fracture events occur in a random fashion, necessitating consideration of probabilistic failure theory (see for instance, Sanderson, 1988; Jordaan and Pond, 2001; Jordaan, 2001). A realistic starting assumption is that the material contains a statistical population of flaws and larger samples are expected to have a higher probability of containing a larger critical flaw.

Hunt and McCartney (1979) developed a statistical treatment of defect populations in a manner that can be applied to the case of inhomogeneous multi-axial stress fields. They start by establishing a relationship between the distribution function of largest defects $Q(x, V)$ for samples of volume V in terms of a material defect distribution function $q(x)$ as given by:

$$Q(x, V) = Vq(x) \exp\{-V \int_x^{\infty} q(x') dx'\} \quad (4.35)$$

The inverse relationship was then derived as:

$$q(x) = \frac{1}{V} \cdot \frac{Q(x, V)}{1 - \int_x^{\infty} Q(x', V) dx'} \quad (4.36)$$

The authors suggest that this equation may be used to determine the material defect distribution function $q(x)$ from $Q(x, V)$, where $Q(x, V)$ may be estimated from strength data obtained from tests on a group of samples of volume V .

The failure probability $S(L)$ of a general component with a defect distribution function $q(x)$ that is subjected to an inhomogeneous stress distribution was also developed. By assuming there was a critical value of stress σ_c , above which all specimens failed, they gave an expression for the average strength of a population of components as:

$$\bar{\sigma} = \int_0^{\sigma_c} e^{-U(L)} dL, \quad (4.37)$$

where L is the maximum principal stress encountered in the component (proportional stressing is assumed; $c(r)$ is the normalized stress tensor and the maximum principal stress $\sigma(r)$ at location r is given by $\sigma(r) = Lc(r)$). $U(L)$ is given by:

$$U(L) = \int_{\Omega} \left\{ \int_{X(Lc(r))}^{\infty} q(x) dx \right\} dV, \quad (4.38)$$

Where Ω denotes the region of space occupied by the component, $X(\sigma)$ is a stress dependent fracture criteria (the authors used a Griffith type criteria), $Lc(r)$ is the maximum principal stress at location r , and $dV = x_1 x_2 x_3$. A useful expression for the distribution function of failure initiating flaws was then given as:

$$F(x) = q(x) \int_{\Omega} \exp \left\{ -U \left(\frac{1}{c(r)} X^{-1}(x) \right) \right\} dV, \quad x_c < x < \infty, \quad (4.39)$$

where x_c is the size of the critical defect corresponding to critical stress σ_c . Hunt and McCartney also highlighted a useful approach for relating the derived failure probability expressions to Weibull theory. While the above model provided much useful insight into the

probabilistic treatment of fracture, Hunt and McCartney assumed that failure is impossible for elements where the maximum principal stress is zero or negative (compressive), limiting its direct application in modeling the effects of shear cracks in spalling fracture.

In modeling the failure of ice, the work of Maes (1992) is also of particular relevance. He developed a probabilistic model of ice failure for a field of flaws in ice subjected to indentation. He started with a specimen containing a randomly dispersed Poisson field of cracks of random original dimensions. He then discretized a specimen of volume V into n elements, each with a volume dV_i . The probability of failure for a given nominal stress σ was given as:

$$\Pr(F | \sigma) = 1 - \prod_{i=1}^n [(1-p) + p(1 - \Pr(S_i | \sigma(x_i)))] \quad (4.40)$$

where F is the event that failure occurs, and p is the probability that a crack is encountered in a given elemental volume ΔV_i . $\Pr(S_i | \sigma(x_i))$ is the probability that the i^{th} element located at coordinates x_i survives (i.e. event S_i) given the stress level $\sigma(x_i)$,

Maes (1992) used criteria which accounted for both time dependent fracture, as well as brittle failure. The criteria for time dependent fracture was based on the rate of crack growth developed by Schapery (1981) for a damaging viscoelastic material. Brittle failure was modeled using a Griffith type fracture criterion for Mode I crack propagation and was based on the maximum positive (tensile) principal stress. Failure in this context was defined as the occurrence of unstable crack propagation. Using a simple stress function, Maes (1992) developed a failure probability distribution to predict the strength of ice based on a brittle elastic fracture criterion and an assumed flaw structure. Considering the special case where the flaw dimensions follow a Pareto distribution with exponent z and the smallest crack size a_1 , Maes (1992) proposed that the failure stress distribution for ice could be expressed as:

$$F_{\sigma}(\sigma) = 1 - \exp \left[-\lambda a_1^z \int_V \left((k-1)c_2(x)S(\sigma) + \left(\frac{Y\hat{\sigma}_1(x)\sigma}{K_{Ic}} \right)^{2(k-1)} \right)^{z/(k-1)} dx \right] \quad (4.41)$$

where λ is the mean crack density, k is a positive constant, c_2 is a positive constant that depends on the state of stress, $S(\sigma)$ is a stress dependent damage measure, K_{Ic} is the plane strain fracture toughness, Y is a geometric scale factor, $\hat{\sigma}_1(x)$ is the maximum principal stress, and σ is the normalized stress tensor at location x (assuming proportional stressing). As with Hunt and McCartney, only tensile fracture was considered in this model.

The classical notion of material strength does not well apply to ice given the dominance of random fracture processes in ice failure. The stress at failure may be dependent on geometry, boundary conditions and other variables, suggesting that a more complete picture of fracture under compressive loading is required. Probabilistic failure models for ice are examined further in Chapter 7.

4.6 High Pressure Zone Behavior at Different Scales

High pressure zones have been observed over a wide range of scales. For small interaction areas, the majority of the load may be transmitted through a single *hpz*. Small-scale ice indentation tests provide valuable insight into the behavior of single, stationary *hpzs*. Early indentation work by Frederking and Gold (1975) provided insight into the ductile behavior of edge-loaded ice plates. Timco (1986) and Finn (1991) reported results of edge indentation tests on floating columnar freshwater ice sheets in the brittle range. A similar series of indentation tests were conducted in the ice basin of the Technical Research Center of Finland by Kärnä and Muhonen (1990), and Muhonen et al. (1992). For a complete historical review of small-scale laboratory tests, the reader is referred to Sanderson (1988).

In small-scale laboratory tests performed by Barrette et al. (2002), a 2 cm spherical indenter was used to study the failure behavior of the ice in the vicinity of a single, stationary *hpz*. The authors found that the crushing process and load cycling were directly linked and were influenced by both temperature and rate. At relatively warm temperatures, in the range of -2 °C, and at a low velocity of 0.2 mm/s, ice fails by a ductile failure mechanism. No extrusion of crushed ice or spalls was seen to occur and a 'smooth' increase in total force was observed. Similar behavior has been modeled previously by Jordaan and Xiao (1992), in

which the authors were able to successfully reproduce the smooth increase in total force. In the tests by Barrette et al. (2002), load cycling behavior periodically begins to appear in low temperature tests performed at $-10\text{ }^{\circ}\text{C}$ and $-20\text{ }^{\circ}\text{C}$ with speeds greater than 2 mm/s and continues for speeds increasing to 10 mm/s. This load cycling was accompanied by the extrusion of crushed ice and the formation of damaged layers at the indentation site. Recent reviews of indentation testing may be found in Mackey (2005) and Wells et al., (2009).

For larger areas, several *hpzs* may interact over the contact zone and may take on different distributions depending on the shape of the ice feature (Jordaan et al., 2008). In the present work on ice sheets, *hpzs* are assumed to be arranged in a line-type configuration, such as that described by Riska et al. (1990). The size of *hpzs* is assumed to scale with the size (thickness) of the ice and they are modeled as being approximately homologous in structure. This has important implications for this study, since average ice thickness for JOIA tests is approximately 0.30 m, while average first-year ice thickness for Molikpaq events is approximately 1.25 m. This assumption is discussed further in section 5.9 of Chapter 5.

Data from past field programs, such as Pond Inlet (Masterson et al., 1992), Rea Point (Masterson et al., 1999), and Hobson's Choice Ice Island (Frederking et al., 1990; Gagnon and Sinha, 1991, Masterson et al., 1993; Gagnon, 1998) provide important insight into *hpz* behavior. Barrette et al. (2002) examined stress scaling in *hpzs* using data from the above field programs, along with data from laboratory tests conducted using scaled-down indenter geometry and equivalent displacement rates (indentation rates were also scaled to maintain strain rate similitude). They found striking similarity between the failure processes and damage zones observed over a broad range of scales, supporting the assumption that *hpzs* scale with thickness. Li et al. (2004) also studied the behavior of *hpzs* at different scales. For low indentation rates damage processes tended to dominate the failure behavior and the measured pressures did not exhibit scale dependence. At higher rates, the occurrence of spalling fracture resulted in a pressure-area scale effect. This work suggests that the key to the local pressure-area scale effect lies in understanding the spalling fracture process. Details of *hpz* behavior are explored in the next chapter.

Chapter 5: High Pressure Zone Behavior and Averaging

5.1 Scope

This chapter focuses on the analysis of small and medium scale experimental results related to the compressive failure of ice. One of the aims was to examine crushing and spalling fracture with particular emphasis on understanding the behavior of high pressure zones (*hpzs*). Results from the analysis of data from sample small-scale experiments are presented, along with results from supplementary numerical simulation of local ice failure (including treatment of damage and spalling). A key objective of this chapter is to gain insights into the nature of crushing and spalling processes observed during medium scale interactions. Tactile pressure data from the Japan Ocean Industries Association (JOIA) medium scale tests have been examined for sample spalling and crushing events.

Local panel pressure data from the JOIA program are analyzed to study correlation between individual panels and a new approach to modeling panel correlations was developed based on the use of composite correlation functions. Global load estimates were extrapolated from local JOIA data using several different approaches, which were compared with measured global pressures to evaluate the effectiveness of each approach. Correlation behavior of panel data from Molikpaq were analyzed and compared with JOIA results. Issues related to correlation and ice thickness effects were discussed and recommendations for further research are made.

5.2 Overview

For design, most methods continue to rely upon empirical data collected from full-scale field measurements. Scale-effects observed in ice pressure behavior have resulted in a large degree of uncertainty associated with the estimation of full-scale loads from small-scale data sets. Rather than use small-scale test results to directly guide design, a more useful approach is to use laboratory work to aid in our understanding of the mechanics associated with ice failure processes. Medium-scale tests offer similar insights regarding material behavior, and provide data useful in assessing pressures acting over local panel areas. Through better understanding of failure processes and associated mechanics, it will be possible to reduce uncertainty and improve design methods.

5.3 Small-scale Ice Indentation Experiments

The study of high pressure zones at small scales has frequently been accomplished through laboratory indentation testing (see for Wells et al., 2009 for a summary of previous indentation testing). Small-scale indentation experiments are often taken as being representative of a single, stationary *hpz*.

The work of Mackey (2005) and Mackey et al. (2007) summarize the results of a series of experiments studying spalling and fracture behavior of polycrystalline ice loaded by a rigid spherical indenter. In this research the relationship between failure stress and distance from the indenter to specimen edge was studied. These results suggest that increasing the distance from the edge increased the stress at which fracture occurred. This effect was attributed to the increased confinement provided by the additional material between the indenter and the free surface. From this research it was clearly established that drops in load are related to the mechanics of spalling.

This work was extended by Wells and her coworkers to examine the role of large grain boundaries and natural flaws in triggering fracture (see for instance, Jordaan et al. (2008), Wells et al. (2009)). Data from these tests are an important source of information regarding spalling and fracture behavior of ice since they combine high-resolution

pressure data and synchronized high speed video. Complete details of the test set-up and results for entire series of indentation experiments are available in Wells et al. (2009). A sample indentation event from this series has been analyzed and the observed damage and spalling behavior were simulated using finite element analysis.

5.3.1 Analysis of Sample Indentation Event

These tests consisted of indenting a milled block of polycrystalline ice using a rigid, spherical-faced indenter. The cylindrical indenter was 20 mm in diameter and had a polished spherical indentation surface with a radius of curvature of 25.6 mm. Air temperatures were maintained at approximately -10°C during testing. Data were recorded at a sampling frequency of 20 kHz and filtered using a 3dB cutoff frequency of 3 kHz. The penetration depth and test speed were set on the test frame controls prior to each experiment. Total force from the load cell, LVDT displacement and high-speed digital video (black and white) were recorded during each test. The load trace and high-speed video data were synchronized based on an electrical synchronizing pulse generated at the beginning of each test. A Tekscan tactile pressure sensor (rated for 25,000 PSI) was used to record pressure at the indentation interface; see Wells et al (2009) for additional detail of the instrumentation and set-up.

Comparison of Damage and Fracture Processes

During test event I07_V5P0_C_062, both damage processes and several large spalls were observed. This test was conducted at an indentation rate of 5 mm/s. The time series data from the LVDT and MTS load cell are shown in Figure 5.1. As shown, the nominal contact area increased linearly with time. Initially, the total force and nominal stress both increased as the indentation proceeded; during this process small spalls occurred intermittently and evidence of local damage (microcracking) around the indentation site was observed.

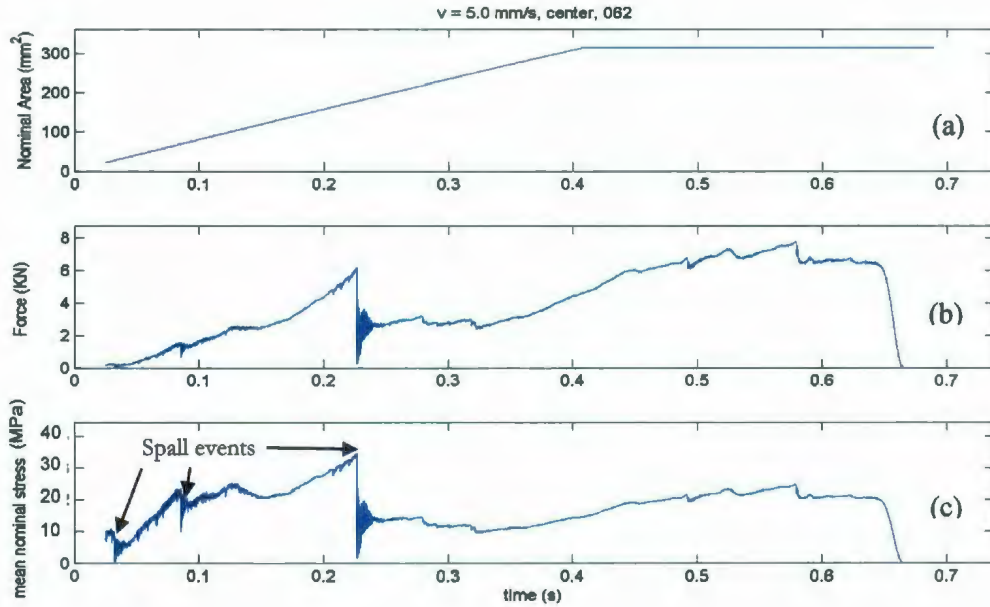


Figure 5.1: LVDT and MTS load cell data for event I07_V5P0_C_062 showing time traces of: (a) nominal indentation area; (b) total force on the indenter; (c) mean nominal stress on indenter; modified from Wells et al. (2009).

In the early stages of the indentation, smaller spalls have a larger relative significance compared with later in the test when a more developed indentation zone has evolved. During later stages of the indentation, as shown in Figure 5.2, dark zones of recrystallized ice are present near the core of the indentation zone. The white regions correspond to the sintered layer of microfractured and crushed ice particles. Detailed examination of Figure 5.2 (a) shows that in some regions, the extruded ice appears to ‘flow’ over the spalled zones, smoothing some of the rough surfaces formed during spalling.

To illustrate the relationship between measured pressure distributions and microstructural changes, the last frame of the tactile pressure sensor data before the test was completed was plotted in Figure 5.2 (b). An outline of the core (red) area of the *hpz* was projected onto the zone indentation for comparison purposes; see Figure 5.2 (c). Good general agreement between the location of the ‘core’ high pressure regions and the recrystallized zones is observed. Some discrepancy between the two is expected since the tactile sensor data corresponds to a given instant in time, while the damage shown in the picture is a consequence of the entire loading history of the specimen.

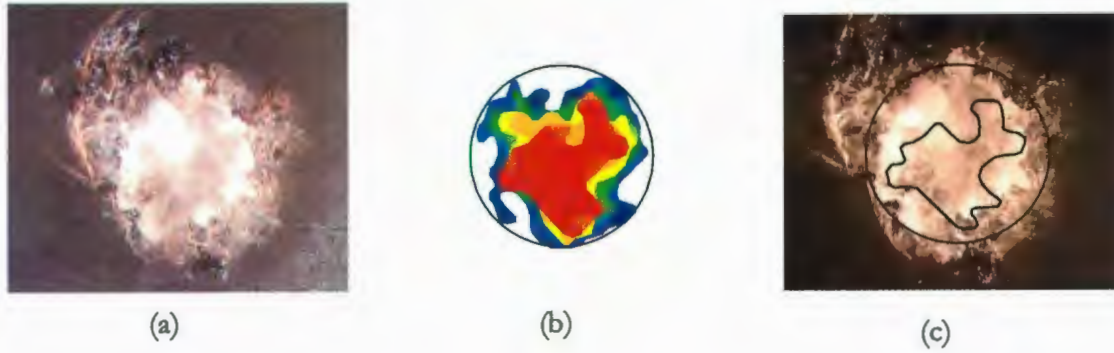


Figure 5.2: Pictures from event I07_V5P0_C_062 showing: (a) indentation zone immediately after testing; (b) pressure distribution given by tactile sensor for last frame before end of test; (c) overlay of *hpz* outline from tactile sensor, showing general agreement between locations of *hpz* 'core' area and darker colored recrystallized zone (photos modified from Wells et al., 2009).

To examine the microstructure of the indentation zone, thin-sections were prepared; see Figure 5.3. As may be seen from these images, the zone of microstructural modification is highly localized into a damage layer immediately adjacent to the indenter. Several types of cracks also form in the zone directly below the indenter. Near the edges of the contact zone, transgranular tensile cracks form, while many of the cracks below the indentation zone form due to shear along grain boundaries.

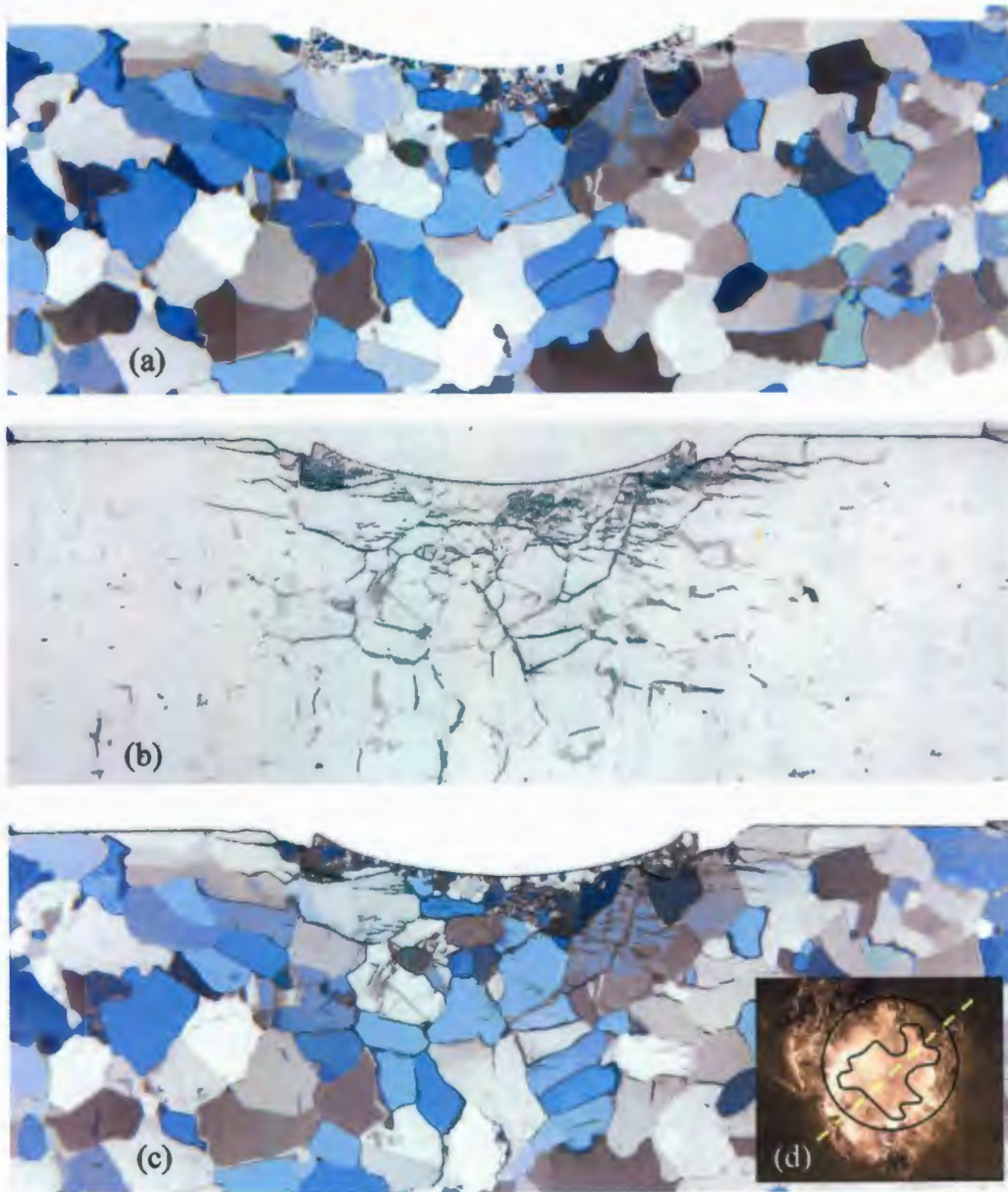


Figure 5.3: Inverted color images of thin-sections from I07_V5P0_C_062 shown under (a) polarized lighting; (b) side-lighting; (c) combined polarized and side-lighting conditions; (d) inset showing plane of thin-section (modified from Wells et al., 2009).

From the above it is evident that microstructure damage and spalling fracture are two distinct, yet interrelated processes. Both play important roles in the formation and evolution of high pressure zones during the compressive failure of ice.

Consequences of Spalling

To examine the consequences of spalling, test event I07_V10P0_C_041 was selected for further analysis. This test corresponded to an indentation depth of 10 mm, at an indentation rate of 10 mm/s. Examination of the synchronized tactile sensor data and total force measurements provided valuable insight into the effects of spalling on the pressure distribution. As shown in Figure 5.4 (a), prior to spalling, a large single *hpz* formed under the indenter, with the center of pressure corresponding well with the center of the indenter (nominal area shown by the black circle). Once fracture occurred, Figure 5.5 (b), a large asymmetric spall was removed from the *hpz* resulting in a significant (approximately 27%) area reduction and a load drop of approximately 50% (see Figure 5.4 (c)). Given that spalls often occur near the edge of the indentation zone, they are generally asymmetric in shape. While large spalls such as the one shown in Figure 5.4 are easily identified from the tactile sensor data, it is evident from the high-speed video footage that many smaller spalls also occur. In reality, spall size is expected to cover a broad spectrum of sizes, with smaller events occurring more frequently than large events. This will be discussed later.

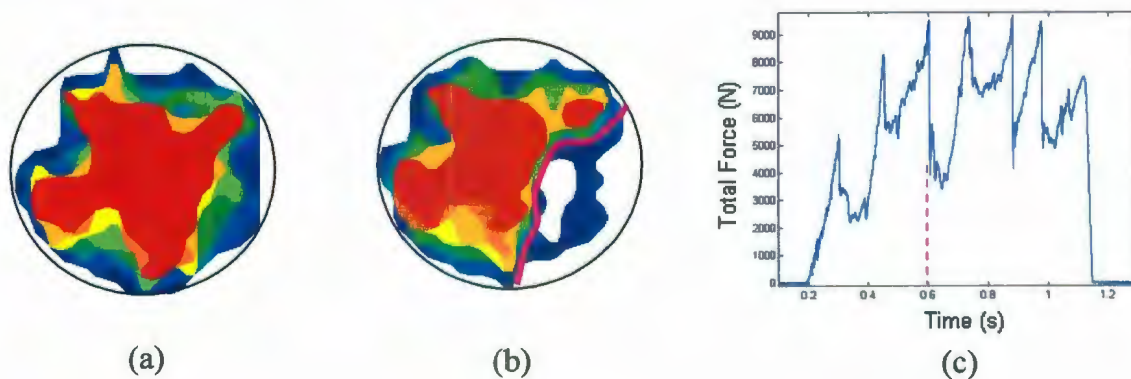


Figure 5.4: Spalling event during test I07_V10P0_C_041: (a) pressure distribution before spalling; (b) pressure distribution after spalling; (c) load drop due to spalling.

To incorporate the above characteristics of the process into a numerical model of ice failure, a finite element model for ice indentation was implemented in ABAQUS.

Finite Element Simulation of Ice Failure

As a starting point, a block of the same dimensions as the ice specimen (20cm x 20cm x 10cm) and an indenter with the same diameter and radius of curvature as the one used in the above experiments were modeled in ABAQUS. The indenter was modeled as a rigid analytical surface (no material model or mesh required) with a reference node located at the center of the contact face. The ice block was meshed using tetragonal 3D stress elements (type C3D4). As may be seen in Figure 5.5, the mesh was biased to give a very fine mesh in the contact zone (approximately 0.5 mm), and a coarser mesh on the remote boundaries (20 mm).

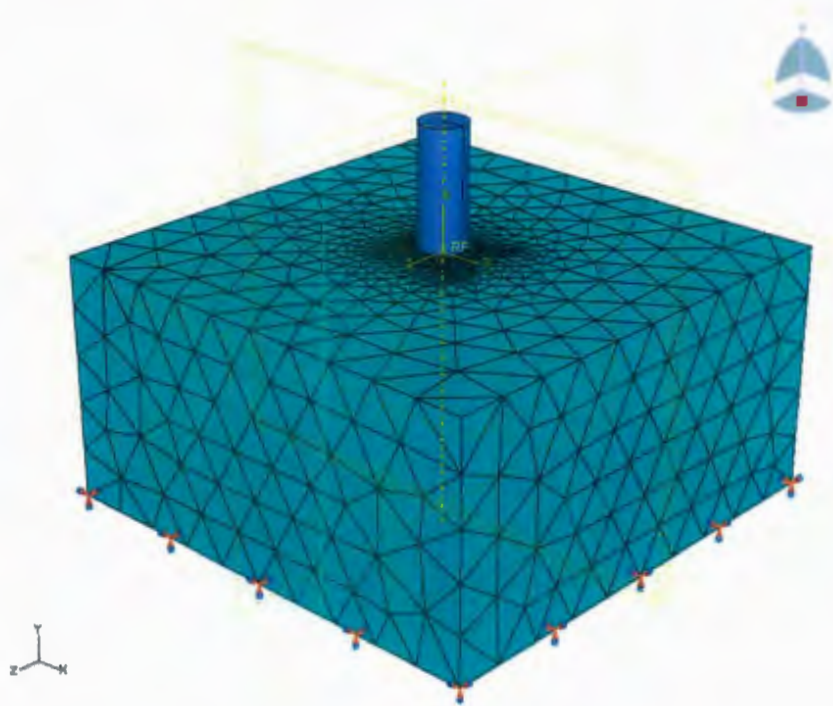


Figure 5.5: Finite element model of ice block and indenter used in indentation analysis.

The ice block was then assigned a user-defined material model using a Fortran UMAT routine developed by Xiao, (1997). This routine models the constitutive behavior of a damaging viscoelastic material using two Schapery damage functions to reflect the dependence of damage on confining pressure. The first function reflects the damage processes, such as microcracking, that are present for low confinement conditions, while the second function reflects the effects of damage under high confinement (i.e. dynamic

recrystallization and local pressure melting). The fundamental theory associated with this routine has been reviewed in Chapters 2 and 3, and is detailed in Xiao (1997). All parametric inputs used with this routine were based on the calibrated parameters used by Li (2007), except for the Elastic Modulus. In the present work an effective modulus of $E = 1.5$ GPa was found to give much better agreement with the measurements. It is assumed here that damaging of the ice during initial contact with the indenter is the source of the reduction of the Elastic Modulus noted above. The values of parameters used in this work are summarized in Table 5.1.

Table 5.1: Calibrated model parameters used for the UMAT routine (from Li, 2007)

Description	Parameter	Value
Elastic modulus	E	1500 (MPa)
Elastic modulus in Kelvin unit	E_K	1500 (MPa)
Poisson's ratio	ν	0.3
Primary creep reference rate	$\dot{\epsilon}_0^d$	1.0×10^{-5}
Secondary creep reference rate	$\dot{\epsilon}_0^c$	1.76×10^{-7}
Creep exponent for Kelvin unit	n	1.0
Creep exponent for Maxwell unit	m	2.5
Volumetric constant	f_3	0.11
Reference stress	s_0	15 (MPa)
Primary creep enhancement parameter	β_d	1
Secondary creep enhancement parameter	β_c	1
Damage function constant	α_1	0.7
Damage function constant	α_2	0.12
Reference pressure	σ_0	15 (MPa)
Low pressure exponent	g	2
High pressure exponent	q	7
Damage function exponent	m_d	2.4

The bottom surface of the ice block was fixed, and the indenter model was positioned such that its vertical axis passed through the centre the block, as shown in Figure 5.5. The indentation process was simulated by applying a fixed displacement rate boundary condition (10 mm/s) to the indenter for a specified amount of time.

The spalls were simulated by partitioning the block geometry into three segments: the main block, spall 1 and spall 2. The spall geometry for the present model was based on an idealization of the shape of surface spalls observed during indentation experiments. The spalls were idealized as being semi-ellipsoids, where the spall depth is a_s , spall width is $2a_s$ and the length is $4a_s$, as shown in Figure 5.6 below.

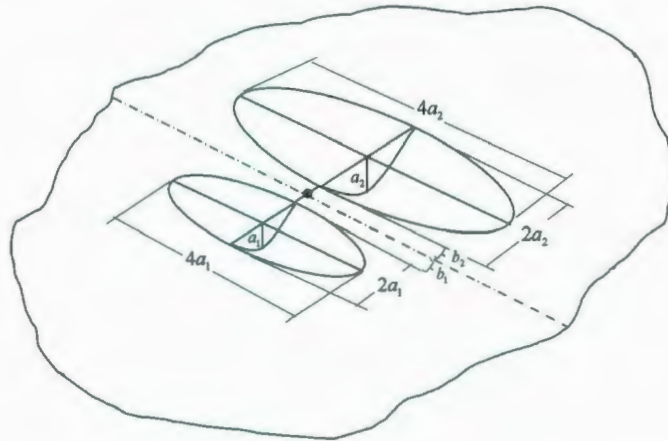


Figure 5.6: Schematic of idealized spall geometry used for finite element analysis.

The first (smaller) spall corresponded to $a_1 = 0.005$ m, and the second (larger) spall corresponded to a characteristic dimension $a_2 = 0.0075$. As shown above, the spalls were oriented such that the semi-major axes are parallel to each other and the edges of the spalls are located at a distance of $b_s = b_1 = b_2 = 0.005$ m from the centre of the block.

While the true spall geometry is more irregular and random during an actual interaction, the above geometry is seen as a reasonable approximation.

During the analysis the spalls were removed at the desired time using the *Model Change input command. This approach assumes that a spall occurs due to a rapid fracture event at some instant in the process, which results in the immediate clearing of the broken ice. This assumption was well supported by observations of rapid clearing of spalls during indentation experiments. For the present analysis, the time at which spalling occurred was selected to coincide with the observed load drops in the measured data.

Using the above analysis the total loads acting on the indenter were simulated and the force was divided by the instantaneous nominal contact area, to give the pressure trace shown in Figure 5.7, the combined damage and fracture numerical model was able to effectively capture many of the salient features of an indentation interaction event. In particular the damage mechanics model was able to well model the loading phase, while the simulated spalls well reproduce the load drop behavior that is characteristic of such fracture events.

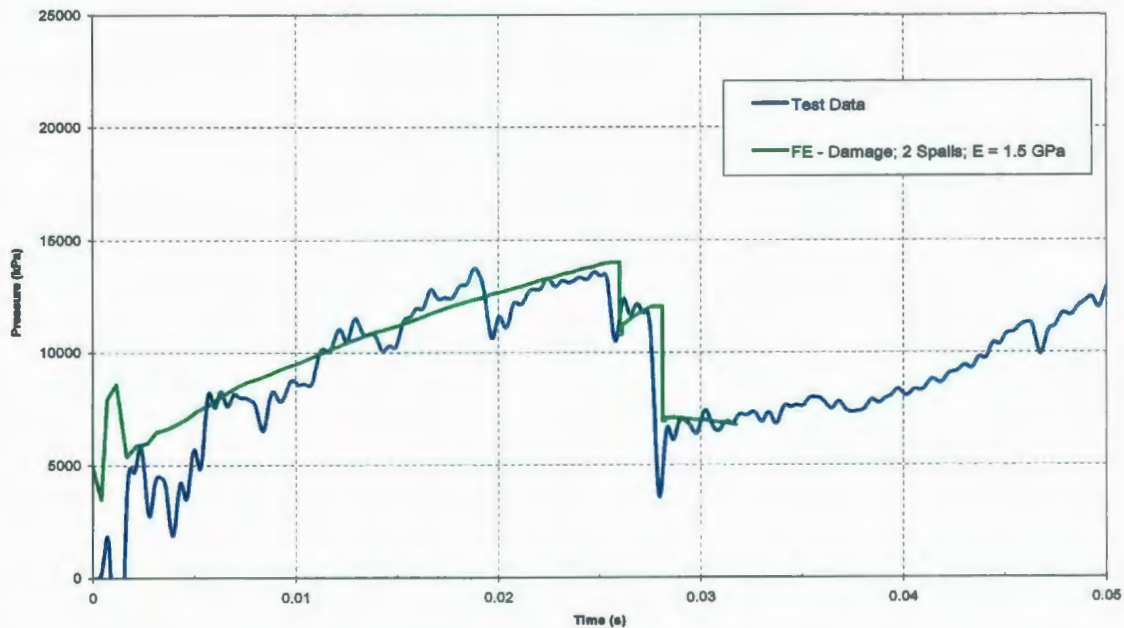


Figure 5.7: Plot of experimental and simulated pressure data from finite element model.

The occurrence of spalls significantly affects the contact geometry. After a spall occurs, the shape and damage state of the remaining ice will largely influence the subsequent stress distribution. Elastic rebound is more likely to result in partial recovery of some of the lost contact area for shallow spalls compared with a deeper spall. If the spall is deep, the localization of stress is more intense and the remaining ice will likely be more prone to further fracture. It is observed during experiments that small secondary failures often follow a large spalling event. This may result from stress localization effects as the loads are redistributed after a fracture event, which in turn may trigger extrusion or further spalling. Local crushing often occurs after a spall and continues until the total load

increases sufficiently to trigger another fracture. The present model cannot simulate extrusion of crushed ice from the damage layer. Inclusion of this capability in future models is recommended.

In developing the above finite element analysis model it also became apparent that the reduction in contact area is not necessarily greater for spalls with larger physical dimensions. Larger spalls that produce lower reductions in contact area may result in smaller load drops than would a spall of smaller physical dimensions which removed more contact area.

In attempting to simulate time series failure behavior using the above approach, the challenges of 'predicting' the exact geometry after each spall became evident. Variation in geometry due to the previous failure will influence the contact area and stress distribution governing the next failure. Even if all material properties and conditions are known, the randomness of the microstructure and other factors influencing the fracture behavior make it impossible to 'predict' the exact size, location and associated load drop that will occur for a given spall. Inherent randomness in the spall characteristics will result in randomness in the failure process. A probabilistic approach is believed to be more appropriate here, since information regarding the extent of load drop due to a spall is much more important in modeling pressure behavior than are the details of spall sizes and locations.

While the above numerical tools provide valuable insight into details of the process, a probabilistic approach to modeling spalling failure is considered to be more appropriate in modeling loads associated with the process. This is explored further in Chapter 7.

5.4 Preliminary Ice Sheet Indentation Tests

To extend the above work to include the study of multiple *hpzs* during edge indentation of an ice sheet, an initial series of small-scale laboratory ice sheet indentation tests were completed. Details of the experimental set-up are provided below.

5.4.1 Test Set-up

Tests were conducted by indenting freshwater columnar ice sheets using a rectangular indenter mounted in the Materials Testing System (MTS) loading frame, as shown in Figure 5.8 (a). Three indenter widths were used in this program: 2.5cm, 5cm, and 10cm. Ice specimens about 50cm high x 50cm wide, covering a range of ice thicknesses from about 2.5 cm to approximately 15cm were tested; see Taylor et al. (2010) for details of test matrices and results. Throughout this program the cold room temperature was maintained at -10°C .

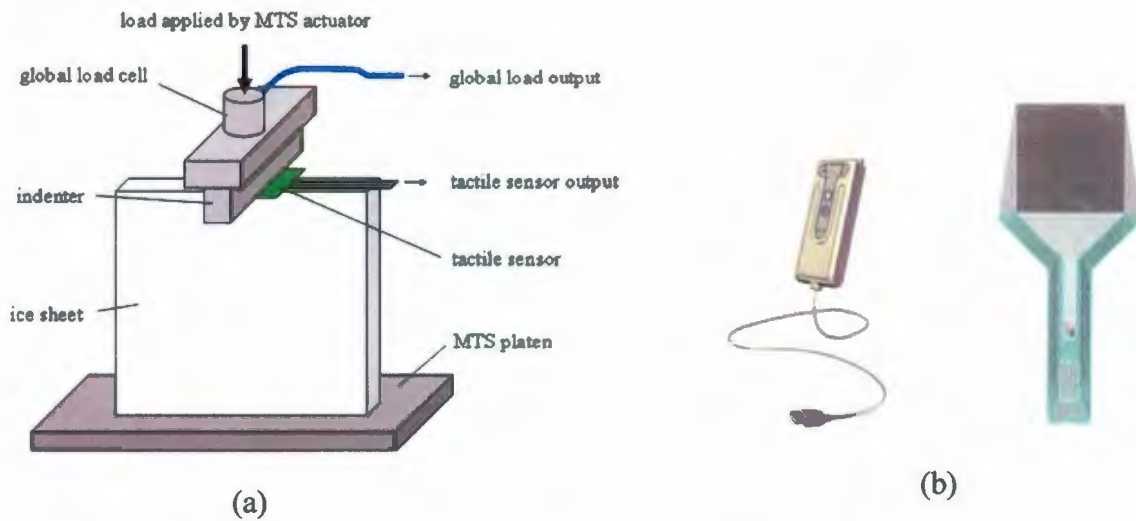


Figure 5.8: (a) Set-up for ice sheet tests; (b) Tekscan USB handle and sensor array.

To measure the spatial pressure and force distributions during indentation a Tekscan tactile pressure sensor was placed at the ice-indenter interface; see Figure 5.8 (b). The tactile sensors used had a 25,000 psi rating and consisted of a 0.004" thick film containing a 44x44 array of sensor elements which record data at a sampling rate of 100 frames per second. Video footage of the experiments was captured using both a standard color camcorder (30 frames per second), and a black and white, high-speed digital video camera (at 1000 fps). The high-speed video was an important tool for helping link load behavior with observed failure processes. Due to the limited storage capacity, high-speed video was not captured for the entire duration of all tests. This was particularly the case for slow speed tests, which had significantly longer test durations.

The selected sample event corresponds to a 5 cm indenter, a 2.55 cm thick ice sheet (with dimensions of approximately 50 cm × 50 cm) and an indentation rate of 0.10 mm/s. During this event, the dominant failure mechanism was a slow crushing process involving considerable extrusion of pulverized ice particles. Due to the unconstrained boundary conditions, many of the test specimens in this series failed by axial splitting before spalling and crushing could be observed (Taylor et al., 2010).

As shown in Figure 5.9 (b), when ice sheet A03 failed under compressive loading, the force was transmitted through small 'line-like' distribution of high pressure zone. During the crushing failure of a specimen, crushed ice is typically ejected from the indentation site. In this particular test the crushed ice was extruded in a horizontally oriented, sintered layer; see Figure 5.10. This layer of damaged ice remained attached to the parent ice sheet throughout the crushing process and grew in lateral extent as the indentation proceeded. This type of formation of crushed ice particles is rare and would not be likely to occur in nature. While this is an interesting observation, the details of sintering (bonding of crushed ice particles under pressure) are beyond the scope of the present work, and so this process is not discussed further here.

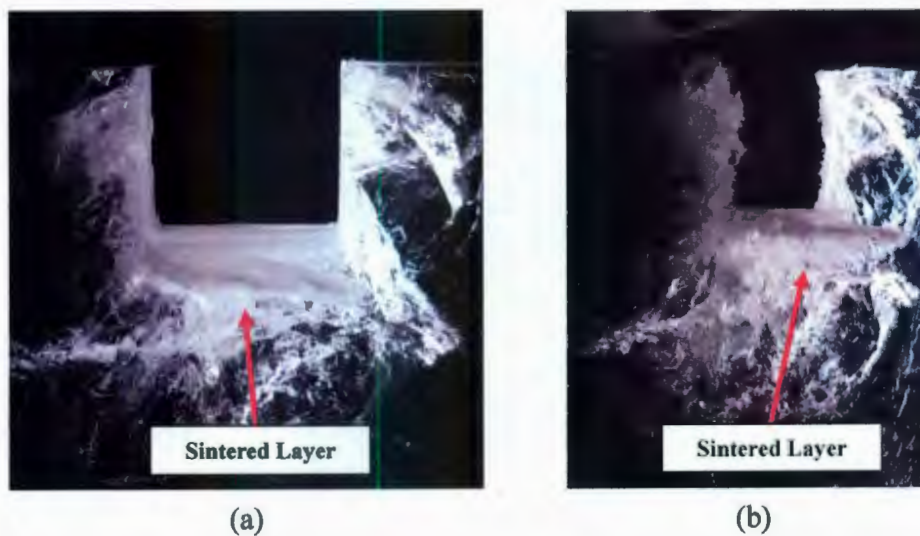


Figure 5.10: Photographs of specimen A03 after testing showing: (a) front view and, (b) isometric view of indentation zone showing sintered layer of extruded ice.

To examine the indentation zone in greater detail, thin-sections of the specimen were prepared. This was accomplished by first rough-cutting the specimen using the bandsaw, and freezing the specimen onto a glass slide. The face of this rough-cut specimen was then smoothed out using the microtome shown in Figure 5.11 (a). The section was then removed from the slide, and refrozen on a new glass slide, positioned with the finished side down. The thickness of the section was reduced by successive passes on the microtome shown in Figure 5.11 (a).

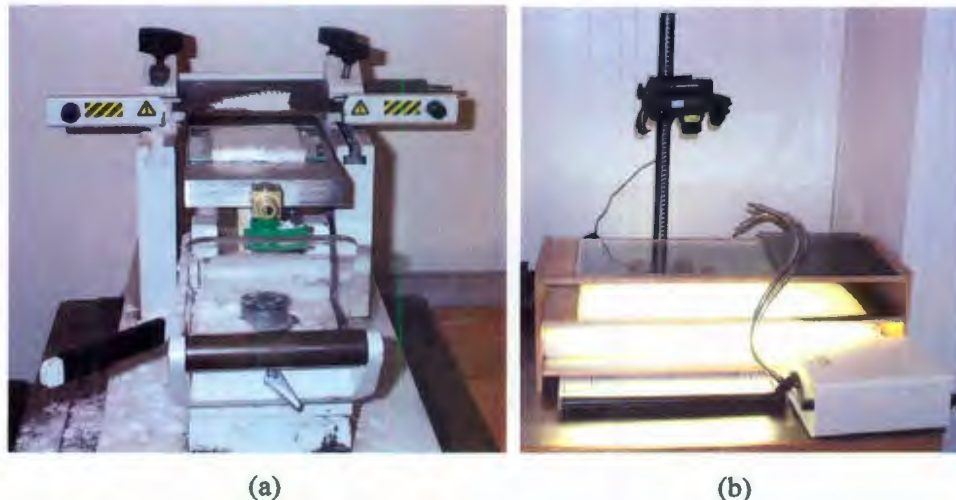


Figure 5.11: (a) Microtome used for thin-sectioning of ice; (b) light table used for lighting thin-sections (photos courtesy of Jennifer Wells).

The microstructure of the specimen was periodically viewed using cross-polarizing light filters and the light table shown in Figure 5.11 (b). As the section was made thinner, grain boundaries and microcracks became more distinct. This process was repeated until a clear image of the grain boundaries was obtained. A description of the specimen storage and thin-sectioning process may be found in Wells et al. (2006).

Thin-sections of specimen A03 reveal a thin layer of finely crushed ice in the zone directly in front of the indenter. As may be seen in Figure 5.12, this layer of crushed ice is accompanied by extensive microcracking and radial cracks emanating from the corners of the indenter. These results provide a clear example of crushed layer formation immediately below the indenter and highlight one of the ways sintering is manifest in the crushing process.



Figure 5.12: Thin-sections of specimen A03 showing: (a) extensive microcracking viewed using side-lighting; (b) microstructure of the ice specimen.

From this series of tests it was evident that boundary conditions play an important role in the mode of fracture that is observed. Further testing at an intermediate scale, for instance at an ice tank facility, is recommended.

5.5 Medium Scale Field Indentation Test (JOIA)

In practice, local pressure data measured from panels with individual areas on the order of 1 m^2 are often used in the estimation of global ice pressures for design. Understanding the relationship between local and global pressure behavior is critical in the development of methodology for design load estimation. The medium-scale field indentation test (MS-FIT) program carried out by the Japan Ocean Industries Association (JOIA) provided pressure data at a resolution previously not available. In the present study, these data have been analyzed to provide detailed information about pressure distributions during ice-structure interactions, offering potential insight into links between *hpzs*, local pressures, and global pressure.

5.5.1 JOIA Program Background

The MSFIT project consisted of over thirty tests carried out over a five year timeframe (1996-2000) in the harbor of Notoro Lagoon in Hokkaido, Japan ($44^{\circ}05'N$, $144^{\circ}10'E$). The testing site was located on a fishing dock in the harbor and the test zones were configured as illustrated in Figure 5.13 below. The site for each test was prepared at selected locations along the waterfront and a 65-ton mobile crane was used to move the test apparatus (Figure 5.14) into position. For some tests naturally grown ice was used, while in other cases the natural ice was removed and a refrozen ice sheet was grown in the test region. A key difference between the two ice types is the presence of snow ice on the top of the naturally grown sheets.

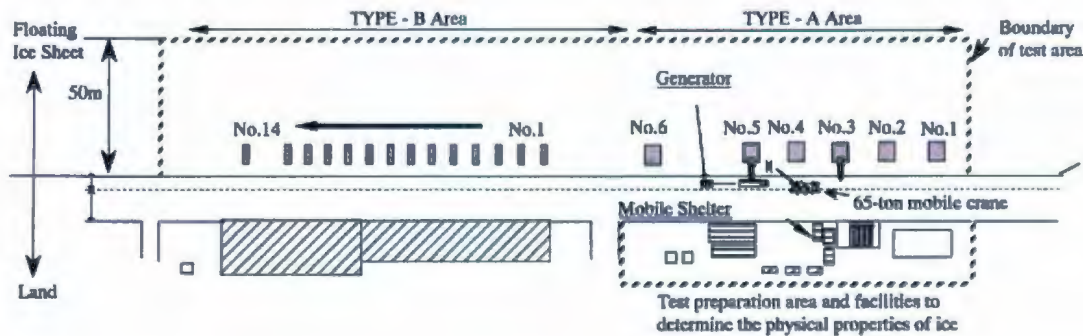


Figure 5.13: Plan view of the test site (Sodhi et al., 1998)

The average ice thickness during these tests was approximately 30 cm. Details of the ice conditions during the program, as well as the physical properties of the ice are presented in Kamio et al. (2000). The natural ice in Notoro Lagoon is brackish first-year ice, with some natural snow cover. In some test cases the natural ice was removed and a refrozen ice sheet was grown, while other tests simply used the naturally grown ice. In the case of natural ice, a layer of snow ice was sometimes present; this was not present on refrozen sheets (Takeuchi et al., 1997).

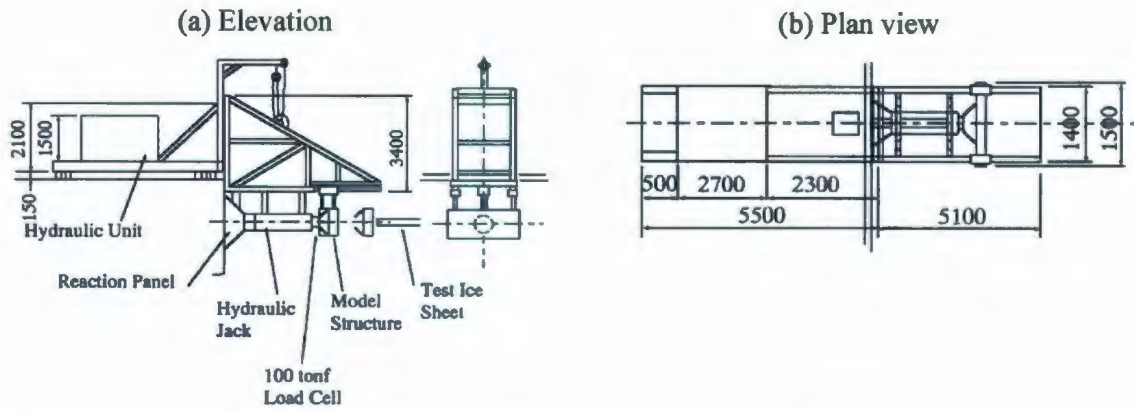


Figure 5.14: Indentation instrumentation and structure: (a) elevation view; (b) plan view (Sodhi et al., 1998).

Displacement rates were held constant for a given test and ranged between 0.03 cm/s to 3 cm/s. In many instances several tests were conducted for a given ice sheet by dividing the stroke into three 35-40 cm sections (maximum stroke was 120 cm). By testing at a different speed for each section, multiple conditions could be studied for each prepared section of ice. A 100 ton-force load cell was mounted between the hydraulic ram and the test beam to measure global loads, though it was later discovered that this load cell did not work for many of the tests. Of interest to the present analysis is the segmented indenter, which consisted of fifteen 10 cm wide panels mounted on a 1.5 m beam. Each local panel was fitted with a 10 metric ton load cell and had a total area of 10 cm (wide) by 40 cm (high); see Figure 5.15.

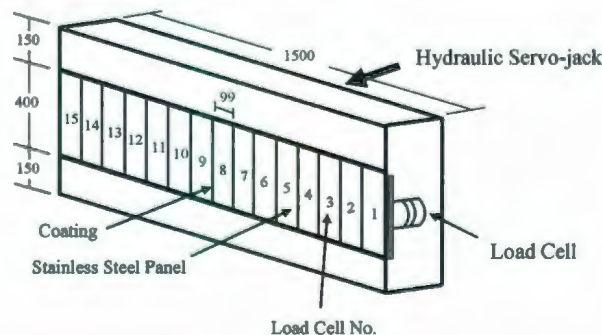


Figure 5.15: Indenter used in MSFIT program; dimensions in mm (after Sodhi et al., 1998)

In 2006, selected data from 1998, 1999 and 2000 seasons became publicly available. During the 1999 season 60 cm wide indenters were used; these results are not considered here. Only those results corresponding to tests with the 150 cm wide indenter (1998, 2000) are included in the present analysis.

In addition to the segmented panels, tactile sensors were fitted to the indenter for some experiments; see Figure 5.16. The primary advantage of the tactile sensors is the high resolution spatial and temporal information provided about the relative pressure distributions in both horizontal and vertical directions as measured across the face of the structure.

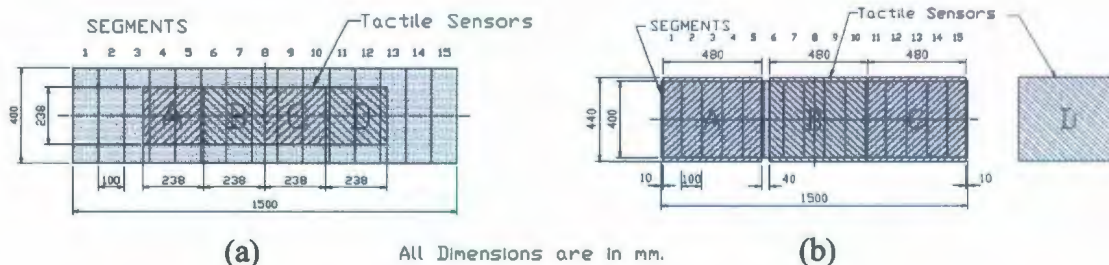


Figure 5.16: Schematic of tactile sensor configurations used in: (a) 1998, 1999; (b) 2000. (after Sodhi et al. (2001))

Takeuchi et al. (1997) provided a discussion of test results from the 1996-1997 seasons. Matsushita and Takawaki (1997) provide a description of early tests on the physical properties and strength characteristics of ice. Kamio et al. (2000) provide a discussion of the physical properties, internal structure and mechanical properties of first-year ice in Notoro Lagoon. Akagawa et al. (2000) analyzed sample cases of tactile pressure sensor and segmented indenter data in the context of peak loads and observed failure modes. In their analysis, Akagawa et al. (2000) observed 'line-like' loading and independent failure zones (high pressure zones). Such 'line-like' loads are readily observable from the tactile pressure sensor data, as shown in Figure 5.17 below.

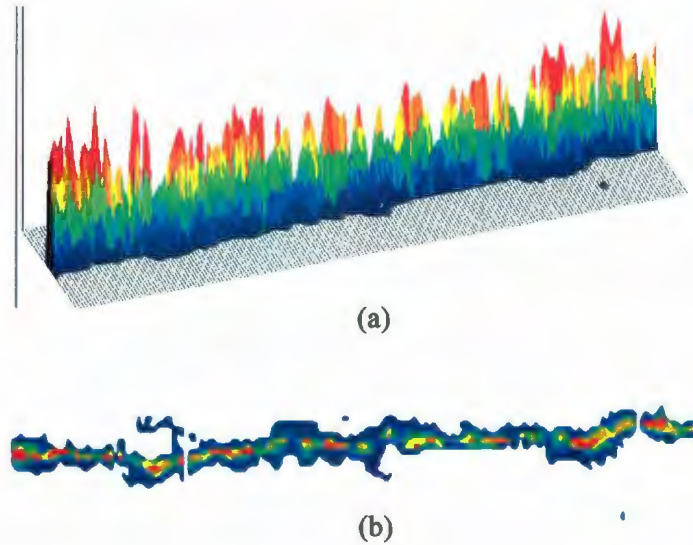


Figure 5.17: Tactile sensor data showing: (a) 3D contour plot; (b) 2D contour map.

Takeuchi et al. (2000) analyzed tactile sensor data for sample events from 1996-1999 (60 cm wide indenters). They concluded that higher correlations between adjacent panels are observed for lower speeds; observed end effects were attributed to the effects of end restraint of the ice sheet. Matsushita et al. (2000) provide a discussion of the various failure modes observed during tests from 1996-1998. Sodhi et al. (2001), Frederking (2004), and Taylor et al. (2008) discussed various aspects of tactile sensor data analysis.

5.6 High Pressure Zone Behavior

Few details of *hpz* characteristics are available in the literature. Since the majority of loads transmitted to both the ice and structure occur through *hpzs*, improved characterization of interface pressures offers an opportunity to enhance understanding of load distributions. This is important in modeling ice failure processes, since the pressure distribution at the interface will significantly affect the stress distribution in the ice. The following analysis aims to establish a means to characterize *hpzs* during the interaction of a vertical walled structure with a level ice sheet.

5.6.1 Analysis of JOIA Tactile Sensor Data

One of the challenges when interpreting data from fixed local panels is the necessity to make inferences about ice failure processes. The mean pressure measured at a local instrumentation panel at a fixed position on a structure is simply the total force acting on the panel averaged over the nominal contact area (panel width \times ice thickness).

Depending on the size of the individual panels relative to *hpzs*, the measured result may be representative of multiple *hpzs*, a single *hpz*, or partial *hpzs* acting on the loaded area. It is not possible to extract detailed *hpz* characteristics from such data. Furthermore, local panel data does not allow the analyst to clearly distinguish between spalling, crushing or other modes of failure. Clearly understanding which failure mechanisms are responsible for the observed behavior is key in the development of physics-based models, since the mechanics associated with each of the failure processes are fundamentally different.

Tactile sensors overcome some of these limitations by providing pressure data at a much higher resolution. The tactile sensor data available from the JOIA test program represents a wealth of information. The detailed nature of these data lends it to a variety of analysis approaches. Tactile pressure sensor data provides valuable information about the formation and evolution of individual high pressure zones during an interaction. The high resolution of these data offer opportunities to more effectively characterize individual *hpzs* than was possible in the past.

Preliminary examination of the tactile data indicates that much of the data is clustered into line-type loading (Riska et al., 1990; Frederking, 2004; Taylor et al., 2008). This supports the assumption of only one *hpz* across the thickness of an ice sheet, which has been used throughout the present study. Since averaging effects require multiple *hpzs*, averaging would primarily be a function of width for such a load distribution, since it is assumed that there is only one *hpz* through the thickness of the ice. Validation of this assumption, particularly for thicker ice (greater than 1 m) is recommended, should such data become available.

During ice-structure interaction significant reductions in ice loads may result from fractures of the ice. Spalling fracture is also associated with the localization of loading

into zones of high pressure. Brittle fracture generally depends on stress, geometry and flaws. The stress conditions most commonly associated with fracture in ice are tensile zones, critical shear zones or combinations of both. The localization of loading into *hpzs* during compressive failure results in considerable spatial and temporal variation in pressure across the structure. The relationship between failure modes and the consequences in terms of contact area and pressure are discussed below; see also Taylor et al., (2008).

5.6.2 Failure Modes and Consequences

The interplay between local surface spalls and the crushing process is important in the relationship between *hpz* evolution and compressive ice failure. The consequences of spalling and crushing are manifest differently in the contact area and pressure distributions of *hpzs*. The consequences of a failure event will depend on the mode of failure that occurs. As a starting point, a sample brittle-type event from the 1998 test program has been analyzed to examine the nature of *hpzs* during compressive failure. A general description of the 1998 test program and results are provided in Nakazawa et al. (1999). The present section is focused on analysis of Tekscan tactile sensor data for the sample event discussed below.

Description of Test

Data for the selected event were collected on January 26, 1998. Details of this test are summarized in Table 5.2 below. The primary reasons for selecting this particular event are that the nominal ice thickness (241 mm) is close to the total height of the tactile film (238 mm) and the time trace suggests that the failure was cyclic and brittle in nature.

Table 5.2: Characteristics of selected event

Indenter Width	1500 mm	Salinity	6.2 ppt
Indenter Height	400 mm	Ice Strength	1 MPa
Indentation Speed	0.3 cm/s	Ice Density	843 kg/m ³
Ice Thickness	241 mm	Ice Temperature	-2.7 °C
Ice Temperature	-2.7 °C	Event Duration	65 seconds

As shown in Figure 5.14, the indenter apparatus used in these tests was mounted in a testing frame and fitted with several types of load measurement instrumentation. Measurement data were collected for global and local segmented panel loads using conventional load cells; see Figure 5.15. Tekscan tactile pressure sensor film was mounted in front of the segmented panels and was used to collect high resolution interfacial pressure measurements; see Figure 5.16. Additional details of the instrumentation may be found in Sodhi et al. (1998).

As illustrated in Figure 5.16 (a), the tactile sensor configuration used in the 1998 tests only partially covered the face of the indenter. Four individual tactile sensors, each consisting of a 44 by 44 array of sensor elements, were connected together to form a continuous 44 by 176 sensor array (for a total of 7744 elements). Each sensor element is nominally 5.4 mm by 5.4 mm and the overall dimension of the sensor array is 238 mm high by 952 mm long. For the selected event, sensor data was sampled at a frequency of 12.5 Hz (one 'frame' every 0.08 seconds). Each 'frame' of data consists of a 44 by 176 matrix of values collected for the specified time interval; each element of the data matrix contains a pressure value for the sensor element having the same element indices in the sensor array. Raw data (integer values ranging between 0 and 255 representing pressure intensity) were collected and later calibrated using the procedure described in JOIA (2006). As discussed by Frederking (2004), the manufacturer of the tactile film indicated that error in any reading on the film may be up to +/- 10%. Correspondingly these pressure data are treated as relative.

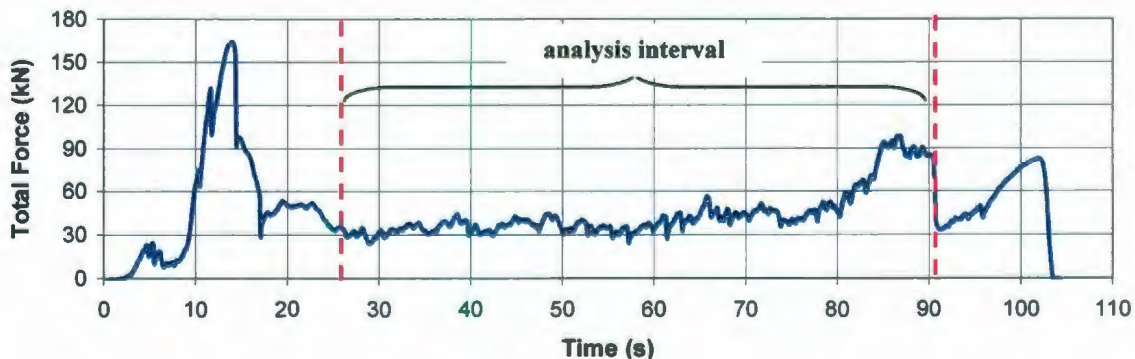


Figure 5.18: Total tactile sensor force vs. time.

The time trace for the total force measured by the tactile film is shown in Figure 5.18 above. A large ‘break-out’ load occurred in the first 25 seconds of the event due to the initial condition resulting from contact of the indenter with the flat sawed edge of the ice. It is interesting to note that, as shown in Figure 5.19 (a), even during the peak of the ‘break-out’ phase of the failure process only approximately 27% of the nominal sensor area was actually under load. After this initial ‘break-out’, the failure process transitioned into a line-type distribution of high pressure zones. During the onset of crushing the total loaded area reduced to approximately 8% of the nominal sensor area; see Figure 5.19 (b).

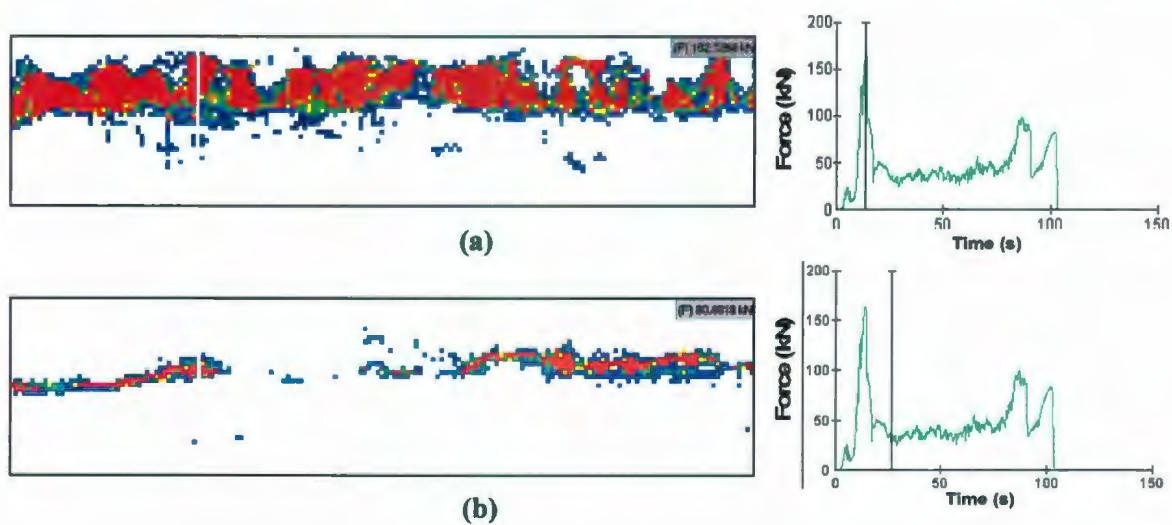


Figure 5.19: Tactile sensor data for (a) peak of ‘break-out’ load; (b) onset of crushing.

For the present work only data from the ‘analysis interval’ between $t = 25$ seconds and $t = 90$ seconds have been considered; see Figure 5.18. Throughout the interaction, *hpzs* were observed to exhibit significant spatial and temporal variation. During the selected interval the average total loaded area was approximately 10% of the nominal sensor area. The average pressure on a loaded sensor element was 2.08 MPa and the average global pressure on the sensor array was 0.208 MPa.

Local Failure Processes: Spalling, Crushing and *hpzs*

Localized failure processes serve to limit load build-up within the ice and consequently limit forces applied to the structure. Examination of the tactile sensor data suggests

spalling, pulverization and extrusion processes are in evidence. In the context of this work, pulverization and extrusion processes are simply referred to as ‘crushing’.

As illustrated in Figure 5.20 (a), crushing is typified by a sudden decrease in *hpz* intensity, without an appreciable shift of the position of the *hpz* (represented below by a centerline). While some variation in area may result from the extrusion of material, significant loss of contact area is generally not expected. Any decrease in total area associated with crushing often occurs near the periphery of the *hpz*.

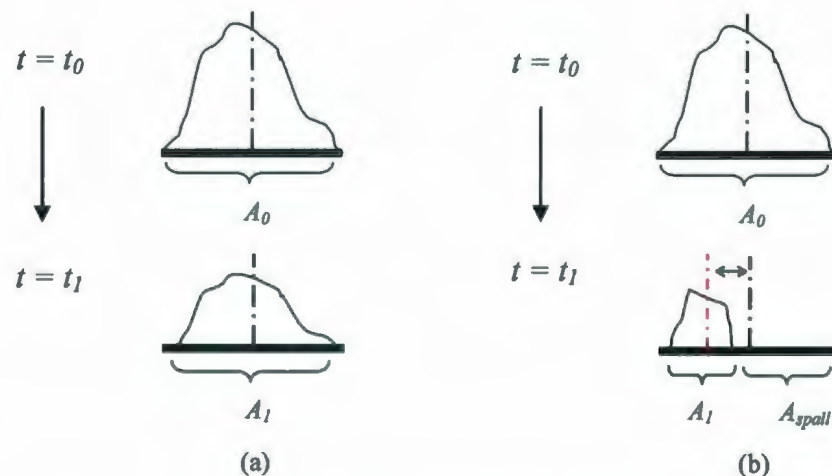


Figure 5.20: Simplified schematic of *hpz* pressure distribution before ($t = t_0$) and after ($t = t_1$) failure for (a) crushing; (b) spalling.

Considering the illustration in Figure 5.20 (b) it may be seen that spalls typically result in appreciable area losses and are often asymmetric in nature (i.e. only on one side of the *hpz*). In addition to affecting the intensity, spalls generally have a more significant effect on the size, shape and position of the *hpz*. These observations are consistent with those found in laboratory experiments reported by Jordaan et al. (2008).

To investigate the occurrence of spalling and crushing failures, data from the tactile sensor array were first divided into four regions, as shown in Figure 5.21.

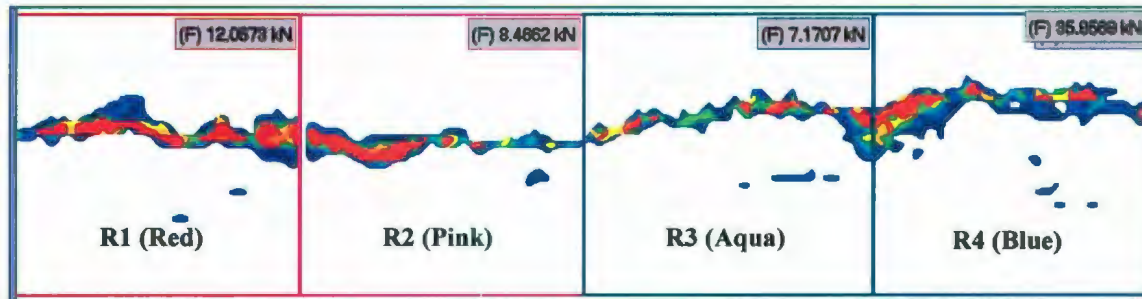


Figure 5.21: Tactile sensor data regions used in the identification of dominant failure events.

To determine if a particular region is associated with the observed load drop, load traces for the data contained within each region were plotted along with the total sensor data; see Figure 5.22. Examination of the load traces and tactile data for each region provided insight into the type of failure process and the associated pressure distribution in the regions dominating the loading behavior.

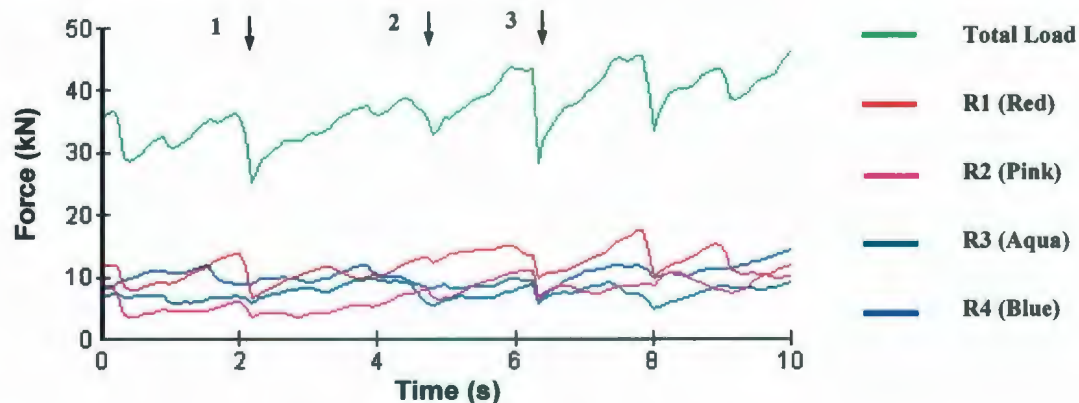


Figure 5.22: Tactile sensor data for interval from 55 to 65 seconds; data correspond to total sensor load, as well as loads for the four regions identified in Figure 5.21.

In an attempt to enhance the understanding of links between failure processes and pressure distributions, both qualitative and quantitative analysis of tactile sensor data have been undertaken. The qualitative approach has been based primarily on visual interpretation of time traces and spatial pressure maps of tactile data. The quantitative approach aims to link decreases in force, area and pressure with various failure types. The

aim of this approach was to aid in the development of criteria for characterizing failure types and their relationship with *hpz* evolution.

Qualitative Interpretation

The degree of influence each region has on the drop in total load for a given failure event has been qualitatively interpreted based on Figure 5.22, as well as the tactile sensor data. Results are summarized in Table 5.3 below. The dominant failure types were also identified for each failure event based on examination of the tactile sensor data. For Failure Event 1, the load drop appears to be dominated primarily by activity in region R1, with some influence from the adjacent region, R2. For Failure Event 2, the decrease in load appears to be most heavily influenced by region R3, while activity in regions R1 and R2 appear to have some effect. During Failure Event 3, there appears to be a rapid load drop across all regions, suggesting a simultaneous failure.

Table 5.3: Classification of the degree of influence of each region on total load drop during identified failure events and assessment of domination failure type using qualitative approach.

Failure Event	Region				Dominant Failure Type
	R1	R2	R3	R4	
1	D	I	I	N	Local Spalling
2	I	I	D	N	Local Crushing
3	D	D	D	D	Simultaneous Crushing

D = Dominant; I = Some Influence; N = Negligible Influence

Two and three dimensional spatial pressure maps corresponding to the instants before and after the load drop for Failure Events 1, 2 and 3 have been plotted in Figures 5.23, 5.24 and 5.25 respectively.

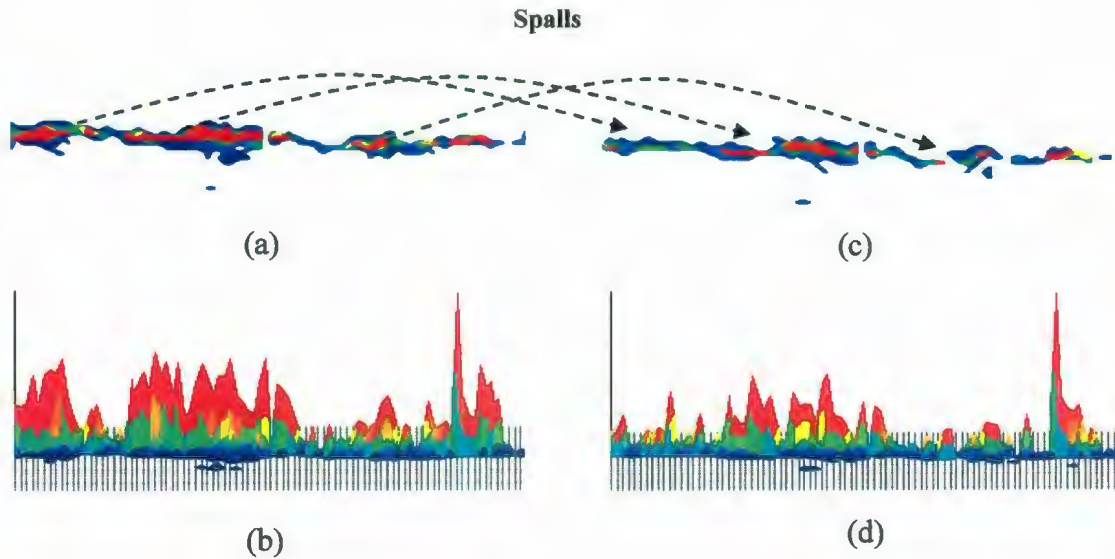


Figure 5.23: Pressure distributions from selected regions for Failure Event 1 (local spalling): (a) 2-D plan view before failure; (b) 3-D view before failure; (c) 2-D plan view after failure; (d) 3-D view after failure.

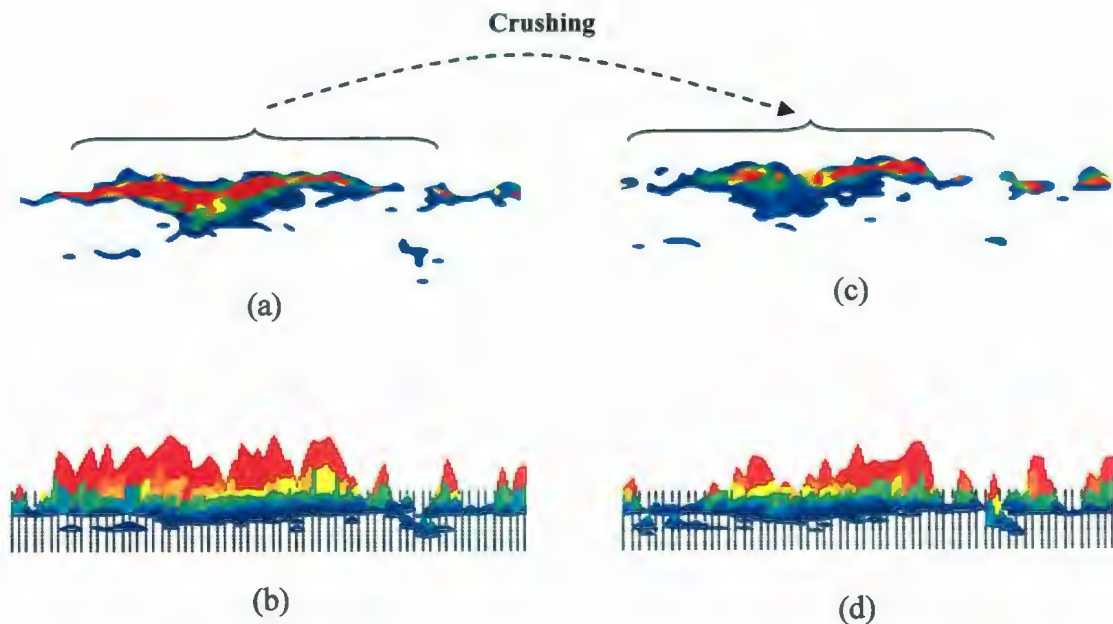


Figure 5.24: Pressure distributions from selected regions for Failure Event 2 (local crushing): (a) 2-D plan view before failure; (b) 3-D view before failure; (c) 2-D plan view after failure; (d) 3-D view after failure.

Comparison of Figures 5.23 and 5.24 illustrates the key differences between spalling failure and crushing failure. Spalling results in appreciable local modification of the shape, intensity and position of *hpzs* and the surrounding area. By comparisons, during crushing the general shape of the contact area does not appreciably change. Rather the extrusion of material along at the face of the indenter results in a decrease in intensity of the *hpz*.

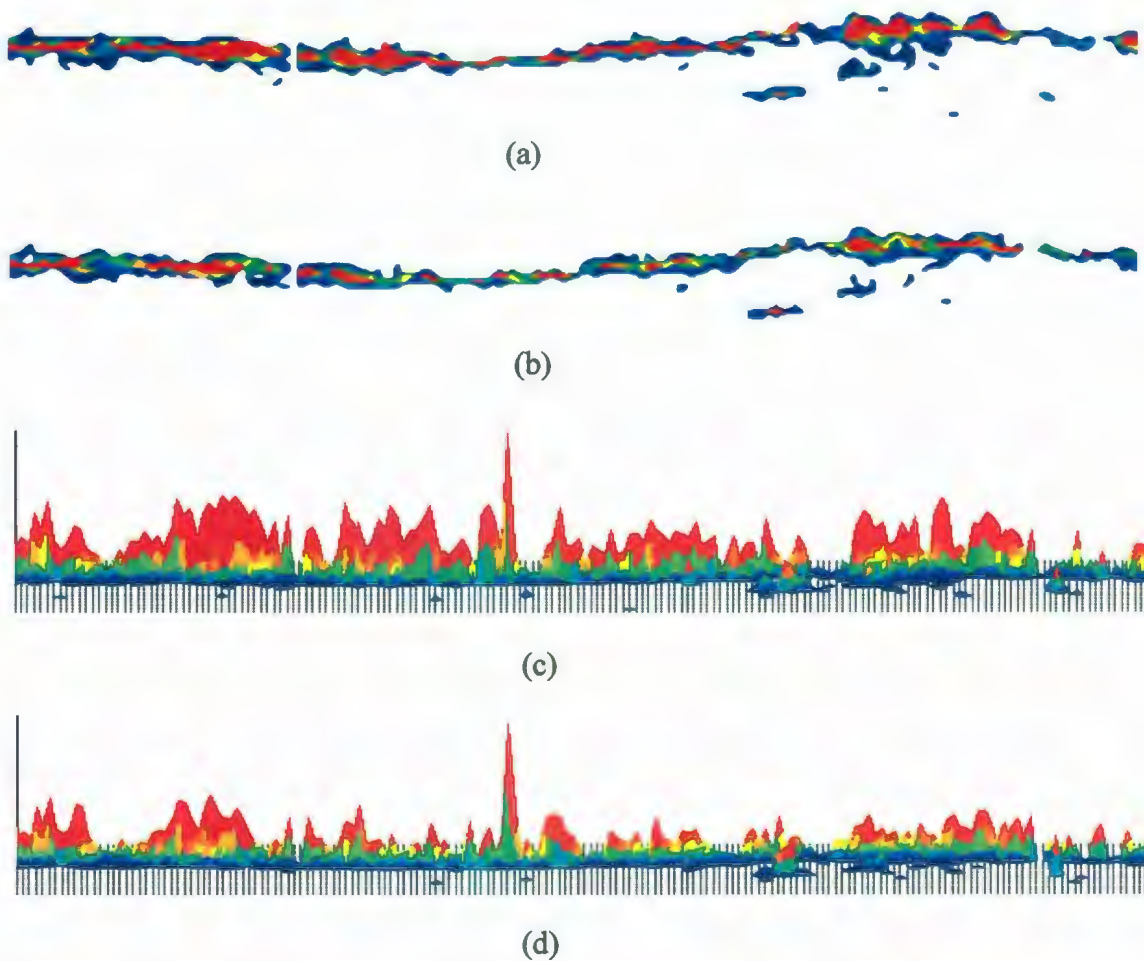


Figure 5.25: Pressure distributions from all regions for Failure Event 3 (simultaneous crushing): (a) 2-D plan view before failure; (b) 2-D plan view after failure; (c) 3-D view before failure; (d) 3-D view after failure.

As may be seen from Figure 5.25, the shape and positions of the *hpzs* do not significantly change during simultaneous crushing. Rather there is a sudden decrease in intensity due to the extrusion of material. As may be seen, most of the area reduction for this failure occurs near the periphery of the *hpzs*, which is characteristic of a crushing type failure.

Quantitative Interpretation

Data were extracted for each region and examined in further detail. The percent of total load drop attributed to each region, as well as the percent decrease in area and pressure within each region were determined. These results well support the qualitative assessment presented in Table 5.3, and have been summarized in Table 5.4.

Table 5.4: Percent drop in force, area and pressure during failure events for each region

Failure Event	Percent Drop in Total Force Attributed to Each Region				Percent Area Reduction in Each Region					Percent Pressure Drop in Each Region				
	R1	R2	R3	R4	R1	R2	R3	R4	Total	R1	R2	R3	R4	Total
1	67	22	9	2	26	-4	-3	12	12	35	40	17	-12	21
2	2	16	60	22	-2	0	2	3	2	4	11	34	9	13
3	25	31	21	22	12	18	10	17	14	19	29	26	21	24

For Failure Event 1, activity in region R1 tends to dominate the drop in total force, which is accompanied by both a sizeable reduction in area and a drop in average pressure over the region. As discussed, this type of response is characteristic of a spalling type failure. There appears to be a moderate load drop in region R2, which has a proportionally larger drop in pressure associated with it. From the tactile sensor data it may be interpreted that a smaller spall occurred in region R2, but the ice fragments did not immediately clear. Rather these fragments maintained contact with the sensor, resulting in slight increase in total contact area in region R2, though they contribute little force. The large pressure drop in region R2 then results from the combination of a moderate drop in load accompanied by the slight increase in contact area.

Results for Failure Event 2 suggest that the drop in total force is dominated by local crushing in region R3, which has a large load drop, small area reduction and significant decrease in pressure intensity associated with it.

For Failure Event 3, the decreases in force, area and pressure are fairly consistent across the width of the indenter suggesting a simultaneous crushing failure. Most of the area reduction for this failure occurs near the periphery of the *hpzs*, which is expected for this type of failure.

Discussion

Local spalling, local crushing and simultaneous crushing failures were observed to occur intermittently across the indenter. The high degree of non-simultaneity observed in these data highlights the importance of using design methods that account for probabilistic averaging effects. Probabilistic averaging results in a standard deviation that is markedly lower for the global load than that of local loads.

5.7 Multiple High Pressure Zones and Averaging

During brittle failure, peak *hpz* loads are generally non-simultaneous, which has considerable implications for estimation of global loads based on local load measurements. Methods based on the assumption that a peak local pressure acts uniformly across the structure (i.e. all points have the same pressure) do not account for the non-simultaneity of ice failure. Extrapolating local loads to estimate global loads without accounting for the statistical averaging of *hpzs* can result in significant conservatism. Since the statistical averaging of *hpzs* reduces the standard deviation of pressures, and the effects of averaging increase for increasing width, averaging will contribute to the pressure-area scale effect; see also Taylor et al., 2007.

5.7.1 Analysis of JOIA Local Pressure Data

The indenter for the tests conducted during the 1998 and 2000 seasons consisted of a 150 cm wide structure segmented into 15 individual panels. These 10 cm wide panels were individually fitted with load cells to measure the force acting on each panel. The segmented panels are contiguously arranged, allowing measured global loads to be compared with those estimated based on single panel estimates. For this reason, this dataset is well-suited for use in the validation of probabilistic averaging methodology.

For this analysis, the JOIA data were divided into three ranges of speed. For all analysis tasks in this study, data is grouped into these three speed categories:

- Slow: < 0.1 cm/s
- Medium: ≥ 0.1 cm/s; ≤ 1.0 cm/s
- Fast: > 1.0 cm/s

The overall objective of the analysis of the JOIA data is to evaluate the probabilistic averaging method used to predict global ice forces from local panel data. While the tactile sensor data provides a high level of detail, the segmented indenters are more analogous to the local pressure panels such as the ones used on Molikpaq. Segmented indenter data has been used for this analysis.

5.7.2 Preparation of Data

Issues such as damaged sensors or data acquisition problems affect the quality of raw data and had to be identified and addressed prior to detailed analysis.

Dataset Selection

The time traces of each sensor of all relevant datasets were reviewed in detail to identify missing or spurious data. Based on this process, a number of data sets were omitted from analysis. Details of the final analysis dataset are summarized in Table 5.5. For identification purposes, event numbers were assigned to each of the JOIA files; cross-references between original JOIA file labels and event numbers used in this analysis are also included in Table 5.5. Events selected for analysis have been limited to those tests for which tactile sensors data are available.

Table 5.5: Selected JOIA Datasets used in probabilistic averaging analysis

Date	Folder Name	Event Number	Width	Velocity	Stroke	Ice Thickness
H9			W(cm)	V(cm/s)	L(cm)	h (cm)
98-01-21	980121-1	01	150	0.3	35	28.7
98-01-22	980121-2	02	150	3	35	28.7
98-01-23	980121-3	03	150	0.03	36	28.7
98/01/23	980122-2	05	150	0.3	35	28.9
98/01/25	980122-4	06	150	0.03	36	28.9
98/01/26	980126-1	07	150	0.3	35	24.1
98/01/27	980126-2	08	150	0.03	36	24.1
98/01/29	980126-4	09	150	3	10	24.1
98/01/28	980128-1	10	150	0.3	35	28.4
98/01/29	980128-2	11	150	0.03	36	28.4
98/01/29	980129-1	12	150	0.3	50	28.2
98/01/30	980129-2	13	150	3	50	28.2
98/02/16	980216-1	14	150	0.03	10	18.6
98/03/02	980228-3_NoTactile	16	150	0.1	50	25.1
02/02/00	02023603	23	150	0.3	64	33.5
02/03/00	02031830	24	150	3.0	65	28.3
02/03/00	02033630	25	150	3.0	65	28.8
02/04/00	02043615	26	150	1.5	65	29.9
02/11/00	02113615	27	150	1.5	65	24.8
02/22/00	02223615	28	150	1.5	63	16.5
02/24/00	02241830	29	150	3.0	64	18.3
02/26/00	02263630	31	150	3.0	20	19.5

Due to the volume of data resulting from this analysis, only representative sample results are presented in this chapter.

Event Definition

During the analysis processes, several types of testing artifacts were identified in the time trace data. These include ramp-up, break-out, stop-under-load and ramp-down portions of the test. Examples of these testing artifacts are shown in the sample event in Figure 5.26.

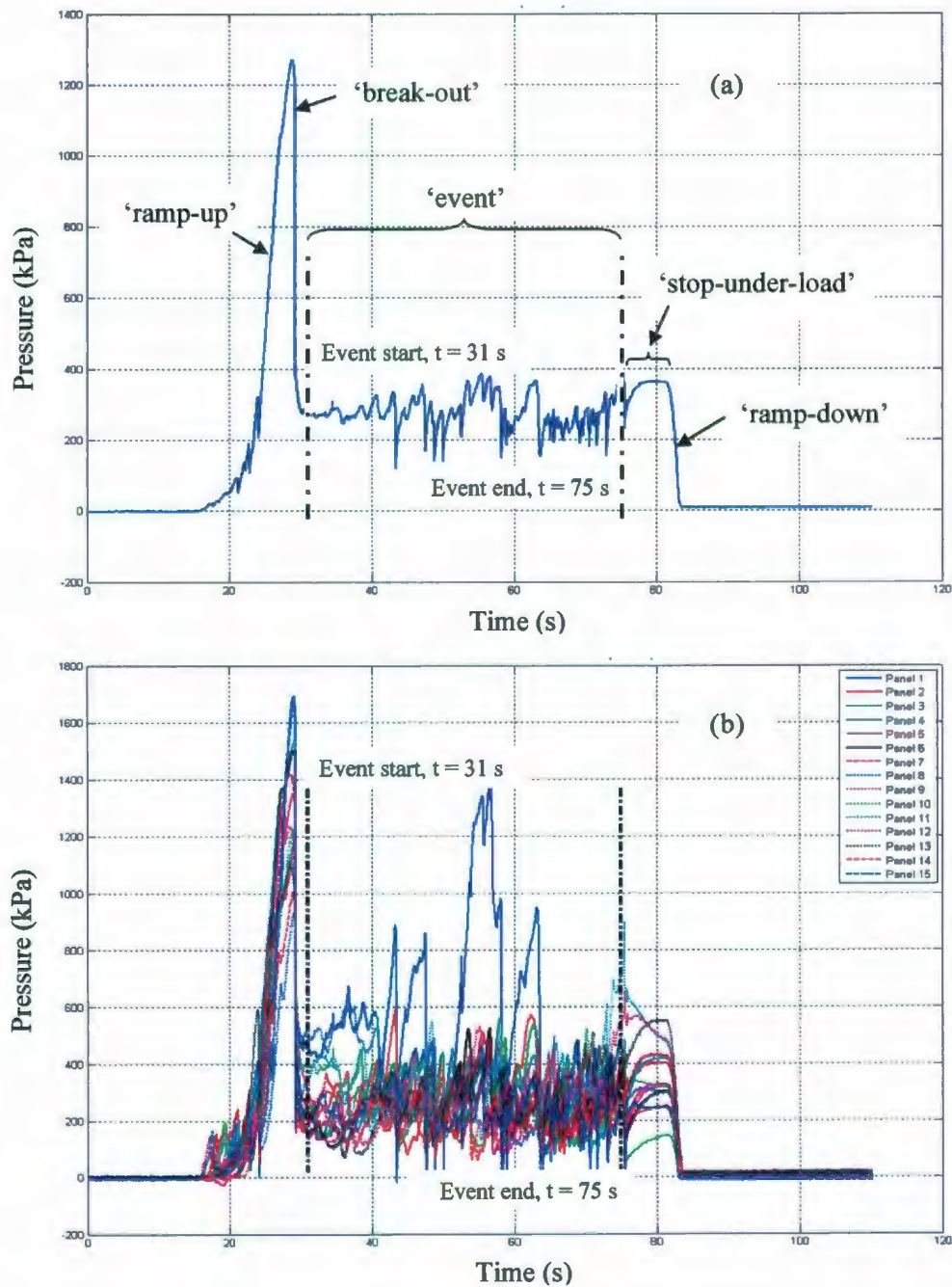


Figure 5.26: Sample event time traces showing: (a) global pressure; (b) local pressures.

To remove these portions of the data, events were defined which correspond to the useable portion of the data. A standardized approach was used in defining events to ensure consistency between tests. To define an event, time traces of the global pressure and local panel pressure data were first plotted, as shown in Figure 5.26.

As shown in Figure 5.26 (a) above, during the initial ramp-up part of some tests, load spikes (also called ‘break-out’ loads) resulted due to the initially near perfect contact between a freshly prepared ice edge and the indenter. This artificial initial condition was denoted as ‘undamaged’ ice on the JOIA data CD. The actual stroke used for most tests was approximately a third of the maximum stroke. This was done to allow testing of multiple conditions for a given ice sheet. The majority of tests were conducted by extending the indenter part way through the ice sheet, then stopping, changing the speed setting and restarting the indentation process. For such tests the initial geometry of the ice was irregular and the ice was denoted as ‘damaged’. Break-out loads were typically not observed for ‘damaged’ initial conditions. For the present analysis, events have been defined in a way which removes data associated with start and end conditions. The analysis conducted in the present work does not distinguish between ‘damaged’ and ‘undamaged’ cases.

The start point of an event was typically taken as the point where trends in the data transitioned from systematic to random behavior. Similarly, the end point was taken as the point where the data transitioned back from random to systematic. For events with ‘break-out’ loads, start points were taken after the initial spike where the data transitioned into more random behavior.

Edge Effects

From the data it was observed that the end panels, P1 and P15, consistently had higher mean and maximum pressures than the other panels (see Figure 5.15 for panel numbering). To check for a systematic edge effect, mean panel pressures were calculated for each panel and then normalized by the mean panel pressure for the middle panel (P8). The middle panel was selected based on elastic indentation theory (Timoshenko and Goodier, 1951), which suggests that the middle panel should have the lowest pressure. Normalizing the pressures in a systematic way allowed for comparison of results from different events. A sample plot of normalized pressure is shown in Figure 5.27; see Taylor et al. (2007) for edge effects analysis results for all events.

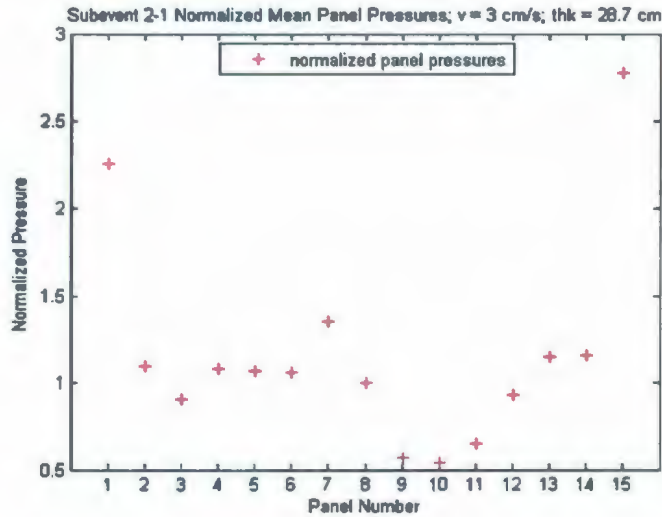


Figure 5.27: Observed edge effects in normalized pressures for event 2-1.

To get a better representation of the mean trend, all event data were grouped according to speed range. The overall mean normalized panel pressures were then calculated using the combined data from all events in each speed range. These results were plotted against the normalized theoretical elastic indentation pressure distribution of Timoshenko and Goodier (1951). As may be observed from Figure 5.28, edge effects were observed for all three speed ranges and agree with the general trends of the Timoshenko solution.

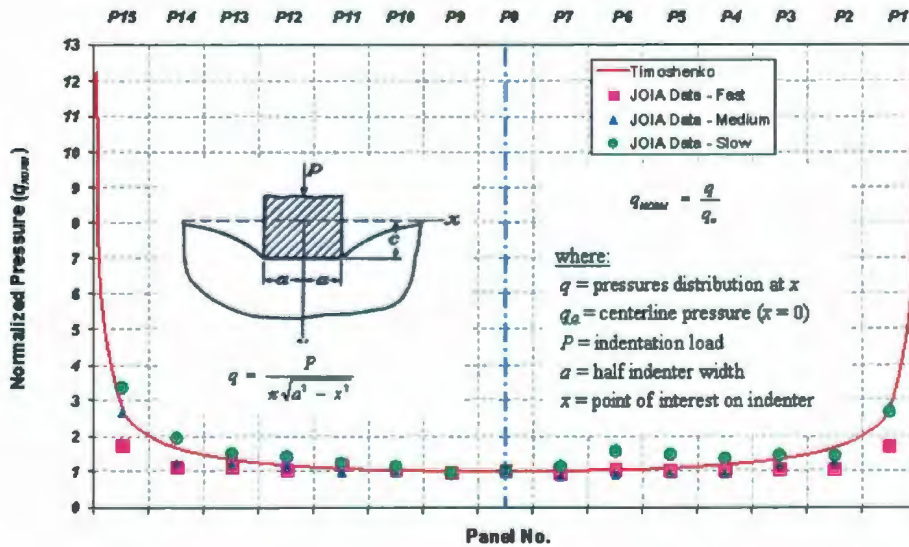


Figure 5.28: Timoshenko elastic solution compared with average normalized JOIA results for three speed ranges considered.

While ice does not strictly behave as an elastic material, the ice sheet behind the local indentation region may be acting as an elastic field, which is contributing to the observed edge effects. As a viscoelastic, damaging material one would expect enhanced microstructural modification accompanied by the formation of spalls and splits near the corners of the indenter. At higher speeds, the occurrence of local spalling at the edges may cause the load to drop, decreasing the average load for the panel. Further work would be needed in this area to definitively identify the causes of observed edge effects.

It is unlikely the edge effects observed in the JOIA data would be present on a full-scale structure. On larger scale structures local failure processes would likely dominate, resulting in imperfect contact conditions. These conditions would lead to a more progressive type of failure, rather than the sort of pressure build-up proposed by the theoretical indentation solution.

In the present work, results have been obtained based on analysis using data for all fifteen indenter segments (P1-P15), as well as for the middle thirteen segments only (P2-P14). Correlation and global load estimation results with and without end panel data are discussed further in the following sections.

Relevant Issues and Assumptions

For the analysis conducted in this study, several key assumptions have been made. These are summarized below. Supporting materials are provided as needed in the appendices identified below.

Global Load Data: All global loads referred to in this study, unless identified otherwise, were obtained by summing individual loads from segmented indenter panels. This approach was deemed more consistent than using oil pressure gauge measurements (erroneous data), or independent global load cell measurements (data not available for most tests). See Appendix B.1 for further detail.

Event Definition Sensitivity: Clearly defining endpoints is more challenging for ductile-type events since other failure modes, such as creep buckling (Sodhi et al., 2001) may affect the load traces. It was found that the standard deviation of pressure was particularly

sensitive to event definition for ductile-type events (important for global load estimation). English versions of project documentation detailing failure mode observations are presently not available, making interpretation of ductile time traces more challenging. Event definitions for ductile-type tests should be revisited should English versions of testing documentation become available. See Appendix B.2 for further discussion.

Sample Spectral Analysis: Preliminary analysis suggested that more harmonic activity is observed for medium and fast events than for slower, ductile-type events. Further work is required to fully assess spectral characteristics of the data. Future efforts to link spectra with failure processes characteristics and correlations would be valuable. See Appendix B.3 for further discussion.

Stationarity: Ice-structure interaction events have been idealized as a random averaging process, and the assumption has been made that the process is stationary for a given time interval. This was found to be a valid assumption for brittle events, and a reasonable starting point for the ductile events. A review of this assumption, particularly for ductile events which may include multiple failure mechanisms, is recommended should additional information become available. See Appendix B.4 for further detail.

5.7.3 Statistical Characteristics of Data

Statistical analysis of all selected datasets was conducted and a series of figures were produced for each event. The first figure plotted for each event provided a summary of key event information, along with a plot illustrating the maximum, mean and standard deviations of all individual panel pressures and global pressures. Figure 5.29 is an example of this type of plot. The next figure generated for the event consisted of a set of time traces and histograms of local pressures for individual panels (P1-P9). An example of this type of plot is shown in Figure 5.30. A third plot was then generated for each event which consisted of time traces and histograms for the remaining local panel pressures (P10-P15), as well as the global pressure; see Figure 5.31. These figures were useful in assessing the general characteristics of the data and performing logical checks.

Plots corresponding to a representative sample of fast (Figures 5.29 to 5.31), medium (Figures 5.32 to 5.34) and slow events (Figures 5.35 to 5.37) are given below.

Statistical Characteristics of Sample Fast Event

From Figure 5.29 it may be seen that the global mean for the event is approximately equal to the local means, while the global standard deviation is consistently lower than the individual panel standard deviations. This is an important check, since it validates the fundamental assumption that probabilistic averaging is present at the scale of the JOIA tests. This provides support for the variance reduction associated with the probabilistic averaging approach used for global pressure estimation.

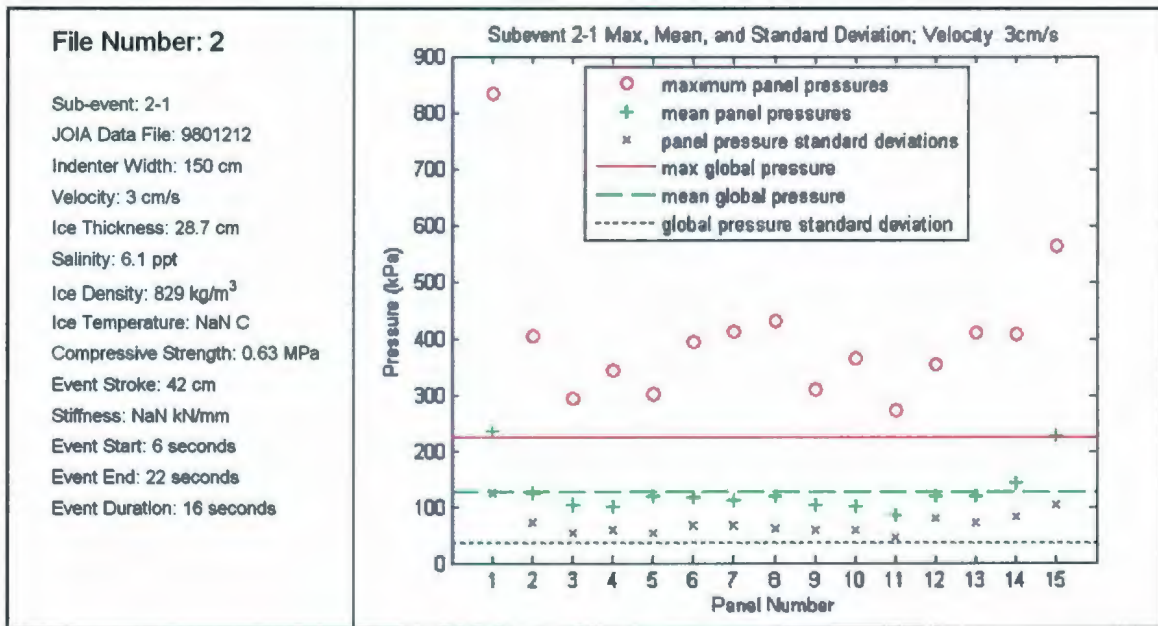


Figure 5.29: Maximum, mean and standard deviation of pressures for sample fast result.

From Figure 5.30 and Figure 5.31, it is observed that the histograms of the data indicate that the local panel pressure distributions are non-Gaussian. Global pressure distributions, which results from the sum of local loads averaged over the total width tends more toward a Gaussian distribution. This is a result of the central limit theorem (CLT), which states generally that if one adds together or averages many random quantities, one gets a random quantity that approaches the normal distribution (Jordaan, 2005).

Subevent 2-1 Local Pressures

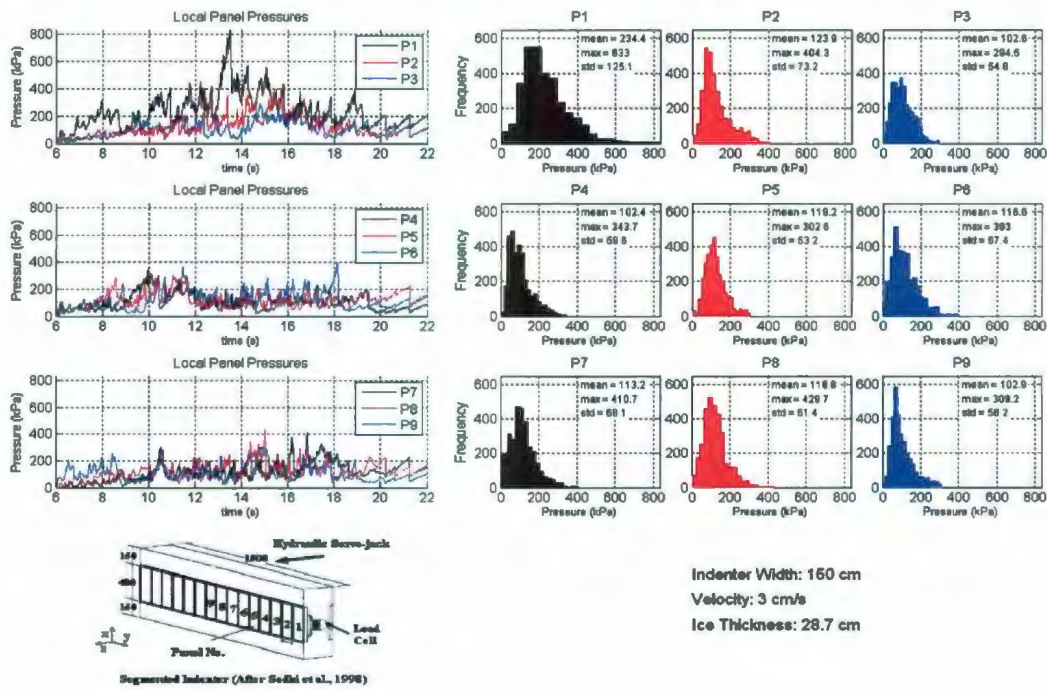


Figure 5.30: Local pressure plots (P1-P9) for sample fast event.

Subevent 2-1 Local and Global Pressures

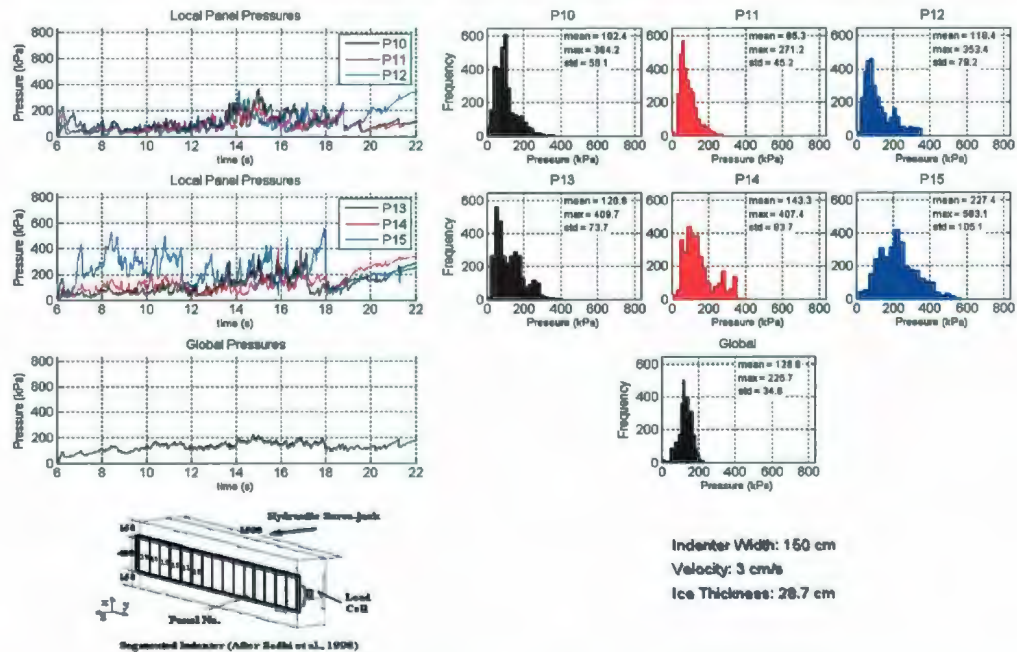


Figure 5.31: Local pressure (P10-P15) and global pressure plots for sample fast event.

Statistical Characteristics of Sample Medium Speed Event

For the medium speed case, it was also observed that the global mean for the event is approximately equal to the local means, as shown in Figure 5.32. The global standard deviation for this event is consistently lower than the individual panel standard deviations, as is expected.

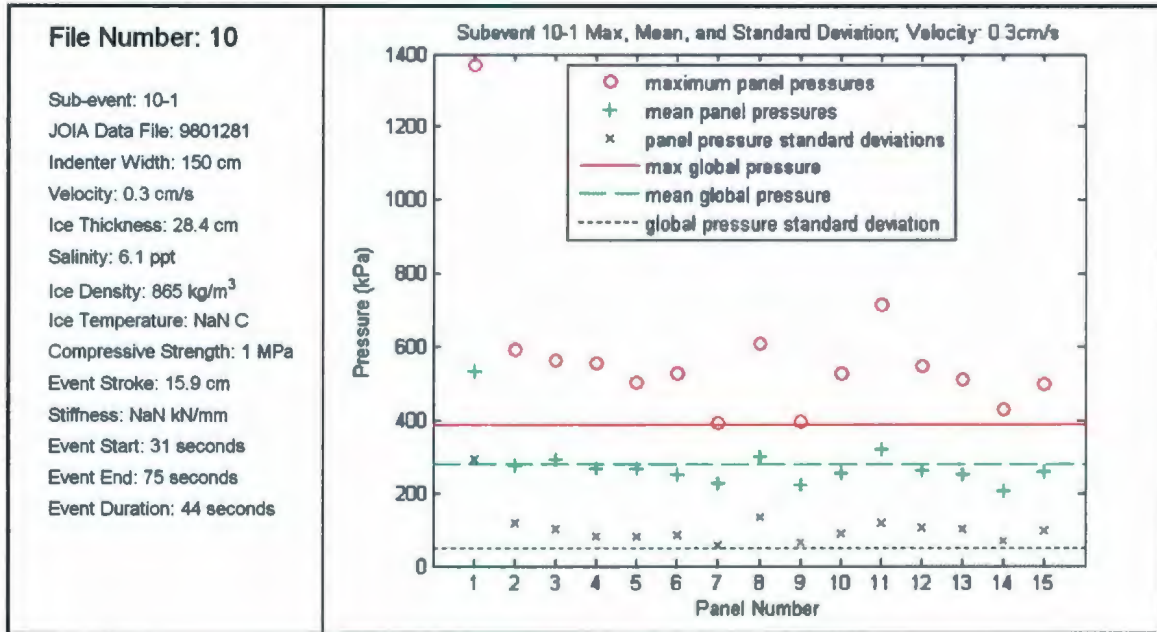


Figure 5.32: Maximum, mean and standard deviation of pressures for sample medium speed event.

The histograms in Figures 5.33 and 5.34 indicate that the pressure distributions for event 10-1 are also non-Gaussian. As for the previous example, the global pressure histogram tends more towards the Gaussian distribution as expected based on the central limit theorem.

Subevent 10-1 Local Pressures

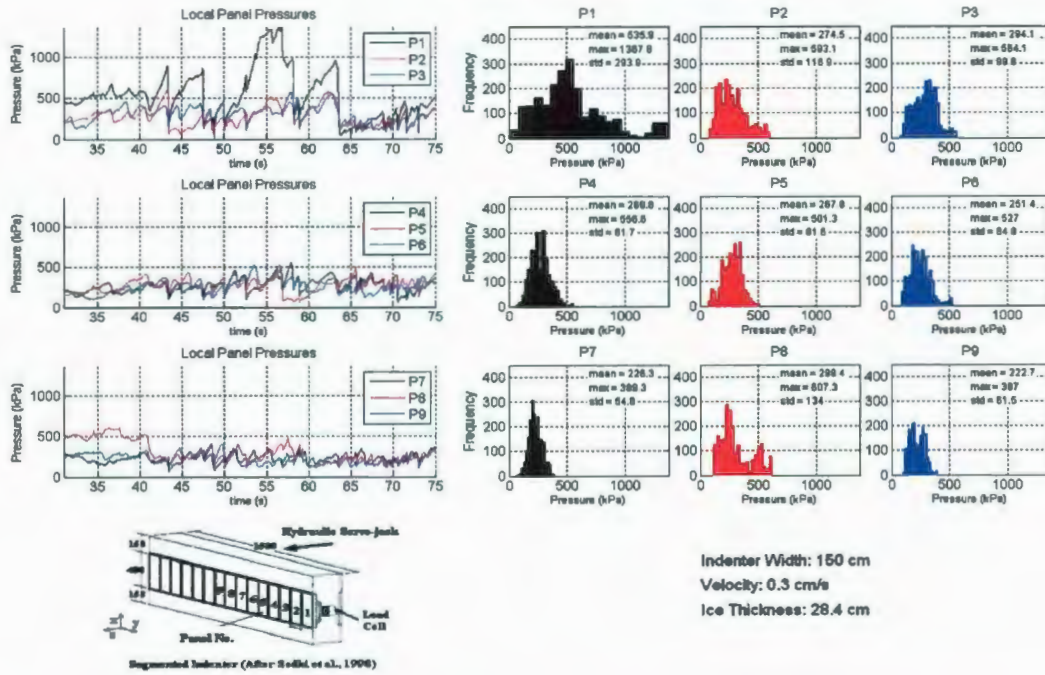


Figure 5.33: Local pressure plots (P1-P9) for sample medium speed event.

Subevent 10-1 Local and Global Pressures

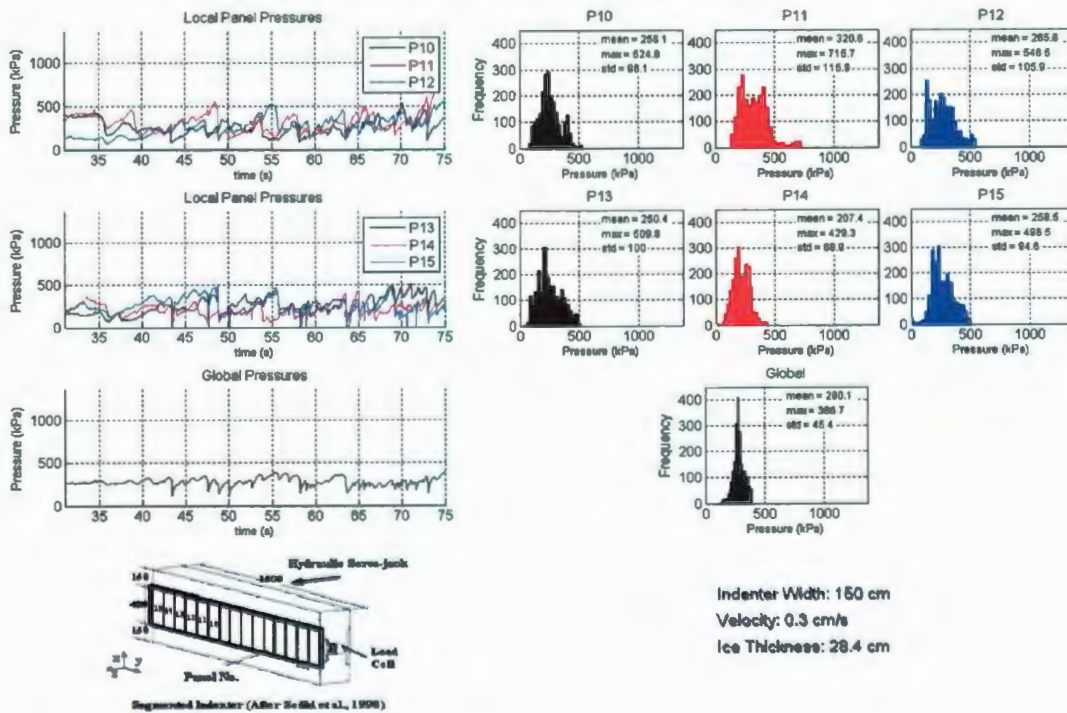


Figure 5.34: Local pressure (P10-P15) and global pressure for medium speed event.

Statistical Characteristics of Sample Slow Event

For the slow example shown in Figure 5.35, similar trends may be observed as for the previous examples. It is noted that for slow events, non-simultaneous aspects of the failure process are less dominant. The observed differences between the standard deviations of the local and global pressures are not as pronounced as in the medium and fast cases.

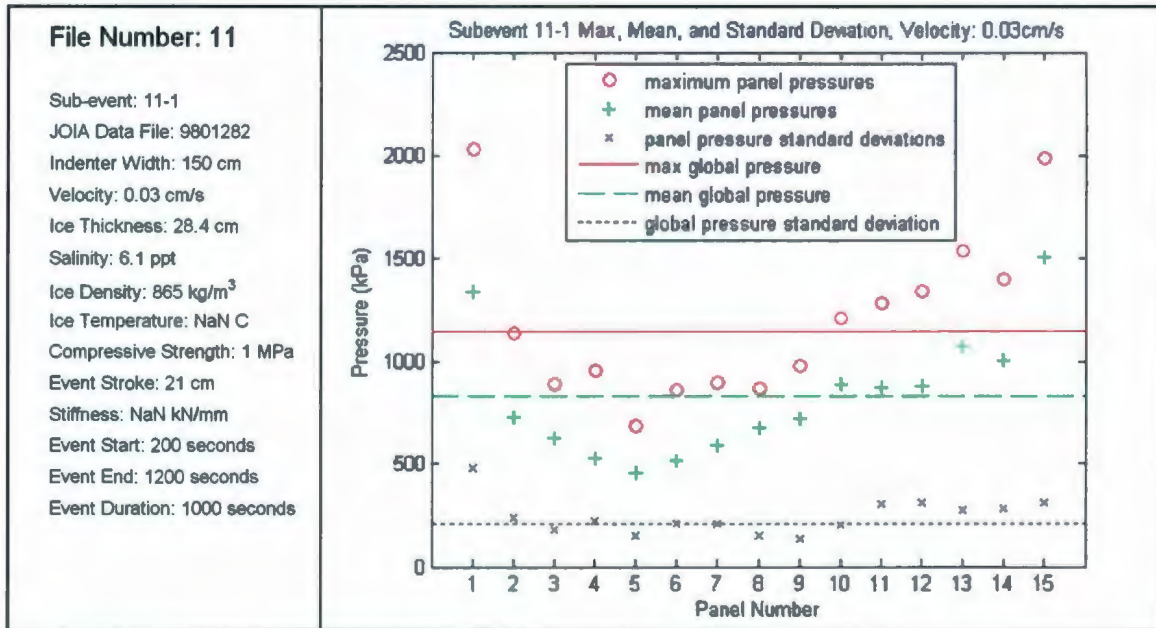


Figure 5.35: Maximum, mean and standard deviation of pressures for sample slow event.

In terms of the pressure distributions, the histograms from Figures 5.36 and 5.37 do not distinctly take on a particular form. The global pressure distribution for the slow case tends to be more uniform than was observed for the medium and fast cases. This is expected since ductile-type failure tends to occur under more uniform loading conditions, while brittle-type failure is more influenced by processes linked to *hpz* formation and evolution.

Subevent 11-1 Local Pressures

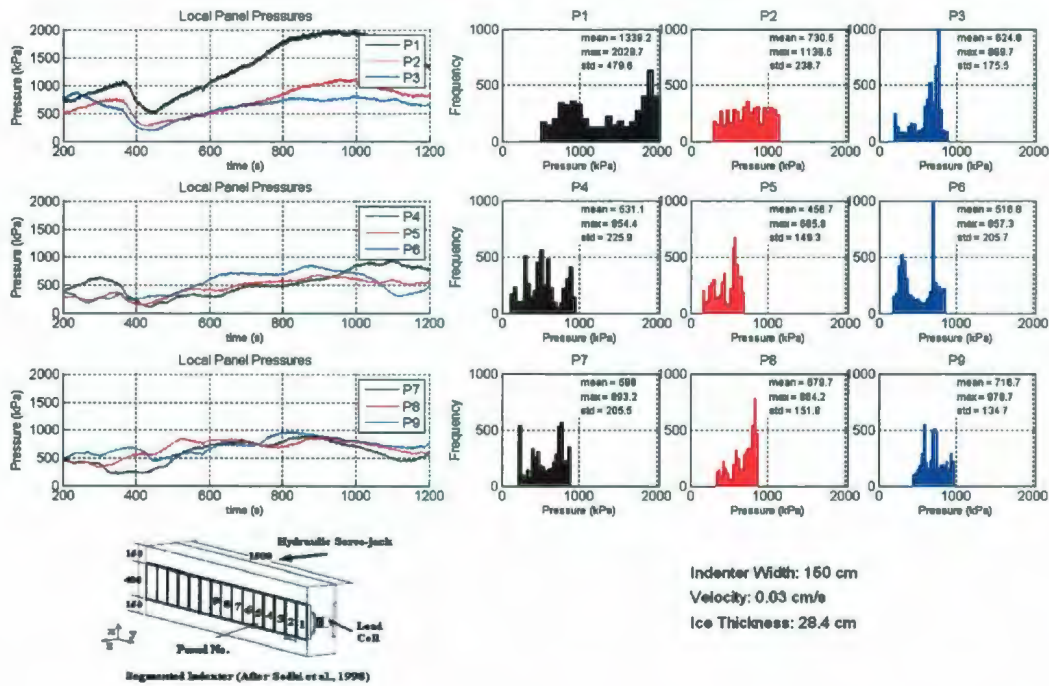


Figure 5.36: Local pressure plots (P1-P9) for sample slow speed event.

Subevent 11-1 Local and Global Pressures

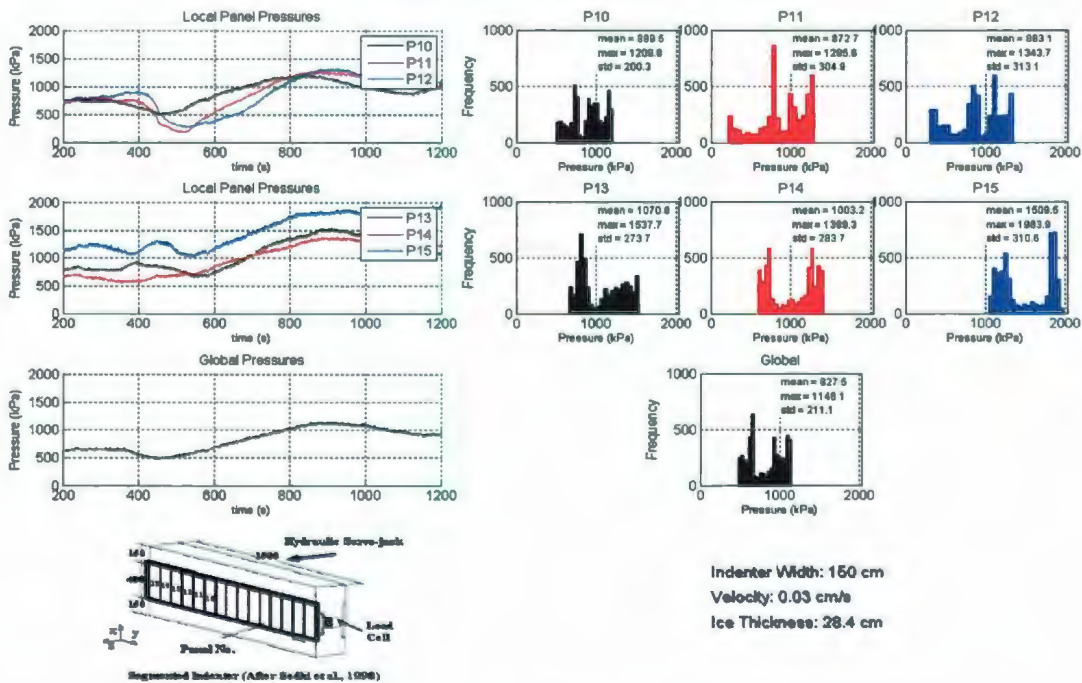


Figure 5.37: Local pressure (P10-P15) and global pressure for sample slow speed event.

Event means and standard deviations of individual panel pressures and global pressures, including edge panels (P1-P15) and excluding edge panels (P2-P14) were calculated for all events. These data were grouped according to speed range. Overall mean, maximum and minimum values of local and global event means were calculated for each speed range. Similarly overall mean, maximum and minimum values of local and global event standard deviations were calculated for each speed range. These data are summarized in Table 5.6.

Table 5.6: Values of local and global event pressures: (a) means; (b) standard deviations.

(a)		Single Panel Mean	Global Mean (P1-P15)	Global Mean (P2-P14)
Fast	Mean	346.8	346.8	323.7
	Max	711.0	709.7	692.0
	Min	124.3	128.8	113.1
Medium	Mean	236.4	236.4	209.3
	Max	487.3	468.8	420.6
	Min	51.1	71.2	47.1
Slow	Mean	717.9	717.9	642.7
	Max	1440.6	1440.6	1422.6
	Min	323.6	332.7	261.7

(b)		Single Panel St Dev	Global St Dev (P1-P15)	Global St Dev (P2-P14)
Fast	Mean	192.0	192.0	180.8
	Max	443.2	355.1	346.7
	Min	45.2	71.1	64.3
Medium	Mean	141.7	141.7	127.3
	Max	695.5	333.9	320.8
	Min	0.0	46.8	31.4
Slow	Mean	135.7	135.7	118.9
	Max	549.4	243.5	220.2
	Min	19.9	38.6	38.4

From the above table it is observed that the values of single panel mean match identically with global mean (P1-P15) values. Similarly, the values of single panel standard deviation match identically with global standard deviation (P1-P15) values. The overall mean values of the single panel standard deviation shown above are equal to the overall mean values of global standard deviation by virtue of the fact that these are averages taken over all events within the speed category. This is a product of arithmetic averaging over multiple events. The standard deviation of local panel pressure for any given event is higher than the corresponding global pressure standard deviation for that event. As expected, excluding the edge panel data tends to decrease the mean and standard deviation.

It is also noted that on average, slow events have higher mean pressures and lower standard deviations than medium and fast cases. This reflects the more uniform loading of the indenter during ductile failure, which results in higher loading with less dominant non-simultaneous behavior. On larger scale structures, it is unlikely that the same degree of uniformity would occur across the entire face of the structure since local failure processes would likely influence the extent of contact. Further work is needed to more fully explore the nature of full-scale loads at slow loading rates.

5.7.4 Probabilistic Averaging: Autoregressive Approach

Probabilistic averaging methodology is used to account for variation in pressures across the width of the structure due to the birth and death nature of *hpzs*. This is of particular importance in extrapolating global loads from local pressure data measured from panels that only partially cover the width of the structure. For the second-order autoregressive model the correlation function $\rho(t)$ has exponential form and is given by Eq. 4.14.

Here τ is taken as the distance between adjacent panels and c is a constant (characteristic correlation length). A typical distance between panels for Molikpaq is approximately 1.13 m, and is approximately 0.10 m for JOIA. The value of c was estimated by calculating $\rho(t)$ as a function of distance τ using Eq. 4.14, comparing with correlation coefficient data obtained from measured data and selecting the c value that gives the best agreement with the measured data.

Based on the central limit theorem, it has been assumed here that the global pressures follow a Gaussian distribution (see section 5.7.3 above for further discussion). Ice pressure has been modeled as a random averaging process with a Gaussian distribution defined by a mean, standard deviation and a second-order autoregressive correlation function in space.

In this analysis the mean global ice pressure is assumed to be equal to the mean local ice pressure. Due to averaging across the width of the structure, the standard deviation of global pressure reduces. The extent of the reduction depends on the width of the loaded

area. The relationship between the standard deviation of the global pressure σ_G and that of the local pressure σ_L based on Eq. 4.15 is given as $\sigma_G = \sqrt{\gamma(T)}\sigma_L$. The term $\sqrt{\gamma(T)}$ is a 'reduction factor' defined as the square root of the variance function $\gamma(T)$ over the averaging distance T , which is taken as the whole structure width in this case. The variance function $\gamma(T)$ was defined in Eq. 4.17.

The above method requires knowledge of the correlation coefficient $\rho(t)$ as a function of distance. Results from the analysis of correlation between pressure measurements from pairs of local panels are presented below. This is followed by a description of two approaches for modeling correlation and the results corresponding to each approach. The first correlation modeling approach, the 'standard' method, relies on a single characteristic correlation length c to model the correlation function $\rho(t)$. The second approach, the 'composite' method models correlation behavior as a weighted linear combination of two correlation terms, based on two values of characteristic correlation length, c_1 and c_2 .

5.7.5 Local Panel Correlation Analysis

The probabilistic averaging approach requires definition of an appropriate characteristic correlation length, which in turn requires knowledge of panel correlation as a function of distance between adjacent indenter panels. To this end, a detailed examination of correlation of the JOIA data has been presented below. For the following analysis only time-averaged spatial correlations have been considered.

Individual Panel Correlations for Speed Ranges

Correlations were calculated for all combinations of two panels for each event and a series of plots was generated. These plots included individual panel correlation plots for all fifteen panels, a 3-D bar chart of the correlation matrix and a 2-D contour map of the correlation matrix. Representative events from each of the three speed ranges have been presented below. Due to the large amount of information resulting from the correlation

analysis, results for only a single sample panel are included below for individual panel correlation plots.

Sample Fast Event

The sample plot shown in Figure 5.38 (a) is a represent pairwise correlation between the noted panel (P7) and all other panels on the indenter for that particular event.

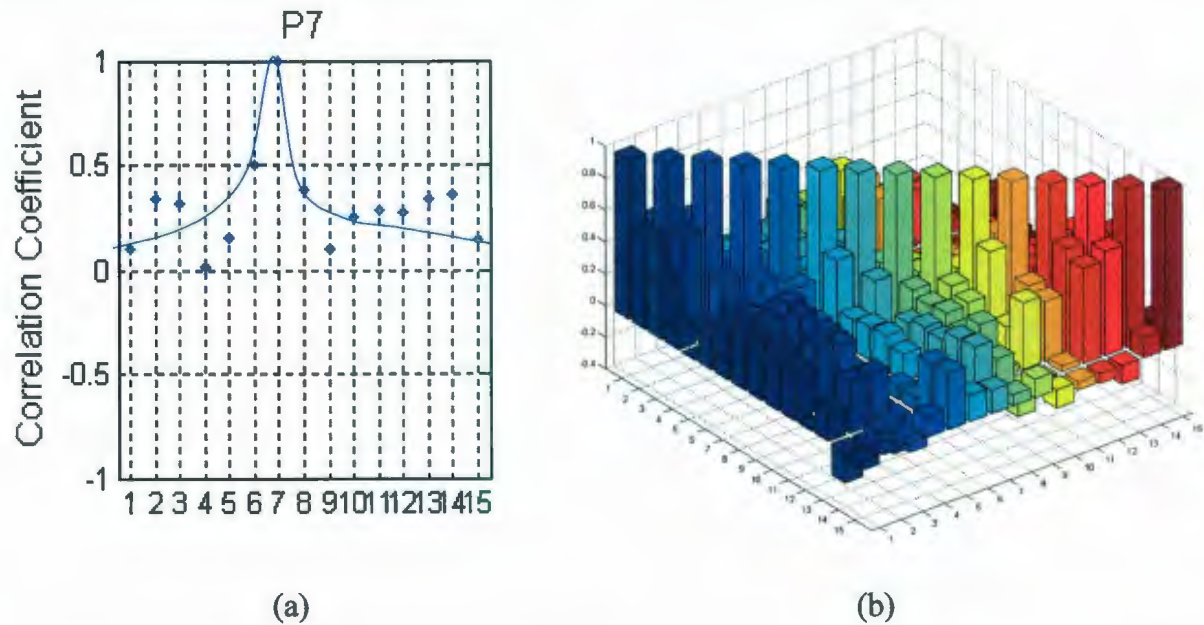


Figure 5.38: (a) Individual panel correlations for sample panel (P7); (b) correlation coefficient matrix 3-D bar chart for sample fast result.

As expected, the correlation between any given panel and itself is unity. It may also be observed that the correlations tend to decrease with increasing distance and are generally higher between a selected panel and the immediately adjacent panels.

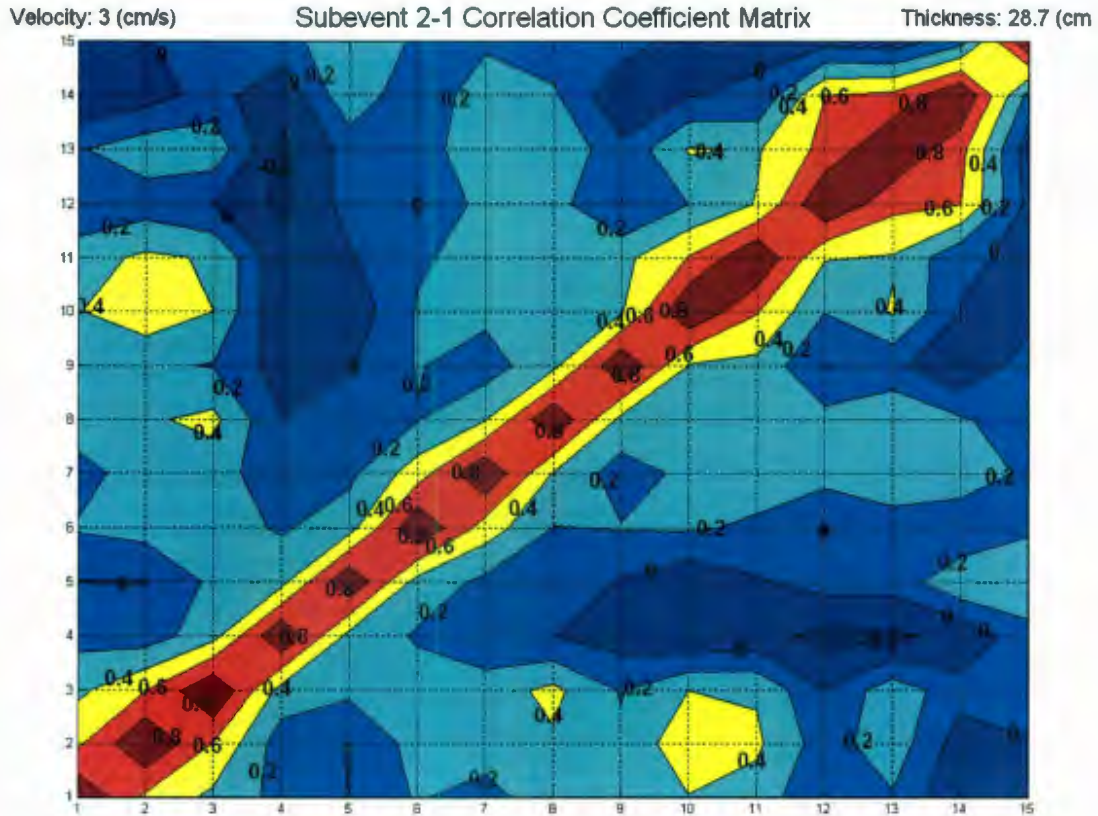


Figure 5.39: Correlation coefficient matrix contour plot; sample fast result (event 2-1)

Figures 5.38 (b) and 5.39 provide alternate graphical representations of the correlation matrix for sample event 2-1. As may be observed, the correlation matrix is symmetrical (i.e. correlation between P1, P2 is the same as P2, P1 – order does not matter). Observed variation in symmetry in the correlation plots in this report are likely artifacts of the plotting routine used rather than a result of asymmetry in the data. Symmetry of the data has been manually confirmed by inspection of the matrices.

From the above correlation plots, it is evident that the highest correlations occur along the diagonal (as expected since correlation equals unity along the diagonal). In the region surrounding the diagonal, the correlations drop off rapidly; immediately adjacent panels have significant correlation, but there is little correlation between panels separated by more than one panel width. This rapid decrease is likely due to the more random nature of the failure processes at faster speeds, which would tend to have a more non-uniform pressure distribution.

Sample Medium Speed Event

Figure 5.40 indicates similar trends for the sample medium speed event; correlations between the selected sample panel (P7) and the immediately adjacent panels are stronger than with distant panels.

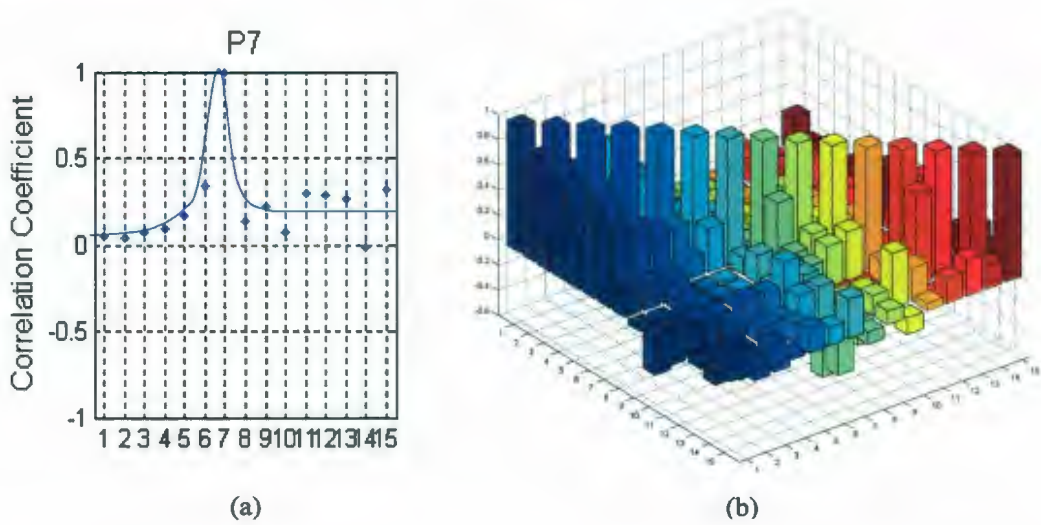


Figure 5.40: (a) Individual panel correlations for sample panel (P7); (b) correlation coefficient matrix 3-D bar chart for sample medium speed event.

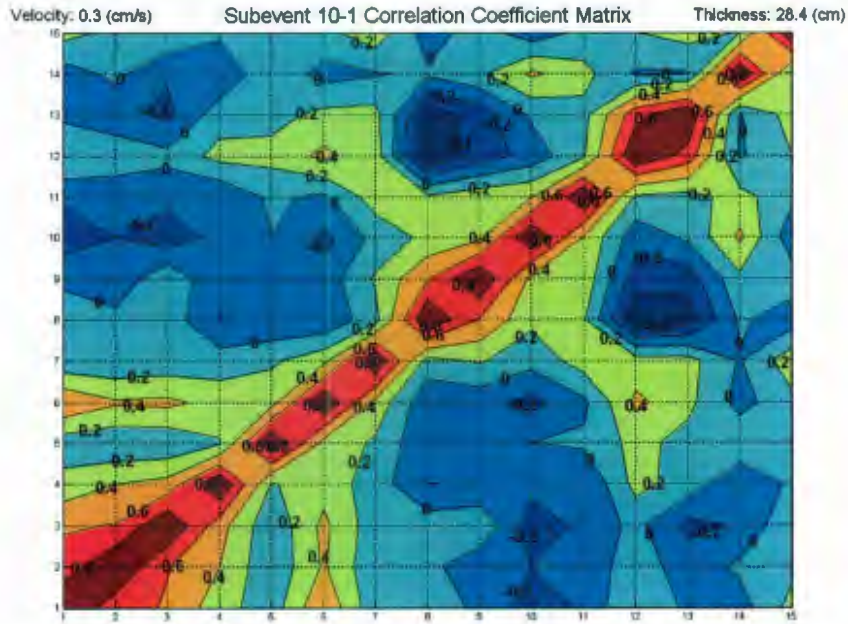


Figure 5.41: Correlation coefficient contour plot; sample medium speed event.

For the sample medium event, correlations also tend to group around the diagonal and decrease considerably with increasing distance away from the diagonal; see Figure 5.40 (b) and Figure 5.41. As with the fast events, the immediately adjacent panels have significant correlation, but there is little correlation between panels separated by more than one panel width. Given the brittle-type failure observed for the medium speed range, the observed correlation relationships are likely influenced by the more dominant non-simultaneous failure processes.

Sample Slow Event

The slow sample event in Figure 5.42 exhibits higher overall correlations than were observed for the medium and fast events. The correlations do not tend to drop off as quickly, and are generally more uniformly distributed. This observation is supported by Figures 5.42 (b) and 5.43, which graphically illustrate the more uniform distribution of correlations.

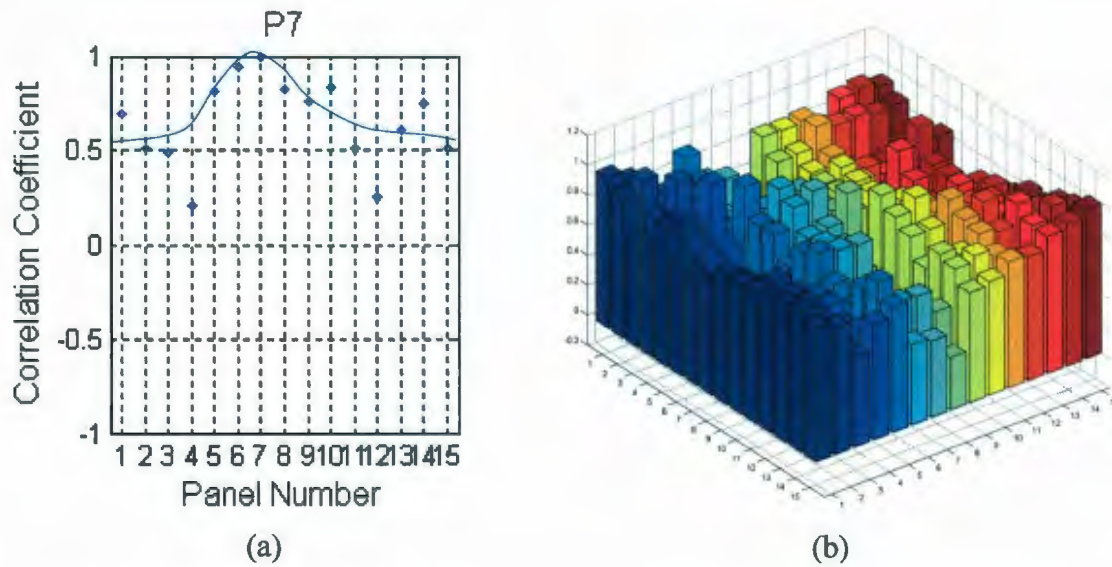


Figure 5.42: (a) Individual panel correlations for sample panel (P7); (b) correlation coefficient matrix 3-D bar chart for sample slow event.

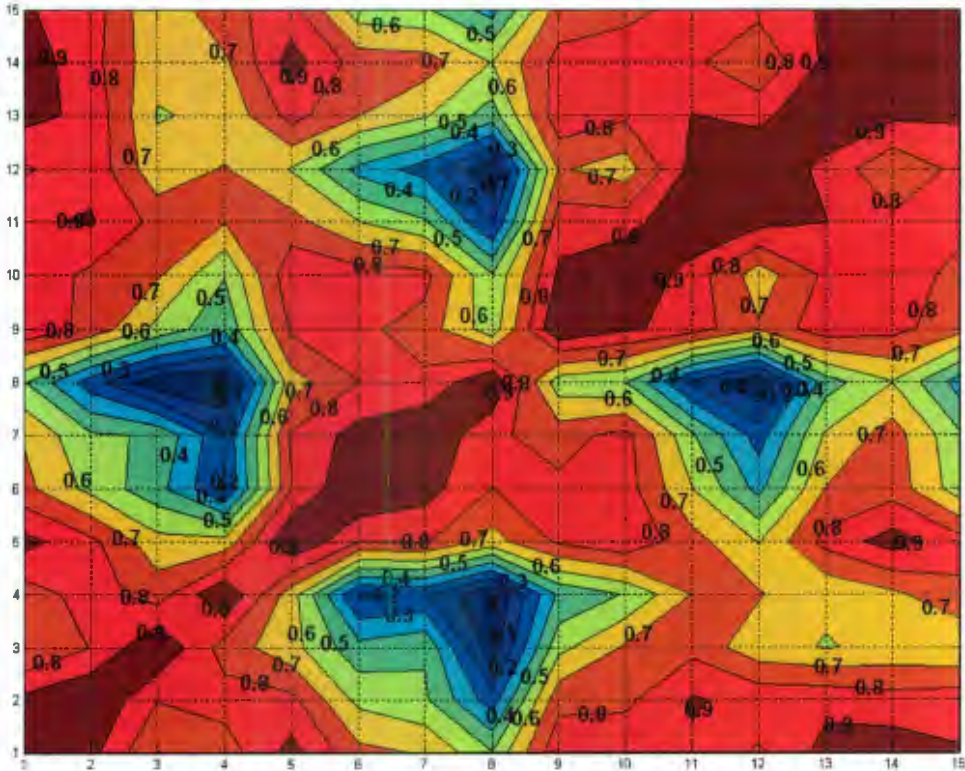


Figure 5.43: Correlation coefficient matrix contour plot; sample slow event.

Figure 5.43 illustrates the more uniform nature of the slow speed event. Quite high correlations are observed at locations other than the diagonal. Significantly high correlations are evident between immediately adjacent panels, as well as between panels separated by significant distances. While some panel combinations have lower correlations (likely a result of random processes), in general the distribution is more uniform for ductile-type events than for brittle conditions.

Average Panel Correlations for Speed Ranges

To get a more accurate representation of correlation trends, panel correlation data for all events in each speed range were compiled, averages over all events in the speed range and plotted. As for the previous section, only sample results for a single panel (P7) is given below. The event averaged individual panel correlation for each of the speed ranges is given in Figure 5.44.

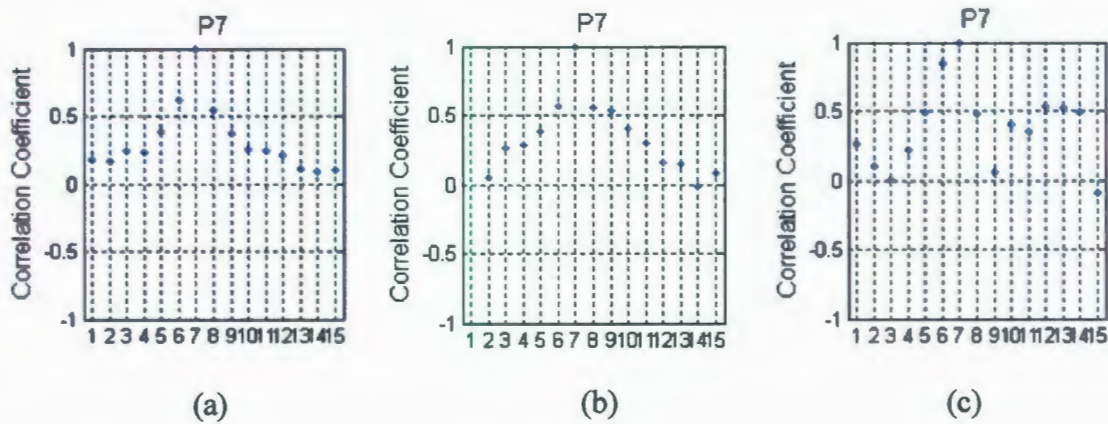


Figure 5.44: Event averaged individual panel correlations for single sample panel (P7) for: (a) all fast events; (b) all medium speed events; (c) all slow events.

Based on the above results it may be concluded that for slower speeds ductile-type failure is expected, resulting in a more uniform pressure distribution and correspondingly higher correlation coefficients across the width of the indenter. For faster speeds the failure is brittle, producing a more random pressure distribution with lower correlation coefficients. The correlations are strongest between adjacent panels and correlation decreases with increasing separation distance.

5.7.6 Correlation Modeling (Standard Approach)

Once correlation information was obtained from the analysis of local panel pressure data, a curve of best-fit was used to estimate the most appropriate value of the characteristic correlation length, c . To this end, JOIA correlation coefficients were plotted as a function of distance, along with correlation coefficients predicted by the autoregressive approach evaluated for various values of c .

Standard Autoregressive Methodology

The method outlined in Jordaan et al. (2006) uses a second-order autoregressive model having a characteristic correlation length, which is related to the correlation coefficient according to Eq. 4.14.

For a given dataset, an appropriate value of characteristic correlation length may be found by calculating the correlation between panels as a function of distance and comparing these data with results obtained using Eq. 4.14 with various values of characteristic correlation length, c . The value of c which gives the best agreement with the panel correlation data is taken as the representative value for the process.

Characteristic Correlation Length Analysis Results (P1-P15)

The initial analysis included edge panel data (P1-P15). Results for the fast, medium and slow results are plotted in Figures 5.45, 5.46, and 5.47 respectively. As shown in Figure 5.45 below, no one particular value of c provided an exact match to the JOIA data. As a conservative estimate, a value of $c = 0.20$ was observed to fit the tail of the data, while over-predicting the correlation for smaller distances.

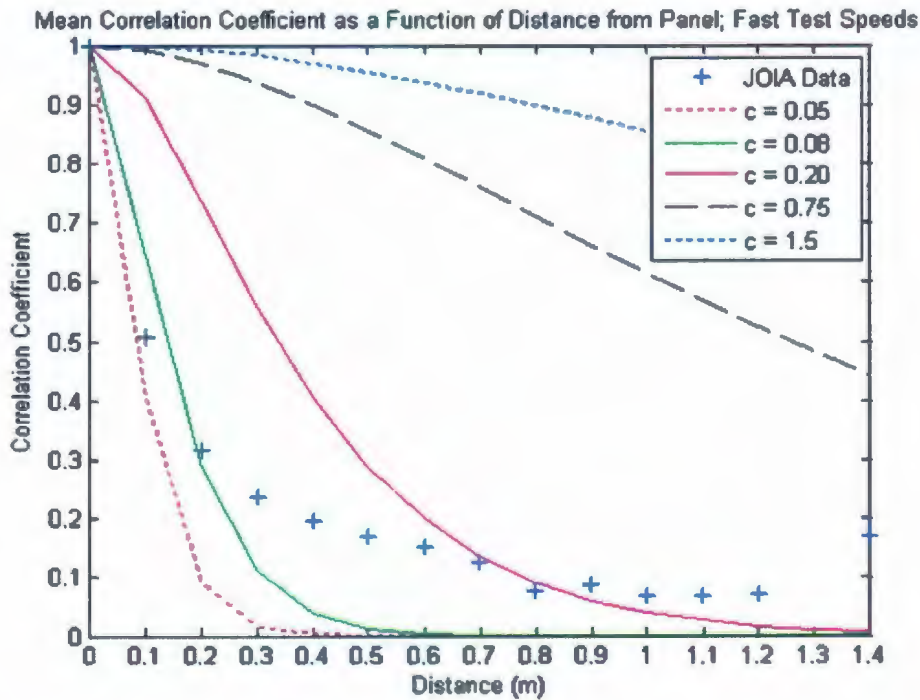


Figure 5.45: Plot of ρ vs. distance; autoregressive fit; fast event data (P1-P15).

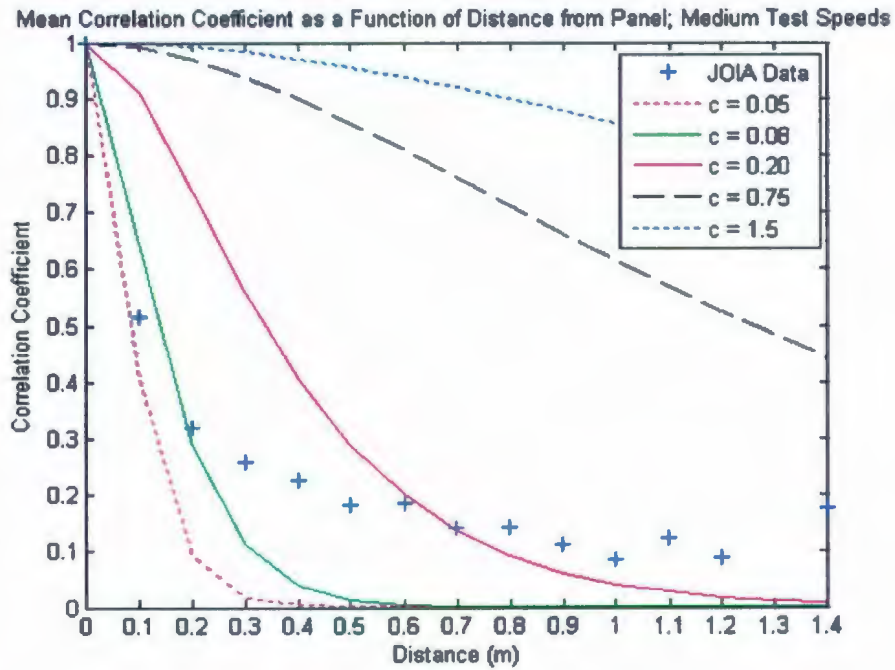


Figure 5.46: Plot of ρ vs. distance; autoregressive fit; medium event data (P1-P15).

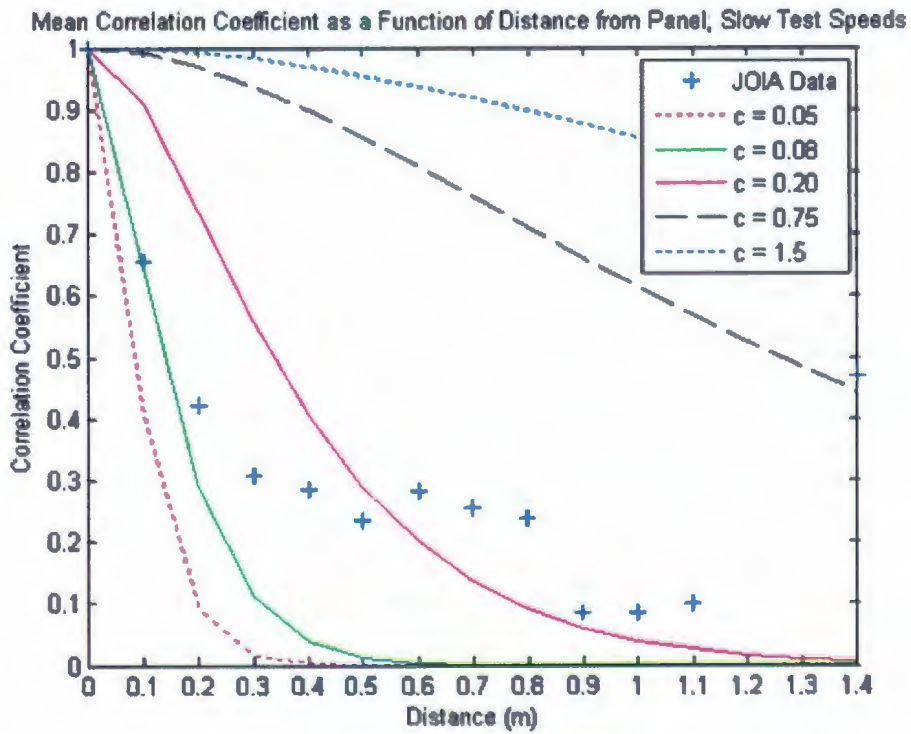


Figure 5.47: Plot of ρ vs. distance; autoregressive fit; slow event data (P1-P15).

Similarly for Figures 5.46 and 5.47, no one particular value of c provided an exact match to the JOIA data. Based on these results, a conservative value of characteristic correlation length of $c = 0.20$ was determined to provide the most appropriate estimation of the data for all speed ranges considered when the autoregressive approach is used.

Characteristic Correlation Length Analysis Results (P2-P14)

To investigate the influence of the edge panel data on the correlation results, the analysis process was repeated excluding edge panel results (P2-P14). Results for the fast, medium and slow results are plotted in Figures 5.48, 5.49, and 5.50 respectively. While the edge panels did not have a significant effect on the fast results, as seen in Figure 5.48, exclusion of the end panels did increase the correlations in the tails of the data for the medium and slow cases. From Figures 5.49 and 5.50 it may be seen that the data tend to asymptote to a value of approximately 0.20 over the range of distances considered. The standard autoregressive approach always asymptotes to zero; to make the tail of the curve match the data a significantly more conservative value of c (equal to 0.5, for instance) would be required. To avoid over conservatism, a compromise had to be made since the standard autoregressive function used does not match the curve shape of the data. Since the correlations of adjacent panels are more important than the correlations of remote panels in terms of their influence on loading, a value of $c = 0.20$ was selected. The rationale for selecting this value was that it provides conservative correlation value over the initial half of the range without being excessively conservative. In the distant regions where the autoregressive curve under predicts the data, the correlation values are very low and would likely only have a negligible effect on load.

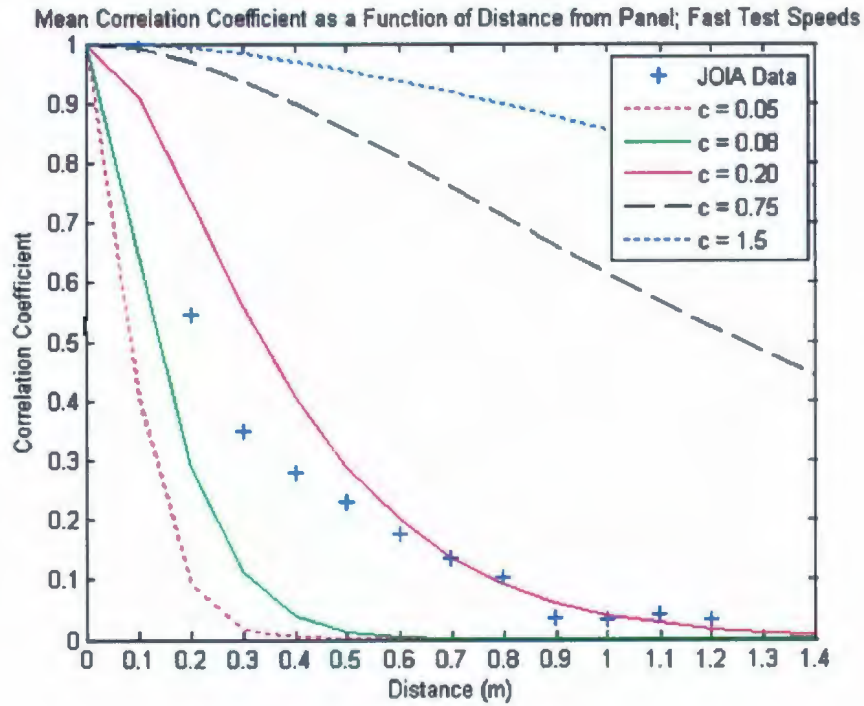


Figure 5.48: Plot of ρ vs. distance; autoregressive fit; fast event data (P2-P14).

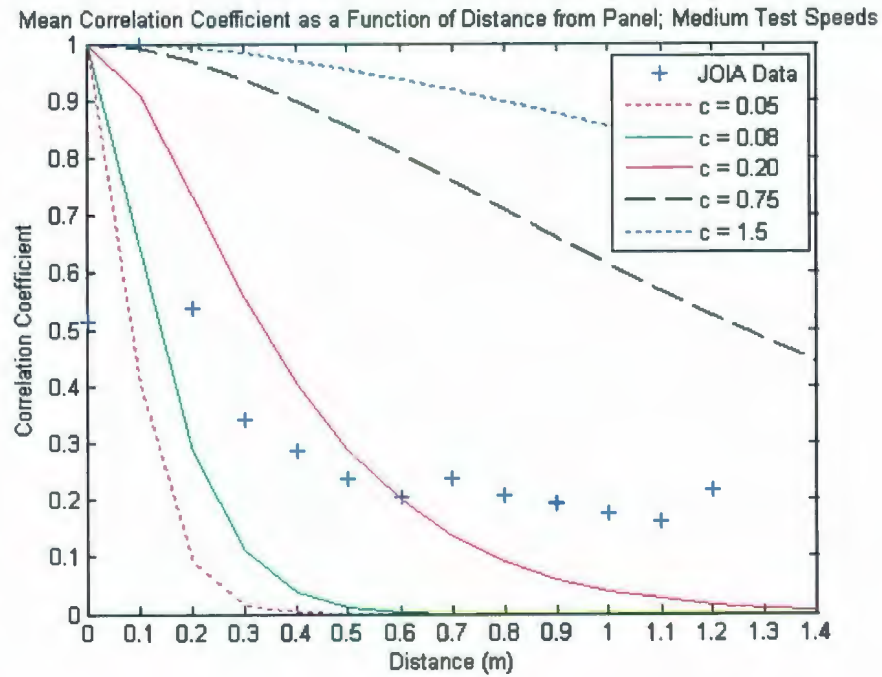


Figure 5.49: Plot of ρ vs. distance; autoregressive fit; medium event data (P2-P14).

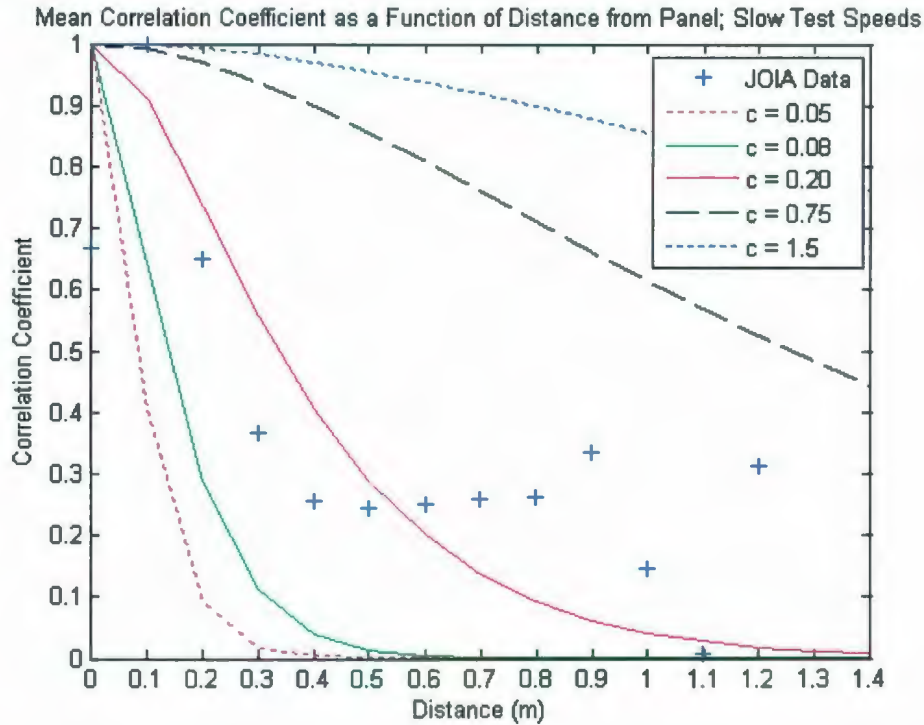


Figure 5.50: Plot of ρ vs. distance; autoregressive fit; slow event data (P2-P14).

The selected value of $c = 0.20$ was used in global load estimation, as discussed in the next chapter. To improve curve-fitting to the selected data, a composite approach was investigated as an alternate to the standard autoregressive approach. This is discussed later in the chapter.

5.7.7 Global Pressure Estimates (Standard Approach)

Upon completion of the correlation analysis, the next task was to estimate global pressure using the selected methods and compare these results with the measured global pressures. Global pressure estimates were determined using a number of analysis approaches and compared with the average measured values of global pressure (with and without end panels). For design, extreme pressures are of interest. In practice, the design value would be selected based on a target level of safety (for instance a design load corresponding to a probability of exceedence of 10^{-4}). For the present purpose, load estimates are based on

the mean plus three standard deviations to allow comparison of more representative design values.

Estimates based on the autoregressive method have been examined using several different approaches. These approaches are discussed below:

- Approach 1: $\mu_{L,i} + \sqrt{\gamma}(3\sigma_{L,i})$. In the first approach, the global pressure is estimated as the sum of the mean individual panel pressure plus three times the individual panel pressure standard deviation multiplied by the variation reduction factor. This method incorporates the autoregressive probabilistic averaging approach to estimate the global pressure based on data from a single panel. This approach is analogous to estimating Molikpaq global pressures based on a single Medof panel.
- Approach 2: $\mu_{L,i} + (3\sigma_{L,i})$. The second approach does not include a variation reduction factor in estimating the global pressure. This approach is simply the sum of the mean individual panel pressure and three times the standard deviation of individual panel pressure. This method is over conservative since it essentially assumes the standard deviation of the global pressure is equal to the standard deviation of the local design pressure. This approach does not account for the effects of averaging across the width of the structure.
- Approach 3: $\mu_{L,avgP1-P15} + \sqrt{\gamma}(3\sigma_{L,avgP1-P15})$. In the third approach, estimates of global pressure are calculated as the sum of the average of all mean panel pressures for the event (P1-P15) plus three times the average panel pressure standard deviation for the event (P1-P15) multiplied by the variation reduction factor. This method is similar to Approach 1, except averages of all the local panel means and standard deviations are used. This approach has been included as a logical check of the results to illustrate how the average estimation (including end panels) compares with the measured global pressure for the event.
- Approach 4: $\mu_{L,avgP2-P14} + \sqrt{\gamma}(3\sigma_{L,avgP2-P14})$. The fourth approach is the same as Approach 3, except the end panels have been excluded from the calculation of the mean and standard deviations. Similarly, this approach has been included as a

logical check of the results to illustrate how the average estimation (excluding end panels) compares with the measured global pressure for the event.

Results for a single representative event have been presented below for each speed range.

Fast Speed Range

The global pressure plot for sample event 2-1 is shown in Figures 5.51.

Subevent-2-1: Estimated Global Pressure (Probabilistic Averaging); Velocity: 3 cm/s; Thickness: 28.7 cm

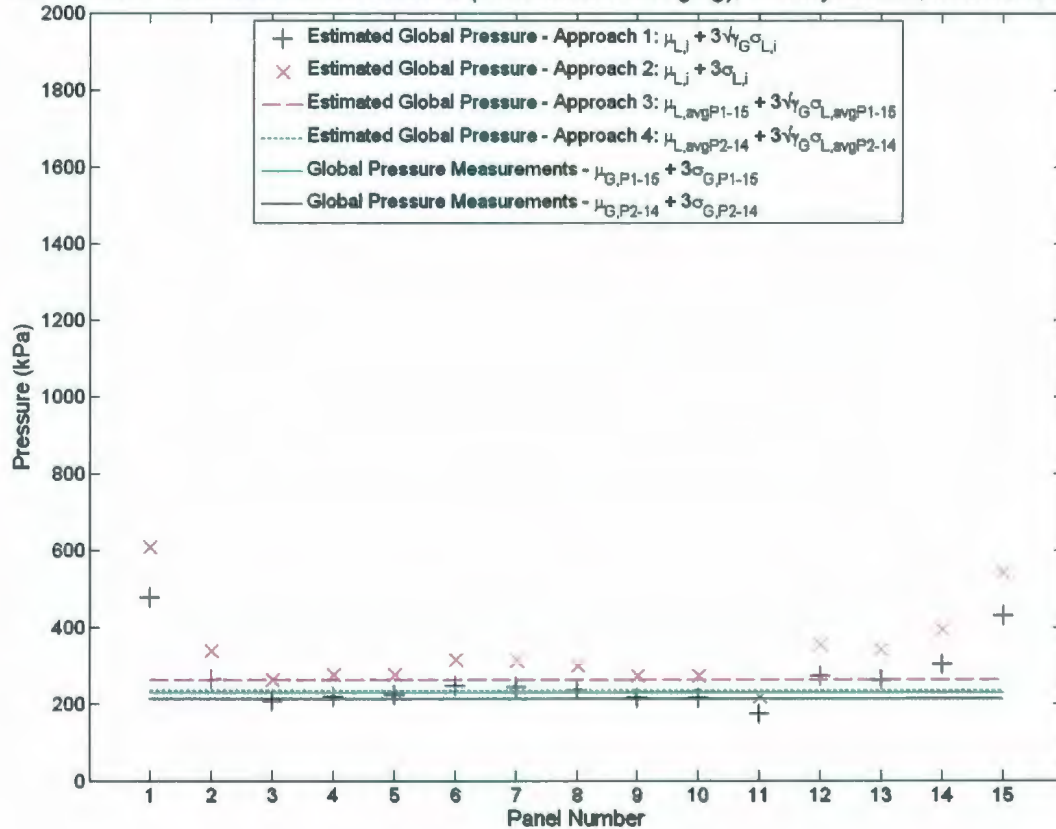


Figure 5.51: Global pressure estimates for event 2-1; $v = 3.0$ cm/s.

A number of important observations may be seen from this figure:

- Average measured global pressures are higher when end panels are included; excluding end panel data lowers the average measured global pressure.
- Estimates determined using the probabilistic averaging approach to calculate global pressure based on individual panels (i.e. Approach 1: $\mu_{L,i} + \sqrt{\gamma}(3\sigma_{L,i})$) are

closely grouped around the measured global pressure values. There is some scatter in these results, but this is expected due to natural variations in local pressures measured on any given panel. Estimates based on end panel data over predict measured global pressures by a large margin.

- Estimates based on Approach 2: $\mu_{L,i} + (3\sigma_{L,i})$, which does not account for probabilistic averaging effects, consistently produces global pressure estimates significantly higher than measured global pressures and higher than estimates found using Approach 1.
- Estimates determined using Approach 3: $\mu_{L,avgP1-P15} + \sqrt{\gamma}(3\sigma_{L,avgP1-P15})$, which includes end panel data, produces higher pressure estimates than those found using Approach 4: $\mu_{L,avgP2-P14} + \sqrt{\gamma}(3\sigma_{L,avgP2-P14})$, which does not include end panel data.
- Approach 3: $\mu_{L,avgP1-P15} + \sqrt{\gamma}(3\sigma_{L,avgP1-P15})$, which includes end panel data, generally produces estimates that are slightly higher than the corresponding measured global pressure (P1-P15). This suggests that on average there is still a slight conservatism in the probabilistic averaging approach.
- Approach 4: $\mu_{L,avgP2-P14} + \sqrt{\gamma}(3\sigma_{L,avgP2-P14})$, which does not include end panel data, produces estimates that are slightly higher than the corresponding measured global pressure (P2-P14). Similarly, this suggests that on average there is still a slight conservatism in the probabilistic averaging approach.

Medium Speed Range

The global pressure plot for sample event 1-1 is shown in Figures 5.52.

Subevent-1-1: Estimated Global Pressure (Probabilistic Averaging); Velocity: 0.3 cm/s; Thickness: 28.7 cm

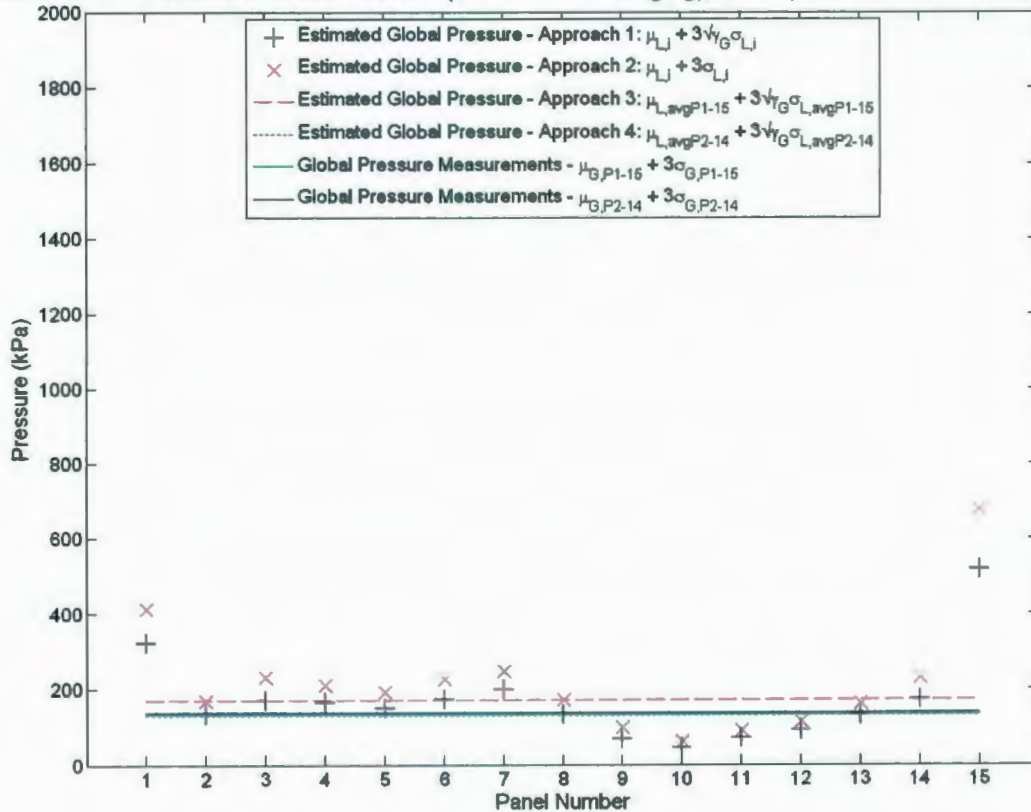


Figure 5.52: Global pressure estimates for event 1-1; $v = 0.30$ cm/s.

Similar observations may be seen from these figures as for the fast event:

- Average measured global pressures are higher when end panels are included.
- Estimates determined using Approach 1: $\mu_{L,i} + \sqrt{\gamma}(3\sigma_{L,i})$ are closely grouped around the measured global pressure values. Scatter due to natural variations in local pressures are observed as expected. Estimates based on end panel data over predict measured global pressures by a large margin.
- Estimates based on Approach 2: $\mu_{L,i} + (3\sigma_{L,i})$, which does not account for probabilistic averaging effects, consistently produces pressure estimates

significantly higher than measured global pressures and higher than estimates found using Approach 1.

- Estimates determined using Approach 3: $\mu_{L,avgP1-P15} + \sqrt{\gamma}(3\sigma_{L,avgP1-P15})$, which includes end panel data, produces higher pressure estimates than those which exclude end panel data, Approach 4: $\mu_{L,avgP2-P14} + \sqrt{\gamma}(3\sigma_{L,avgP2-P14})$.
- Approach 3: $\mu_{L,avgP1-P15} + \sqrt{\gamma}(3\sigma_{L,avgP1-P15})$, which includes end panel data, generally produces estimates that are slightly higher than the corresponding measured global pressure (P1-P15). This suggests that on average there is slight conservatism in the probabilistic averaging approach.
- Approach 4: $\mu_{L,avgP2-P14} + \sqrt{\gamma}(3\sigma_{L,avgP2-P14})$, which does not include end panel data, produces estimates that are slightly higher than the corresponding measured global pressure (P2-P14). This suggests that on average there is slight conservatism in the probabilistic averaging approach.

Slow Speed Range

The global pressure plot for sample event 3-1 is shown in Figures 5.53. The following observations may be made from this figure:

- Average measured global pressures are higher when end panels are included.
- Estimates determined using Approach 1: $\mu_{L,i} + \sqrt{\gamma}(3\sigma_{L,i})$ are grouped around the measured global pressure values. Scatter due to natural variations in local pressures were larger than those observed for fast and medium events. Estimates based on end panel data over predict measured global pressures by a large margin.
- Estimates based on Approach 2: $\mu_{L,i} + (3\sigma_{L,i})$, which does not account for probabilistic averaging effects, consistently produces pressure estimates significantly higher than measured global pressures and higher than estimates found using Approach 1.

- Estimates calculated using Approach 3: $\mu_{L,avgP1-P15} + \sqrt{\gamma}(3\sigma_{L,avgP1-P15})$, which includes end panel data, produces higher pressure estimates than those which exclude end panel data, Approach 4: $\mu_{L,avgP2-P14} + \sqrt{\gamma}(3\sigma_{L,avgP2-P14})$.
- Approach 3: $\mu_{L,avgP1-P15} + \sqrt{\gamma}(3\sigma_{L,avgP1-P15})$, which includes end panel data, generally produces estimates that are higher than the corresponding measured global pressure (P1-P15), though for subevent 8-1 the estimated global pressure was lower than the measured global pressure, as shown in Figure 5.53.
- Approach 4: $\mu_{L,avgP2-P14} + \sqrt{\gamma}(3\sigma_{L,avgP2-P14})$, which does not include end panel data, generally produces estimates that are slightly higher than the corresponding measured global pressure (P2-P14), though for subevent 8-1 the estimated global pressure was lower than the measured global pressure, as shown in Figure 5.53.

Subevent-3-1: Estimated Global Pressure (Probabilistic Averaging); Velocity: 0.03 cm/s; Thickness: 28.7 cm

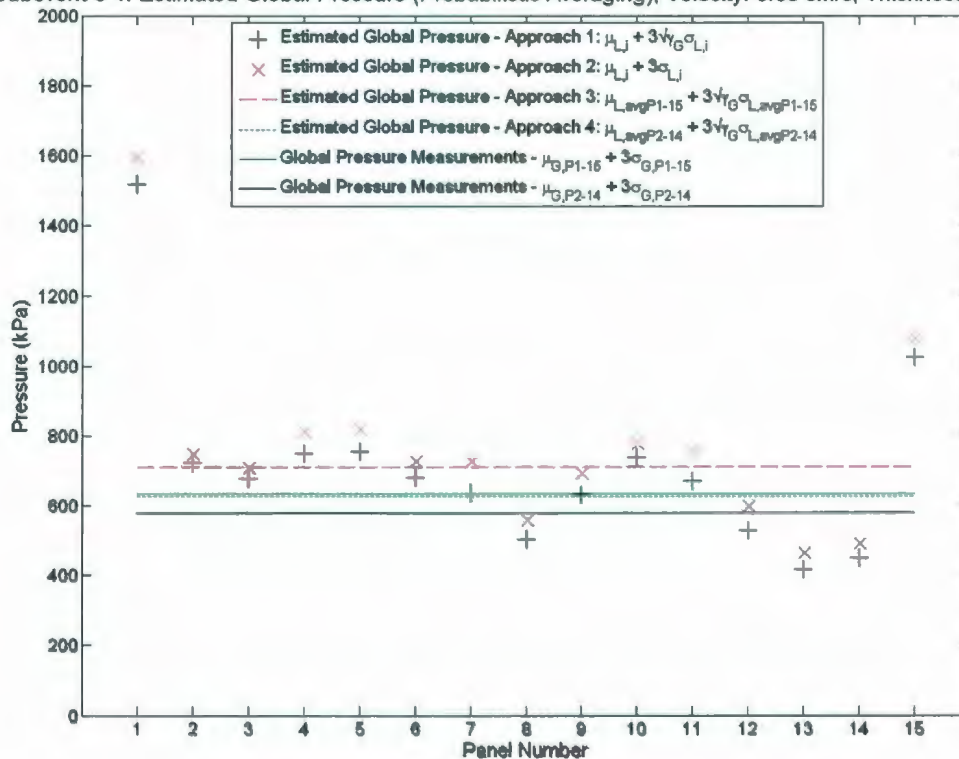


Figure 5.53: Global pressure estimates for event 3-1; $v = 0.03$ cm/s.

To assess the effectiveness of each global load estimation approach, the percent error between the estimated and measured pressures were calculated for all events. The events were grouped according to speed range and the mean, maximum and minimum of all panels for all events in the selected speed range were calculated. The average means, maximums and minimums for each speed range were calculated as shown in Table 5.7 below. For these calculations the measured global pressure used corresponds to panels P2-P14 (i.e. no end panels).

Table 5.7: Percent error in global pressure estimates (autoregressive) compared with measured global pressure.

		Approach 1 (Prob Avg)	Approach 2 (No Prob Avg)	Approach 3 (Prob Avg; P1-15)	Approach 4 (Prob Avg; P2-14)
Slow (Ductile)	Mean Estimation Error	0%	12%	13%	0%
	Max Estimation Error	76%	89%	30%	8%
	Min Estimation Error	-54%	-47%	1%	-10%
Medium (Brittle)	Mean Estimation Error	12%	44%	33%	12%
	Max Estimation Error	122%	196%	58%	28%
	Min Estimation Error	-67%	-55%	7%	-4%
Fast (Brittle)	Mean Estimation Error	10%	42%	10%	10%
	Max Estimation Error	73%	125%	31%	23%
	Min Estimation Error	-37%	-18%	4%	1%

As may be observed from Table 5.7, the probabilistic averaging method works well for estimating global pressures. Approach 2, which did not account for probabilistic averaging, typically overestimated the measured global pressure by a significant margin. By comparison Approach 1, which is based on the probabilistic averaging methodology, had a considerably smaller mean estimation error. Based on these results it may be concluded that in general, probabilistic averaging approach produces a better estimate of measured global pressure than the approach without probabilistic averaging.

To explore potential ways to further improve global pressure estimation the use of a composite correlation model was implemented.

5.7.8 Correlation Modeling (Composite Approach)

For the second-order autoregressive model used above, it was assumed that correlation coefficient data would take the same form as the exponential expression in Equation 4.14. The composite correlation approach used below has been implemented as a potential way to extend the flexibility of the probabilistic averaging method for cases where the correlation data does not strictly adhere to the exponential form.

Composite Correlation Autoregressive Methodology

For correlation data that are not well modeled by the 'standard' method used above, Vanmarcke (1983) developed a composite correlation function which is a weighted, linear combination of correlation coefficients. For the present work, only two weighted terms have been used (hereafter referred to as the 'composite' approach). The correlation function given by this method may be written as:

$$\rho(\tau) = \sum_i q_i \rho_i(\tau) = q_1 \rho_1(\tau) + q_2 \rho_2(\tau), \quad (5.1)$$

where q is a weighting factor corresponding to each of the correlations functions, ρ . The correlation coefficients ρ_1 and ρ_2 may be based on any correlation function; for this analysis the autoregressive function described in Equation 4.14 was used. In implementing the composite approach, values of ρ_1 and ρ_2 are selected through appropriate choice of corresponding characteristic correlation lengths, c_1 and c_2 . Values of q_1 and q_2 are based on appropriate weighting required to fit the curve to correlation data. For preliminary evaluation purposes, a trial and error curve fitting approach has been used to determine values of c_1 , c_2 , q_1 , and q_2 . Future efforts to improve curve-fitting methodology may be beneficial.

The composite approach is applied to the variation reduction equation through the expression:

$$\gamma(T) = \sum_i q_i \gamma_i(T) = q_1 \gamma_1(T) + q_2 \gamma_2(T), \quad (5.2)$$



where the weighting factors q_1 and q_2 are determined from correlation fitting associated with Equation 4.14 and the variation reduction values γ_1 and γ_2 are determined by evaluating Equation 4.17 with values c_1 and c_2 respectively.

Characteristic Correlation Length Analysis Results

Plots of composite correlation curves fitted to the data are shown in Figures 5.54, 5.55, and 5.56 for the fast, medium and slow data respectively. From the figures below it may be seen that the composite approach better models the data than does the standard autoregressive method. The values of c_1 , c_2 , q_1 and q_2 selected for each event have been plotted on each figure. Further exploration of the composite approach in terms of its effects on load estimation is recommended.

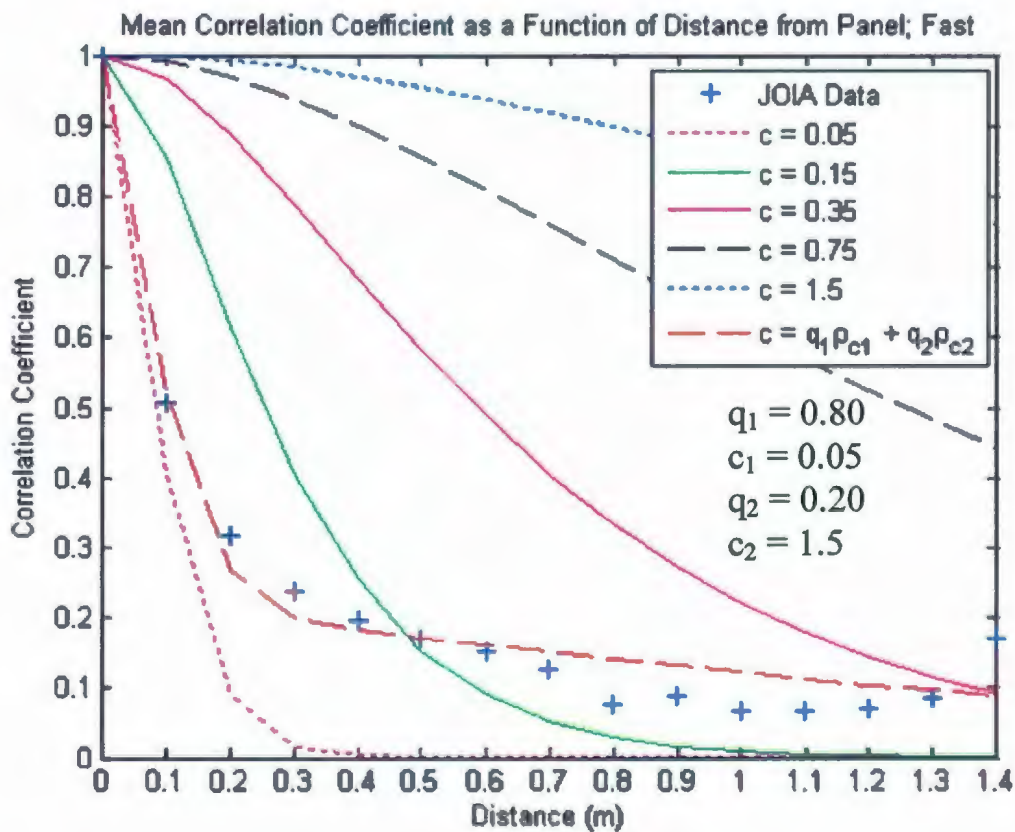


Figure 5.54: Plot of ρ vs. distance; composite fit; fast event data (P2-P14).

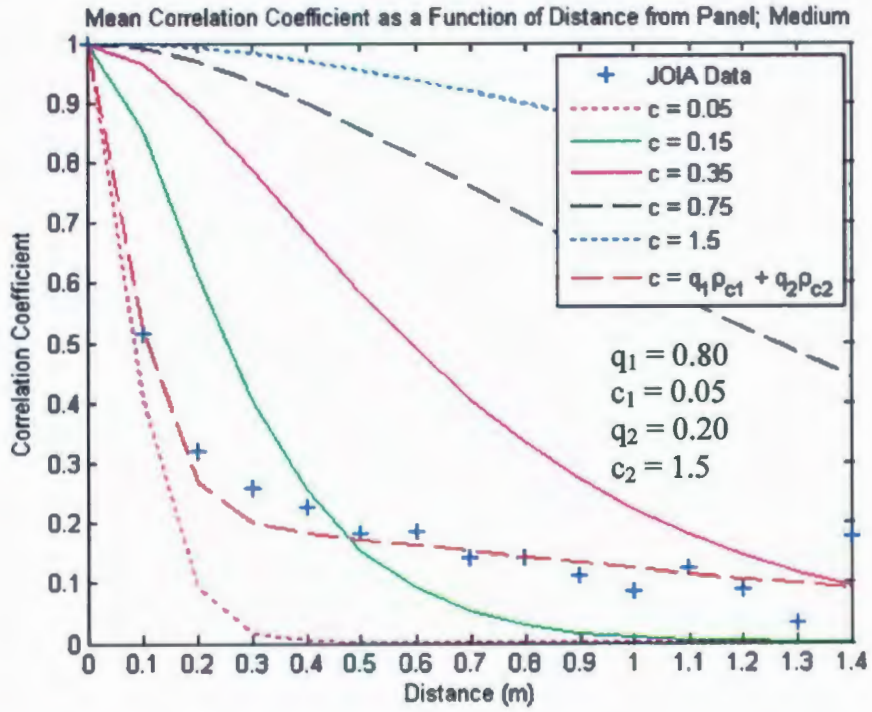


Figure 5.55: Plot of ρ vs. distance; composite fit; medium event data (P2-P14).

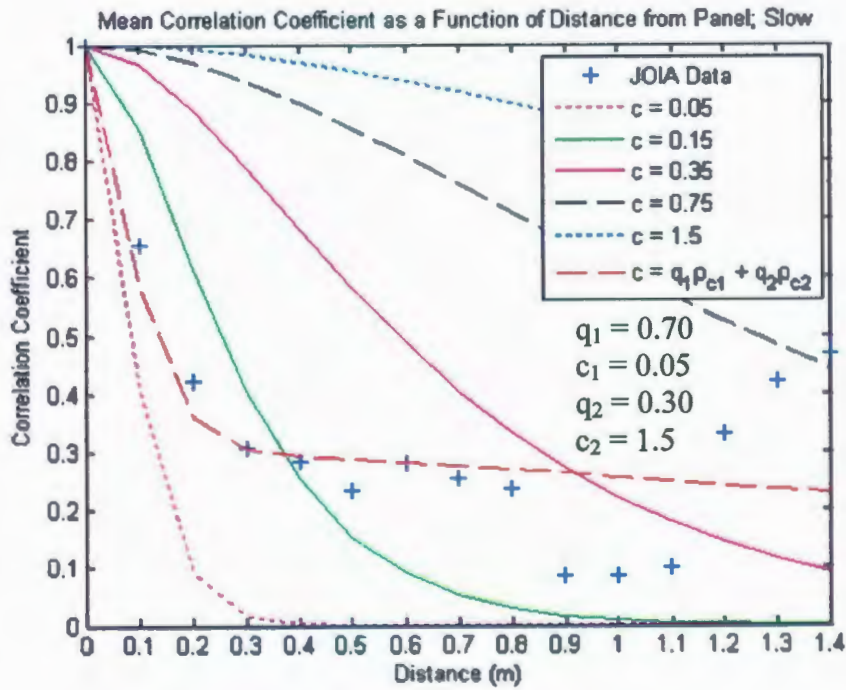


Figure 5.56: Plot of ρ vs. distance; composite fit; slow event data (P2-P14).

Global load estimates based on the composite approach were generated to assess the effects of this alternate correlation modeling approach on load estimation.

5.7.9 Global Pressure Estimates (Composite Approach)

To evaluate the composite approach, a selected sample event from each of the speed ranges was analyzed. As with the standard autoregressive approach, four different global load estimation approaches were considered for comparative purposes:

- Approach 1: $\mu_{L,i} + \sqrt{\gamma}(3\sigma_{L,i})$
- Approach 2: $\mu_{L,i} + (3\sigma_{L,i})$
- Approach 3: $\mu_{L,avgP1-P15} + \sqrt{\gamma}(3\sigma_{L,avgP1-P15})$
- Approach 4: $\mu_{L,avgP2-P14} + \sqrt{\gamma}(3\sigma_{L,avgP2-P14})$

The key difference here is that the variance reduction factors were based on the composite formulation. The global pressures estimates corresponding to each of the sample events are plotted in Figures 5.57, 5.58, and 5.59 for the fast, medium and slow events respectively.

The following general observations may be seen from these figures:

- Average measured global pressures are higher when end panels are included.
- Estimates determined using Approach 1: $\mu_{L,i} + \sqrt{\gamma}(3\sigma_{L,i})$ are grouped around the measured global pressure values. Scatter due to natural variations in local pressures are observed for all events; scatter appears to be somewhat larger for the slower event than for fast and medium events. Estimates based on end panel data generally over predict measured global pressures by a significant margin.
- Approach 2: $\mu_{L,i} + (3\sigma_{L,i})$, which does not account for probabilistic averaging effects, consistently produces pressure estimates significantly higher than measured global pressures and higher than estimates found using Approach 1.

- Approach 3: $\mu_{L,avgP1-P15} + \sqrt{\gamma}(3\sigma_{L,avgP1-P15})$, which includes end panel data, produces higher pressure estimates than Approach 4: $\mu_{L,avgP2-P14} + \sqrt{\gamma}(3\sigma_{L,avgP2-P14})$, which exclude end panel data.
- Approach 3: $\mu_{L,avgP1-P15} + \sqrt{\gamma}(3\sigma_{L,avgP1-P15})$, generally produces estimates that are higher than the corresponding measured global pressure (P1-P15).
- Approach 4: $\mu_{L,avgP2-P14} + \sqrt{\gamma}(3\sigma_{L,avgP2-P14})$, which does not include end panel data, produces estimates that are slightly higher than the corresponding measured global pressure (P2-P14).

Subevent-2-1: Estimated Global Pressure (Probabilistic Averaging); Velocity: 3 cm/s; Thickness: 28.7 cm

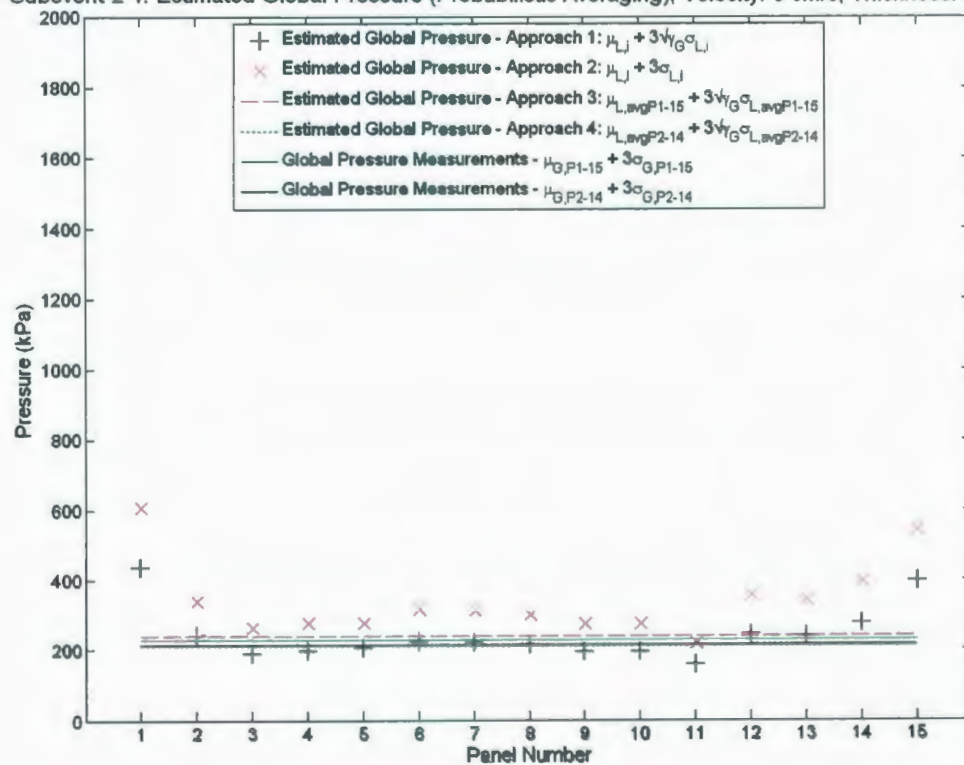


Figure 5.57: Global pressure estimates for event 2-1 (composite approach).

Subevent-10-1: Estimated Global Pressure (Probabilistic Averaging); Velocity: 0.3 cm/s; Thickness: 28.4 cm

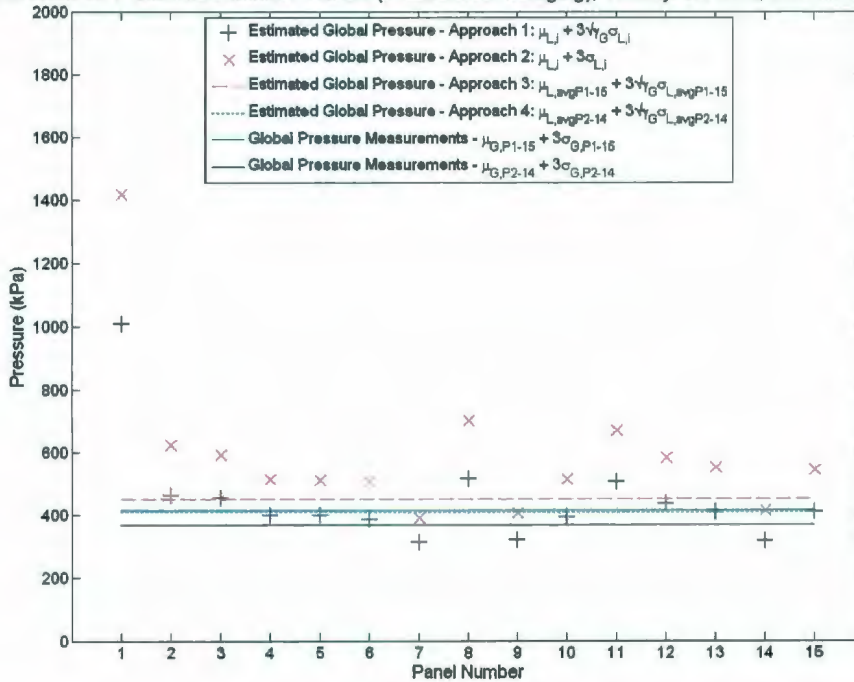


Figure 5.58: Global pressure estimates for event 10-1 (composite approach).

Subevent-3-1: Estimated Global Pressure (Probabilistic Averaging); Velocity: 0.03 cm/s; Thickness: 28.7 cm

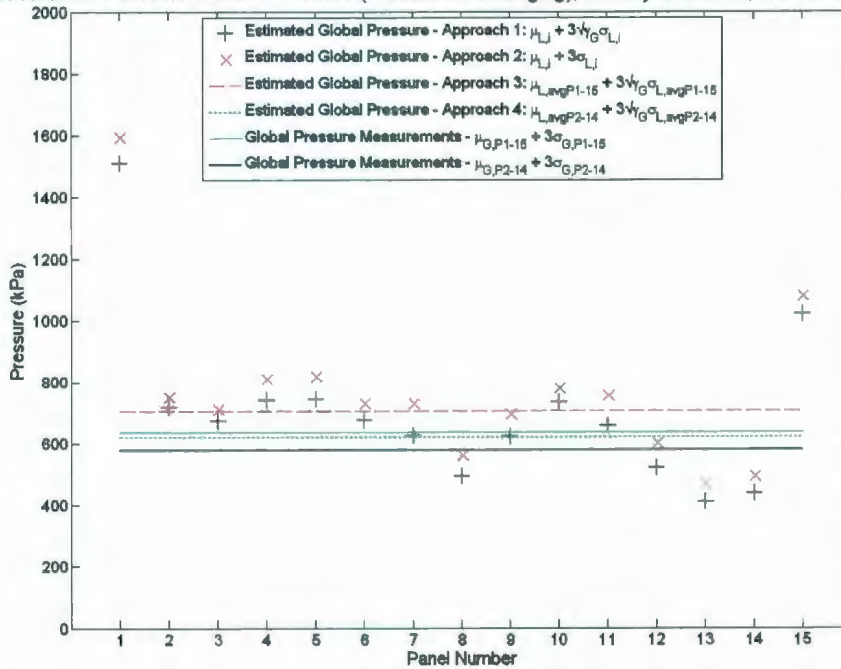


Figure 5.59: Global pressure estimates for event 3-1 (composite approach).

As with the analysis based on the standard correlation model, the percent error between the estimated and measured pressures were calculated for all events. The events were grouped according to speed range and the mean, maximum and minimum of all panels for all events in the selected speed range were calculated. The average means, maximums and minimums for each speed range were calculated as shown in Table 5.8 below. For these calculations the measured global pressure used corresponds to panels P2-P14 (i.e. no end panels).

Table 5.8: Percent error in global pressure estimates (composite) compared with measured global pressure (based on P2-P14)

		Approach 1 (Prob Avg)	Approach 2 (No Prob Avg)	Approach 3 (Prob Avg: P1-15)	Approach 4 (Prob Avg: P2-14)
Slow (Ductile)	Mean Estimation Error	-2%	12%	11%	-2%
	Max Estimation Error	75%	89%	29%	7%
	Min Estimation Error	-55%	-47%	-2%	-12%
Medium (Brittle)	Mean Estimation Error	2%	44%	21%	2%
	Max Estimation Error	97%	196%	43%	15%
	Min Estimation Error	-71%	-55%	-2%	-13%
Fast (Brittle)	Mean Estimation Error	0%	42%	0%	0%
	Max Estimation Error	56%	125%	18%	11%
	Min Estimation Error	-43%	-18%	-5%	-7%

As may be observed, the probabilistic averaging method on average produced more accurate global pressure estimates than were obtained using Approach 2, which did not account for probabilistic averaging. Approach 2 typically overestimated the measured global pressure by a significant margin. As with the previous analysis, it may be concluded that in general, the probabilistic averaging approach produces better estimates of the measured global pressure than the approach without probabilistic averaging.

5.7.10 Comparison of Global Pressure Estimation Approaches

Three different formulations for estimating global pressures based on local panel pressure data have been compared below. These include: probabilistic averaging (autoregressive); probabilistic averaging (composite); direct extrapolation with no probabilistic averaging. Mean, max and minimum estimation error for the probabilistic averaging approach based on both autoregressive and composite fitting, as well as for the estimates produced without probabilistic averaging are summarized in Table 5.9.

Table 5.9: Percent error for different global pressure estimation approaches

		Approach 1: (Prob Avg) Autoregressive	Approach 1: (Prob Avg) Bilinear	Approach 2: (No Prob Avg)
Slow (Ductile)	Mean Estimation Error	0%	-2%	12%
	Max Estimation Error	76%	75%	89%
	Min Estimation Error	-54%	-55%	-47%
Medium (Brittle)	Mean Estimation Error	12%	2%	44%
	Max Estimation Error	122%	97%	196%
	Min Estimation Error	-67%	-71%	-55%
Fast (Brittle)	Mean Estimation Error	10%	0%	42%
	Max Estimation Error	73%	56%	125%
	Min Estimation Error	-37%	-43%	-18%

Based on the above results, it may be concluded that including probabilistic averaging in global pressure estimation significantly reduces the mean estimation error. On average, Approach 2, which does not account for probabilistic averaging, significantly overestimated the measured global load. For the probabilistic averaging analysis, results obtained using the composite approach had lower mean estimation errors than those obtained with the standard autoregressive approach. Results suggest that the probabilistic averaging method offers clear advantages and further improvement may be possible through use of a composite approach. Further work is recommended to more fully explore the details of the composite approach prior to implementation of the method in global load estimation.

5.8 Full-scale Data Analysis

5.8.1 Global Load Estimation Using Molikpaq Data

Ice load measurements on the Molikpaq, Amauligak I-65 deployment represent an important set of full-scale data for use in the estimation of global ice loads. Significant discrepancies exist within the literature regarding ice loads estimated from the Medof panels. Jordaan et al. (2006) apply probabilistic averaging in analyzing the Medof panel data, taking into account the fact that only a portion of the structure was instrumented. This approach estimates a global pressure standard deviation that is appropriate for

extrapolation to determine face loads. In modeling, an ice-structure interaction event has been treated as a stationary, random averaging process.

The Medof data has many fluctuations due to fractures, splits, and variations in ice thickness. If these aspects were quantified it would be possible to develop models to account for these effects. Since there is no basis to develop physical reasoning to explain the non-stationarity, it is idle to state that there is a non-stationary process as it cannot be properly modeled. Load fluctuations during ice-structure interaction rather are considered as background random events within a stationary process. For the given time intervals, the process is therefore treated as stationary.

Jordaan et al. (2006), statistical averaging significantly reduces the variance of global pressure. This indicates that the use of measurements based on Medof panels without accounting for probabilistic averaging will result in overestimates of the global pressure. This observation was confirmed with the JOIA data.

An important difference between the JOIA and Molikpaq data results from the scale of the structure, which has important implications in how data are interpreted. Further discussion of these differences is presented below.

5.8.2 Discussion of Scale Issues: JOIA vs. Molikpaq Scale

In terms of correlation results for the Molikpaq and JOIA data, a number of factors needed to be considered for each of these datasets. The mechanics of the stress field are different at large scale. Large-scale fracture would be more important at the Molikpaq scale, since an ice-structure interaction would result in a much larger stressed volume of ice and correspondingly exposure to a larger field of flaws. Probabilistic averaging effects would also be more dominant for a large structure, since localized events are averaged over a larger width resulting in decreased global variance. Ice thicknesses for the Molikpaq data (approximately 1.25 m) are significantly thicker than for the JOIA data (approximately 0.3 m). Since it has been assumed that *hpz* size scales with ice thickness, and *hpz* behavior influences pressure correlation, the thickness of the ice may also influence correlation behavior. In addition, the JOIA tests were conducted over an

average exposure distance (stroke) of approximately 35 cm, compared with much larger exposure distances for Molikpaq events. Further investigation of the effects of duration on correlation at various scales is recommended.

To aid in the discussion of scale issues, a sample Molikpaq event is discussed below. The selected event is a mixed crushing and creep event with extrusion; this event was recorded on March 8, 1986. Data for this event were recorded by Medof panels, which were configured as illustrated in Figure 5.60 below.

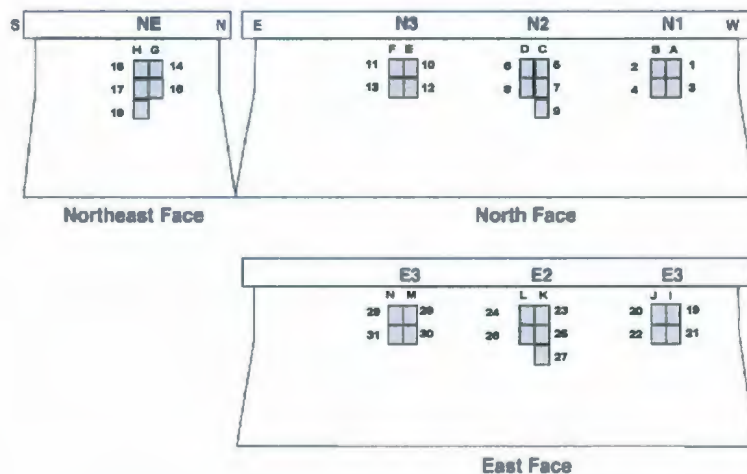


Figure 5.60: Molikpaq Medof panel configurations.

During an ice loading event on the Molikpaq, partial loading of the face of the structure commonly occurred. As shown in Figure 5.61, under such conditions global loads continuously act on the structure, yet local panels are only loaded intermittently. During the JOIA tests, all local panels are continuously loaded during a global event. The intermittent nature of local loading on the Molikpaq is illustrated in Figure 5.61 (a).

If correlations between columns of Molikpaq panels are analyzed for the entire global event, the analysis is dominated by two distinct local loading scenarios. The first consists of periods of time having near zero loads; during the second period of time, both columns are loaded to higher pressures. As illustrated in Figure 5.61 (b), correlation analysis results are influenced by the fact that the data are clustered into a low pressure grouping and a high pressure grouping. Analysis results indicate a high correlation coefficient

(approximately 0.79) between Columns E and F during the global event. Correlation information obtained in this manner does not necessarily reflect the correlation of the columns during a local loading event. Rather this suggests that during a global event, if Column E is experiencing a period of relatively high pressure, Column F will likely experience a period of high pressure. This is distinctly different from the loading conditions in the JOIA experiments.

For the JOIA tests considered, all local panels are loaded during a global event. When calculating correlation between two panels in this way, the presumption is that both local panels are always active. In the context of the Molikpaq data, a comparable correlation analysis would only focus on local 'subevents' where both columns of panels are active, as is illustrated in Figure 5.61 (a).

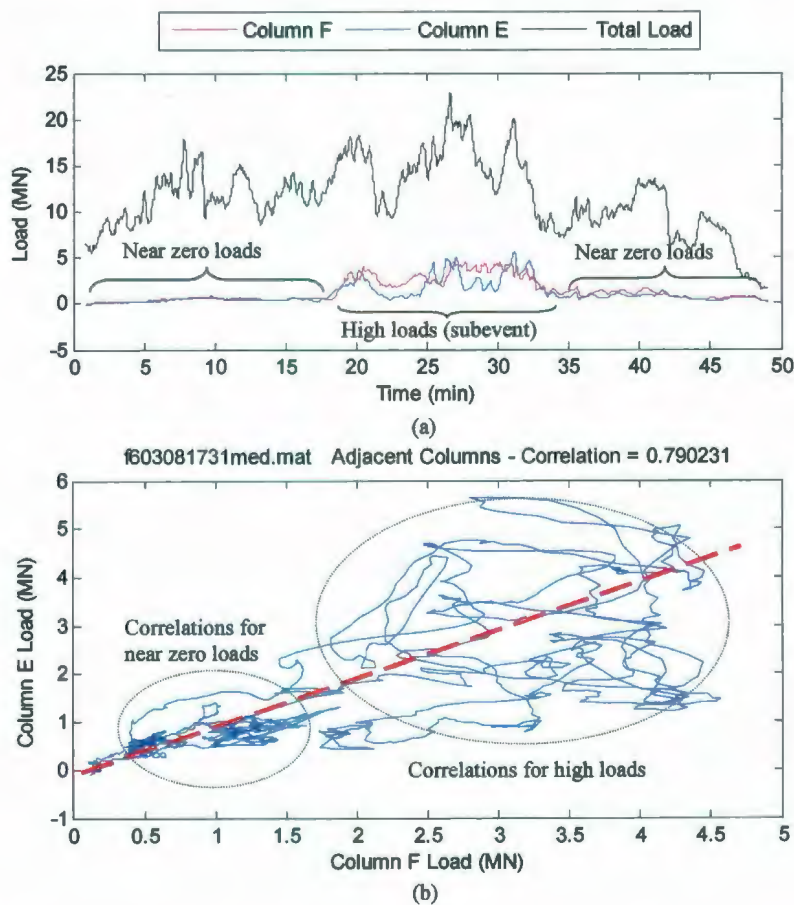


Figure 5.61: Molikpaq sample event: (a) global and local load traces; (b) comparative plot of column data illustrating apparent correlation.

Analysis of the Molikpaq local subevent yields quite different correlation results than analysis of the global event. As shown in Figure 5.62, if focus is placed on the active subevent region, the correlations coefficient is approximately -0.071 , compared with approximately 0.79 for the entire global event.

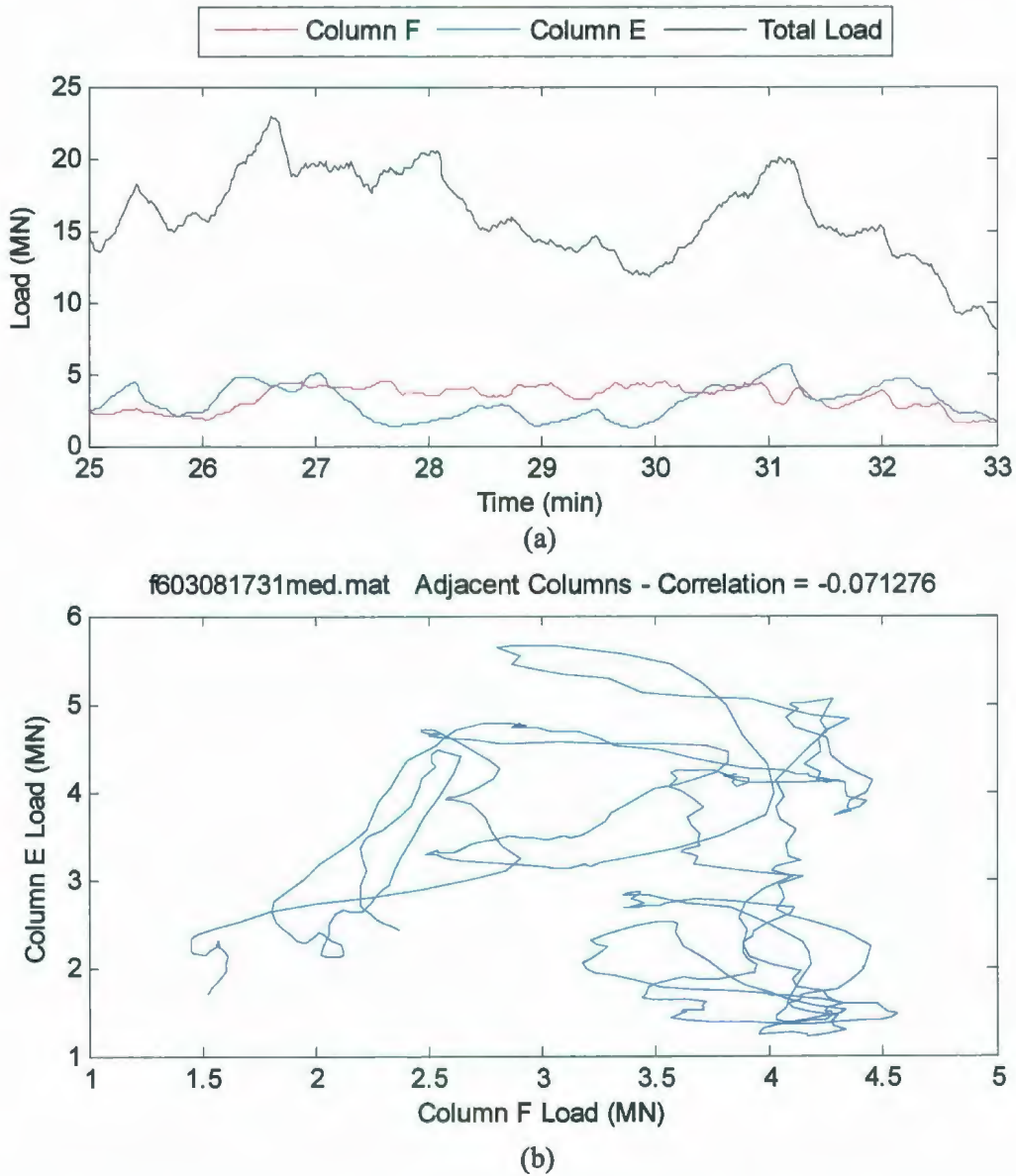


Figure 5.62: Molikpaq local subevent: (a) global and local load traces; (b) comparative plot of column data illustrating local correlation.

To compare properly Molikpaq and JOIA data, it would first be necessary to sift through the Molikpaq data to identify and analyze local subevents. While a detailed reanalysis of Molikpaq data is beyond the scope of the present work, an initial comparison of the Molikpaq and JOIA datasets is considered below. Detailed comparison of the correlation data between the JOIA, Molikpaq and STRICE datasets represents an important direction for future work.

5.8.3 Molikpaq Correlation Analysis (Standard)

First-year ice events for the 1986 Molikpaq, Amauligak I-65 deployment were sorted into fast and slow groups corresponding to speeds greater than and less than 0.05 m/s respectively. As illustrated in Figure 5.60, Medof panels were vertically clustered into columns of two or three panels. For this preliminary analysis it has been assumed that the middle row of panels provides representative estimates of correlations between pairs of panels (or columns). Only data for the middle panels have been included in this analysis. The time traces for these data were inspected and an initial attempt was made to identify and isolate local loading subevents from each global event. Correlations between pairs of panels have only been examined for panels from the same face. Analysis was based on panels 3, 4, 7, 8, 12 and 13 for the North face, panels 16 and 17 for the Northeast face and panels 21, 22, 25, 26, 30 and 31 for the East face.

Correlations were determined for selected pair combinations and tabulated as a function of spacing between panel pairs. Since the Medof panels only covered approximately 10% of the width of the faces and were located at fixed positions, correlation information is available only for distance intervals corresponding to spacing between panel pairs. Correlation data for all slow and fast events were grouped according to distance. Average correlation values corresponding to each interval were calculated for both speed ranges. These average correlation values were plotted as a function of distance, along with JOIA data from the corresponding speed category. These plots are shown in Figures 5.63 and 5.64 for fast and slow speeds respectively.

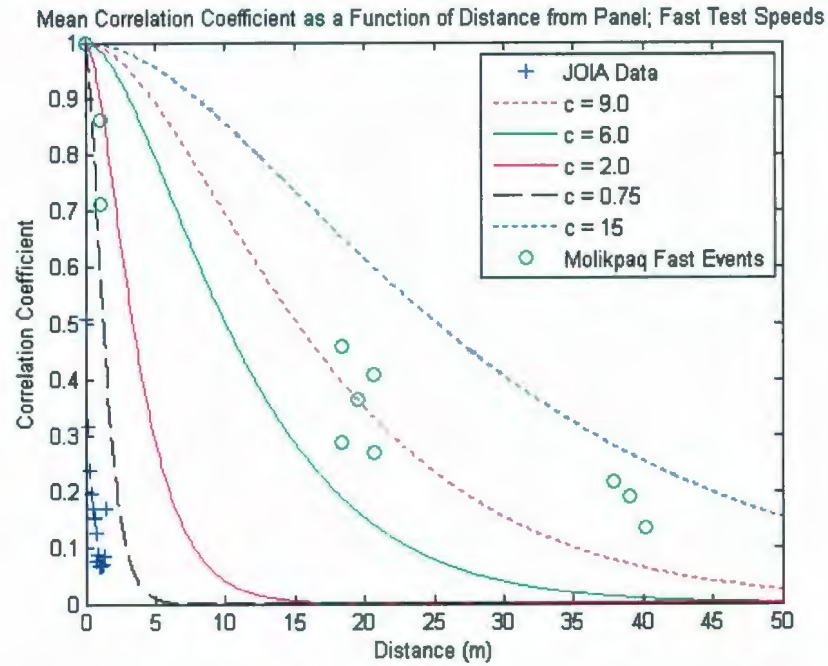


Figure 5.63: Comparison of JOIA and Molikpaq correlations: fast events (autoregressive).

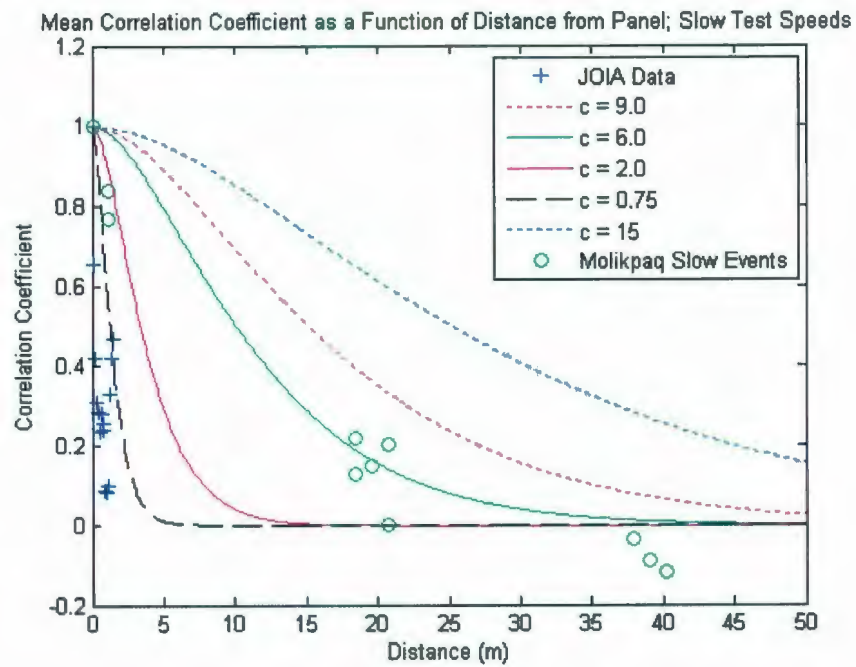


Figure 5.64: Comparison of JOIA and Molikpaq correlations: slow events (autoregressive).

Significant differences in correlation as a function of distance exist between Molikpaq and JOIA datasets; further investigation into the causes of these differences is needed.

5.8.4 Molikpaq Correlation Analysis (Composite)

To investigate the suitability of using the composite approach to model the Molikpaq correlations, composite fits to correlation data were plotted in Figures 5.65 and 5.66 for fast and slow events, respectively.

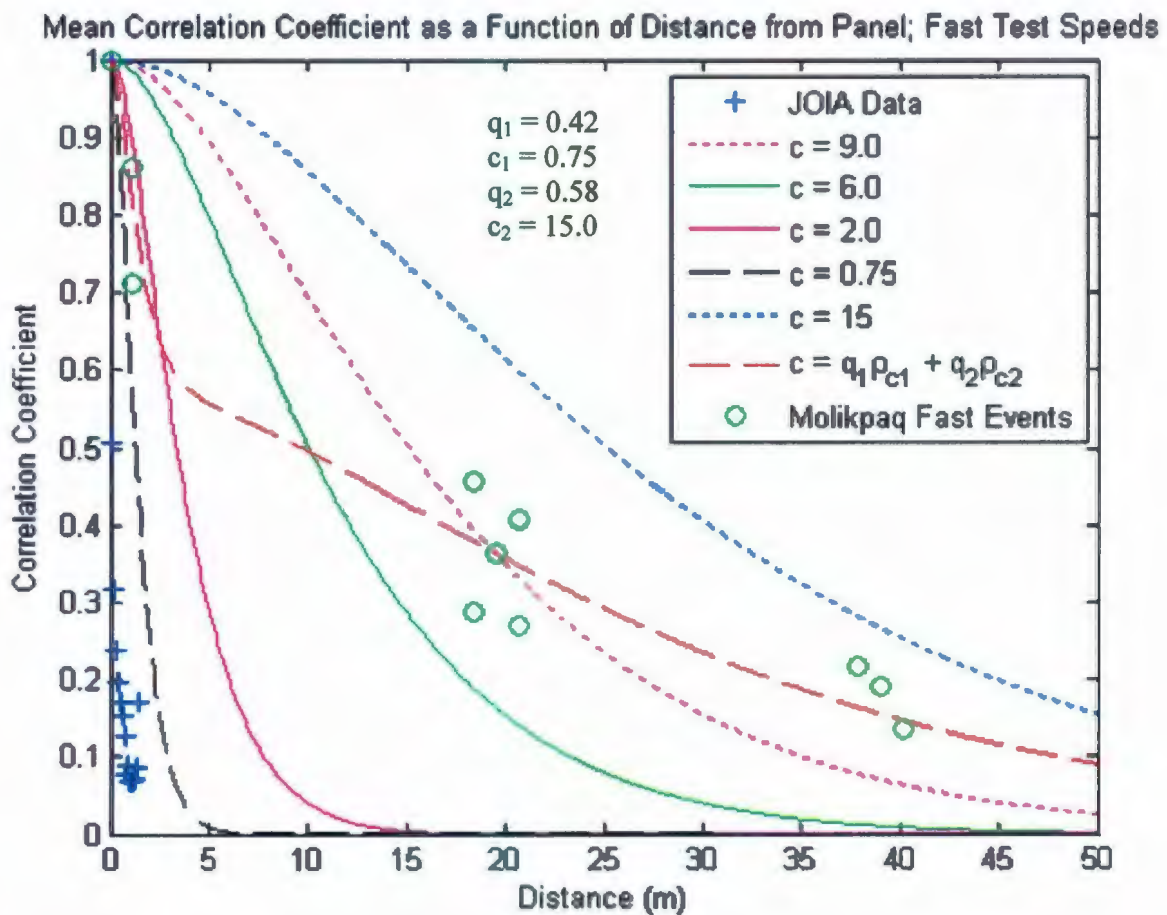


Figure 5.65: Comparison of JOIA and Molikpaq correlations: fast events (composite).

As may be observed from the above figure, the composite approach demonstrates better capabilities in model the correlation data for the Molikpaq.

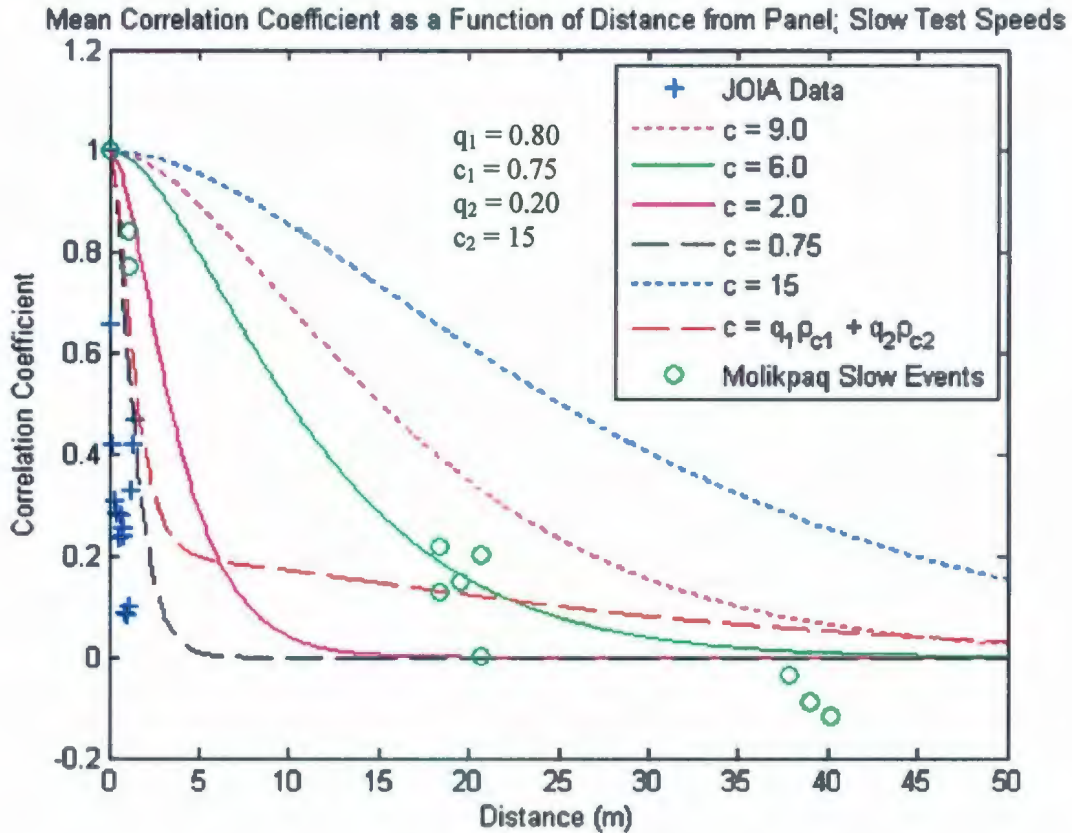


Figure 5.66: Comparison of JOIA and Molikpaq correlations: slow events (composite).

Similarly, the composite approach provided more flexibility in modeling the correlation data for the slow event data. Further analysis of the relationship between JOIA and Molikpaq results is recommended. As a preliminary investigation of possible factors influencing scaling, the dependency of results on ice thickness was examined.

5.8.5 Correlation Scaling: Preliminary Investigation

As an initial attempt to investigate scaling associated with correlation data for the Molikpaq and JOIA data, the correlation was assumed to scale with thickness. Since it is assumed that $hpzs$ scale with thickness, it follows that the distance over which averaging takes place should also be a function of thickness.

In light of these implications, the lag distance τ in Eq. 4.14 should be normalized by thickness h to give a lag ratio instead of lag distance. Normalizing the lag distance by thickness yields the expression:

$$\rho(t) = \left[1 + \frac{|\tau/h|}{c'} \right] e^{-|\tau/h|/c'}, \quad (5.3)$$

where c' is a dimensionless parameter that is characteristic of the process. Normalizing the correlation distance by the ice thickness gave the results presented in Figures 5.67 and 5.68 for fast and slow events respectively.

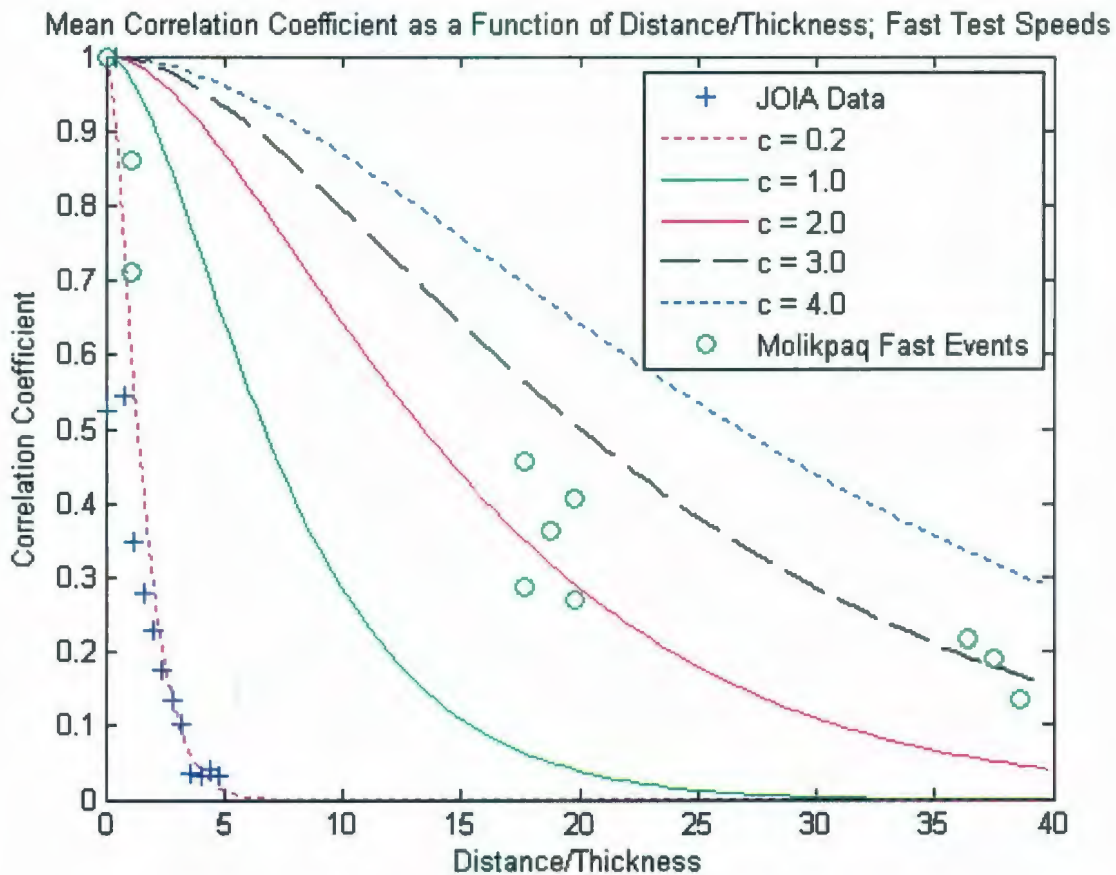


Figure 5.67: Comparison of JOIA and Molikpaq correlations: fast events (non-dimensionalized by thickness).

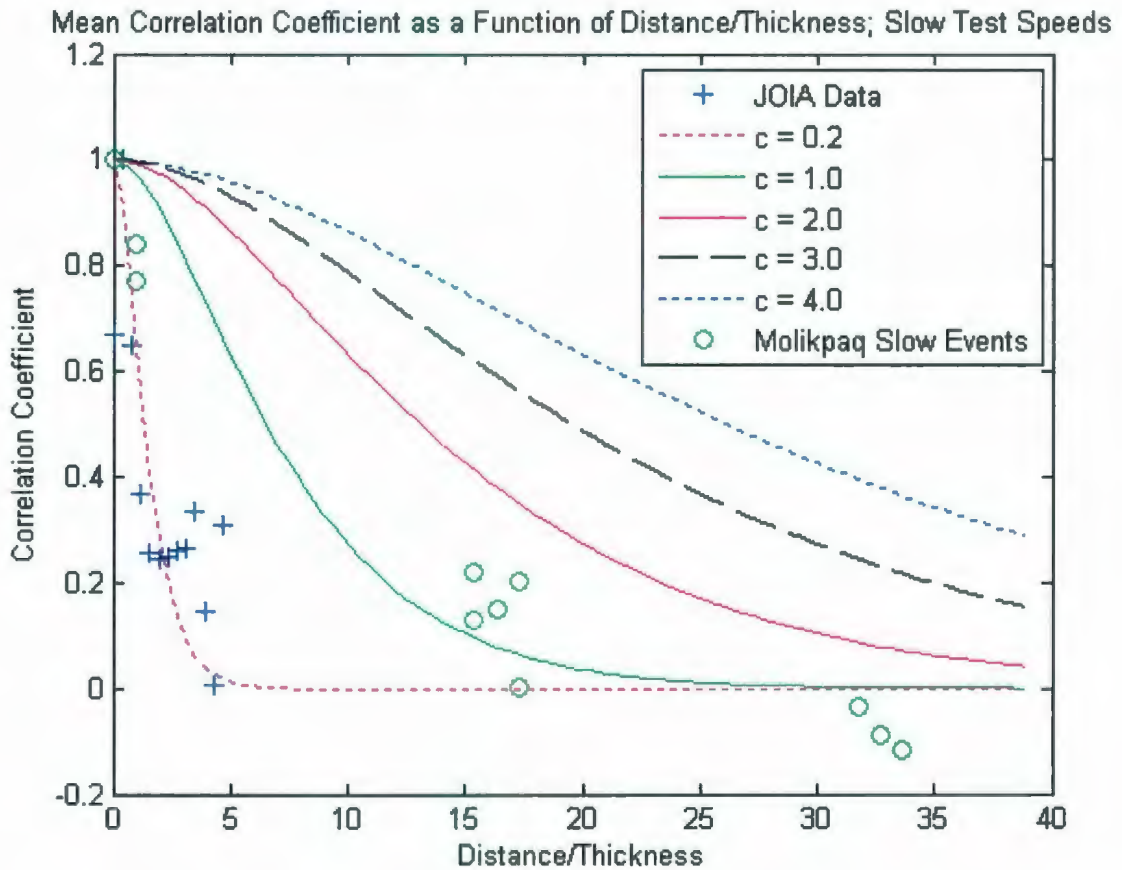


Figure 5.68: Comparison of JOIA and Molikpaq correlations: slow events (non-dimensionalized by thickness).

As may be observed above, non-dimensionalizing by thickness does reduce the discrepancies between the datasets, but does not fully explain the differences. Further work is required to more completely explore details of correlations in Molikpaq data and to more fully relate JOIA and Molikpaq results.

5.8.6 Discussion of Results

Failure behavior in evidence in JOIA pressure data was reflective of first-year ice behavior reported in the literature. From the segmented panel data edge effects were observed for the end panels, P1 and P15. Results were compared for cases that included and excluded the end panels. In general, pressure results obtained for the analysis cases excluding the end panels (i.e. for panels P2-P14) yielded the most appropriate results. Since these edge effects would not be expected a larger scales, end panels should not be included in JOIA data analyzed to compare with full-scale data (i.e. Molikpaq).

Ice mechanics show that the failure mode of ice changes with speed; this is clearly reflected in the data. Non-simultaneous aspects of failure were observed for all events considered, though it was more dominant for higher speed tests. From the JOIA data, it was observed that the measured global standard deviation was lower than the local pressure standard deviations, particularly for higher speeds where non-simultaneous aspect of failure are more dominant. This suggests that probabilistic averaging processes are present at the scale of the JOIA tests. On this basis, it may be concluded that in general, the same probabilistic averaging principles apply to the JOIA data as to the Molikpaq data. For full-scale structures, the variation reduction associated with probabilistic averaging is more significant than for the scale of the JOIA tests, due to the much larger width of a full-scale structure over which averaging would take place.

Correlations of JOIA panel data were examined, with emphasis on modeling the correlations using the autoregressive correlation function. In general it was observed that correlations were found to be lower for higher speeds due to increased randomness associated with non-simultaneous failure. Similarly, lower speed tests had higher correlations due to the more uniform nature of the ductile failure processes present in that speed range. Correlation as a function of distance was explored for the JOIA data. Based on comparison of correlation curves and correlation data, a constant value of characteristic correlation length ($c = 0.20$ m) was chosen for analysis using the autoregressive method. Composite fitting was explored as an alternative approach to improve correlation modeling. Both approaches were used in the estimation of global pressures.

Estimates of global pressure using local pressure data were determined using a number of approaches. Results were obtained using an autoregressive probabilistic averaging approach, a composite probabilistic averaging approach and an approach based on linear extrapolation of local panel data (which did not account for probabilistic averaging). Estimates were produced using each method and compared with measured global pressure data for the indenter.

Event averaged mean error between measured and estimated global loads for the three speed ranges considered have been summarized in Table 5.10. These results indicate that on average, the autoregressive method offered substantially less estimation error than the linear extrapolation (no probabilistic averaging) approach.

Table 5.10: Event averaged mean estimation error for various estimation approaches

	No Probabilistic Averaging	Probabilistic Averaging (Autoregressive)	Probabilistic Averaging (Bilinear)
Slow (Ductile)	12%	0%	-2%
Medium (Brittle)	44%	12%	2%
Fast (Brittle)	42%	10%	0%

For brittle failure, simple averaging (no probabilistic averaging) resulted in an average overestimation of about 40%. The composite approach exhibited potential to improve the estimation capabilities of the probabilistic averaging method. Further work to explore details of the composite approach has been recommended.

In some instances observation of JOIA results did not fully reflect expected full-scale results. For example, in the JOIA results, the slow ductile-type failures give larger total loads than the brittle cases. This resulted largely from the near uniform contact conditions across the entire width of the structure during the slow tests. Such conditions are not representative of full-scale; geometric irregularities, partial loading, fracture or other localized failure would influence full-scale contact conditions. Further review and analysis of Molikpaq data would be beneficial to examine creep cases; emphasis to date has been primarily on crushing. The mechanics of the stress field would be different at large scale than that of the JOIA scale.

At large scale, fracture is more important since both the stressed volume of ice and associated stressed field of flaws would be larger. In addition, probabilistic averaging effects are expected to be more dominant for large structures due to averaging over a larger area.

Issues associated with correlation analysis of Molikpaq data were discussed. Correlations of Molikpaq panel pressures were examined using autoregressive and composite approaches. Observed differences in Molikpaq and JOIA correlation data were attributed to issues association with the different scale of the structures. In light of *hpz* scaling associated with the thicker ice conditions of Molikpaq results, an initial attempt to scale correlation by thickness was made. Further work is needed with regards to the study of Molikpaq panel correlations and the relationship between the scales of both sets of tests.

Overall the JOIA data contain a wealth of information related of probabilistic averaging, *hpz* characterization and spatial pressure correlations. The JOIA data are a particularly valuable data set for development and validation of methodology. STRICE and Molikpaq results are more appropriate for direct use in ice load estimation. Detailed analysis and comparison of JOIA, STRICE and Molikpaq data in the context of pressure correlation and probabilistic averaging would be very beneficial. Analysis of JOIA tactile film data to improve understanding of the effects of speed and thickness on *hpz* size, density and distribution is recommended. Efforts to link failure behavior with correlation structure and spatial and temporal variations in pressure represent an important direction for future work.

5.9 Summary and Conclusions

From the analysis of sample small-scale indentation results it was observed that the interplay of damage and spalling play an important role in the localization of contact into *hpzs*. In simulating the ice failure process spall size, location and shape are important factors affecting the extent of load drop resulting from a fracture event. These aspect are quite complex to model and idealizations based on observations from experiments were required. The finite element simulations (which incorporated damage and spalling) yielded good agreement with load behavior for the selected case.

In modeling ice loads the primary interests are the peak loads at which spalls occur and how much load drops after a given event. The details of spall geometry and position are only of interest insofar as how they affect the load drop after a spall. A probabilistic treatment of spalling fracture is seen as more appropriate given the random nature of spalling and the focus on modeling the peak pressures and associated failure consequences.

Sample results were examined from a series of small-scale ice sheet edge indentation tests. From this work the main conclusions were: (1) the boundary conditions of ice specimens greatly affect the fracture behavior; (2) crushing is typically preceded by local spalling which localizes contact into *hpzs*; (3) multiple *hpzs* occur in a line-type configuration even for small scales (ice thickness on the order of several cm); (4) at slower loading rates (0.10 mm/s) processes such as local pressure melting and sintering occur in the layer; under appropriate conditions this can lead to the lateral growth of a layer of sintered ice as ice is extruded from the contact zone.

The JOIA tactile pressure data are an excellent source of information, with the potential to offer much richer insights into the details of ice failure than can be obtained from panel measurements alone. Characteristics of high pressure zones were investigated from a sample tactile pressure event. It was observed that during crushing, the loaded area is on average about 10% of the nominal area. Qualitative and quantitative descriptions of how spalling and crushing processes are manifest in the tactile data have been provided. A high degree of non-simultaneity was observed throughout the process, highlighting the need for probabilistic averaging.

Further efforts to explore links between correlation structure, *hpz* characteristics, and observed failure behavior are needed. The assessment of statistical aspects of *hpz* characteristics such as size, frequency, persistence and intensity is an important direction for further research. Further work may also examine the frequency of occurrence of each type of failure and explore links between these processes.

Future studies may expand on the above work to include probabilistic averaging analysis using tactile pressure sensor data and compare with results from the segmented panel analysis. Analysis of JOIA tactile film data to improve understanding of the effects of speed and thickness on *hpz* size, density and distribution is recommended.

To study probabilistic averaging and evaluate methods for estimating global loads based on local pressure measurements, segmented panel data from the JOIA program were analyzed. Edge effects were observed for the end panels (P1, P15). Comparison of results for cases that included and excluded end panels suggest that exclusion of end panels from the analysis is most appropriate. From the data it was evident that the measured global standard deviation was lower than local pressure standard deviations, which is consistent with probabilistic averaging theory. This was particularly the case for higher speeds where non-simultaneous aspects of failure are more dominant.

From correlation analysis of the JOIA panel data it was observed that correlations were generally lower for higher speed interaction as a result of increased randomness associated with non-simultaneous failure. Higher correlations were typically observed for lower speed tests due to the more uniform nature of failure at those speeds. Standard autoregressive correlation functions were fitted to JOIA panel correlation data plotted as function of distance. A characteristic correlation length value of $c = 0.20$ m was chosen for analysis using the autoregressive method. The use of composite correlation functions was also explored and provided a promising alternate approach for correlation modeling. Further work to explore links between temporal variation in correlation and failure behavior is an important direction for future work.

Estimates of global pressure using local pressure data were calculated using three approaches: (1) standard correlation probabilistic averaging; (2) composite correlation probabilistic averaging; (3) linear extrapolation of local pressures (no probabilistic averaging).

Comparison of estimates obtained for each approach indicate that the standard correlation probabilistic averaging method offered substantially lower average estimation error compared with the linear extrapolation approach. The composite correlation approach yielded promising results and further work to explore details of this approach is recommended.

From the JOIA data it was observed that the slow ductile-type events had larger total loads than brittle failure events. This has been attributed to the near uniform contact conditions across the entire width of the structure during the slow tests. Higher correlations result in reduced averaging effects, which mean less reduction in global pressure standard deviations and a higher overall global load estimate. Such conditions are not believed to be representative of full-scale since fracture, partial loading or other localized failure would affect the contact conditions at full-scale. At large scale, fracture is also likely to be more important since both the stressed volume of ice and associated stressed field of flaws would be larger. For large structures where averaging takes place over a much larger area, probabilistic averaging effects are expected to be more dominant. Further review and analysis of Molikpaq data to examine creep cases is recommended, since emphasis to date has been primarily on crushing.

To compare the JOIA results with full-scale data, correlations of Molikpaq panel pressures were examined using both the standard and composite correlation modeling approaches. Issues associated with the different scale of the structures resulted in observed differences in Molikpaq and JOIA correlation data. Since *hpzs* are assumed to scale with ice thickness, an initial attempt to scale correlation by thickness was made to account for the different ice conditions. Recall that it has been assumed here that there is a single *hpz* across the thickness of an ice sheet (i.e. no averaging across the thickness). For thicker ice, the possibility of multiple *hpzs* per unit thickness may result in averaging across the thickness leading to potentially higher correlations for thicker ice. Further work is needed in this area and characteristics of *hpzs* for thick ice should be investigated should tactile sensor data become available. Investigation of the effects of event duration on correlation modeling is also recommended.

From the above analysis it was evident that the dependence of local pressure on ice thickness is an important area for further study. The dependence of ice pressure of thickness is explored in Chapter 6.

Chapter 6: Pressure-Thickness

Scaling From Data

6.1 Scope

The primary aim of this chapter is to study the thickness effect present in full-scale data for local panels approximately of unit width. Data from indentation experiments on ice with remote edges are examined for various speeds. Ice-structure interaction data from the STRICE dataset were shown to exhibit clear scale effects of pressure with thickness. Comparison of STRICE data with Molikpaq, JOIA and Cook Inlet sets suggested that Molikpaq data were systematically higher than other data. To account for this observation an optional recalibration factor was applied to the Molikpaq data to examine results with and without a recalibration correction. Additional optional analysis filters were used for each dataset to evaluate the influence of factors such as event duration and the removal of rafted ice events. For the specified combinations of analysis filters, mean and standard deviations of pressure were plotted. Power law curves of the form $P_{avg} = Ch^D$ and $P_{std} = Eh^F$ were fitted to these data. A comparison of results for each analysis case was used to guide the selection of a case that is most representative of the observed ice behavior. Parameter values corresponding to the selected case was taken as being representative of the pressure-thickness scale effect.

6.2 Overview

From the pressure-area effect it follows that for a region of an ice feature of constant width pressure should decrease for increasing ice thickness. As shown in Figure 6.1, for a region of an ice feature of constant width, pressure should decrease for increasing ice thickness. This thickness effect will be explored to provide insight into the underpinning mechanics of the scale dependent behavior of ice during compressive failure.

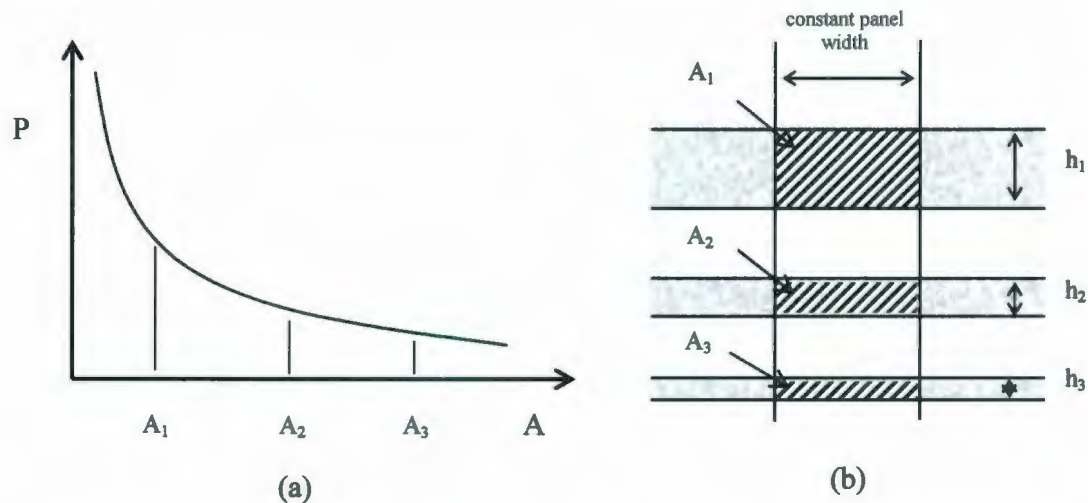


Figure 6.1: Illustration of (a) pressure-area effect; (b) increasing area for constant width panel with increasing thickness.

To gauge the extent of the effects of the top and bottom free surfaces on the scale effect, results for tests on confined specimens (remote boundaries) are first analyzed. This is followed by a detailed analysis of thickness scaling in full-scale data.

6.3 Scale Effect for Remote Ice Edges

Li et al. (2004) studied the behavior of high pressure zones at different scales. The authors conducted a series of small-scale indentation tests with four different sizes of spherical indenters (10mm, 20mm, 40mm and 100mm in diameter) and confined ice specimens. Three series of tests were conducted for three different orders of displacement rates; grain sizes

were also scaled with indenter size. Corresponding event data from medium scale field tests (Sinha and Cai, 1992; Masterson et al., 1999) were also analyzed along with the laboratory results. The results considered are summarized in Table 6.1 below.

Table 6.1: Displacement rates for the three test series (a, b and c) each with five indenter sizes; details of test results are provided in Li et al. (2004).

Indentor	Displacement rate (mm/sec)		
	Series (a)	Series (b)	Series (c)
Rate of data acquisition (Hz)	500	1000	3000
1	0.01	0.1	1
2	0.02	0.2	2
3	0.04	0.4	4
4	0.10	1.0	10
Field tests	1.00	10.0	100

Li et al. (2004) also examined the relationship between stress and nominal contact area for the different test series. In all tests, specimens were confined, which suppressed large edge spalls (since the only free surface is the indentation face).

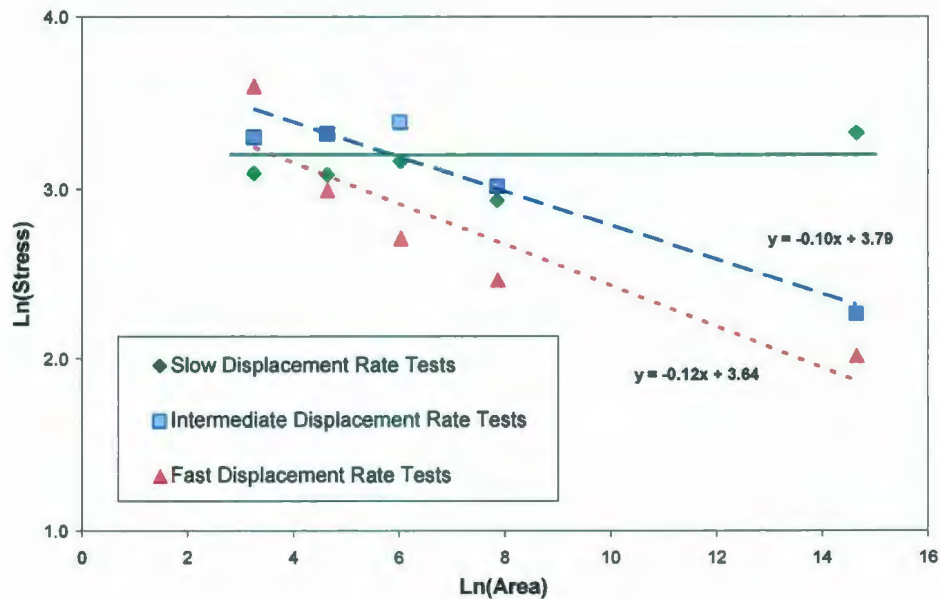


Figure 6.2: Indentation test scale effects for different speeds (after Li et al., 2004)

For the intermediate and high speed tests, surface spalls occurred, as local fractures initiated in the zone below the indenter and deviated towards the indentation face of the specimen. As may be seen in Figure 6.2, even in the absence of the top and bottom ice edges, scale-effects were observed for intermediate and fast displacement rates, but not for slow displacement rates.

From Figure 6.2 it is observed that for slow displacement rate tests, results exhibit little scale effect, as expected for classical (in this case, damaging viscoelastic) material behavior. As the displacement rate is increased, spalling fracture results in the localization of contact into zones of high pressure. For the above results, the spalls were primarily surface spalls (as opposed to edge spalls). This is expected, since the specimens are confined resulting in little effect from the remote ice edges. The occurrence of spalling fractures is believed to be key in the scale effect observed for the faster displacement rate test results shown in Figure 6.2.

The fact that neither surface spalls nor the associated scale effect are present during slower speed tests is strong evidence of the link between fracture and the scale effect. At intermediate and fast speeds, scale effects due to fracture processes are present. Remote top and bottom ice edges introduce negligible free surface effects resulting in few edge spalls. Under these conditions, surface spalls still occur and are the likely cause of the observed scale dependent behavior. Scale effects observed in full-scale data for ice sheets with thicknesses between approximately 0.2 m and 2.0 m are examined below.

6.4 Pressure-Thickness Effect in STRICE Data

Field data were collected from the lighthouse Norstromsgrund, shown in Figure 6.3 (a), during two European Union funded projects carried out over four winter seasons from 1999-2003. The lighthouse Norstromsgrund is founded at a water depth of about 14 m and has a water line diameter of about 7.2 m. It is located in the Northern Baltic Sea approximately 60 km offshore of Lulea in Sweden; see Figure 6.3 (b).



(a)



(b)

Figure 6.3: (a) Norstromsgrund lighthouse; (b) lighthouse location (Kärnä and Yan, 2006).

The lighthouse was outfitted with nine force measuring load panels, each with an individual area 1.2 m wide x 1.6 m high and a load capacity of 3000 kN. As illustrated in Figure 6.4(a), the panel array covered approximately 167 degrees of the structure. The northern Baltic Sea has a salinity of about 1ppt and experiences about 1000 freezing-degree-days (based on 2002-2003 season). At this location, only first year ice is encountered, with a maximum level thickness of approximately 0.6m.

The primary source of ice crushing data gathered from the lighthouse during the winters of 1999-2003 is Kärnä and Yan (2006). In this report, the authors used spectral characteristics of the signals to identify stationary events of continuous ice crushing. The authors identified events as being either brittle crushing or low velocity crushing. In this report load panel data was converted into mean ice pressures and mean standard deviations of pressure using the following expressions:

$$\text{Mean Ice Pressure [MPa]} = \frac{\text{Mean Ice Force [kN]}}{\text{Panel Width [m]} \times \text{Ice Thickness [m]} \times 1000}$$

$$\text{Mean Standard Deviation [MPa]} = \frac{\text{Mean Standard Deviation [kN]}}{\text{Panel Width [m]} \times \text{Ice Thickness [m]} \times 1000}$$

Based on information presented in Kärnä and Yan (2006) it has been determined that only events where the panels were measuring the full load were used in the STRICE analysis.

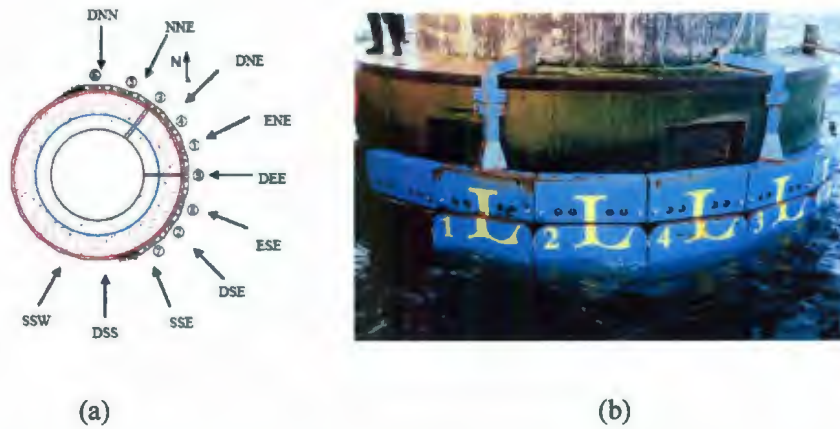


Figure 6.4: STRICE measurement panels: (a) schematic of panel numbering and orientation; (b) mounting configuration (Kärnä and Yan, 2006).

From an initial analysis of the STRICE data it was observed that a distinct pressure thickness effect is present in the mean event pressure data; see Figure 6.5 below.

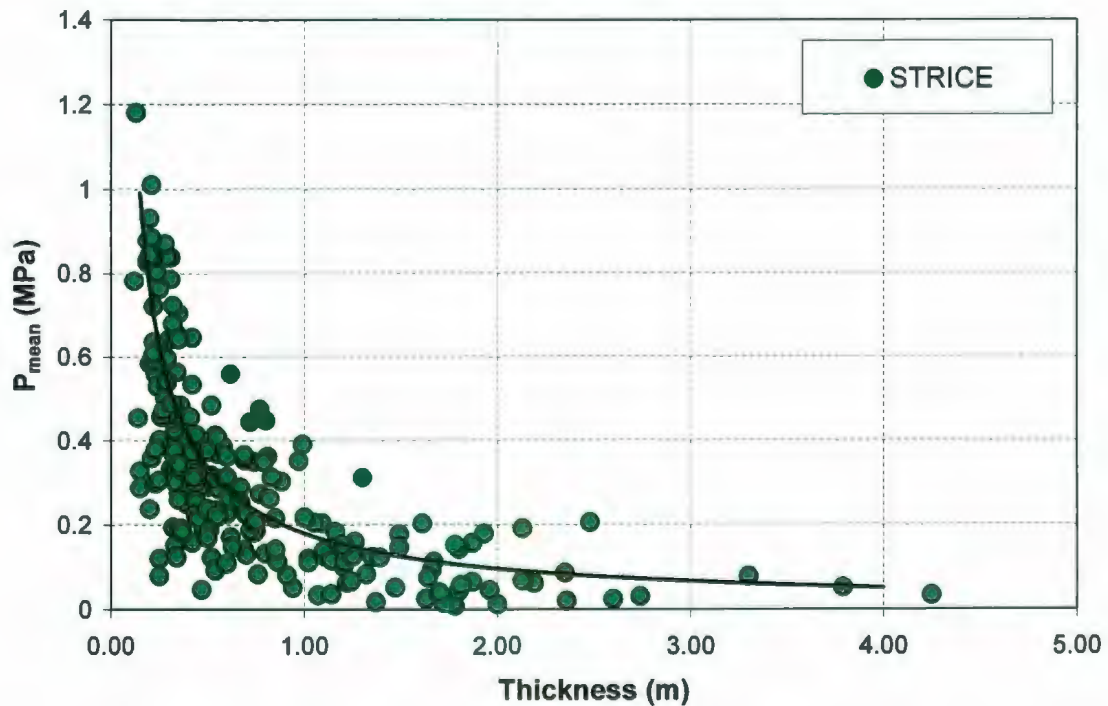


Figure 6.5: Mean local pressure versus ice thickness for STRICE event data.

To study pressure-thickness scale effects in other datasets, full-scale data from Molikpaq, JOIA and Cook Inlet were analyzed and compared with the STRICE data. This analysis is described below.

6.5 Thickness Effects in Full-scale Pressure Data

The following work examines the dependence of local pressure, measured by a panel of approximately unit width (1 m), on the thickness of the ice. Initial efforts focus on establishing a more consistent comparison of the Molikpaq data with other available datasets. Given the differences between these datasets, as well as their associated measurement uncertainties, direct comparisons of individual events or parts of an event are not considered. There will be variation, even for a given ice thickness, from one event to another. The only meaningful option is to assess and compare the statistical parameters of each set of events.

Full-scale data from the Molikpaq, as well as two European Union (EU) field measurement programs, 'Validation on Low Level Ice Forces on Coastal Structures' (LOLEIF) and 'Measurements on Structures in Ice' (STRICE), have been analyzed. In the present work, data from both EU projects are collectively referred to as the STRICE dataset. Measurement data from Cook Inlet and the Japan Ocean Industries Association (JOIA) medium-scale field indentation program are included in the analysis.

Mean pressure-thickness data analyzed on a per event basis is shown in Figure 6.6. A trend of decreasing pressure with increasing ice thickness is evident. The data in Figure 6.6 correspond to a variety of interaction widths. A more meaningful analysis requires a comparison of pressures for interactions acting over regions of the same width.

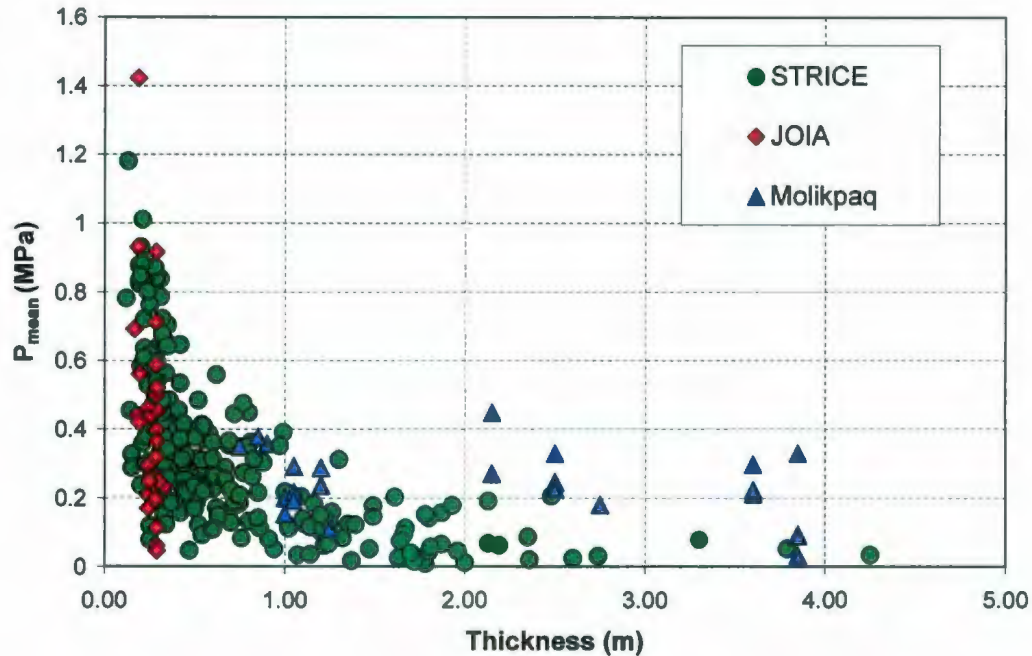


Figure 6.6: Illustration of pressure-thickness effect based on pressure data for individual events for JOIA, STRICE and Molikpaq data.

To allow for a comparison of pressure-thickness data, differences between the available datasets have been identified and are discussed below in an attempt to establish a consistent basis for analysis. Where possible, events have been selected and processed in a way which allows for the analysis of similar types of events from each dataset. Pertinent background information, along with a description of the analysis procedures used for each dataset are given below.

6.5.1 Detailed Analysis and Filters for Molikpaq Data

Data available from the 1985/1986 deployment of the Molikpaq mobile arctic caisson structure at Amauligak I-65 in the Canadian Beaufort Sea are considered. Details of the structure and its deployments are available in the open literature (see for instance, Rogers et al., 1988). This dataset includes multiple interactions of a wide, vertically-sided structure with both first-year and multi-year ice. The Molikpaq was instrumented with thirty-one Medof panels to measure local ice forces, each with a capacity of 20 MN.

These panels were installed on the north, northeast and east face of the caisson in groups of four or five (see Figure 6.7) and positioned with the bottom of the top panel approximately 0.2 m below the waterline.

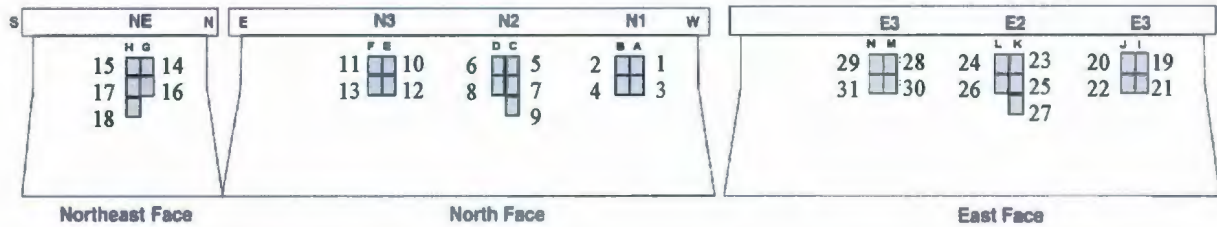


Figure 6.7: Medof panel array numbering (letters represent columns).

These panels were configured to measure the total force acting over the panel area (1.135 m wide by 2.715 m high). Slightly more than 10% of the length of each the north and east faces are covered with panels. During most of the interactions the Molikpaq performed well under ice loading, though on several occasions the structure experienced significant cyclic loading. During the ice loading event of April 12, 1986 liquefaction near the edge of the sand core occurred (Jefferies and Wright, 1988). Data corresponding to interactions covering a wide range of ice thicknesses, including thick multi-year ice features are available and are of interest in exploring scale effects. This dataset presents a wealth of information about full-scale behavior.

The Medof panels were configured in columns of two panels (i.e. Figure 6.7 panels 11 and 13), or in columns of three panels (i.e. Figure 6.7, panels 5, 7 and 9). For two panel columns, the Medof panels reached depths of 2.915 m, while the three panel columns covered ice interactions to a depth of 5.63 m. This has implications in the selection of appropriate column data for different events. As a general rule, ice loads have only been taken from columns which have instrumented panels covering the entire thickness of the ice, to ensure loads are captured across the entire ice thickness. This is illustrated in Figure 6.8 below.

One exception to this rule is noted for interactions on the Northeast face. As noted by Gulf Canada Ltd. (1987), panel 17 did not function throughout the entire 1985-1986 season and panels 14 and 15 were damaged during flaring operations on December 20, 1985 and did not work after that date. To address this issue, event data from the panels on the NE face were

individually examined to verify which panels were working correctly for the events of interest. Event data for malfunctioned panels were filtered out. Since panel 15 (top left) and panel 17 (middle left) both did not work, data from the entire left column of NE panels were discarded. For the right NE column, panel 14 (top right) did not work. Discarding the entire right NE column would result in the omission of all NE event data. Rather than entirely discard the data from the NE face, it was decided that the measurements from panel 16 would be taken as representative NE column loads for thin ice events.

This is seen as a reasonable assumption since spalling of the ice edge would likely result in negligible loads on the top panel, with the majority of load being transmitted through the middle panel. As with all other two panel columns, for thicker ice events, data for this column were omitted from the analysis; see Figure 6.8 (b) and (c).

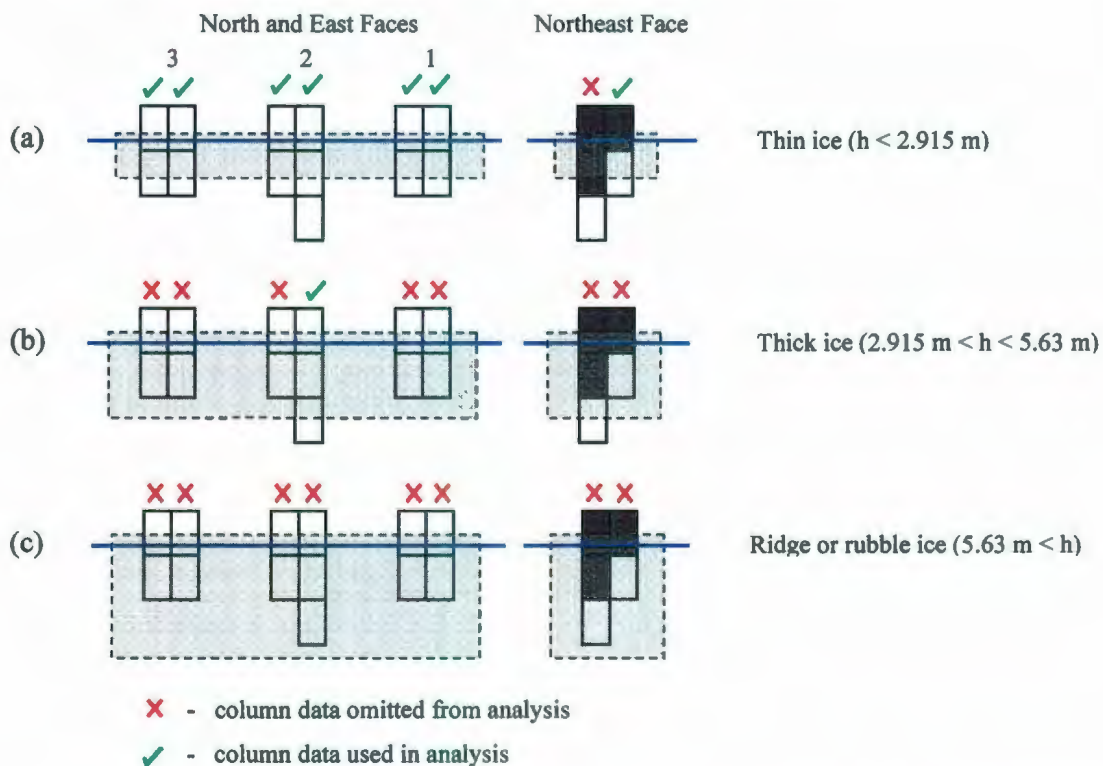


Figure 6.8: Illustration of selected columns of Medof panel data (dark panels represent broken panels) used for: (a) thin ice events; (b) thick ice events; (c) ridge/rubble events.

In reality there may be some load acting on the top panel of the NE column (i.e. panel 14), which would result in an actual pressure that is higher than those based on panel 16 only. Overall the number of events to which this applies is small, and the effects on the individual events are not expected to be significant. It has also been assumed here that the probability of loads below the bottom panels is unlikely given the quoted ice thickness values, though uncertainty associated with ice thicknesses is a likely contribution to the variation of the Molikpaq data.

In assessing the statistical characteristics of Molikpaq event data, significant effort has been placed to using an approach that is consistent with the analysis of the STRICE data. Since it was not possible to analyze directly the STRICE data (time series data are not publicly available), event means and standard deviations for STRICE have been obtained from Kärnä and Yan (2006). Based on this report it has been determined that the STRICE dataset contains only continuous crushing events, for which all panels are loaded for the entire duration of the event as stated in Kärnä and Yan (2006). A review of various event descriptions and lists (see for instance Rogers et al., 1988) resulted in the selection of relevant Molikpaq events for further analysis.

To provide a set of events comparable with STRICE, individual Molikpaq events were screened and processed. First all vertical groups of panels (e.g. panels 11 and 13) were combined to give column loads. Sections of the column load data files were then selected based on the global attributes of the interaction (i.e. start or stop of the event or a period of no load). In one instance, panel 9 experienced overloading for part of the event (event f605120301 on May 12, 1986); this portion of the event was filtered out. The selected data from each of the loaded columns were then linked together in series to form a single event load trace; see Figure 6.9.

Next the linked time trace for each event (i.e. linked data from all loaded columns) was examined in detail. These data were then trimmed to remove periods of low local loads corresponding to clearing, sliding or other processes acting locally on the given columns of panels. This produced time traces for 'continuous' crushing events with an 'effective' duration; see Figure 6.9 (b). For thick ice events where the bottom of the ice is below the

bottom of the middle panels, only the columns with three panels per column were analyzed to ensure ice loads were measured for the entire thickness. This process was repeated for all events in the analysis set. Details of the individual events used for each one, and additional detail of the data trimming process used are provided in Appendix C.1 and Appendix C.2, respectively. All analysis cases here only use single columns of data (i.e. corresponding to a single panel width); no combined columns are used.

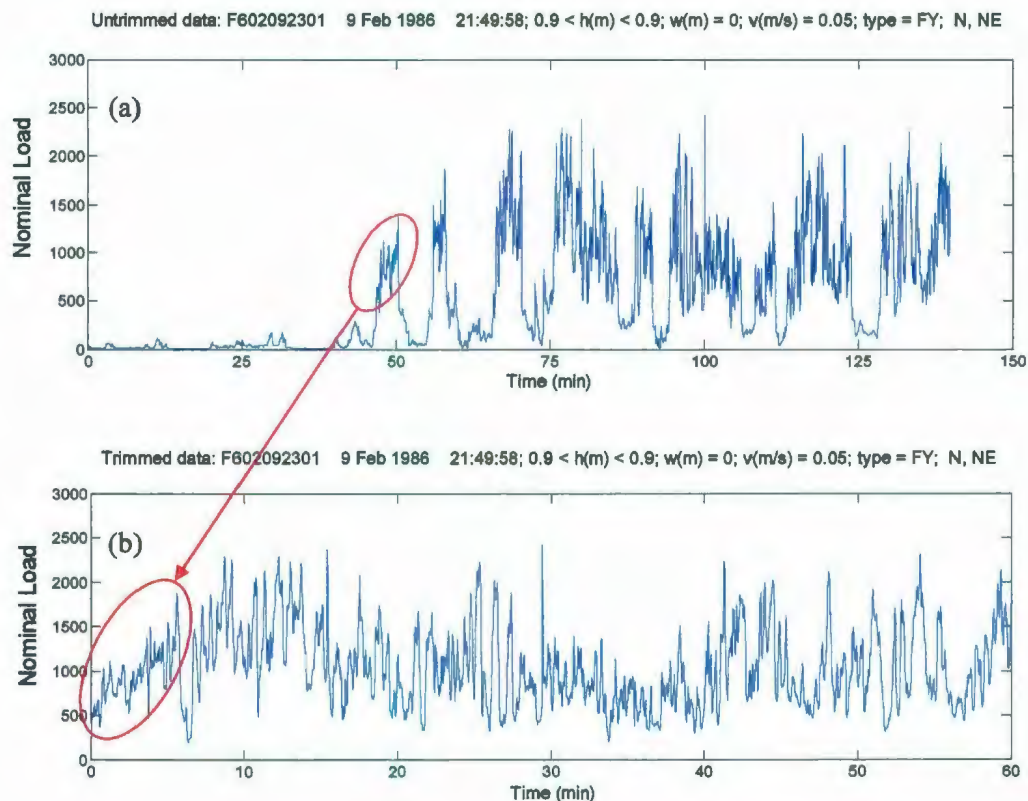


Figure 6.9: Plots showing a sample Molikpaq event with: (a) linked untrimmed data, and (b) linked trimmed data.

The Molikpaq fast files used in this analysis were collected at a sampling rate of 1 Hz. Jefferies and Wright (1988) stated that the response time of the Medof panels to a step change in load was of the order of 5 to 10 seconds. Some of the high frequency loads were effectively damped out (averaged) and the panel could not capture processes with frequencies above about 0.5 Hz to 3 Hz. As a result, Medof panel measurements could not capture process frequencies over the same range as the STRICE instrumentation.

Given the lower effective sampling rate of the Molikpaq data, it would be expected that for similar events, the standard deviations of pressure should be higher for STRICE than for the Molikpaq. The extent to which the difference in sampling rate affects the data is not clear. For the present analysis, no correction has been made to account for the difference in sampling frequencies, since time series data are not available for STRICE. Should these data become available, this could be explored by comparing STRICE statistical parameters for unfiltered event data, as well as for data that is either resampled at the same rate as the Molikpaq data or alternatively averaged using a moving average with a time window that is representative of the Medof panel response time.

Comparing the sample Molikpaq event in Figure 6.9 with the sample STRICE event shown in Figure 6.10 illustrates the general agreement between the forms of the processed data for both datasets.

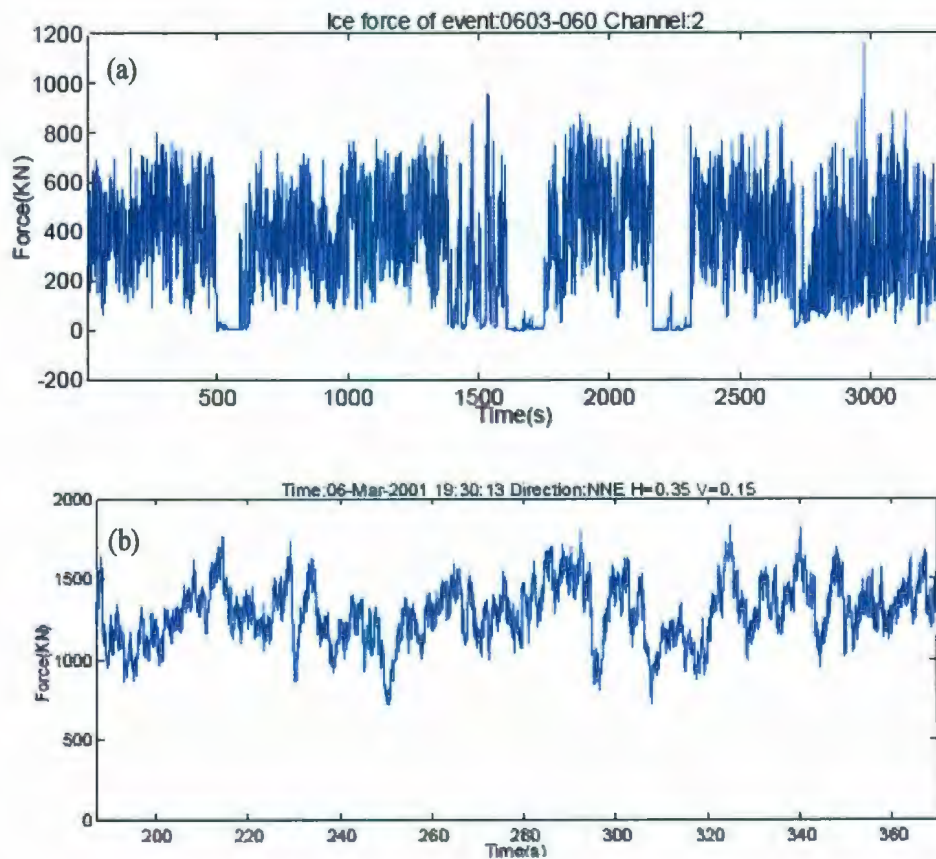


Figure 6.10: Data for a sample STRICE event: (a) untrimmed data and (b) a trimmed event (after Kärnä and Yan, 2006).

The duration of individual events is also an important consideration. Short events do not provide a sufficiently large sample to give a representative estimate of the statistical parameters, resulting in more uncertainty about how well the statistics characterize the process. This is an issue for all datasets, but this is of most relevance to the STRICE and Molikpaq datasets. Duration information is not available for the Cook Inlet dataset; these data were not included in analyses which studied the effects of duration. For the JOIA data, the duration of the events was determined by the stroke of the hydraulic ram used in the tests. JOIA events are much shorter in duration than STRICE and Molikpaq events.

The issue of event duration was treated by weighting the means and standard deviations in determining averages to reflect the duration of individual events. This approach is preferred, since it does not completely remove the data but rather assigns more weight to the longer duration events. The premise here is that longer duration events have greater statistical significance since they represent larger samples of the processes of interest.

Duration weighting is accomplished by populating an array containing event means (or standard deviations) where the number of repeat entries for each given event is proportional to the duration. The number of replications of an event n_i is equal to the duration of the i^{th} event in minutes truncated to one decimal place and multiplied by 10. For instance, an event with a duration of 15.6 minutes has its event mean entered into the overall mean pressure array 156 times. A second event, having a duration of 10.3 minutes would have 103 entries in the overall mean pressure array. In this manner, longer duration events have a proportionally larger influence on the overall mean. This option can only be applied to data where duration information is available (i.e. not for Cook Inlet). Using this technique it is possible to examine if duration length significantly affect the mean and standard deviation estimates.

Another difference between the STRICE and Molikpaq data is related to the configuration of panels. The STRICE program used a contiguous arrangement of panels (see Figure 6.4), while the Molikpaq panels were distributed across the face of the structure in clusters of two columns as shown in Figure 6.7. Consideration of temporal and spatial correlations is important when combining pressures from adjacent or remote columns to estimate pressures acting over a wider area, as with the probabilistic averaging analysis in Chapter 5. Since the

emphasis here is on pressures corresponding to a single panel width, such correlations do not enter into the analysis. Trimmed data for the Molikpaq columns were linked in series to give a representative single panel event with an effective duration. These data were then analyzed in a manner consistent with the single panel data analyzed from STRICE.

Recalibration Correction

In Jordaan et al. (in preparation), it was the judgment of the authors that the historical publically reported Medof panel derived ice loads for the Molikpaq 1985-86 deployment were of the order two times too high. Their reanalysis of data from non Medof panel instrumentation, the May 12, 1986 decelerating floe impact analysis, geotechnical information and possible softening of the Medof panels suggested that a recalibration factor of about 0.5 should be applied to the Medof panel data.

An initial comparison of uncorrected Molikpaq and STRICE results corresponding to a similar range of ice thicknesses highlights the discrepancy between the Molikpaq data and other data sets; see Figure 6.11. The Molikpaq results are consistently higher than other measurements corresponding to the same ice thicknesses. Recalibration to account for this discrepancy yields much better agreement between the data sets.

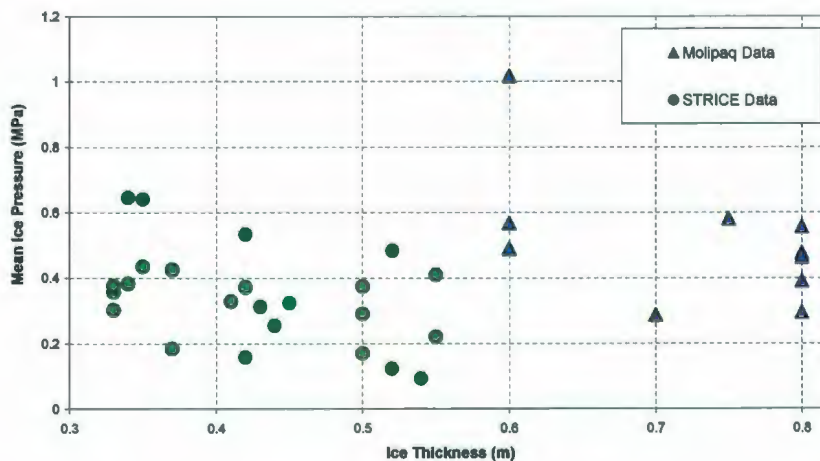


Figure 6.11: Initial comparison of STRICE and Molikpaq results corresponding to similar ice conditions, showing the discrepancy between values measured on each structure.

To account for the recalibration factor, an optional correction factor was implemented in the present analysis. The purpose of this correction factor is to allow for an assessment of the degree of consistency between Molikpaq and other datasets both with and without the Molikpaq corrections. When this option is used final pressure estimates (means and standard deviations) for the Molikpaq data are multiplied by 0.5. When this option is turned off, the Molikpaq pressure values given are the uncorrected values.

6.5.2 Filters for STRICE Data

Based on information presented by Kärnä and Yan (2006) it was determined that data corresponding to ice thickness greater than 1.5 m or less than 0.2 m should be omitted. For this reason, all events with thickness above 1.5 m or below 0.2 m have been discarded. The authors also suggested that while rafted ice can have more or less the same strength as corresponding level ice, there is uncertainty associated with both the extent of consolidation of the rafted ice, and its strength. Since the competent level ice has an upper limit of approximately 0.6 m for this region, an optional level ice filter was used for some analysis cases, as is discussed below. From the STRICE data obtained from Kärnä and Yan (2006) relevant brittle crushing and low velocity crushing events were selected.

Two optional analysis filters, one for level ice and the other for event duration were implemented for the STRICE dataset.

Level Ice Filter

Given the ice conditions in the Baltic Sea, an upper limit on level ice thickness was taken as $h \leq 0.6\text{m}$. This filter removes all thicker (likely rafted) ice from the analysis.

Duration Filter

This option is used to remove events which have an overall duration of less than 10 minutes to study the effect of removing short duration events.

6.5.3 Filters for JOIA Data

As discussed in Chapter 5, the JOIA medium-scale field indentation test (MSFIT) project consisted of over thirty tests carried out over a five year timeframe (1996-2000). Only results corresponding to tests with the 150 cm wide indenter (1998, 2000) have been included in the present analysis. From these data, only measurements corresponding to the center 13 panels of the indenter were included (for a total width of 130 cm) since the edge effects were identified with the end panels; see Chapter 5 for further discussion of the edge effects. For the thickness scaling analysis the JOIA events required no screening parameters since the tests were conducted under controlled conditions and the relevance of individual events to the present work could be more clearly determined. The short duration of individual events, which was limited by the stroke of the hydraulic ram used, is discussed later in the chapter.

6.5.4 Filters for Cook Inlet Data

Cook Inlet has been the site of concentrated oil and gas development since the early 1960s. The ice cover in Cook Inlet is typically thin first-year ice with maximum thickness often less than 0.5m. The salinity is in the range of 4-6 ppt and the ice is subject to vigorous tidal action. During the mid-1960s, 14 offshore structures were built in this region, with several being instrumented for ice forces during the 1963-1969 period (Sanderson, 1988). Instrumented piles were typically fitted with strain gauges to measure bending strain under load. The primary source of published data for this region is Blenkarn (1970).

Time series data are not available for the Cook Inlet measurements. In the following analysis, the steady ice load values reported by Blenkarn (1970) have been used to estimate mean pressures on the test structure. Standard deviations of pressure were not reported. These data were originally reported in units of thousands of pounds (kip) per foot in diameter and a corresponding value of thickness was provided. These values were converted into units of pressure (MPa) for an area of unit width (m) by converting the force per unit width to metric units and dividing by thickness.

Level Ice Filter

Blenkarn (1970) indicated that the limit of ice growth for the Cook Inlet region is on the order of 0.5 m. For this reason, an optional filter was used to remove data corresponding to ice thicknesses above 0.5m. Beyond this thickness, the ice is assumed to be rafted ice or refrozen brash ice.

The processing options used with this dataset are summarized in Table 6.2 for the various analysis cases considered. It is noted that standard deviations of pressure and event durations are not available for these data. Cook Inlet data is absent from all portions of the analysis related to discussion of standard deviation of pressure and event duration.

6.5.5 Thickness Scaling Analysis Results

In light of the above assessment of the datasets, an analysis matrix was compiled to compare data processed using various combinations of the identified event screening criteria; see Table 6.2. These combinations of screening criteria were selected to illustrate the relationship between the Molikpaq and other datasets, while examining the influence of various factors on the observed trends.

Table 6.2: Description of cases considered in analysis

Case	Molikpaq	STRICE	JOIA	Cook Inlet
1	Softening Correction Off Unweighted Mean	Level Ice Filter On Duration Filter Off	No Filters	Level Ice Filter On
2	Softening Correction On Unweighted Mean	Level Ice Filter On Duration Filter Off	No Filters	Level Ice Filter On
3	Softening Correction Off Weighted Mean	Level Ice Filter On Duration Filter Off	No Filters	Excluded
4	Softening Correction On Weighted Mean	Level Ice Filter On Duration Filter Off	No Filters	Excluded
5	Softening Correction On Unweighted Mean	Level Ice Filter On Duration Filter On	No Filters	Level Ice Filter On
6	Softening Correction On Weighted Mean	Level Ice Filter On Duration Filter On	No Filters	Excluded
7	Softening Correction On Unweighted Mean	Level Ice Filter Off Duration Filter Off	No Filters	Level Ice Filter Off
8	Softening Correction On Unweighted Mean	Level Ice Filter On Duration Filter On	No Filters	Excluded
9	Softening Correction Off Unweighted Mean	Level Ice Filter On Duration Filter On	Excluded	Excluded
10	Softening Correction On Unweighted Mean	Level Ice Filter On Duration Filter On	Excluded	Excluded
11	Softening Correction Off Weighted Mean	Level Ice Filter On Duration Filter On	Excluded	Excluded
12	Softening Correction On Weighted Mean	Level Ice Filter On Duration Filter On	Excluded	Excluded

For each of the analysis cases, power law curves were fitted to the data. The assumed forms for the power law curves were: $P_{avg} = Ch^D$; $P_{std} = Eh^F$. Values of these parameters are discussed below for each of the analysis cases. Results for individual cases have been grouped into pairs which have used similar analysis options. Confidence intervals on future response (also referred to as ‘prediction intervals’) have been included in the analysis.

Analysis Pair 1: Case 1 and Case 2

Data for this pair were analyzed using unweighted means for the assessment of mean pressure and standard deviations. The STRICE data were filtered to only include level ice, but were not filtered by event duration. JOIA data were not filtered and the Cook Inlet data only included results corresponding to level ice thicknesses. Molikpaq data were analyzed with the recalibration correction turned off for Case 1, and turned on for Case 2.

For Case 1, a recalibration correction was not applied to the Molikpaq data. Results for the mean pressure data for this case are shown in Figure 6.12 (a) and standard deviation of pressure data are in Figure 6.12 (b). As may be observed in Figure 6.12 (a), the uncorrected Molikpaq mean pressure data are significantly higher than the other data and have a wider degree of variability. The power law fitted to the mean pressure data has parameters $C = 0.407$ and $D = -0.128$. Similarly for standard deviation of pressure data shown in Figure 6.12 (b), the Molikpaq dataset has significantly higher values than the standard deviations for other datasets. The power law fitted to the standard deviation of pressure data has parameter values $E = 0.228$ and $F = 0.106$.

For Case 2, a recalibration correction factor was used for the Molikpaq data. The mean pressure and standard deviation of pressure data are shown in Figures 6.13 (a) and 6.13 (b), respectively. As shown in Figure 6.13 (a), the corrected Molikpaq mean pressure data are much more consistent with the STRICE, JOIA and Cook Inlet data and a distinct pressure-thickness effect is observed. Similarly the standard deviation data for the corrected Molikpaq results in Figure 6.13 (b) are in much better agreement with STRICE and JOIA than were the uncorrected results shown for Case 1. For this case the curve fit parameters for the mean pressure data were found to be $C = 0.287$ and $D = -0.401$, and $E = 0.15$ and $F = -0.185$ for the standard deviation of pressure.

Analysis Pair 2: Case 3 and Case 4

For these cases duration weighted means were used in the assessment of mean pressure and standard deviations. The STRICE data were filtered to only include level ice, but were not filtered by event duration. The JOIA data were not filtered and Cook Inlet data are excluded, since event durations are not known for these data. Molikpaq data were included with the recalibration correction turned off for Case 3, and turned on for Case 4.

Case 3 did not include corrections to the Molikpaq data for panel recalibration. From Figures 6.14 (a) and (b) it may be observed inconsistencies between the uncorrected Molikpaq mean pressure data and other datasets dominates the trends for this case. The use of weighted means has little impact on these results, since the mismatch between the uncorrected Molikpaq and other datasets dominates the results. The curve fit parameters were found to be

$C = 0.392$ and $D = -0.058$ for the mean pressure data and $E = 0.345$ and $F = 0.273$ for the standard deviation of pressure.

In Case 4, a recalibration correction was applied to the Molikpaq data. It may be observed from the mean pressure data in Figure 6.15 (a) and the standard deviation of pressure data in Figure 6.15 (b) that there is more consistency between the Molikpaq, STRICE and JOIA data for this case. Both mean and standard deviation results support a decreasing pressure thickness trend. The curve fit parameters for this case were found to have values of $C = 0.212$ and $D = -0.429$ for the mean pressure and $E = 0.179$ and $F = -0.098$ for the standard deviation of pressure.

Analysis Pair 3: Case 5 and Case 6

This analysis pair used recalibration corrected Molikpaq data. STRICE data were filtered using the level ice and all events with duration less than 10 minutes were filtered out. JOIA data were not filtered.

For Case 5, unweighted means were used, and Cook Inlet data were filtered to include only level ice. From Figure 6.16 (a) it is observed that a good fit to the mean pressure data is obtained. The mean pressure data were well represented by a curve with parameter values $C = 0.299$ and $D = -0.384$. The standard deviation of pressure data are plotted in Figure 6.16 (b). Power law parameter values of $E = 0.167$ and $F = -0.182$ were obtained for a curve fitted to these data. A distinct decreasing pressure-thickness trend is observed for both mean and standard deviation results.

For Case 6, duration weighting was used and Cook Inlet data were excluded, since no duration information is available for this set. It may be observed from Figure 6.17 (a) that the curve fitted to the mean pressure data has parameters $C = 0.211$ and $D = -0.392$. While these parameter values well model the data for thin ice, the curve does not well bound the pressure values for thicker ice. The standard deviation of pressure results are plotted in Figure 6.17 (b). A power law curve of the form $P = Eh^F$ was fitted to these data and yielded parameter values of $E = 0.179$ and $F = -0.11$. While a trend of decreasing pressure with

increasing thickness is observed for these results, the resulting power law fit does not bound the data as well as the curve fit parameters obtained for Case 5.

Analysis Pair 4: Case 7 and Case 8

For these analysis cases, corrected Molikpaq data were used, along with STRICE and JOIA data. Case 7 did not include any filtering for duration or for thicker rafted ice. Unfiltered Cook Inlet data were also included for this case. In Case 8, level ice and duration filters were used for the STRICE data and Cook Inlet data were excluded. In both cases, unweighted means were used in the assessment of overall mean and standard deviation of pressures.

The mean pressure data, along with associated mean curve and 95% confidence intervals on future response for Case 7 are shown Figure 6.18 (a). The parameter values for the curve fitted to these data are $C = 0.242$ and $D = -0.539$. From this plot it may be observed that the fitted curve tends to provide a better representation of the data for thinner ice, than for thick ice. Similarly in Figure 6.18 (b) a power law curve and associated confidence intervals on future response were fitted to the unweighted standard deviation of pressure data. The fitted curve had parameter values of $E = 0.116$ and $F = -0.387$ for the standard deviation results. As may be observed in this plot, a decreasing pressure-thickness trend is evident, with the curve well bounding the data for this analysis case.

The unweighted mean pressure curve, confidence intervals on future response and mean pressure data for Case 8 are given in Figure 6.19 (a). A curve with power law parameter values of $C = 0.273$ and $D = -0.377$ were fitted to these data. The standard deviation results, along with the fitted power law curve and associated confidence intervals on future response are shown in Figure 6.19 (b). The curve shown in this figure has parameter values of $E = 0.167$ and $F = -0.182$. As in previous analysis cases, a trend of decreasing pressure with increasing thickness is evident. It may be observed from Figure 6.19 that the fitted curves well bound the data over the range of thicknesses included in this analysis.

Analysis Pair 5: Case 9 and Case 10

A main focus of this analysis pair was to examine results based solely on the STRICE and Molikpaq data (JOIA and Cook Inlet were excluded). STRICE data were filtered using both

the level ice filter and the duration filter. The overall mean and standard deviation of pressures were evaluated using unweighted means for both cases. For Case 9, Molikpaq data were not corrected for recalibration. A recalibration correction factor was applied to the Molikpaq data for Case 10.

The unweighted mean and standard deviation of pressure curves for Case 9 are given in Figure 6.20. The power law curve parameters for the mean pressure data are $C = 0.44$ and $D = -0.113$, and $E = 0.286$ and $F = 0.022$ for the standard deviation results. As in other cases which did not use a recalibration correction, the Molikpaq data are not consistent with the other datasets and data are not well represented by the curve fits.

The results for Case 10 are given in Figure 6.21 (a) for mean pressure, and Figure 6.21 (b) for standard deviation of pressure. Parameter values of $C = 0.278$ and $D = -0.408$ were obtained for the mean pressure power law fit. Similarly for the standard deviation results, parameter values were found to be $E = 0.172$ and $F = -0.273$. From these data a clear trend of decreasing pressure with increasing thickness is observed. As shown in Figure 6.21, the above power law curves well bound the data for both mean and standard deviation results. As with other analysis cases, the Molikpaq data to which a recalibration correction factor had been applied were much more consistent with the STRICE results than were the uncorrected data.

Analysis Pair 6: Case 11 and Case 12

This analysis pair also examined results based solely on the STRICE and Molikpaq data (JOIA and Cook Inlet were excluded). The STRICE data were filtered using both the level ice filter and the duration filter. For these cases, duration weighted means were used for both cases. Molikpaq data were not corrected for recalibration for Case 11. For Case 12 a recalibration correction factor was applied to the Molikpaq data.

The mean pressure and standard deviation of pressure results for Case 11 are given in Figure 6.22 (a) and Figure 6.22 (b), respectively. For the mean pressure power law fit, parameter values of $C = 0.392$ and $D = -0.038$ were obtained. Similarly, parameter values of $E = 0.348$ and $F = 0.229$ were obtained for the standard deviation results. It is again

observed that uncorrected Molikpaq data are not consistent with the STRICE data and are not well represented by the fitted curves.

The recalibration corrected Molikpaq data used in Case 12 showed much better agreement with the STRICE data. The mean pressure data for this case is given in Figure 6.23 (a), along with the associated power law curve and 95% confidence intervals on future response. Power law parameter values of $C = 0.211$ and $D = -0.383$ were fitted to the mean pressure data. As shown in Figure 6.23 (b), standard deviation of pressure data have been fitted with a power law curve ($E = 0.179$ and $F = -0.117$). A trend of decreasing pressure with increasing thickness is evident. As in earlier analysis cases using duration weighted means, the confidence intervals on future response do not bound the data as well as the unweighted analysis. Improved techniques for weighting should be explored.

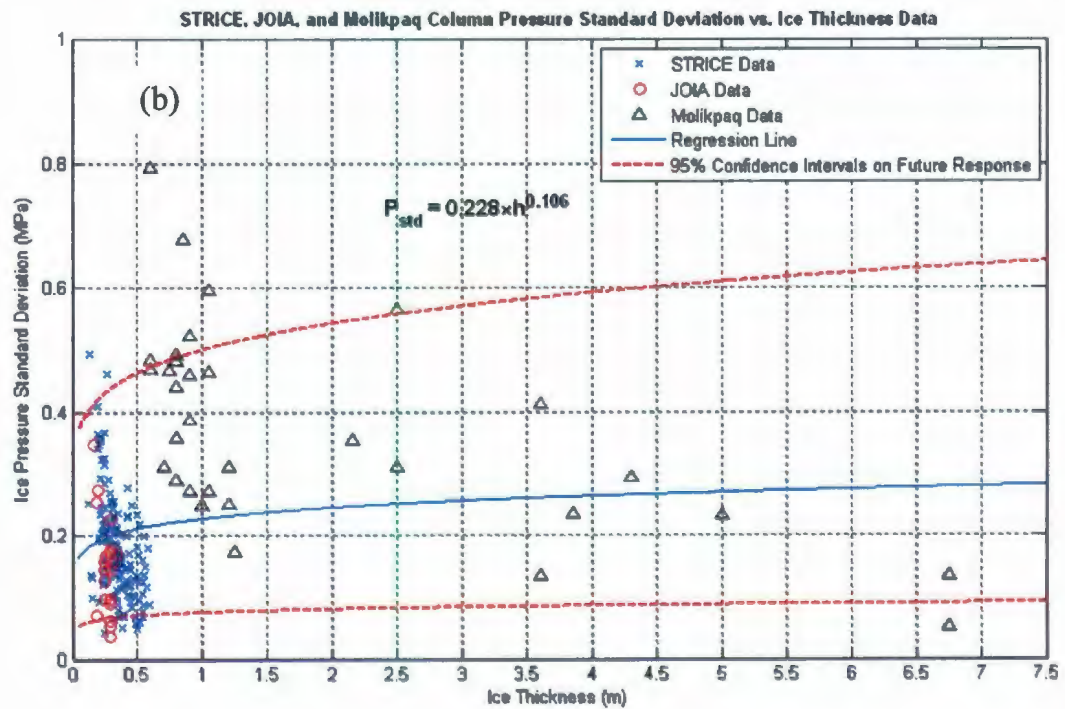
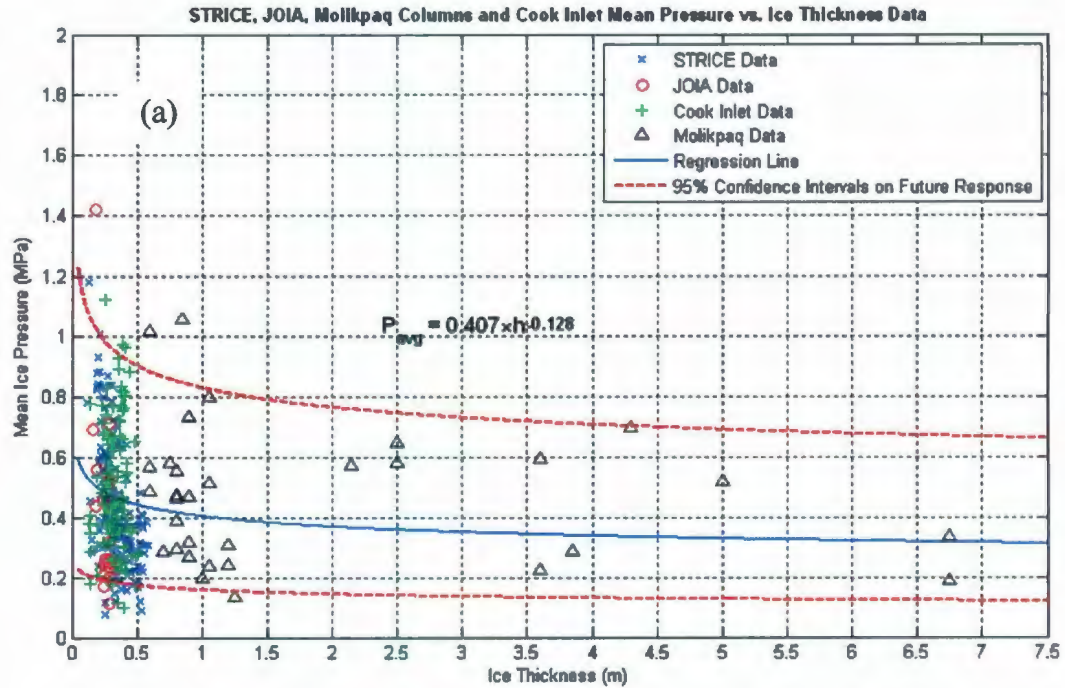


Figure 6.12: Case 1 (Mollkpaq recalibration correction off; STRICE level ice filter on, duration filter off; JOIA unfiltered; Cook Inlet level ice filter on; unweighted mean) data and curve fits for: (a) mean pressure results; (b) standard deviation of pressure results.

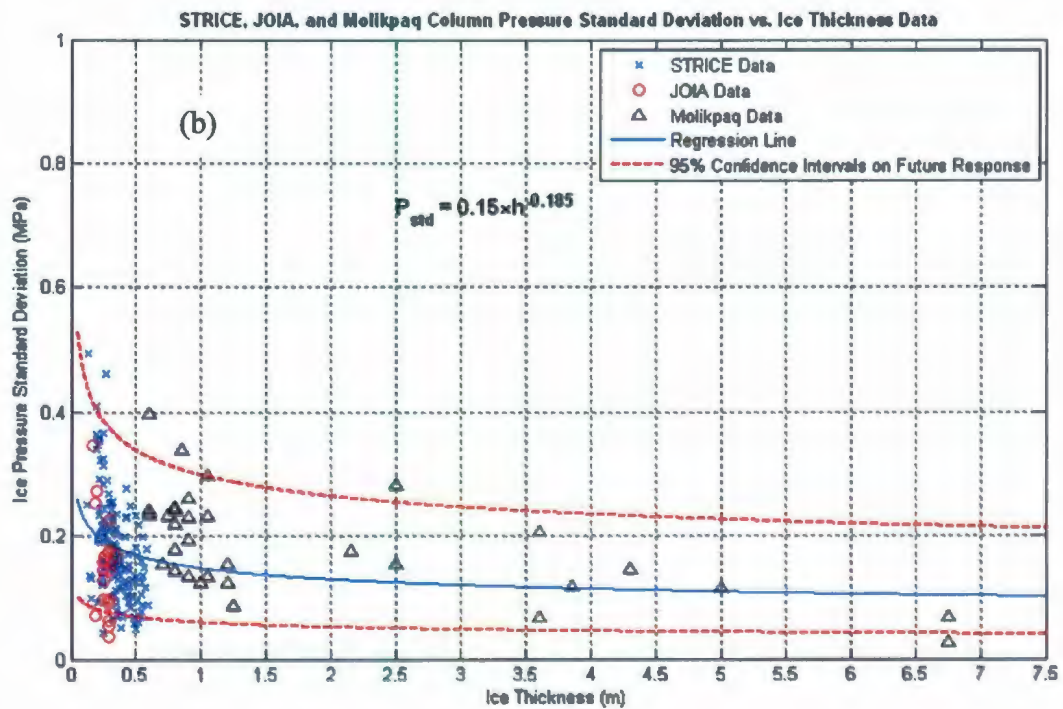
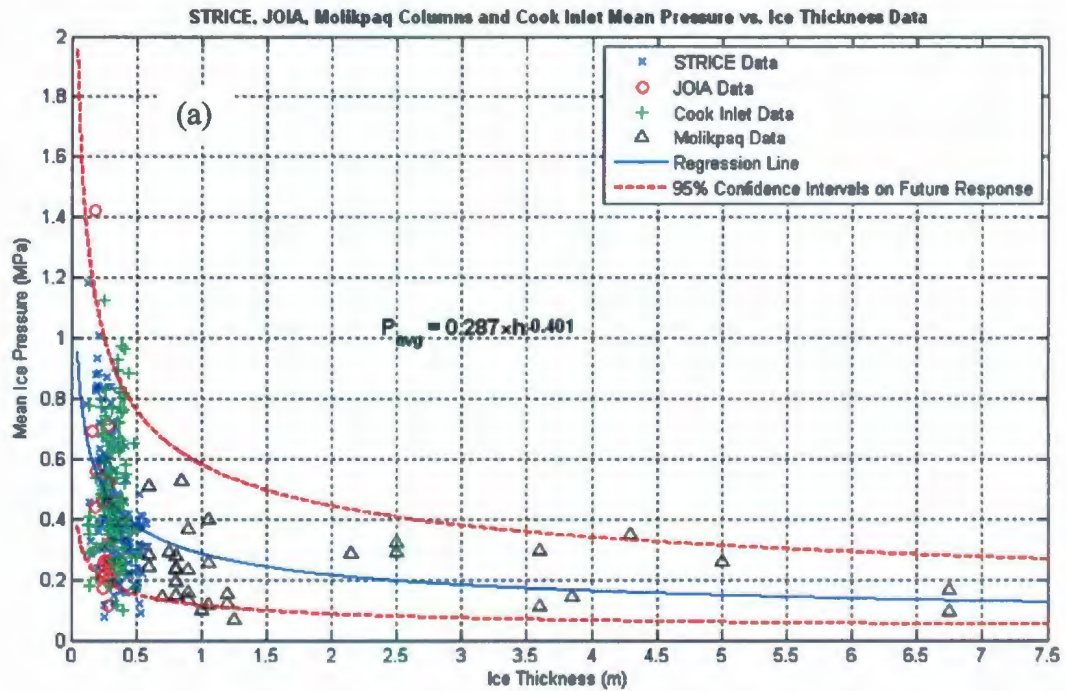


Figure 6.13: Case 2 (Molikpaq recalibration correction on; STRICE level ice filter on, duration filter off; JOIA unfiltered; Cook Inlet level ice filter on; unweighted mean) data and curve fits for: (a) mean pressure results; (b) standard deviation of pressure results.

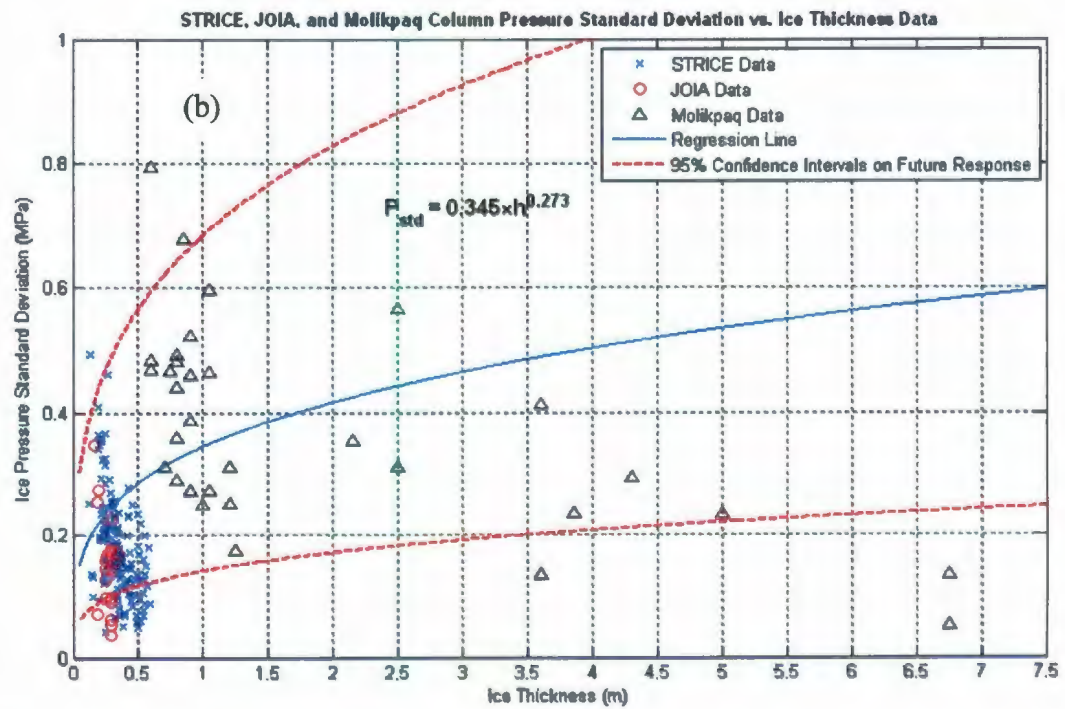
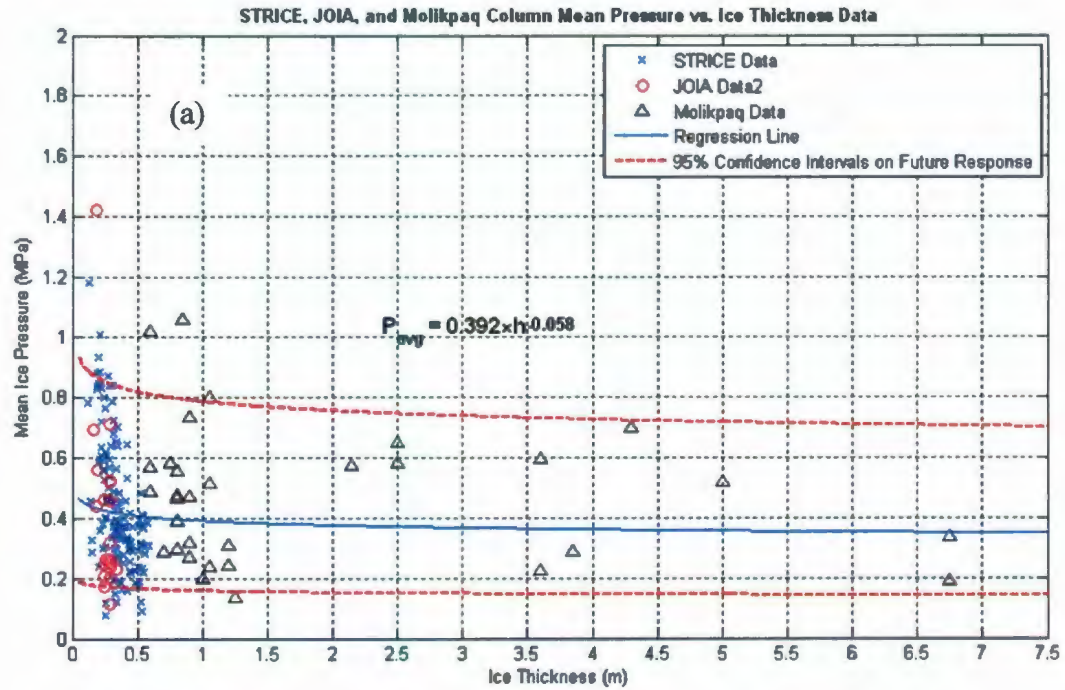


Figure 6.14: Case 3 (Molikpaq recalibration correction off; STRICE level ice filter on, duration filter off; JOIA unfiltered; Cook Inlet data excluded; weighted mean) data and curve fits for: (a) mean pressure results; (b) standard deviation of pressure results

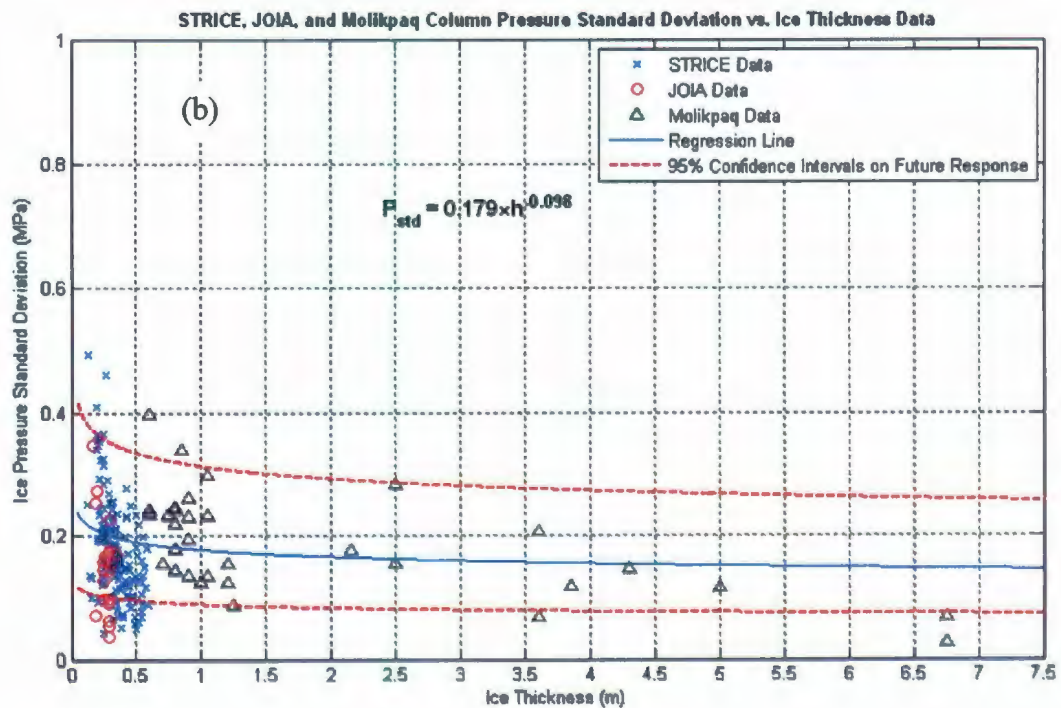
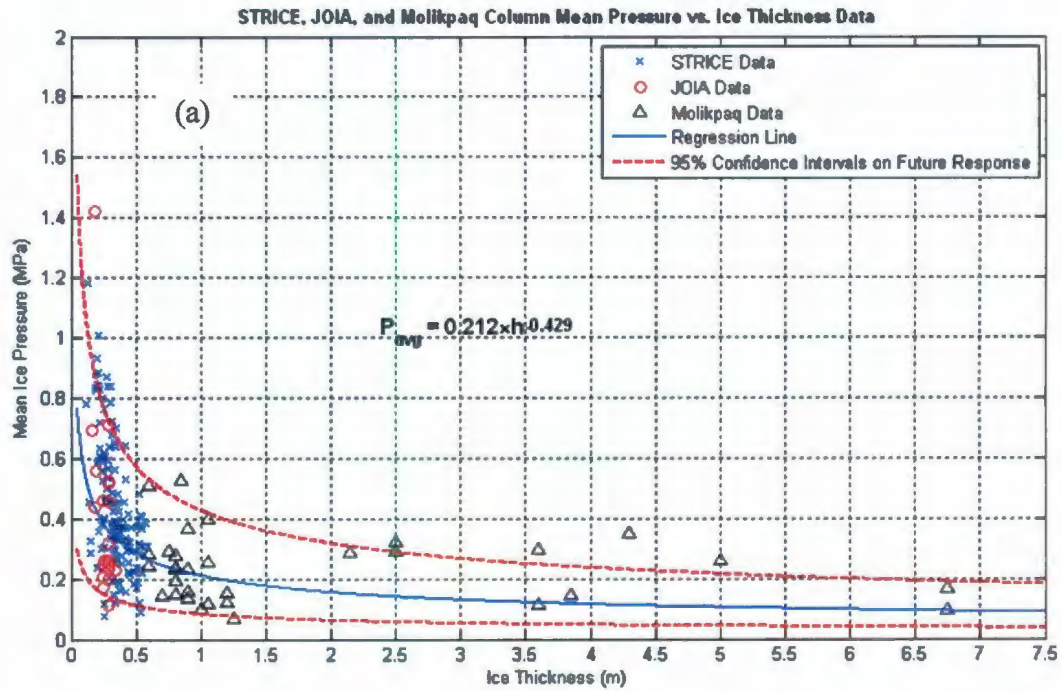


Figure 6.15: Case 4 (Molikpaq recalibration correction on; STRICE level ice filter on, duration filter off; JOIA unfiltered; Cook Inlet excluded; weighted mean) data and curve fits for: (a) mean pressure results; (b) standard deviation of pressure results.

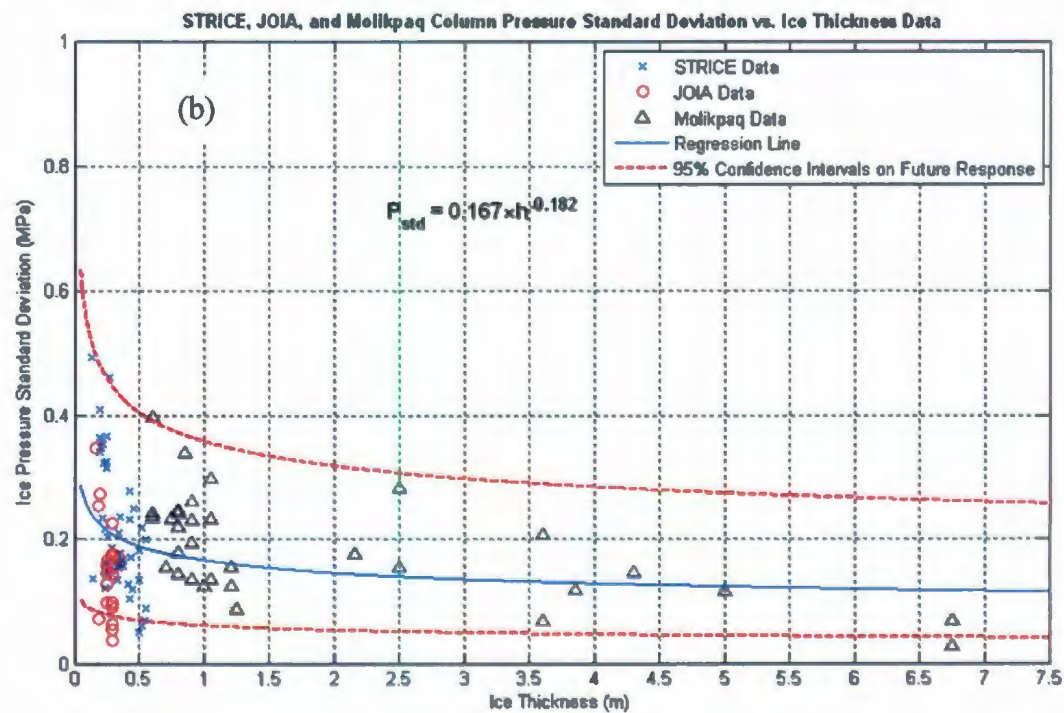
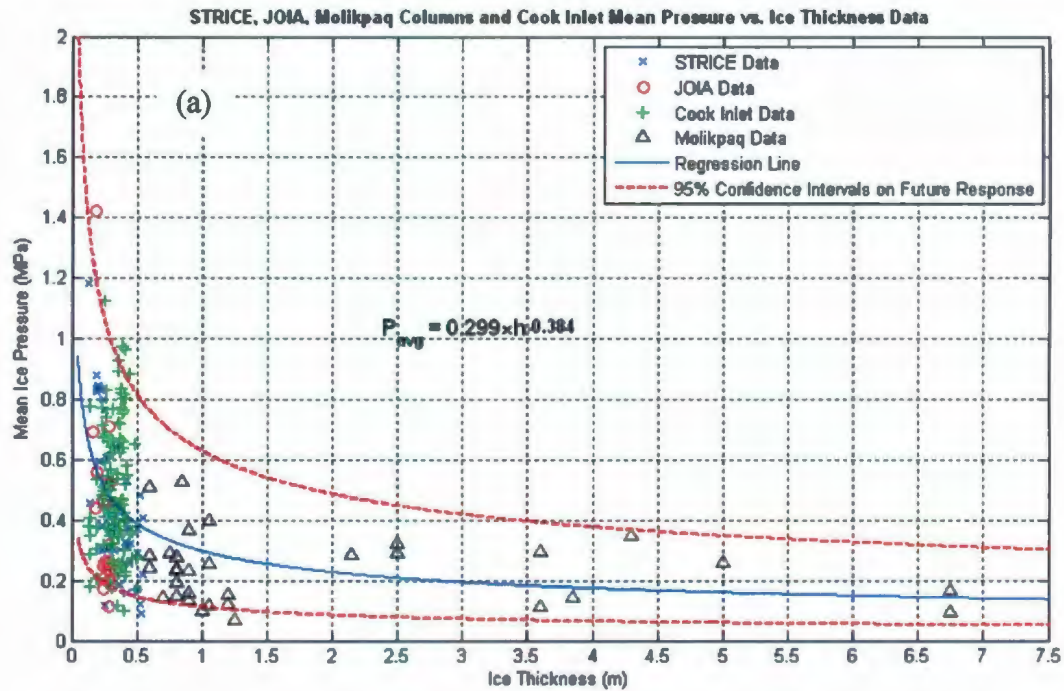


Figure 6.16: Case 5 (Molikpaq recalibration correction on; STRICE level ice filter on, duration filter on; JOIA unfiltered; Cook Inlet level ice filter on; unweighted mean) data and curve fits for: (a) mean pressure results; (b) standard deviation of pressure results.

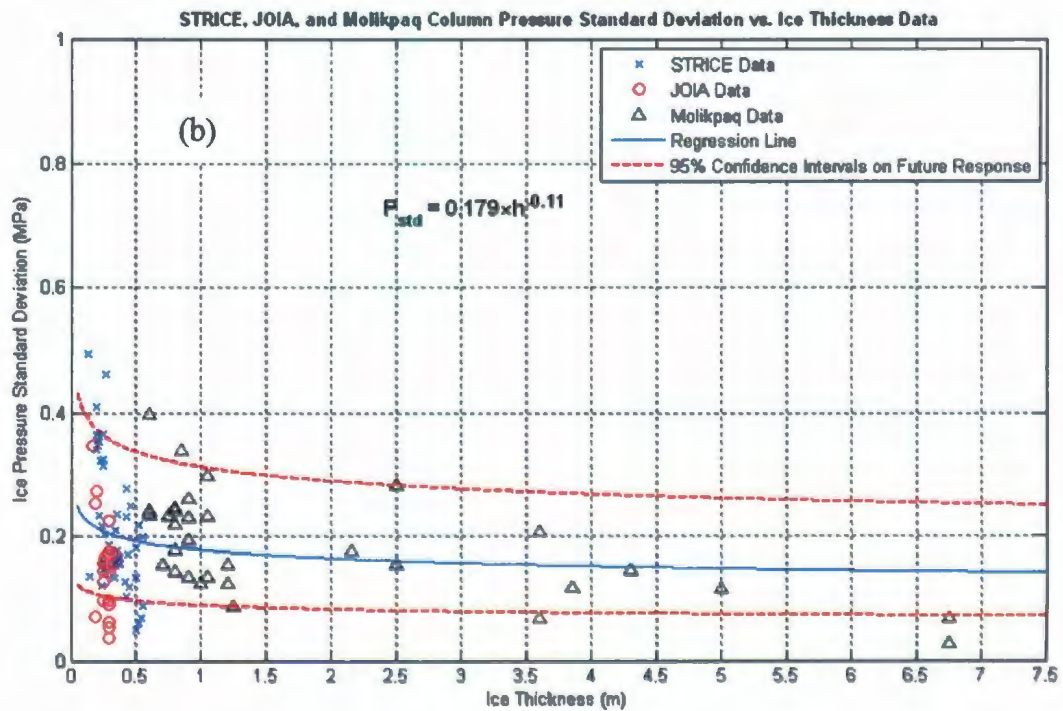
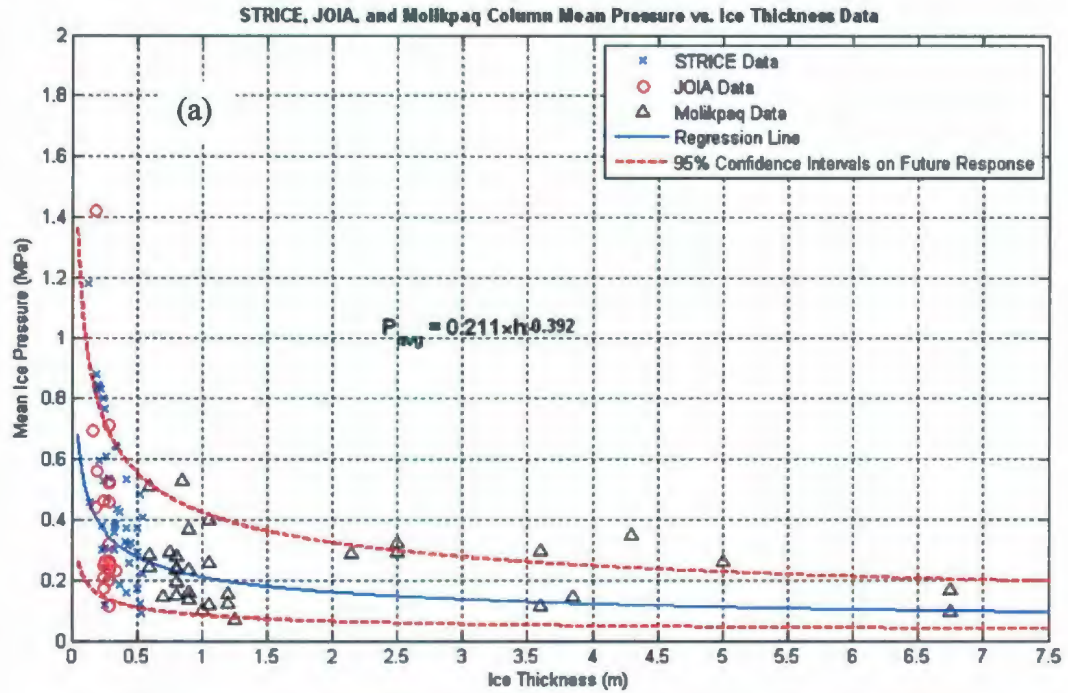


Figure 6.17: Case 6 (Molikpaq recalibration correction on; STRICE level ice filter on, duration filter on; JOIA unfiltered; Cook Inlet data excluded; weighted mean) data and curve fits for: (a) mean pressure results; (b) standard deviation of pressure results.

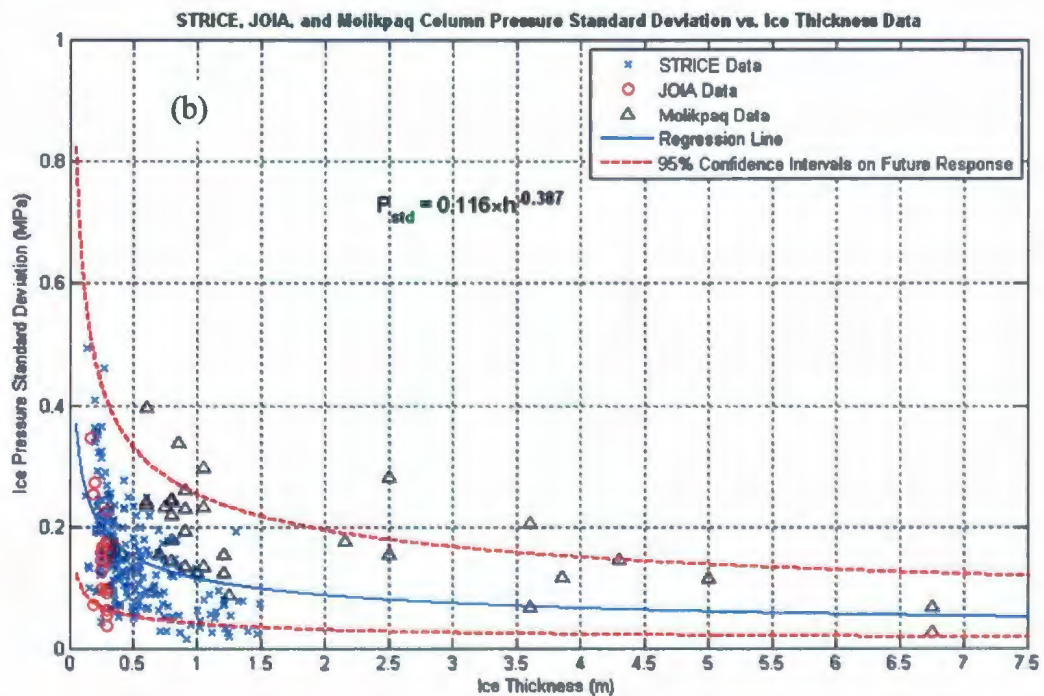
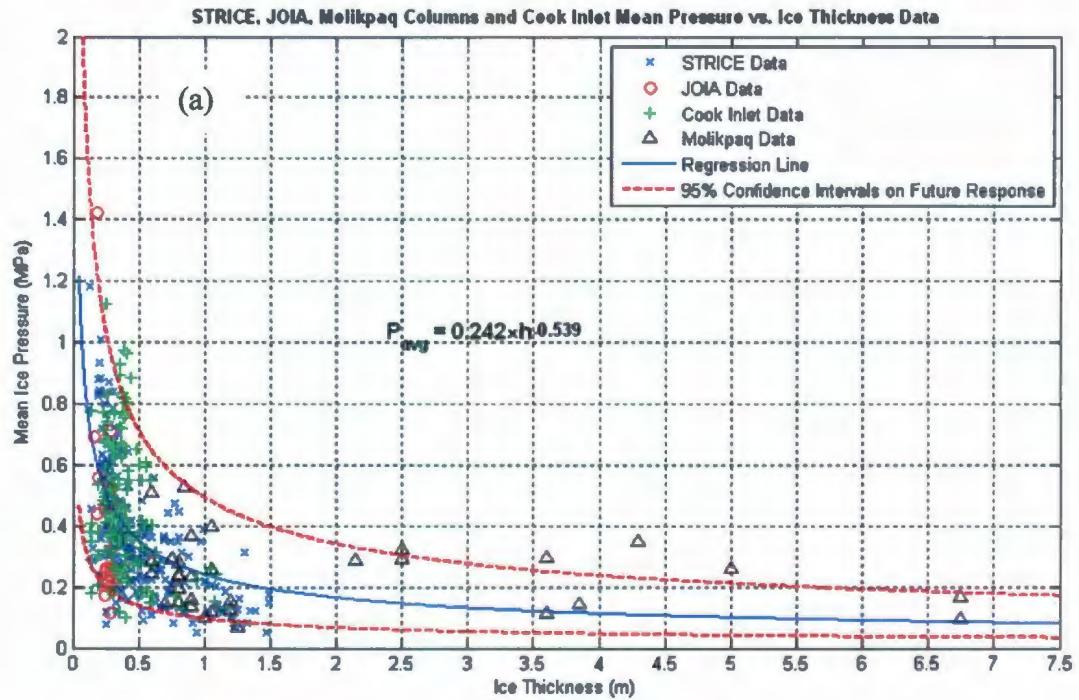


Figure 6.18: Case 7 (Molikpaq recalibration correction on; STRICE level ice filter off, duration filter off; JOIA unfiltered; Cook Inlet data level ice filter off; unweighted mean) data and curve fits for: (a) mean pressure results; (b) standard deviation of pressure results

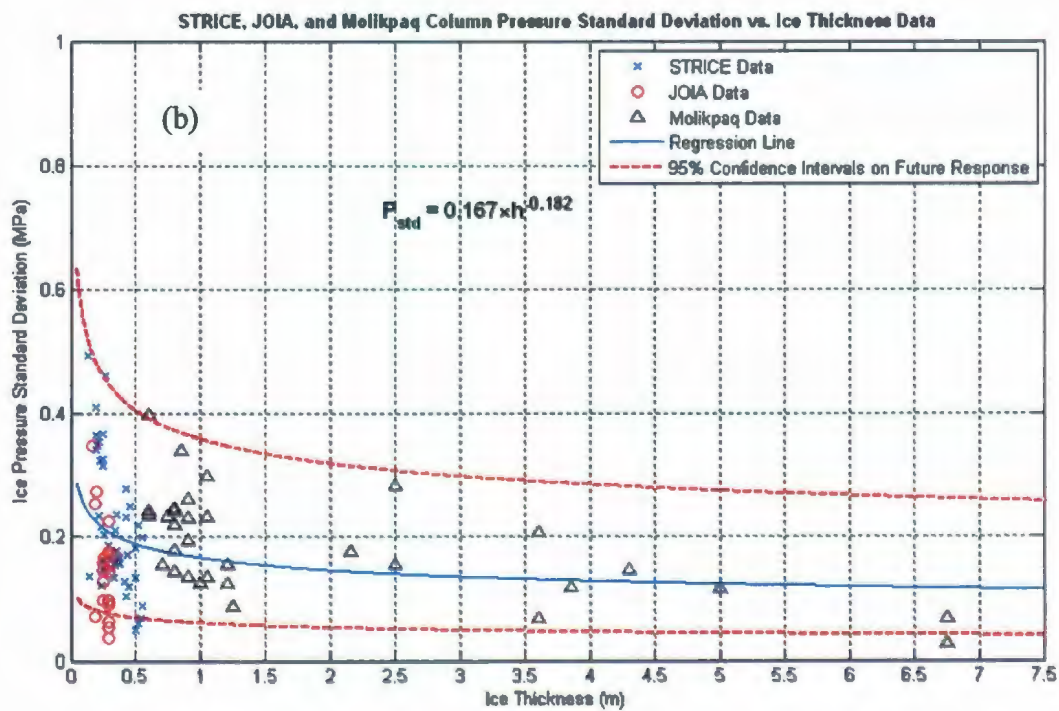
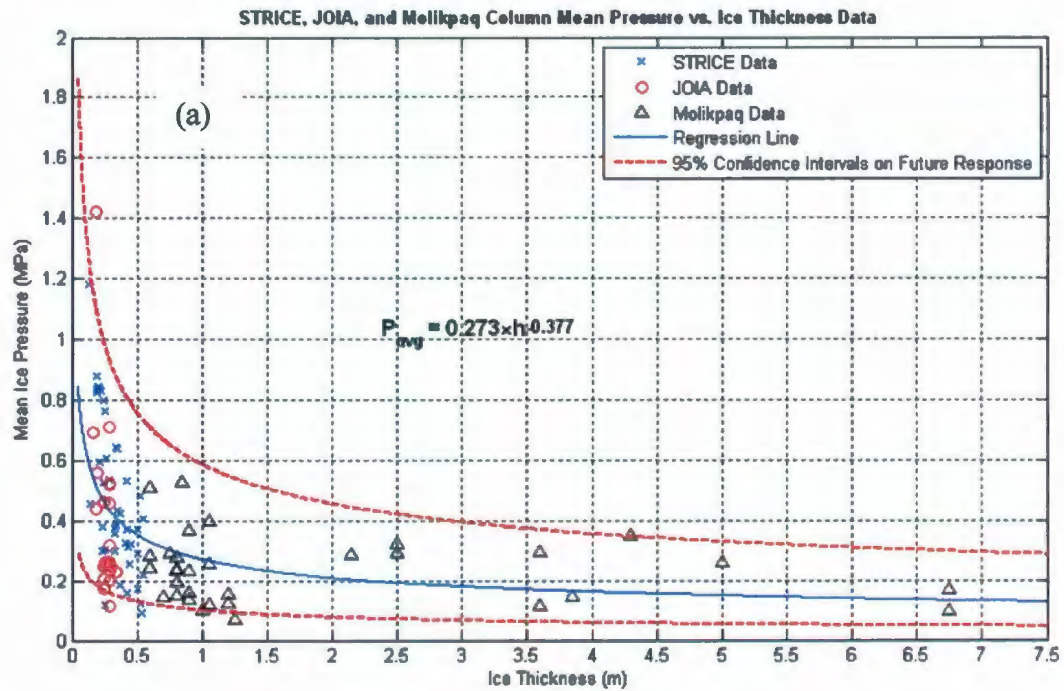


Figure 6.19: Case 8 (Molikpaq recalibration correction on; STRICE level ice filter on, duration filter on; JOIA unfiltered; Cook Inlet data excluded; unweighted mean) data and curve fits for: (a) mean pressure results; (b) standard deviation of pressure results.

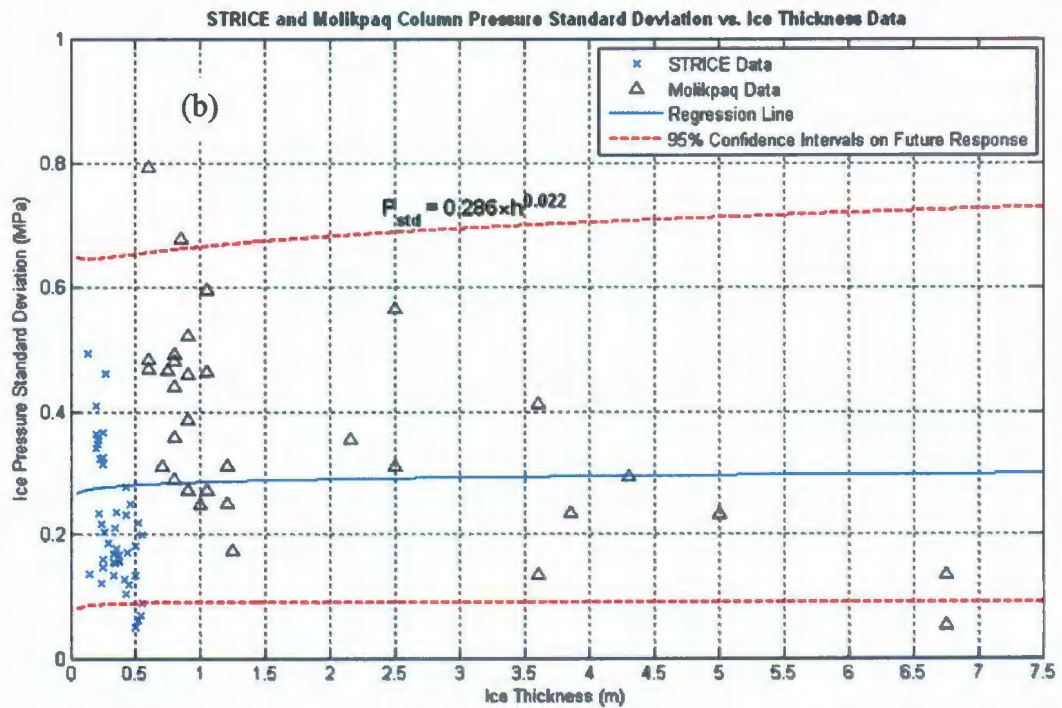
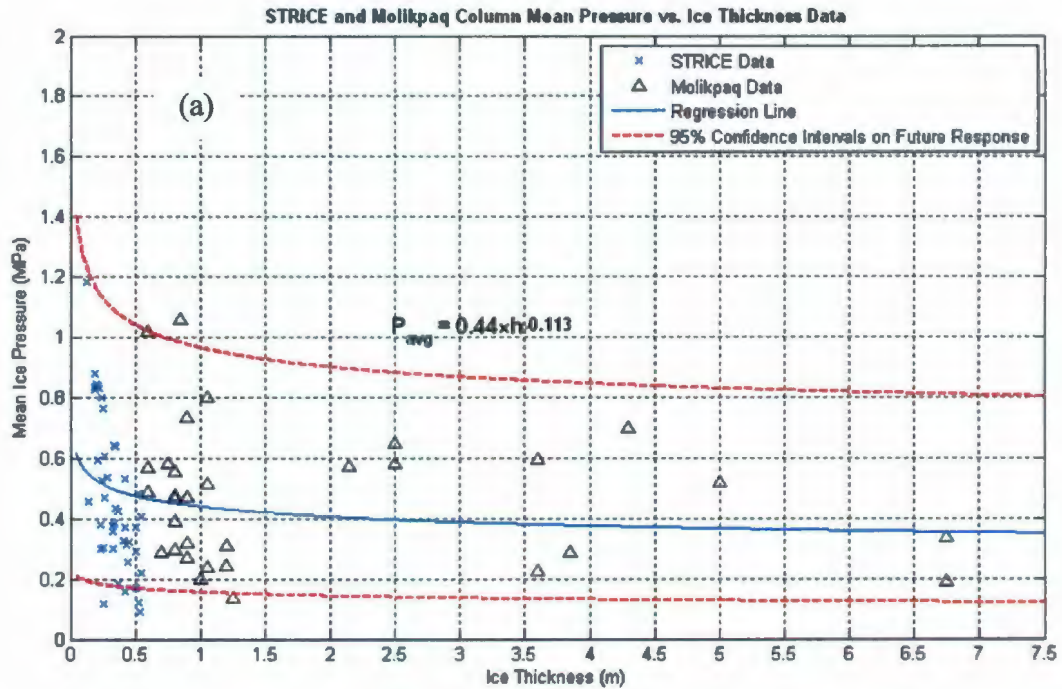


Figure 6.20: Case 9 (Molikpaq recalibration correction off; STRICE level ice filter on, duration filter on; JOIA excluded; Cook Inlet data excluded; unweighted mean) data and curve fits for: (a) mean pressure results; (b) standard deviation of pressure results.

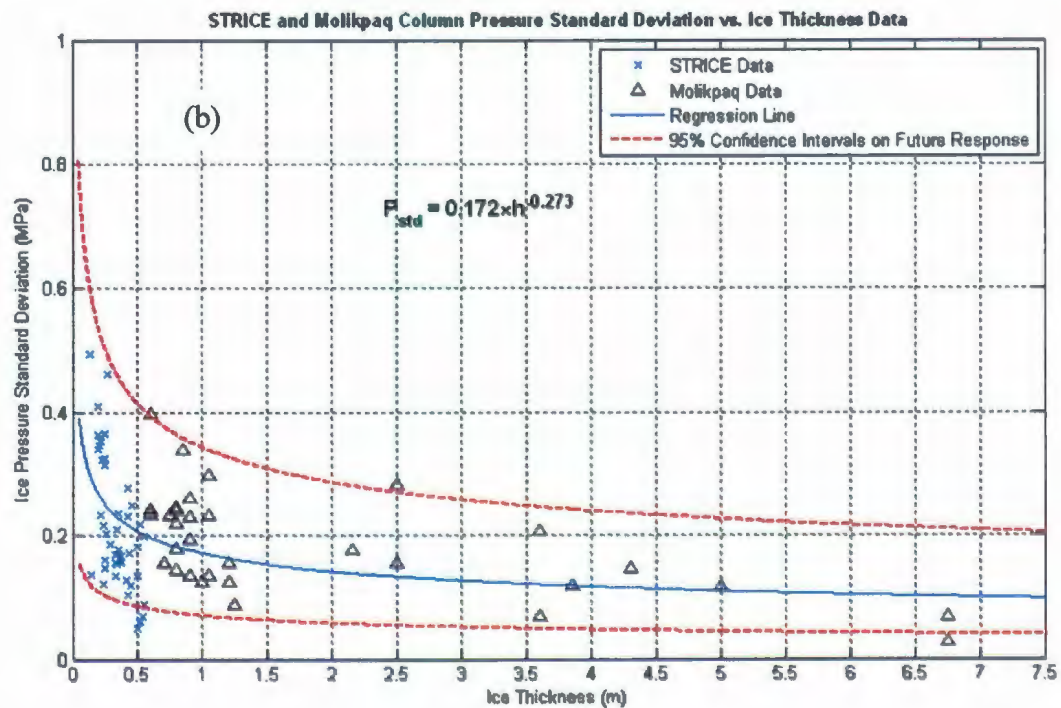
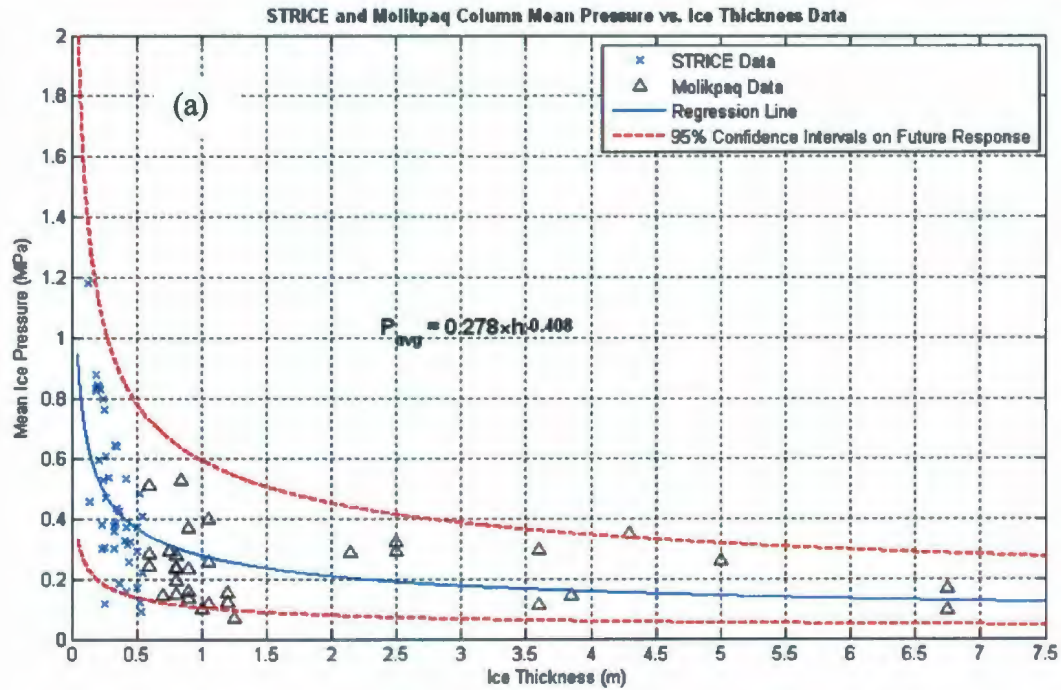


Figure 6.21: Case 10 (Molikpaq recalibration correction on; STRICE level ice filter on, duration filter on; JOIA excluded; Cook Inlet data excluded; unweighted mean) data and curve fits for: (a) mean pressure results; (b) standard deviation of pressure results.

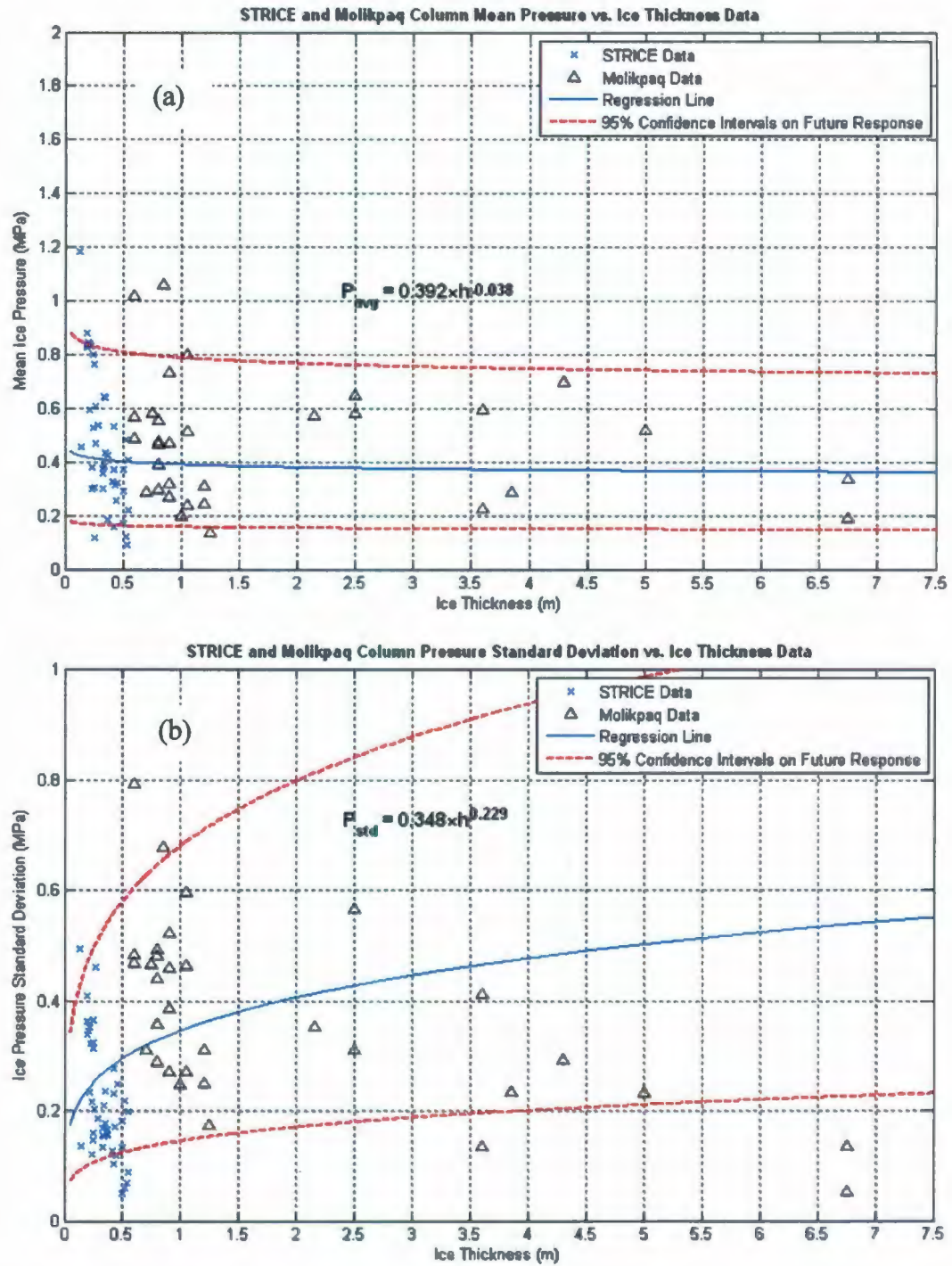


Figure 6.22: Case 11 (Molikpaq recalibration correction off; STRICE level ice filter on, duration filter on; JOIA excluded; Cook Inlet data excluded; weighted mean) data and curve fits for: (a) mean pressure results; (b) standard deviation of pressure results.

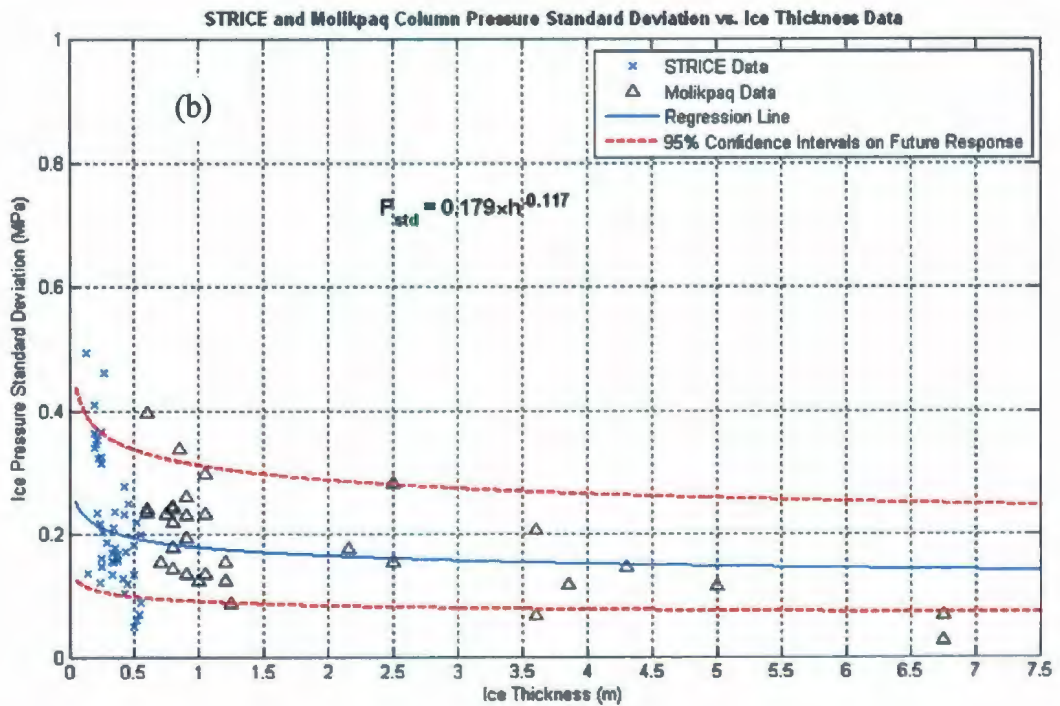
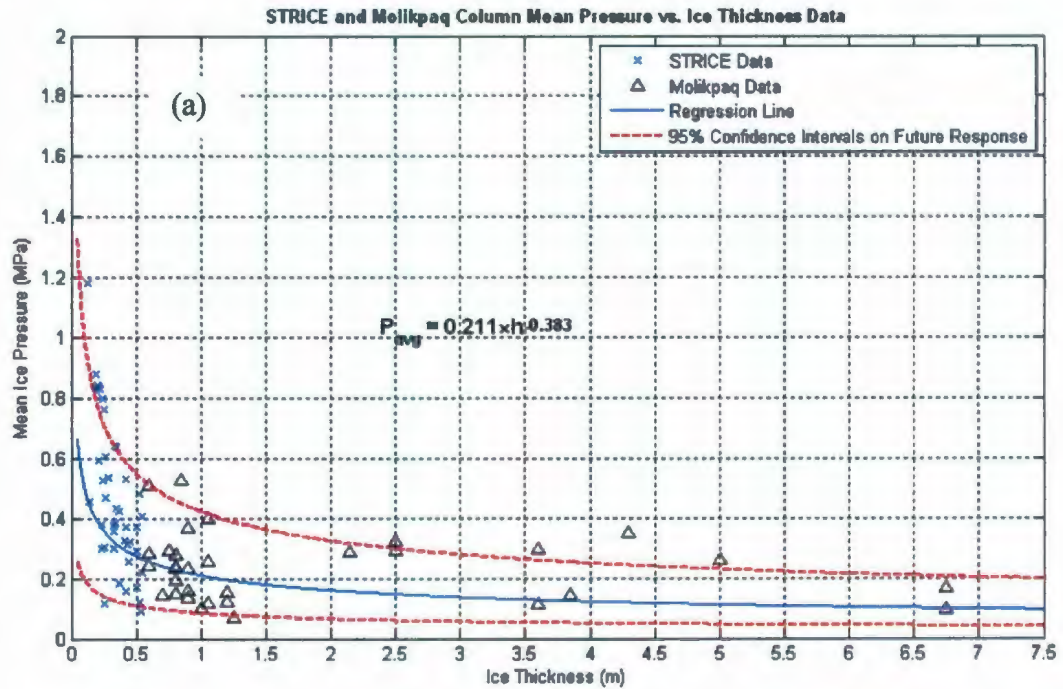


Figure 6.23: Case 12 (Molikpaq recalibration correction on; STRICE level ice filter on, duration filter on; JOIA excluded; Cook Inlet data excluded; weighted mean) data and curve fits for: (a) mean pressure results; (b) standard deviation of pressure results.

6.5.6 Discussion

From the above results it is evident that average local pressures do scale with ice thickness. To assess which analysis case is most representative of the observed pressure-thickness trends, a discussion of different analysis options is given below. The aim in comparing the different cases is to assess which set of analysis criteria produce the most appropriate power law fit to represent the observed pressure-thickness scale effect. Parameter values for each analysis case have been summarized in Table 6.3.

Table 6.3: Power law parameters fit to mean and standard deviation data for analysis cases

Case	$P_{avg} = Ch^D$		$P_{std} = Eh^F$	
	C	D	E	F
1	0.407	-0.128	0.228	0.106
2	0.287	-0.401	0.150	-0.185
3	0.392	-0.058	0.345	0.273
4	0.212	-0.429	0.179	-0.098
5	0.299	-0.384	0.167	-0.182
6	0.211	-0.392	0.179	-0.110
7	0.242	-0.539	0.116	-0.387
8	0.273	-0.377	0.167	-0.182
9	0.440	-0.113	0.286	0.022
10	0.278	-0.408	0.172	-0.273
11	0.392	-0.038	0.348	0.229
12	0.211	-0.383	0.179	-0.117

Effect of recalibration correction

Examining the power law parameters given in Table 6.3, as well as the data presented in Figures 6.12 through 6.23, it is evident that the recalibration correction has a considerable impact on the consistency between the Molikpaq and other datasets. This is particularly evident for standard deviation data (compare for instance Case 11 with Case 12). For cases with uncorrected data, the fitted power law curves for the standard deviation of pressure data often have positive exponents, and yield very poor agreement with the data; see for example Figure 6.22 (b). By comparison, when the Molikpaq data is corrected to account for panel recalibration (i.e. Figure 6.23 (b)) significant improvements in the agreement between the Molikpaq and other data results. On this basis it may be concluded that correcting the

Molikpaq data to account for panel recalibration results in more consistency between the Molikpaq, STRICE, JOIA and Cook Inlet datasets.

Effect of duration weighting

As discussed earlier in the chapter, duration weighting was used in some analysis cases to assign more statistical weight to events with longer durations. For most cases, (i.e. Case 3 and Case 4) using weighted means did not improve the accuracy of the curve fits in bounding the datasets. Depending on the filtering criteria used, different numbers of data points from each dataset are used in the analysis. Sets with more points, or longer total duration have more influence on the fitted curve. In some cases, the result of duration weighting was to produce trend lines which provided a good fit to the data for thin ice, but which did not well bound the data for thick ice events. This may be observed by comparing the unweighted values from Case 10 (Figure 6.21) with those found using weighted means in Case 12 (Figure 6.23). From these figures it is evident that the thin ice events dominate in the weighting process, which results in poor agreement for thicker ice. In general it may be concluded that there are less data for thick ice events, and events in this range have shorter total duration, resulting in a weighting scheme which is biased towards thin ice events.

Effect of STRICE event duration

The effect of removing short duration events from the STRICE dataset may be assessed by comparing Case 2 and Case 5. Duration filters for short STRICE events (less than 10 minutes) were used for Case 5, but not used for Case 2. Comparing Figure 6.13 with Figure 6.16, it may be observed that filtering the short duration STRICE events results in curve fits which better bound the datasets. On this basis it is recommended that the short duration events should be filtered out.

Effect of level ice filters

While thicker ice event data are available within the STRICE and Cook Inlet datasets, the main focus here has been placed on competent level ice. The effect of including the thicker, rafted ice in the analysis may be assessed by comparing Case 7 (level ice filters off; Figure 6.18) with Case 2 (level ice filters on; Figure 6.13). As may be observed from Figure 6.18,

including the thicker ice data in the analysis results in more inconsistencies between the datasets and results in trend lines which do not bound the data as well as those in Figure 6.13. As discussed earlier in the chapter, uncertainties are associated with the degree of consolidation and strength of the thicker, rafted ice. Based on these results it may be concluded that level ice filters are appropriate and only competent ice should be included in the pressure-thickness analysis.

Effect of excluding Cook Inlet and JOIA data

Limited information is available for the Cook Inlet dataset making it difficult to assess which factors influence the data. For instance, if very short duration events were used in the calculation of mean pressures the resulting values may not well represent the true mean pressure during the interaction. In addition, it is not clear if the events correspond to continuous crushing, creep or other failure modes. JOIA events have very short durations and only cover a very narrow range of ice thicknesses. For these reasons, the effects of excluding the Cook Inlet and JOIA datasets have been considered here to gauge how strongly they influence the power law fits to the mean pressure data. Examining the trend lines and prediction intervals for Figures 6.12 through 6.23, it may be observed that the analysis cases that include only the STRICE and Molikpaq data yield the most definitive results.

Checking of regression assumptions

In the above analysis, the power law parameters were estimated by taking logarithms of the data and using a linear least squares fit to estimate the regression parameters. To check normality of the distribution of residuals, a histogram of the residuals was plotted. For the sample case presented in Appendix C.3 (analysis case 10), the data support the assumption of normally distributed residuals with approximately constant variance. In terms of goodness of fit, the observation is made that the residuals behave randomly, which suggests that the model fits the data well; residuals displaying a pattern would indicate a poor fit, but no such pattern is in evidence. Further work to examine the possibility of using other distributions in estimating confidence intervals may be considered in the future. For analysis case 10 the sample consisted of 73 data points and the correlation coefficient of the transformed data was found to be approximately -0.64. The sparseness of available pressure-thickness data presents

challenges for estimating model parameters, which highlights the importance of properly accounting for modeling uncertainties when estimating loads based on empirical results.

6.6 Summary and Conclusions

Based on the above analysis it may be concluded that a definitive pressure thickness relationship was observed for full-scale panel measurements. A panel of constant width experiences decreasing pressure over the loaded area for increasing ice thickness. This is in general agreement with the well known pressure-area scale effect for ice. In the absence of a recalibration correction for the Medof panel, the trends of the Molikpaq data are not consistent with the other data. Accounting for recalibration yields results that are much more consistent with those observed from the STRICE, JOIA and Cook Inlet datasets.

A representative power law for the pressure-thickness effect observed in the STRICE and corrected Molikpaq data (Case 10), may be modeled using the power law curves:

$$P_{avg} = 0.278h^{-0.408}, \quad (6.1)$$

$$P_{std} = 0.172h^{-0.273}. \quad (6.2)$$

For the analyses performed here, more data exists for thin ice events than for thick ice. As a result, duration weighting results in trends that are highly influenced by the thin ice events. Duration weighting was observed to produce curves which did not bound the thick ice event data as well as curves based on unweighted values. Further work is recommended to examine more fully the influence of duration weighting and determine a more effective approach. It was also noticed during the above analysis that time based weighting assigns a higher weight to the slower speed events (this was particularly the case for the JOIA results). For full-scale data this results from the fact that it takes a longer time for a slow moving floe to cover the same interaction distance compared with a fast moving floe. A possible alternative approach to explore in future work is the use of interaction distance (duration x speed) as a weighting measure in the assessment of overall mean and standard deviations.

The analysis of indentation data for ice specimens with remote edges earlier in the chapter suggests a clear link between the onset of spalling fracture (at higher speeds) and the onset of scale dependent pressure behavior. This result suggests that spalling fracture is a key aspect of the observed pressure thickness scale effect. Theoretical aspects of spalling fracture and thickness scaling of pressure are investigated in Chapter 7.

Chapter 7: Theoretical Analysis of Pressure-Thickness Scaling

7.1 Scope

In this chapter the spalling failure of ice was studied with the aim of establishing a sound theoretical basis for linking the observed pressure-thickness scale effect with probabilistic aspects of spalling fracture. The first section of this chapter provides an overview of an idealized ice failure process, and includes analysis results for a sample JOIA event taken as a benchmark for comparison with the theoretical results. The idealized ice edge geometry and loading distributions are defined. Finite element analysis was applied to model the elastic stress distribution in the near field region of an ice sheet subject to a parabolic pressure distribution. Stress analysis results are used as inputs into subsequent probabilistic models. A Weibull (tensile) failure model was applied to ice and used to estimate the probability of failure for the selected analysis case. To study more explicitly the links between ice failure and flaws, a probabilistic fracture mechanics (PFM) model has been developed. This model accounts for both tensile and compressive (shear) fracture modes. The PFM model was then implemented to study the dependence of pressure on thickness. The influence of ice edge shape and the effect of *hpz* eccentricity on pressure scaling were also studied using the PFM model. Recommendations for future work are made.

7.2 Introduction

In developing a theoretical model of ice failure, it was first necessary to characterize the failure process and establish a benchmark to guide model development and parameter selection. It was also necessary to make simplifying assumptions and to define geometry and loading conditions.

7.2.1 Overview of the Ice Failure Process

During an interaction between a vertical-walled structure and an ice sheet, pressure tends to increase monotonically as the ice advances. Depending on factors such as the damage state, stress conditions and characteristics of flaws in the ice, either crushing failure or spalling fracture may result in a drop in load. Crushing failure can result in either random or cyclic load drops during an interaction; see Figure 7.1 (a). Since the present analysis is focused on spalling fracture, the pressure (corresponding to a nominal area determined by the product of the ice thickness and the unit (1m) width of a measurement panel) during a crushing event is modeled as an equivalent mean value of monotonically increasing pressure. The overall ice failure process, as depicted in Figure 7.1 (a) is then assumed to be a sequence of successive individual fracture events, such as the one depicted in Figure 7.1 (b).

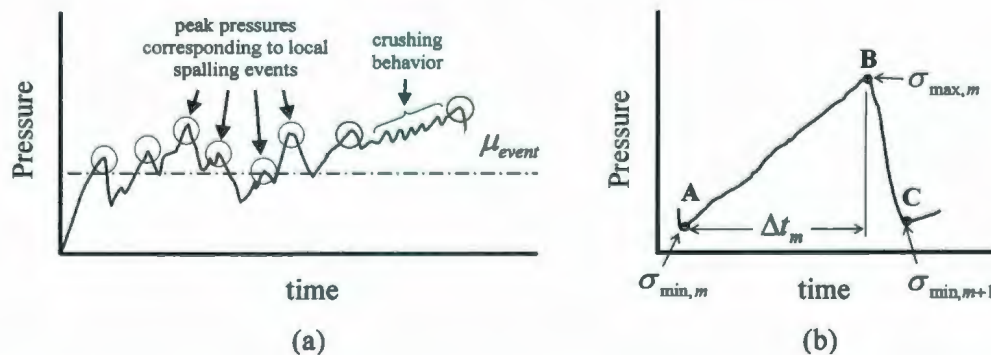


Figure 7.1: Illustrations of: (a) an idealized pressure time trace showing peak pressures, crushing behavior and overall event mean pressure; (b) idealization of a fracture event comprised of a loading phase (AB), a fracture event (B) and a consequence phase (BC).

As illustrated in Figure 7.1 (b), each spalling fracture event may be characterized by three distinct points: (A) the pressure starts from some minimum value and begins to increase monotonically as the ice floe advances; (B) at some critical value of pressure an unstable fracture event occurs, resulting in the limiting of local load build up and the onset of a drop in load as the spall is removed; (C) the spall has been expelled and contact forces are redistributed, which results in the end of one fracture event, and the beginning of a new event.

During the first phase the load increases at a rate that depends on factors such as the drift speed of the ice floe, as well as the local ice conditions (for instance, the extent of softening, ice edge geometry). The second phase, the occurrence of a peak pressure, is assumed to be governed by fracture mechanics. At some given stress level fracture initiates at internal stress raisers (for instance, large, favorably oriented grain boundaries). Sufficiently stressed tensile cracks may propagate in an unstable manner, while shear cracks may grow stably until they interact with a free surface. Upon becoming unstable, a propagating crack is assumed to grow rapidly resulting in the separation of a spall of ice from the edge of the ice sheet. Since fracture depends on flaw size, location, orientation, density and the local stress field, a distribution of peak pressures is expected.

The third phase, the drop in load, will depend on the extent of the spall (i.e. size, location, and shape), the clearing process and how the load is redistributed following failure. It is assumed here that the failed ice clears immediately from the contact zone and that a new high pressure zone results. Each successive *hpz* is assumed to have a parabolic load distribution, with ice edge geometry as defined in the section below. Analysis here is focused on modeling the process up to the point of failure (i.e. up to Point B in Figure 7.1 (b)).

7.2.2 Analysis of Tactile Sensor Data for Sample Event

To guide model development and assist with the calibration of parameters, a representative sample event from the JOIA dataset was analyzed. The aim of this task was to characterize statistical attributes of the process.

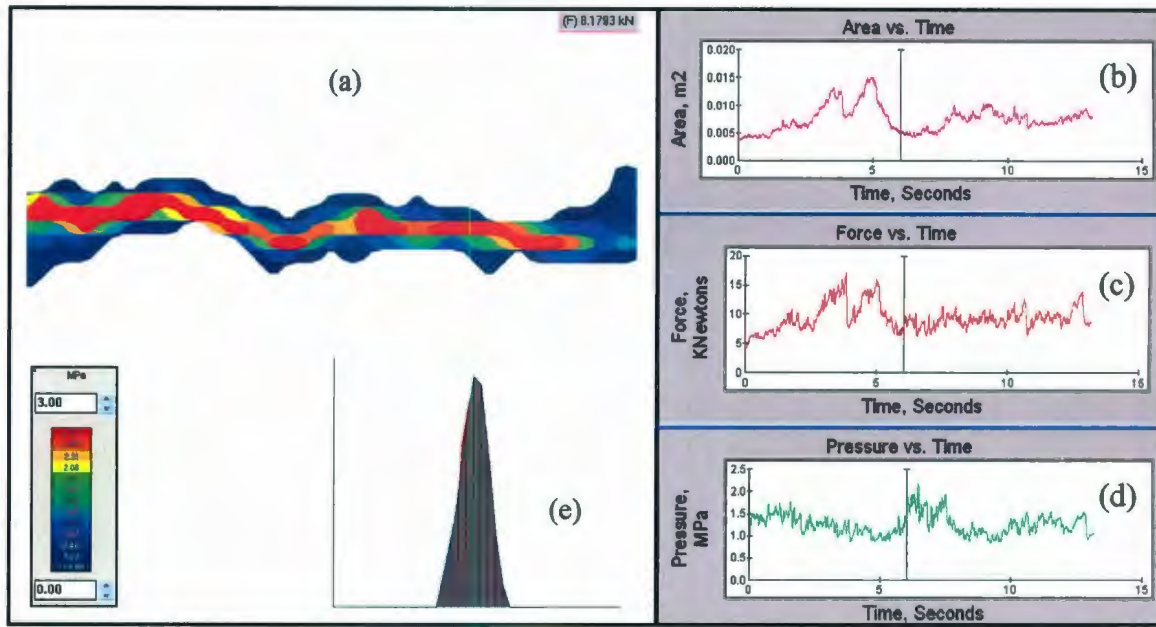


Figure 7.2: Results from analysis of tactile data for sample JOIA event, showing: (a) pressure distribution at $t \approx 6$ sec; (b) time series plot of contact area; (c) time series plot of total forces; (d) time series plot of contact pressure; (e) cross-section of pressure through an *hpz*.

The selected event (980121-2; see Table 5.5 for details) corresponded to a fast indentation rate (3 cm/s) and an ice thickness of 28.7 cm; see Figure 7.2. The tactile sensor for this event consisted of a single panel containing a 44×44 array of sensor elements (sensels), with overall panel dimensions of approximately $0.229\text{m} \times 0.229\text{m}$. The nominal area would be panel width (0.229m) \times ice thickness (0.287m), giving a value of approximately 0.07m^2 . From the tactile data, the mean contact area was determined to be approximately 0.008m^2 , as is calculated from the product of the number of active sensels and the area of each individual sensel. This indicates that the contact area is approximately 10% of the nominal area for the given event. This agrees well with the tactile data analysis results from Chapter 5.

The mean contact area is modeled as being approximately 10% of the nominal area. Assuming a panel is fully loaded across the width, this suggests that an *hpz* with average height $2q$ corresponds to approximately 10% of the ice thickness h , yielding the assumed geometric relationship $2q = 0.1 \times h$.

For this event, the mean overall pressure was approximately 0.1425 MPa, as calculated by dividing the average force by the nominal area, and the standard deviation of overall pressure was found to be 0.0331 MPa. The mean contact pressure (total force over the average contact area), was about 1.3 MPa.

It is recognized that the ice for the JOIA test program is columnar ice. Columnar ice compressed across the columns, as is the case during ice-structure interaction, has brittle crushing strength that is essentially indistinguishable from that of granular ice of the same grain size (Schulson and Duval, 2009). This suggests fracture processes are governed by similar size flaws for both cases. In the present model flaws are assumed to be randomly oriented. It is recommended that the effects of preferential flaw orientation be examined in future work.

7.2.3 Problem Definition for Analysis of Ice Edge Spalling

Unstable crack growth emanating from the competent ice in the near field region behind the contact zone is assumed to be the primary mechanism resulting in spalling fracture. In the probabilistic fracture mechanics (PFM) model developed in this chapter, expressions for the probability of spalling as a function of stress, random flaw size and orientation have been developed, implemented in Matlab and used to study the pressure-thickness scale effect. It is assumed that tensile fracture is unstable and compression (shear) induced fracture is stable until a crack reaches a free surface, after which it becomes unstable.

As a result of spalling and progressive failure, the shape of the edge of the ice sheet geometry evolves throughout the interaction processes. While the true shape at any given instant may be somewhat irregular, to a reasonable approximation, the edge can be modeled as a truncated wedge. Matskevitch and Jordaan (1996) showed that certain geometries promote the formation of local zones of tensile and shear stresses. For a three-dimensional ice sheet, the edge geometry may be idealized as shown in Figure 7.3. Since an ice sheet is very wide in the z direction, it is assumed here that negligible strain occurs in this direction (i.e. $\epsilon_z = 0$). This allows for approximation using a two-dimensional plane strain analysis. This is discussed in further detail later in the chapter.

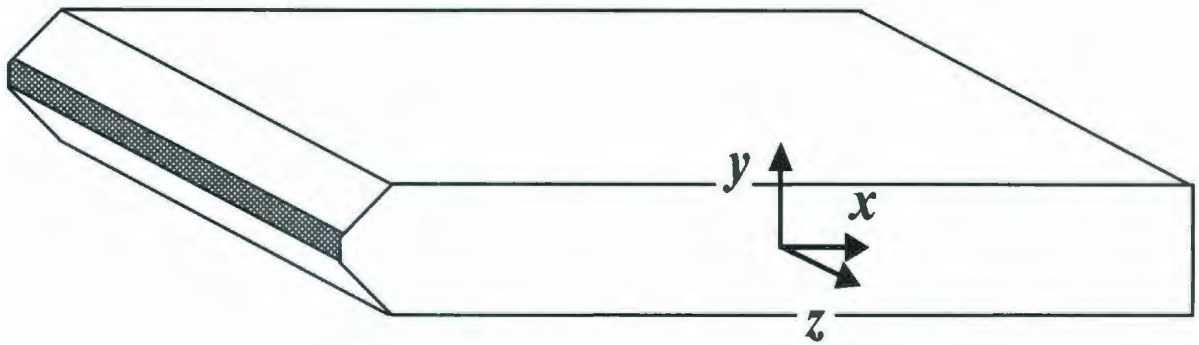


Figure 7.3: Three dimensional idealization of semi-infinite ice sheet.

For a two-dimensional analysis, the ice edge geometry has been idealized as shown in Figure 7.4. The contact zone at the interaction interface is assumed to have a width of $2q$, which is assumed to be a fixed percent of the total ice thickness h ; see Figure 7.4 (a).

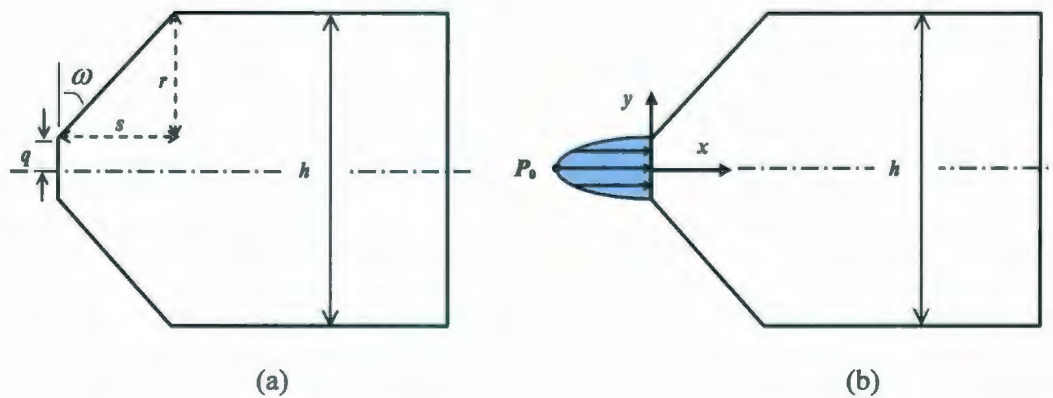


Figure 7.4: Two dimensional idealization of ice edge on interaction face, showing (a) edge geometry; (b) assumed pressure distribution.

Based on analysis results for the sample JOIA event considered in Section 7.2.2, the contact width has been modeled as being 10% of the overall ice thickness (i.e. contact width = $2q = 0.1 \times h$). The ice edge shown in Figure 7.4 has been modeled as having an ‘effective taper angle’, ω (in degrees). The slope of this edge has been defined by the rise r and run s ,

where $\tan \omega = s/r$. From geometry, the rise r is a fixed proportion of thickness ($r = h/2 - q = 0.45h$) for an h pz centered in the thickness of the sheet. The run s has been specified in the model based on the analysis case selected ($s = 0$ corresponds to a flat, vertical ice edge).

The pressure has been assumed to follow a parabolic distribution (see Figure 7.2 (e); see also earlier damage mechanics analysis by Xiao, 1991). This is taken to represent the pressure corresponding to a vertical slice through the center of a single elongated h pz. For the above geometry, the equation for the parabolic distribution is given as:

$$P(y) = 1 - 400 \frac{y^2}{h^2} . \quad (7.1)$$

As shown in Figure 7.4 (b), the maximum peak pressure P_0 occurs at $x = 0$, and the pressure is zero at $y = \pm q$. Since the parabolic pressure distribution above is defined in terms of the peak pressure P_0 at the center of the distribution, it is of interest to also calculate the mean contact pressure (i.e. average pressure over contact area), as well as the overall mean pressure (i.e. average pressure taken over entire thickness). The total force is the area under the parabolic pressure curve (with base = $2q$, and the height = P_0), as given by the expression:

$$F_{Total} = \frac{2}{3} (2q)(P_0) . \quad (7.2)$$

The mean contact pressure \bar{P}_c is the total force divided by the contact width $2q$, given as:

$$\bar{P}_c = \frac{2/3(2q)(P_0)}{2q} = \frac{2}{3} P_0 . \quad (7.3)$$

The overall mean pressure \bar{P}_h is the total force taken over the ice thickness h . Substituting the contact width definition ($2q = h/10$) into Eq. 7.2 and dividing by h , we may write:

$$\bar{P}_h = \frac{2/3(h/10)(P_0)}{h} = \frac{1}{10} \left(\frac{2}{3} P_0 \right) = \frac{\bar{P}_c}{10}. \quad (7.4)$$

Using the above expressions, it is possible to calculate the mean contact pressure \bar{P}_c and the mean overall pressure \bar{P}_h corresponding to a given peak pressure P_0 and a contact zone of width $2q$. Details of the stress analysis are discussed below.

7.3 Elastic Stress Field Analysis

For local fracture of an ice sheet specimen, the region of interest is the near field zone adjacent to the interaction interface. In the present work, focus is placed on the elastic field in the region behind the damage layer; see section 3.2.3 for discussion of the elastic approximation of ice. It is assumed here that the spalling fractures must emanate from the ‘competent’ ice in the elastic field. The highly damaged ice in the layer is locally very soft, and will fail due to material mismatch, not as a result of brittle crack propagation. As illustrated in Figure 7.6, zones of shear and tension in the near field region are believed to be the most probable sites for unstable crack growth leading to the formation of spalls.

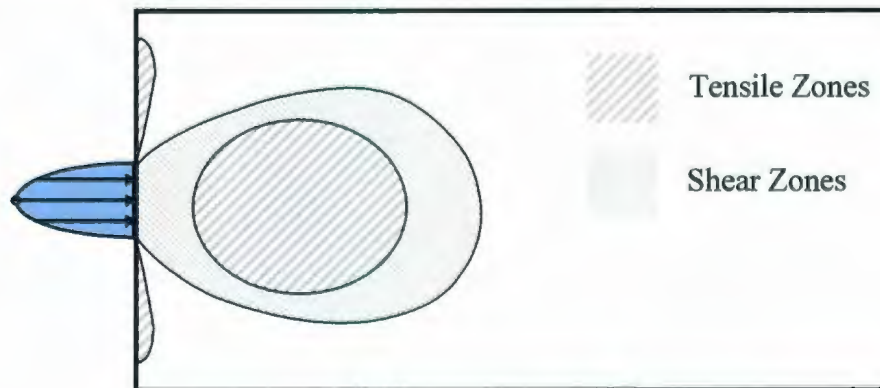


Figure 7.5: Illustration of zones for potential shear and tensile cracking.

As a starting point for a probabilistic failure analysis, it is important to model the stress in this zone. Strictly speaking ice is a damaging, viscoelastic medium. For faster loading rates, such as those of interest here, the analysis may be simplified by considering only the linear elastic stresses. This assumption has been used here.

7.3.1 Background

The assumption of plane strain conditions has been made for this region based on the extent of lateral constraint offered through the width of the ice sheet. Since an ice sheet is assumed to be very wide relative to the thickness of the ice, the out of plane strain components are assumed to be negligible. The strain tensor can then be approximated as:

$$\varepsilon_{ij} = \begin{bmatrix} \varepsilon_{11} & \varepsilon_{12} & 0 \\ \varepsilon_{21} & \varepsilon_{22} & 0 \\ 0 & 0 & 0 \end{bmatrix}. \quad (7.5)$$

The corresponding stress tensor σ_{ij} for these conditions is:

$$\sigma_{ij} = \begin{bmatrix} \sigma_{11} & \sigma_{12} & 0 \\ \sigma_{21} & \sigma_{22} & 0 \\ 0 & 0 & \sigma_{33} \end{bmatrix}. \quad (7.6)$$

While a non-zero value of stress σ_{33} is required to maintain the out of plane constraint, to allow for a two-dimensional analysis the stress tensor for plane strain is simplified as given in Eq. 7.7 (defining $\sigma_{11} = \sigma_x$, $\sigma_{22} = \sigma_y$ and $\tau_{xy} = \tau_{yx} = \sigma_{12} = \sigma_{21}$).

$$\sigma_{ij} = \begin{bmatrix} \sigma_x & \tau_{xy} \\ \tau_{xy} & \sigma_y \end{bmatrix}. \quad (7.7)$$

Similarly the strain tensor was reduced to the two-dimensional case by eliminating all empty (zero) elements from Eq. 7.5. Unless stated otherwise, the fracture toughness values used throughout this study also correspond to plane strain conditions.

In studying ice fracture both shear and tensile stresses are of interest. From continuum mechanics it has been shown for an element subject to combined normal and shear stresses that a plane of maximum principal stresses may be defined which experience zero shear. On this basis it is possible to describe the stress state of individual elements in terms of elemental principal stresses, σ_1 and σ_2 . Finite element analysis solutions have been used to estimate

the three stress components (σ_x , σ_y and τ_{xy}) for each element. As illustrated in Figure 7.6, these three stress components can be reduced to two stress components by transforming them to the principal plane (recall that there is zero shear on the principal plane).

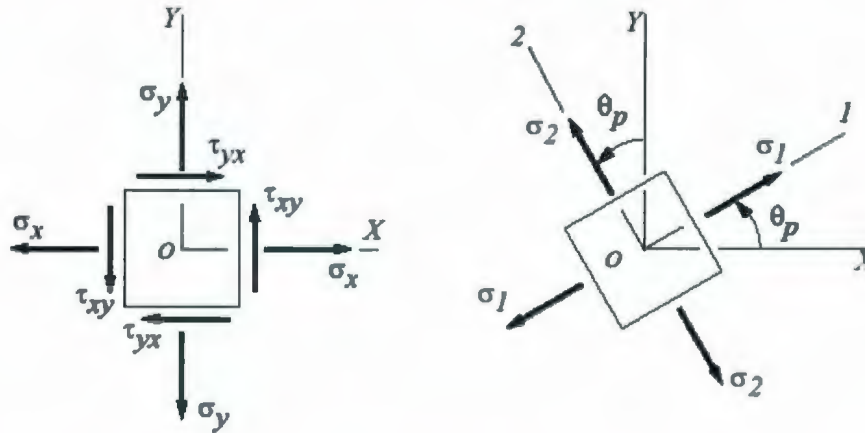


Figure 7.6: Illustration of element stress components for a two-dimensional general state of stress (left) and stress components after transformation to the principal plane (right).

The magnitudes of the principal stress components are found using the equation:

$$\sigma_{1,2} = \frac{\sigma_x + \sigma_y}{2} \pm \sqrt{\left(\frac{\sigma_x - \sigma_y}{2}\right)^2 + \tau_{xy}^2}, \quad (7.8)$$

where σ_1 is the maximum principal stress and σ_2 is the minimum principal stress. The convention in Eq. 7.6 is that tension is positive, compression is negative. The principal angle θ_p , as shown in Figure 7.6, may be found using the expression:

$$\tan 2\theta_p = \frac{2\tau_{xy}}{\sigma_x - \sigma_y}. \quad (7.9)$$

Recalling Mohr's circle for a two-dimensional state of stress (Figure 7.7), we see that three possible combinations of principal stress states may exist: biaxial tension, tension with lateral confinement or biaxial compression. It is recognized that for plane strain conditions, there will be some non-zero, out of plane component of stress, so the term 'biaxial' is not strictly

correct. For simplicity, the term ‘biaxial tension’ is used to refer to the case where both σ_1 and σ_2 are tensile. Similarly, ‘biaxial compression’ refers to the case where both σ_1 and σ_2 are compressive. The ‘tension with lateral confinement’ case refers to an element with tensile σ_1 and compressive σ_2 .

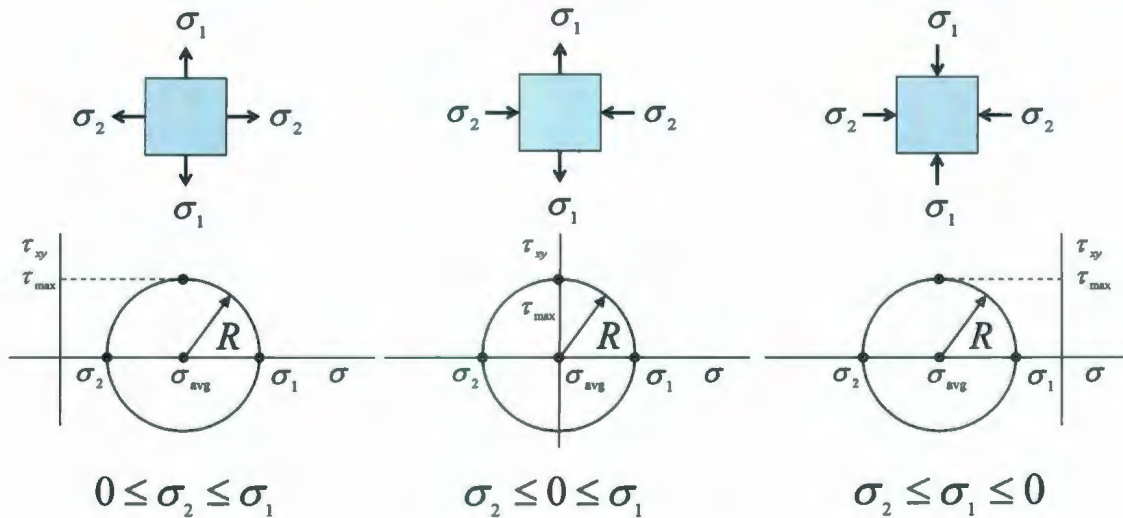


Figure 7.7: Mohr's circle for a two-dimensional element subject to: loading case 1 (left); loading case 2 (centre); loading case 3 (right).

For the Weibull failure model, only positive (tensile) principal stresses are of interest, since it is assumed in this model that elements with zero or negative (compressive) principal stresses cannot fail. In the probabilistic fracture mechanics model developed later in this chapter, three loading cases are specified to account for all possible stress states. These three loading cases are referred to as: (1) ‘biaxial tension’; (2) ‘tension with lateral confinement’; (3) ‘biaxial compression’. To solve the elastic stresses for the geometry and loading conditions specified in Figure 7.7, finite element analysis solutions were generated using the software package ABAQUS.

7.3.2 Finite Element Implementation

Finite element analysis solutions were generated using the software package ABAQUS. For the analysis case of interest, the geometry of the ice edge was created in the ABAQUS part

module and meshed with quadrilateral plane strain elements (type CPE4R). Throughout the present analysis, a constant mesh size of 0.01m x 0.01m was used.

The ice edge geometry was defined based on the parameters outlined in Figure 7.4. The sample meshed geometry shown in Figure 7.8 corresponds to an effective taper angle of $\omega = 0$ (i.e. a flat edge), an overall thickness of $h = 1.0$ m and a contact area with dimensions $2q = 0.1$ m. Based on preliminary analysis, it was determined that a region with a length in the x-direction of about $1.5h$ encapsulates the near field stresses. Since only the results from the near field zone are of interest in the present work, the model geometry was partitioned at a distance of $1.5h$ from the front edge. To model the semi-infinite length of the idealized ice sheet in the x-direction, the overall length of the specimen was defined such that portion of the model beyond the near field zone is about $10h$. A fixed boundary condition was applied to the remote rear face of the model.

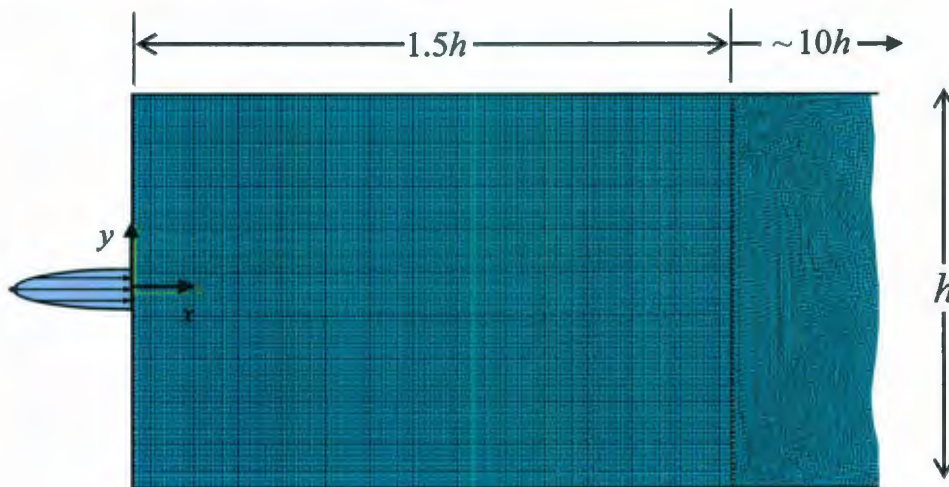


Figure 7.8: Meshed geometry for sample analysis case.

The material model applied to the specimen was a linear elastic model with $E = 9.0$ GPa, and $\nu = 0.3$. The parabolic pressure function given by Eq. 7.2 was implemented and applied over the contact zone. A magnitude of $P_0 = 1.0$ MPa was specified for the pressure function. The selected outputs for the model included the element volumes, stress components at the element centroids and the coordinates of the element centroids.

Once the analysis is completed, a field output report is generated to export the desired information (element volumes, element centroids, and stress components σ_{xx} , σ_{yy} , τ_{xy}) to a .txt file that could be imported into Matlab. Contour plots of stress components σ_{xx} and σ_{yy} are shown in Figure 7.9 (a) and Figure 7.9 (b), respectively for the sample event.

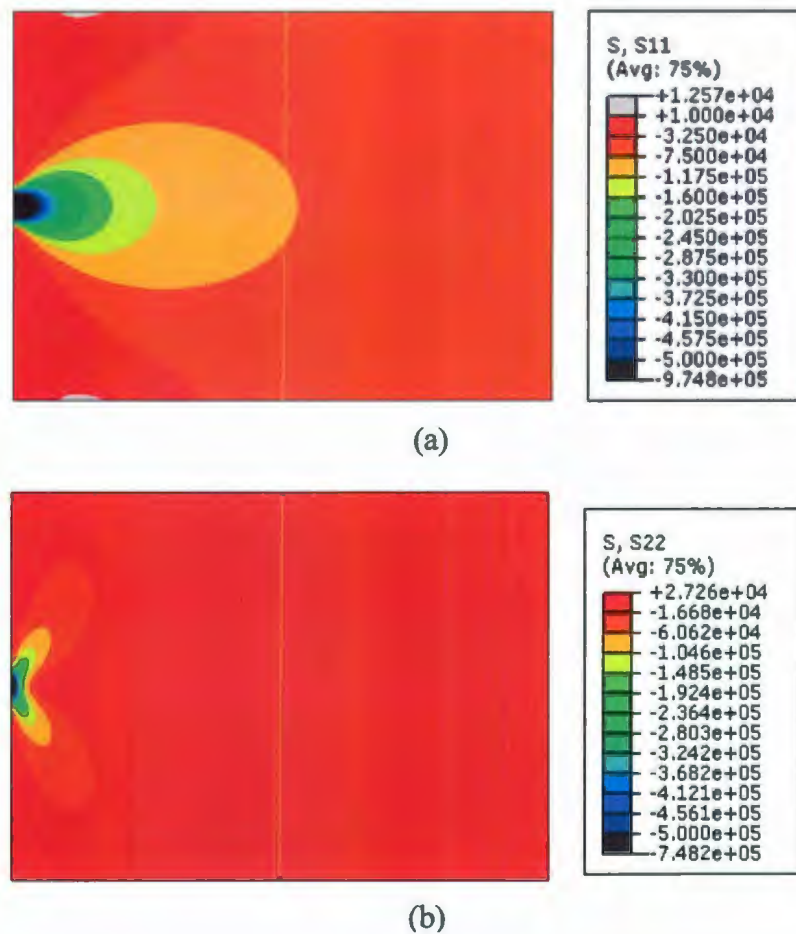


Figure 7.9: Stress contour plots for sample event showing: (a) σ_{xx} ; (b) σ_{yy} .

Inside the Matlab environment, the elemental volumes and stress components were compiled and the principal stresses were calculated using Eq. 7.8. Similarly, the principal angles were calculated using Eq. 7.9. These outputs of this stress analysis were then taken as inputs into the probabilistic failure models described below.

7.4 Weibull Failure Model

As discussed in Chapter 4, weakest-link models were developed for tensile loading where failure of a link leads to failure of the specimen (Weibull, 1951). Weibull's approach did not directly consider the influence of the flaw distribution, but rather modeled specimen failure using a material function to characterize behavior. In the analysis below it is assumed that the peak pressure distribution may be modeled by a weakest link process based on Weibull theory modified to account for heterogeneous stress conditions.

7.4.1 Overview of Weibull Model

For the present analysis, the discretized form in Eq. 4.19 is of greatest interest. Assuming $\sigma_0 = 0$ and substituting Eq. 4.21 into Eq. 4.19 yields the expression:

$$F_w(\sigma) = 1 - \exp \left[-\frac{1}{v_0} \sum_{i=1}^n \left(\Delta V_i \left(\frac{\sigma(x_i)}{\sigma_w} \right)^{\alpha_w} \right) \right], \quad (7.10)$$

where $\sigma(x_i)$ is taken as the maximum principal stress in the i^{th} element at location x_i . Here proportional stressing was assumed, allowing the stress in each element to be normalized by a reference stress value r as given by:

$$\sigma(x_i) = r\sigma'(x_i), \quad (7.11)$$

where $\sigma'(x_i)$ is the normalized stress distribution. In the present analysis, the function $\sigma'(x_i)$ was solved from the array of elemental stresses $\sigma(x_i)$ obtained from a finite element solution for the desired geometry and loading. The reference state r used to define $\sigma'(x_i)$ throughout the present work corresponded to a peak *hpz* pressure of $r = P_0 = 1.0$ MPa. The $\sigma(x_i)$ array was then normalized by dividing by the scalar value P_0 , to give the array $\sigma'(x_i)$. Once the $\sigma'(x_i)$ array was determined, elemental stresses could be calculated for any other value of r using Eq. 7.11. Substituting Eq. 7.11 into Eq. 7.10 gives:

$$F_W(\sigma) = 1 - \exp \left[-\frac{1}{v_0} \sum_{i=1}^n \left(\Delta V_i \left(\frac{r\sigma'(x_i)}{\sigma_W} \right)^{\alpha_W} \right) \right], \quad (7.12)$$

Classical Weibull theory is only valid for specimens in tension, where brittle failure (i.e. unstable fracture) is assumed to occur once the strength of the weakest link is exceeded. On this basis, only the subset of elements with positive (tensile) principal stresses were included in the analysis. Jordaan (2005) discusses the subset of tensile elements in terms of a 'reduced volume' concept. In the present study, Eq. 7.12 has been implemented in a Matlab routine using stress and volume information from finite element solutions. In this routine, only tensile elements are included; elements with zero or negative maximum principal stresses are assumed to have a failure probability of zero.

7.4.2 Implementation of Weibull Model (Tension Only)

Values for the model parameters (v_0, σ_W, α_W) used in this analysis were based on the work of Parsons et al. (1992). These values are summarized in Table 7.1.

Table 7.1: Weibull parameter values for freshwater ice (after Parsons et al., 1992)

Parameter	Specimen Volume		
	$V = 0.027 \times 10^{-2} \text{ m}^3$	$V = 0.216 \times 10^{-2} \text{ m}^3$	$V = 2.197 \times 10^{-2} \text{ m}^3$
α_W	4.380	4.403	4.765
σ_W	0.940	1.044	2.210
v_0	10^{-2} m^3	10^{-2} m^3	10^{-2} m^3

Using the three sets of parameter values from Table 7.1, a sample specimen with overall thickness of $h = 1.0 \text{ m}$, a contact area with a dimensions $2q = 0.1 \text{ m}$ and an effective taper angle of $\omega = 0$ (i.e. a flat edge) was examined; see Figure 7.9 for sample contour plots of stress for this specimen. Failure probability estimates for each of the above sets of parameters are given in Figure 7.10.

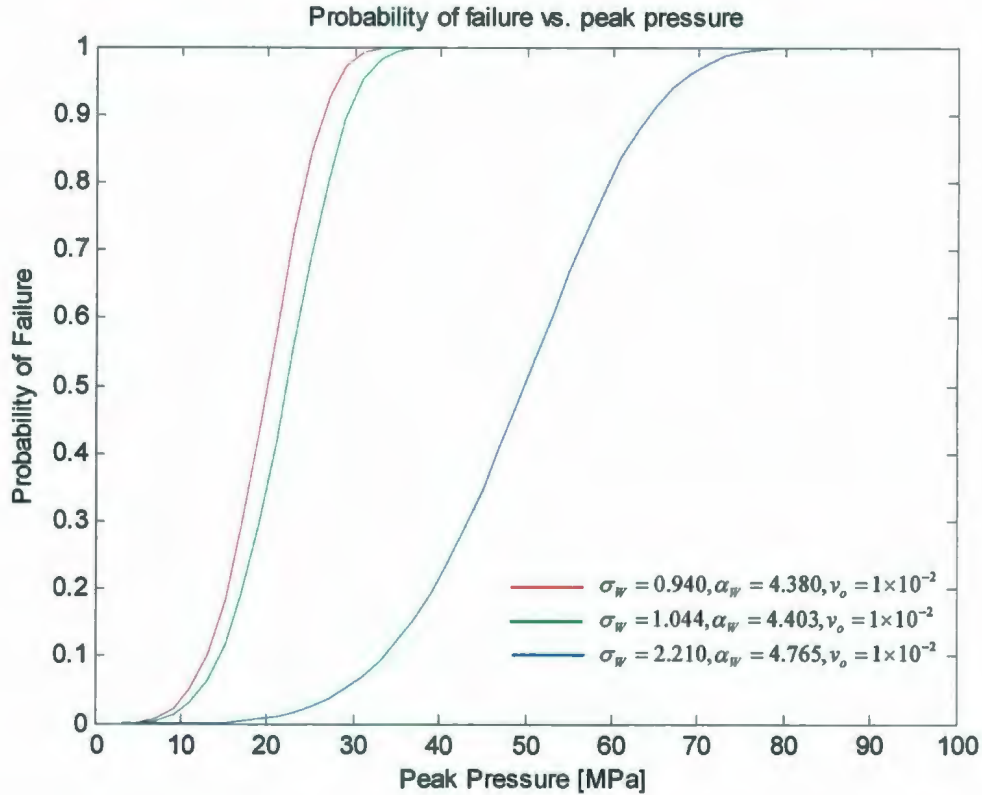


Figure 7.10: Results of Weibull analysis corresponding to three sets of model parameters.

From Figure 7.10 it is evident that the peak pressure estimates obtained using a Weibull failure model (which includes only the contributions of tensile volumes) are orders of magnitude higher than failure pressures observed in the benchmark data considered in Section 7.2.2. During ice structure interactions shear cracks are routinely observed in zones of compression. Regions of the ice subject to conditions other than pure tension play an important role in the fracture behavior of ice. Given that Weibull theory is only applicable for tensile volumes, a probabilistic fracture mechanics approach that accounts for contributions of both shear and tensile cracks has been developed. This model is discussed below.

7.5 Probabilistic Fracture Mechanics Model

Flaws play a central role in the fracture behavior of brittle materials. In classical fracture mechanics, flaws are generally treated as idealized internal cracks or surface flaws in the material and are characterized by specific geometry. A wide variety of closed form solutions

exist in fracture mechanics literature for elastic bodies with cracks; see for example Broek (1986). For engineering problems which may be approximated by these cases, or from the superposition of these cases, a solution may be readily obtained. For materials such as ice, which contain fields of such flaws, a probabilistic approach is required.

7.5.1 Overview of Model

The work of Maes (1992) and Hunt and McCartney (1979) was used as a starting point. As discussed in Section 7.3.2, a parabolic load distribution is assumed. The present model focuses only on linear elastic fracture. Focus is placed on the failure behavior of an ice specimen containing a distribution of flaws that is subject to stress from a single *hpz*. A model of the weakest-link variety is seen as the best starting point.

Maes (1992) started by discretizing a specimen of volume V into n elements, each with a volume dV_i . For a specimen containing randomly dispersed cracks of random original dimensions the probability of F (the event that the specimen fails), given a nominal stress σ was given as:

$$\Pr(F | \sigma) = 1 - \prod_{i=1}^n [(1-p) + p\{1 - \Pr[S_i | \sigma(x_i)]\}], \quad (7.13)$$

where p is the probability that a crack is encountered in a given elemental volume ΔV_i , and $\Pr(S_i | \sigma(x_i))$ is the probability that the i^{th} element survives (event S_i) at the given stress level $\sigma(x_i)$ for the element located at coordinates x_i . For an elastic solid subject to a monotonically increasing load the stress tensor σ_{ij} may be expressed as the product of a scalar r and a normalized stress tensor σ'_{ij} , given as:

$$\sigma_{ij} = r\sigma'_{ij}. \quad (7.14)$$

This concept, commonly referred to as the proportional stressing assumption, has been employed in this study.

One of the main limitations of previous models is the assumption that cracks only propagate in the tensile regions of the specimen. It is evident from observation of compressive ice failure processes that fractures emanate from compressive zones, largely resulting from shear along crack-like grain boundaries. The mechanics of brittle cracking under compressive loading have been examined in detail by Ashby and Hallam (1986), Sanderson (1988) and others. The probabilistic fracture mechanics (PFM) model described below treats fracture differently for both tensile and compressive zones, and calculates the overall probability of spalling based on a specimen subject to a parabolic pressure distribution that is increased monotonically.

The specimen of total volume V has been discretized into $i = 1 \cdots n$ elements, each with elemental volume dV_i . Elemental stresses σ_i have been estimated based on stress analysis for specimens without flaws. Quasi-static conditions are assumed. It has been assumed that the presence of flaws does not significantly affect the initial stress distribution, allowing approximation of elemental stresses based on an elastic analysis of a specimen containing no flaws.

The specimen is modeled as containing a Poisson field of flaws with a maximum average density of about one flaw per grain. Flaws are assumed to have length $2a$ that is on the order of $0.65d_g$, where d_g is the mean grain size (Cole, 1986). Grain size is modeled based on distribution information reported in the literature (for instance, Kamio et al., 2003). Interaction and linkage effects are not included in the present model.

In the present work, a failure event F is defined as the occurrence of a spalling fracture (local failure), rather than a complete specimen failure (global failure). The probability of a spall occurring is taken as the probability of unstable crack propagation anywhere in the specimen. The event that the i^{th} element fails, resulting in a local fracture, is defined as event E_i .

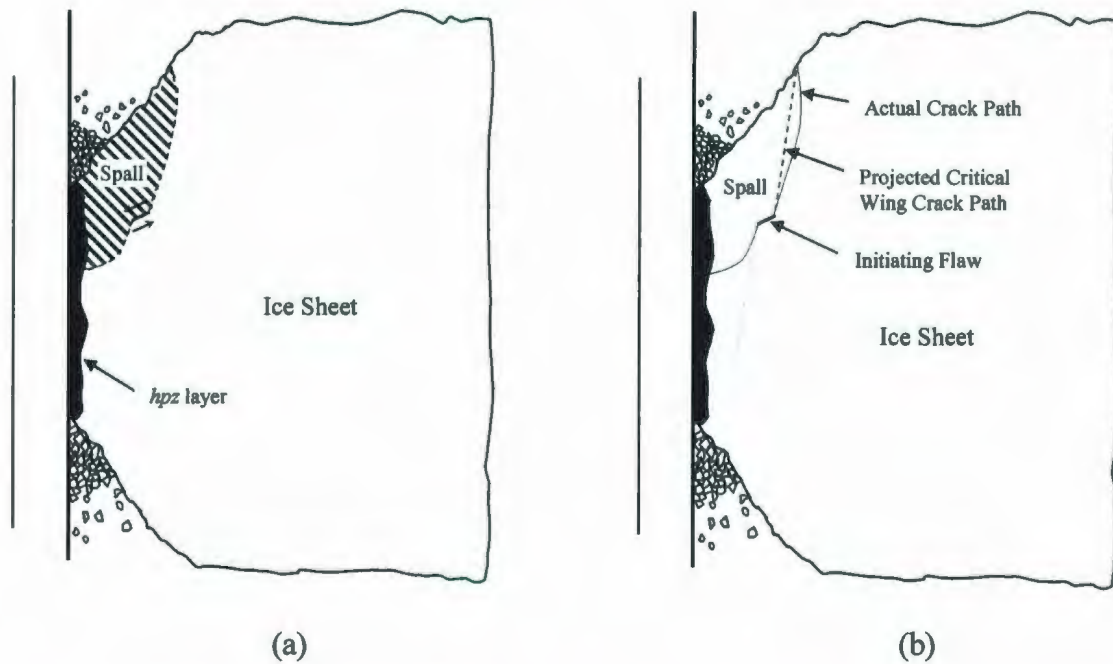


Figure 7.11: Spalling fracture idealization, showing: (a) shear crack spalling mechanism; (b) wing crack growth model used to estimate probability of spalling.

An idealization of the shear crack mechanism of spalling is shown in Figure 7.11 (a). Unstable crack propagation is assumed to occur when either (1) a tensile crack is stressed at a level greater than the critical stress level, or (2) a shear crack under compression grows in a stable manner to sufficient length where the crack intersects the nearest free surface of the ice sheet; see Figure 7.11 (b). For the shear crack model, the projected crack length is calculated as the distance between each end of the initiating flaw and the nearest free surface, taken along the line of action of the maximum principal (compressive) stress. The critical projected crack length is taken as the minimum of the lengths of the wing cracks projected from each end of the initial flaw; see Figure 7.11 (b).

The analysis routines were set-up as a post-processing task which used outputs from stress analysis carried out using the finite element package ABAQUS; see Section 7.3.2 for further discussion of stress analysis. These elemental stress inputs from ABAQUS have been combined with the crack growth and propagation models of Anderson (2005) for tension, and Ashby and Hallam (1986) for compression (see Figure 7.12). Details are discussed later in the chapter.

Based on the distributions of stress and flaws, the probability of a spall occurring is calculated as the sum of elemental probabilities of unstable crack propagation in the specimen.

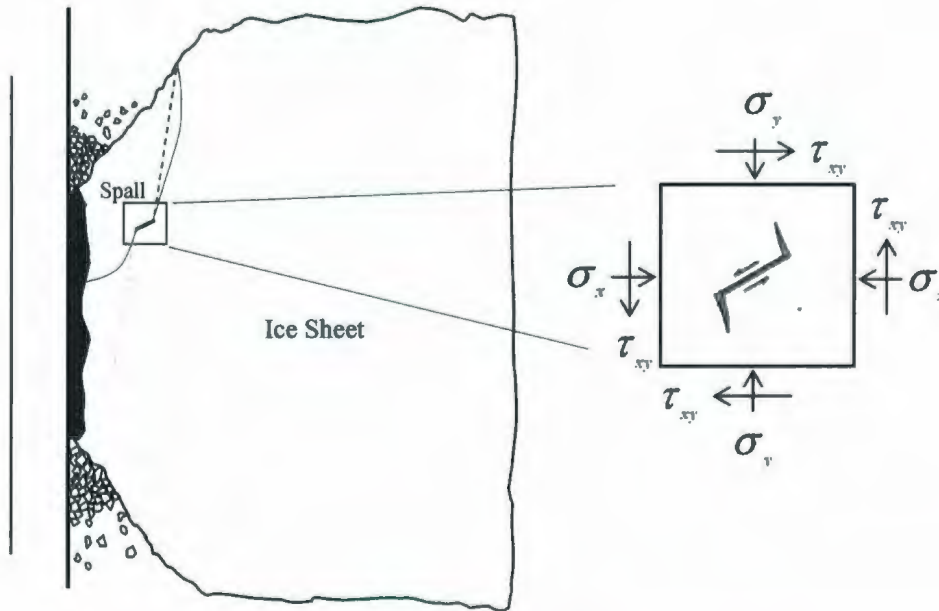


Figure 7.12: Illustration of combined elemental stress and idealized wing crack analysis

Elemental volumes, centroidal coordinates, and stress components (normal and shear) were exported from ABAQUS as a text file, and were imported into the Matlab environment. The flowchart presented in Fig. 7.13 outlines the structure of the PFM routine. The normal and shear stresses are transformed to principal planes, and the magnitudes of the principal stress components, and the principal angles were computed.

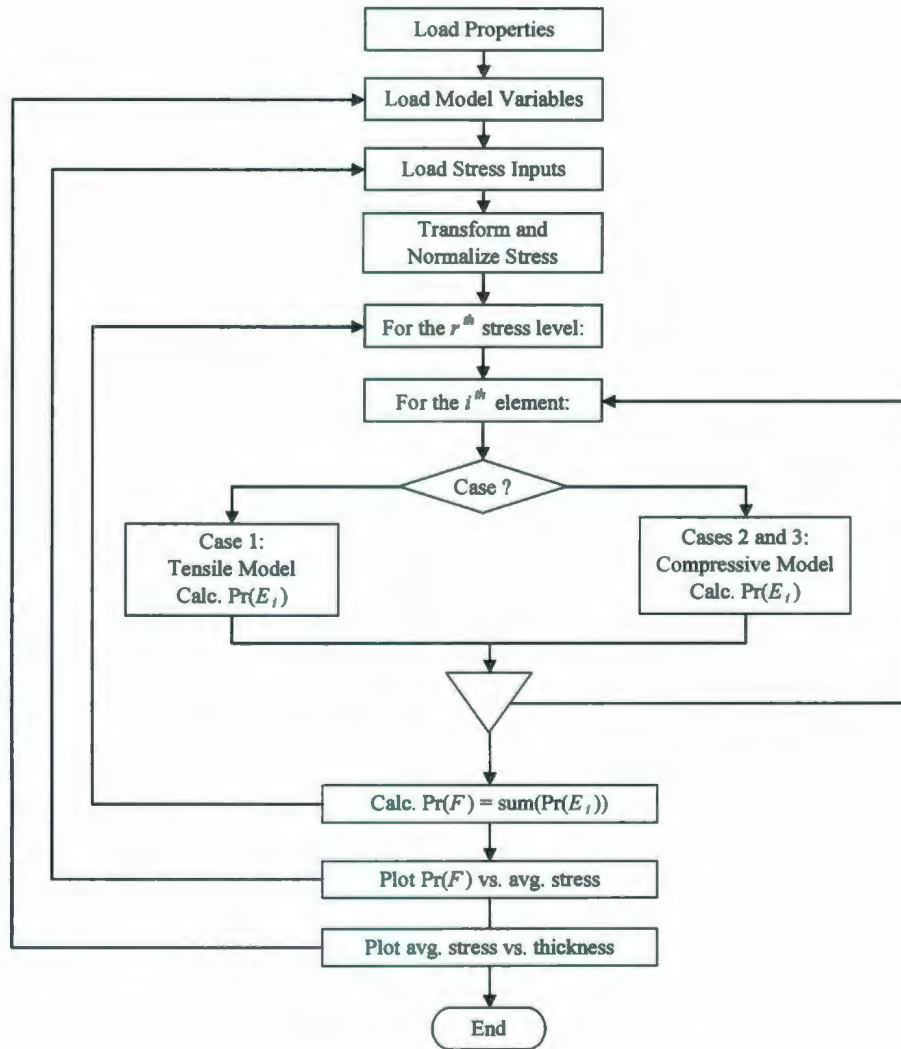


Figure 7.13: Structure of probabilistic fracture mechanics analysis main routine

Material properties, such as Young's modulus ($E = 3.5 \text{ GPa}$, $\nu = 0.3$, $K_{Ic} = 0.1 \text{ MPa}\sqrt{\text{m}}$) are coded into the model. Temperature was assumed to be -3°C for all analysis cases. The grain size distribution is assumed to follow a Weibull distribution and values for the scale parameter, A_G and shape parameter, B_G are specified in the routine. All of the above parameter values are based on conditions reported from the JOIA program; see Kamio et al., 2003. The spatial crack distribution is modeled as a Poisson process, represented by an average flaw density per unit volume ρ_c . The upper limit of flaw density is taken as one flaw per grain (Cole, 1986), but other values of crack density have also been explored, since not all flaws are necessarily active.

Elastic elemental stresses were modeled as the product of a normalized stress tensor σ'_{ij} and a scalar magnitude r ; see Eq. 7.14. The stress scalar r is a reference value, taken here as corresponding to the peak value of the parabolic *hpz* pressure distribution. The σ'_{ij} tensor was normalized by dividing the stress tensor σ_{ij} from the finite element analysis by the reference state $P_0 = 1.0$ MPa. This allowed all elemental stresses to be incrementally scaled up from some arbitrary low stress state to a value of r corresponding with a failure probability of unity. Here the initial value of $r = 0.01$ MPa was used and stress was increased incrementally by $\Delta r = 0.01$ MPa for each cycle of the loop. In each iteration the updated value of r was multiplied by the normalized stress tensor to estimate the values of elemental stress due to the monotonically increasing load. This allowed for the evaluation of failure probability as a function of increasing *hpz* pressure.

In the PFM routine, the elemental principal stress components are evaluated and the appropriate loading case is identified for each element:

- loading case 1: 'biaxial tension'
- loading case 2: 'tension with lateral confinement'
- loading case 3: 'biaxial compression'

This was repeated for all elements. Depending on the identified loading case of each element, either a tensile or compressive crack model is used to evaluate the elemental failure probability. The primary physical difference between a crack subject to lateral tension and one subject to lateral compression (confinement) is the absence or presence of crack face contact. Cracks experiencing lateral tension are assumed to not have any contact between the crack faces (i.e. no normal or frictional components). By comparison, confined cracks are assumed to have sliding contact along the crack faces, which must be accounted for in the fracture mechanics solution. A review of the mechanics of wing cracks based on the works of Kachanov (1982), Nemat-Nasser and Horii (1982), Ashby and Hallam (1986) and others has been provided in Chapter 3. The elemental fracture models used for these two cases are described in the sections below.

7.5.2 Crack Model I: Tensile Crack (No Confinement)

To model tensile elements containing a single flaw, we consider a two dimensional plane strain solution for an element containing a single elliptical through crack. Schapery (1975) and Brockway and Schapery (1978) reported that the neighborhood of the crack tip P in Figure 7.14 may be assumed to be in a state of plane strain provided: (i) the length α of the failure zone is small compared to the distance to the nearest geometric feature, (ii) α is small compared to the radius of curvature of the crack edge at P , (iii) the value of σ_z away from P can be neglected in comparison to that of σ_y near P . Given that the ice is approximately elastic for the loading rates considered, the length of the non-linear failure zone is very small. This length will be negligible relative to the distance to a surface and the radius of curvature of the crack edge at P satisfying conditions (i) and (ii). Since the value of σ_z is assumed to be much smaller than the in-plane stresses, condition (iii) is also satisfied. On this basis, the assumption of plane strain conditions is appropriate here.

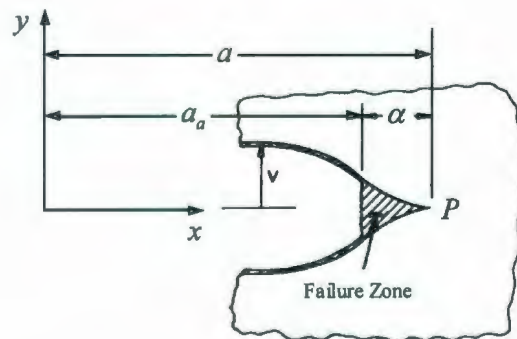


Figure 7.14: Cross-section of an idealized crack (Schapery, 1975)

Anderson (2005) provided an idealized model for the general case where a crack oriented at some angle β relative to the principal axis is subjected to biaxial tension; see Figure 7.15. Using this idealization, the likelihood of fracture may be related to the maximum principal stress and a distribution of flaws of random size and orientation.

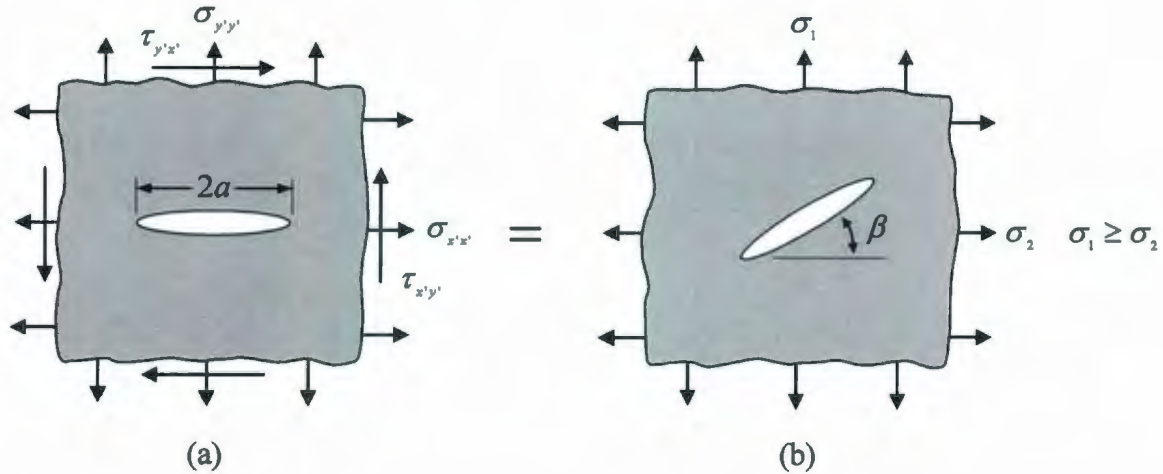


Figure 7.15: Through crack in an infinite plate for general case where the principal stress is not perpendicular to the crack plane in terms of: (a) general state of stress; (b) maximum principal stress (modified from Anderson, 2005).

For an elastic medium the case of biaxial tension may be modeled using superposition of the stress intensity factors for both tensile stress components. The stress intensity factor for a specimen in uniaxial tension at angle $\beta = 0$ is:

$$K_{I0} = \left(\frac{2}{\pi}\right)\sigma\sqrt{\pi a} \quad (7.15)$$

where σ is the maximum principal stress on the element and a is the crack half-length. When stress increases to a level such that the stress intensity at the crack tip exceeds a critical level, the crack will propagate. As discussed in Chapter 2, a flaw that is not orthogonal to the applied normal stress will initially experience combined Mode I and II loading. Applying the principle of superposition for the case of biaxial tension, Anderson (2005) gave the expression for the Mode I stress intensity factor for a flaw at angle β as:

$$K_I = K_{I0}(\cos^2 \beta + B \sin^2 \beta) \quad (7.16)$$

Similarly the Mode II stress intensity factor may be expressed as:

$$K_{II} = K_{I0}(\sin \beta \cos \beta)(1 - B) \quad (7.17)$$

where B is the biaxiality ratio, defined as $B = \sigma_2 / \sigma_1$. As illustrated in Fig. 7.16 (a), the crack will propagate in the direction of the maximum energy release rate. The propagation direction depends on B and β . This deviation from the initial flaw orientation may be described in terms of a kink angle α relative to the original crack plane; see Fig. 7.16 (b).

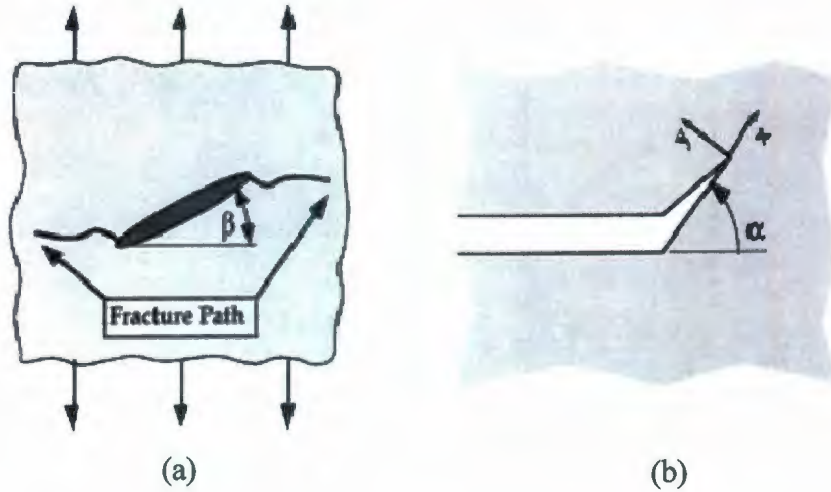


Figure 7.16: Illustrations showing (a) fracture path deviating from the original crack plane for uniaxial loading; (b) infinitesimal kink at the tip of a macroscopic crack (modified from Anderson, 2005).

The crack propagation direction is taken as the direction which maximizes the local Mode I stress intensity factor $k_I(\alpha)$ at the kink tip (which corresponds to $k_{II}(\alpha) = 0$). The local stress intensity factor for Mode I loading at the kink tip may be defined as:

$$k_I(\alpha) = K_{I0} [(\cos^2 \beta + B \sin^2 \beta)C_{11}(\alpha) + (\sin \beta \cos \beta)(1 - B)C_{12}(\alpha)] \quad (7.18)$$

The parameters C_{11} and C_{12} are functions of α given by:

$$C_{11} = \frac{3}{4} \cos\left(\frac{\alpha}{2}\right) + \frac{1}{4} \cos\left(\frac{3\alpha}{2}\right) \quad (7.19)$$

$$C_{12} = -\frac{3}{4} \left[\sin\left(\frac{\alpha}{2}\right) + \sin\left(\frac{3\alpha}{2}\right) \right] \quad (7.20)$$

The energy release rate $G(\alpha)$ for the kinked crack is then given by:

$$G(\alpha) = \frac{k_I^2(\alpha) + k_{II}^2(\alpha)}{E} \quad (7.21)$$

where E is the elastic modulus and k_I and k_{II} are the local Mode I and Mode II stress intensity factors. As discussed in Anderson (2005), the flaw will only propagate in the direction of maximum G , which also corresponds to $k_{II} = 0$. This simplification allows Eq. 7.21 to be reduced to:

$$G(\alpha) = \frac{k_I^2(\alpha_*)}{E} \quad (7.22)$$

where α_* is the angle at which both G and k_I exhibit a maximum and $k_{II} = 0$. It is assumed here that the crack growth will initiate along α_* . Since the critical kink angle α_* will depend on the orientation angle β of the flaw relative to the normal stress, the maximum energy release rate also varies with β . The optimum propagation angle α_* may then be calculated as a function of β ; see Figure 7.17. As indicated by Anderson (2005), the G_{\max} criterion depends not only on the initial crack orientation angle β , but also the biaxiality ratio B .

For tensile loading, unstable crack growth occurs when the energy release rate G at the crack tip exceeds a critical value, which for ice is approximately $G_C = 1 \text{ J/m}^2$ (see for instance Timco and Frederking, 1986). Exceedence of this value is assumed to result in unstable crack propagation for tensile loading.

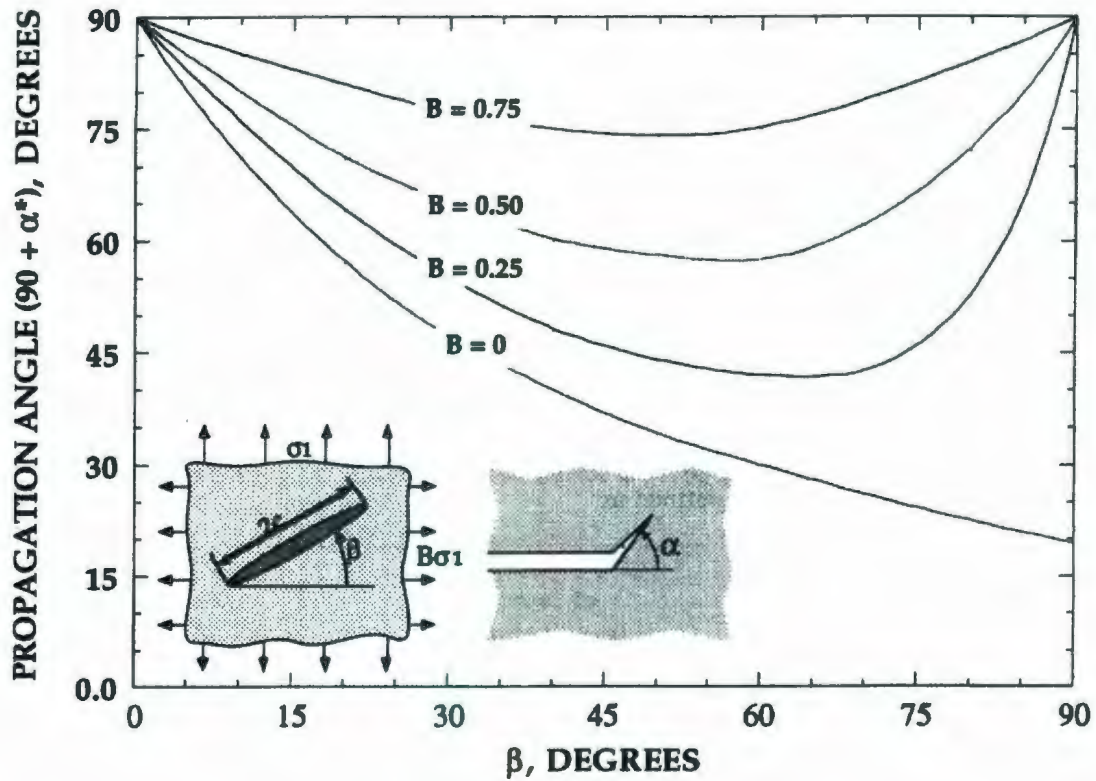


Figure 7.17: Optimum propagation angle for crack oriented at angle β relative to normal stress as a function of biaxiality (Anderson, 2005).

An early version of the PFM model was used to estimate the probability of failure based on only the tensile zones of the specimen. These early simulations yielded failure pressures an order of magnitude greater than those expected based on data analysis. These early results highlighted the importance of mixed-mode fracture in shear zones. Subsequent versions also modeled shear fracture processes associated with compressive zones.

Implementation of Crack Model I

The above elemental fracture models were implemented in Matlab to allow for simulation of spalling probabilities as a function of the stress state and flaw distributions. The main functionality of the Matlab routine for Crack Model I is embodied in Fig. 7.18.

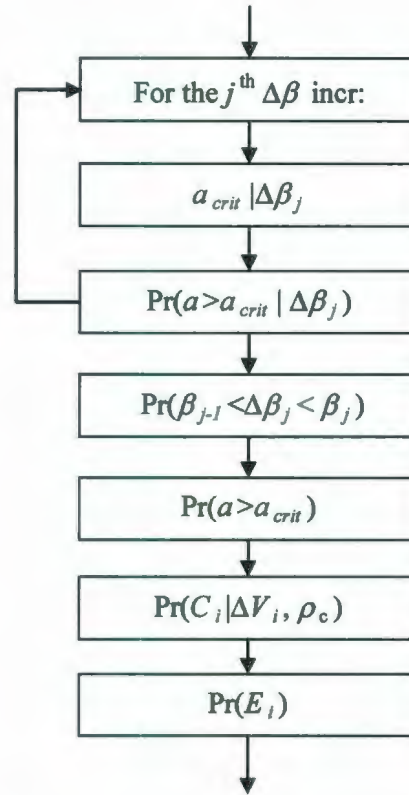


Figure 7.18: Structure of failure probability routine for unconfined tensile element.

Recall from Eq. 7.22 that a tensile crack is assumed to propagate along the direction α_* that maximizes the energy release rate G . In the PFM routine the value of α_* is found by evaluating expression 7.21 over the range $\alpha = -180^\circ$ to 180° and solving for the value of α which maximizes $k_I(\alpha)$.

Substituting Eq. 7.15 into Eq. 7.18 yields an expression for the Mode I stress intensity factor k_I at the kink crack-tip as:

$$k_I(\alpha_*) = \left(\frac{2}{\pi}\right) \sigma_1 \sqrt{\pi a} \left[(\cos^2 \beta + B \sin^2 \beta) C_{11}(\alpha_*) + (\sin \beta \cos \beta) (1 - B) C_{12}(\alpha_*) \right], \quad (7.23)$$

where σ_1 is the maximum (tensile) principal stress. Fracture is assumed to occur when the local stress intensity factor exceeds the fracture toughness of ice. Substituting the fracture

toughness K_{Ic} for k_j into Eq. 7.23 and solving for the crack half-length a yields an expression for the critical crack half-length, a_{crit} as:

$$a_{crit}(\beta) = \frac{1}{\pi} \left[\frac{\pi K_{Ic}}{2\sigma_1[(\cos^2 \beta + B \sin^2 \beta)C_{11}(\alpha_*) + (\sin \beta \cos \beta)(1 - B)C_{12}(\alpha_*)]} \right]^2. \quad (7.24)$$

For the tensile crack model, the orientation β of the crack relative to the principal axis is assumed to be in the range 0 to 90 degrees and to follow a random uniform distribution. Numerical implementation of this distribution was accomplished by discretizing the distribution into b increments of width $\Delta\beta_j$, where $j = 1, 2, \dots, b$. In evaluating Eq. 7.24 for each $\Delta\beta_j$ increment, the value of β used corresponds to the midpoint of the $\Delta\beta_j$ interval of interest, and may be calculated as $\bar{\beta}_j = (\beta_j + \beta_{j-1})/2$. This is shown graphically in Figure 7.19.

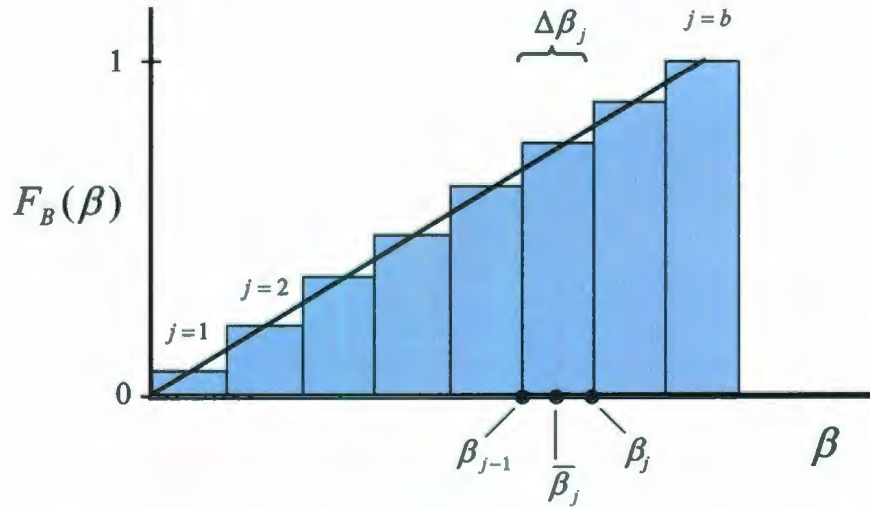


Figure 7.19: Discretization of flaw orientation distribution *cdf* into b intervals of width $\Delta\beta_j$.

Since any orientation is equally likely, the probability of an angle being in any given $\Delta\beta_j$ increment is:

$$\Pr(\beta_{j-1} < \beta < \beta_j) = F_B(\beta_j) - F_B(\beta_{j-1}) = 1/b. \quad (7.25)$$

For any given orientation and stress level, cracks longer than the critical length a_{crit} will propagate in an unstable manner.

The above expressions allow for the calculation of a_{crit} for each $\Delta\beta_j$ interval. For each value of a_{crit} , the probability of brittle propagation is equal to the probability that the crack is longer than the critical length, as given by:

$$\Pr(a \geq a_{crit} | \Delta\beta_j) = [1 - F_A(a_{crit}(\bar{\beta}_j))] \quad (7.26)$$

where $F_A(a_{crit}(\bar{\beta}_j))$ is the cumulative distribution function (*cdf*) of the crack size distribution evaluated at $a_{crit}(\bar{\beta}_j)$ for the interval $\Delta\beta_j$. The total probability of the element containing a critical length crack over all possible β is then:

$$\Pr(a \geq a_{crit}) = \frac{1}{b} \sum_{j=1}^b \Pr(a \geq a_{crit} | \Delta\beta_j) \quad (7.27)$$

The probability of any random element failing must also account for the probability that the given element contains a crack. We define C_i as the event that the i^{th} element contains a crack. The probability of an element with volume ΔV_i containing a crack $\Pr(C_i)$ is given by:

$$\Pr(C_i) = \Delta V_i \times \rho_c, \quad (7.28)$$

where the mean crack density ρ_c is specified in the model. The maximum number of grains per cubic meter can be estimated based on the volume of an average sized grain. The event that the element fails (i.e. triggers a local fracture) is defined as event E_i . The probability of an element failing is then the probability that it contains a flaw multiplied by the probability that the flaw is greater than the critical crack length:

$$\Pr(E_i) = \Pr(C_i) \times \Pr(a \geq a_{crit}) = \Pr(C_i) \times (1 - F_A(a_{crit})). \quad (7.29)$$

Using these expressions it is possible to estimate the probability of an unstable crack occurring in a given element that is subjected to tensile stresses. Using the above expressions

the probability of failure may be found for each tensile element. Once all elemental failure probabilities are found, they are summed over all elements to give the total probability of local (spalling) failure.

7.5.3 Crack Model II: Shear Crack (Subject to Confinement)

While tensile loading causes separation of the crack faces (i.e. no contact), compressive loading will often result in contact between opposing crack surfaces. Frictional forces acting along the crack interface are an important additional component of the crack mechanics. As stress increases, the crack tries to slide (shear) along the length of the crack, leading to the formation of tensile zones at the crack tips as shown in Figure 7.20 (a); the convention used in the shear crack analysis is that tension is positive, compression is negative, thus σ_1 is the most negative (most compressive) and σ_2 is the most positive (least compressive) principal stress. At a certain critical level of stress, tensile 'wing cracks' form and begin to propagate (Kachanov, 1982). Initially the wing cracks begin to grow perpendicular to the crack ends, eventually aligning themselves with the principal axis of compression as they elongate. The classic works of Nemat-Nasser and Horii (1982) and Ashby and Hallam (1986) detail the mechanics associated with compressive crack growth.

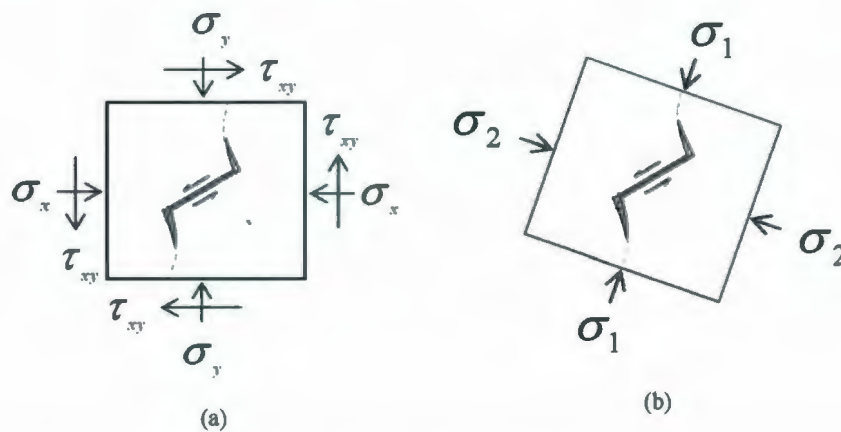


Figure 7.20: Through crack in an infinite plate for general case where the principal stress is not perpendicular to the crack plane in terms of: (a) general state of stress; (b) maximum principle stress.

Ashby and Hallam (1986) present an approximate analytical solution for wing crack nucleation and growth based on the idealization shown in Figure 7.20. For a crack of length $2a$, lying at an angle ψ to the direction of principal compression, wing cracks form and grow stably to length ℓ . The authors suggest that cracks in the approximate range of orientations between 30° and 60° relative to the maximum principal compression will nucleate since these angles are most favorable for sliding.

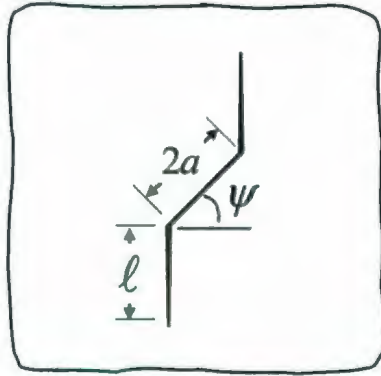


Figure 7.21: Idealized wing crack geometry.

Flaws oriented at angles outside this range require significantly higher stresses to form cracks. For the present analysis, it has been assumed that cracks within the above range of orientations have a nucleation probability equal to unity. Cracks outside this range have a nucleation probability of zero.

The general result of Ashby and Hallam (1986) is:

$$K_{Ic} = \frac{\sigma_1 \sqrt{\pi a}}{(1 + \Lambda)^{3/2}} \left[1 - \lambda - \mu(1 + \lambda) - \frac{\sqrt{3}\lambda\Lambda}{\Gamma} \left[\frac{\Gamma\Lambda}{\sqrt{3}} + \frac{1}{\sqrt{3}(1 + \Lambda)^{1/2}} \right] \right], \quad (7.30)$$

where K_{Ic} is the fracture toughness, a is the half-length of the original crack, ℓ is the length of a single wing crack and $\Lambda = \ell/a$. The parameter Γ is a constant with a value of approximately 0.4, $\lambda = \sigma_2/\sigma_1$ (ratio of confinement to compression) and μ is the coefficient of friction across the crack. The details of the derivation of Eq. 7.30 are included in Appendix A.1. Ashby and Hallam (1986) applied this model to cases with lateral tension, as well as to those with lateral compression. Given the values of the stress components and the

initial crack length the above expression can be used to estimate the equilibrium wing crack length by solving iteratively for the value of Λ required to give a stress concentration value equal to the fracture toughness of ice.

For narrow cylindrical specimens used in laboratory testing, wing cracks may split the ice into vertical beams. Ashby and Hallam (1986) gave solutions for finite width specimens and used beam theory to account for bending of these 'beams' as a result of sliding along the precursor crack. In this study, it is assumed that the majority of precursor cracks are in the interior of the material, and any 'beams' that may form would be sufficiently stiff as to have negligible effects on wing crack stress intensity and associated crack growth. No modifications have been made to Eq. 7.30 to account for bending effects on narrow beams of ice.

An expression for the internal static coefficient of friction of ice (i.e. between the opposing crack faces) is given as a function of temperature T_f (in degrees C) by Hallam (1986) as:

$$\mu = \frac{-0.39T_f}{3.18 - 0.39T_f} \quad (7.31)$$

The above expressions allow the stable crack length to be evaluated as a function of stress. As illustrated in Figure 7.22 the elemental stress components can be transformed to obtain the principal stresses acting on the element and the orientation of the initial crack can be defined relative to the principal axis. This allows stress components obtained from a finite element analysis to be used in the assessment of stable crack length.

Failure (i.e. local spalling fracture) is assumed to occur when a crack becomes unstable. Hallam (1986) reported that crack extension in compression is stable, and a crack must extend until it reaches free surfaces or until it interacts with other cracks, resulting in instability. In the PFM, unstable crack propagation is assumed to occur when one of the individual 'wings' grows to a sufficient length to reach a free surface. This critical length ℓ_k depends on the location of the activated precursor crack, the precursor crack length and the propagation direction.

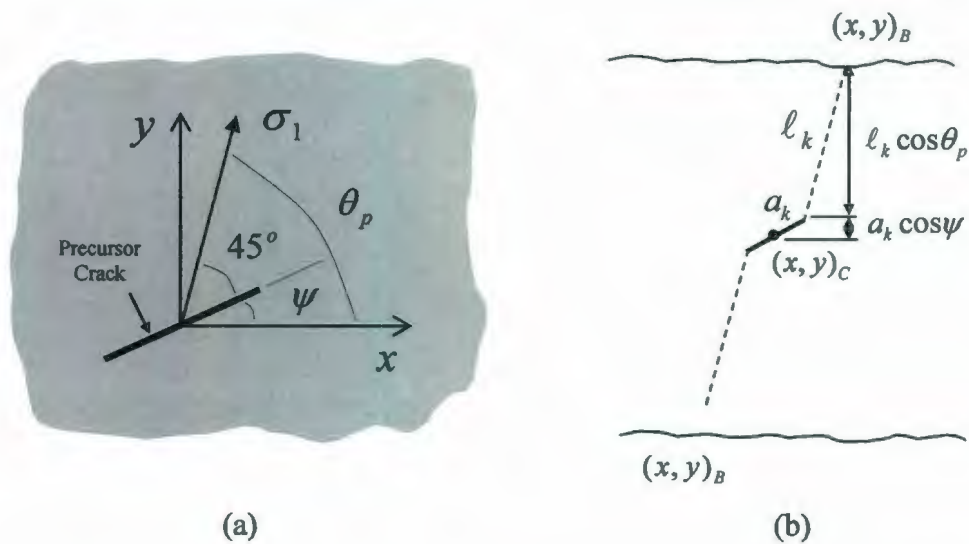


Figure 7.22: Illustration of: (a) orientation of the principal stress, and precursor flaw relative to the horizontal plane; (b) projected intersection of a wing crack with the free surface.

As illustrated in Figure 7.22 (a), θ_p is the angle between the principal stress axis of the element and the horizontal plane. The angle ψ is measured between the precursor flaw axis and the horizontal plane. Ashby and Hallam (1986) suggest an approximate range of precursor crack orientations between 30° and 60° relative to the maximum principal compression will nucleate wing cracks since these angles are most favorable for sliding. Here calculations have been based on an assumed mean orientation angle of 45° relative to the axis of principal compression. This allowed for the calculation of ψ as $\psi = \theta_p - 45^\circ$. From Figure 7.22 (b), it may be seen that the boundary coordinates of the top and bottom free surfaces are given as $(x, y)_B$.

If we take a line of action parallel to the principal compressive stress axis and project it through the end of the precursor crack, this line will also intersect with the nearest free surface of the ice. This is shown in Figure 7.22 (b) as dashed lines for both the top and bottom surfaces. The critical wing crack length ℓ_k will be the shortest of these two lengths, and the end point of ℓ_k at the point of intersection with the free surface is given by the x-coordinate x_B and the y-coordinate y_B .

The centroid of the precursor crack is defined by the x-coordinate x_C and the y-coordinate y_C . The precursor flaw half-length is given as a_k . In the PFM routine, the y_C and y_B values are known from geometry, and the distance between them is simply the difference of these two values. This distance is also equal to the sum of the projected lengths of the precursor crack half-length a_k and the critical wing crack length, ℓ_k (as projected on a vertical plane). Equating these two distances, we may write:

$$y_B - y_C = \ell_k \cos \theta_p + a_k \cos(\psi). \quad (7.32)$$

Rearranging the above equation to solve for ℓ_k gives:

$$\ell_k = \frac{y_B - y_C - a_k \cos(\psi)}{\cos \theta_p}. \quad (7.33)$$

From this expression it may be seen that for a fixed location in a given specimen, the critical wing crack length will depend on the precursor crack length. Since the precursor crack half-length distribution $F_A(a)$ is defined in the model, the *cdf* of this distribution can be divided into k intervals of width Δa_k . The mean precursor crack half-length \bar{a}_k corresponding to a given Δa_k interval has been taken as the midpoint value of the k^{th} interval; see Figure 7.23 below.

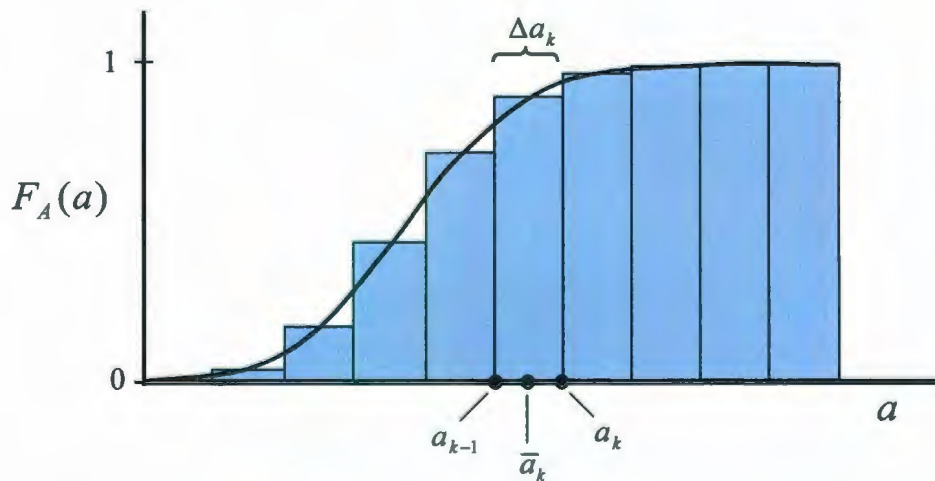


Figure 7.23: Discretization of flaw size distribution *cdf* into k intervals of width Δa_k .

The probability of a random flaw having a half-length a which is in the range Δa_k may be found using the expression:

$$\Pr(a_{k-1} \leq \Delta a_k \leq a_k) = F(a_k) - F(a_{k-1}) \quad (7.34)$$

In the present analysis, both the distance from the centroid to the top surface, and the distance from the centroid to the bottom surface have been calculated for each element. The minimum of these two values is then used for the purpose of calculating the instability criteria. Recall that it has been assumed in the above model that wing cracks will propagate from precursor flaws oriented between 30° and 60° relative to most compressive principal stress axis. To simplify the above criteria, it has been assumed that the mean orientation of the precursor crack relative to the principal axis (45°) may be used to provide a representative estimate of the average critical wing crack length. The orientation ψ of the precursor crack relative to the horizontal plane is then $\psi = \theta_p - 45^\circ$, as shown in Figure 7.22 (a). For each Δa_k interval the elemental failure probability may be found by solving for the corresponding critical wing crack length ℓ_k using the expression:

$$\ell_k = \frac{y_B - y_C - a_k \cos(\theta_p - 45^\circ)}{\cos \theta_p} \quad (7.35)$$

The Λ ratio corresponding to the critical wing crack length, for a given Δa_k interval is defined as:

$$\Lambda_k = \ell_k / a_k \quad (7.36)$$

Substitution of a_k and Λ_k into the crack-tip stress intensity expression into Eq. 7.30 gives:

$$K_{I,k} = \frac{\sigma_1 \sqrt{\pi a_k}}{(1 + \Lambda_k)^{3/2}} \left[1 - \lambda - \mu(1 + \lambda) - \frac{\sqrt{3} \lambda \Lambda_k}{\Gamma} \left[\frac{\Gamma \Lambda_k}{\sqrt{3}} + \frac{1}{\sqrt{3}(1 + \Lambda_k)^{1/2}} \right] \right] \quad (7.37)$$

If $K_{I,k} \geq K_{Ic}$ there is sufficient stress concentration at the crack tip to cause propagation to the free surface, which is assumed to result in unstable crack propagation in the remaining

wing crack. If $K_{I,k} < K_{Ic}$ the length of the stable crack will not be of sufficient length to reach the free surface, and unstable propagation does not result for the given stress level.

Implementation of Crack Model II

For the compressive crack model, the approach used was similar to that used for the tensile case. The Matlab routine developed for Crack Model II is illustrated in Fig. 7.24.

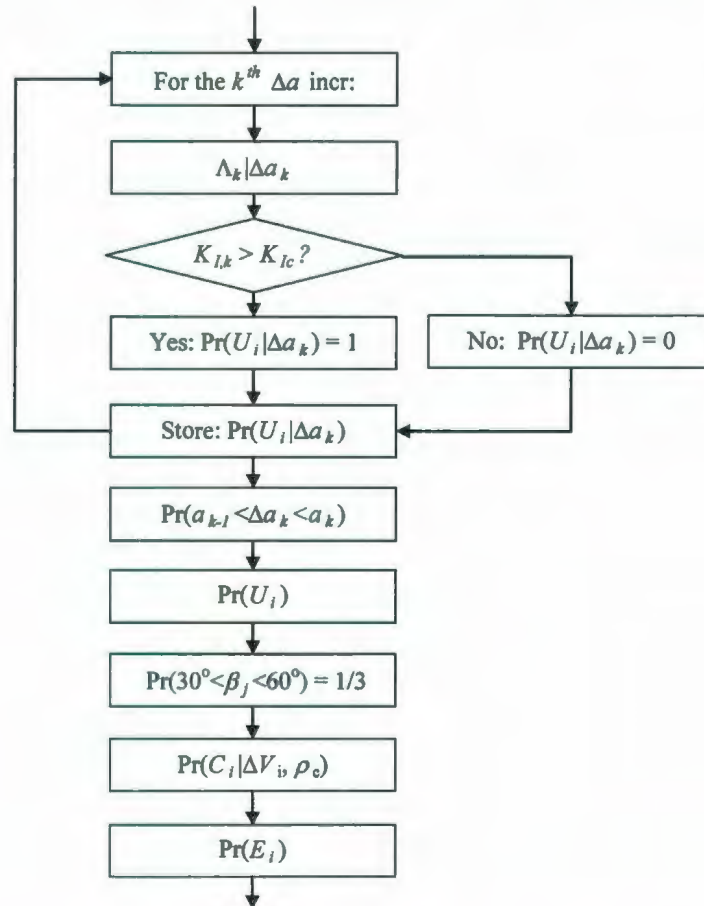


Figure 7.24: Structure of confined crack element failure probability routine

For a crack subject to compressive principal stresses, we start by looping through each of the k^{th} increments of the crack size distribution, where each interval is of width Δa_k . For each value Δa_k , the local crack tip stress intensity factor $K_{I,k}$ corresponding to the critical wing crack length ℓ_k is calculated. This value is then compared with the plane strain fracture toughness of the material K_{Ic} . If the local stress intensity $K_{I,k}$ exceeds the fracture toughness,

then it is assumed that there is sufficient energy to cause the crack to propagate to the free surface and thus become unstable. If $K_{I,k}$ is less than K_{Ic} , the stable crack length will be less than that required to reach the free surface, and the crack will not become unstable. Recalling that U_i is the event that unstable crack propagation occurs, we may write:

$$\Pr(U_i | \Delta a_k) = 1, \quad \text{if } K_{I,k} \geq K_{Ic}. \quad (7.38)$$

$$\Pr(U_i | \Delta a_k) = 0, \quad \text{if } K_{I,k} < K_{Ic}. \quad (7.39)$$

This process is repeated for each of the k^{th} increments of Δa_k . The probability that a random crack with half-length a is in the increment Δa_k (i.e. in the range $a_{k-1} \rightarrow a_k$) is given by the expression: $\Pr(a_{k-1} \leq a \leq a_k) = F_A(a_k) - F_A(a_{k-1})$, where $F_A(a)$ is the *cdf* of the distribution of the crack half-lengths. Using this value, the total probability of unstable propagation for the i^{th} crack is given as:

$$\Pr(U_i) = \Pr(U_i | \Delta a_k) \times \Pr(a_{k-1} \leq a \leq a_k). \quad (7.40)$$

Since only cracks oriented favorably for sliding (between 30° to 60° from to the principle compressive stress axis) will be active, the probability of a crack propagating also depends on the probability that it is favorably oriented. Assuming each orientation angle is equally likely, the probability of it being in the range favorable for sliding is:

$$\Pr(30^\circ \leq \beta_b \leq 60^\circ) = 30^\circ / 90^\circ = 1/3. \quad (7.41)$$

Where C_i is the event that the i^{th} element contains a crack, and ρ_c is the mean crack density, the probability of an element with volume ΔV_i containing a crack $\Pr(C_i)$ is then:

$$\Pr(C_i) = \Delta V_i \times \rho_c, \quad (7.42)$$

The overall failure probability of the i^{th} element at the given stress level $\Pr(E_i)$ is then the product of the probabilities that the element contains a crack, that this crack is favorably

oriented, and that it becomes unstable at the given stress level. This is expressed mathematically as:

$$\Pr(E_i) = \Pr(C_i) \times \Pr(30^\circ \leq \beta_b \leq 60^\circ) \times \Pr(U_i). \quad (7.43)$$

In the PFM routine, $\Pr(E_i)$ is calculated and stored for each element and the overall spalling failure probability $\Pr(F)$ of the specimen at the given stress level is calculated as the sum of elemental failure probabilities, as given by:

$$\Pr(F) = \sum_{i=1}^n \Pr(E_i) \quad (7.44)$$

7.6 Investigation of Scaling Behavior using PFM Model

To implement the model, stress analysis results for all specified geometries were imported from ABAQUS. The parameter values used throughout the analysis were the baseline values given in Table 7.2, unless otherwise specified; these values are based on ice properties reported from the JOIA program (Kamio et al., 2003).

Table 7.2: Summary of baseline parameters used in PFM model

Description	Parameter	Value
Elastic modulus	E	3.5 GPa
Poisson's ratio	ν	0.3
Fracture toughness	K_{Ic}	0.1 MPa \sqrt{m}
Temperature	T	- 3 °C
Grain size distribution (Weibull scale parameter)	A_G	0.009 m
Grain size distribution (Weibull shape parameter)	B_G	3.323
Mean crack density	ρ_C	$1 \times 10^5 \text{ m}^{-2}$

One of the largest uncertainties at present is the density of active flaws in the ice. While an upper bound of 1 flaw per grain has been used to estimate the maximum crack density (Cole,

1986), the number of active flaws during an actual interaction is unknown. As discussed in Section 7.6.2 below, results were found to be less sensitive to ρ_c for flaw densities above about $\rho_c = 10^5 \text{ m}^{-2}$. Based on this result, a value of $\rho_c = 10^5 \text{ m}^{-2}$ was used to represent the mean density of active cracks.

7.6.1 Thickness Scaling for Flat Ice Edge ($\omega = 0^\circ$)

To investigate the dependence of pressure on thickness for ice with a flat edge ($\omega = 0^\circ$), four self-similar geometries scaled by thickness were analyzed. Details of these cases are summarized in Table 7.3. The parameters given in Table 7.3 correspond to the geometry defined in Figure 7.4.

Table 7.3: Matrix of analysis cases used to study thickness effect for flat ice edge.

Case	ω	h	$2q$	r	s
3	0°	0.2	0.020	0.090	0.000
6	0°	0.5	0.050	0.225	0.000
9	0°	1.0	0.100	0.450	0.000
12	0°	2.0	0.200	0.900	0.000

For each of these cases, the spalling failure probability distributions as a function of overall mean pressure \bar{P}_h (see Eq. 7.4) were calculated. To examine which type of probability distribution gave the best agreement with the data, exponential, gamma, Gumbel and Weibull distributions were fitted to sample data using a curve fitting routine; see Appendix D for sample results. From this work it was observed that the Gumbel distribution best models the data, particularly the tail of the distribution which is of most interest in modeling the extreme pressures of interest in design.

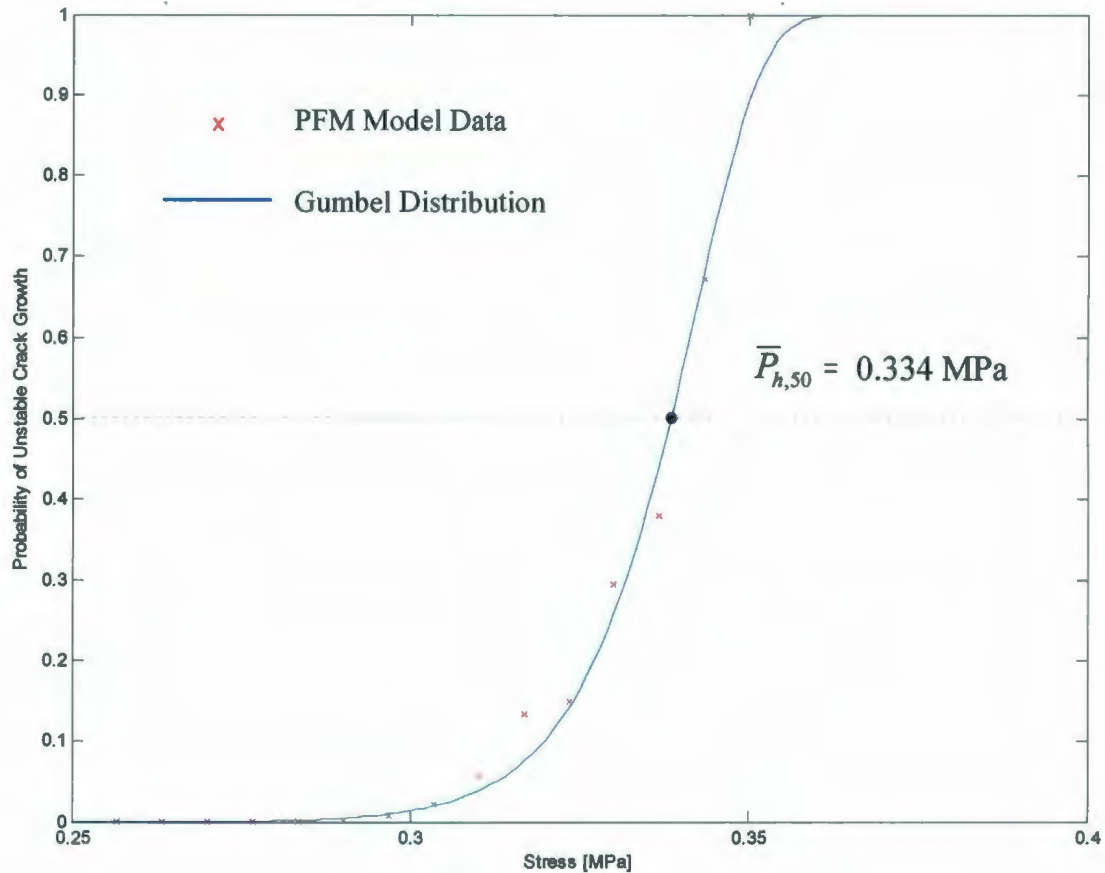


Figure 7.25: Probability of spalling as a function of stress for Case 3 ($h = 0.2\text{m}$).

The spalling probability distribution $P_F(\sigma)$ for Case 3 is shown in Figure 7.25. These data are well fit by a Type I Extremal (Gumbel) distribution with parameters $\mu = 0.334$; $\sigma = 9.9 \times 10^{-3}$. For the purposes of evaluating the scale effect, the pressure corresponding to a 50% probability of exceedence is used for all cases throughout this study, and is denoted $\bar{P}_{h,50}$ as shown in Figure 7.25. For Case 3 a value of $\bar{P}_{h,50} = 0.334 \text{ MPa}$ was obtained.

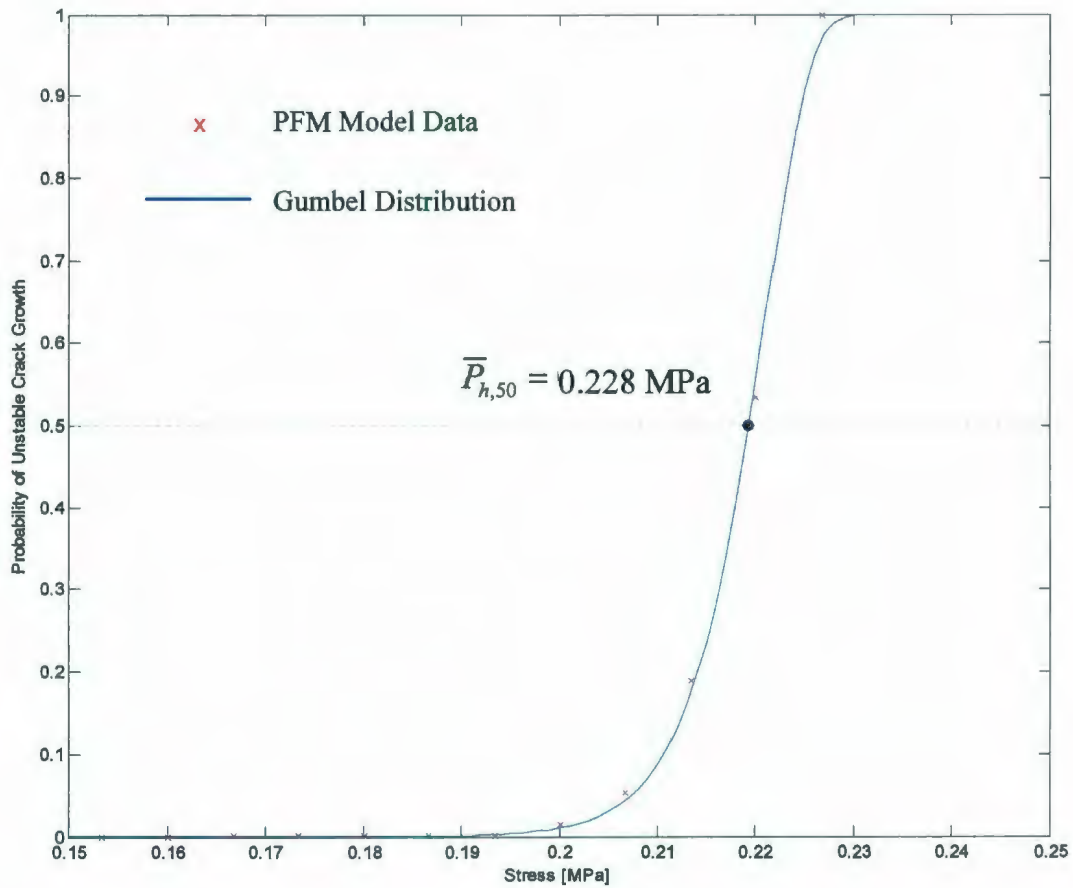


Figure 7.26: Probability of spalling as a function of stress for Case 6 ($h = 0.5\text{m}$).

For Case 6, the distribution for the probability of spalling given in Figure 7.26 had a mean overall pressure of $\bar{P}_{h,50} = 0.228 \text{ MPa}$. This distribution was well fitted by a Type-I Extremal (Gumbel) distribution with parameters $\mu = 0.228$; $\sigma = 4.6 \times 10^{-3}$.

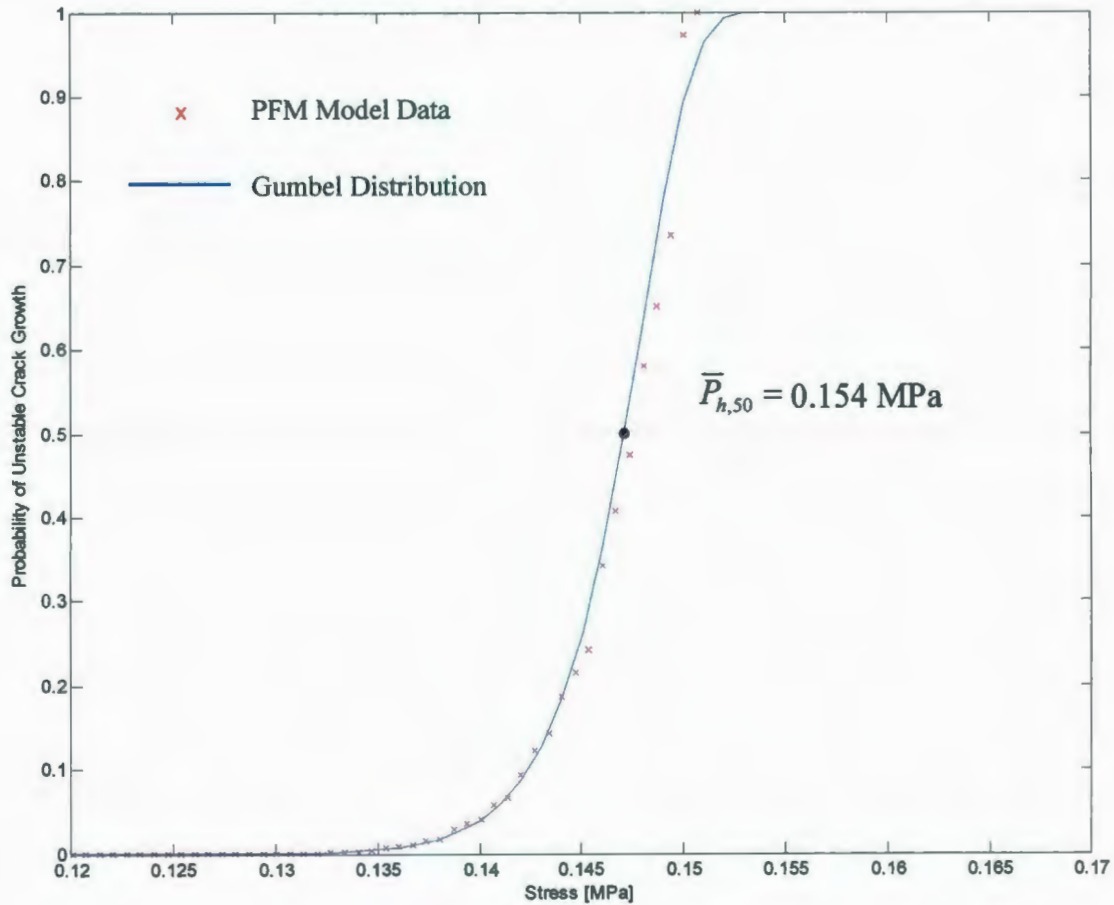


Figure 7.27: Probability of spalling as a function of stress for Case 9 ($h = 1.0\text{m}$).

For Case 9, the spalling failure distribution had a mean overall pressure of

$\bar{P}_{h,50} = 0.154 \text{ MPa}$ was fitted by a Type-I Extremal (Gumbel) distribution with parameters

$\mu = 0.154$ and $\sigma = 2.5 \times 10^{-3}$; see Figure 7.27.

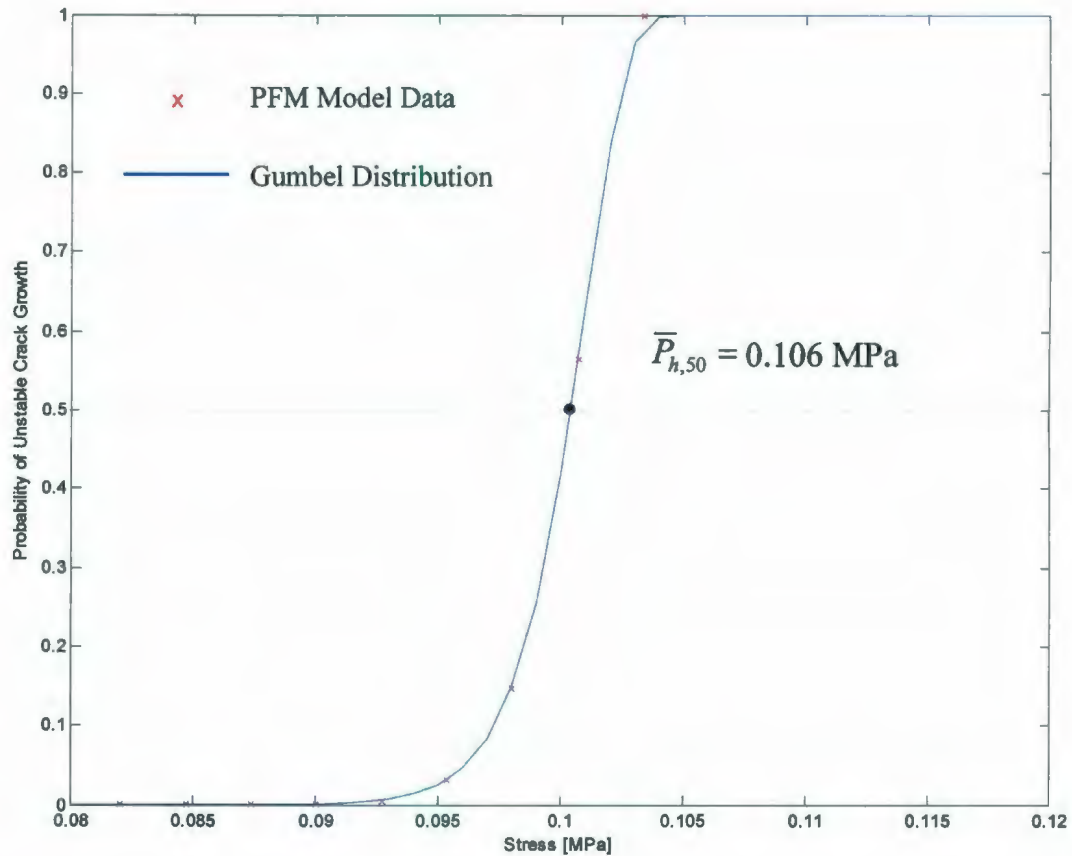


Figure 7.28: Probability of spalling as a function of stress for Case 12 ($h = 2.0\text{m}$).

For Case 12, a value of $\bar{P}_{h,50} = 0.106$ MPa was observed. The spalling distribution shown in Figure 7.28 was fitted by a Gumbel distribution with parameters $\mu = 0.106$, and $\sigma = 1.65 \times 10^{-3}$.

Compiling the $\bar{P}_{h,50}$ results for the above analysis cases we get the values shown in Table 7.4, and plotted in Figure 7.29.

Table 7.4: Values of $\bar{P}_{h,50}$ for Case 3, Case 6, Case 9, and Case 12.

Parameter	Case 3 ($h = 0.2\text{m}$)	Case 6 ($h = 0.5\text{m}$)	Case 9 ($h = 1.0\text{m}$)	Case 12 ($h = 2.0\text{m}$)
$\bar{P}_{h,50}$	0.334 MPa	0.228 MPa	0.154 MPa	0.106 MPa

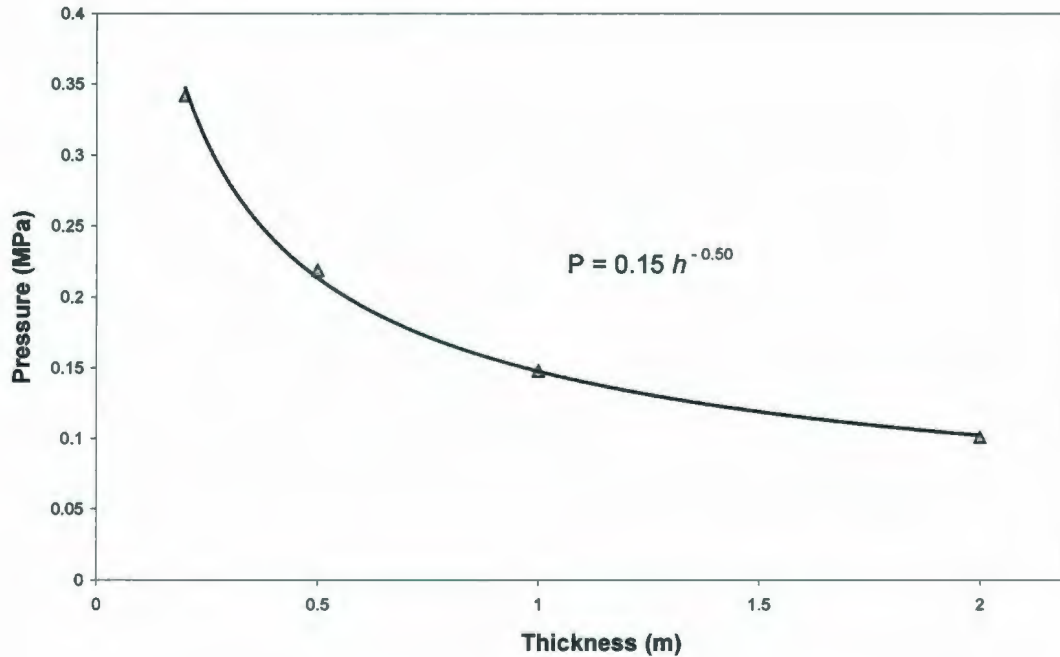


Figure 7.29: Pressure-thickness plot for $\bar{P}_{h,50}$ data from Table 6.4.

From the pressure-thickness plot in Figure 7.29 it is observed that clear scale effect is predicted from theory, and a power-law relationship has been fitted to these data, given by:

$$P = 0.15h^{-0.50} . \quad (7.45)$$

Recall from Section 7.2.2 that the sample event had a thickness of $h = 0.287\text{m}$, a mean pressure of $\mu_e = 0.1425\text{ MPa}$ and a standard deviation of $\sigma_e = 0.0331\text{ MPa}$. Using Eq. 7.45 for an ice thickness of $h = 0.287\text{m}$ we find that the value of peak pressure estimated by the theoretical model is:

$$P_{p,th} = 0.28\text{ MPa} . \quad (7.46)$$

Defining peak pressure in terms of mean and standard deviation of pressure, we may write:

$$P_{p,e} = \mu_e + S \cdot \sigma_e , \quad (7.47)$$

where S is a constant corresponding to the specified probability of exceedence. Substituting $\mu_e = 0.143\text{ MPa}$ and $\sigma_e = 0.033\text{ MPa}$ into Eq. 7.47, gives:

$$P_{p,e} = 0.143 + S \cdot (0.033) \text{MPa}, \quad (7.48)$$

Equating Eq. 7.48 with Eq. 7.46 and solving gives $S \approx 4.5$, suggesting that the theoretical model corresponds to approximately $\mu_e + 4.5\sigma_e$. This result suggests that the PFM model well bounds the benchmark data, providing strong support for the validity of the PFM approach. Broader comparisons of model results with data are recommended. Time series simulations would be required to explore more fully the relationship between the mean, standard deviation and peak pressure, since factors such as interaction speed, distance and duration play an important role in determining extreme pressures.

7.6.2 Effect of Ice Edge Shape

Throughout an interaction, the ice edge shape will evolve as a direct result of local failure processes. To study the influence of the edge geometry on the overall thickness, twelve different analysis cases have been examined. These cases consist of a combination of four ice thickness values, and the three spalling angle configurations defined by the geometry shown in Figure 7.30.

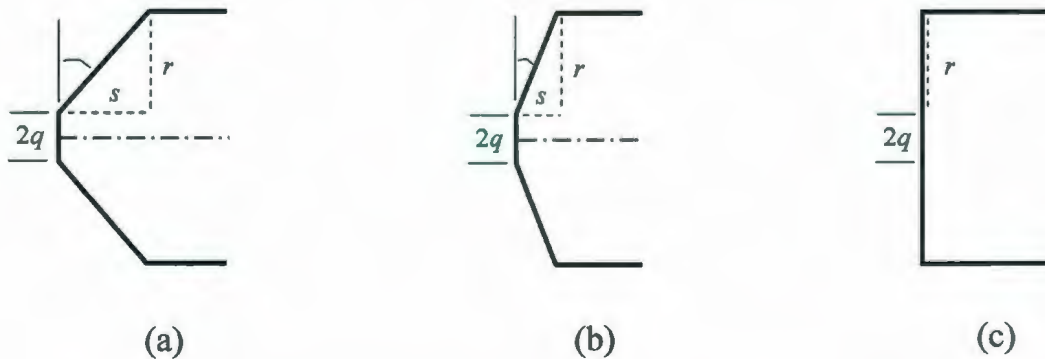


Figure 7.30: Geometric configurations considered: (a) $\omega = 45^\circ$; (b) $\omega = 20^\circ$; (c) $\omega = 0^\circ$.

The geometric parameters corresponding to each analysis case are given in Table 7.5.

Table 7.5: Matrix of model geometry for analysis of effects of ice edge shape.

Case	ω	h	q	r	s
1	45°	0.2	0.010	0.090	0.090
2	20°	0.2	0.010	0.090	0.030
3	0°	0.2	0.010	0.090	0.000
4	45°	0.5	0.025	0.225	0.225
5	20°	0.5	0.025	0.225	0.075
6	0°	0.5	0.025	0.225	0.000
7	45°	1.0	0.050	0.450	0.450
8	20°	1.0	0.050	0.450	0.150
9	0°	1.0	0.050	0.450	0.000
10	45°	2.0	0.100	0.900	0.900
11	20°	2.0	0.100	0.900	0.300
12	0°	2.0	0.100	0.900	0.000

For each of the above analysis cases, spalling failure distributions were obtained and $\bar{P}_{h,50}$ values were extracted. The $\bar{P}_{h,50}$ results were grouped by angle (i.e. Cases 1, 4, 7, 10 ($\omega = 45^\circ$); Cases 2, 5, 8, 11 ($\omega = 20^\circ$); Cases 3, 6, 9, 12 ($\omega = 0^\circ$)). Each of these groups represents a set of self-similar geometries scaled by thickness. Pressure-thickness plots, such as the one given in Figure 7.29 were generated for each group, and a power-law of the form $P = CA^D$ was fitted to each curve. The values of the pressure coefficient C and pressure exponent D corresponding to each ω were extracted from each pressure versus thickness curve.

To investigate the sensitivity of the results to the flaw density ρ_c , simulations were carried out using five flaw densities: $\rho_c = 10^3, 10^4, 10^5, 5 \times 10^5, 10^6 \text{ m}^{-2}$. This was accomplished by simply carrying out the above analysis five times, each time using a different value of ρ_c .

Results for the effect of taper angle ω on the pressure coefficient C and pressure exponent D are plotted in Figures 7.31 and 7.32, respectively. In both figures, the values are plotted as a function of flaw density to show the sensitivity of the results to ρ_c .

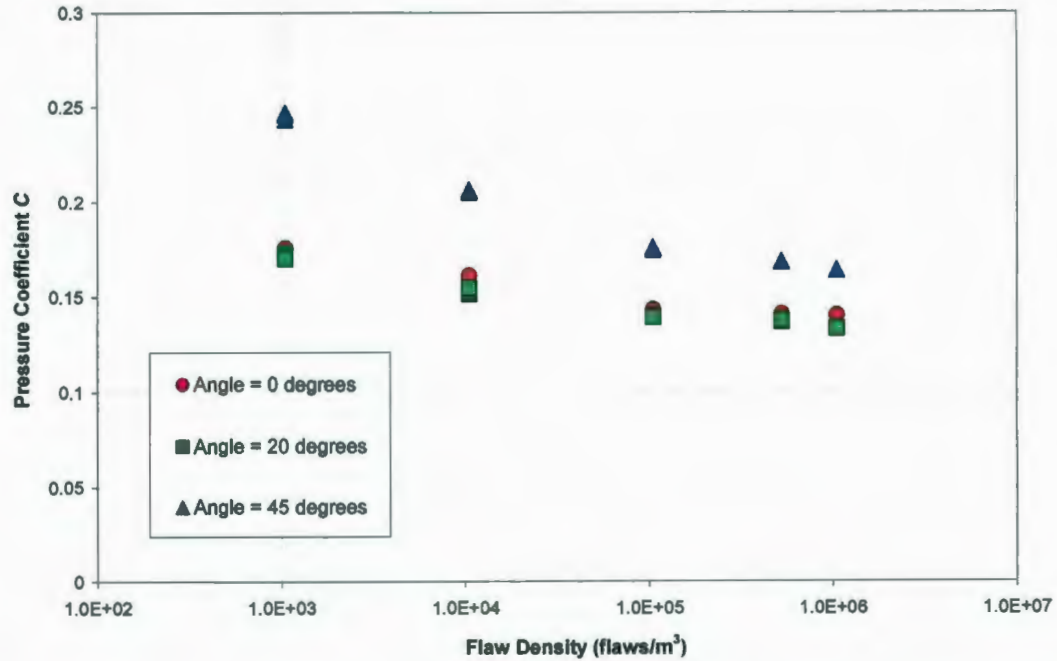


Figure 7.31: Plot of pressure coefficient C as a function of flaw density ρ_c for three different effective taper angles.

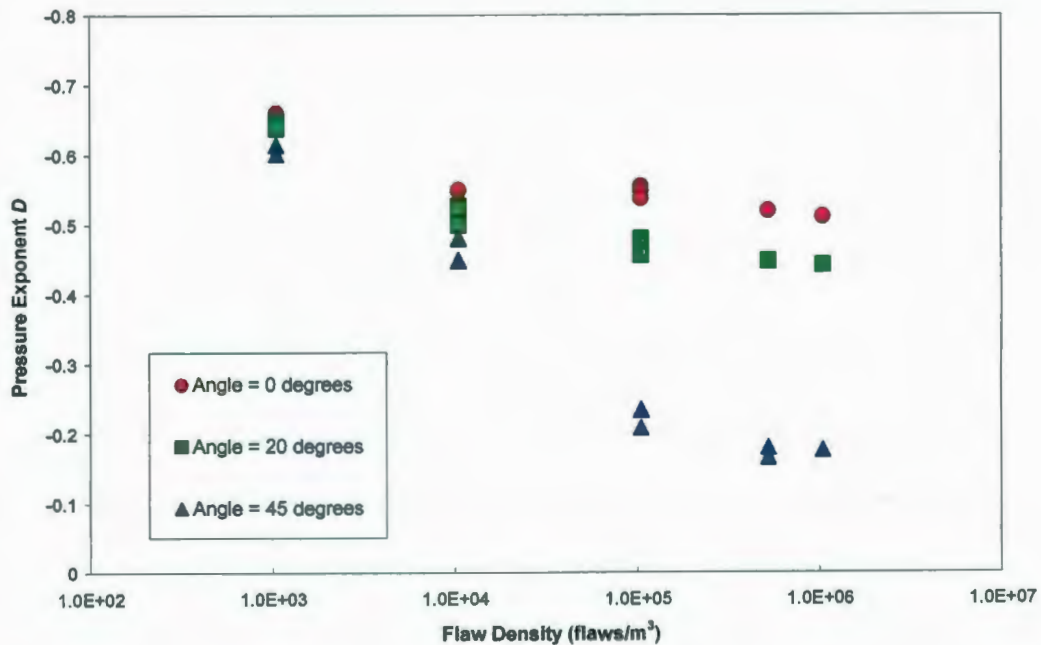


Figure 7.32: Plot of pressure exponent D as a function of flaw density ρ_c for three different effective taper angles.

It may be seen from both Figure 7.31 and Figure 7.32 that the results are much less sensitive to flaw density in the range above $\rho_c = 10^5 \text{ m}^{-2}$. Based on this observation, the simplifying assumption that the active number of cracks is about $\rho_c = 10^5 \text{ m}^{-2}$ has been made. This assumption is used throughout the analysis.

From the above analysis it is evident that the effective taper angle of the ice edge affects the pressure required to trigger a local fracture event. The influence is particularly strong for steeper taper angles. Higher values of the coefficient C correspond to the higher taper angles, and decrease as the effective taper angle is reduced. This indicates that higher pressures are required to trigger fractures events in highly tapered edges, compared with flatter edges. In other words, spalls occur more easily for flat ice edges, than for tapered edges. Local fracture becomes less likely as the ice edge becomes more tapered (i.e. after a period of spalling activity). From Figure 7.32, it is observed that the scale effect weakens for increasing taper angle (smaller values of exponent D).

Tapering of the ice edge is a consequence of spalling. Local damage processes (including small surface spalls) tend to reduce the effective taper angle through crushing and removal of material from the layer immediately adjacent to the contact zone. This observation serves as an explanation for the interplay between spalling and crushing. Spalling produces 'sharp' taper angles, which results in stress localization in a manner that supports damage, crushing and extrusion; damage results in strain localization due to softening in the layer, resulting in crushing failures which 'flatten' the edge, which in turn produces (after a number of cycles) conditions that support spalling fracture. Further work is recommended to explore more fully the influence of effective taper angles on spalling, and to investigate more clearly the links between spalling and crushing.

7.6.3 Effect of Proximity to the Edge

Line-type loads are generally concentrated near the horizontal centerline of an ice sheet (i.e. mid thickness) because spalls near the edge are more likely to occur at lower pressures. Due to the random nature of the processes involved in hpz formation there will be some variation in the location of the $hpzs$ relative to the centerline. Brittle indentation theory (see for

instance Lawn, 1993) suggests that the distance from the point of application of the load to the edge of the specimen has a significant effect on the loads required to trigger fracture. For the present analysis, eccentricity effects are examined for a flat ice edge (i.e. taper angle of $\omega = 0^\circ$).

To examine the effects of eccentricity on failure probability, four parametrically defined eccentricity values were modeled (see Figure 7.33). Recall that q is a geometric parameter defined in terms of thickness h as $q = 0.05h$.

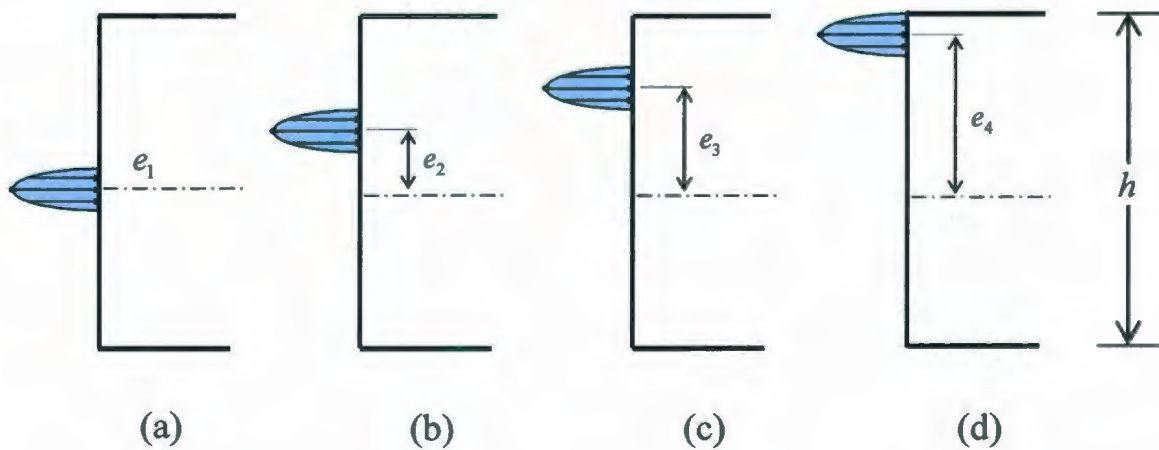


Figure 7.33: Four eccentricity cases: (a) $e_1 = 0q$; (b) $e_2 = 3q$; (c) $e_3 = 6q$; (d) $e_4 = 9q$.

The geometry for each model was based on the parameters shown in Figure 7.34; details for each case are summarized in Table 7.6.

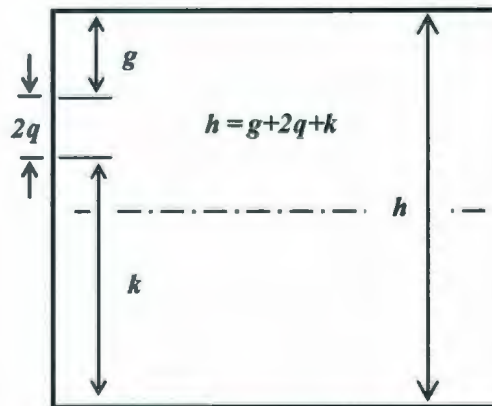


Figure 7.34: Model geometry used for study of eccentricity effects.

Table 7.6: Matrix of model geometry for analysis cases used to study eccentricity effects.

Case	h	q	e/q	g	k	
3	0.2	0.010	0	0.090	0.090	$e_1 = 0q$
6	0.5	0.025	0	0.225	0.225	
9	1.0	0.050	0	0.450	0.450	
12	2.0	0.100	0	0.900	0.900	
15	0.2	0.010	3	0.060	0.120	$e_2 = 3q$
18	0.5	0.025	3	0.150	0.300	
21	1.0	0.050	3	0.300	0.600	
24	2.0	0.100	3	0.600	1.200	
27	0.2	0.010	6	0.030	0.150	$e_3 = 6q$
30	0.5	0.025	6	0.075	0.375	
33	1.0	0.050	6	0.150	0.750	
36	2.0	0.100	6	0.300	1.500	
39	0.2	0.010	9	0.000	0.180	$e_4 = 9q$
42	0.5	0.025	9	0.000	0.450	
45	1.0	0.050	9	0.000	0.900	
48	2.0	0.100	9	0.000	1.800	

Simulations were conducted for each of the above cases (the density of flaws was assumed to be $\rho_c = 10^5 \text{ m}^{-3}$ based on discussions from Section 7.6.2). To study the influence of eccentricity on pressure-thickness scale effect, results for the above cases were grouped into four self-similar groups of geometries scaled by thickness, as shown in Table 7.6. Pressure thickness plots were generated for each of these groups in the same manner as discussed in Section 7.6.1 and power-law curves of the form $P = CA^D$ were fitted to each pressure thickness plot.

The pressure coefficient C and pressure exponent D corresponding to each eccentricity case was extracted. These results have been plotted in Figure 7.35 and Figure 7.36, respectively.

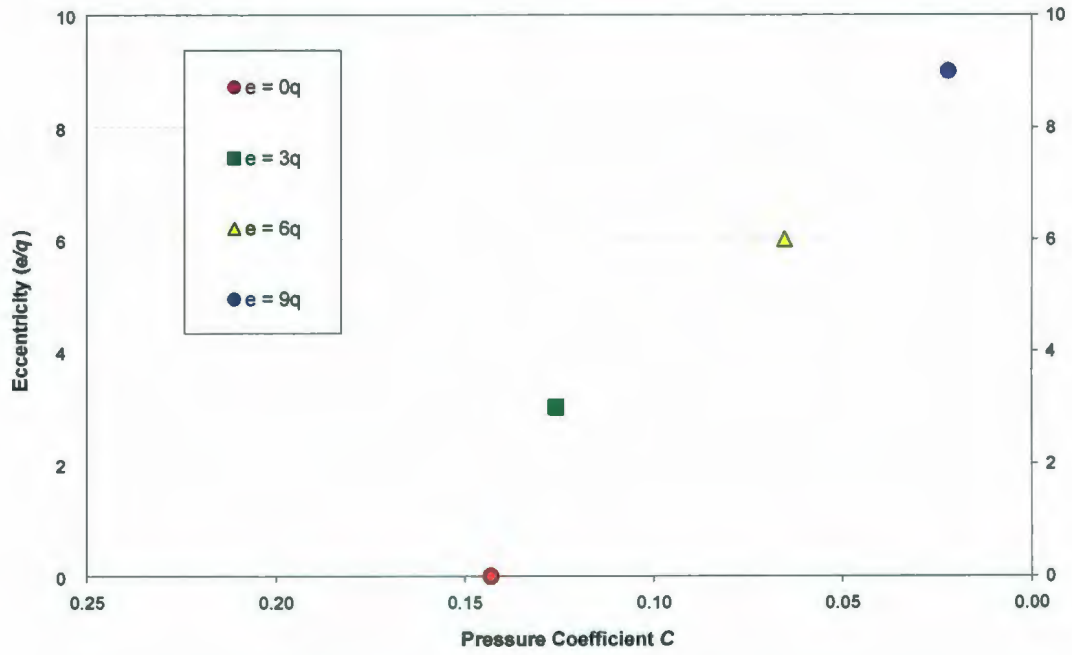


Figure 7.35: Plot of pressure coefficient C for each of the eccentricity cases.

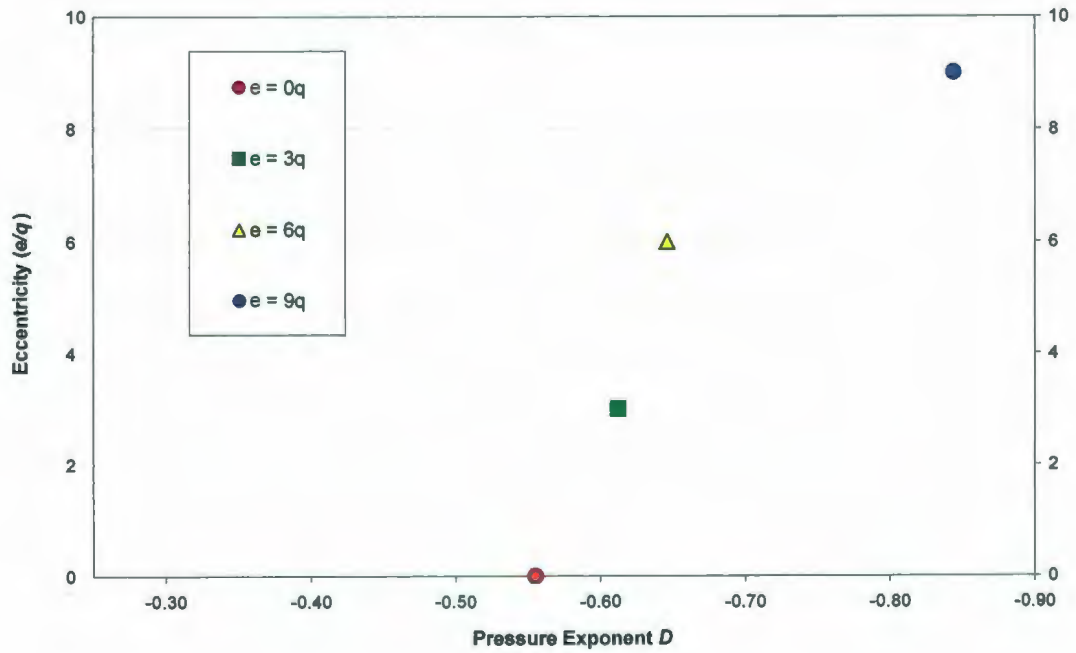


Figure 7.36: Plot of pressure exponent D for each of the eccentricity cases.

From Figure 7.35 it may be seen that the pressure coefficient C decreases as the center of the hpz moves away from the centerline of the ice sheet. This is a logical result, since the stress distribution is influenced by the presence of the free surface, and cracks emanating from behind the contact zone have to grow less before instability results (i.e. cracks have to cross a smaller distance to reach a free surface when the hpz is nearer to the edge). It may be observed from Figure 7.36 that the pressure exponent D gets larger (more negative) for $hpzs$ positioned closer to edge. This indicates that the scale effect is stronger (i.e. load drops off faster with thickness) for $hpzs$ positioned near the edge.

For an ice sheet, the maximum distance from a free surface corresponds to a distance of $h/2$. High pressure zones at locations closer to a free edge (i.e. further from the center) would likely fail sooner. Such $hpzs$ would not likely contribute significantly to the extreme pressures of interest in design. For this reason, it may be concluded that $hpzs$ centered about the middle of the ice thickness are more likely to occur and are of most relevance in modeling design ice pressures (i.e. are most representative of the $hpzs$ creating peak loads).

7.7 Discussion and Conclusions

In this chapter probabilistic approaches to modeling spalling fracture during ice-structure interaction were considered. For the present analysis, the ice failure process was idealized as a sequence of spalling events, and variations in loading due to crushing were represented by a monotonically increasing mean pressure. To establish a benchmark for comparison, a sample JOIA event was analyzed; the mean and standard deviation of these data were calculated and used to compare with theoretical results. Idealized ice edge geometry and loading functions were defined. Details of the elastic stress analysis, including a discussion pertinent to plane strain assumptions, was given. Sample finite element analysis results and a discussion of elastic stresses were presented. Stress analysis was carried out using the software ABAQUS. Elemental stress and volume outputs from these finite element solutions were used as inputs into probabilistic models developed in Matlab.

Probabilistic aspects of failure were first examined using a Weibull approach. A discussion of theory used in the model was given, followed by a description of its implementation. Only

tensile volumes were considered in this model, since this theory assumes a zero failure probability for elements with zero or negative (compressive) stress. Results were provided for a sample case (flat ice edge, $h = 1.0$ m, $2q = 0.1$ m); three sets of Weibull parameters (from Parsons et al., 1992) were used to estimate failure probability distributions. Failure pressure estimates from this model were found to be orders of magnitude higher than the benchmark data. This discrepancy was attributed to the 'tensile failure only' assumption, since cracks are often observed emanating from compressive zones (shear cracks) during the compressive failure of ice.

To account for the effects of both tensile and compressive (shear) fracture processes, a probabilistic fracture mechanics model was developed. Failure in this model was defined as the occurrence of a local spall. It was assumed that a local fracture (spall) resulted if unstable crack growth occurred anywhere in the specimen (i.e. in any element). The PFM routine was programmed to distinguish between elements in biaxial tension, biaxial compression or compression with lateral tension. Two crack models were used: one for tension only elements, and one for elements subject to compression. For tensile elements, unstable crack growth was assumed to occur once the energy release rate at the crack tip exceeded the critical value. For compressive elements, crack growth is stable. An instability (failure) criteria was developed based on the proximity of a given flaw to the nearest free surface; unstable crack growth was assumed to have occurred when one side of a crack intersects with a free surface. Equations accounting for the influence of flaw size, orientation, and crack density on the elemental failure probability were developed for both crack models. For a given state of stress, the total failure probability for the specimen was taken as the sum of elemental failure probabilities.

Proportional stressing was assumed, allowing elemental stress to be incrementally scaled with increasing applied pressure. The overall failure probability was determined for each incremental value of stress. These results were then used to model the probability distribution of spalling failure as a function of mean overall ice pressure (taken over the nominal area). Spalling probability distribution results were examined for several sample cases, and were found to be well modeled by a Type-I Extremal (Gumbel) distribution.

To study the scale dependence of ice pressure on thickness, four geometrically self-similar cases (scaled by thickness) were analyzed. The mean failure stress for each of these cases (taken as corresponding to a failure probability of 50%) was extracted and plotted against thickness. This result showed a clear theoretical scale effect in peak (spalling) pressure due to probabilistic aspects of fracture. The pressure-thickness data were found to follow a power law relationship:

$$P = 0.15h^{-0.50}$$

This relationship was compared with the benchmark data and found to correspond to about $\mu_e + 4.5\sigma_e$, where μ_e and σ_e are the event mean and standard deviation of pressure, respectively for the benchmark data. This initial result provides strong support for the validity of the PFM approach, though broader comparisons of model results with data are recommended.

The PFM model was then implemented to study the influence of ice edge shape (taper angle). From this analysis it was observed that higher pressures are required to cause spalling in specimens with more tapered edges (i.e. flatter edges spall more readily). From the pressure exponent results it was observed that stronger scale effects (i.e. larger values of D) are associated with flatter edges compared with highly tapered edges. This result serves as a possible explanation for the interplay between spalling and crushing. The occurrence of spalls produces geometry that supports crushing, while crushing produces geometry that supports spalling. This is an interesting and important area of research. Further work is recommended to more fully explore the observed behavior and to investigate the links between spalling and crushing.

Simulations aimed at studying the effect of *hpz* eccentricity on pressure scaling were then conducted using the PFM model. From this analysis it was observed that *hpzs* positioned nearer to an edge require considerably less pressure to trigger a spall. It was also observed that the pressure-thickness data corresponding to locations nearer to an edge exhibit a stronger scale effect (i.e. larger pressure exponent D). It was concluded that *hpzs* centered about the middle of the ice thickness are of most relevance in modeling design ice pressures (i.e. are most representative of the *hpzs* creating peak loads).

Recommendations for future work include expanding the model to include stress updating in the crack growth models and to explore time-dependent crack growth. The study of theoretical factors influencing consequences of spalling (i.e. shape, location and size of spall) was identified as an area requiring further research. Expansion of the model to include a three dimensional spalling analysis is recommended to account for variation in *hpz* characteristics across the width of a structure. Incorporation of the PFM model into time series simulations for modeling ice loads is recommended to allow for a broader comparison with full-scale data.

Chapter 8: Conclusions

8.1 Summary and Conclusions

The main focus of this study was scale effect associated with compressive ice failure. Emphasis was placed on understanding the behavior of high pressure zones, and the processes responsible for their formation and evolution, with particular focus on spalling fracture. Probabilistic averaging, arising from the non-simultaneous nature of multiple *hpzs* acting over an area has been examined. Methodology for extrapolating full-scale pressures from local panel pressures based on probabilistic averaging methodology has been studied. The trend of decreasing pressure with increasing thickness for a panel of unit width was explored using full-scale data. Spalling fracture was identified as being both a major factor affecting *hpz* behavior and a main cause of observed scale effects in ice pressure. To study theoretical aspects of spalling fracture and the pressure-thickness scale effect, probabilistic failure models were developed.

8.1.1 Critical Analysis of Scale Effects

From the examination of data and theory related to scale effects in ice it was concluded that the two primary contributors to the scale dependence of ice pressure behavior are: (i) statistical averaging effects, and (ii) effects associated with mechanics. Statistical aspects of scale effect result from the averaging of non-simultaneous loads acting across the width of a structure. Scale effects due to mechanics include contributions due to the mechanics of fracture, and the probabilistic nature of spalling, which limits local loads during an interaction.

8.1.2 Analysis of High Pressure Zones

To study the behavior of a single *hpz*, sample test data from small-scale indentation tests were analyzed. These results highlighted the importance of the interplay between damage and spalling in *hpz* formation and evolution. Failure processes observed during small-scale experiments were simulated in the finite element package ABAQUS using a damaging, viscoelastic material model, and element removal techniques (for spalling). The finite element simulations yielded good agreement with load behavior for the selected case. From this work it was concluded that the severity of the consequences of fracture (i.e. reduction of contact area and drop in load) are dependent on many factors, such as the size, location and shape of the spall. Modeling all of these aspects would be quite complex, and idealizations based on experimental observations were made. Given the random nature of spalling fracture it was concluded that a probabilistic approach was appropriate.

As part of this research program, preliminary small-scale ice sheet edge indentation tests were carried out. From the results of these tests it was concluded that the fracture behavior of small specimens are highly influenced by boundary conditions. In events where crushing was observed, contact was first localized into *hpzs* through the formation of spalls. Even for the small ice thicknesses considered in this program (order of several centimeters), line-type configurations of multiple *hpzs* were observed during crushing. During one experiment, a continuous layer of extruded sintered ice was observed to 'grow' laterally from the contact zone due to the sintering of crushed ice particles as they were extruded from the layer.

From the analysis of tactile pressure sensor data from the JOIA program, characteristics of high pressure zones were investigated for a sample event. The contact area during a crushing event was observed to correspond to about 10% of the nominal area. From the analysis of crushing and spalling processes as manifested in the tactile data, it was observed that significant non-simultaneity occurs during the compressive failure of ice, highlighting the need for probabilistic averaging methodology.

8.1.3 Study of Probabilistic Averaging Effects

Local panel pressure data from the JOIA program were analyzed to study probabilistic averaging and evaluate methods for extrapolating global pressure estimates using local pressure data. The end panels (P1, P15) were observed to exhibit edge effects and data from these end panels were not included in the final analysis. The standard deviations of local pressure data were higher than the standard deviations of measured global pressure data, particularly for higher speeds events where non-simultaneous aspects of failure are more dominant. These observations are consistent with probabilistic averaging theory, which provides strong support for use of these methods in estimating global loads from local pressure data. The effects of averaging are expected to be more pronounced at full-scale, since averaging takes place over a much larger width. Probabilistic averaging is believed to be an important contributor to the observed pressure-area scale effects. For design the conservative assumption of a fully loaded width is often taken, though large global fracture events would likely further reduce global loads (particularly those resulting in a reduction of the loaded width of the structure).

For higher speed interactions, individual panel correlations were generally observed to be lower than were typically observed for lower speed tests. This was attributed to the random nature of high speed interactions, compared with the more uniform failure behavior observed at lower speeds. The individual panel correlation data were plotted as a function of the distance between panels and used to assess the autoregressive correlation functions required for the probabilistic averaging analysis. A value of $c = 0.20$ m (characteristic correlation length) was chosen for analysis using the autoregressive method. A new approach based on a linear combination of correlation functions (referred to as the composite approach) was found to give promising results as an alternate method for modeling correlation.

Local pressure data were used to produce estimates of global pressure based on three different approaches. These included: (1) standard correlation probabilistic averaging; (2) composite correlation probabilistic averaging; (3) linear extrapolation of local pressures (no probabilistic averaging). These estimates were compared to the measured global loads and the average estimation error associated with each method was calculated. The standard

correlation probabilistic averaging method was found to result in substantially lower average estimation error compared with the linear extrapolation approach. Results obtained using the composite correlation approach were promising and further investigation of this method is recommended.

To study correlation behavior at full-scale, local panel pressure data from the Molikpaq were analyzed using both the standard and composite correlation modeling approaches. These results were compared with those from the JOIA data and observed differences due to the different scale of the structures were discussed. An initial attempt to scale correlation by thickness was made to account for the different ice conditions; further work on correlation scaling is recommended.

8.1.4 Analysis of Thickness Scaling in Full-scale Data

From the pressure-area effect it follows that a panel of constant width should experience decreasing pressure as a function of increasing ice thickness. The analysis of indentation data for ice specimens with remote edges indicated a clear link between the onset of spalling fracture (at higher speeds) and the onset of scale dependent pressure behavior. This suggests that the pressures required to trigger spalling fractures should exhibit the same dependence on ice thickness as does the measured pressure data.

To study the relationship between pressures and ice thickness, full-scale data were analyzed for panels of approximately unit width. From these data a distinct offset was observed in the Molikpaq data compared with other datasets. In the absence of a recalibration correction the trends of the Molikpaq data were not consistent with the STRICE, JOIA and Cook Inlet datasets. Accounting for recalibration of the Medof panels was found to give results for the Molikpaq that are more consistent with those of the other datasets.

Representative power law curves were fit to data for a variety of analysis cases based on different combinations of data filters. The results that were determined to be most representative of the pressure-thickness effect observed in the STRICE and corrected

Molikpaq data followed the relationship $P_{avg} = 0.278h^{-0.408}$ and $P_{std} = 0.172h^{-0.273}$ for the mean and standard deviation of pressure, respectively.

Duration weighting was explored as a technique to weight the contributions of individual events based on record length. Longer events were more influential in the calculation of the overall statistical characteristics of the ensemble data than were shorter duration events. It was concluded that the duration weighting approach produced curves which did not bound the data well for thick ice events. This was attributed, in part, to the fact that more data exists for thin ice events than for thick ice, and duration weighting resulted in trends that were highly influenced by the thin ice events. It was also observed that that a weighting scheme based on duration (time) assigns a higher weight to slower speed events, since it takes a longer time to cover the same interaction distance for slow speed interactions.

8.1.5 Theoretical Modeling of Spalling Fracture and Scale Effects

To simplify the theoretical analysis, variations in loading due to crushing were represented by a monotonically increasing mean pressure and the ice failure process was idealized as a sequence of spalling fracture events. The mean μ_e and standard deviation σ_e of pressure data for a sample JOIA event were calculated to establish a benchmark for comparison with theoretical results. Definitions of the idealized ice edge geometry, parabolic pressure distribution and plane strain assumptions used in the elastic stress analysis were given. A discussion of the elastic stress analysis (carried out using the software ABAQUS) was presented, along with sample finite element solution results. Outputs from the finite element analysis (element centroidal coordinates, stress components and element volumes) were exported from ABAQUS and imported into Matlab as inputs into the probabilistic failure analysis routines.

A probabilistic model based on Weibull theory was developed. Since this theory assumes a zero failure probability for elements with zero or negative (compressive) stress, only elements with tensile stresses were included in this analysis. Three sets of Weibull parameters (from Parsons et al., 1992) were used to estimate failure probability distributions for a representative sample case (flat ice edge, $h = 1.0$ m, $2q = 0.1$ m). Failure pressure

estimates obtained from this analysis were orders of magnitude higher than the pressures observed from the benchmark data. This discrepancy was attributed to the assumption that failure is only possible in tensile elements. During the compressive failure of ice, shear cracks are frequently observed to nucleate and grow from compressive regions of the ice. From the results of this model, it was concluded that both tensile and shear cracks must be included in the probabilistic model.

Using a probabilistic fracture mechanics approach, the effects of both tensile and compressive (shear) cracks were modeled based on a flaw distribution linked to grain size and elastic stresses estimated using finite element analysis. Here failure was defined as the occurrence of spalling fracture (i.e. unstable crack growth) in any element. Separate crack models were used for tensile elements, and for elements subject to compressive loading. Crack growth under compressive conditions was assumed to be stable until one of the wings of a shear crack was of sufficient length to intersect with the nearest free surface; instability (spalling) was assumed to occur once this condition was satisfied. For tensile cracks, exceedence of the critical energy release rate at the crack tip was taken as the critical condition for unstable crack growth. For each of the crack models, equations were developed to allow for estimation of the elemental failure probability based on the assumed flaw size, orientation, and crack density distributions. The total probability of failure for the specimen given as specific state of stress was then calculated as the sum of all elemental failure probabilities.

The elemental stresses were defined as being proportional to the peak *hpz* pressure, allowing stresses to be scaled with pressure. The overall failure probability of a given specimen was evaluated as a function of increasing stress, which was incrementally ramped up until a failure probability of unity was reached. The spalling failure probability as a function of the mean overall pressure (over the nominal area) was then plotted; these data were found to be well fitted by Type-I Extremal (Gumbel) probability distributions.

The dependence of pressure on ice thickness was studied based on four geometrically self-similar cases that we scaled by thickness. The mean failure stresses (i.e. corresponding to a failure probability of 50%) were compiled for all of these cases and plotted against thickness.

From these results a clear theoretical scale effect in peak (spalling) pressure was observed, which followed the power law relationship, $P_{p,th} = 0.15h^{-0.50}$. This relationship was found to correspond to a peak pressure of about $\mu_e + 4.5\sigma_e$, where μ_e and σ_e are the event mean and standard deviation of pressure for the benchmark data. This result suggests that the peak pressures predicted by the PFM are in good agreement with the expected range of peak pressures estimated from the benchmark data. Time series simulations are required to provide more meaningful statistical comparisons of the PFM model results with data.

To study the effect of ice edge shape (taper angle) on the scale effect, the PFM model was implemented for a combination of cases comprised of three taper angles, and four thicknesses (twelve total). These results indicate that specimens with flatter edges tend to spall at lower pressures, while those with more tapered edges spall less readily. Larger values of the pressure exponent D were observed for specimens with flatter edges, suggesting that stronger scale effects are associated with small taper angles compared with highly tapered edges. It was concluded that this result serves as a possible explanation for the interplay between crushing and spalling failure. Spalls produce geometry that localizes contact in a manner that supports crushing, while crushing (often over several cycles) tends to 'flatten' the ice edges, producing geometry that supports spalling. More work is required in this area to further investigate the links between crushing and spalling.

To study the influence of *hpz* eccentricity on the pressure-thickness scale effect a series of simulations were conducted using the PFM model based on a combination of four eccentricity values with four ice thicknesses (sixteen cases total). It was observed from these results that the mean peak (failure) pressure decreases for increasing eccentricity (i.e. *hpzs* located nearer to an edge are expected to trigger spalling at considerably lower pressures). Larger values of the pressure exponent D were also observed (i.e. stronger scale effects) for *hpzs* positions nearer to an edge. From this analysis it was concluded that *hpzs* centered about the middle of the ice thickness are the zones most likely to create the peak pressures that are of interest in design. The assumption that *hpzs* are located at the center of the ice sheet is seen as most appropriate.

From the above results it may be concluded that the PFM model produced more realistic estimates of ice pressure behavior than were found using the Weibull (tensile only) model. This observation suggests that the shear cracking mechanism is a key component of the spalling process, which in turn appears to be the primary cause of the local pressure-thickness effect.

Overall it may be concluded, that the probabilistic fracture mechanics approach developed in this thesis provides good agreement with results and trends observed from full-scale interactions. Probabilistic aspects of random spalling fracture are believed to be the key factor governing the scale-effect associated with local ice pressure behavior. For the conditions of interest for design (i.e. assuming no global fracture) probabilistic averaging is believed to be a main contributor to the global pressure scale effect. From the analysis of tactile pressure sensor data, the non-simultaneous failure behavior of ice (and hence probabilistic averaging) has been linked to random (spalling) fracture events. It is believed that improved understanding of the spalling process (and its interplay with crushing failure) is key to improving the state of knowledge regarding scale effects in ice. Through improved understanding and modeling of random spalling and its role in non-simultaneous failure, it is believed that greater clarity of the links between local and global pressure behavior will emerge.

8.2 Recommendation for Future Work

During the course of this research program, a number of recommendations for future work emerged. One of the areas identified for further research is the study of *hpz* behavior during full-scale interactions. At present tactile pressure sensor data does not exist for interactions with thick ice. Throughout this study it was assumed that on average there is only a single *hpz* across the thickness of the ice. This assumption was verified for small and medium scale thicknesses up to about 30cm, but this cannot be verified for thicker ice. From the analysis of panel correlation data, higher correlations as a function of distance were observed for full-scale than for medium scale data. The possibility of multiple *hpzs* per unit thickness was identified as a potential source of the higher correlations. Further work is needed to explore

full-scale *hpz* characteristics and correlation behavior. Investigation of the effects of event duration on correlation modeling is also recommended.

From the analysis of JOIA tactile sensor data a number of recommendations were made. The need for further investigation of the links between correlation structure, *hpz* characteristics, and observed failure behavior was identified. The assessment of statistical aspects of *hpz* characteristics such as size, density, frequency, persistence and intensity is an important direction for further research. An assessment of the influence of ice thickness and interaction speed on these characteristics is needed. Further work may also examine the frequency of occurrence of spalling and crushing failures and explore links between these processes.

From the analysis of JOIA segmented panel data it was observed that the slow interaction events had larger total loads than brittle failure events. This was attributed to the more uniform contact conditions across the entire width of the structure during the slow tests. Such conditions are not believed to be representative of full-scale since fracture, partial loading or other localized failure would affect the contact conditions at full-scale. Fracture is also likely to be more important at larger scales since both the stressed volume of ice and the associated field of flaws would be larger. Further review and analysis of Molikpaq data to examine creep cases is recommended, since emphasis to date has been primarily on crushing.

In analyzing pressure-thickness behavior in full-scale data it is recommended that alternatives to the duration weighting method used here be explored to identify a more effective approach (recall that unweighted data were used in the final curve fits selected). The use of interaction distance as a weighting measure was recommended as a possible alternative approach to explore in future work.

The probabilistic fracture mechanics model gave promising results, and a number of recommendations for further development have been made. One area is to expand the crack growth models to include stress updating at the crack tip by mapping the stresses along the mean trajectory of the crack. Expanding the model to include the effects of time-dependent crack growth would also be a worthwhile improvement. To model the consequences of spalling, which is dependent on factors such as the shape, location and size of the spall, further study is required. To account for variation in *hpz* characteristics across the width of a

structure, and attempt to link probabilistic averaging with spalling failure, expansion of the model to include a three dimensional spalling analysis is recommended. To allow for broader comparison of PFM results with full-scale data, further work is recommended to more fully exercise the PFM model and incorporate it into time series simulations for modeling ice loads. Extension of this model to other applications involving floe splitting or interactions with icebergs is recommended.

In conclusion, the results of the above research are promising and are believed to provide strong support for continued research in the development and application of probabilistic fracture mechanics to the study of scale effects in compressive ice failure and to guide the development of methods for the estimation of design ice pressures.

Bibliography

Abdel-Tawab, K., Rodin, G.J., 1995. Inelastic effects in fracture of columnar-grained ice. *Ice Mechanics -1995*, AMSE AMD-Vol. 207, 49-63.

Akagawa, S., Nakazawa, N., Sakai, M., 2000. Ice failure mode predominantly producing peak-ice-load observed in continuous ice load records. *Proceedings of the 10th International Offshore and Polar Engineering Conference*. 2000. p. 613.

Anderson, T.L., 2005. *Fracture mechanics: fundamentals and applications*, 3rd edition. CRC Press. Boca Raton, FL.

Ashby, M.F., Palmer, A.C., Thouless, M., Goodman, D.J., Howard, M.W., Hallam, S.D., Murrell, S.A.F., Jones, N., Sanderson, T.J.O., Ponter, A.R.S., 1986. Non-simultaneous failure and ice loads on arctic structures. *Offshore Technology Conference 1986*. Houston. Paper No. OTC 5127, pp. 399-404.

Ashby, M.F., and Hallam, S.D., 1986. The failure of brittle solids containing small cracks under compressive stress states. *Acta Metallurgica*. Vol. 34, No. 3, pp.497-510, 1986.

Ashby, M.F., and Sammis, C.G., 1990. The damage mechanics of brittle solids in compression. *PAGEOPH*, 133: 489-521.

Atkins, A.G., and Mai, Y.W., 1985. *Elastic and plastic fracture*. Ellis Horwood.

Barnes, P., Tabor, D., Walker, J.C.F., 1971. The friction and creep of polycrystalline ice. *Proc. R. Soc. London. Ser. A* 324: 127-55.

Barrette, P., Pond, J., and Jordaan, I., 2002. Ice damage and layer formation in small scale indentation experiments. *Ice in the Environment, Proceedings of the 16th international Symposium on Ice, IAHR, Dunedin, New Zealand, 2002*, vol. 3:246-253.

Barrette, P., Pond, J., Li, C., and Jordaan, I.J., 2003. Laboratory scale indentation of ice. Technical Report PERD/CHC 4-81. Report prepared for The National Research Council of Canada, Program Energy Research and Development (PERD).

Batdorf, S.B., and Heinisch Jr., H.L., 1978. Weakest link theory reformulated for arbitrary fracture criterion. *Journal of the American Ceramic Society* 61, pp. 355–358.

Bazant, Z.P., Kim, J.K., 1985. Fracture theory for non-homogeneous brittle materials with application to ice. *Proceedings of the ASCE Arctic '85 Conference, San Francisco*. pp. 917-930.

Bazant, Z.P., Planas, J., 1998. *Fracture and size effect in concrete and other quasibrittle materials*. CRC Press. Boca Raton, FL.

Bhat, S.F., 1990. Modeling of size effect in ice mechanics using fractal concepts. *Journal of Offshore Mechanics and Arctic Engineering*. 112(4), pp. 370-376.

Biot, M.A., 1954. Theory of stress-strain relations in anisotropic viscoelasticity and relaxation phenomena. *Journal of Applied Physics*, Vol. 25, pp. 1385-1391.

Blanchet, D., DeFranco, S.J., 1996. Global first-year ice loads: scale effect and non-simultaneous failure. *Proceedings 14th IAHR Symposium on Ice, Beijing, China*. p. 203-213.

Bolotin, V.V., 1969. *Statistical methods in structural mechanics*. Holden-Day. (Translated from Russian by Samuel Aroni).

Brockway, G.S., and Schapery, R.A., 1978. Some viscoelastic crack growth relations for orthotropic and prestrained media. *Engineering Fracture Mechanics*. Vol. 10, pp. 453-468. Pergamon Press.

Broek, D., 1986. Elementary engineering fracture mechanics. pp. 9-12, 22-24, 99-104, Martinus Nijhoff Publishers, Boston.

Bruce, J., 2009. Level ice interaction with sloping and conical offshore structures. M.Eng. Thesis. Memorial University, St. John's, NL, Canada.

Budianski, B., and O'Connell, R., 1976. Elastic moduli of a cracked solid. *International Journal of Solids and Structures*. 12, 81-97.

Cammaert, A.B., Muggeridge, D.B., 1988. Ice interaction with offshore structures. Van Nostrand Reinhold. New York.

Cole, D.M., 1986. Effect of grain size on the internal fracturing of polycrystalline ice. CRREL Report 86-5.

Cole, D.M., 1988. Crack nucleation in polycrystalline ice. *Cold Regions Science and Technology*. 15. pp. 79-87.

Conrad, N., 1976. On microcrack growth and arrest in simulated fibrous composites. Mechanics and Materials Research Center, Texas A&M University, College Station, Report MM 3168-76-10.

Cormeau, A., Jordaan, I.J., and Maes, M., 1986. Development of a model for progressive damage in ice. Det Norske Veritas (Canada) Ltd. Calgary, Alberta.

Cotterell, B. and Rice, J., 1980. Slightly curved or kinked cracks. *International Journal of Fracture* 16, 155-169.

Croasdale, K.R., 1975. Ice forces on marine structures. Proceedings 3rd IAHR Symposium on Ice. Hanover, NH. 1975. pp. 317-337.

Croasdale, K.R., Morgenstern, N.R., Nuttal, J.B., 1977. Indentation tests to investigate ice pressures on vertical piers. *Journal of Glaciology*. 19(81). pp. 301-312.

Croasdale, K.R., 1984. The limited driving force approach to ice loads. Offshore Technology Conference 1984. Houston. Paper No. OTC 4716, pp. 57-64.

Crocker, G.B., Croasdale, K.R., McKenna, R.F., English, G.M., Guzzwell, J. and Bruneau, S.J., 1997. C-CORE iceberg impact experiment-phase 2, final report. C-CORE, Memorial University of Newfoundland, Newfoundland.

CSA S474-04, 2004 General requirements, design criteria, the environment, and loads. CSA Standard S474-04, Canadian Standards Association. February 2004.

Daley, C., 1991. Ice edge contact, a brittle failure process model. Dissertation, Acta Polytechnica Scandinavica, Me 100, Helsinki, 92 pp.

Daley, C., Tuhkuri, J., Riska, K., (1998). The role of discrete failures in local ice loads, Cold Regions and Science Technology, 1998, 27, 197.

Danielewicz, B.W., and Metge, M., 1981. Ice forces on Hans Island, 1980. APOA Project No. 180.

DeFranco, S.J., and Dempsey, J.P., 1990. Crack growth stability in S2 ice. IAHR Symposium, Espoo, Finland.

Dempsey, J.P., 1996. Scale effects on the fracture of ice. The Johannes Weertman Symposium. The Minerals, Metals and Materials Society, 1996. pp 351-361.

Dempsey, J.P., 1999. Research trends in ice mechanics. Research Trends in Solid Mechanics. USNC/TAM Committee, 1999.

Dempsey, J., Adamson, R., and Mulmule, S., 1999. Scale effects on the in-situ tensile strength and fracture of ice, part 2: first year sea ice at Resolute, N.W.T. International Journal of Fracture 95, 347-366.

Dempsey, J.P., 1991. The fracture toughness of ice. Ice-Structure Interaction. (ed. S.J. Jones, R.F. McKenna, J. Tillotson, I.J. Jordaan) Springer-Verlag, Berlin Heidelberg. 109-145.

Derradji-Aouat, A., Evgin, E., Sinha, N.K., 1990. Finite element calculations of ice pressure on rigid structures. Proceedings of 9th OMAE. Houston, Texas. pp. 75-81.

Derradji-Aouat, A., 2005. Explicit FEA and constitutive modeling of damage and fracture in polycrystalline ice – simulation of ice loads on structures. Proceedings of 18th POAC. Potsdam, New York. Vol. 1, pp. 225-238.

Derradji-Aouat, A., and Evgin, E., 2001. A constitutive model for isotropic freshwater ice. *Can. Geotech. J.* 38, 818–827.

Dunwoody, A.B., (1991) Non-simultaneous ice failure. A report to Amoco Production, Tulsa, OK.

Duval P., Ashby, M.F., Anderman, I., (1983) Rate-controlling processes in the creep of polycrystalline ice. *J Phys Chem* 87: 40667-4074.

Elvin, A.A, Shyam Sunder, S., 1996. Microcracking due to grain boundary sliding in polycrystalline ice under uniaxial compression. *Acta mater.* Vo. 44. No. 1, pp.43-56.

Evans, A.G., 1978. A general approach for the statistical analysis of multiaxial fracture. *Journal of the American Ceramic Society.* 61, pp. 302–308.

Evans, A.G., Palmer, A.C., Goodman, D.J., Ashby, M.F., Hutchinson, J.W., Ponter, A.R.S., and Williams, G.J., 1984. Indentation spalling of edge loaded ice sheet, IAHR Ice Symposium, Hamburg.

Findley, W.N., Lai, J.S. and Onaran, K., 1976. Creep and relaxation of nonlinear viscoelastic materials. North-Holland Publishing Company.

Finn, D., 1991. Vertical and inclined edge-indentation of freshwater ice sheets. M.Eng Thesis, Memorial University, St. John's, NL, Canada.

Fransson, L., Olofsson, T., Sandkvist, J., 1991. Observations of the failure process in ice blocks crushed by a flat indenter. Proceedings of 11th International Conference on Port and Ocean Engineering under Arctic Conditions, St. John's, Canada. vol. 1, pp. 510-514.

Frederking, R., 1998. Pressure area relation in the definition of ice forces. In Proceedings of 8th IAHR International Symposium on Ice, Volume 2, Montreal, Canada, pp. 431–437.

Frederking, R.M.W., 2004. Ice pressure variations during indentation. Proceedings of the 17th IAHR International Symposium on Ice. 2004. Vol. 2. p. 307.

Frederking, R. and Gold, L.W., 1975. Experimental study of edge loading of ice plates. Canadian Geotechnical Journal, 12, 4:456-463.

Frederking, R.M.W., Blanchet, D., Jordaan, I.J., Kennedy, K., Sinha, N.K., Stander, E., 1989. Field tests on ice indentation at medium scale, ice island. National Research Council of Canada Report CR 5866.1.

Frederking, R.M.W., Jordaan, I.J., and McCallum, J.S., 1990. Field tests of ice indentation at medium scale: Hobson's Choice ice island 1989. Proceedings of 10th International Symposium on Ice, IAHR' 90, Espoo, Finland, Vol. 2, pp. 931-944.

Freudenthal, A.M., 1968. Statistical approach to brittle fracture. Fracture, ed., H. Liebowitz, Vol. II. pp. 591-619.

Frost, H., 1995. Mechanisms of crack nucleation in ice. Ice Mechanics. ASME. 207. pp. 1-8.

Frost, H., 2001. Mechanisms of crack nucleation. Engineering Fracture Mechanics. 68 (2001) 1823-1837.

Gagnon, R.E., and Sinha, N.K., 1991. Energy dissipation through melting in large scale indentation experiments on multi-year sea ice, Proceedings of OMAE, Vol. IV, pp. 157-161.

Gagnon, R.E., 1998. Analysis of visual data from medium scale indentation experiments at Hobson's Choice Ice Island. Cold Regions Science and Technology. 28:45-58.

Glen, J.W., 1955. The creep of polycrystalline ice, Proceedings Royal Society of London, Piccadilly, London, W., Ser. A, Vol. 228, pp.519-538.

Glen, J.W., 1975. The mechanics of ice: cold regions science and engineering monograph II-C2b. Cold Regions Research and Engineering Laboratory, Hanover, New Hampshire. p. 29-33.

- Gold, L.W., 1963. Crack formation in ice plates by thermal shock. *Can J Phys* 1963; 41: 1712-28.
- Gold, L.M., 1972. The failure process in columnar-grained ice. Technical Paper No. 369, Division of Building Research, NRC.
- Griffith, A.A., 1920. Phenomena of rupture and flow in solids. *Philos. Trans. R. Soc. London, Ser. A221*, pp. 163-198.
- Gulf Canada Resources Ltd., 1987. Dynamic horizontal ice loading on an offshore structure; phase 1A: Molikpaq performance at Amauligak I-65, Vol. 3 - Instrumentation. (CHC 14-3).
- Hallam, S.D., 1986. The role of fracture in limiting ice force. *Proceedings of IAHR Ice Symposium, Iowa*. pp. 287-319.
- Hallam, S.D., Duval, P., Ahsby, M.F., 1986. A study of cracks in polycrystalline ice under uniaxial compression. *Proceedings of 7th Symposium on the Physics and Chemistry of Ice, Grenoble. Journal de Physique, Colloque C1, Supplement au No. 3, Tom. 48 (1987)*. Pp. 303-311.
- Hayes, D. J., 1975. Origins of the energy balance approach to fracture, *Journal of Strain Analysis*, 10 (4), 195-197.
- Hobbs, P.V., 1974. *Ice physics*. Clarendon Pres, Oxford.
- Hoek, E., and Bieniawski, Z.T., 1965. Brittle fracture propagation in rock under compression. *International Journal of Fracture*. 1, 137-155.
- Horii, H. and Nemat-Nasser, S., 1983. Overall moduli of solids with microcracks: load-induced anisotropy. *Journal of Mechanics and Physics of Solids*, Vol. 31, No. 2, pp. 155-171.
- Hunt, R.A. and McCartney, L.N., 1979, A new approach to Weibull's statistical theory of brittle fracture, *Int. Journal of Fracture*, 15.
- Hutchinson, J.W. and Suo, Z., 1992. Mixed mode cracking in layered materials. *Advances in Applied Mechanics*. Academic Press, Vol. 29, pp. 63-191.

Inglis, C.E., 1913. Stresses in a plate due to the presence of cracks and sharp corners. Transactions of the Institute of Naval Architects. 55, 219-230.

Irwin, G.R., 1957. Fracture. Handbuch der physic. 6. Springer-Verlag, Berlin.

ISO 19906. Petroleum and natural gas industries – arctic offshore structures. ISO Draft International Standard. ICS 75.180.10.

Jayatilaka, A.D.S, Trustrum, K., 1977. Statistical approach to brittle fracture. Journal of Materials Science. 12: 1426-1430.

Jefferies M.G. and Wright, W.H., 1988. Dynamic response of Molikpaq to ice-structure interaction. OMAE, Houston, Texas.

Joensuu, A., Riska, K., 1989. Contact between ice and structure (in Finnish). Laboratory of Naval Architecture and Marine Engineering. Helsinki University of Technology, Espoo, Finland, Report M-88.

Johnston, M.E., Croasdale, K.R., Jordaan, I.J., 1998. Localized pressures during ice-structure interaction: relevance to design criteria. Cold Regions Science and Technology. 27. pp. 105-117.

Jonas, J.J. and Muller, F., 1969. Deformation of ice under high internal shear stresses, Canadian Journal of Earth Sciences, Vol. 6, pp.963-968.

Jordaan, I.J., 2001. Mechanics of ice-structure interaction. Engineering Fracture Mechanics; 68:1923-1960

Jordaan, I.J., 2005. Decisions under uncertainty: probabilistic analysis for engineering decisions. Cambridge University Press. 672 pp.

Jordaan, I.J., Hewitt, K., Frederking, R., Bruce, J. and Sudom, D., (In Preparation). 'Re-evaluation of pressures and loads measured on the Molikpaq structure, 1985-6 season'. Paper in preparation for POAC 2011 conference.

Jordaan, I. and McKenna, R., 1988. Constitutive relations for creep of ice. Proceedings of 9th IAHR International Symposium on Ice, Vol. 3, Sapporo, Japan, pp. 47–58.

Jordaan, I.J., and McKenna, R.F., 1989. Processes of deformation and fracture of ice in compression. Proceedings IUTAM/IAHR Symposium on Ice-Structure Interaction, St. John's, NL, Canada. pp. 283-310.

Jordaan, I.J., McKenna, R.F., Duthinh, D., Fuglem, M.K., Kennedy, K.P., Maes, M.A., Marshall, A., 1990. Development of new ice load models. Report for Canada Oil and Gas Lands Administration (COGLA) by C-CORE, Memorial University, St. John's. p. 206.

Jordaan, I. J. and Xiao, J., 1992. Interplay between damage and fracture in ice-structure interaction. Proceedings of the 11th International Symposium on Ice, IAHR, Banff, Alberta, 1992, Vol 3: 1448 – 1467.

Jordaan, I.J., Xiao, J., Zou., B., 1993. Fracture and damage of ice: towards practical implementation. Proceedings of 1st Joint Mechanics Meeting of ASME, ASCE, SES. Charlottesville, Virginia. AMD163 (Ice Mechanics). pp. 251-260.

Jordaan, I.J., Maes, M.A., Brown, P.W. and Hermans, I.P., 1993. Probabilistic analysis of local ice pressures. Journal of Offshore Mechanics and Arctic Engineering, Vol. 115, pp.83-89.

Jordaan, I., Fuglem, M., and Matskevitch, D., 1996. Pressure-area relationship and the calculation of global forces. In the Proceedings of 13th International Symposium on Ice, Volume 1, Beijing, China, pp. 166–175.

Jordaan, I., Matskevitch, D., and Meglis, I., 1997. Disintegration of ice under fast compressive loading. Proceedings of the Symposium on Inelasticity and Damage in Solid subject to Microstructural Change, St. John's, Newfoundland, pp. 211–231.

Jordaan, I.J., and Pond, J., 2001. Scale effects and randomness in the estimation of compressive ice loads. Proceedings, IUTAM Symposium on Scaling Laws in Ice Mechanics and Ice Dynamics, 43-54. 2001. Kluwer Academic Publishers.

Jordaan, I., Frederking, R. and Li, C., 2006. Mechanics of ice compressive failure, probabilistic averaging and design load estimation. Proceedings of 18th International Symposium on Ice, IAHR, Sapporo, Japan, Vol. 2, pp.223-230.

Jordaan, I.J., Taylor, R., Reid, S., 2007. Fracture, probabilistic averaging and the scale effect in ice-structure interaction. Proceedings of POAC 2007. Dalian, China.

Jordaan, I.J., Wells, J., Xiao, J., Derradji-Aouat, A., 2008. Ice crushing and cyclic loading in compression. Proceedings 19th IAHR Symposium on Ice, Vancouver, British Columbia, Canada.

Kachanov, L., 1958. On the creep rupture time. *Izv. An SSSR, Otd. Tekhn. Nauk.* (8), 26–31.

Kachanov, M.L., 1982. A microcrack model of rock inelasticity, part II: propagation of microcracks. *Mechanics of Materials*, 1 (1982) 29-41.

Kachanov, M., 1993. Elastic solids with many cracks and related problems. *Advances in Applied Mechanics*. 30.

Kalifa, P., Duval, P. and Ricard, M., 1989. Crack nucleation in polycrystalline ice under compressive states. Proceedings, OMAE, A.S.M.E., Vol. 4, pp. 13-21.

Kamesaki, K., Tsukuda, H., Yamauchi, Y., 1997. Experimental studies on non-simultaneous failure characteristics of vertical sided indentors. Proceedings of 7th International Offshore and Polar Engineering Conference, Honolulu, USA. Vol II., pp. 387-393.

Kamio, Z., Takawaki, T., Matsushita, H., et al., 2000. Medium scale field indentation tests: physical characteristics of first-year sea ice at Notoro Lagoon, Hokkaido. Proceedings of the Tenth International Offshore and Polar Engineering Conference. p. 562.

Kamio, Z., Matsushita, H., and Strnadel, B., 2003. Statistical analysis of ice fracture characteristics. *Engineering Fracture Mechanics*. 70 (2003). 2075-2088.

Kanninen, M.F., 1973. An augmented double cantilever beam model for studying crack propagation and arrest. *International Journal of Fracture*. Vol. 9. No. 1. March 1973. The Netherlands.

Kanninen, M. F. and Popelar, C. H., 1985. *Advanced Fracture Mechanics*. pp. 31-36, 39-42, 282. Oxford University Press, New York.

Karna, T., Muhonen, A., 1990. Preliminary results from ice indentation tests using flexible and rigid indenters. *Proceedings 10th IAHR Symposium on Ice*, Espoo, Finland, Vol. 3, p. 261-275.

Kärnä, T. and Yan, Qu., 2006. Analysis of the size effect in ice crushing - edition 1. VTT Technical Report, RTEU50-IR-6/2005.

Karr, D., 1985. A damage mechanics model for uniaxial deformation of ice. *Journal of Energy Resources Technology*. 107, 363–368.

Karr, D. and Choi, K., 1989. A three-dimensional constitutive damage model for polycrystalline ice. *Mechanics of Materials*. 8, 55–66.

Kendall, K., 1978. Complexities of compression failure. *Proc. R. Soc., London A361*, 245–263.

Kheisin, D.E. and Cherepanov, N.V., 1976. Change of ice structure in the zone of impact of a solid body against the ice cover surface. *Problems of the Arctic and Antarctic*, Edited by Treshnikov, A.F., Issue 33-35, pp. 239-245.

Kobayashi, S., 1971, *Journal of Society of Material Science of Japan*. 20, 164,

Korzhavin, K., 1971. Action of ice on engineering structures. *Cold Regions Research and Engineering Laboratory*, draft translation, Hanover, NH, p. 319.

Krajcinovic, D., 1983. Constitutive equations for damaging materials. *Journal of Applied Mechanics* 50, 355–360.

- Krajcinovic, D., 1985. Continuous damage mechanics revisited: Basic concepts and definitions. *Journal of Applied Mechanics* 52, 829–834.
- Kry, P.R., 1978. A statistical prediction of effective ice crushing stresses on wide structures. *Proceedings of the 5th International IAHR Conference, Lulea, Sweden, Part 1:33-47.*
- Kujala, P., 1996. Modelling of non-simultaneous ice crushing as a Poisson random process. *International Journal of Offshore and Polar Engineering, Vol. 6, No. 2. pp. 138-143.*
- Lawn, B., 1993. *Fracture of brittle solids.* Cambridge, UK: Cambridge University Press.
- Li, C., 2003. Finite element analysis of ice-structure interaction with a viscoelastic model coupled with damage mechanics. M.Eng Thesis, Memorial University, St. John's, NL, Canada.
- Li, C., 2007. Probability and fracture mechanics applied to ice load estimation and associated mechanics. Ph.D Thesis, Memorial University, St. John's, NL, Canada.
- Li, C., Jordaan, I.J., Barrette, P., 2005. Strain localization and fracture of cylindrical ice specimens under confining pressure. *Proceedings of 18th POAC. Potsdam, New York. Vol. 1, pp. 213-224.*
- Mackey, T., 2005. Laboratory indentation of polycrystalline ice: an investigation of fracture. M.Eng Thesis, Memorial University, St. John's, NL, Canada.
- Mackey, T., Wells, J., Jordaan, I.J., Derradji-Aouat, A., 2007. Experiments on the fracture of polycrystalline ice. *Proceedings of POAC 2007. Dalian, China.*
- Maes, M.A., Jordaan, I.J., Cormeau, A. and Baldwin, J. 1986. Probabilistic theories for the failure of sea ice. *Proceedings, Int. Conf. on Ice Tech., M.I.T., Boston, 37-54.*
- Maes, M.A. 1992. Probabilistic behaviour of a Poisson field of flaws in ice subjected to indentation. *IAHR Ice Symposium, Banff, Alberta, vol 2 pp 871-882.*
- Masterson, D.M., Nevel, D.E., Johnson, R.C., Kenny, J.J., Spencer, P.A., 1992. The medium scale iceberg impact test program. *Proceedings IAHR Symposium. Banff, AB.*

Masterson, D. and Spencer, P., 1992. Reduction and analysis of 1990 and 1989 Hobson's Choice ice island indentation tests data. Report prepared by Sandwell Inc.

Masterson, D.M., Frederking, R.M.W., Jordaan I.J., Spencer, P.A., 1993. Description of multiyear ice indentation tests at Hobson's Choice ice island – 1990. Proceedings of 12th International Conference on Offshore and Arctic Engineering. Vol. 4. Glasgow. pp. 145-55.

Masterson, D. M., Spencer, P. A., Nevel, D. E. and Nordgren, R. P. 1999. Velocity effects from multiyear ice tests. Proceedings 18th OMAE Conference. S. John's, Canada, 1999.

Matlock, H., Dawkins, W.P., Panak, J.J., 1969. A model for the prediction of ice-structure interaction. Proceedings of the 1st Offshore Technology Conference, Vol. 1, OTC 1066, Houston, TX, pp. 687-694.

Matlock, H., Dawkins, W.P., Panak, J.J., 1971. Analytical model for ice-structure interaction. Proceedings of ASCE, J. Eng. Mech. Div., Aug. 1971.

Matskevitch, D.G., Jordaan, I.J., 1996. Spatial and temporal variations of local ice pressures. Proceedings of OMAE 1996. Vol. IV. pp. 83-91.

Matsushita, H., Takawaki, T., Hirayama, K.I., 1997. Medium scale field indentation tests - physical properties and strength of the ice sheet. Proceedings of the 7th International Offshore and Polar Engineering Conference. Vol. 2. p. 368.

Matsushita, H., Kamio, Z., Sakai, M., et al., 2000. Consideration of failure mode of a sea ice sheet. Proceeding of 10th International Offshore and Polar Engineering Conference. p. 577.

McKenna, R.F., Meyssonier, J., and Jordaan, I.J., 1989. Peak pressures from a damage model for ice in compression. Proceedings of OMAE 1989, the Hague, Netherlands, Vol. IV, pp. 67-73.

McKenna, R.F., Jordaan, I.J., and Xiao, J., 1990. Analysis of damage and energy flow in the crushed layer during rapid ice loading. Proceedings of IAHR Symposium on Ice, Espoo, Finland, Vol. 3, pp. 231-245.

Meglis, I., Melanson, P., and Jordaan, I., 1999. Microstructural change in ice: II. creep behavior under triaxial stress conditions. *Journal of Glaciology* 45 (151), 438–448.

Melanson, P.M., 1998. Damage and microstructural change in laboratory grown ice under high pressure zone conditions. M. Eng. Thesis, Memorial University, St. John's, NL, Canada.

Melanson, P.M., Meglis, I.L., Jordaan, I.J. and Stone, B.M., 1999. Microstructural change in ice: I. Constant-deformation-rate tests under triaxial stress conditions. *Journal of Glaciology*, Vol. 45, No.151, pp. 417-422.

Mellor, M., 1983. Mechanical behaviour of sea ice, U.S. Army Cold Region Research and Engineering Lab, Hanover, CRREL Report 83-1.

Michel, B., 1978. *Ice mechanics*. Les Presses de l'Université Laval. Quebec.

Muggeridge, K. and Jordaan, I., 1999. Microstructural change in ice: III. observations from an iceberg impact zone. *Journal of Glaciology* 45 (151), 449–455.

Muhonen, A., Karna, T., Eranti, E., Riska, K., Jarvinen, E., Lehmus, E., 1992 *Laboratory Indentation Tests with Thick Freshwater Ice*. Vol. I. VTT Research Notes 1370. 106p.

Mulmule, S., Adamson, R., and Dempsey, J., 1995. Large-scale in-situ ice experiments, part 2: modeling aspects. *Ice Mechanics* 207, 129–146.

Murrell, S.A.F., Sammonds, P.R. and Rist, M.A., 1991. Strength and failure modes of pure ice and multi-year sea ice under triaxial loading. *Proceedings of Symposium on Ice Structure Interaction, IUTAM / IAHR, St. John's, NF, Canada*, pp. 339-361.

Nadreau, J.P., Michel, B., 1984. Ice properties in relation to ice forces. *Proceedings of 2nd State-of-the-Art IAHR Working Group on Ice Forces, Hamburg*.

Nakazawa, N., Sakai, M., et al., 2000. Ice failure mode predominantly producing peak-ice-load observed in continuous ice load records. *Proceedings of the 10th International Offshore and Polar Engineering Conference*. p. 613.

Nemat-Nasser, S. and Horii, H., 1982. Compression induced non-planar crack extension with application to splitting, exfoliation and rockburst. *Journal of Geophysical Resources*. 87. 6805-6821.

Niell, C.R., 1975. Force fluctuations during ice-floe impact on piers. *Proceedings of IAHR Symposium*. Leningrad. pp. 44-50.

Nixon, W.A., 1996. Wing crack models of the brittle compressive failure of ice. *Cold Regions Science and Technology*. 24. pp. 41-55.

Nordell, B., 1990. Measurement of a P-T coexistence curve for ice-water mixture. *Cold Regions Science and Technology*, 19: 83-88.

Palaniswamy, K. and Knauss, W., 1978. On the problem of crack extension in brittle solids under general loading. *Mechanics Today*, 4.

Palmer, A.C., Sanderson, T.J.O., 1991. Fractal crushing of ice and brittle solids. *Proc. R. Soc. London. Ser. A* 433, pp. 469-477.

Palmer, A.C., Goodman, D.J., Ashby, M.F., Evans, A.G., Hutchinson, J.W. and Ponter, A.R.S., 1983. Fracture and its role in determining ice forces on offshore structures. *Annals of Glaciology*. 4:216-221

Palmer, A. C., Dempsey, J. P., 2007. Understanding the size effect. *Proceedings of POAC '07*, 2007, 363, Dalian, China.

Parsons, B.L., 1991. The size effect of nominal ice failure pressure, fractals, self-similarity and non-stationarity. *Proceedings of 11th International Conference on Port and Ocean Engineering under Arctic Conditions*, St. John's, Canada. vol. 1, pp. 457-470.

Parsons, B.L., Lal, M., Williams, F.M., Dempsey, J.P., Snellen, J.B., Everard, J., Slade, T., and Williams, J., 1992. The influence of beam size on the flexural strength of sea ice, freshwater ice, and iceberg ice. *Philosophical Magazine A*, Vol. 66, No. 6, 1017-1036.

Passchier, C.W., Trouw, R.A.J., 2005, *Microtectonics*. Springer-Verlag. Berlin.

Peyton, H.R., 1966. Sea ice strength. University of Alaska, Geophysical Institute, Report No. UAG R-182.

Poirier, J.P., 1985. Creep of crystals. Cambridge University Press, London.

Pounder, E.R., 1965. The physics of ice. Pergamon Press. London.

Raj, R., Ashby, M.F., 1971. On grain boundary sliding and diffusion creep. Metall Trans. 2. 1113-1127.

Reid, S.G., 1991. Flaws in the failure prediction model of glass strength. Proceedings of the 6th International Conference on Application of Statistics and Probability in Civil Engineering, Mexico City. pp. 111-117.

Rice, J., 1968. A path-independent integral and the approximate analysis of strain concentration by notches and cracks. Journal of Applied Mechanics. 191-309.

Riska, K., Frederking, R., 1987. Development of a model for penetration into ice. Report to Joint Research Project Arrangement I between Technical Research Center of Finland and National Research Council of Canada, Espoo. p. 57.

Rist, M.A., Murrel, S.A.F. and Sammonds, P.R., 1988. Experimental results on the failure of polycrystalline ice under triaxial stress conditions. Proceedings of 9th IAHR Conference, Sapporo, pp. 118-127.

Rist, M., Jones, S., and Slade, T., 1994. Microcracking and shear fracture in ice. Annals of Glaciology 19, 131-137.

Rist, M. and Murrel, S., 1994. Ice triaxial deformation and fracture. Journal of Glaciology. 40 (135), 305-318.

Rodin, G., 2000. On fracture of warm ice. In the Proceedings of IUTAM Symposium on Scaling Laws in Ice Mechanics and Ice Dynamics, Potsdam, New York, pp. 207-216.

Rogers, B, Hardy, M.D., Jefferies, M.G, Wright, B.D., 1998. Klohn-Crippen DynaMAC: Molikpaq ice loading . PERD/CHC Report 14-62.

Sammis, C., King, G., Biegel, R., 1987. The kinematics of gouge deformation. *Pure Appl. Geophy.* 125, 777-812.

Sanderson, T.J.O., 1988. Ice mechanics: risks to offshore structures. p. 88-92. Graham & Trotman, London.

Schapery, R.A., 1962. A simple collocation method for fitting viscoelastic models to experimental data. GALCIT SM 61-23 A, California Institute of Technology.

Schapery, R.A., 1969. On the characterization of nonlinear viscoelastic materials. *Polymer Engineering Science*. Vol. 9, pp. 295-310.

Schapery, R.A., 1975. A theory of crack initiation and growth in viscoelastic media: I. theoretical development. *International Journal of Fracture*, Vol. 11, No. 1: 141-159.

Schapery, R.A., 1981. On viscoelastic deformation and failure behaviour of composite materials with distributed flaws. *Advances in Aerospace Structures and Materials*, The American Society of Mechanical Engineers, pp.5-20.

Schapery, R.A., 1984. Correspondence principles and a generalized J integral for large deformation and fracture analysis in viscoelastic media. *International Journal of Fracture*. Vol. 25, pp. 195-223.

Schapery, R.A., 1988. A theory of mechanical behavior of elastic media with growing damage and other changes in structure. Mechanics and Materials Center, Texas A&M University, College Station, Texas, Report No. MM 5762-88-1.

Schapery, R.A., 1989. Models for the deformation behavior of viscoelastic media with distributed damage and their applicability to ice. *Proceedings IUTAM/IAHR Symposium on Ice Structure Interaction*. St. John's, NL, Canada, pp. 191-230.

Schapery, R.A., 1997. Nonlinear viscoelastic and viscoplastic constitutive equations based on thermodynamics. *Mechanics of Time-Dependent Materials*, Vol. 1, pp. 209-240.

Schulson, E.M., 1987. The fracture of ice Ih. *Journal of Physics*. 48-C1: 207-220.

Schulson, E.M., 1990. The brittle compressive fracture of ice. *Acta Metallica et Materiala*. 38: 1963-1976.

Schulson, E.M. and Cannon, N.P., 1984. The effect of grain size on the compressive strength of ice. *IAHR Ice Symposium, Hamburg*. Pp. 24-38.

Schulson, E.M., Jones, D.E. and Kuehn, G.A., 1991. The effect of confinement on the brittle compressive fracture of ice. *Annals of Glaciology*, Vol. 15, pp.216-221.

Schulson, E.M., 2001. Brittle failure of ice. *Eng. Fracture Mechanics*, 68(17-18), pp. 1839-1887.

Schulson, E.M., and Duval, P., 2009. *Creep and fracture of ice*. Cambridge University Press, UK.

Seng-Kiong, T. and Shyam Sunder, S., 1985. Constitutive modeling of sea ice with applications to indentation problems. *CSEOE Research Report No. 3*, MIT, Cambridge, Massachusetts.

Shi, Q., Huang, Y., Song, A., Tong, J., 2002. Non-simultaneous failure of ice in front of multi-leg structures. *China Ocean Engineering*, Vol. 16, No. 2, pp. 183-192.

Shyam Sunder, S., Wu, M.S., 1990. Crack nucleation due to elastic anisotropy in polycrystalline ice. *Cold Region Science and Technology*. 18. pp. 29-47.

Sih, G., 1973. Some basic problems in fracture mechanics and new concepts. *Engineering Fracture Mechanics* 5, 365-377.

Sih, G. C. and Liebowitz, H., 1968. *Fracture: an advanced treatise*. Liebowitz, H. editor. p. 89-91, Academic Press, New York.

Sih, G.C., and Tzou, D.Y., 1983. Mechanics of nonlinear crack growth: effect of specimen size and loading steps. *Proceedings of conference on modeling problems in crack tip mechanics*.

Singh, S., 1993. Mechanical behaviour of viscoelastic material with changing microstructure. Ph.D Thesis, Memorial University, St. John's, NL, Canada.

Sinha, N.K., 1979. Grain boundary sliding in polycrystalline materials. *Phil. Mag. A*, Vol. 40, pp. 825-842.

Sinha, N.K., 1982. Delayed elastic strain criterion for first cracks in ice. *Proc. of the symposium on deformation and failure of granular materials*, Rotterdam: Balkema. pp. 323-330.

Sinha, N.K., 1984. Intercrystalline cracking, grain-boundary sliding, and delayed elasticity at high temperatures. *J. Mater Sci.* 19. pp. 359-376.

Sinha, N., 1989. Elasticity of natural types of polycrystalline ice. *Cold Regions Science and Technology* 17, 127-135.

Sodhi, D.S, 1998. Non-simultaneous crushing during edge indentation of freshwater ice sheets. *Cold Regions Science and Technology.* 27 (1998). pp. 179-195.

Sodhi, D.S., Takeuchi, T., Kawamura, M., Nakazawa, N., Akagawa, S., 2001. Measurement of ice forces and interfacial pressures during medium-scale indentation tests in Japan. *POAC '01.* p. 617.

Sodhi, D.S., Takeuchi, T., Nakazawa, N., Akagawa, S., Saeki, H., 1998. Medium-scale indentation tests on sea ice at various speeds. *Cold Regions Science and Technology.* 28. pp. 161-182.

Smith, E., Barnby, J.T., 1967. Crack nucleation in crystalline solids. *Metal Sci J.* 1. pp. 56-64.

Smith, T.R., and Schulson, E.M., 1993. The brittle compressive failure of fresh-water columnar ice under biaxial loading. *Acta Metall. Mater.*, Vol. 41, pp. 153-163.

Stroh, A.N., 1957. A theory of the fracture of metals. *Adv Phys* 1957. 6. pp. 418-465.

Suo, Z., 1990. Delamination specimens for orthotropic materials. *Journal of Applied Mechanics*. 57: 627-634.

Takeuchi, T., Saeki, H., 1994. Ice load on wide structure in non-simultaneous failure of ice sheet by shot noise model. *Proceedings of IAHR Ice Symposium*. Trondheim, Norway. Vol. 1, pp. 219-228.

Takeuchi, T., Akagawa, S., Kawamura, M., et al., 2000. Examination of factors affecting total ice load using medium field indentation test data. *Proceedings of 10th International Offshore and Polar Engineering Conference*. p. 607.

Takeuchi, T., Masaki, T., Akagawa, S., et al., 1997. Medium-scale indentation tests (MSFIT) - ice failure characteristics in Ice/Structure interactions. *Proceedings of 7th International Offshore and Polar Engineering Conference*. Vol. 2. p. 376.

Taylor, R.S., Jordaan, I.J., Derradji-Aouat, A., and Bugden, A., 2010. Laboratory investigation of compressive failure of freshwater ice sheets. *Technical Report*. National Research Council of Canada.

Taylor, R.S., Frederking, R., and Jordaan, I. J. 2008. The nature of high pressure zones in compressive ice failure. *Proceedings 19th IAHR Symposium on Ice*, Vancouver, British Columbia, Canada.

Taylor, R.S., Jordaan, I.J., Li, C., and Sudom, D., 2009. Local design pressures for structures in ice: analysis of full-scale data. *Proceedings of OMAE 2009*. Honolulu, USA.

Taylor, R.S., Fuglem, M., Jordaan, I.J., Frederking, R.M.W, 2007. Analysis of JOIA data: probabilistic averaging for global load estimation. *Technical Report - Ian Jordaan and Associates*.

Thouless, M., Evans, A., Ashby, M., and Hutchinson, J., 1987. The edge cracking and spalling of brittle plates. *Acta Metall* 35, 1333–1341.

Timco, G.W., 1986. Indentation and penetration of edge-loaded freshwater ice sheets in the brittle range. *Journal of Offshore Mechanics and Arctic Engineering*. Vol. 109. pp. 287-294

Timco, G.W., 1987. Ice-structure interaction tests with ice containing flaws. *Journal of Glaciology*. Vol. 33., No. 114, pp. 186-194.

Timco, G. and Frederking, R., 1986. The effects of anisotropy and microcracks on the fracture toughness of freshwater ice. In the Proceedings of the 5th International OMAE Conference, Volume 4, Tokyo, Japan, pp. 341-348.

Timoshenko, S., and Goodier, J.N., 1951. *Theory of elasticity*, second edition. McGraw-Hill.

Tomin, M., Cheung, M., Jordaan, I.J., and Corneau, A., 1986. Analysis of failure modes and damage processes of freshwater ice in indentation tests. *Proceedings of OMAE*, Tokyo, Vol. IV, pp. 453-460.

Tuhkuri, J., 1993. Laboratory tests of ship structures under ice loading. Vol. 1, Helsinki University of Technology Ship Laboratory, Report M-166. Otaniemi, p. 171.

Tuhkuri, J., 1994. Analysis of ice fragmentation process from measured particle size distributions of crushed ice. *Cold Regions Science and Technology*. 23: 69-82.

Urabe, N. and Yoshitake, A., 1981. Fracture toughness of sea ice-in-situ measurement and its application. *Proceedings of 6th IAHR International Symposium on Ice*, Vol. 1, pp. 356-365.

Urai, J.L., Means, W.D.M. and Lister, G.S., 1986. Dynamic recrystallization of minerals. *American Geophysical Union, Geophysical Monograph* 36, pp. 161-199.

Vanmarcke, E., 1983. *Random fields: analysis and synthesis*. MIT Press, Cambridge, MA. 382 pp.

Van Mier, J.G.M., 1997. *Fracture processes of concrete*. CRC Press. Boca Raton.

Varsta, P., 1983. On the mechanics of ice load on ships in level ice in the Baltic Sea. *Dissertation*. Technical Research Center of Finland, VTT Pub 11, Espoo, p. 91.

Veitch, B., Tuhkuri, J., 1997. Indentation contact and penetration by a semi-circular indenter. *International Journal of Offshore and Polar Engineering*. Vol. 7, No. 1, 16-21.

Vernon, R.H., 1981. Optical microstructure of partly recrystallized calcite in some naturally deformed marbles. *Tectonophysics*, Vol. 78, pp. 601-612.

Wei, Y., Dempsey, J.P., 1991. Fractographic examinations of fracture in polycrystalline S2 ice. *Journal of Materials Science*. 26. (1991). 5733-5740.

Weibull, W. 1951. A statistical distribution function of wide applicability. *J. Appl. Mech.* 18.

Wierzbicki, T., 1985. Spalling and buckling of ice sheets. In *Civil Engineering in the Arctic Offshore*, pp. 953–961.

Weiss, J. and Schulson, E.M., 1995. The failure of fresh-water granular ice under multiaxial compressive loading. *Acta Metallurgica et Materialia*, Vol. 43, pp. 2303-2315.

Wells, J., I. Jordaan, A. Derradji, and A. Bugden, 2006. Laboratory investigation of the fracture behavior of polycrystalline ice with embedded monocrystals. Technical report. Prepared for Institute for Ocean Technology, National Research Council (IOT/NRC).

Wells, J., Jordaan, I.J., Derradji-Aouat, A., and Bugden, A., 2009. Laboratory investigation of the fracture behavior of polycrystalline ice – phase II. Technical Report. National Research Council of Canada.

Xiao, J., 1991. Finite element modeling of damage processes in ice-structure interaction. M.Eng Thesis. Memorial University of Newfoundland. St. John's, NL, Canada.

Xiao, J., 1997. Damage and fracture of brittle viscoelastic solids with application to ice load models. Ph. D Thesis, Memorial University, St. John's, NL, Canada.

Xiao, J., and Jordaan, I.J., 1991. Modeling of fracture and production of discrete ice pieces. Canada Oil and Gas Lands Administration (COGLA) Report.

Xiao, J., and Jordaan, I.J., 1996. Application of damage mechanics to ice failure in compression. *Cold Regions Science and Technology*. Vol. 24, pp. 305-322.

Zou, B., 1996. Ships in ice: the interaction process and principles of design. Ph.D Thesis. Memorial University of Newfoundland. St. John's, Canada.

Zou, B., Xiao, J., and Jordaan, I., 1996. Ice fracture and spalling in ice-structure interaction. *Cold Regions Science and Technology* 24, 213–220.

Appendix A: Related Mechanics

A.1 Derivation of Wing Crack Stress Intensity Factor

The following section details the derivation of the expressions given by Ashby and Hallam (1986) used in the development of the PFM model.

Wing Crack Initiation

We start with an infinite elastic plate containing a crack of initial length $2a$, and subject to principal stresses σ_1 and σ_2 , as shown in Fig. A.1. The convention used here is that tension is positive, compression is negative, thus σ_1 is the most negative (most compressive) and σ_2 is the most positive (least compressive) principal stress. The precursor crack is oriented at an angle ψ to the x_1 axis. Stresses act on the crack plane and the shear (σ_{xy}) and normal (σ_{xx}) components are due to the remote stress field, where the implicit sign convention is that σ_{xy} is always positive and σ_{xx} is always negative. The shear stress may be defined as:

$$\sigma_{xy} = \frac{\sigma_2 - \sigma_1}{2} \sin 2\psi = \tau \sin 2\psi . \quad (\text{A1.1})$$

Similarly, the normal stress may be given as:

$$\sigma_{xx} = \frac{\sigma_2 + \sigma_1}{2} + \frac{\sigma_2 - \sigma_1}{2} \cos 2\psi = \sigma + \tau \cos 2\psi . \quad (\text{A1.2})$$

The wing cracks will initiate in the direction θ which maximizes K_I , which corresponds to an angle of $\theta_c = 0.392\pi = 70.5^\circ$. This yields a stress intensity for wing crack initiation as:

$$K_I = \frac{2}{\sqrt{3}} \sigma'_{xy} \sqrt{\pi a}. \quad (\text{A1.6})$$

Ashby and Hallam (1986) suggest that the most dangerous crack is the one lying at the angle ψ which maximizes K_I . Substituting Eq. A1.3 into Eq. A1.6 and maximizing gives $\tan 2\psi = 1/\mu$. At the crack tips, the local stress field is predominantly shear in character on the plane of the precursor crack, but normal stresses act on planes at an angle θ to the crack tip, which causes Mode I wing cracks to grow from the crack tips. Wing cracks will initiate in the direction θ which maximizes the local Mode I stress intensity factor (also the direction of maximum tensile stress) at the precursor crack tip. Using Eq. A1.1 and A1.2 with $\tan 2\psi = 1/\mu$, the maximum K_I value may be found as:

$$K_I = \left\{ \frac{\pi a}{3} \right\}^{1/2} \left\{ (\sigma_2 - \sigma_1)(1 + \mu)^{1/2} + \mu (\sigma_1 + \sigma_3) \right\}. \quad (\text{A1.7})$$

For proportional loading, where $\sigma_2 = \lambda\sigma_1$, the maximum value of K_I may be expressed as a function of the principal stress σ_1 as:

$$K_I = \frac{-\sigma_1 \sqrt{\pi a}}{\sqrt{3}} \left\{ (1 - \lambda)(1 + \mu^2)^{1/2} - (1 + \lambda)\mu \right\}. \quad (\text{A1.8})$$

This may be reorganized to give a general crack initiation criterion:

$$\frac{\sigma_1 \sqrt{\pi a}}{K_{Ic}} = \frac{-\sqrt{3}}{[(1 - \lambda)(1 + \mu^2)^{1/2} - (1 + \lambda)\mu]}. \quad (\text{A1.9})$$

Here the term $\lambda = \sigma_2 / \sigma_1$ and wing crack initiation is assumed to occur when $K_I = K_{Ic}$ (i.e. when stress intensity factor equals fracture toughness). The above results hold while σ_{xx} is compressive, since tensile normal stresses will result in crack separation, resulting in a

disappearance of the frictional component $\mu\sigma_{xx}$. Since the new crack concentrates σ_{xx} and σ_{xy} , the stress $\sigma_{\theta\theta}$ acting on a plane at an angle θ to that crack, at a distance r from the crack tip may be written as:

$$\sigma_{\theta\theta} = -\frac{3\sigma_{xy}\sqrt{\pi a}}{2\sqrt{2\pi r}} \sin\theta \cos\frac{\theta}{2} - \frac{\sigma_{xx}\sqrt{\pi a}}{\sqrt{2\pi r}} \cos^3\frac{\theta}{2}. \quad (\text{A1.10})$$

As defined previously, if we take $K_I = \sigma_{\theta\theta}\sqrt{2\pi r}$, we get:

$$K_I = -\frac{3}{2}\sqrt{\pi a} \cos\frac{\theta}{2} \left\{ \sigma_{xy} \sin\theta + \sigma_{xx} \cos^2\frac{\theta}{2} \right\}. \quad (\text{A1.11})$$

If we take $\tau = \frac{1}{2}(\sigma_2 - \sigma_1)$ and $\sigma = \frac{1}{2}(\sigma_2 + \sigma_1)$, Eq. A1.12 may be written as:

$$K_I = -\frac{3}{2}\sqrt{\pi a} \cos\frac{\theta}{2} \left\{ \tau \sin 2\psi \sin\theta + (\sigma + \tau \cos 2\psi) \cos^2\frac{\theta}{2} \right\}. \quad (\text{A1.12})$$

Maximizing K_I with respect to θ using Eq. A1.11, we get:

$$\sigma_{xx} \tan(\theta/2) + 2\sigma_{xy} \tan^2(\theta/2) - \sigma_{xy} = 0. \quad (\text{A1.13})$$

Then maximizing K_I with respect to ψ using Eq. A1.12 gives:

$$\tan 2\psi = 3 \tan \theta / 2. \quad (\text{A1.14})$$

Using this pair of simultaneous equations for θ and ψ we may define the critical crack angle and the propagation direction. If only σ_{xx} exists, the only solution for Eq. A1.13 is that $\theta = 0$ and from Eq. A1.14, $\psi = 0$, and the specimen fails by simple tensile fracture. In the case where only σ_{xy} exists, the crack closes, but without friction. For this case, Eq. A1.13 gives $\theta = 70.5^\circ$, and Eq. A1.14 gives $\psi = 45^\circ$. For the case where both σ_{xx} and σ_{xy} exist, Ashby and Hallam (1986) suggest that a solution may be obtained by first substituting Eq.

A1.14 into Eq. A1.13 and then substituting the definitions of σ_{xx} and σ_{xy} and writing $R = \sigma / \tau [= (\lambda + 1) / (\lambda - 1)]$ to give:

$$3R \tan 2\psi - 6 \sin 2\psi \tan^2 2\psi = 0. \quad (\text{A1.15})$$

For the tensile fracture initiation stress, $\psi = 0$ and $\theta = 0$ and the initiation conditions become:

$$\sigma_2 \sqrt{\pi a} = K_{Ic}. \quad (\text{A1.16})$$

As mentioned above, Eq. A1.9 is only valid for compressive normal stress, since tensile σ_{xx} causes the crack to open and the frictional force $\mu\sigma_{xx}$ disappears. As noted by Ashby and Hallam (1986), it is reasonable to approximate crack initiation by Eq. A1.9 truncated by Eq. A1.16. The remaining portion of the solution is found by rewriting A1.15 to give:

$$\frac{3R}{\cos 2\psi} - 6 + 2 \tan^2 2\psi = 0. \quad (\text{A1.17})$$

Replacing $\cos 2\psi$ by $(1 + \tan^2 2\psi)^{-1/2}$ gives a quadratic expression in $\tan^2 2\psi$ as:

$$4 \tan^4 2\psi - (24 + 9R^2) \tan^2 2\psi + 36 - 9R^2 = 0. \quad (\text{A1.18})$$

Solving Eq. A1.18 yields

$$\tan^2 2\psi = 3 + \frac{9}{8} R^2 \pm \frac{3}{8} (64R^2 + 9R^4)^{1/2}; \quad + \text{ for } R < 0; \quad - \text{ for } R \geq 0, \quad (\text{A1.19})$$

Substituting Eq. A1.14 into Eq. A1.12 and using the definitions of σ and τ gives:

$$\frac{\sigma_1 \sqrt{\pi a}}{K_{Ic}} = \frac{2(9 + \tan^2 2\psi)^{3/2}}{(\lambda - 1)[(\lambda + 1)/(\lambda - 1) + \cos 2\psi \sin 2\psi \tan 2\psi]}. \quad (\text{A1.20})$$

The fracture initiation surface may be calculated in stress space using the above expressions by choosing a value of R (or λ), calculating ψ using Eq. A1.17, evaluating σ_1 from Eq. A1.20, and then calculating σ_3 from the definition of λ .

Wing Crack Propagation

To model wing crack growth, we start by considering the potential energy of a body containing a wing crack, such as the one idealized in Figure 2, where the wing cracks are assumed to be straight and parallel to the principal compressive axis. If we let the crack be pinned together so as to prevent any relative motion of the crack faces and then load the specimen to stress σ_1, σ_2 , the stored elastic energy due to the remote field is U_0 . If these pinning constraints are removed and the precursor crack is allowed to slide, the faces of the wing cracks will separate and open. As a result of this motion, the tractions will do work W on the specimen. There will also be stored elastic energy components associated with the mode I stress intensity field due to the wedging action U_I , as well as the mode II stress intensity field due to the sliding action along the crack face U_{II} . Based on these contributing factors, Ashby and Hallam gave an expression for the potential energy of the body plus its loads as:

$$P = U_0 + U_I + U_{II} - W . \quad (\text{A1.21})$$

Prior to the onset of sliding, the tractions acting on the faces of the precursor crack are:

$$\begin{aligned} T_s &= \sigma_{xy} + \mu\sigma_{xx} , \\ T_n &= \sigma_{xx} . \end{aligned} \quad (\text{A1.22})$$

For the wing cracks, the tractions acting on the crack faces are:

$$\begin{aligned} T_s &= 0 , \\ T_n &= \sigma_2 . \end{aligned} \quad (\text{A1.23})$$

The traction T_s on the precursor crack is relaxed due to the work associated with displacement arising from sliding along the crack face. Since the displacement is in the plane

of the crack, the normal traction T_n does no work. Over the face of the wing crack, the normal traction T_n is relaxed and it does work on the crack faces (since it resists crack opening). For a linear elastic system, the total work done is then:

$$W = \frac{1}{2} \sum \text{Force} \times \text{Displacement} = \frac{1}{2} \int_{S_1} 2T_s u_s(x) dS_1 + \frac{1}{2} \int_{S_2} 2T_n u_n(x) dS_2, \quad (\text{A1.24})$$

where $\pm u_s(x)$ are the shear displacements over the surface S_1 of the precursor crack and $\pm u_n(x)$ are the normal displacements over the surface S_2 of the wing cracks. Assuming the kinked crack is straightened out to a straight crack of length $2(\ell + a)$, the sliding displacements of the faces of the precursor crack $u_s(x)$ are given by

$$u_s(x) = \pm \frac{\alpha_1 \delta \{(\ell + a)^2 - x^2\}^{1/2}}{(\ell + a)}, \quad (\text{A1.25})$$

where α_1 is a constant (~ 1) that accounts for the kinked shape of the crack, x is measured from the centre of the crack, and 2δ is the maximum relative sliding displacement. Assuming the normal displacement of the wing crack face $u_n(x)$ decreases linearly with distance to the tip, we may write:

$$u_n = \pm \alpha_2 \delta \left\{ \frac{\ell + a - x}{\ell + a} \right\}, \quad (\text{A1.26})$$

where α_2 is another geometric shape constant. Inserting Eq. A1.25 and Eq. A1.26 into Eq. A1.24 and integrating gives:

$$W = \alpha_1 (\sigma_{xy} + \mu \sigma_{xx}) a B \delta \{ [1 - 1/(1 + \Lambda)^2]^{1/2} + (1 + \Lambda) \arcsin[1/(1 + \Lambda)] \} + \alpha_2 \sigma_2 a \Lambda B \delta \quad (\text{A1.27})$$

where $\Lambda = \ell / a$. Expanding terms as a power series yield, Ashby and Hallam rewrote the equation as:

$$W = 2\alpha_1 (\sigma_{xy} + \mu \sigma_{xx}) a B \delta \{ 1 - 1/6(1 + \Lambda)^2 \} + \alpha_2 \sigma_2 a \Lambda B \delta. \quad (\text{A1.28})$$

In the above expression, the first group of terms represents the work done by shearing tractions acting on the surface of the precursor crack, T_s . The second group of terms is the work done against the confining stress σ_2 as the wing crack opens. Since the first group of terms is almost independent of Λ , Eq. A1.28 may be approximated as:

$$W = 2aB\delta\{\alpha_1(\sigma_{xy} + \mu\sigma_{xx}) + \alpha_2\sigma_2 \Lambda / 2\}. \quad (\text{A1.29})$$

The displacement term δ may be resolved into a normal component δ_n taken relative to the average plane of the crack (at angle θ to the X_1 axis), and an in-plane shear component δ_s , where:

$$\delta^2 = \delta_n^2 + \delta_s^2. \quad (\text{A1.30})$$

The components of the above equation are given as:

$$\delta_n = \delta \sin \theta = \frac{\delta \Lambda \sin \psi}{(\sin^2 \psi + (\cos \psi + \Lambda)^2)^{1/2}} \approx \frac{\Lambda \delta}{\sqrt{2(1 + \Lambda)}}. \quad (\text{A1.31})$$

$$\delta_s = \delta \cos \theta = \frac{\delta(1 + \Lambda \cos \psi)}{(\sin^2 \psi + (\cos \psi + \Lambda)^2)^{1/2}} \approx \frac{\delta}{1 + \Lambda} \quad (\text{A1.32})$$

For an infinite body, the elastic stress field associated with the opening displacement $2\delta_n$, applied to the centre of a crack of length $2(\ell + a)$ will have an elastic energy that must be of the form: $U_I = \alpha_3 E_0 B \delta_n^2$, where α_3 is a constant (to be determined; it is roughly $4/\pi$). The elastic stress field associated with the shear displacement $2\delta_s$ also contributes a component of elastic energy of the form: $U_{II} = \alpha_3 E_0 B \delta_s^2$. Since the total elastic energy U_T is the sum of both the normal and shear contributions, we may write:

$$U_T = \alpha_3 E_0 B \delta^2. \quad (\text{A1.33})$$

Finding the minimum potential energy of the body with respect to the displacement δ (for a constant crack length) allows for determination of the extent of sliding. This may be found using the expression:

$$\frac{d}{d\delta} \{U_0 + U_T - W\} = 0. \quad (\text{A1.34})$$

Since the stored elastic energy due to the remote stress field is independent of the displacement, (i.e. $dU_0/d\delta = 0$), Eq. A1.34 may be simplified and the Eq. A1.33 and Eq. A1.29 may be substituted for the U_T and W , respectively to give:

$$\delta = \frac{a}{E_0} \left\{ \frac{\alpha_1}{\alpha_2} (\sigma_{xy} + \mu\sigma_{xx}) + \frac{\alpha_2}{2\alpha_3} \sigma_3 \Lambda \right\}. \quad (\text{A1.35})$$

For the case of simple compression ($\sigma_2 = 0$), the displacement reduces to:

$$\delta = -\frac{a\sigma_1}{2E_0} \frac{\alpha_1}{\alpha_3}. \quad (\text{A1.36})$$

This expression is independent of the wing crack length, which results from the approximation of Eq. A1.28 by Eq. A1.29. The expression given by Eq. A1.35 may be considered the limiting sliding displacement δ corresponding to a large value of Λ (i.e. $\Lambda \gg 1$). As the wing crack is wedged open due to the sliding of the precursor crack, the normal component of displacement δ_n applied at the centre of a crack of length $2(\ell + a)$ contributes to the mode I stress intensity factor,

$$K_I^n = \frac{\beta_n E_0 \delta_n}{(1+a)^{1/2}}, \quad (\text{A1.37})$$

where $\beta_n \approx 0.4$. Similarly, the shear displacement δ_s contributes to the mode I stress intensity factor at the wing crack tip according to:

$$K_I^s = \frac{\beta_s E_0 \delta_s}{(\ell + a)^{1/2}}, \quad (\text{A1.38})$$

Where $\beta_s \approx 1.0$. As discussed by Ashby and Hallam, observations of crack propagation show that the wing cracks initiate at an angle of $\sim 70^\circ$ to the precursor crack, in response to the stress intensity K_I^s given by Eq. A1.38. Once the crack has extended sufficiently ($\ell \approx a$), the wing rotates and aligns with the principal compressive direction. Beyond this point, the crack growth is dominated by the stress intensity due to the wedging action, K_I^n as modeled by Eq. A1.37. Ashby and Hallam accommodate this transition by multiplying K_I^s by the factor $1/(1 + \Lambda)^{1/2}$, which for $\ell \approx a$, reduces K_I^s by a factor of $1/\sqrt{2}$. Using this adjustment, the total stress intensity factor at the crack tip is:

$$K_I = K_I^n + K_I^s / (1 + \Lambda)^{1/2}, \quad (\text{A1.39})$$

Using the equations for K_I^s (Eq. A1.38), K_I^n (Eq. A1.37), δ (Eq. A1.35) and the definitions of δ_n (Eq. A1.31) and δ_s (Eq. A1.32), the stress intensity factor may be expanded to:

$$K_I = \frac{\sqrt{\pi a}}{\sqrt{\pi}(1 + \Lambda)^{3/2}} \left\{ \frac{\alpha_1}{\alpha_3} (\sigma_{xy} + \mu \sigma_{xx}) + \frac{\alpha_2}{2\alpha_3} \sigma_2 \Lambda \right\} \times \left\{ \beta_n \Lambda + \frac{1}{(1 + \Lambda)^{1/2}} \right\}, \quad (\text{A1.40})$$

To solve for the constants α_1 / α_3 and $\alpha_2 / 2\alpha_3$, the limits of small and large Λ are applied. For the limiting case where $\Lambda = 0$, Eq. A1.40 reduces to the initiating criterion (Eq. A1.8) provided:

$$\frac{\alpha_1}{\alpha_3} = \frac{2\sqrt{2\pi}}{\sqrt{3}}. \quad (\text{A1.41})$$

For the case where $\Lambda \gg 1$ and σ_2 is positive (tensile), the stress intensity must reduce to $\sigma_2 \sqrt{\pi \ell}$, which only results if:

$$\frac{\alpha_2}{\alpha_3} = \frac{2\sqrt{2\pi}}{\beta_n}. \quad (\text{A1.42})$$

Combining these results gives the stress intensity factor as:

$$K_I = \frac{\sqrt{\pi a}}{(1 + \Lambda)^{3/2}} \left\{ \frac{2}{\sqrt{3}} (\sigma_{xy} + \mu \sigma_{xx}) + \frac{\sigma_2 \Lambda}{\beta_n} \right\} \times \left\{ \beta_n \Lambda + \frac{1}{(1 + \Lambda)^{1/2}} \right\}, \quad (\text{A1.43})$$

The strain energy at the wing crack tip due to sliding of the main crack causes the wing to grow until K_I at the tip of the wing crack falls to K_{Ic} . Using $\beta_n \approx 0.4$ based on the work of Tada et al. (1973), writing $\lambda = \sigma_2 / \sigma_1$ and substituting Eq. A1.1 and Eq. A1.2 for σ_{xx} and σ_{xy} , respectively, Ashby and Hallam gave the final expression for the mode I stress intensity at the crack tip as:

$$K_I = \frac{-\sigma_1 \sqrt{\pi a}}{(1 + \Lambda)^{3/2}} \{1 - \lambda - \mu(1 + \lambda) - 4.3\lambda\Lambda\} \times \left\{ 0.23\Lambda + \frac{1}{\sqrt{3}(1 + \Lambda)^{1/2}} \right\}. \quad (\text{A1.44})$$

Since compressive crack growth is stable, the wing cracks will grow (i.e. Λ increases) until $K_I = K_{Ic}$. Physically, the above expression covers three regimes of crack behavior. When $\lambda = 0$, Eq. A1.44 reduces to the initiation criteria. When Λ is about unity (depending on λ), K_I is dominated by the wedging action of the main crack. As the wing crack grows further, K_I becomes greatly influenced by the confining stress σ_2 , since this stress acts over the entire crack length $2(\ell + a)$, whereas the maximum compressive stress σ_1 only acts on the angle portion of the crack (i.e. on the precursor crack). When the confining stress σ_2 is zero or compressive, the crack growth is always stable; when σ_2 is tensile (even when it is very small), the crack eventually becomes unstable. For the case where the confining stress is zero, Eq. A1.44 reduces to:

$$\frac{\sigma_1 \sqrt{\pi a}}{K_{Ic}} = \frac{-\sqrt{\Lambda}}{0.23(1 - \mu)}. \quad (\text{A1.45})$$

The application of these equations to ice are discussed in further detail in Sanderson (1988).

A.2 Radial and Circumferential Cracking

During ice structure interactions, global fractures (radial and circumferential cracks) will sometimes occur. For design these modes of fracture cannot be relied upon to always occur or to always cause drops in load when they do occur. The extreme pressures of interest in design are assumed to occur when these types of fracture do not. For completeness, radial and circumferential cracking are discussed below.

Radial Cracking

This mode refers to any type of fracture which ‘radiates’ away from the contact zone (i.e. crack grows in a direction that is normal to the contact surface). During small-scale indentation tests, cracks which form directly below the indenter and are approximately perpendicular to the indenter surface are often classified as radial cracks; in the context of the present work, these types of fractures have been associated with local spalling. During interactions between ice sheets and vertical-walled structures, in-plane splitting forces may also result in cracks that propagate perpendicular to the contact surface (in-plane splitting; also termed ‘cleavage’ fracture), which has been modeled as a contributing mechanism of spalling fracture.

Radial cracking in the context of the present work refers to a global fracture mechanism, defined by through-thickness cracks which emanate radially from the contact zone (sometimes called floe splitting). This type of fracture, depicted in Figure A.2, results primarily from tensile stresses in the far-field zone of the ice sheet. For rectangular indenters, stress concentrations at the corners of the structure can promote the formation of radial cracks at the edges of the indenter, as shown in Figure A.2 (b). Such edge effects are likely more dominant during smaller scales tests where contact geometry is more uniform. At larger scales, irregularities in local geometry tend to redistribute loads in a more random fashion.

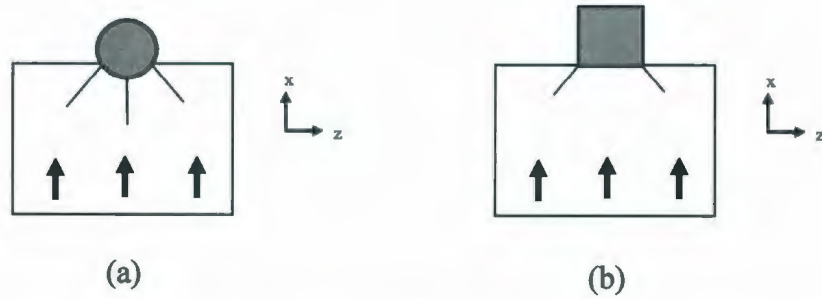


Figure A.2: Idealization of radial cracking during ice-structure interaction for: (a) cylindrical indenter; (b) rectangular indenter.

Palmer et al. (1983) in their investigation of the role of fracture in limiting ice loads on offshore structures outlined an initial theory of radial cracking to generate an order-of-magnitude estimate of cracking forces. Their work concluded that radial cracks can form at relatively low loads when ice interacts with offshore structures, which suggests radial cracks form readily in nature. Observations from Hans Island (Danielewicz and Metge, 1981) showed that radial cracks do indeed form in nature, though load drops due to radial cracking are not certain. In their model, Palmer and his coworkers treated the conditions near the contact zone as being approximately plane strain. The authors related the contact pressure P_M during indentation to the force on the structure P using Hertzian contact theory, given by

$$P_M = \left(\frac{2PE}{\pi Dt(1-\nu^2)} \right)^{1/2} \quad (\text{A2.1})$$

where D is the structure diameter, t the ice thickness, E is Young's modulus, and ν is the Poisson ratio. In the region near the indentation, the normal stress across a plane of symmetry will be compressive, and tensile in the far field region. The authors idealized a radial crack as an edge crack in a semi-infinite plate wedged open by opposing crack-opening forces as shown in Figure A.3.

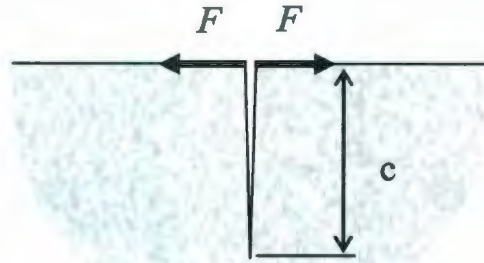


Figure A.3: Idealization of radial crack (after Palmer et al., 1983).

For this configuration the stress intensity factor was given as

$$K_{Ic} = 1.461 \left(\frac{F}{t\sqrt{c}} \right) \quad (\text{A2.2})$$

where F is the crack-opening force ($F = \alpha P$, where α is a proportionality constant), and c is the crack length. Reorganizing Eq. (A2.2) gives the crack length as

$$c = 2.13 \left(\frac{\alpha P}{K_{Ic} t} \right)^2 \quad (\text{A2.3})$$

From this expression it is seen that the crack length grows stably, but rapidly (proportional to P^2) as the indentation force is increased. The authors suggest that such cracks are advancing into the elastic region far from the contact and the result ought not to be sensitive to the details of the stress-strain relationship of the ice.

Based on the work of Lawn and his coworkers on axisymmetric indentation in ceramics, Palmer et al. (1983) suggested a value of $\alpha = 0.5$ for Eq. (A2.3). When remote stresses s are present in the ice cover, the stress-intensity factor was given as

$$K_I = 1.461 \left(\frac{\alpha P}{t\sqrt{c}} \right) + 1.12 \left(\frac{s}{\sqrt{\pi c}} \right) \quad (\text{A2.4})$$

For the case where the stress intensity factor equals the fracture toughness, the authors gave expressions for crack length and force required for unstable crack growth as

$$P = 0.086K_{ic}^2 t / \alpha s \quad (\text{A2.5})$$

$$c = 0.071(K_{ic} / s)^2 \quad (\text{A2.6})$$

Citing a numerical example, the authors concluded that even very small transverse tensile stresses substantially reduce the force needed to cause an ice sheet to fracture.

Correspondingly, transverse compressive stresses tend to have a stabilizing effect.

The stable growth of radial cracks does not directly lead to other kinds of fracture and may not itself limit the maximum ice force. Tensile stresses within individual 'sectors' can lead to the development of additional radial cracks and the splitting of the ice into progressively smaller sectors. Palmer et al. (1983) suggest that subsequent radial cracks are on the order of the initial crack length. At very high crack densities the length of subsequent cracks would likely diminish.

Unlike spalling, radial cracks are not typically associated with the removal of ice from the contact area. Radial cracking resulting in the breaking of the ice cover into smaller 'sectors' makes the cracked ice sheet more susceptible to flexural buckling than an intact sheet. As a result of the lower flexural rigidity, circumferential cracking is more probable for radially cracked specimens. Both radial cracking and mixed radial/circumferential cracking are observed to be more prevalent for higher aspect ratios (width/thickness) and higher strain rates (Palmer et al., 1983; Timco, 1986). The mixed radial/circumferential cracking mode limits maximum forces through the creation of rubble ice fragments, which break away and ride up over the uncracked sheet.

Circumferential Cracking

This is a type of flexural failure attributed to bending stresses resulting from eccentric compressive forces acting on the ice sheet, or vertical forces due to rubble accumulation, or interaction with a sloped structure. For vertical-walled structures, eccentricities in the applied load can result from variations in thickness across the width of the structure, as well as variations in the contact area resulting from local failure processes. The accumulation of ice rubble and fragments near the interface during an interaction further affects the line of action

of ice loads. Circumferential cracking is more prevalent when combined with radial cracking which reduces the flexural rigidity of the ice. Flexural failure of ice is also of particular importance in the design of ice-breaking vessels.

As a consequence of very low fracture toughness, fracture is an extremely important process in the compressive failure of ice. Early work on fracture processes in ice often assumed uniform contact at the interaction interface and used classical mechanics solutions based on elasticity or plasticity theory. Some models, such as those of Matlock et al. (1969, 1971), focused on trying to reproduce observed loading behavior observed during repeated flexural (circumferential) failure of ice against the legs of jacket pile structure.

Matlock and coworkers developed one of the earliest process models based on observations of data from offshore platforms in Cook Inlet (Peyton, 1966). As illustrated in Figure A.4, Matlock modeled the structure as a damped single degree of freedom system with mass M , damping c and stiffness k . In this model, the ice was represented by a series of cantilever beams which exerted a force proportional to the beam deflection resulting from the movement of the ice against the structure. The beam was modeled as elastic up to the point of fracture, which corresponded with some critical level of deflection. Upon fracture, the load dropped and the beam was discarded from the model. The model outputted displacements, velocities and accelerations of the structure, which was useful in describing some of the dynamic characteristics of the structures. Since this model did not capture the physics of the failure processes, it was unable to effectively predict loads.

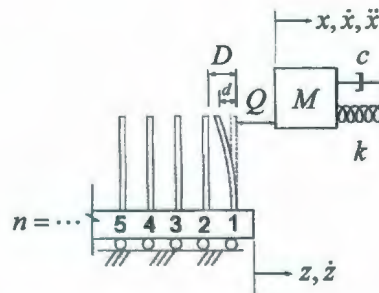


Figure A.4: Early ice failure model developed by Matlock (1969).

Flexural failure, rubble accumulation and ridge formation are also important processes associated with circumferential fracture, but are beyond the scope of the present work. The reader is referred to Bruce (2009) for further discussion of this topic.

A.3 Dimensional Analysis

Dimensional analysis may be used as a tool to assess the likely material property responsible for the scale effect in ice. The classical problem of ice mechanics, and the one considered in the present work, is that of a uniform sheet of ice of thickness h failing against a vertical-sided structure of width w . From the Buckingham-Pi theorem we know that the relationship between these parameters must be expressible as a relationship between dimensionless groups:

$$\frac{F}{h^A w^B X} = f(w/h), \quad (\text{A3.1})$$

where F is the force applied to the ice, h is the ice thickness, w is the contact width, A and B are constants, and X is an unknown quantity with dimensions which makes Eq. A3.1 dimensionless. This requires the dimensions of X to be:

$$[X] = [ML^{1-A-B}T^2]. \quad (\text{A3.2})$$

If we know A and B , then the dimensions of X can be deduced (i.e. units of X depends on A and B). If we assume that pressure is some function of area and aspect ratio, we can rewrite the contact pressure as:

$$\frac{F}{wh} = X (hw)^{\frac{1}{2}(A+B)-1} \left(\frac{w}{h}\right)^{\frac{1}{2}(B-A)} f\left(\frac{w}{h}\right). \quad (\text{A3.3})$$

Simplifying gives:

$$F = X (hw)^{\frac{1}{2}(A+B)} \left(\frac{w}{h}\right)^{\frac{1}{2}(B-A)} f\left(\frac{w}{h}\right). \quad (\text{A3.4})$$

Force has dimensions $[MLT^{-2}]$. The terms h and w both have fundamental units of length $[L]$, resulting in dimensionless aspect ratio terms. Considering the dimensions of Eq. A3.5 we see that:

$$[MLT^{-2}] = [X][L^2]^{\frac{1}{2}(A+B)}. \quad (A3.6)$$

Simplifying Eq. A3.6 we find that the units of X are dependent on A and B as given by:

$$[X] = [ML^{1-(A+B)}T^{-2}]. \quad (A3.7)$$

If $A + B = 2$,

$$[X] = [ML^{-1}T^{-2}] = [\text{stress}]. \quad (A3.8)$$

This suggests characteristic units of stress. If $A + B = 1.5$, the implied dimension has dimensions of fracture toughness:

$$[X] = [ML^{-1/2}T^{-2}]. \quad (A3.9)$$

Palmer and Dempsey (2007) examined various ice pressure equations in the context of the above dimensional analysis. Based on their results the authors concluded that dimensional analysis indicates that a property with the same units of fracture toughness governs the scale effect in ice. This suggests fracture is a primary contributor to the scale effect associated with ice pressure; this idea is explored later in the chapter.

If it is assumed that the only relevant quantities during an ice-structure interaction are the ice force F , the contact area A , and the fracture toughness K , then the only dimensionless group that can be formed is $F/A^{3/4}K$. As discussed by Palmer (1991), this dimensionless group must remain a constant, meaning that the force per unit area (pressure) must follow the proportionality:

$$F/A \propto A^{-1/4} K. \quad (A3.10)$$

On this basis, the pressure behavior is expected to scale according to $A^{-1/4}$. While this result points to the presence of a scale effect due to fracture, dimensional analysis only requires agreement of the units, it does not require that the characteristic length dimension specifically be associated with area, or crack length. For spalling fracture, many other characteristic length dimensions may be relevant. This might include the distance from the center of an *hps* to the edge of the ice sheet, a characteristic crack or flaw length (possibly linked to grain size), the total ice thickness, the interaction width, characteristic dimensions of individual *hps*, or any other parameter with the primitive dimensions of length. While dimensional analysis does support the notion that scale effects are associated with fracture, it does not provide insights into the details of the physical processes responsible for the scale effect.

Appendix B: JOIA Data Information

B.1 Global Load Data

Three measures of global load were included in the spreadsheets on the CD containing the JOIA data. The first was direct measurement using an independent 100 ton-force load cell. The second measure was taken as the sum of all loads measured on the individual panels across the width of the segmented indenter. The third global load measure was based on pressure gauge output from the hydraulic unit. A comparison of loads based on pressure gauge output and those based on summing panel loads suggests the pressure gauge data may be erroneous, as shown in Figure B.1. Global loads based on pressure gauge output have not been considered in any further detail in this report.

This was further complicated when it was discovered that independent global load data from the 100 ton-force load cell were not available on the data CD for most tests. The only remaining option then was to estimate global loads as the sum of local panel loads. To validate this approach, an estimate based on summed local loads was compared with available independent global load cell data.

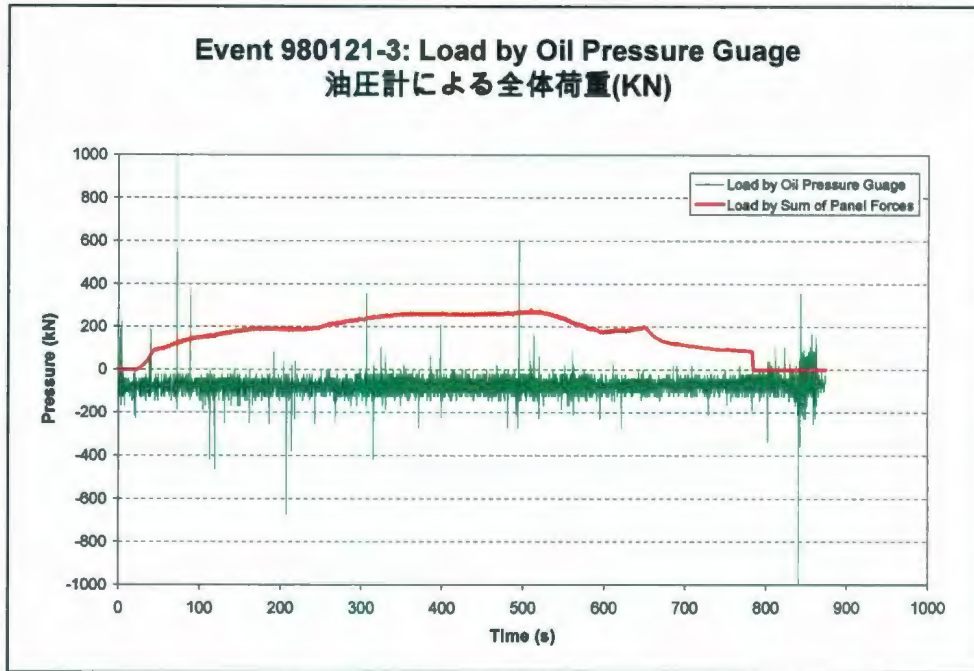


Figure B.1: Comparison of global loads based on summation of local panel loads and pressure gauge measurements for a selected sample event.

From Figure B.2 it is seen that there is very good agreement between the independently measured global loads and the summation global loads for the sample event shown.

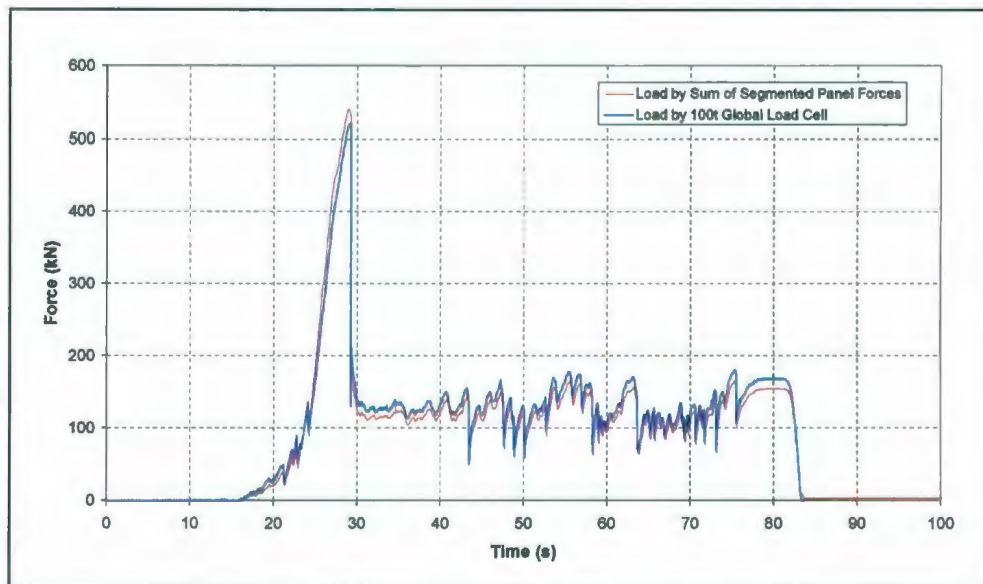


Figure B.2: Comparison of global loads based on summation of local panel loads and load measured by 100t load cell for Event 980128-1 (0.3 cm/s).

The strong linearity between the two measures, shown in Figure B.3, suggests that the summation approach provides an accurate representation of the global loads measured by the independent 100 ton-force load cell.

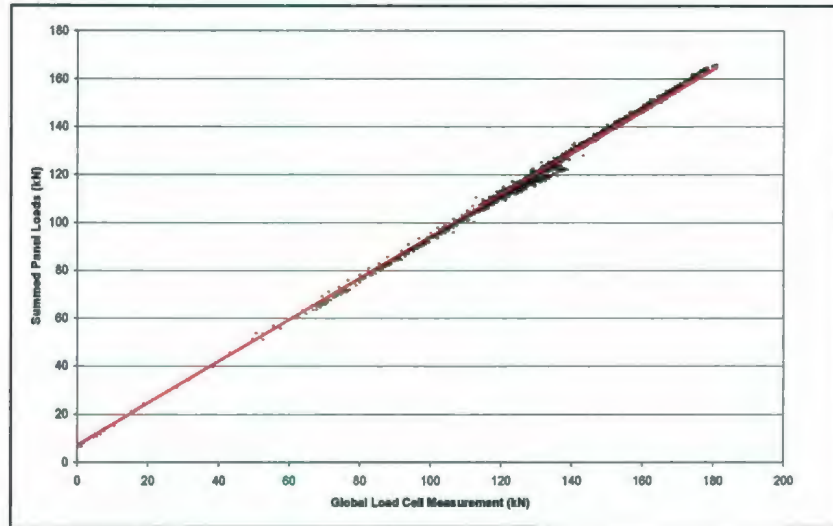


Figure B.3: Plot of global loads based on summation of local panel loads against load measured by 100t load cell for JOIA event 980128-1 (0.3 cm/s).

In light of the available options, it was decided that the most consistent approach for obtaining global loads was to sum individual panel loads across the width of the indenter. While this global load measurement is not independent of the panel loads, these results match well with the independent global load cell data and could be used consistently for all datasets. All global loads referred to in this study, unless identified otherwise, were obtained by summing individual loads from segmented indenter panels.

B.2 Event Definition Sensitivity

Fast and medium speed events exhibited brittle-type failure. Such events typically had well-defined endpoints. This resulted in less uncertainty in terms of definition of appropriate start and end points for the selected data. For ductile-type events, such as the one shown in Figure B.4, clearly defining endpoints is somewhat more challenging. Given the greater degree of uncertainty in ductile event definition, it was determined that a brief examination of

sensitivity to end point selection was warranted, as a number of alternative definitions are possible for such an event.

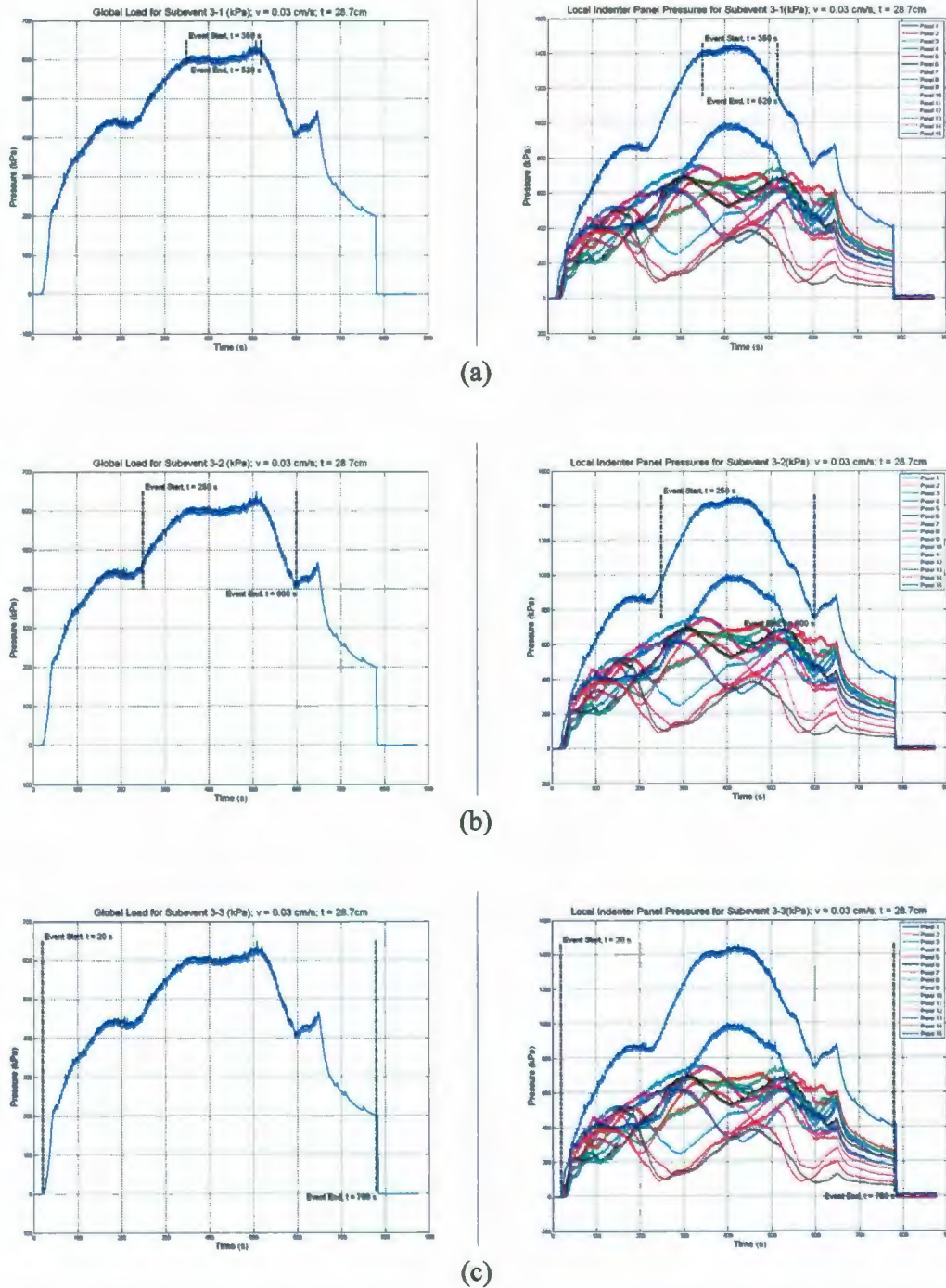


Figure B.4: Endpoint sensitivity: (a) Subevent 3-1 (start=350s; end=520s); (b) Subevent 3-2 (start=250s; end=600s); (c) Subevent 3-3 (start=20s; end=780s).

To examine the effects of end-point selection on the mean and standard deviation of the local and global pressures, three alternative definitions were taken for Event 3. The alternative definitions are shown in the context of the global and local pressure in Figure B.4. It is noted that the values of the end-points were intentionally varied by a large margin to examine several possible approaches to defining a ductile-type event. As shown in the table below, variation in end point definition for ductile tests impacts the mean and has a very significant impact on the standard deviation.

Table B.1: Effect of end-point selection on mean and standard deviation of global pressure and average panel pressure.

	Global Pressure		Average Panel Pressure	
	μ	σ	μ	σ
Sub-event 3-1	606.2	10.8	606.2	55.1
Sub-event 3-2	567.7	55.4	567.7	101.8
Sub-event 3-3	441.6	145.7	441.6	175.4

The sensitivity of the standard deviation to event definition is particularly noteworthy, since global load estimation is highly dependent on the standard deviation. For this reason, it the global load estimates for the ductile cases would be expected to be sensitive to the event definition.

While non-simultaneous aspects are less dominant in ductile-type events, other failure modes, such as creep buckling may influence results (Sodhi et al., 2001), further complicating event definition. English versions of project documentation detailing failure mode observations made during testing are presently not available, making interpretation of ductile time traces more challenging. Further work would be recommended to examine sensitivity and other such issues in further detail prior to applying this method to estimate loads for ductile-type failure at full-scale. Further efforts to acquire English versions of testing documentation may assist in the interpretation of the ductile event time traces.

B.3 Sample Spectral Analysis

As part of the initial investigation of general characteristics of the JOIA data, a sample event from each of the speed ranges was selected for spectral analysis.

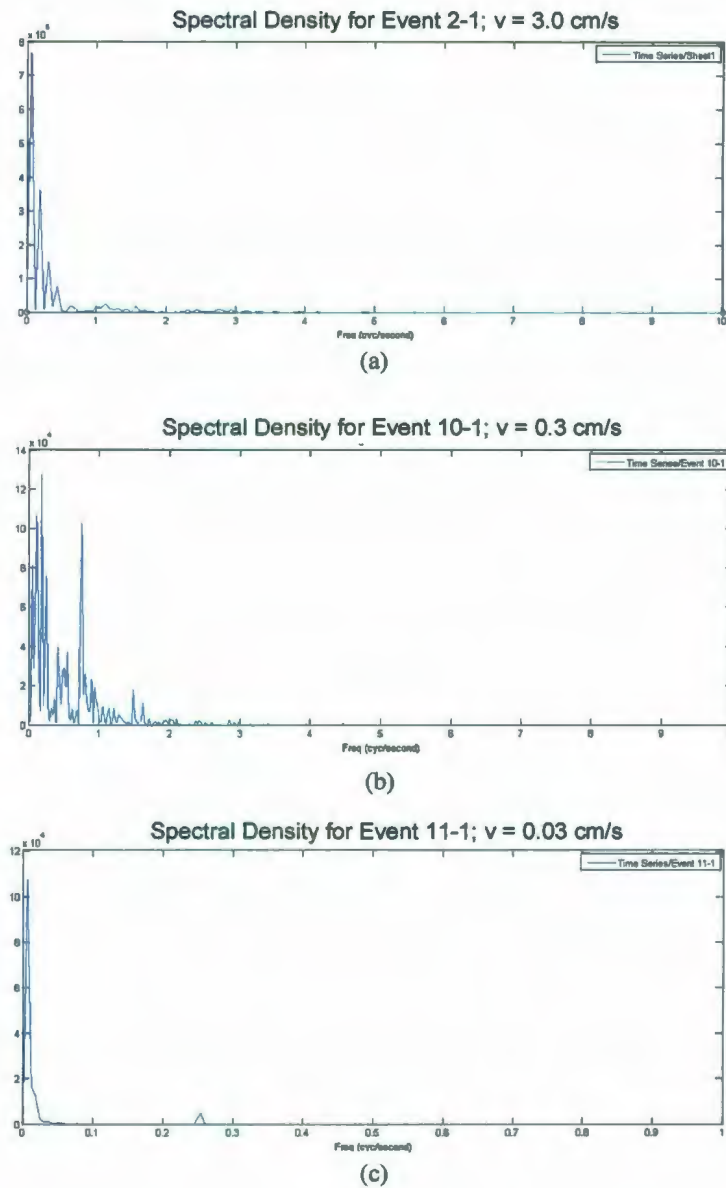


Figure B.5: Spectral density for (a) Event 2-1; $v=3.0$ cm/s; (b) Event 10-1; $v=0.3$ cm/s; (c) Event 11-1; $v=0.03$ cm/s

Spectral plots for the selected cases are shown in Figure B.5. From this figure it is noted that more harmonic activity is observed for medium and fast events than for the slower, ductile-

type event. The low frequency spike shown in Figure B.5 (c) for the slow speed event is likely an artifact of the test program. Further work is required to fully assess spectral characteristics of the data. Results suggest that efforts to link spectra to failure processes and correlations would be valuable. Investigation of links between increased harmonic activity and the presence of more dominant non-simultaneous failure processes in both medium and fast events is of interest.

B.4 Stationarity

Ice-structure interaction events have been idealized as a random averaging process, and the assumption has been made that the process is stationary. To examine the stationarity of the data, two sample events have been analyzed by dividing the data into multiple intervals and investigating the influence of interval selection on means and standard deviations.

Representative brittle and ductile cases have been considered below. The four analysis intervals and corresponding global means and standard deviations are given in the Tables B.2 and B.3 for representative brittle and ductile events, respectively.

Table B.2: Global pressures for different analysis intervals – Event 2 (brittle).

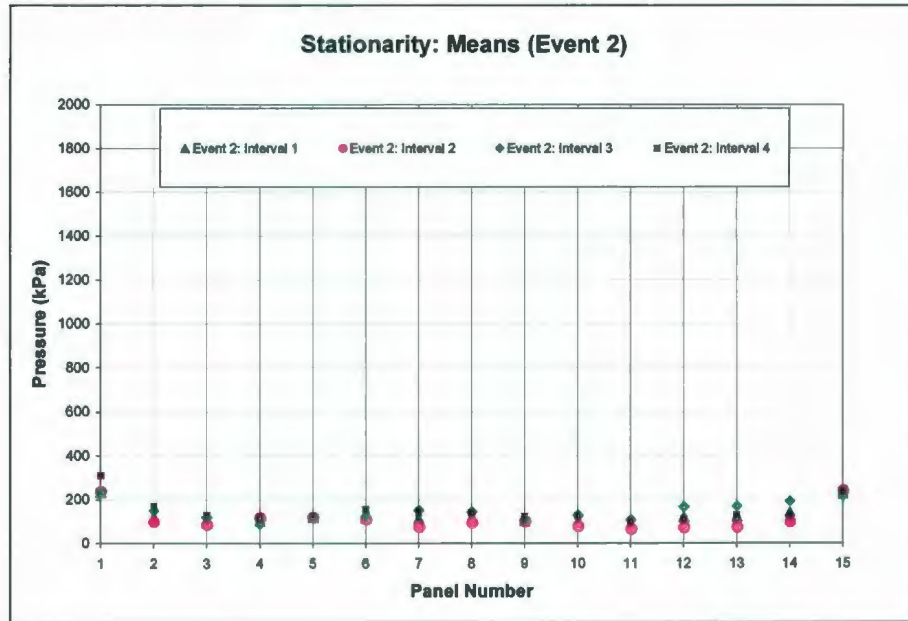
Event 2 (Brittle)	Start Time (s)	Stop Time (s)	μ_{global}	σ_{global}
Interval 1:	6	22	113.1	64.3
Interval 2:	6	14	90.7	51.0
Interval 3:	14	22	135.5	61.8
Interval 4:	10	18	129.5	61.6

Table B.3: Global pressures for different analysis intervals – Event 11 (ductile).

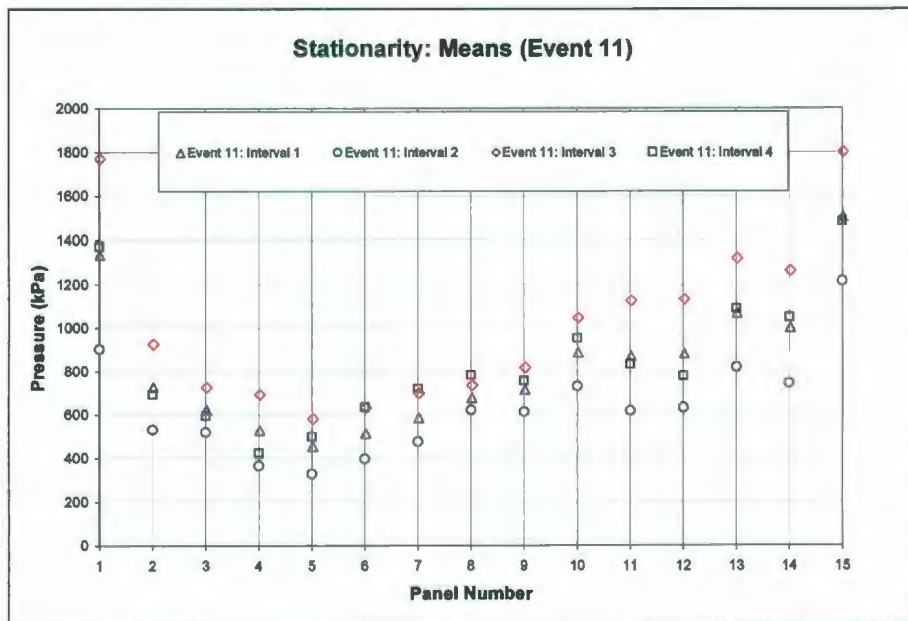
Event 11 (Ductile)	Start Time (s)	Stop Time (s)	μ_{global}	σ_{global}
Interval 1:	200	1200	735.7	220.2
Interval 2:	200	700	569.4	153.0
Interval 3:	700	1200	901.9	110.6
Interval 4:	450	950	754.7	210.1

For both cases, Interval 1 corresponds to the full event, Interval 2 is the first half of the event, and Interval 3 is the second half of the event. The length of Interval 4 is half the event, but the interval starts quarter way through the event. The local panel means and standard

deviations for each of the four intervals have been plotted in Figures B.6 and B.7 respectively. The start and stop times for the analysis intervals shown in these plots correspond to those defined in Tables B.2 and B.3.

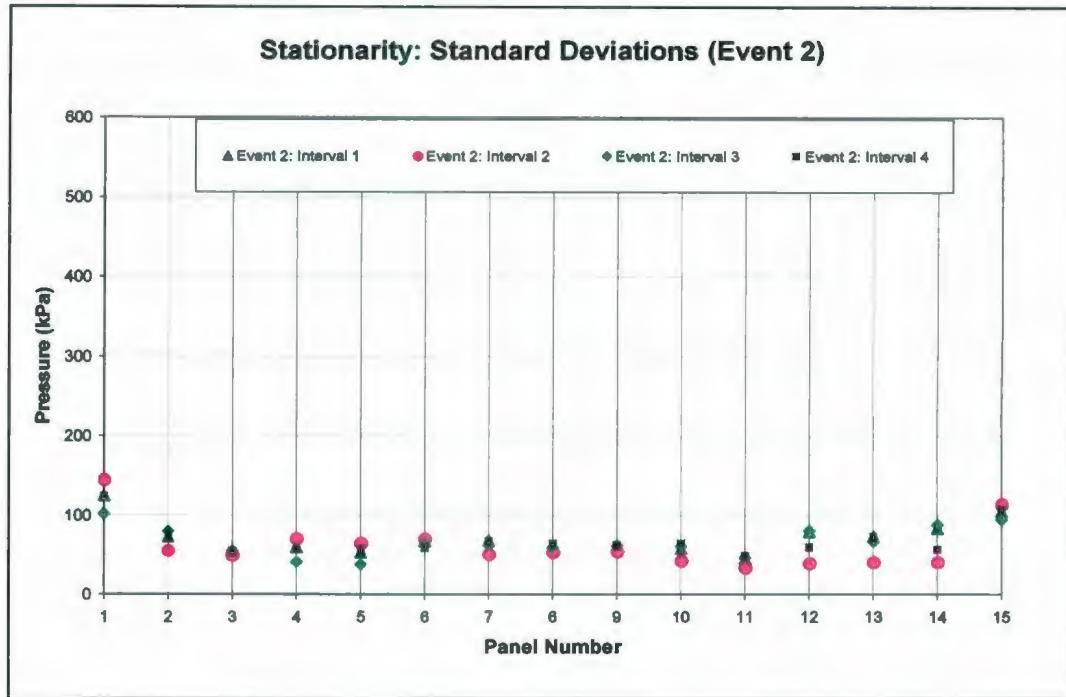


(a)

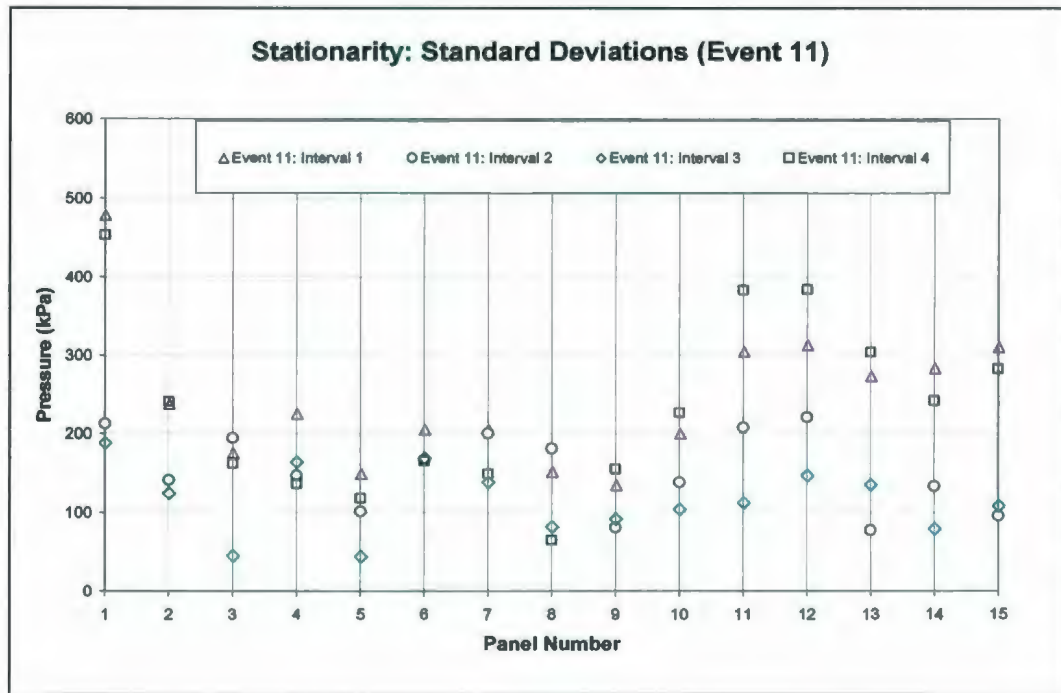


(b)

Figure B.6: Comparison of mean local panel pressures analyzed for multiple intervals for: (a) sample brittle event (Event 2); (b) sample ductile event (Event 11).



(a)



(b)

Figure B.7: Comparison of local panel pressure standard deviations analyzed for multiple intervals for: (a) sample brittle event (Event 2); (b) sample ductile event (Event 11).

From these figures it may be observed that the means and standard deviations of the brittle event are closely clustered together for all intervals considered, while the ductile means and standard deviations have more scatter. This suggests that brittle events are reasonably stationary over the given time interval.

Sodhi et al. (2001) reported that in some ductile events, creep buckling was observed. The presence of a different failure mechanism may affect the means and standard deviations of different data intervals. As discussed previously, the unavailability of field notes in English or other such documentation has made defining 'events' more challenging. Identifying data associated with creep buckling cannot be reliably done without such information. A comprehensive analysis of all data sets to further examine stationarity is recommended.

On this basis, it was decided that the stationarity assumption is valid for brittle events. Until further information for ductile events becomes available to allow for treatment of different failure mechanisms, the assumption of stationarity is seen as a reasonable starting point, but requires further investigation.

Appendix C: Data Analysis Details

C.1 Molikpaq Events

fastfile	h_1 (m) ¹	h_2 (m) ²	v (m/s)	Ice Type ³	Loaded Face(s) ⁴
f602080201	0.9	1.2	0.2	FY	NE
f606021301	1.8	2.5	0.01	MY	E
f605120301	1.5	3.5	0.17	FY/MY	N
f603081731	4.3	4.3	0.04	MY	N
f604121201	4	6	0.01	MY	E
f511271201	1.2	1.2	0.75	FY/MY	E, NE
f512160801	1.2	1.2	0.42	FY/MY	E
f601071801	1	1.5	0.3	FY	E, NE
f602062201	0.8	1.2	0.13	FY	E, NE
f602070301	0.9	1.2	0.1	FY	E, NE
f602072301	0.9	0.9	0.2	FY	E, NE, N
f602080101	0.9	1.2	0.2	FY	E, NE
f602170401	0.5	0.7	0.04	FY	E
f602171600	0.7	0.8	0.04	FY	E, N
f602280821	0.8	0.9	0.05	FY	E, NE, N
f604121400	3.6	3.6	0.01	MY	E
f603081603	3.7	4	0.04	MY	NE, N
f604121101	3.6	3.6	0.01	MY	E
f605221301	2	3	0.06	MY	E, NE
f602021701	0.6	0.6	0.08	FY	E, NE
f602070401	0.9	0.9	0.2	FY	E, NE
f602171401	0.8	0.8	0.05	FY	E, NE, N
f602171901	0.8	0.8	0.04	FY	E, N
f511121901	0.8	0.8	0.57	FY	N
f511171301	0.8	0.8	0.1	FY	N
f511191901	0.9	0.9	0.06	FY	NE, N
f511241501	0.6	0.6	0.1	FY	E
f602030501	0.8	0.8	0.05	FY	N
f602092301	0.9	0.9	0.05	FY	NE, N
f602150501	0.7	0.7	0.04	FY	E
f603071520	3.5	10	0.05	MY	N
f603071603	3.5	10	0.05	MY	N

¹ h_1 = lower limit of available ice measurements

² h_2 = upper limit of available ice measurements

³ FY = first-year ice; MY = multi-year ice

⁴ E = East face; NE = Northeast face; N = North face

C.2 Explanation of Event Trimming Process

To clarify the trimming process used, consider the example of event F602192301.

Step 1: Trim the data from the beginning and end of the crushing interaction (see Figure C.1).

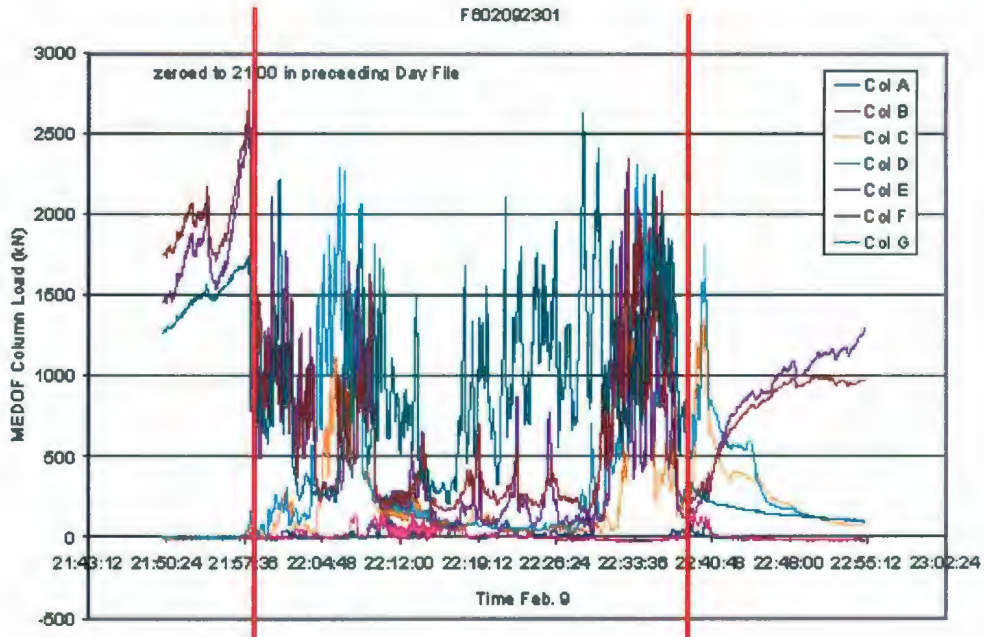


Figure C.1: All column data plotted for the interaction interval corresponding to the identified crushing event; the first red line demarks the onset of crushing; the second red line demarks the end of the event.

Step 2: Plot the data trimmed in Step 1 for each individual column and link them together to form a single pressure trace shown; see Figure C.2.

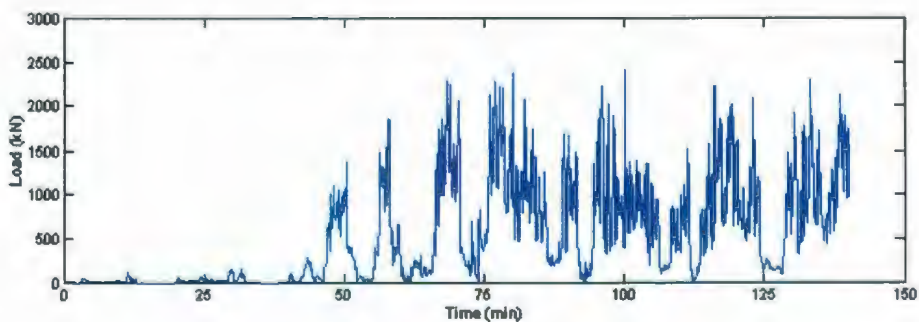


Figure C.2: Linked single column data from Step 2.

Step 3: The data from Step 2 were trimmed by identifying the intervals of low or no loads, which were then removed from the dataset. As a guideline the removed sections had a mean duration below about 0.25 MPa for more than 2 minutes.

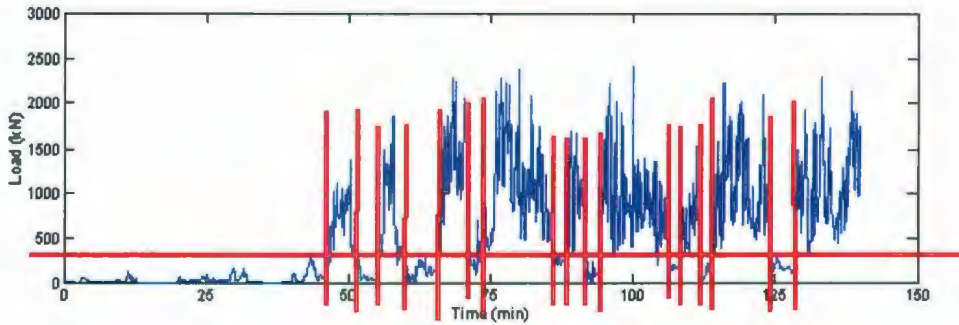


Figure C.3: Trimming points identified for all linked single column data.

Step 4: Remove all periods of low pressure an link remaining data to give a 'continuous' event with an 'effective duration', as shown in Figure C.4.

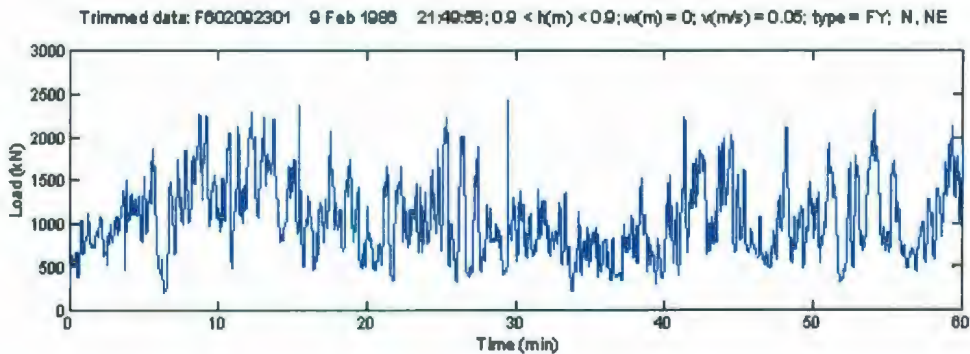


Figure C.4: Trimmed, linked single column 'continuous' event data for the given file.

C.3 Residuals of Pressure Data for Analysis Case 10

To examine the normality of the residuals for analysis case 10, the plots shown in Figure C.1 were generated.

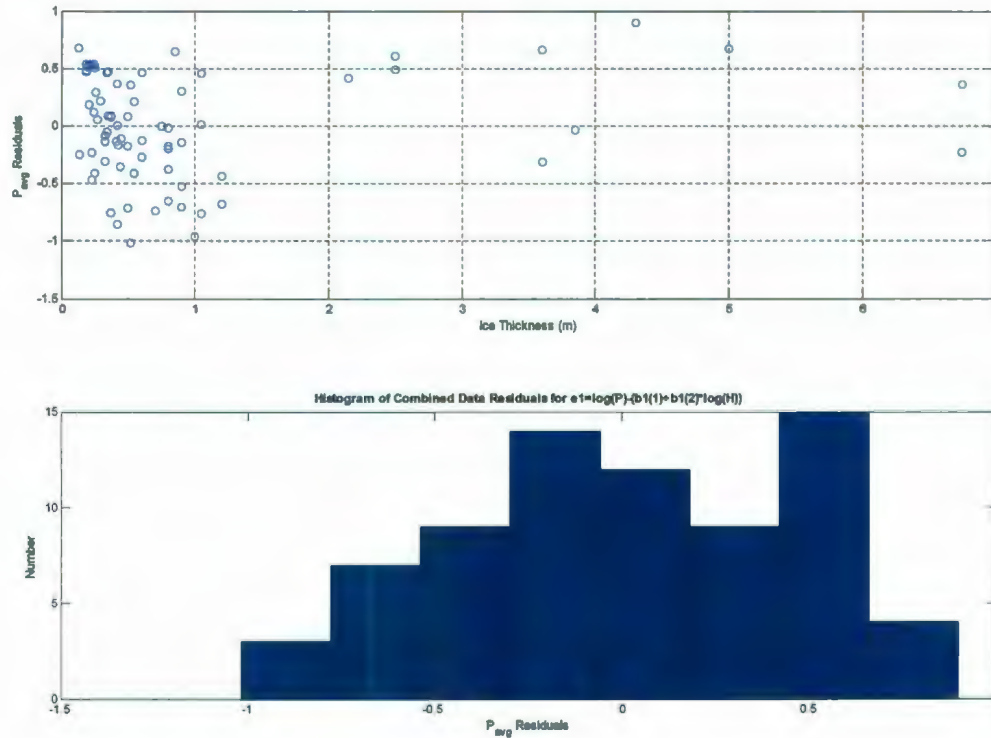


Figure C.5: Plots of: residuals of mean pressure vs. ice thickness (top), and histogram of residuals (bottom).

Appendix D: Distribution Fitting

D.1 Sample Probability Plot

To examine which type of probability distribution gave the best agreement with the data, several fits were tried using a curve fitting routine. Figure D.1 below includes best fit curves for exponential, gamma, Gumbel and Weibull distributions fitted to the data (plotted on Gamma probability paper). From this figure it may be observed that the Gumbel distribution best models the data, particularly in the tail of the distribution.

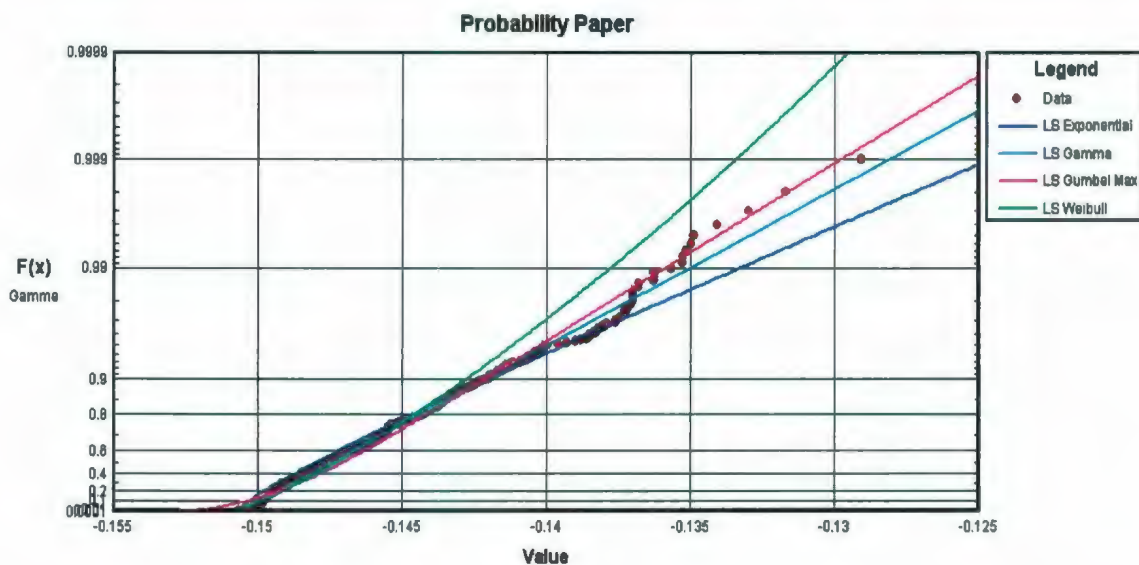


Figure D.1: Trimmed, linked single column 'continuous' event data for the given file.



